Dushantha Nalin K. Jayakody · John Thompson
Symeon Chatzinotas · Salman Durrani *Editors*

Wireless Information and Power Transfer: A New Paradigm for Green Communications

Springer

Wireless Information and Power Transfer: A New Paradigm for Green Communications

Dushantha Nalin K. Jayakody • John Thompson
Symeon Chatzinotas • Salman Durrani
Editors

Wireless Information and Power Transfer: A New Paradigm for Green Communications

Springer

Editors
Dushantha Nalin K. Jayakody
Department of Software Engineering,
Institute of Cybernetics
National Research Tomsk
Polytechnic University
Tomsk, Russia

Symeon Chatzinotas
Interdisciplinary Centre for Security
University of Luxembourg
Esch-sur-Alzette, Luxembourg

John Thompson
School of Engineering
University of Edinburgh
Institute for Digital Communications
Edinburgh, UK

Salman Durrani
College of Engineering
and Computer Science
The Australian National University
Canberra, Aust Capital Terr, Australia

ISBN 978-3-319-56668-9 ISBN 978-3-319-56669-6 (eBook)
DOI 10.1007/978-3-319-56669-6

Library of Congress Control Number: 2017943674

Printed on acid-free paper

This Springer imprint is published by Springer Nature
The registered company is Springer International Publishing AG
The registered company address is: Gewerbestrasse 11, 6330 Cham, Switzerland

To my parents Amara Dewndarage and Linton Jayakody

Dushantha Nalin K. Jayakody

Preface

The concept of wireless information and power transfer provides researchers with a unique set of challenges which is quite distinct from their traditional fixed power supply. New approaches in, wireless power transmission (or transfer) (WPT) is paramount as it helps us to overcome the scarcity of electric power when electric power is supplied wirelessly.

The necessities of communication systems are a burgeoning issue that is already straining operating budgets and attracting the attention of policymakers around the globe. Communication technologies continue to be a central element of the transition to smart, energy-efficient and sustainable lifestyles. Radio frequency (RF) energy transfer and harvesting techniques have recently become alternative methods to power next-generation wireless networks. This book features the latest research findings in the area of wireless energy harvesting through RF wireless power transfer and simultaneous information and power transfer in light of the emerging area of the Internet of Things.

All living and machine entities rely on both information and power for their existence. Although these two entities are work harmoniously, in traditional engineering design; information and power are handled by separate systems with limited interaction. Indeed, wireless energy harvesting (WEH) through radio waves has already found various applications (such as the radiofrequency identification (RFID) technology, healthcare monitoring, etc.), but radio wave-based communication and power transfer have largely been designed separately. The contributions in this book aim at achieving a breakthrough in the design of WPT networks whilst delivering simultaneously high quality to this rapidly evolving area. This book brings together the latest findings in wireless information and power transfer in order to disseminate state-of-the-art results and inspire future research in this field. This introduces a new paradigm of green communications.

The editors would like to express their gratitude to all the contributors for their full cooperation during the entire authoring and production process and their patience through the reviewing rounds and specifically to Himal A. Suraweera, Salman Durrani, Nalin D. K. Jayakody, Shree Krishna Sharma, Symeon

Chatzinotas, Wanchun Liu, Xiangyun Zhou, Nafiseh Janatian, Ivan Stupia, Luc Vandendorpe, Christos Masouros, Yunfei Chen, Weisi Guo, Muhammad Ismail, Mohamed Kashef, Khalid A. Qaraqe, Ioannis Katsidimas, Sotiris Nikoletseas, Theofanis P. Raptis, Christoforos Raptopoulos, Fahira Sangare, Zhu Han, Mohammadali Mohammadi, Batu K. Chalise and Sotiris Nikoletseas.

Furthermore, a special thanks goes out to the reviewing team for providing constructive feedback and improving the quality of the content: Himal Suraweera, Pan Cao, Nalin D. K. Jayakody, Cristian Rusu, Mohammad Ali Mohammadi, Bin Chen, Batu Chalise, Sumit Gautam, Dang Khoa Nguyen, Christos Masouros, Yunfei Chen and Muhammad Ismail.

The writing of this book would not have been possible without the support of many friends and colleagues. This work was funded, in part, by the Ministry of Education and Science of the Russian Federation Grant No. 02.G25.31.0190 dated 27.04.2016 and performed in accordance with Russian Government Resolutions No. 218 of 09.04.2010; by various funding schemes of the Ministry of Education and Science, Russia; by the FNR-FNRS bilateral project "InWIP-NETs: Integrated Wireless Information and Power Networks"; by the Australian Research Council's Discovery Project funding scheme (project number DP140101133); by the Norwegian-Estonian Research Cooperation Programme through grant EMP133; and by the Estonian Research Council through research grant PUT405. Authors also acknowledged the contribution of the COST Action on Inclusion Radio Communications (IRACON) CA15104.

Finally, the editors would like to thank Mary E. James and Brinda Megasyamalan from Springer for their support in bringing this book to completion.

Tomsk, Russia — Dushantha Nalin K. Jayakody
Edinburgh, UK — John Thompson
Esch-sur-Alzette, Luxembourg — Symeon Chatzinotas
Canberra, ACT, Australia — Salman Durrani

Contents

Part I Emerging Topics of Wireless Information and Power Transfer

1 Introduction, Recent Results, and Challenges in Wireless Information and Power Transfer 3
Dushantha Nalin K. Jayakody, Shree K. Sharma, and Symeon Chatzinotas

2 Full-Duplex Wireless-Powered Communications 29
Mohammadali Mohammadi, Batu K. Chalise, and Himal A. Suraweera

3 Multi-Objective Resource Allocation Optimization for SWIPT in Small-Cell Networks 65
Nafiseh Janatian, Ivan Stupia, and Luc Vandendorpe

4 Harvesting Signal Power from Constructive Interference in Multiuser Downlinks 87
Christos Masouros

5 Energy Harvesting for Wireless Relaying Systems 123
Yunfei Chen

6 Multi-Scale Energy Harvesting 157
Weisi Guo, Yansha Deng, Arumugam Nallanathan, Bin Li, and Chenglin Zhao

Part II Energy Harvesting Protocols For Wireless Sensor and Related Areas

7 RF Energy Harvesting Networks: Existing Techniques and Hardware Technology 189
Fahira Sangare and Zhu Han

8 Wireless Powered Sensor Networks 241
Wanchun Liu, Salman Durrani, and Xiangyun Zhou

9 Spectrum and Energy Harvesting Protocols for Wireless Sensor Nodes 271
Mansi Peer and Vivek Ashok Bohara

10 Efficient Wireless Power Transfer Maximization Algorithms in the Vector Model 297
Ioannis Katsidimas, Sotiris Nikoletseas, Theofanis P. Raptis, and Christoforos Raptopoulos

11 Enabling Green Heterogeneous Cellular Networks via Balanced Dynamic Planning 323
Muhammad Ismail, Mohamed Kashef, Erchin Serpedin, and Khalid A. Qaraqe

Index 359

Authors' Biography

Symeon Chatzinotas (S'06–M'09–SM'13) received his M.Eng. degree in telecommunications from Aristotle University of Thessaloniki, Thessaloniki, Greece, and M.Sc. and Ph.D. degrees in electronic engineering from the University of Surrey, Surrey, UK, in 2003, 2006 and 2009, respectively. He is currently a research scientist with the SIGCOM Research Group, Interdisciplinary Centre for Security, Reliability and Trust, University of Luxembourg, Luxembourg, managing H2020, ESA and FNR projects. In the past, he has worked on numerous R&D projects for the Institute of Informatics and Telecommunications, National Centre for Scientific Research "Demokritos"; Informatics and Telematics Institute, Centre for Research and Technology Hellas; and Mobile Communications Research Group, Centre for Communication Systems Research, University of Surrey, Surrey, UK. He has authored more than 120 technical papers in refereed international journals, conferences and scientific books. His research interests include multiuser information theory, cooperative/cognitive communications and wireless network optimisation. He was the corecipient of the 2014 Distinguished Contributions to Satellite Communications Award and Satellite and Space Communications Technical Committee, IEEE Communications Society and CROWNCOM 2015 Best Paper Award. He is one of the editors of the book *Cooperative and Cognitive Satellite Systems* (Elsevier, 2015) and was involved in co-organising the first international workshop on Cognitive Radios and Networks for Spectrum Coexistence of Satellite and Terrestrial Systems (CogRaN-Sat) in conjunction with the IEEE ICC 2015, London, UK, June 8–12, 2015.

Salman Durrani received his B.Sc. (first-class honours) degree in electrical engineering from the University of Engineering and Technology, Lahore, Pakistan, in 2000. He received his Ph.D. degree in electrical engineering from the University of Queensland, Brisbane, Australia, in December 2004. He has been with the Australian National University, Canberra, Australia, since 2005, where he is currently senior lecturer in the Research School of Engineering, College of Engineering and Computer Science.

His research interests are in wireless communications and signal processing, including machine-to-machine and device-to-device communication, wireless energy harvesting systems, stochastic geometry modelling of finite area networks and synchronisation in communication systems. He has co-authored more than 100 publications to date in refereed international journals and conferences. He was a recipient of the 2016 IEEE ComSoc Asia-Pacific Outstanding Paper Award. He was the chair of the ACT Chapter of the IEEE Signal Processing and Communications Societies from 2015 to 2016. He currently serves as an editor of the *IEEE Transactions on Communications*. He is a member of Engineers Australia and a senior fellow of the Higher Education Academy, UK.

Dushantha Nalin K. Jayakody (M'14) received the B.Eng. degree (with first-class honors) from Pakistan and was ranked as the merit position holder of the University (under SAARC Scholarship). He received the M.Sc. degree in Electronics and Communications Engineering from Eastern Mediterranean University, Cyprus (under the University full graduate scholarship) and ranked as the first merit position holder of the department. He received the Ph.D. degree in Electronics and Communications Engineering from the University College Dublin, Ireland. Currently, he is a Professor at the Institute of Cybernetics, National Research Tomsk Polytechnic University, Russia, where he also serves as the Director of Tomsk Infocomm Lab. From 2014 to 2016, he has held a Research Fellow positions at the University of Tartu, Estonia and University of Bergen, Norway. Dr Jayakody has received the best paper award from the IEEE International Conference on Communication, Management and Information Technology (ICCMIT), Warsaw, Poland in April 2017. Dr. Jayakody is a Member of IEEE and has served as session chair or technical program committee member for various international conferences, such as IEEE PIMRC 2013/2014, IEEE WCNC

2014/2016, and IEEE VTC 2015. He currently serves as a lead guest editor for the Elsevier Physical Communications Journal and MDPI Information journal. Also, he serves as a reviewer for various IEEE Transactions and other journals.

John Thompson (SM'13) received his B.Eng. and Ph.D. degrees from the University of Edinburgh, Edinburgh, UK, in 1992 and 1996, respectively. He holds a personal chair in signal processing and communications with the School of Engineering, University of Edinburgh, Edinburgh, UK. He specialises in antenna array processing, cooperative communication systems and energy-efficient wireless communications. His work in these areas is highly cited, and his h-index is currently 21 according to Web of Science. Mr. Thompson is a distinguished lecturer for the IEEE Communications Society for 2014–2015. He was the lead editor of the *IEEE Communications Magazine* special issue on "5G Wireless Communication Systems: Prospects and Challenges", published in February and May 2014. He was an elected member at large for the Board of Governors of the IEEE Communications Society from 2012 to 2014. He is also serving as a tutorial co-chair for the 2015 IEEE International Conference on Communications in London, UK.

Vivek Ashok Bohara received his Ph.D. degree from the School of EEE, Nanyang Technological University (NTU), Singapore, in 2011. From 2011 to 2013, he was a postdoctoral researcher (Marie Curie fellowship) in ESIEE Paris, Université Paris-Est. He joined IIIT-Delhi in 2013 where he is currently working as an assistant professor. His research interests are towards next-generation communication technologies such as device-to-device communication, carrier aggregation and digital predistortion algorithms. He received first prize in the National Instruments ASEAN Virtual Instrumentation Applications Contest in 2007 and 2010. He was also the recipient of best poster award at IEEE ANTS 2014 and IEEE COMSNETS 2015 and 2016 conferences.

Batu K. Chalise received his M.Sc. and Ph.D. degrees in electrical engineering from the University of Duisburg-Essen, Germany. He has been a faculty member with the Department of Electrical Engineering and Computer Science, Cleveland State University, OH, since fall of 2015. From 2013 to 2015, he was a wireless systems research engineer with ArrayComm, San Jose, CA, where he worked on LTE and LTE-A communication systems. He was a postdoctoral research fellow with the Center for Advanced Communications, Villanova University, Villanova, PA, from 2010 to 2013. He has held various research and teaching positions at the University of Duisburg-Essen; Université Catholique de Louvain, Belgium; and Villanova University.

His current research interests include signal processing for wireless and radar communications and machine learning. In wireless communications, he is mainly interested in full duplex, cooperative, cognitive, massive multi-antenna and energy harvesting communications.

Dr. Chalise is an associate editor of the *EURASIP Journal on Wireless Communications and Networking*. He serves as a Technical Program and Organizing Committee member in various IEEE conferences. He received an exemplary reviewer award from the IEEE Communications Society in 2013. He is a senior member of the IEEE and the recipient of 2016 US Air Force Research Lab Summer Faculty Fellowship.

Yunfei Chen (S'02–M'06–SM'10) received his B.E. and M.E. degrees in electronic engineering from Shanghai Jiao Tong University, Shanghai, P.R. China, in 1998 and 2001, respectively. He received his Ph.D. degree from the University of Alberta in 2006. He is currently working as an associate professor at the University of Warwick, UK. His research interests include wireless communications, cognitive radios, wireless relaying and energy harvesting.

Yansha Deng received her Ph.D. degree in electrical engineering from Queen Mary University of London, UK, in 2015. She is currently a postdoctoral research fellow with the Department of Informatics, King's College London, UK. Her research interests include massive MIMO, HetNets, molecular communication, cognitive radio, cooperative networks and physical layer security.

Weisi Guo received his M.Eng., M.A. and Ph.D. degrees from the University of Cambridge. He is currently an assistant professor at the University of Warwick and a faculty fellow at the Alan Turing Institute (ATI). He is an investigator in a number of projects funded by the Royal Society, Lloyd's Register Foundation, British Council and US Air Force. He is the recipient of the IET Innovation Award 2015 and IEEE Best Paper Award 2014 and a finalist in the Bell Labs Prize 2014 and semi-finalist in the Bell Labs Prize 2016. He has published over 80 peer-reviewed papers, and his research interests are in the areas of networks, molecular communications and urban science.

Zhu Han (S'01–M'04–SM'09–F'14) received his B.Sc. degree in electronic engineering from Tsinghua University, in 1997, and M.Sc. and Ph.D. degrees in electrical and computer engineering from the University of Maryland, College Park, in 1999 and 2003, respectively.

From 2000 to 2002, he was an R&D engineer of JDSU, Germantown, Maryland. From 2003 to 2006, he was a research associate at the University of Maryland. From 2006 to 2008, he was an assistant professor at Boise State University, Idaho. Currently, he is a professor in the Department of Electrical and Computer Engineering as well as in the Department of Computer Science at the University of Houston, Texas. His research interests include wireless resource allocation and management, wireless communications and networking, game theory, big data analysis, security and smart grid. Dr. Han received an NSF Career Award in 2010, the Fred W. Ellersick Prize of the IEEE Communications Society in 2011, the EURASIP Best Paper Award for the *EURASIP Journal on Advances in Signal Processing* in 2015, the IEEE Leonard

G. Abraham Prize in the field of communication systems (best paper award in IEEE JSAC) in 2016 and several best paper awards in IEEE conferences. Currently, Dr. Han is an IEEE Communications Society distinguished lecturer.

Muhammad Ismail received his B.Sc. and M.Sc. degrees (Hons.) in electrical engineering (electronic and communications) from Ain Shams University, Cairo, Egypt, in 2007 and 2009, respectively, and Ph.D. degree in electrical and computer engineering from the University of Waterloo, Waterloo, ON, Canada, in 2013. He is currently an assistant research scientist with the Electrical and Computer Engineering Department, Texas A&M University at Qatar, Doha, Qatar, and an IEEE senior member. Dr. Ismail is a co-author of two research monographs by Wiley-IEEE Press and Springer, and he has presented two tutorials in the IEEE WCNC 2016 and the IEEE GLOBECOM 2015. He is a corecipient of best paper awards in the IEEE ICC 2014, the IEEE GLOBECOM 2014, the SGRE 2015 and the Green 2016. Dr. Ismail was an editorial assistant of the *IEEE Transactions on Vehicular Technology* from 2011 to 2013. He has been an associate editor of the *IEEE Transactions on Green Communications and Networking* since 2016 and the *IET Communications* since 2014. He is serving as a TPC co-chair in the IEEE VTC Fall 2017 and has served as a TPC co-chair in the IEEE VTC Fall 2016, the publication and publicity chair in the CROWNCOM 2015, the Web chair of the IEEE INFOCOM 2014 and a TPC member in several IEEE conferences.

Nafiseh Janatian received her B.Sc. degree in electronic engineering from Sharif University of Technology, Tehran, Iran, in 2006. She received her M.Sc. and Ph.D. degrees in communication systems from Isfahan University of Technology, Isfahan, Iran, in 2009 and 2015, respectively. From February to August 2013, she was a visiting research assistant at the Institute for Infocomm Research (I2R), Agency for Science, Technology and Research (A*STAR), Singapore. Since September 2015, she has been working as a postdoctoral fellow at the Institute of Information and Communication Technologies, Electronics and Applied Mathematics (ICTEAM), Université Catholique de Louvain (UCL), Louvain-la-Neuve, Belgium. Her main research interests include the application of statistical signal processing and optimisation theory to wireless communications with the current focus on beamforming and resource allocation design in simultaneous wireless information and power transfer (SWIPT) networks.

Mohamed Kashef received his B.Sc. and M.Sc. degrees (Hons.) in electronic and electrical communications engineering from Cairo University, Cairo, Egypt, in 2006 and 2009, respectively, and Ph.D. degree in electrical engineering from the University of Maryland, College Park, MD, USA, in 2013. He is currently a postdoctoral research associate with Texas A&M University at Qatar, Doha, Qatar, and an IEEE member. His research interests generally include wireless communication systems and networks, visible light communication networks and optimisation of stochastic systems.

Ioannis Katsidimas is a Ph.D. student under the supervision of Professor Sotiris Nikoletseas, at the Computer Engineering and Informatics Department of the University of Patras, Greece. Also, he is a researcher at the Computer Technology Institute and Press "Diophantus", Greece.

His research interests include wireless power transfer algorithms in ad hoc communication networks, wireless sensor networks and Internet of Things. Currently, he participates in the Privacy Flag EU project.

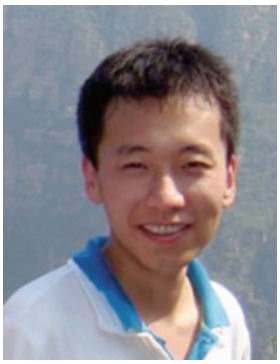

Bin Li received his bachelor's degree in electrical information engineering from Beijing University of Chemical Technology (BUCT) in 2007 and Ph.D. degree in communication and information engineering from Beijing University of Posts and Telecommunications (BUPT) in 2013. Then, he joined BUPT at 2013, and now, he is an associate professor of the School of Information and Communication Engineering (SICE). His current research interests are focused on statistical signal processing for wireless communications, e.g. molecular communications, millimetre-wave (mm-wave) communications and cognitive radios (CRs). He has published more than 70 journal and conference papers. He received 2011 ChinaCom Best Paper Award, 2015 IEEE WCSP Best Paper Award and 2010 and 2011 BUPT Excellent Ph.D. Student Award Foundation.

Wanchun Liu received her B.Sc. and M.S.E. degrees in electronic and information engineering from Beihang University, Beijing, China. She is currently pursuing her Ph.D. degree at the Research School of Engineering, Australian National University, Canberra, Australia. Her research interest lies in the field of wireless communications and includes wireless communication networks powered by energy harvesting and backscatter communications.

She was a TPC member of VTC'17-Spring and the GLOBECOM workshop on wireless energy harvesting communication networks at GLOBECOM'16. She is also a TPC member of GLOBECOM'17.

Christos Masouros (SMIEEE, MIET) received his diploma degree in electrical and computer engineering from the University of Patras, Greece, in 2004 and M.Sc. by research and Ph.D. in electrical and electronic engineering from the University of Manchester, UK, in 2006 and 2009, respectively. In 2008, he was a research intern at Philips Research Labs, UK. Between 2009 and 2010, he was a research associate in the University of Manchester and between 2010 and 2012 a research fellow in Queen's University Belfast. He has held a Royal Academy of Engineering Research Fellowship between 2011 and 2016.

He is currently a senior lecturer in the Communications and Information Systems Research Group, Department of Electrical and Electronic Engineering, University College London. His research interests lie in the field of wireless communications and signal processing with particular focus on green communications, large-scale antenna systems, cognitive radio, interference mitigation techniques for MIMO and multicarrier communications. He was the recipient of the Best Paper Award in the IEEE GLOBECOM conference 2015 and has been recognised as an exemplary editor for *IEEE Communications Letters* and as an exemplary reviewer for *IEEE Transactions on Communications*. He is an associate editor for *IEEE Communications Letters* and guest editor for the *IEEE Journal of Selected Topics in Signal Processing* issue "Exploiting Interference Towards Energy Efficient and Secure Wireless Communications".

Mohammadali Mohammadi received his B.S. degree in electrical engineering from Isfahan University of Technology, Isfahan, Iran, and his M.S. and Ph.D. degrees in electrical engineering from K. N. Toosi University of Technology, Tehran, Iran, in 2005, 2007, and 2012, respectively. From November 2010 to November 2011, he was a Visiting Researcher at the Research School of Engineering, Australian National University, Canberra, A.C.T., Australia, working on cooperative networks. He is currently an Assistant Professor with the Faculty of Engineering, Shahrekord University, Shahrekord, Iran. His research interests include cooperative communications, energy harvesting and green communications, full-duplex communications, and stochastic geometry.

Arumugam Nallanathan is professor of wireless communications in the Department of Informatics at King's College London (University of London). He served as the head of Graduate Studies in the School of Natural and Mathematical Sciences at King's College London, 2011/2012. He was an assistant professor in the Department of Electrical and Computer Engineering, National University of Singapore, from August 2000 to December 2007. His research interests include 5G wireless networks, Internet of Things (IoT) and molecular communications. He published more than 300 technical papers in scientific journals and international conferences. He is a corecipient of the Best Paper Award presented at the IEEE International Conference on Communications 2016 (ICC2016) and IEEE International Conference on Ultra-Wideband 2007 (ICUWB 2007). He is an IEEE distinguished lecturer. He has been selected as a Thomson Reuters Highly Cited Researcher in 2016. He is an editor for *IEEE Transactions on Communications* and *IEEE Transactions on Vehicular Technology*. He was an editor for *IEEE Transactions on Wireless Communications* (2006–2011), *IEEE Wireless Communications Letters* and *IEEE Signal Processing Letters*. He served as the chair for the Signal Processing and Communication Electronics Technical Committee of the IEEE Communications Society and Technical Program chair and member of Technical Program Committees in numerous IEEE conferences. He received the IEEE Communications Society SPCE outstanding service award 2012 and IEEE Communications Society RCC outstanding service award 2014.

Sotiris Nikoletseas is a professor at the Computer Engineering and Informatics Department of the University of Patras, Greece. Also, he is the director of the Sensors Lab and a scientific consultant of the Algorithms Group at the Computer Technology Institute and Press "Diophantus" (CTI), Greece. He has been a visiting professor at the Universities of Geneva, Ottawa and Southern California (USC).

His research interests include algorithmic aspects of wireless sensor networks and the Internet of Things (IoT), wireless energy transfer protocols, probabilistic techniques and random graphs, probabilistic algorithms and algorithmic engineering. He has published 3 books and 200+ research papers and has delivered several invited talks and tutorials. He has coordinated several externally funded R&D projects.

Mansi Peer joined as a Ph.D. scholar at Indraprastha Institute of Information Technology (IIIT)-Delhi, India, in 2016. She has received her B.Tech. (2014) and M.Tech. (2016) degrees from the National Institute of Technology (NIT), Srinagar, and IIIT-Delhi, respectively. Her research areas include cooperative relaying, cognitive networks and RF energy harvesting, and currently, she is working in the device-to-device communication domain.

Khalid A. Qaraqe (S'00) was born in Bethlehem. Dr. Qaraqe received a B.S. degree in EE from the University of Technology, Bagdad, Iraq, in 1986, with honors. He received an M.S. degree in EE from the University of Jordan, Jordan, Amman, Jordan, in 1989, and he earned his Ph.D. degree in EE from Texas A&M University, College Station, TX, in 1997. From 1989 to 2004 Dr. Qaraqe has held a variety of positions in many companies and he has over 12 years of experience in the telecommunication industry. Dr. Qaraqe has worked on numerous GSM, CDMA, and WCDMA projects and has experience in product development, design, deployments, testing, and integration. He joined the department of Electrical and Computer Engineering of Texas A&M University at Qatar, in July 2004, where he is now a professor.

Dr. Qaraqe research interests include communication theory and its application to design and performance, analysis of cellular systems, and indoor communication systems. Particular interests are in mobile networks, broadband wireless access, cooperative networks, cognitive radio, diversity techniques, and 5G systems.

Dr. Theofanis P. Raptis is a postdoctoral research fellow at the National Research Council (CNR), Pisa, Italy. Previously, he was a researcher at the Computer Technology Institute and Press "Diophantus", Greece. He received his Ph.D. from the Computer Engineering and Informatics Department, University of Patras, Greece.

His research interests include wireless power transfer algorithms in ad hoc networks, as well as future Internet platforms and test beds. He has co-authored more than 35 publications in acclaimed international refereed journals, conferences and books and has participated in several European Union-and national-funded R&D projects (AUTOWARE, IoT Lab, DISFER, SHARPEN, HOBNET).

Dr. Christoforos Raptopoulos got his Ph.D. entitled "Design and Analysis of Algorithms for Random and Evolutionary Networks" under the supervision of Professor Paul G. Spirakis, from the Computer Engineering and Informatics Department in the University of Patras, Greece, in 2008. He worked as a postdoc at the University of Paderborn and Heinz Nixdorf Institute (HNI) in Germany and as a research fellow ("Bourse d'excellence") at the Computer Science Department of the University of Geneva.

His research interests include evolutionary dynamics, dynamic and evolutionary networks, average case analysis of algorithms and random graphs. He has been the principal investigator of the SHARPEN project (Structural and Algorithmic Properties of Dynamic and Evolutionary Networks) and has participated in several EU projects on fundamental aspects of networks (MULTIPLEX, IoT Lab, HOBNET, FRONTS, FLAGS, AEOLUS).

Fahira Sangare (M'10) received his B.E. degree in electrical, electronic and information engineering from Nagaoka University of Technology, Japan, in 2005 and M.E.E. in electrical engineering from the University of Houston, Texas, in 2013. From 2005 to 2016, he was an electrical engineer for Schlumberger, the world's largest oilfield service company, in various countries (Japan, the USA, Canada and Mexico).

He is currently pursuing a Ph.D. in electrical engineering at the University of Houston. His research interests include mathematical optimisation, wireless sensor networks, RF energy harvesting, embedded software and system design.

Erchin Serpedin is a Professor in the Department of Electrical and Computer Engineering, Texas A&M University, College Station, TX, USA. He received a specialization degree in signal processing and transmission of information from Ecole Superieure D'Electricite (SUPELEC), Paris, France, in 1992, an M.Sc. degree from the Georgia Institute of Technology, Atlanta, USA, in 1992, and a Ph.D. degree in electrical engineering from the University of Virginia, Charlottesville, USA, in January 1999. Dr. Serpedin is the author of 3 research monographs, 1 textbook, 15 book chapters, 140 journal papers, and 250 conference papers. His research interests include signal processing, biomedical engineering, bioinformatics, and machine learning. Dr. Serpedin is currently serving as an Associate Editor of the *IEEE SIGNAL PROCESSING MAGAZINE*. He served as an Associate Editor of a dozen of journals, such as the *IEEE TRANSACTIONS ON INFORMATION THEORY, IEEE TRANSACTIONS ON SIGNAL PROCESSING, IEEE TRANSACTIONS ON COMMUNICATIONS, IEEE SIGNAL PROCESSING L ETTERS, IEEE COMMUNICATIONS LETTERS, IEEE TRANSACTIONS ON WIRELESS COMMUNICATIONS, Signal Processing* (Elsevier), *Physical Communications* (Elsevier), *EURASIP Journal on Advances in Signal Processing*, and as a Technical Chair for five major conferences. He is an IEEE Fellow.

Shree Krishna Sharma received an M.Sc. degree in information and communication engineering from the Institute of Engineering, Pulchowk, Nepal; an M.A. degree in economics from Tribhuvan University, Nepal; an M.Res. degree in computing science from Staffordshire University, Staffordshire, UK; and a Ph.D. degree in wireless communications from the University of Luxembourg, Luxembourg, in 2014. Dr. Sharma worked as a Research Associate at Interdisciplinary Centre for Security, Reliability and Trust (SnT), University of Luxembourg, for two years, where he was involved in EU FP7 CoRaSat project, EU H2020 SANSA, ESA project ASPIM, as well as Luxembourgish national projects Co2Sat, and SeMIGod. He is currently working as a Postdoctoral Fellow at Western University, Canada. His research interests include 5G and beyond wireless systems, Internet of Things (IoT), adaptive optimization of distributed communication, computing and caching resources, cognitive and cooperative communications, and interference mitigation and resource allocation in heterogeneous wireless networks.

In the past, Dr. Sharma was involved with Kathmandu University, Dhulikhel, Nepal, as a Teaching Assistant, and he also worked as a Part-Time Lecturer for eight engineering colleges in Nepal. He worked in Nepal Telecom for more than

four years as a Telecom Engineer in the field of information technology and telecommunication. He is the author of more than 75 technical papers in refereed international journals, scientific books, and conferences. He received an Indian Embassy Scholarship for his B.E. study, an Erasmus Mundus Scholarship for his M.Res. study, and an AFR Ph.D. grant from the National Research Fund (FNR) of Luxembourg. He received Best Paper Award in CROWNCOM 2015 conference, and for his Ph.D. thesis, he received "FNR award for outstanding PhD Thesis 2015" from FNR, Luxembourg. He is a member of IEEE and has been serving as a reviewer for several international journals and conferences; and also as a TPC member for a number of international conferences including IEEE ICC, IEEE Globecom, IEEE PIMRC, and IEEE ISWCS.

Ivan Stupia received his M.Sc. degree in telecommunications engineering and Ph.D. degree in information engineering from the University of Pisa, Italy, in 2004 and 2009, respectively. In 2011, he joined the Institute of Information and Communication Technologies, Electronics and Applied Mathematics (ICTEAM) of the Université Catholique de Louvain.

His expertise and general interests span the areas of wireless communications and signal processing with special emphasis on radio resource allocation, interference management techniques, cooperative networking, wireless power transfer and green and cost-effective design of cellular networks. His current research topics focus on the application of game theory and multi-objective optimisation to the design of self-adaptive and self-organising networks.

Himal A. Suraweera received his B.Sc. Engineering (First Class Honors) degree from the University of Peradeniya, Sri Lanka, in 2001, and his Ph.D. degree from Monash University, Australia, in 2007.

He is a Senior Lecturer at the Department of Electrical & Electronic Engineering, University of Peradeniya. From January 2011 to May 2013, he was a Post-Doctoral Research Associate at the Singapore University of Technology and Design, Singapore. From July 2009 to January 2011, he was with the National University of Singapore, Singapore, as a Research Fellow. From February 2007 to June 2009, he was a Research Fellow at Victoria University, Australia. He was awarded the Mollie Holman medal and the Kenneth Hunt medal upon graduating from Monash University, IEEE ComSoc Asia-Pacific Outstanding Young Researcher Award in 2011, and WCSP Best Paper Award in 2013.

Dr. Suraweera serves on the editorial boards of *IEEE TRANSACTIONS ON WIRELESS COMMUNICATIONS*, *IEEE TRANSACTIONS ON GREEN COMMUNICATIONS AND NETWORKING,* and Series on Green Communications and Networking of the *IEEE JOURNAL ON SELECTED AREAS IN COMMUNICATIONS*. He was an editor for *IEEE COMMUNICATIONS LETTERS* during 2010–2015. He was a co-chair of the Signal Processing for Communications Symposium, GLOBECOM '15. His research interests include relay networks, energy harvesting wireless communications, full duplex communications, physical layer security, and MIMO systems.

Luc Vandendorpe (M'93, SM'99, F'06) was born in Mouscron, Belgium, in 1962. He received his degree (summa cum laude) in electrical engineering and Ph.D. degree from the Université Catholique de Louvain (UCL), Louvain-la-Neuve, Belgium, in 1985 and 1991, respectively. Since 1985, he has been with the Communications and Remote Sensing Laboratory, UCL, where he first worked in the field of bit rate reduction techniques for video coding. In 1992, he was a visiting scientist and a research fellow at the Telecommunications and Traffic Control Systems Group, Delft University of Technology, the Netherlands, where he worked on spread spectrum techniques for personal communication systems. From October 1992 to August 1997, he was a senior research associate of the Belgian NSF, UCL, and an invited assistant professor. He is now a full professor with the Institute of Information and Communication Technologies, Electronics and Applied Mathematics, UCL. His research interests include digital communication systems and more precisely resource allocation for OFDM(A)-based multicell systems, MIMO and distributed MIMO, sensor networks, UWB-based positioning and wireless power transfer. He is a TPC member for numerous IEEE conferences (VTC, GLOBECOM, SPAWC, ICC, PIMRC and WCNC). He was a co-technical chair for the IEEE ICASSP 2006. He served as an editor for Synchronization and Equalization of the *IEEE Transactions on Communications* between 2000 and 2002 and as an associate editor of the *IEEE Transactions on Wireless Communications* between 2003 and 2005 and the *IEEE Transactions on Signal Processing* between 2004 and 2006. He was the chair of the IEEE Benelux joint chapter on communications and vehicular technology between 1999 and 2003. He was an elected member of the Signal Processing for Communications Committee between 2000 and 2005 and an elected member of the Sensor Array and Multichannel Signal Processing Committee of the Signal Processing Society between 2006 and 2008 and between 2009 and 2011. Luc Vandendorpe is a fellow of the IEEE.

Chenglin Zhao received his bachelor's degree in radio technology from Tianjin University in 1986, master's degree in circuits and systems from Beijing University of Posts and Telecommunications (BUPT) in 1993 and Ph.D. degree in communication and information system from Beijing University of Posts and Telecommunications in 1997. At present, he serves as a professor in Beijing University of Posts and Telecommunications, Beijing, China. His research is focused on emerging technologies of short-range wireless communication, cognitive radios and 60GHz millimetre-wave communications.

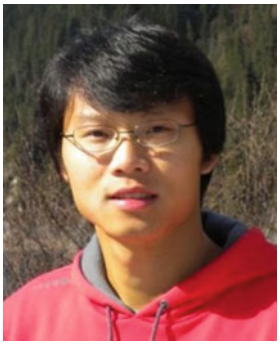

Xiangyun Zhou received his B.E. (Hons.) degree in electronic and telecommunications engineering and Ph.D. degree in telecommunications engineering from the Australian National University in 2007 and 2010, respectively. From 2010 to 2011, he worked as a postdoctoral fellow at the UNIK – University Graduate Center, University of Oslo, Norway. He joined the Australian National University in 2011 and currently works as a senior lecturer. His research interests are in the fields of communication theory and wireless networks.

Dr. Zhou currently serves on the editorial board of *IEEE Transactions on Wireless Communications* and *IEEE Communications Letters*. He also served as a guest editor for the *IEEE Communications Magazine*'s feature topic on wireless physical layer security in 2015 and the *EURASIP Journal on Wireless Communications and Networking*'s special issue on energy harvesting wireless communications in 2014. He was a co-chair of the ICC workshop on wireless physical layer security at ICC'14, ICC'15 and ICC'16. He was also a co-chair of the GLOBECOM workshop on wireless energy harvesting communication networks at GLOBECOM'16.

He was the chair of the ACT Chapter of the IEEE Communications Society and Signal Processing Society from 2013 to 2014. He is a recipient of the Best Paper Award at ICC'11 and IEEE ComSoc Asia-Pacific Outstanding Paper Award in 2016.

Introduction

Wireless power transfer (WPT) through RF signals has a long and rich history. Indeed, it has been more than 120 years since the first pioneering experimental work was accomplished by Nikola Tesla in 1899. Recently, wireless information and power transfer has been acknowledged as a significant means to prolonging the lifetime of energy-constrained wireless devices and networks. The evolution of this technology has been rapid, and it is now being considered for most of the beyond 5G technologies, with new commercial products being showcased every year in the Consumer Electronics Show. WPT is a technology whose time has come. The reason is the proliferation of the number of Internet-connected devices, which is set to explode even further with the coming of the Internet of Things (IoT). For instance, industry forecasts predict that the number of IoT-connected devices will exceed 25 billion by 2025, whilst the number of mobile subscribers will exceed 7 billion by the same year. Typically, energy-limited wireless devices are generally powered by batteries with a limited operating time. Whilst recharging the batteries can extend the lifetime of the device/network to a certain extent, it usually experiences high costs and may not be very convenient in certain cases like toxic environments, building structures or inside human bodies, etc. Thus, RF energy harvesting through ambient environment or other ways is an attractive solution to power wireless devices in the future. In particular, RF signal-sourced wireless power transfer methods are especially appealing to low-energy-consumption devices in IoT.

Since RF signals can carry energy and information at the same time, simultaneous wireless information and power transfer (SWIPT) is an interesting new area of research that has attracted increasing attention by academia and industry. However, a unified research framework in this area of research is still in the infancy stage, although notable results are reported in this book. Radio frequency (RF) energy transfer and harvesting techniques have recently become alternative methods to power next-generation wireless networks. As this emerging technology enables proactive energy replenishment of wireless devices, it is advantageous in supporting applications with quality of service (QoS) requirements. The level of the ambient RF signals is unceasingly growing because of wireless systems such

as mobile base stations, Wi-Fi applications, TV and radio base stations, wireless routers and other systems that exploit wireless networks. Hence, wireless power transfer and wireless energy harvesting systems are drawing more attention and becoming more efficient. Furthermore, these systems are much less affected by weather circumstances as compared with other energy harvesting systems. However, they have some challenges such as low power density and high sensitivity. In the contemporary era, the available frequency resources are getting rarer as a result of spectrum segmentation and increased number of connected devices. Furthermore, the power consumed by our modern communication applications and networks is becoming a warning factor in the dialogue of global warming, resulting in the idea of green and sustainable radio. Consequently, it becomes vital to define and explore new wireless network designs which have the ability to support higher system throughput and energy efficiency whilst providing large-scale coverage and availability.

In this direction, we present an overview of the WPT including system architecture, RF wireless power transfer techniques and existing applications. We demonstrate the idea of WPT is exploited in emerging areas such as full duplex communication, cooperative wireless communications, interference exploitation, etc. WPT/SWIPT applications of WSNs are also of a particular interest in this book. These systems absorb ambient RF signals in the environment. The book aims at bringing and structuring the state-of-the-art research findings in WPT/SWIPT and presenting these to postgraduate students, companies and researchers. The book will also serve as a reference book in the area of RF wireless power transfer and RF energy harvesting for researchers, engineers and postgraduate and doctoral students. The book contains two parts, i.e. Part I deals with the emerging topics of wireless information and power transfer and Part II contains interesting applications and background of WPT in wireless sensor networks and related areas.

Part I: Emerging Topics of Wireless Information and Power Transfer

In recent years, research on RF energy harvesting or WPT-assisted communication has created innovative paradigms. In this context, we term WPT as energy scavenging through RF signals for far fields, with a significant attention to the information processing angle as it is central to wireless communications. In this section, we discuss some emerging topics of wireless information and power transfer.

Chapter 1 focuses on surveying and presenting an introduction to the wireless information and the power transfer area. This chapter provides an overview and introduction to simultaneous wireless information and power transfer (SWIPT) systems, with a particular focus on emerging techniques associated with SWIPT. The chapter explores various key design issues in the development of SWIPT-assisted emerging wireless communication technologies including those related

to 5G communications. The chapter also provides interesting research ideas and directions for future work.

Chapter 2 studies the full duplex communication together with the WPT. Full duplex (FD) radios that can simultaneously transmit and receive on the same frequency channel have emerged as a solution to potentially double the spectral efficiency. In this chapter, the authors overview the state-of-the-art advances in FD communications and WPT. Specifically, FD wireless-powered network design with examples from (a) bidirectional topology, (b) relay topology and (c) hybrid access point topology is presented. Then, the chapter presents FD to design energy and spectrally efficient future wireless communication network. In particular, in each topology, the chapter analyses the system performance and considers beamforming design to optimise the performance. In addition, the impact of beamforming strategy and various system/energy harvesting parameters on the performance is discussed in detail. Finally, future research directions and open problems associated with FD and WPT are identified.

Chapter 3 investigates the concept of SWIPT for small-cell networks and investigates the resource allocation optimisation for SWIPT in small-cell networks. The chapter considers a small-cell network with multiple-input single-output SWIPT system model and addresses the problem of joint transmit beamforming and receiver time switching design. The design problem is formulated as a non-convex multi-objective optimisation problem with the goal of maximising the harvested energy and information data rates for all users simultaneously. The proposed multi-objective optimisation problem is introduced employing the weighted Chebyshev method. In this scenario, the trade-off between the maximisation of the energy efficiency of information transmission and the maximisation of the wireless power transfer efficiency is studied by means of resource allocation using a multi-objective optimisation framework.

Chapter 4 presents the latest developments in the area of interference exploitation for harvesting useful signal power. This complements existing work on energy harvesting and wireless power transfer, where wireless interference acts not only as a source of RF energy for powering the transceiver hardware but also as a source of useful signal energy for enhancing signal detection. This chapter complements Chap. 1 by providing the state of the art in the area of RF energy harvesting with interference exploitation, where constructive interference is harvested both as useful signal power and as an RF energy source. This is more potentially an interesting research direction. There is only a limited work done to date.

Chapter 5 presents different aspects of energy harvesting relaying systems. First, the performance of energy harvesting relaying systems with or without interference is analysed in terms of different performance measures. This analysis helps to show the benefit of energy harvesting relaying. Then, a new energy harvesting relaying protocol that allows the source node to harvest energy from the relay node during the relaying phase is examined. Finally, the channel estimation problem for energy harvesting relaying is discussed, where pilots used in channel estimation are transmitted using the harvested energy.

Chapter 6 reviews the state-of-the-art technologies that allow multi-scale wireless devices to simultaneous harvest energy and transmit data. The energy efficiency of systems in general determines its operational sustainability. Harvesting energy is a crucial technology for a variety of wireless systems that have limited access to a reliable electricity supply or recharging sources. As such, these devices need to harvest electricity from alternative sources such as the natural environment or wireless signals. A variety of wireless systems and devices fit this profile, from relatively power-hungry macro-base stations deployed in remote regions to nanoscale sensors in in vivo environments.

Part II: RF Energy Harvesting Protocols for Wireless Sensors and Related Areas

The future Internet of Things (IoT) will connect trillions of devices, where wireless sensors will play an important part. Due to the large scale of such networks, battery replacement is a crucial issue for the massive number of wireless sensors. To efficiently address the finite sensor lifetime problem in IoT, techniques such as energy harvesting-powered and wireless power transfer-powered WSNs are promising solutions.

Chapter 7 presents an introduction to RF energy harvesting techniques, describing the underlying electronics hardware design, showing the current state-of-the-art applications and commercially available products and finally expanding to future applications and challenges ahead. This chapter surveys the general architecture of a harvester from both anticipated and ambient RF origins, in order to meet the future demand for self-powered devices. All the subsystems of the harvester were discussed, including the antenna design, matching circuit, rectifier, power management and energy storage. In addition, potential RF signal scavenging applications and techniques beyond wireless sensor node power were explored, such as long-distance electrical power distribution, SWIPT, beamforming and cognitive radio.

Chapter 8 summarises the state-of-the-art WSNs, EH-based WSNs and wireless power transfer techniques and then motivates wireless power transfer-based WSNs. Also, it presents the major design challenges for wireless power transfer-based status monitoring WSNs, including accurate modelling of sensor energy costs and metrics to take into account the age of the sensed information. Then, the chapter introduces a novel solution to one of the challenges. Specifically, it introduces a harvest-then-use protocol and considers two complementary performance metrics to measure the timeliness of the status monitoring WSN, i.e. update cycle and update age. Moreover, the chapter investigates a framework of analysis for both the update cycle and the update age, which takes into account both the energy cost of sensing and transmission.

Chapter 9 proposes a simultaneous approach of using cooperative spectrum sharing and energy harvesting techniques for enhancing the quality of service (QoS) of next-generation wireless networks. The vision of creating a sustainable and smart planet has encouraged researchers to move towards more energy-efficient and user-friendly technologies giving rise to the notion of 5G standard. 5G standard is envisioned to bring with itself the ability to alleviate the problems of spectrum underutilisation and energy inefficiency. Earlier, these two issues were tackled separately; however, this chapter addresses these issues jointly.

Chapter 10 introduces a model which arises naturally from fundamental properties of the superposition of energy fields. This model has been shown to be more realistic than other one-dimensional models that have been used in the past and can capture super-additive and cancellation effects. Under this model, the chapter defines two new interesting problems for configuring the wireless power transmitters so as to maximise the total power in the system, and it proves that the first problem can be solved in polynomial time. The chapter presents a distributed solution that runs in pseudo-polynomial time and uses various knowledge levels, and it provides theoretical performance guarantees. Finally, the chapter designs three heuristics for the second problem and evaluates them experimentally.

Chapter 11 relates to heterogeneous cellular networks via balanced dynamic planning. Generally, network operators exploit temporal and spatial fluctuations in call traffic load to save energy by switching off their lightly loaded base stations (BSs), a technique that is referred to as dynamic planning. This chapter quantifies the impact of dynamic planning on mobile users' service quality for data calls in both uplink and downlink. It proposes dynamic planning frameworks with balanced energy efficiency that account for the service quality of mobile users both at the downlink and uplink based on a two-timescale decision problem. Simulation results demonstrate that the balanced dynamic planning frameworks can save energy for the network operators and provide service quality guarantee for mobile users in the downlink and the uplink as compared with an unbalanced (traditional) dynamic planning benchmark.

Part I
Emerging Topics of Wireless Information and Power Transfer

Chapter 1
Introduction, Recent Results, and Challenges in Wireless Information and Power Transfer

Dushantha Nalin K. Jayakody, Shree K. Sharma, and Symeon Chatzinotas

1.1 Introduction

Radio communications have become one of the pillars on which our Society relies for carrying out many daily tasks. Today, the number of connected devices is increasing exponentially, reflecting not only enthusiastic smartphone adoption but also increasing connectivity of machines, etc. Some theoretical foundations have to be revisited and groundbreaking technologies are to be discovered during the coming decade. Today, wireless services are dominated by packet data transfer over the cellular and Wi-Fi networks. The cellular networks account for the majority of the world's wireless ICT power consumption, with 6 million macro-cells worldwide consuming a peak rate of 12 billion Watts. The rapid growth in the Internet-of-Things (IoT) sector is set to increase the energy consumption of small devices dramatically. While many such small devices are sensor motes with a power consumption that is in the order of a Watt or less, the sheer number of such devices (25 billion) is set to consume more power than the cellular networks worldwide. Therefore, it is important to address the emerging challenge of energy efficiency for connected small devices.

D.N.K. Jayakody (✉)
Department of Software Engineering, Institute of Cybernetics, National Research Tomsk Polytechnic University, Tomsk, Tomskaya Oblast, Russia
e-mail: nalin.jayakody@ieee.org

S.K. Sharma
University of Western Ontario, London, ON, Canada N6A 3K7,
e-mail: sshar323@uwo.ca

S. Chatzinotas
Interdisciplinary Centre for Security, University of Luxembourg, Esch-sur-Alzette, Luxembourg
e-mail: Symeon.Chatzinotas@uni.lu

D.N.K. Jayakody et al. (eds.), *Wireless Information and Power Transfer: A New Paradigm for Green Communications*, DOI 10.1007/978-3-319-56669-6_1

Mobile communications system in the upcoming years will have to face massively diverse tasks and expectations. Current 3G and 4G technologies such as high-speed packet access (HSPA) and long-term evolution (LTE) will evolve in that route, but there are also many advantages brought up by fifth-generation (5G) mobile communications technologies. Some interesting projects also feature this new targeting technology era of 5G, for example, EU-funded FP7 project METIS [1], an industry-wide consortium with the target to explore mobile and wireless enablers for the 2020 information civilization.

As shown in [2], the projected expansion of the global carbon footprint from 2007 to 2020 is contributed by mobile devices, and network architecture devices as a one of the main stakeholders. As per the prognosis, the overall carbon footprint of mobile communications surges almost linearly until 2020 with an annual increase of 11 Mto CO_2, an increase equivalent to the annual emissions of the whole of 2.5 million EU households. It is clear that one of the immense challenges is to encounter the future necessities and potentials in a reasonable and sustainable way. Low energy consumption is important to accomplish in this dialogue. Currently, the mobile operator's energy bill is a cumulative part of their OPEX (operational expenditure), and with the future needs and opportunities there is a clear danger that this may increase even more if nothing is done. This is also vital in terms of sustainability; even though mobile communications currently subsidize a segment of a percent to the global CO_2 footprint [2], it is central to uphold or even lessen this in the future. Hence, *low energy consumption* (WPT does not necessarily imply low energy consumption, as the power transfer efficiencies are quite low) *is a key design goal for future mobile communication systems*. RF energy harvesting (RFEH) through ambient energy can help to improve the amount of energy that a single node can harvest.

Initial work on wireless power transfer (WPT) focused on long-distance and high-power applications. However, both the low efficiency of the transmission process and the health concerns for such high-power applications prevented their further development. Therefore, on the one hand, most recent WPT research has focused on short-distance power transmission through inductive coupling [3] (e.g., charging mobile phones, medical implants, and electrical vehicles). Conversely, recent advances in silicon technology have significantly reduced the energy demand of many wireless devices. As wireless sensor nodes and transceivers become more power efficient, we envision that radio waves will not only become a major source of power for operating these devices, but also *their information and power transmission aspects will be unified,* e.g., *power line communications*. In this direction, simultaneous wireless information and power transfer (SWIPT) technology can offer significant gain in lifetime, reducing charging cycles and improving energy efficiency, transmission delay, power consumption, and interference management by superposing information and power transfer. *A new analytical approach that takes into account both the information flow and power transfer can contribute towards a significant engineering revolution and lead to potential new applications and services for future 5G wireless networks.*

Wireless connected devices (smartphones, etc.) are increasing. Information and power are two fundamental notions with critical impact on all aspects of life. Rollout of IoT will lead to the massive deployment of sensor nodes and information exchange, making it impractical to recharge/control these devices. Therefore, recharging devices wirelessly presents a new opportunity. The fundamental objective of the project is to address the challenging problem of SWIPT in future communication networks. *As a sustainable solution to prolong the lifetime of energy-constrained wireless networks, energy harvesting (EH) technique has recently drawn significant attention.* Apart from the conventional renewable energy sources, such as solar and wind, radio frequency (RF) signals radiated by ambient transmitters can be treated as a viable new opportunity for EH. Many future applications could benefit from SWIPT; for example, wireless implants can be charged and calibrated concurrently with the same signal. *The research on SWIPT/WPT will have an impact on different applications,* e.g.*, SWIPT could be the only option to deploy nodes at remote locations as well as in body-centric and industrial applications.*

The successful communication between two terminals solely powered by ambient radio signals, such as the existing cellular signals, has already been treated in [3, 4]. Wirelessly powered communications networks (WPCNs) under different setups have been studied in [5] to enable energy transfer in hybrid cellular networks. In [6], a medium access control (MAC) protocol was proposed for wireless sensor networks (WSNs) powered by WPCN. The nodes of WSN interfere with each other and also contribute to the RF energy that can be harvested. WPCN was considered for cognitive radio networks in [7], where secondary transmitters harvest ambient RF energy from the signals sent by nearby active primary transmitters. SWIPT has been employed in the cooperative scenario in the literature [2, 8–10], in which relay transmissions can be powered by EH from the incoming signals. However, a vast number of challenges remain open for research, e.g., multi-node scenario with SWIPT, relay selection, physical layer network coding (PLNC), a tailored SWIPT technique for novel channel coding schemes, multi-objective optimization (MOO) in multiuser SWIPT, and enhanced receiver architectures for SWIPT.

The recent literature focuses on the development of circuits and communication techniques for efficient energy harvesting (EH) from the ambient electromagnetic radiation (WPT technology); the recent cost action IC1301 on Wireless Power Transmission for Sustainable Electronics focuses on the development of efficient wireless power transmission technologies and strategies. However, this area is still in its infancy. Several current EU projects (e.g., Zero Power EU, SWAP, E-CROPS, SCAVANGE, etc.) focus on utilizing conventional EH sources (e.g., solar, vibration, wind, etc.) to increase the operational autonomy of wireless communication systems. In contrast to the state of the art, which predominantly distinguishes information and power transfer, one main objective of this project is to study the fundamental benefits of SWIPT in future wireless networks.

The radio wave-based information and power transfer has largely been designed separately, as shown in Fig. 1.1.

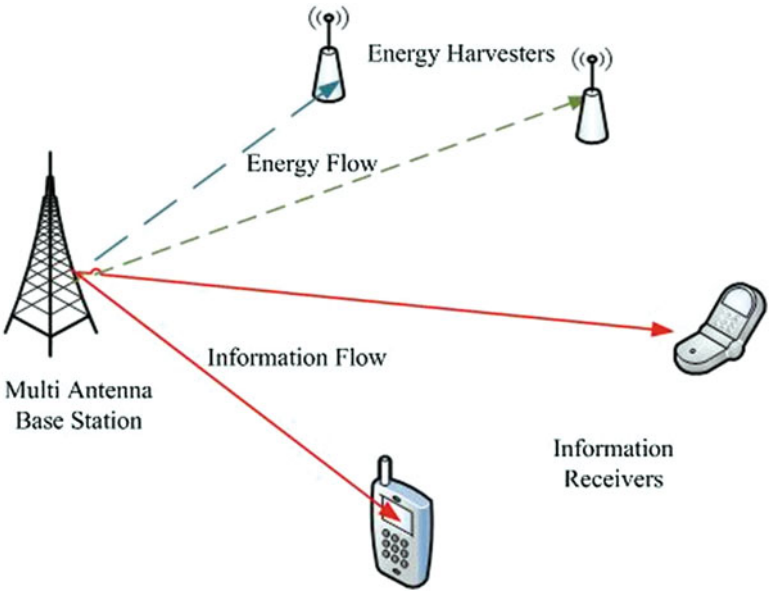

Fig. 1.1 Wireless transmission of power and information to multiple connected devices

The chapter is organized as follows. In Sect. 1.2, we introduce main technologies associated with RFEH. Then, in Sect. 1.3, we focus on emerging technologies like mmWave assisted SWIPT, Massive MIMO enabled MIMO, etc. Subsequently, we present recommendations and future directions of SWIPT in Sect. 1.4. Finally, we provide the summary of this chapter in Sect. 1.5.

1.2 Main Schemes

1.2.1 RF Wireless Energy Harvesting

Energy harvesting or energy scavenging is the process of converting energy that is obtained from external energy sources such as wind, thermal, kinetic, and solar energy into electricity. The environment contains a good source of available energy rather than the energy stored in batteries or super capacitors. There has been considerable growth of interest relating to RFEH as the demand of WSNs, number of radio transmitters, and mobile base stations continues to increase [11]. RFEH becomes a propitious solution to wireless networks with limited lifetime. Power supply of RF energy harvesting network (RF-EHN) has been maintained at a certain rate from an RF environment built from billions of radio transmitters, mobile phones, mobile base stations, and television broadcast systems around the world.

Therefore, the wireless devices now can harvest energy from RF signals according to the power requirement at the time. As a result of this technique, various forms of practical applications such WSNs, wireless body networks, and wireless charging systems for wireless devices have been found by RF-EHNs [12, 13]. In RFEH, radio signals are used as a channel to transfer energy in the form of electromagnetic radiation with a frequency range from 300 GHz to as low as 3 kHz. Ambient signals arising from TV broadcasting, Wi-Fi, and GSM signals, etc. can be considered here as sources.

1.2.2 Wireless Power Transfer

WPT is an innovative concept for use of electricity that was originally devised by Nikola Tesla in the 1890s. WPT refers to the transmission of electrical energy from a power source by means of electromagnetic fields, to an electrical component or a portion of a circuit that consumes electrical power without the aid of wired interconnections. The WPT system contains a transmitter connected to the main power source, which transforms main power to a time variant electromagnetic field and one or more receiver devices to receive and harvest energy from the electromagnetic field. Two factors, long-distance transmission and high power, have been more focused during early efforts on WPT. Nonetheless, further development of these factors ended to due to low efficiency of the power transmission process and health concerns related to high-power applications. Therefore, most WPT research start to continue in two distinct regions, non-radiative (near field) and radiative (far field). The fields in these regions have different characteristics and different WPT techniques are used to transfer power. The amount of WPT depends on various factors like placement of power beacon, antenna array scheme, transmitted power, etc. However, high frequency signals with very high transmitted power may not be feasible due to severe attenuation and blockage effects.

1.2.3 Simultaneous Wireless Information and Power Transfer

In SWIPT, both information and RF energy are conveyed from the source to the destination and, therefore, SWIPT is suitable for low-power operation. Simultaneous wireless information and power transfer (SWIPT) is a recently developed technique, which allows signals that carry information to also be used to harvest energy. Fundamental design changes are required in wireless communication networks to have an efficient SWIPT. Reception reliability and information transfer rates are conventionally used to assess performance of the wireless network [14]. The trade-off between energy harvested and information rates becomes an important factor to access performance once users in the system perform energy harvesting using RF signals [14]. In [14], an ideal receiver is used, which has the ability to perform

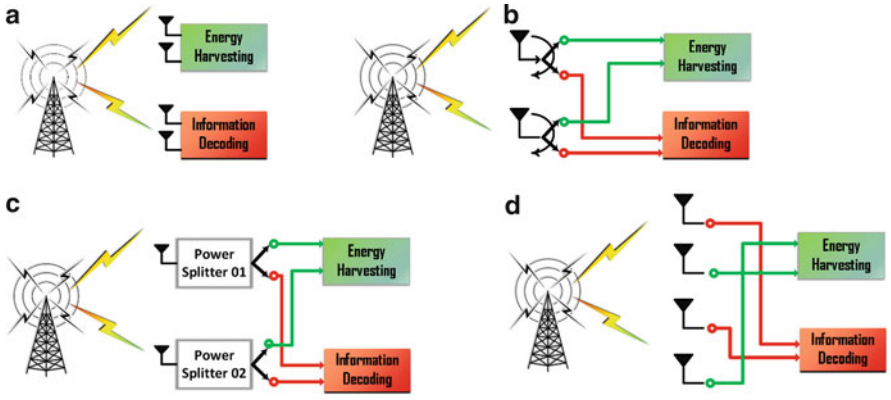

Fig. 1.2 Various simultaneous wireless information and power transfer (SWIPT) antenna architectures. (**a**) Separate receiver architecture. (**b**) Time switching architecture. (**c**) Power splitting architecture. (**d**) Antenna switching architecture

energy harvesting (EH) and information decoding (ID) simultaneously. Two circuit receivers are used in the receiver architecture proposed in [15] to perform EH and ID separately. Applications of smart antenna technologies in SWIPT MIMO and relaying were considered in [16]. The possibility of further improvements in WPT energy efficiency is opened up by the use of these smart antenna technologies.

Next we present some basic antenna architecture associated with SWIPT. Conventional architectures may not be suitable for SWIPT [17, 18] due to various power sensitivity. Antenna switching architecture is given in Fig. 1.2a. The antenna array is separated into two sets: energy harvester and the information receiver. Then, the architecture allows to perform energy harvesting and information decoding independently and simultaneously. The antenna architecture based on time-switching mode is shown in Fig. 1.2b, allows the network node to switch and use either the information decoding antenna or the RFEH antenna for the received RF signal. Based on the preset power level or power allocation optimization mechanism, Fig. 1.2c, divide the incoming power stream into two sections; information decoding and RFEH. Finally in Fig. 1.2d, a nantenna-switching equips an energy harvesting antenna and information decoding antenna. They observe different channels and take the advantage of spatial multiplexing. Compared to time-switching and power-splitting protocols, the antenna switching protocol is comparatively easy and appealing for practical SWIPT architecture design.

In the next section, as shown in Fig. 1.3, we provide SWIPT enabled emerging technologies in different application areas. Figure 1.3 provides various enabling SWIPT techniques for emerging wireless communication areas such as Massive Multiple-Input Multiple-Output (MIMO), Bistatic Scatter Radio, Cooperative Non-Orthogonal Multiple Access (NOMA), Multiuser MIMO, Broadband wireless systems, etc. All these emerging technologies are included in the following paragraphs in conjunction with the latest literature in the field.

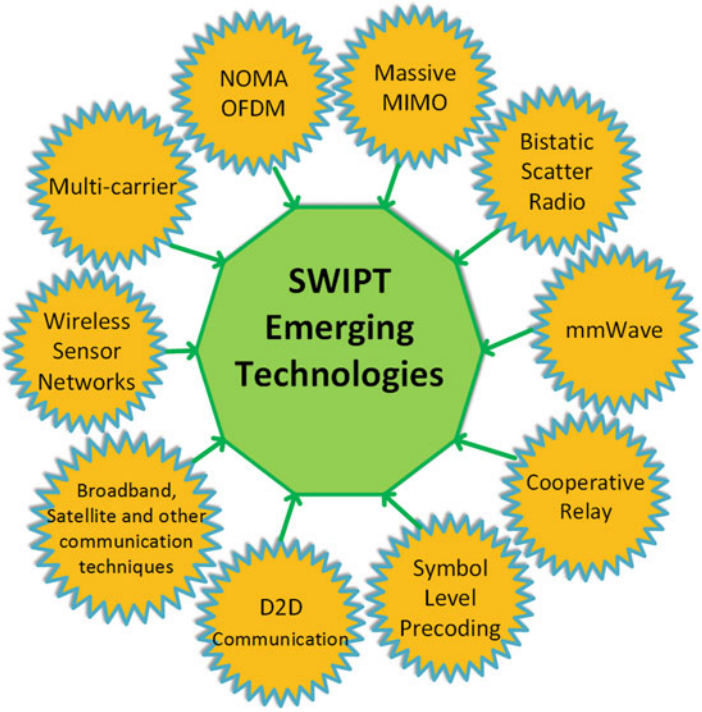

Fig. 1.3 Various emerging areas of SWIPT associated technologies

1.3 Emerging Technologies Associated with Simultaneous Wireless Information and Power Transfer/Wireless Power Transfer

1.3.1 Wireless Power Transfer/Simultaneous Wireless Information and Power Transfer Assisted Cooperative Relaying

Over the past decade, cooperative wireless diversity techniques have rekindled within the research community. Usage of WPT/SWIPT also becomes an interesting avenue for self-powered relaying [19]. A generic example of cooperative relay scheme is given in the following Fig. 1.4. In the first timeslot, an access point (or base station) transmits wireless RF energy and information simultaneously. The relay nodes (Relay 1 and Relay 2) are equipped with two antennas, i.e., one antenna for energy harvesting (EH) and other for information decoding (ID). In the second time slot, the relay harvests energy from the access point and utilizes it for information decoding as well as for retransmitting the signal to the destination using PLNC. Figure 1.4 shows the downlink (DL) and in the uplink (UL), relays

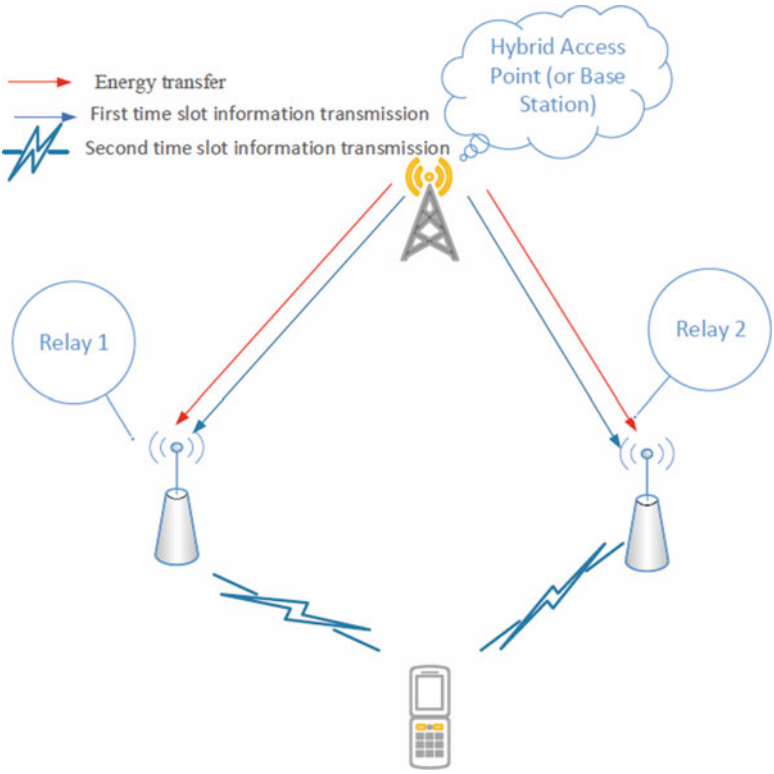

Fig. 1.4 Parallel relay scheme cooperative communications system with self-powered relay nodes

can also harvest energy from the RF signals of the UL transmission. This way, the relay can be a self-powered device. Such a wireless system can be powered in the presence of Wi-Fi or using ambient signals. Resource allocation cooperative relay algorithm design for SWIPT systems includes the following aspects/system design protocols:

1. *Harvest-then-Cooperate Scheme*: In this scheme, authors in [20, 21] propose a protocol related to first harvest RF energy in the relay node then use harvested energy for cooperation, in which the source and relay harvest energy from the an access point or power beacon in the downlink and work cooperatively in the uplink. The resource allocation and performance measuring parameters like throughput, amount of energy, etc. are analyzed for three-node scheme in [20] and for multiple access relay scheme in [22] and [23], it extends for multi user and multi antenna scenarios, respectively.
2. *Harvest-use scheme*: In this scheme, the harvested energy cannot be stored in the battery, but should be utilized for the operational energy needs [24]. This scheme offers a trade-off between the EH time and communication time from

the relay node. It was found that the FD seems to be an attractive and promising technology for HU-assisted cooperative relay communications.

3. *Self-Energy Recycling:* In this technique, a part of the energy (loop energy) that is used for information transmission by the relay is used for harvested and reused in addition to the dedicated energy sent by the source. In this scheme, the relay can functions in full-duplex mode with simultaneous energy harvesting and information transmission.
4. *Interference Aided Harvesting*: An interference aided RFEH operation is introduced in [25] for cooperative wireless relaying systems. In particular, energy-strained relays harvest energy from the received information bearing signal and co-channel interference signals. Then it uses that harvested energy to cover the energy expenses to transmit decoded signal to the destination.

Note that some of above approaches have some overlaps; however, the aforementioned sectorization is based on their more prominent features.

1.3.2 Bistatic Scatter Radio for Energy Harvesting

A scatter radio is defined as a radio which works based on the principle of communications by means of reflected power [26]. This communication principle is commonly used in Radio Frequency IDentification (RFID) systems, which are extensively being used in object tracking and supply chain monitoring. In RFID systems, an RFID tag communicates its identification number to a reader and also additional information stored in its memory in some cases [27]. For short distances (less than 2–5 m), the tags (also called passive tags) can derive their received power from the signal received from the reader and the communication distance is determined by the ability of the tag to extract the energy level from the received signal. However, for moderate/long-distance applications, the tag (also called semi-passive tag) consists of a battery in order to operate the backscatter modulator and tag state machine and use the same backscatter mechanism for the communication purpose [27, 28].

In the commonly used RFID systems, a carrier emitter and a reader are placed in a single reader box, which is called as a monostatic RFID architecture. In other words, the transmit antenna, which generates the carrier signal, and the receive antenna, which is used to demodulate the reflected signal coming from the RFID tag, are components of the same equipment [29]. However, there are several disadvantages of this monostatic architecture such as high round-trip path loss and limited communication ranges with the passive tags.

In order to address the aforementioned disadvantages of monostatic RFID structure, there is an emerging concept of bistatic architecture in which the carrier signal emitter is dislocated from the reader where backscattered signals are received. This architecture is characterized by easier setup with multiple carrier emitters and

one centralized reader and also provides long-range scatter radio communication for sensor networks [29].

Traditional wireless communication transmission is operated by costly battery supported system. However, this pulls down the attention of biologic electric potential (EP) signals (from one or multiple plants). In [30], low-cost, batteryless, and wireless approach presented proof-of-concept for the "plant-as-sensor-and-battery" idea. Here, a self-powered, EP wireless sensor is constructed that harvests near-maximum energy from the plant itself and, then, forwards the EP signal. It can travel approximately 10 m with a single switch. This technique uses the low-cost and low-power bistatic scatter radio principles and contributes to the green energy.

One of the main challenges in realizing SWIPT systems is to find a reliable source for RFEH purpose. In this regard, the carrier emitters of bistatic radar systems, which are essential parts of bistatic scatter ratio, can act as potential sources for RFEH. By exploiting the scatter radio emitter's transmissions, much more ambient energy can be captured.

1.3.3 Simultaneous Wireless Information and Power Transfer with Symbol Level Precoding

In contrast to the traditional concept that interference is always considered to be harmful, there is an emerging concept of treating constructive interference among the users as a source of useful signal energy [30–32]. With the knowledge of both the instantaneous Channel State Information (CSI) and the data symbols at the Base Station (BS), the received interference can be classified as either constructive or destructive. The destructive interference deteriorates the detection performance whereas constructive one moves the received symbols away from the decision thresholds of the constellation, thus improving the signal detection performance [30].

The available precoding for wireless downlink transmission can be broadly grouped into: (1) user-level precoding, (2) group level precoding, and (3) symbol level precoding [31]. The first technique is dependent on the CSI of individual users and the second technique is dependent on the CSI of each user group. On the other hand, the symbol level precoding technique, also called data-aided precoding, requires CSI knowledge as well as the symbols of the users. Besides the possibility of using constructive interference as a source of useful information signal, this can be used as a source of electrical wireless energy for energy harvesting purpose [30]. For this purpose, symbol level precoding can be employed in order to exploit the constructive interference for information decoding and energy harvesting purposes. In this context, authors in [30] have recently extended the conventional SWIP beamforming techniques in the context of symbol level precoding by exploiting the interference signal as:

1. A source of electrical signal for energy harvesting, and
2. A source of useful information signal [33].

The existing literature in symbol level precoding has mostly focused on a single cell scenario. The investigation of this approach in practical multicell scenarios is challenging due to the need of high level of collaboration among base stations in order to acquire the knowledge of symbols of the users. In this context, future works should focus on the feasibility of SWIPT systems with symbol level precoding in practical multicell systems, and also they should focus towards the reduction of communication resource overhead.

1.3.4 Secure Wireless Power Transfer/Simultaneous Wireless Information and Power Transfer Transmission

As already indicated, in SWIPT, RF signal is used to harvest the energy at the receiver end. In order to expedite the EH process, the transmitter is able to emit a highly boosted signal. This may likewise prompt to an expanded defenselessness to eavesdropping because of a higher potential for data spillage when the receiver is malevolent. In line with this, a new paradigm of quality of service (QoS) matter raised in communications systems with SWIPT frameworks, which is imperative to handle [34]. In particular, privacy and authentication have progressively become major areas for wireless communications. Also, physical layer security has emerged as a new layer of defense to acquire perfect secrecy communications besides to the cryptography—more amount to upper layers and expensive technique [35, 36]. Cooperative relay secure transmission with PHY layer security improvements received significant attention [37–40]. In [37], maximize the secrecy rate with the help of SWIPT enabled AF relays, limited by the EH power constraints of individual relays by jointly optimizing the cooperative beam forming relays.

By employing separated receiver mode, i.e., particular receiver assigned for confidential information decoding and the rest of the receivers are assigned for EH, some works focus on the SWIPT assisted PHY layer security. In [15, 41, 42], the artificial noise will be used to interfere with the eavesdropper for secrecy information nodes as well as operate as the primary source of EH for non-ID receivers—this method does not suit for colocated antennas where the user simultaneously receives secrecy ID and performs EH. In [41, 42], optimize the aggregate harvested power of all users while satisfying secrecy rate requirements of individual users over an orthogonal frequency division multiple access (OFDMA) [22]. In [15], the secrecy performance analysis using secrecy outage and secrecy capacity metrics has been studied for single-input multiple-output SWIPT systems and in [38–40, 43], SWIPT assisted secrecy issues addressed in non-perfect CSI for the same system setup.

Fig. 1.5 Millimeter Wave (MmWave) assisted SWIPT/wireless power transfer (WPT) scheme. This shows how the mmWave assisted SWIPT enabling the universal access of 5G networks

1.3.5 Simultaneous Wireless Information and Power Transfer Assisted Millimeter Wave Communications

In the presence of low frequency, bearing signal offers less power transfer efficiency and ultimately affects the quality of experience of the user. As the availability of large spectrum resources at higher frequencies (above 6 GHz) is vital, Millimeter Wave (mmWave) communications present as a key candidate for future 5G communications as shown in Fig. 1.5. In general, mmWave is identified as a promising avenue for WPT due to the following reasons; very high frequencies, narrow beam, large array gains, and dense network with mmWave base stations. As with the new IoT wave, many low powered connected devices are expected to deploye, mmWave RF signal can be used to harvest energy substantially.

A scheme demonstrating *harvest and use strategy* is applied in [36] where the user harvests energy from the corresponding base station through mmWave signals, then uses the harvested energy to transmit information messages. The overall (energy-and-information) coverage probability is improved by use of optimizing technique over the power-splitting ratio in order to receive signal (optimally

portion) between the energy harvesting and the information decoding modules using mmWave assisted SWIPT in [36, 44]. Here, authors maximize the network-wide energy coverage for a given user population by optimizing the antenna geometry. In [45], a prototype is developed for 24 GHz rectenna. This demonstrates the feasibility of wireless energy harvesting and information transmission by use of millimeter wave.

Unfortunately, as high frequency bands inherently suffer from poor penetration and diffraction, they present as research challenges to use mmWave for SWIPT/WPCN assisted wireless networks. Also, limited amount of work considered mmWave for SWIPT/WPCN. There is a huge gap in the research on mmWave assisted SWIPT in information processing and hardware development point of view. Many of current setup cannot be used directly for higher frequencies like above 6 GHz.

1.3.6 Simultaneous Wireless Information and Power Transfer/Wireless Power Transfer Enabled Wireless Sensor Network

The WSN has come to significant attention with the new embarkation of IoT as WSNs will play a crucial part there. These devices are small in nature but, generally, place in hazardous or remote areas where human access is limited. Therefore, replacing the batteries or supplying stable power source is an issue for WSNs. In this section, we propose a hybrid time-switching and power-splitting spectrum sharing protocol for energy harvesting wireless sensor nodes [46]. In WSNs, power ingestion is usually divided into three parts as in [47]: sensing, data processing, and communication. As compared to sensing and data processing, communication is a costly functionality in a typical sensor node [48]. Hence, local data processing is important in order to minimizing power utilization of WSNs. As the failure of any node can significantly cause the structure to be rerouting and inefficient in terms of reliability, improving the lifespan of WSNs is an important issue for future IoT. This takes introduction to alternative energy sources like SWIPT for WSNs. Figure 1.6 depicts a WSN architecture energized by solar power and WPT techniques. Certain types of sensors may only consider WPT and can discard information depending on the application. The WSN may be distributed over a wide range of area (many kilometers) especially for a WSN user. At the same time, sensor nodes can be situated in the unreachable locations, or the real site of each sensor node can be unidentified. Also, a WSN may consist of dozens, hundreds, or even thousands of sensor nodes. Under these circumstances, it is also very useful to have WPT and information processing capabilities embedded to the sensors.

In [49], authors focus on the development of network deployment and their routing strategy. The idea is to minimize the total recharging cost to improve the lifespan of WSNs. Using the assumption that the sensors can continuously be

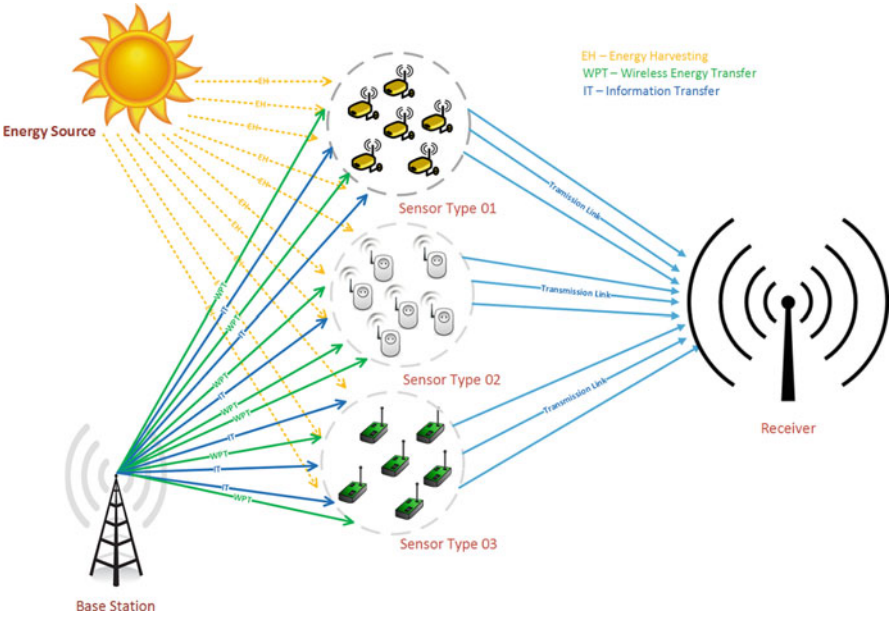

Fig. 1.6 This depicts a wireless sensor network (WSN) architecture supported by solar and WPT

recharged before their power is exhausted and have complete knowledge of CSI, an optimization problem formulates using joint network deployment and routing. A few prototype implementations of sensor nodes using RFEH is investigated in [50, 51]. By utilizing the benefits offered by SWIPT, low-power wireless sensor nodes deployed in healthcare sector can be energized during their operations, and this will subsequently improve the QoE at the end-users [12].

Some work has suggested the use of wireless energy charger application for WSN as it supports the mobility [52, 53]. A practical Real-Time Wireless Recharging Protocol for dynamic wireless recharging in sensor networks is proposed in [54]. The real-time recharging framework supports single or multiple mobile vehicles and similarly, a collaborative wireless charging scheme is presented in [55, 56]. Recharging selected nodes in remote area with Unmanned Aerial Vehicles (UAVs) delivers a solution that presently can recharge a single node. The authors in [57] simulated a limited recharging system and presented evidence of effectiveness of recharging a single node. However, this does not describe a robust system model and work is limited to simulations. Prototype based implementation for such energy harvesting architecture is provided in [57, 58].

A substantial amount of work concentrating the aspect of wireless energy harvesting and relatively less work concentrate on SWIPT enabled WSNs [59]. Exploitation of inference based energy harvesting techniques is not yet largely investigated. Physical layer redesign of SWIPT enabled WSNs is a timely requirement to furthering research with solid theoretical framework.

1.3.7 RF Energy Harvesting Enabled Internet of Things Networks

Recently, the trend of introducing energy harvesting concepts in IoT networks is increasing. In many IoT applications such as environmental monitoring, the sensors may need to rely on the harvested energy due to the unavailability of a fixed and reliable power supply. By incorporating energy harvesting capabilities in IoT devices, the self-sustainability of IoT networks can be significantly enhanced. However, the harvested RF energy may not be sufficient to handle the continuous operation of IoT sensors and it is important to reduce the energy consumption of the sensors deployed over a wide area. In this regard, one promising solution is to incorporate caching at the aggregator nodes/access points so that the sensing data can be stored temporarily and can be forwarded to the requested users without the need of activating the sensors. Following this approach, authors in [60] evaluated the performance of a caching mechanism in an IoT-enabled sensing system assuming that a sensor is capable of harvesting RF energy from the radio environment. It has been shown that the incorporation of caching ability reduces the power consumption of the energy-harvesting-based sensor and hence improves the overall sensing performance.

In cooperative relay systems used for IoT applications, a relay's battery quickly drains out since it has to support other nodes for their communication. One way to address this problem is to incorporate energy harvesting capability at the relay nodes of IoT networks. With this energy harvesting capability and opportunistic relaying, the inactive nodes can utilize their idle time in recharging their batteries. In this context, authors in [61] studied an energy harvesting-based relay selection scheme considering the residual batteries of the relays and the channel distribution function of both large-scale and small-scale fading. Furthermore, the contribution in [62] analyzed the fundamental limitations of energy harvesting-based Machine to Machine (M2M) communication systems and derived the corresponding theoretical bounds by using the Shannon theorem and IEEE 802.1ah channel models.

In addition, maintenance of batteries in IoT devices can be a significant problem for IoT networks since they are easily prone to wear and tear. The currently used rechargeable batteries have a fixed life-cycle and they need to be periodically replaced. Moreover, power converters used in the sensor devices are usually heavy, costly, and lossy [63]. In order to address these issues, authors in [63] proposed a technique to perform converter-less and storage-less energy harvesting. The proposed scheme uses a power management unit which can perform maximum power point tracking of the solar energy while providing almost fixed voltage to the IoT devices and is recommended to be a promising solution for energy management in IoT networks.

1.3.8 Multicarrier Simultaneous Wireless Information and Power Transfer Systems

In the context of multicarrier SWIPT systems, several existing literature have studied the performance of SWIPT in Orthogonal Frequency Division Multiplexing (OFDM)-based wireless systems [64–67]. The contribution in [64] investigated the performance of SWIPT receivers considering a single user OFDM channel and has provided an upper bound for the rate-energy trade-off for the considered system setup. It has been shown that there exists a trade-off between the achievable rate and the harvested energy, leading to the rate-energy trade-off in the considered system setup. Furthermore, the authors in [65] studied SWIPT for broadband wireless systems, which employ OFDM and transmit beamforming in order to create a set of parallel sub-channels with the objective of simplifying the resource allocation mechanism. Subsequently, authors proposed power control mechanisms for SWIPT in the context of multiuser multiantenna OFDM setting taking circuit-power constraints into account. However, in [68], only the carriers which have been assigned to a specific user are utilized for energy harvesting purpose for that particular user assuming a fixed subcarrier allocation. Furthermore, the authors in [66] studied the performance of SWIPT in an OFDM-based multiuser single-antenna system by employing a Power-Splitting (PS) technique at the receiver. Subsequently, the following two sets of receiver architectures were analyzed: (1) the first set considering arbitrary power-splitting ratios to split the received power into continuous sets of power streams, and (2) the second set with the fixed PS ratios to divide the received power level into a discrete set of power streams. It has been demonstrated that system energy efficiency can be enhanced by employing RFEH in the interference limited regime and multiantenna receivers are beneficial to enhance the system capacity rather than enhancing the system energy efficiency [66].

Moreover, authors in [67] studied the performance of SWIPT systems in OFDM-based multiuser wireless systems considering broadcast transmission from a fixed access point to a set of distributed user terminals. In their analysis, authors considered two multiple access schemes, namely, Time Division Multiple Access (TDMA) and OFDMA. In the first scheme, Time Splitting (TS) approach was used in such a way that information receiver of a particular user operates in the scheduled time slot for that user whereas the energy receiver operates in all other time periods. However, in the second approach, the PS approach is applied at each receiver considering that all subcarriers share the same PS ratio at each receiver. In the abovementioned two settings, authors in [14] subsequently addressed the problem of weighted sum-rate maximization over all the users by adapting the time/frequency power allocation and either PS or TS ratio considering the constraints of minimum harvested energy constraint on each user and total and/or peak transmit power constraint.

Most of the existing SWIPT literature have focused on narrowband receivers for energy harvesting and information decoding purposes. In this regard, one of the interesting future research directions is to investigate suitable RFEH techniques in

order to harvest energy based on wideband transmitted signal and also to explore wideband SWIPT receiver architectures. In this direction, one of the promising research directions is to investigate suitable techniques to enable the utilization of all the unused carriers for energy harvesting and the information bearing carrier for information decoding. For this purpose, the SWIPT receiver should be able to support multiple frequency bands. Moreover, another interesting research direction is to explore RFEH from multiple sources, which are operating in different sets of frequencies, simultaneously.

1.3.9 Massive Multiple-Input Multiple-Output Enabled Simultaneous Wireless Information and Power Transfer Systems

Another important application area of SWIPT is massive MIMO [23], which uses a very large number of antennas and has been considered as one of the promising technologies in order to meet the capacity demands of 5G wireless. The massive MIMO setting facilitates the SWIPT operation in a way that the antennas can be partitioned into two different sets for information decoding and energy harvesting. Massive MIMO system not only enables the multiplexing of signals among spatially distributed user terminals but also focuses its transmitted energy towards the directions of interest. Besides, in a multicast setting, massive MIMO SWIPT has been shown to achieve both high spectral efficiency and high energy efficiency.

Several recent works in the literature have applied SWIPT in massive MIMO systems in various settings. Authors in [69] proposed an antenna partition strategy in order to divide the antennas at the receiver for energy harvesting and information decoding purpose and subsequently analyzed the rate-energy trade-off in interference-aware massive MIMO systems. Furthermore, the contribution in [70] studied wireless energy transfer enabled massive MIMO system consisting of one hybrid energy and data access point having fixed power supply and with a large-scale antenna array. In the considered setup, a number of distributed single-antenna users are based on the wireless energy transferred from the hybrid access point for uplink transmission and use frame-based transmissions with each frame divided into the following three phases: (1) uplink channel estimation, (2) downlink WPT, and (3) uplink wireless information transfer [70]. Moreover, authors in [71] studied the wireless energy transfer enabled massive MIMO considering superimposed pilot-based channel estimation. It has been shown that even with simpler linear detection method, this scheme provides better achievable rate than that of the conventional pilot-based schemes.

In addition, the contribution in [72] employed energy beamforming for SWIPT in large-scale MIMO systems with the objective of achieving long-distance wireless energy transfer. Subsequently, a resource allocation scheme was proposed by jointly optimizing the transmit power and the transfer time. Besides, the contribution in

[73] investigated SWIPT in multi-way relay networks with massive MIMO by considering power-splitting and time-switching receiver architectures. In this setup, authors derived closed-form expressions for asymptotic symmetric sum rate and subsequently studied the energy-rate trade-off.

Although a large number of degree of freedoms available in massive MIMO systems provide performance benefits for both information decoding and energy harvesting, several issues such as balancing rate-energy trade-off in the presence of interference, low-complexity antenna partition methods, joint transmit beamforming and receive power-splitting design, pilot contamination, imperfect CSI acquisition, and synchronization issues need to be addressed.

1.3.10 Low-Power Consumption Channel Codes for Simultaneous Wireless Information and Power Transfer/Wireless Power Transfer Enabled Systems

A proper channel coding technique is needed for SWIPT enabled communication systems since the receiving signal can contain corrupted information such as noise, interference, fading, etc. and the available energy budget is extremely limited for self-powered nodes. Polar codes [74] and LDPC codes can be potential channel coding techniques in SWIPT enabled 5G communications. A method for efficiently constructing polar codes is presented and analyzed in [75], and it applies in cooperative communications in [75]. Polar codes can be decoded by using successive cancellation (SC) or the belief propagation (BP) algorithms. However, unlike SC decoders, performance optimizations for BP decoders are not yet much explored. An early stopping criterion for polar BP decoding to reduce energy dissipation and decoding latency is proposed in [76]. In [77], it is shown that polar codes are suitable for DF and compress-and-forward relaying in relay channels with orthogonal receivers.

A low-power decoder design approach for generic quasi-cyclic low-density parity-check (QC-LDPC) codes based on the layered min-sum decoding algorithm is given in [78] and a low-power high-throughput LDPC decoder using non-refresh embedded DRAM is designed in [79]. Turbo codes have been used in 3G cellular standard. These codes achieve lower bit error rates at the expense of high-computational complexity as compared to LDPC and Polar codes. Therefore, for mobile communication devices, designing energy efficient Turbo decoders is of great importance. In [80], present a MAP-based Turbo decoding algorithms with energy-quality trade-offs for various channel models.

However, an energy efficient Polar and LDPC coding scheme for SWIPT enabled communication systems is needed. Interesting researcher's motivation for developing a low-power consuming and adapting coding techniques suitable for SWIPT/WPT depended wireless communication system is an encouraging research direction. As the turbo codes have the benefits of low interconnect complexity and

inherent flexibility, in [81] it is demonstrated that they facilitate high-throughput flexible channel coding gain at lower implementation complexities as compared to LDPC and polar codes. They further explained that the turbo codes offer an additional benefit of backwards compatibility to 3G and 4G standards, which is favorable for cellular communications industry in terms of cost savings. This again brings the research community works on channel coding to investigate the best suit coding technique for energy efficient deployment in 5G standards.

1.4 Research Challenges and Future Directions

1.4.1 Hardware Impairment

Many of the research work focused on SWIPT have not yet focused on hardware impairments in the SWIPT enabled communication networks. Several hardware impairments such as in-phase/quadrature-phase (I/Q) imbalances, high-power amplifier nonlinearity, and oscillator phase noise that can decrease the quality of the transmitter. The effect of realistic relay transceiver structures on the outage probability and throughput of WPT has been analyzed and confirmed in [82] based on two-way decode-and-forward (DF) cognitive network in the influence of transceiver impairment [83]. Moreover, DF in EH systems with multiple antennas are also studied in [84] under the existence of transmitted hardware impairment. However, hardware impairment can have various effects on SWIPT enabled communication systems. It is an interesting research direction to exploit the effects of hardware impairment in different SWIPT enabled wireless communication systems. In addition, we strongly recommend that future research on SWIPT and SWIPT emerging technologies needs to pay extra attention to hardware impairment.

1.4.2 Internet of Things

Internet of things (IOT) is an evolving area that is based on connecting all types of electronic devices to the Internet. IoT essentially connects people, processes, data, and every possible things together in order to fulfill modern needs of society. One of the main deployment challenges in IoT is to maintain reliable communication with the low-cost and power limited IoT devices. In general, most of the IoT devices are battery operated and sometimes can be located in remote areas such as devices in a vessel in the middle of the deep ocean, military devices, etc. [85]. Therefore, charging those batteries sometimes can be economically impracticable; hence, SWIPT integration to IoT devices can be a promising solution to overcome this major issue in IoT.

1.4.3 Information-Theoretic Framework

Information-theoretic framework examines fundamental limits of SWIPT/SPT from an information-theoretic perspective. A proper theoretical framework has not yet been developed for SWIPT technology. Since SWIPT recently has only been introduced, a theoretical framework for trustworthiness evaluation could raise the possibility of merging SWIPT with existing communication technologies. In this regard, implementing rigorous theoretic frameworks for SWIPT systems can be an interesting and valuable research area.

1.4.4 Full-Duplex Transceiver Design

Full-duplex (FD) communication is an enabled technology for 5G as it improves the throughput. Inherently, it suffers from self-inference issues. In order to use FD incorporation with SWIPT, a robust SI cancelling algorithm enabled low-power transceiver design is needed. This forms a new direction for researchers interested in this avenue. A test bed design by incineration of nonlinearity in the circuit design and suitable mathematical modeling will optimize the EH capacity of the rectifier.

1.4.5 Satellite Communications

Satellite assisted SWIPT is an interesting application via radio frequency beam. As many satellites are solar-powered, we could use solar energy harvesting to power up the satellite and then to use it to initiate wireless power transmission to the ground stations via microwave beams and also participate in the information transmission [86]. This is designed in geostationary orbit, 36,000 km above the Earth's surface. In Fig. 1.7, we demonstrate a future idea of using solar-powered satellite for SWIPT. This can use SWIPT application as the satellite can transmit information and power for low-power consumed base stations and mobile base stations such as drones, etc. This can also be used to energize UAVs while supporting the idea of *ubiquitous energy*. Future researchers may pay attention to such satellite assisted SWIPT based drones, base stations, or similar applications and support the idea of "*ubiquitous energy*" becoming a reality.

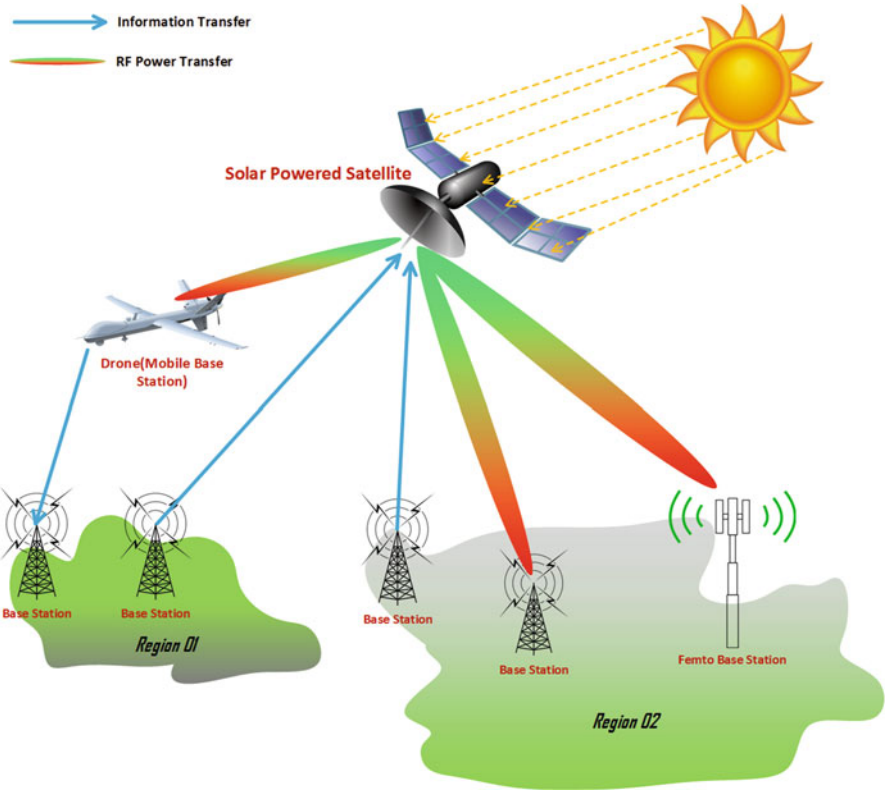

Fig. 1.7 Usage of a solar-powered satellite to develop SWIPT assisted scheme together with mobile base stations and regular base stations

1.4.6 Simultaneous Wireless Information and Power Transfer Assisted Vehicular Communications

M. Hutin and M. Le-Blanc proposed a device and technique for powering an electrical vehicle (EV) inductively in 1894 using an approximately 3-kHz AC generator [87]. However, even after a century ago this avenue of WPT using RF signals has not picked up by researchers or R & D companies to a greater extent. In the early twenty-first century, the microwave power transmission to micro aerial vehicle (MAV) [87] and Mars observation airplane projects were deployed. They have used microwave power transmission systems directed towards small airplanes. They were proposed and developed in Japan. SWIPT is an excellent possible technology to reduce or even eliminate the fuel requirements of an airplane or drone. Hence, further research on SWIPT assisted UAV, small aircrafts, and other vehicular activities propose a promising research direction.

1.5 Conclusions

This chapter presents an introduction, and recent results of simultaneous wireless information and power transfer. We presented a comprehensive introduction on the WPT and SWIPT with focus on architecture and enabling techniques. Then, we present most emerging wireless 5G related technologies together with SWIPT/WPT. Finally, we have discussed on the future directions and practical challenges in RFEH techniques including SWIPT. The incorporation of RFEH technique with 5G key areas brings about novel research issues and areas. This will form a motivation and the basis for future research in this unique area.

Acknowledgements This work was partially funded by the Russian Federal budget funds for research work (Fundamental research, applied research and experimental development) through the grant No. 3942 and performed in accordance with Russian Government Resolutions No. 2014/226 of 2017, FNR-FNRS bilateral project "InWIP-NETs: Integrated Wireless Information and Power Networks. Authors also acknowledged the contribution of the COST Action on Inclusion Radio Communications (IRACON) CA15104.

References

1. EU funded research project FP7 METIS. (Mobile and wireless communications Enablers for the Twenty-twenty Information Society, Nov 2012 to Apr 2015), https://www.metis2020.com.
2. A. Fehske, G. Fettweis, J. Malmodin, G. Biczók, The global footprint of mobile communications: The ecological and economic perspective. IEEE Commun. Mag. **49**(8), 55–62 (2011)
3. N. Shinohara, Power without wires. IEEE Microw. Mag. **12**(7), S64–S73 (2011)
4. X. Zhou, R. Zhang, C.K. Ho, Wireless information and power transfer: Architecture design and rate-energy tradeoff, in *IEEE Global Communications Conference*, 2012, pp. 3982–3987
5. J.R. Smith, *Wirelessly Powered Sensor Networks and Computational RFID* (Springer, New York, 2013)
6. K. Huang, V. Lau, Enabling wireless power transfer in cellular networks: Architecture, modeling and deployment. IEEE Trans. Wirel. Commun. **13**(2), 902–912 (2014)
7. P. Nintanavongsa, M. Naderi, K. Chowdhury, Medium access control protocol design for sensors powered by wireless energy transfer, in *Proceedings IEEE INFOCOM*, 2013
8. D.W.K. Ng, E.S. Lo, R. Schober, Wireless information and power transfer: Energy efficiency optimization in OFDMA systems. IEEE Trans. Wirel. Commun. **12**(12), 6352–6370 (2013)
9. Z. Ding, S.M. Perlaza, I. Esnaola, H.V. Poor, Power allocation strategies in energy harvesting wireless cooperative networks. IEEE Trans. Wirel. Commun. **13**(2), 846–860 (2014)
10. I. Krikidis, Simultaneous information and energy transfer in large-scale networks with/without relaying. IEEE Trans. Commun. **62**(3), 900–912 (2014)
11. H. Nishimoto, Y. Kawahara, T. Asami, Prototype implementation of ambient RF energy harvesting wireless sensor networks, in *2010 IEEE Sensors*, Kona, HI, 2010, pp. 1282–1287
12. X. Zhang, H. Jiang, L. Zhang, C. Zhang, Z. Wang, X. Chen, An energy-efficient ASIC for wireless body sensor networks in medical applications. IEEE Trans. Biomed. Circ. Syst **4**(1), 11–18 (2010)
13. R.C. Johnson, H.A. Ecker, J.S. Hollis, Determination of far-field antenna patterns from near-field measurements. Proc. IEEE **61**(12), 1668–1694 (1973)
14. R. Zhang, C.K. Ho, MIMO broadcasting for simultaneous wireless information and power transfer. IEEE Trans. Wirel. Commun. **12**(5), 1989–2001 (2013)

15. D. Ng, E. Lo, R. Schober, Robust beamforming for secure communication in systems with wireless information and power transfer. IEEE Trans. Wirel. Commun. **13**(8), 4599–4615 (2014)
16. N.M.B. Medepally, Voluntary energy harvesting relays and selection in cooperative wireless networks. IEEE Trans. Wirel. Commun. **9**, 3543–3553 (2010)
17. X. Lu, P. Wang, D. Niyato, D.I. Kim, Z. Han, Wireless networks with RF energy harvesting: A contemporary survey. IEEE Commun. Surv. Tutor. **17**(2), 757–789 (2015)
18. X. Zhou, R. Zhang, C.K. Ho, Wireless information and power transfer: Architecture design and rate-energy tradeoff, in *IEEE Transaction on Communications*, 2008, pp. 4754–4767
19. A.A. Nasir, X. Zhou, S. Durrani, R.A. Kennedy, Relaying protocols for wireless energy harvesting and information processing. IEEE Trans. Wirel. Commun. **12**(7), 3622–3636 (2013)
20. H. Chen, Y. Li, J.L. Rebelatto, B.F. Uchoa-Filho, B. Vucetic, Harvest-then-cooperate: Wireless-powered cooperative communications. IEEE Trans. Signal Process. **63**(7), 1700–1711 (2015)
21. Y. Liu, Wireless information and power transfer for multirelay-assisted cooperative communication. IEEE Commun. Lett. **20**, 784–787 (2016)
22. M. Zhang, Y. Liu, R. Zhang, Artificial noise aided secrecy information and power transfer in OFDMA systems. IEEE Trans. Wirel. Commun. **15**, 3085–3096 (2016)
23. G. Yang, C.K. Ho, R. Zhang, Y.L. Guan, Throughput optimization for massive mimo systems powered by wireless energy transfer. arXiv **1403**, 3991 (2014)
24. I. Krikidis, G. Zhang, B. Ottersten, Harvest-use cooperative networks with half/full-duplex relaying, in *Proceedings of IEEE Wireless Communications and Networking Conference*, 2013, pp. 4256–4260
25. A.A. Nasir, X. Zhou, S. Durrani, R.A. Kennedy, Relaying protocols for wireless energy harvesting and information processing, in *IEEE Transaction on Wireless Communication*, 2013, pp. 3622—3636
26. H. Stockman, Communication by means of reflected power. Proc. IRE **36**(10), 1196–1204 (1948)
27. N. Fasarakis-Hilliard, P.N. Alevizos, A. Bletsas, "Coherent detection and channel coding for bistatic scatter radio sensor networking, in *2015 IEEE International Conference on Communications (ICC)*, London, 2015, pp. 4895–4900
28. V. Liu, A. Parks, V. Talla, S. Gollakota, D. Wetherall, J.R. Smith, Ambient backscatter: Wireless communication out of thin air, in *Proceedings ACM SIGCOMM*, 2013
29. G. Vannucci, A. Bletsas, D. Leigh, A software-defined radio system for backscatter sensor networks. IEEE Trans. Wirel. Commun. **7**(6), 2170–2179 (2008)
30. C. Konstantopoulos, E. Koutroulis, N. Mitianoudis, A. Bletsas, Converting a plant to a battery and wireless sensor with scatter radio and ultra-low cost. IEEE Trans. Instrum. Meas. **65**(2), 388–398 (Feb. 2016)
31. M. Alodeh, S. Chatzinotas, B. Ottersten, in *2015 IEEE Global Communications Conference (GLOBEM), Constructive Interference through Symbol Level Precoding for Multi-Level Modulation*, 2016, pp. 1–6
32. M. Alodeh, S. Chatzinotas, B. Ottersten, Constructive multiuser interference in symbol level precoding for the MISO downlink channel. IEEE Trans. Signal Process. **63**(9), 2239–2252 (2015)
33. D. Kwon, H.S. Kang, D.K. Kim, Robust interference exploitation-based precoding scheme with quantized CSIT. IEEE Commun. Lett. **20**(4), 780–783 (2016)
34. G. Pan, C. Tang, T. Li, Y. Chen, Secrecy performance analysis for SIMO simultaneous wireless information and power transfer systems. IEEE Trans. Commun. **63**(9), 3423–3433 (2015)
35. G. Pan, H. Lei, Y. Deng, L. Fan, J. Yang, Y. Chen, Z. Ding, On secrecy performance of MISO SWIPT systems with TAS and imperfect CSI. IEEE Trans. Commun. **64**, 3831–3843 (2016)
36. L. Wang, M. Elkashlan, R.W. Heath, M. Di Renzo, K.K. Wong, Millimeter wave power transfer and information transmission, in *2015 IEEE Global Communications Conference (GLOBECOM)*, San Diego, CA, 2015

37. H. Xing, K. Wong, A. Nallanathan, R. Zhang, Wireless powered cooperative jamming for secrecy multi-AF relaying networks. IEEE Trans on Wireless Commun **1**(4), 372–375 (2012)
38. L. Dong, Z. Han, A. Petropulu, H. Poor, Improving wireless physical layer security via cooperating relays. IEEE Trans. Signal Process. **58**(3), 1875–1888 (2010)
39. Y. Yang, Q. Li, W.-K. Ma, J. Ge, P.C. Ching, Cooperative secure beamforming for AF relay networks with multiple eavesdroppers. IEEE Signal. Process. Lett. **20**(1), 35–38 (2013)
40. J. Li, A.P. Petropulu, S. Weber, On cooperative relaying schemes for wireless physical layer security. IEEE Trans. Signal Process. **59**(10), 4985–4997 (2011)
41. L. Liu, R. Zhang, K.C. Chua, Secrecy wireless information and power transfer with MISO beamforming. IEEE Trans. Signal. Proc. **62**(7), 1850–1863 (2014)
42. H. Xing, L. Liu, R. Zhang, Secrecy wireless information and power transfer in fading wiretap channel, in *Proceedings in IEEE International Conference on Communication (ICC)*, June 2014, pp. 5402–5407
43. M. Zhang, Y. Liu, Energy harvesting for physical-layer security in OFDMA networks. IEEE Trans Info Forensics Sec **11**(1), 154–162 (2015)
44. T.A. Khan, A. Alkhateeb, R.W. Heath, Millimeter wave energy harvesting. IEEE Trans. Wirel. Commun. **15**(9), 6048–6062 (2016)
45. S. Ladan, A.B. Guntupalli, K. Wu, A high-efficiency 24 GHz rectenna development towards millimeter-wave energy harvesting and wireless power transmission. IEEE Trans. Circuits. Syst. Regular Papers **61**(12), 3358–3366 (2014)
46. M. Peer, N. Jain, V.A. Bohara, A hybrid spectrum sharing protocol for energy harvesting wireless sensor nodes, in *IEEE 17th international workshop on signal processing advances in wireless communications (SPAWC)*, 2016, pp. 1–6
47. V. Gungor, G. Hancke, Industrial wireless sensor networks: Challenges, design principles, and technical approaches. IEEE Trans. Ind. Electron. **56**(10), 4258–4265 (2009)
48. I.F. Akyildiz, T. Melodia, K. Chowdhury, A survey on wireless multimedia sensor networks. Comput. Netw. **51**(4), 921–960 (2007)
49. B. Tong, Z. Li, G. Wang, W. Zhang, How wireless power charging technology affects sensor network deployment and routing, in *Proceedings of IEEE International Conference on Distributed Computing Systems (ICDCS)*, Genoa, Italy, 2010, pp. 438–447
50. H. Nishimoto, Y. Kawahara, T. Asami, Prototype implementation of ambient RF energy harvesting wireless sensor networks, in *Proceedings of IEEE Sensors*, Kona, HI, 2010
51. Z. Popovic, E.A. Falkenstein, D. Costinett, R. Zane, Low power far-field wireless powering for wireless sensors. Proc. IEEE **101**(6), 1397–1409 (2013)
52. S. Gua, C. Wang, Y. Yang, Mobile data gathering with wireless energy replenishment in rechargeable sensor networks, in *International Conference on Computer Communications*, 2013, pp. 1932–1940
53. S. Gua, C. Wang, Y. Yang, Joint mobile data gathering and energy provisioning in wireless rechargeable sensor networks. IEEE Trans. Mob. Comput. **13**(12), 2836–2852 (2014)
54. C. Wang, J. Li, F. Ye, Y. Yang, Netwrap: An ndn based real-time wireless recharging framework for wireless sensor networks. IEEE Trans. Mob. Comput. **13**(6), 1283–1297 (2014)
55. L. Xie, Y. Shi, Y.T. Hou, H.D. Sherali, Making sensor networks immortal: An energy renewal approach with wireless power transfer. IEEE ACM Trans. Networking **20**(6), 1748–1761 (2012)
56. S. Zhang, J. Wu, S. Lu, Collaborative mobile charging. IEEE Trans. Comput. **64**(3), 654–667 (2015)
57. E.B. Johnson, C. Detweiler, Charge selection algorithms for maximizing sensor network life with UAV-based limited wireless recharging, in *2013 IEEE Eighth International Conference on Intelligent Sensors, Sensor Networks and Information Processing*, Melbourne, VIC, 2013, pp. 159–164
58. M.Y. Naderi, K.R. Chowdhury, S. Basagni, W. Heinzelman, S. De, S. Jana, Experimental study of concurrent data and wireless energy transfer for sensor networks, in *2014 IEEE Global Communications Conference*, Austin, TX, 2014, pp. 2543–2549

59. M.Y. Naderi, K.R. Chowdhury, S. Basagni, W. Heinzelman, S. De, S. Jana, Experimental study of concurrent data and wireless energy transfer for sensor networks, in *2014 IEEE Global Communications Conference*, Austin, TX, 2014, pp. 2543–2549
60. D. Niyato, D.I. Kim, P. Wang, L. Song, A novel caching mechanism for Internet of Things (IoT) sensing service with energy harvesting, in *2016 IEEE International Conference on Communications (ICC)*, Kuala Lumpur, 2016, pp. 1–6
61. H. Kawabata, K. Ishibashi, S. Vuppala, G. Abreu, Robust relay selection for large-scale energy harvesting IoT networks. IEEE Int. Things J. (99), 1
62. J. Rinne, J. Keskinen, P.R. Berger, D. Lupo, M. Valkama, Feasibility and fundamental limits of energy-harvesting based M2M communications, in *2016 IEEE 27th Annual International Symposium on Personal, Indoor, and Mobile Radio Communications (PIMRC)*, Valencia, Spain, 2016, pp. 1–6
63. H.G. Lee, N. Chang, Powering the IoT: Storage-less and converter-less energy harvesting, in *20th Asia and South Pacific Design Automation Conference*, Chiba, 2015, pp. 124–129
64. P. Grover, A. Sahai, Shannon meets Tesla: Wireless information and power transfer, in *2010 IEEE International Symposium on Information Theory*, 2010, pp. 2363–2367
65. K. Huang, E. Larsson, Simultaneous information and power transfer for broadband wireless systems. IEEE Trans. Signal Process. **61**(23), 5972–5986 (2013)
66. D.W.K. Ng, E.S. Lo, R. Schober, Wireless information and power transfer: Energy efficiency optimization in OFDMA systems. IEEE Trans. Wirel. Commun. **12**(12), 6352–6370 (December 2013)
67. X. Zhou, R. Zhang, C.K. Ho, Wireless information and power transfer in multiuser OFDM systems. IEEE Trans. Wirel. Commun. **13**(4), 2282–2294 (2014)
68. P. Grover, A. Sahai, Shannon meets Tesla: wireless information and power transfer, in *Proceedings IEEE International Symposium on Information Theory (ISIT)*, Austin, TX, 2010
69. H. Wang, W. Wang, X. Chen, Z. Zhang, Wireless information and energy transfer in interference aware massive MIMO systems, in *2014 IEEE Global Communications Conference*, Austin, TX, 2014, pp. 2556–2561
70. G. Yang et al., Throughput optimization for massive mimo systems powered by wireless energy transfer. IEEE J. Select. Areas Commun. **33**(8), 1640–1650 (2015)
71. J. Li, H. Zhang, D. Li, H. Chen, On the performance of wireless-energy-transfer-enabled massive mimo systems with superimposed pilot-aided channel estimation. IEEE Access **3**, 2014–2027 (2015)
72. X. Chen, X. Wang, X. Chen, Energy-efficient optimization for wireless information and power transfer in large-scale MIMO systems employing energy beamforming. IEEE Wireless Commun. Lett. **2**(6), 667–670 (2013)
73. G. Aruma Baduge, E. Larsson, V. Poor, Wireless information and power transfer in multi-way massive MIMO relay networks. IEEE Trans. Wirel. Commun. **99**, 1
74. R. Blasco-Serrano, R. Thobaben, M. Andersson, V. Rathi, M. Skoglund, Polar codes for cooperative relaying. IEEE Trans. Commun. **60**(11), 3263–3273 (2012)
75. I. Tal, A. Vardy, How to construct polar codes. IEEE Trans. Inf. Theory **59**(10), 6562–6582 (2013)
76. H. Kong, C. Xing, S. Zhao, P. Shi, Cooperative coding scheme using polar codes, in *Proceedings of 2012 2nd International Conference on Computer Science and Network Technology*, Changchun, 2012, pp. 602–606
77. B. Yuan, K.K. Parhi, Early stopping criteria for energy-efficient low-latency belief-propagation polar code decoders. IEEE Trans. Signal Process. **62**(24), 6496–6506 (2014)
78. K. He, J. Sha, L. Li, Z. Wang, Low power decoder design for QC-LDPC codes, in *Proceedings of 2010 IEEE International Symposium on Circuits and Systems*, Paris, 2010, pp. 3937–3940
79. Y.S. Park, D. Blaauw, D. Sylvester, Z. Zhang, Low-power high-throughput LDPC decoder using non-refresh embedded DRAM. IEEE J. Solid State Circuits **49**(3), 783–794 (2014)
80. J. Kaza, C. Chakrabarti, Design and implementation of low-energy turbo decoders. IEEE Trans. Very Large Scale Integr. (VLSI) Sys. **12**(9), 968–977 (2004)
81. R.G. Maunder, The 5G channel code contenders, AccelerComm White Paper, Aug 2016, 1–13

82. D.K. Nguyen, D.N.K. Jayakody, S. Chatzinotas, J. Thompson, J. Li, Wireless energy harvesting assisted two-way cognitive realy networks: Protocol design and performance analysis, in *IEEE Access*, 2016
83. S. Lee, R. Zhang, K. Huang, Opportunistic wireless energy harvesting in cognitive radio networks. IEEE Trans. Wirel. Commun. **12**(9), 4788–4799 (2013)
84. V.P. Tuan, S.Q. Nguyen, H.Y. Kong, Performance analysis of energy-harvesting relay selection systems with multiple antennas in presence of transmit hardware impairments, in *International Conference SUBMITTED on Advanced Technologies for Communications (ATC)*, Hanoi, Vietnam, 2016, pp. 126–130
85. S.K. Sharma, T.E. Bogale, S. Chatzinotas, X. Wang, L.B. Le, Physical layer aspects of wireless IoT, in *International Symposium on Wireless Communication Systems (ISWCS)*, Poznan, pp. 304–308, 2016
86. URSI, White paper on solar power satellite (SPS) systems and report of the ursi inter-commission working group on SPS, in *URSI Inter-commission Working Group on SPS*, 2007
87. K. Miyashiro, F. Inoue, K. Maki, K. Tanaka, S. Sasaki, K. Komurasaki, Sequentially rotated array antenna for wireless power transmission to an MAV (in Japanese), in *IEICE Technical Report, WPT2012–30*, 2012, pp. 59–61

Chapter 2
Full-Duplex Wireless-Powered Communications

Mohammadali Mohammadi, Batu K. Chalise, and Himal A. Suraweera

2.1 Introduction

Wireless communications have seen a rapid progress since the invention of the radio around the turn of the twentieth century by Guglielmo Marconi. Proliferation of wireless applications, smart phones, and devices has profoundly impacted the everyday lives of people. In most communication systems, radio terminals have a dual role as transmitters and receivers. Such role has been traditionally carried out by employing half-duplex (HD) operation, meaning that the radio terminals transmit and receive in orthogonal time or frequency channels. However, this requires additional spectrum which, in fact, is scarce. In their quest to find a solution for this spectrum scarcity problem, academic and industrial communities have focused on full-duplex (FD) communications, where the terminals are allowed to transmit and receive simultaneously over the same frequency band [1, 2].

The history of FD wireless dates back to around 1940s when the principle was mainly used in radar systems [1]. However, until very recently, FD was not considered to be feasible due to the effects of self-interference (SI). This view has been radically changed since prototypes and efficient SI cancellation algorithms

M. Mohammadi (✉)
Faculty of Engineering, Shahrekord University, Shahrekord 115, Iran
e-mail: m.a.mohammadi@eng.sku.ac.ir

B.K. Chalise
Department of Electrical Engineering and Computer Science, Cleveland State University, Cleveland, OH 44115-2214, USA
e-mail: batu.k.chalise@ieee.org

H.A. Suraweera
Department of Electrical and Electronic Engineering, University of Peradeniya, Peradeniya 20400, Sri Lanka
e-mail: himal@ee.pdn.ac.lk

D.N.K. Jayakody et al. (eds.), *Wireless Information and Power Transfer: A New Paradigm for Green Communications*, DOI 10.1007/978-3-319-56669-6_2

have emerged through the development of electronics and antenna theory [3–5]. In FD systems, the significant power difference between the transmitted signal and the received signal causes SI. Such strong SI can saturate the front end of the receiver to cause severe performance degradation [6–8].

Present methods to mitigate SI in FD transceivers can be classified into two broad categories as: analog and digital SI cancellation techniques [4]. Further, analog domain SI cancellation techniques can be subdivided into passive suppression techniques and active analog techniques. Examples of former include the placement of a radio frequency (RF) absorber to block the path between the transmitter and receiver, polarization and the deployment of directional antennas [9]. These methods rely on propagation path loss for attenuation of the transmitted signal at the receiver. On the other hand, active analog cancellation techniques rely on methods such as specific antenna placement and the use of delay lines to cancel the RF analog signal. Other options for SI cancellation exist in the digital domain, where with the help of reference signals and adaptive filtering, SI can be estimated and removed. Often a combination of both analog and digital cancellation methods are required to reduce the SI up to tolerable levels and to make FD operation practical [10]. Nevertheless, perfect SI cancellation is not possible due to nonlinear distortion caused by transmitter and receiver imperfections [7].

The use of FD has already been advocated for small cells, wireless local area networks (WLANs), and fifth generation (5G) systems [1, 2, 8, 11]. In addition, applications of FD technology in cognitive radio systems [12] and physical layer security [13] have also been considered. For example, simultaneous sensing and data transmission function allowed by FD radios can improve the sensing performance and secondary throughput in cognitive radio systems. Transmission of artificial noise to interfere the eavesdropper is an effective technique used for improving the wireless security. To this end, FD radios allow simultaneous transmission of jamming signals and reception of useful signals and hence become a natural solution to improve the secrecy.

2.1.1 Wireless-Powered Communications

Emergence of multi-media rich wireless applications has created a high demand for energy. Terminals in contemporary wireless networks are either connected to the electrical grid or rely on batteries for operation. Therefore, limited operational lifetime of such wireless terminals imposes strict constraints on the network performance. In this context, energy harvesting communications have emerged as a viable solution to supply power to wireless devices by letting them scavenge energy from resources such as photovoltaic, wind, vibrational, thermoelectric, and RF signals [14]. Already, tremendous research progress has been achieved to bring energy harvesting from an interesting theoretical concept to a technological maturity [15–17].

Energy harvesting from solar, wind, etc. present significant challenges due to the intermittent nature of these sources [14]. An alternative reliable source of energy that can overcome this issue is offered by ambient and directed RF signals. It is well accepted that RF sources can provide a controllable energy flow to replenish the depleted energy supply of wireless nodes and sensors [18]. However, to realize such wireless-powered communication systems, several key design aspects are yet to be comprehensively investigated. These include efficient beamforming design [19, 20], resource allocation [21], optimized power beacon (PB) placement [22], and waveform design [23]. In addition, characteristics of the propagation environment is an important factor for wireless power transmission and the received power level depends on the range of frequencies used [24]. Accordingly, in the existing literature, depending on the nature of both the source that is used to harvest RF energy and the receiver architecture, three main approaches have been identified as (1) wireless energy harvesting, (2) wireless power transfer (WPT), and (3) simultaneous wireless information and power transfer (SWIPT).

- **Wireless energy harvesting**: This approach refers to harvesting energy from the ambient RF signals available in the environment. While solutions based on TV broadcasting, WiFi, and GSM signals have been developed, an issue with the approach is the variable nature of the ambient RF signal sources. Moreover, the approach is also sensitive to several factors such as path loss and shadowing effects as well as the choice of the rectifier since often a range of frequencies must be scanned in order to harvest sufficient amounts of energy.
- **Wireless power transfer**: WPT refers to harvesting energy using dedicated external sources such as a transmitter or a PB [18]. Available solutions to perform WPT can be divided into two categories: (1) near-field and (2) far-field. Popular methods of near-field WPT include inductive power transfer between nearby coils or magnetic resonance coupling. Although such methods exhibit high conversion efficiency, they are not suitable for mobile applications due to very short distances. On the other hand, far-field methods rely on the radiative nature of wave propagation. The history of far-field WPT can be traced back to Nicola Tesla's experiments in the last century. Although the experiments ended up in failure, they opened the way for more recent developments in microwave WPT [25].

  The gains of WPT depend on several factors such as the placement of PBs and the ability of the antenna array to focus the radiated power in the desired user direction. Moreover, frequency of the signal used for WPT has an impact on the performance and the sharpness of the beam increases with the signal frequency. However, high frequency signals such as millimeter waves are subject to severe attenuation and blockage effects. Hence, an optimum frequency must be selected to achieve a high WPT efficiency.
- **Simultaneous wireless information and power transfer**: Varshney in [26] proposed a new form of WPT coined as SWIPT. In SWIPT, both information and RF energy are conveyed from the source to the destination and, therefore, SWIPT is suitable for low power operation. Also SWIPT saves spectrum by

simultaneously transmitting information and energy using the same waveform. Several researchers have looked into practical ways of implementing SWIPT receivers [19]. The two main architectures described in the literature include the time-switching (TS) receiver and power-splitting (PS) receiver. A TS receiver operates by allowing the terminal to adaptively switch between the information and energy receiver over orthogonal time periods. A PS receiver, on the other hand, splits the incoming RF signal into two streams with different power levels, one for information reception and one for energy harvesting. If multiple antennas are present, SWIPT architectures based on antenna switching can be implemented where antennas are divided into two disjoint sets, one for information reception and other for energy harvesting [27].

2.1.2 Full-Duplex Wireless-Powered Communications

FD and WPT can be combined to realize communications with improved performance. Several attractive features of FD wireless-powered communications include:

- In many cases of interest, FD wireless-powered systems exhibit higher throughput gains as compared to their HD counterparts.
- As shown in [28, 29], undesirable SI component can be converted into an extra source of energy harvesting in FD wireless-powered communications. Hence, FD radios that can recycle the energy of the transmitted signal can be designed. Also, it is beneficial to use multiple antennas to harvest practical amounts of energy [27]. This approach can be coupled with FD communications, since spatial-domain SI cancellation can be implemented for improved performance [7].
- A FD base station (BS) can receive information and transfer energy to a set of disjoint terminals at the same time. Such a possibility is helpful for rapidly responding to the energy demands of the terminals and efficiently managing the perpetual operation of the network [11, 30, 31].
- FD nodes capable of WPT are ideal for 5G small cell implementation. In general, FD radios are unable to transmit with very high power due to possible generation of SI, while path loss significantly limits the energy harvesting performance. Hence, FD and WPT when combined together will offer benefits in terms of the increased spectral and energy efficiency.

2.1.3 Recent Results

This subsection presents a comprehensive survey of the state-of-the-art techniques on FD wireless-powered communication systems. There are three main topologies investigated in the literature. The first topology refers to the case of FD bi-directional

communications where one or both nodes of the point-to-point system apply TS or PS architecture to perform energy harvesting and information decoding. In particular, so far FD WPT [32] and FD SWIPT [33–35] bi-directional systems have been studied. In [32], a multi-antenna bi-directional FD WPT system, in which a device powered by WPT from an energy transmitter communicates with an information receiver over the same frequency band, has been considered. Specifically, the achievable rate associated with the link from the device to the information receiver has been maximized by jointly optimizing the energy beamforming at the energy transmitter and information beamforming at the device subject to transmit power constraints. In [33], optimal transmit beamforming vector at a FD access point (AP), PS ratio at the FD mobile station (MS), and transmit power of the FD MS have been designed to minimize the system's weighted sum transmit power. However, authors in [33] have assumed perfect SI cancellation, and therefore, the effect of SI is not included in the results. In [34], an antenna pair selection scheme has been introduced to improve the performance of a FD wireless-powered bi-directional system. Optimum design of the PS ratio and transmit power for SWIPT, in a FD bi-directional communication system with dual-antenna nodes, was analyzed in [35]. The FD wireless-powered bi-directional system model has also been extended to include the cases of physical layer security in [36] and machine-to-machine communication for the internet-of-things (IoT) [37].

The second topology studied in the literature is the FD relay topology. To this end, [28, 38–43] have investigated the three-node FD relay channel and WPT. In [38], throughput of a single-antenna dual-hop FD relaying system, assuming a TS-based receiver, has been studied with the aim of characterizing the fundamental trade-off between the energy harvesting and communication periods. Note that most contemporary wireless standards promote the use of multiple antenna terminals, and hence there is a need to understand the performance under more general antenna setups [44]. The concept of "self-energy recycling" in the context of WPT has been proposed in [28, 29], where the FD node regains a portion of its own transmit energy via the SI channel. The integration of SI for WPT and optimal beamforming design at the relay have been studied in [39]. A FD multi-antenna relaying system with SWIPT has been considered in [40], where the source and relay transceiver have been designed based on the minimum mean-square-error criterion.

The incorporation of the harvest-use model and TS-based FD relaying have been considered in [41]. The results in [41] demonstrate that the FD mode can outperform the HD counterpart. PS-based FD relaying with the harvest-use and harvest-store-use models have been studied in [42], where the relay periodically switches between two rechargeable batteries for charging and discharging during two consecutive time slots of each block. The optimal PS ratio that maximizes the end-to-end signal-to-interference-plus-noise ratio (SINR) and the trade-off between the end-to-end SINR and recycled self-power have also been characterized. In [43], assuming a dual-hop FD relaying system, the PS parameter and energy consumption proportion in the case of single-antenna transceivers have been jointly optimized. As concluded in this study, self-energy recycling has a limited effect and relaying is useful only when the direct source-to-destination link is very weak.

The third topology presented in the literature is the FD hybrid AP topology where data from users in the uplink channel and energy to the users in the downlink channel are transmitted and received simultaneously [45–48]. The work in [45] considered a wireless-powered communication network, where a hybrid FD AP broadcasts energy to a set of users and receives information from another set of users via time-division multiple access at the same time. Under perfect and imperfect SI cancellation at the AP, the time allocation for the downlink energy transfer and the uplink information transfer and the transmit power allocation have been jointly optimized. The same system setup has been considered in [46], where a sum-throughput maximization problem and a total-time minimization problem have been studied. In [47], considering a multi-user scenario, the case of orthogonal frequency division multiplexing has been studied by jointly optimizing the subcarrier scheduling and power allocation. In [48], a resource allocation algorithm design for a SWIPT system consisting of a FD BS, multiple single-antenna HD users, and multiple energy harvesters equipped with multiple antennas has been presented. A FD multiuser multiple-input multiple-output (MIMO) system has been studied in [49], where uplink users first harvest energy via BS energy beamforming before transmitting their information to the BS, while at the same time the BS transmits information to the users in the downlink channel. The FD hybrid BS topology has also been extended to physical layer security in [50], where the transmitter covariance matrix and receive combining vector at the multi-antenna hybrid BS have been jointly optimized to maximize the weighted uplink and downlink secrecy sum rate. Hardware feasibility of FD and WPT has also been demonstrated in [51], where an AP and a sensor node transmit data to each other while the AP simultaneously delivers power to the sensor.

Table 2.1 shows the summary of recent results discussed above on FD wireless-powered communication systems.

2.1.4 Chapter Organization

The aim of this chapter is to analyze and optimize the performance of FD wireless-powered communications. The presented analysis considers general multiple antenna setups, while the effect of residual SI is modeled specifically to show the corresponding performance insights of practical significance. In particular, we consider bi-directional, relay, and hybrid AP enabled FD wireless-powered communications with precoder design and parameter optimization in Sects. 2.2–2.4, respectively. In Sect. 2.5 we discuss future research challenges related to FD wireless-powered communications and conclusions are drawn in Sect. 2.6.

Notation: We use bold upper case letters to denote matrices, bold lower case letters to denote vectors. $\|\cdot\|$, $(\cdot)^{\dagger}$, $(\cdot)^{-1}$, and $\mathrm{tr}(\cdot)$ to denote the Euclidean norm, conjugate transpose operator, matrix inverse, and the trace of a matrix, respectively;

Table 2.1 Summary of recent results on FD wireless-powered communication systems

Literature	Topology	Wireless energy transfer receiver technique	Architecture	Design objective
[32]	Bi-directional	WPT	TS	Maximizing the achievable rate
[33]	Bi-directional	SWIPT	PS	Minimizing the sum transmit power
[34]	Bi-directional	SWIPT	–	Antenna pair selection
[35]	Bi-directional	SWIPT	PS	Maximizing the sum rate
[36]	Bi-directional	SWIPT	TS	Improving the physical layer security
[28]	Relay (AF)	SWIPT	TS	Maximizing the throughput. Self-energy recycling is assumed
[38]	Relay (AF/DF)	SWIPT	TS	Optimizing the TS parameter
[39, 40]	Relay (AF)	SWIPT	TS-PS	Beamforming optimization
[41]	Relay (AF/DF)	SWIPT	TS	Maximizing the channel capacity
[42]	Relay (DF)	SWIPT	PS	Maximizing the e2e SINR
[43, 44]	Relay (DF)	SWIPT	PS-TS	Maximizing the information rate
[45–47]	AP	WPT	–	Maximizing the sum-throughput of uplink transmissions
[48]	AP	WPT	–	Minimizing the uplink/downlink transmit power
[49]	AP	WPT	TS	Maximizing the sum rate
[50]	AP	WPT	–	Maximizing the weighted sum secrecy rate

$\Pr(\cdot)$ denotes the probability; $f_X(\cdot)$ and $F_X(\cdot)$ denote the probability density function (pdf) and cumulative distribution function (cdf) of the random variable (RV) X, respectively; $\mathscr{CN}(\mu, \sigma^2)$ denotes a circularly symmetric complex Gaussian RV x with mean μ and variance σ^2; $W(x)$ is the Lambert W-function, defined as the solution for W in $W\exp(W) = x$ [52]; $\Gamma(a)$ is the Gamma function; $\Gamma(a, x)$ is upper incomplete Gamma function [53, Eq. (8.350)]; $K_\nu(\cdot)$ is the νth order modified Bessel function of the second kind [53, Eq. (8.432)]; $\psi(x)$ is the psi (digamma) function [53, Eq. (8.360.1)]; $E_n(x)$ is the E_n-function [53], and $G_{pq}^{mn}\left(z \mid \begin{smallmatrix} a_1 \cdots a_p \\ b_1 \cdots b_q \end{smallmatrix}\right)$ denotes the Meijer G-function [53, Eq. (9.301)].

2.2 Full-Duplex Wireless-Powered Bi-directional Communications

In this section, we propose optimum and suboptimum schemes to enlarge the boundary of the BS-MS rate region for a FD wireless-powered bi-directional communication system.

2.2.1 System Model

As shown in Fig. 2.1, we consider FD bi-directional communications between an N-antenna BS and a MS with two antennas [54]. Specifically, the BS has M_T transmit antennas and $(N - M_T)$ receive antennas. At the MS side, one antenna is used for transmission and the other for reception. Since the MS is usually power limited and the uplink rate is the bottleneck, we consider a case where the BS first transmits energy to the MS, which will be used by the MS for the subsequent uplink transmission.

The communication takes place in two phases with duration α and $(1-\alpha)$, respectively. In phase I, the BS transmits energy to the MS. Suppose the transmit power of BS in this phase is P_{BS}, then the received energy is $E = \alpha P_{\mathsf{BS}} \lambda\left(\mathbf{H}_{\mathrm{BM}} \mathbf{H}_{\mathrm{BM}}^{\dagger}\right)$, where the channel between the BS and the MS is denoted as $\mathbf{H}_{\mathrm{BM}}$ and $\lambda(\cdot)$ returns the maximum eigenvalue of a matrix. In phase II, the BS and the MS communicate to each other using FD operation. The MS's transmit power can be written as $p_m = \kappa P_{\mathsf{BS}} \lambda\left(\mathbf{H}_{\mathrm{BM}} \mathbf{H}_{\mathrm{BM}}^{\dagger}\right)$ with $\kappa \triangleq \frac{\alpha\eta}{1-\alpha}$ where η is RF-to-DC energy conversion efficiency coefficient. The conversion efficiency, and thus the coefficient value depends on several factors, such as the efficiency of the rectenna and power efficiency of the hardware circuit that converts the received RF signals to DC voltage [15]. The

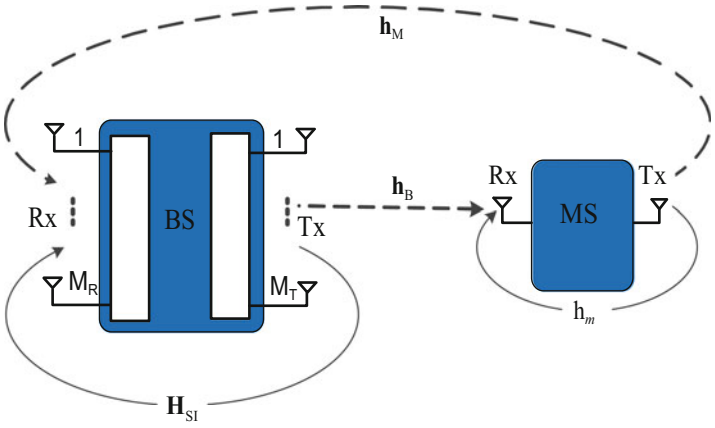

Fig. 2.1 FD wireless-powered bi-directional communication system

channels from the BS to MS and from the MS to BS are denoted by $\mathbf{h}_B^\dagger \in \mathbb{C}^{1\times M_T}$ and $\mathbf{h}_M \in \mathbb{C}^{(N-M_T)\times 1}$, respectively. FD operation causes SI at the BS and MS receive antennas. The SI channels are $\mathbf{H}_{\mathsf{SI}} \in \mathbb{C}^{(N-M_T)\times M_T}$ and h_M at the BS and MS, respectively. The transmit beamformer at the BS is $\mathbf{w}_t$ and the noise power at the BS and MS is denoted by σ_b^2 and σ_m^2, respectively.

By using the minimum mean-square-error receiver at the BS, the BS and MS achievable rates are, respectively, calculated as [54]

$$r_B = (1-\alpha)\log_2\left(1+\frac{p_m}{\sigma_b^2}\left(\|\mathbf{h}_M\|^2 - \frac{|\mathbf{h}_M^\dagger \mathbf{H}_{\mathsf{SI}}\mathbf{w}_t|^2}{\sigma_b^2+\|\mathbf{H}_{\mathsf{SI}}\mathbf{w}_t\|^2}\right)\right), \tag{2.1}$$

$$r_M = (1-\alpha)\log_2\left(1+\frac{|\mathbf{h}_B^\dagger \mathbf{w}_t|^2}{\sigma_m^2+p_m|h_m|^2}\right). \tag{2.2}$$

The maximum achievable rate at the BS has been derived in [54] as

$$R_B^{\max} = (1-\alpha^*)\log_2\left(1+\frac{\alpha^*}{1-\alpha^*}\frac{b\|\mathbf{h}_M\|^2}{\sigma_b^2}\right), \tag{2.3}$$

where $\alpha^* = \left(\exp\left(W\left(\frac{\tilde{b}-1}{\mathrm{e}}\right)+1\right)-1\right)/\left(\tilde{b}+\exp\left(W\left(\frac{\tilde{b}-1}{\mathrm{e}}\right)+1\right)-1\right)$ and $\tilde{b} = b\frac{\|\mathbf{h}_M\|^2}{\sigma_b^2}$ with $b = \eta P_{\mathsf{BS}}\lambda\left(\mathbf{H}_{\mathsf{BM}}\mathbf{H}_{\mathsf{BM}}^\dagger\right)$. The MS-BS rate region can be obtained by maximizing the MS rate while confirming that the BS-rate is equal to a certain value R_B. By solving this optimization problem for all R_B, where $R_B \in [0, R_B^{\max}]$ and $R_B^{\max}$ is the maximum value of BS rate, we obtain the MS-BS rate region. As such, the optimization problem for a given R_B is expressed as

$$\max_{\|\mathbf{w}_t\|^2\le P_{\mathsf{BS}},\, 0\le\alpha\le 1,\, p_m} (1-\alpha)\log_2\left(1+\frac{|\mathbf{h}_B^\dagger \mathbf{w}_t|^2}{\sigma_m^2+p_m|h_m|^2}\right)$$

$$\text{s.t.} \quad (1-\alpha)\log_2\left(1+\frac{p_m}{\sigma_b^2}\left(\|\mathbf{h}_M\|^2 - \frac{|\mathbf{h}_M^\dagger \mathbf{H}_{\mathsf{SI}}\mathbf{w}_t|^2}{\sigma_b^2+\|\mathbf{H}_{\mathsf{SI}}\mathbf{w}_t\|^2}\right)\right) = R_B,$$

$$p_m = \frac{\alpha\eta P_{\mathsf{BS}}\lambda\left(\mathbf{H}_{\mathsf{BM}}\mathbf{H}_{\mathsf{BM}}^\dagger\right)}{(1-\alpha)}. \tag{2.4}$$

The optimization problem (2.4) is a complicated non-convex optimization with respect to (w.r.t.) $\mathbf{w}_t$ and α. However, (2.4) can be solved efficiently by finding optimum $\mathbf{w}_t$ for a given α and vice-versa. Since α is scalar valued, the optimum solution can be ascertained by using one-dimensional search w.r.t. α.

2.2.2 *Joint Optimization of Beamformer and Time-Splitting Parameter*

In this subsection, optimum and suboptimum schemes for solving the joint optimization of the beamformer, $\mathbf{w}_t$, and TS parameter, α, are presented.

2.2.2.1 Optimum Scheme

The optimum scheme corresponds to finding $\mathbf{w}_t$ that maximizes the end to end SINR for a given α. Since α is scalar valued, the jointly optimal solution of $\mathbf{w}_t$ and α can be obtained by using one-dimensional search w.r.t. α. The computational complexity of line search is minimized by exploiting the nature of the optimization problem (2.4).

1. *Optimization of* $\mathbf{w}_t$: First consider the problem of optimizing $\mathbf{w}_t$ for a given α. In this case, the optimization problem (2.4) is expressed as

$$\begin{aligned} \max_{\|\mathbf{w}_t\|^2 \le P_{\mathsf{BS}}} \quad & (1-\alpha)\log\left(1+\frac{|\mathbf{h}_B^\dagger \mathbf{w}_t|^2}{\sigma_m^2 + p_m|h_m|^2}\right) \\ \text{s.t.} \quad & (1-\alpha)\log_2\left(1+\frac{p_m}{\sigma_b^2}\left(\|\mathbf{h}_M\|^2 - \frac{|\mathbf{h}_M^\dagger \mathbf{H}_{\mathsf{SI}}\mathbf{w}_t|^2}{\sigma_b^2 + \|\mathbf{H}_{\mathsf{SI}}\mathbf{w}_t\|^2}\right)\right) = R_B. \end{aligned} \tag{2.5}$$

   Since $\log(1+x)$ is a monotonically increasing function of $x \triangleq \frac{|\mathbf{h}_B^\dagger \mathbf{w}_t|^2}{\sigma_m^2 + p_m|h_m|^2}$ and the denominator, $\sigma_m^2 + p_m|h_m|^2$, of x is independent of $\mathbf{w}_t$, (2.5) can be solved from

$$\max_{\|\mathbf{w}_t\|^2 \le P_{\mathsf{BS}}} \quad |\mathbf{h}_B^\dagger \mathbf{w}_t|^2 \qquad \text{s.t.} \ \frac{|\mathbf{h}_M^\dagger \mathbf{H}_{\mathsf{SI}}\mathbf{w}_t|^2}{\sigma_b^2 + \|\mathbf{H}_{\mathsf{SI}}\mathbf{w}_t\|^2} = \Gamma_B, \tag{2.6}$$

   where $\Gamma_B \triangleq \|\mathbf{h}_M\|^2 - \frac{\sigma_b^2}{p_m}\left[2^{\frac{R_B}{1-\alpha}} - 1\right]$. It is clear that the objective function in (2.6) is maximized with $\|\mathbf{w}_t\|^2 = P_{\mathsf{BS}}$. This optimization problem is non-convex due to the fact that it is the maximization of a quadratic function with a quadratic equality constraint. Moreover, (2.6) does not admit a closed-form solution. However, it can be efficiently and optimally solved using semi-definite programming. For this purpose, define $\mathbf{V}_B \triangleq \mathbf{w}_t\mathbf{w}_t^\dagger$ and relax the rank-one constraint, $\mathrm{rank}(\mathbf{V}_B) = 1$. The relaxed optimization is

$$\begin{aligned} \max_{\mathbf{V}_B} \ & f(\alpha, p_m) = \mathrm{tr}(\mathbf{V}_B \mathbf{h}_B \mathbf{h}_B^\dagger) \\ \text{s.t.} \ & \mathrm{tr}(\mathbf{V}_B \mathbf{H}_{\mathsf{SI}}^\dagger \mathbf{h}_M \mathbf{h}_M^\dagger \mathbf{H}_{\mathsf{SI}}) = \Gamma_B\left(\sigma_b^2 + \mathrm{tr}(\mathbf{V}_B \mathbf{H}_{\mathsf{SI}}^\dagger \mathbf{H}_{\mathsf{SI}})\right), \end{aligned}$$

$$\text{tr}(\mathbf{V}_B) = P_{\text{BS}}, \mathbf{V}_B \succeq 0. \tag{2.7}$$

The optimization problem (2.7) is a standard semi-definite relaxation (SDR) problem with only two equality constraints. Therefore, according to Shapiro–Barvinok–Pataki (SBP) rank reduction theorem [55], there exists a rank-one optimum solution of $\mathbf{V}_B$. Let $\mathbf{V}_B^*$ be the optimum solution of (2.7). Since $\mathbf{V}_B^*$ is rank-one matrix, the optimum solution $\mathbf{w}_t^*$ is obtained $\mathbf{w}_t^* = \sqrt{P_{\text{BS}}}\tilde{\mathbf{u}}\tilde{\mathbf{u}}^\dagger$, where $\tilde{\mathbf{u}}$ is the eigenvector corresponding to a non-zero eigenvalue of $\mathbf{V}_B^*$.

2. *Optimization of* $\mathbf{w}_t$ *and* α: In order to jointly optimize $\mathbf{w}_t$ and α, the SDR problem (2.7) can be solved using an one-dimensional (or line search) search over α where $0 \leq \alpha \leq 1$. However, this line search can be limited to a small segment, and therefore the number of required SDR optimizations can be significantly minimized. To illustrate this, let the objective function in (2.5), for a given $\mathbf{w}_t^*$, be defined as

$$f(\alpha) = (1-\alpha)\log_2\left(1 + \frac{\mu}{c + \frac{\alpha b}{1-\alpha}}\right), \tag{2.8}$$

where $\mu = \frac{|\mathbf{h}_B^\dagger \mathbf{w}_t^*|^2}{|h_m|^2}$ and $c = \frac{\sigma_m^2}{|h_m|^2}$. The derivative of $f(\alpha)$ can be written as

$$\frac{df(\alpha)}{d\alpha} = -\log_2(g(\alpha)) - \frac{b\mu g(\alpha)^{-1}}{(1-\alpha)\log(2)}\left(c + \frac{\alpha b}{1-\alpha}\right)^{-2}, \tag{2.9}$$

where $g(\alpha) = 1 + \frac{\mu}{c + \frac{\alpha b}{1-\alpha}} \geq 0, \forall \alpha \in [0,1]$. It is clear from (2.9) that $\frac{df(\alpha)}{d\alpha} < 0$ for all α, i.e., $f(\alpha)$ is a monotonically decreasing function of α. This means that the maximum value of the objective function is achieved when α is minimum, provided that the equality constraint is fulfilled. However, as $\alpha \to 0$, $\Gamma_B \to \infty$, i.e., the infeasibility of the SDR optimization problem (2.7) increases. Consequently, the optimum α is the minimum α for which (2.7) is feasible. The output $\mathbf{V}_B$ of such feasible SDR provides the optimum $\mathbf{w}_B$. In a nutshell, the proposed optimum solution can be summarized as follows:

1. Define a fine grid of α in steps of $\partial\alpha$. Start with $\alpha = 0$.
2. Solve (2.7) with the increment of $\partial\alpha$.
3. If feasible, stop and output α and $\mathbf{V}_B$.
4. If not, go to step (2).

2.2.2.2 Suboptimal Scheme

The scheme presented in Sect. 2.2.2.1 requires an extensive optimization. Hence, in order to find a low-complexity closed-form solution, we can enforce a ZF constraint so that the designed transmit beamformer $\mathbf{w}_t$ ensures no SI for the FD operation at the BS. To realize this, it is easy to check from (2.4) that the following condition is sufficient,

$$\mathbf{w}_t^{\dagger}\mathbf{H}_{\mathsf{SI}}^{\dagger}\mathbf{h}_M = 0. \tag{2.10}$$

1. *Optimization of* $\mathbf{w}_t$: Substituting (2.10) into (2.4), the resulting optimization problem for a given α can be re-expressed as [54]

$$\begin{aligned} \max_{\mathbf{w}_t} \quad & |\mathbf{h}_B^{\dagger}\mathbf{w}_t|^2 \\ \text{s.t.} \quad & \|\mathbf{w}_t\|^2 \le P_{\mathsf{BS}} \\ & \mathbf{w}_t^{\dagger}\mathbf{H}_{\mathsf{SI}}^{\dagger}\mathbf{h}_M = 0. \end{aligned} \tag{2.11}$$

   Using a standard Lagrangian multiplier method and skipping the corresponding details, the closed-form solution of $\mathbf{w}_t$ is expressed as $\mathbf{w}_t^* = \sqrt{P_{\mathsf{BS}}}\frac{\mathbf{B}\mathbf{h}_B}{\|\mathbf{B}\mathbf{h}_B\|}$ where $\mathbf{B} = \mathbf{I} - \frac{\mathbf{H}_{\mathsf{SI}}^{\dagger}\mathbf{h}_M\mathbf{h}_M^{\dagger}\mathbf{H}_{\mathsf{SI}}}{\|\mathbf{H}_{\mathsf{SI}}^{\dagger}\mathbf{h}_M\|^2}$.

   Accordingly, the corresponding objective function becomes $|\mathbf{h}_B^{\dagger}\mathbf{w}_t|^2 = P_{\mathsf{BS}}\|\mathbf{B}\mathbf{h}_B\|^2$.
2. *Optimization of* α: Obviously, the transmit beamformer $\mathbf{w}_t^*$ is independent of α. Therefore, the optimization problem (2.4) w.r.t. α is equivalent to

$$\begin{aligned} \max_{0\le\alpha\le 1} \quad & f(\alpha) \triangleq (1-\alpha)\log_2\left(1+\frac{\mu}{c+\frac{\alpha b}{1-\alpha}}\right) \\ \text{s.t.} \quad & (1-\alpha)\log_2\left(1+\frac{\alpha}{1-\alpha}\tilde{b}\right) = R_B. \end{aligned} \tag{2.12}$$

   The optimum α would be zero if there were no equality constraint (or the constraint with $R_B = 0$). In the presence of equality constraint with $R_B > 0$, it is clear that the optimum α is the smallest α that satisfies the equality constraint. The following proposition presents α.

Proposition 1. *When equality constraint is feasible (i.e.,* $R_B \le R_B^{\max}$*), the optimum* α *is given by*

$$\alpha^{\text{opt}} = \frac{-\frac{1}{R_B\log(2)}W\left(-\frac{R_B\log(2)}{b\gamma}\mathrm{e}^{R_B\log(2)\left(1-\frac{1}{b}\right)}\right) - \frac{1}{\tilde{b}}}{1-\frac{1}{R_B\log(2)}W\left(-\frac{R_B\log(2)}{\tilde{b}}\mathrm{e}^{R_B\log(2)\left(1-\frac{1}{b}\right)}\right) - \frac{1}{\tilde{b}}}. \tag{2.13}$$

Proof. The equality constraint for the BS rate is expressed as

$$\log\left(1+\frac{\alpha}{1-\alpha}\tilde{b}\right) = R_B\log(2)\left(\frac{\alpha}{1-\alpha}+1\right). \tag{2.14}$$

Define $y \triangleq 1 + \frac{\alpha}{1-\alpha} b$. Then, after simple manipulations, (2.14) can be expressed as

$$\left(-\frac{R_B \log(2)}{\tilde{b}} y\right) \mathrm{e}^{-\frac{R_B \log(2)}{\tilde{b}} y} = \left(-\frac{R_B \log(2)}{\tilde{b}}\right) \mathrm{e}^{R_B \log(2)\left(1-\frac{1}{\tilde{b}}\right)}. \tag{2.15}$$

Using the Lambert-W function, y in (2.15) is expressed as

$$y = \frac{-\tilde{b}}{R_B \log(2)} W\left(-\frac{R_B \log(2)}{\tilde{b}} \mathrm{e}^{R_B \log(2)\left(1-\frac{1}{\tilde{b}}\right)}\right). \tag{2.16}$$

Note that $\frac{R_B \log(2)}{\tilde{b}} \mathrm{e}^{R_B \log(2)\left(1-\frac{1}{\tilde{b}}\right)} \leq \frac{1}{\mathrm{e}}$ is required to have a real value of y. If not, the equality constraint is not feasible for given $\tilde{b}$ and R_B where $R_B \leq R_B^{\max}$. Substituting y in (2.16), we obtain

$$\frac{\alpha}{1-\alpha} = \frac{-1}{R_B \log(2)} W\left(-\frac{R_B \log(2)}{\tilde{b}} \mathrm{e}^{R_B \log(2)\left(1-\frac{1}{\tilde{b}}\right)}\right) - \frac{1}{\tilde{b}}$$

which yields the optimum α^{Opt} given in (2.13).

We now corroborate our analysis with the numerical examples to reveal the behavior of the MS-BS rate region. The distance between the BS and MS is set to 10 meters, whereas the path loss exponent is taken as 3. The noise powers, σ_b^2 and σ_m^2, are fixed to -70 dBm. Figure 2.2 shows the rate regions obtained with the optimum and suboptimum methods for $M_T = 2$ and 3, when $N = 5$, $P_{\mathsf{BS}} = 30$ dBm, whereas the corresponding regions for $P_{\mathsf{BS}} = 0$ dBm are shown in Fig. 2.3. The channel coefficients (excluding the path attenuation) for all channels are taken as independent and identically distributed (i.i.d.) $\mathscr{CN}(0, 1)$ RVs. All results correspond to averaging of 100 independent channel realizations. The BS rate is varied from 0 to $R_B^{\max}$. The achieved BS-MS rate regions are also shown for the HD mode. Note that, in the HD mode, the information transmission period of $(1-\alpha)$ is equally divided for the BS to MS and then the MS to BS communications. Due to the HD protocol, the BS and MS can utilize all of their antennas for transmit and receive beamforming as in standard MIMO communications. Thus, the BS and MS information rates are, respectively, given by

$$\begin{aligned} r_{B,H} &= \frac{1-\alpha}{2} \log_2\left(1 + \frac{\alpha}{1-\alpha} \frac{\eta P_{\mathsf{BS}} \lambda^2(\mathbf{H}_{\mathrm{BM}} \mathbf{H}_{\mathrm{BM}}^{\dagger})}{\sigma_b^2}\right), \\ r_{M,H} &= \frac{1-\alpha}{2} \log_2\left(1 + \frac{P_{\mathsf{BS}} \lambda(\mathbf{H}_{\mathrm{BM}} \mathbf{H}_{\mathrm{BM}}^{\dagger})}{\sigma_m^2}\right). \end{aligned} \tag{2.17}$$

It can be observed from Figs. 2.2 and 2.3 that the maximum value of the MS rate is obtained when R_B is minimum, whereas the minimum value is obtained when R_B takes maximum value. Moreover, the BS-rate is much smaller than the MS-

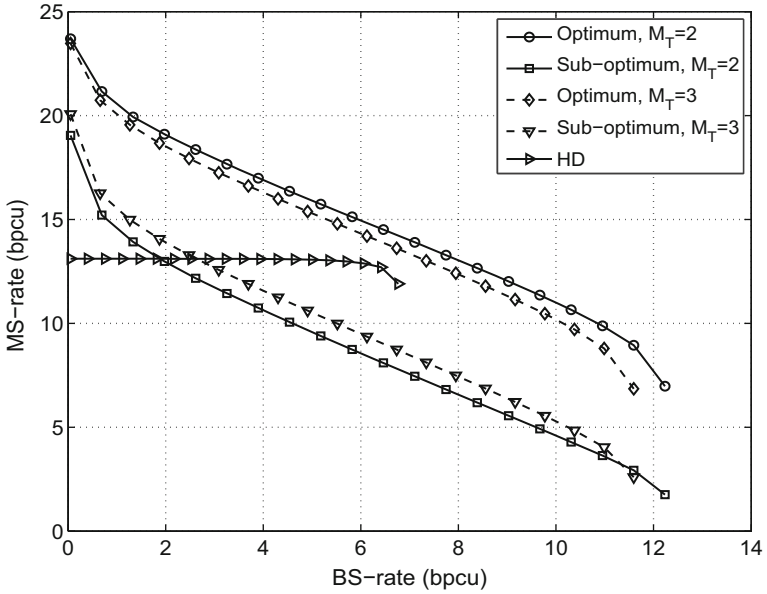

Fig. 2.2 MS-BS rate region with $P_{\mathrm{BS}} = 30\,\mathrm{dBm}$, and $M_T = 2, 3$

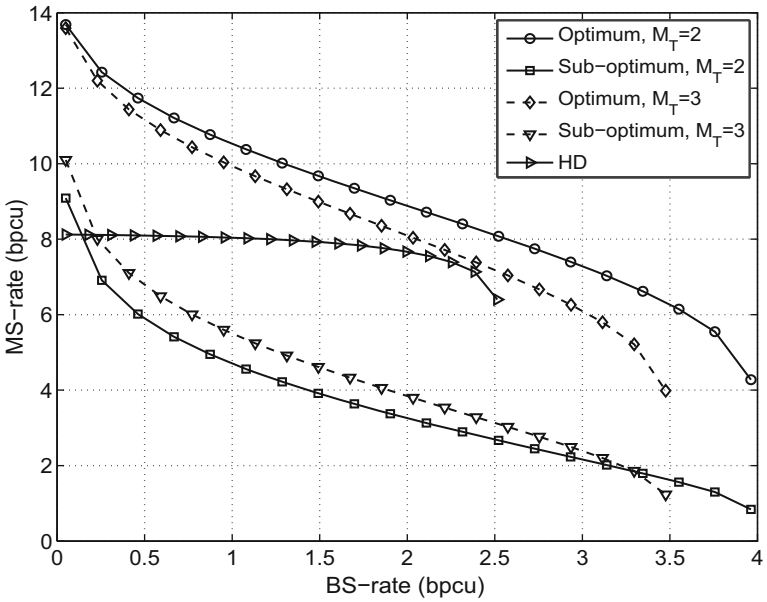

Fig. 2.3 MS-BS rate region with $P_{\mathrm{BS}} = 0\,\mathrm{dBm}$, $M_T = 2, 3$, and $N = 5$

rate. This is due to the fact that the former is limited by the transmit power of the MS which depends on the harvested power. Both figures show that the optimum method performs much better than the suboptimum approach. Moreover, when M_T increases, the obtained maximum BS rate decreases, whereas the maximum MS rate remains almost unchanged in the optimum method and increases in the suboptimum method. Figure 2.2 shows that the maximum BS and MS rates obtained with the optimum method are almost double of the corresponding rates of the HD mode. However, when the BS rate increases, the MS rate decreases rapidly in the FD mode, whereas it only decreases gradually in the HD mode. The advantage of the FD mode over the HD mode diminishes as P_{BS} decreases, as seen from Fig. 2.3. As a final observation, the advantage of the optimum method is more pronounced for smaller values of M_T.

2.3 Full-Duplex Wireless-Powered Relay Communications

The source-relay-destination topology is another widely considered system model in the current FD literature [1]. When FD relays are employed, information from the source can be transferred to the destination in one time slot, and thus the spectral efficiency bottleneck of using HD relays can be resolved. FD operation of the relays offers clear benefits for use in modern wireless networks [56]. As an example, the self-backhauling capability of FD relays has been identified as a useful feature for their use in dense 5G indoor networks [57]. Furthermore, FD relays with limited transmit power can be carefully placed in order to cover coverage gaps, although several relays would be required. While important results on FD relays with fixed and reliable power supplies have been reported in the literature, as outlined in Sect. 2.1.3, FD wireless-powered relay communications is still in infancy and deserves more investigation.

Consider a two-hop FD decode-and-forward relay system where the relay is powered using WPT from the source signals. Specifically, below we design optimum and suboptimum receive and transmit beamformers at the multiple antenna relay and optimize the TS parameter to characterize the instantaneous throughput and delay-constrained throughput.

2.3.1 System Model

Figure 2.4 shows a FD decode-and-forward relay system consisting of one source S, one relay R, and one destination, D [44]. Both S and D are equipped with a single antenna, while R is equipped with two sets of antennas, i.e., M_R receiving antennas and M_T transmitting antennas. The relay has no external power supply and employs the TS protocol to receive energy from S. Hence, the entire communication process is divided into two phases, i.e., for a transmission block time T, α fraction

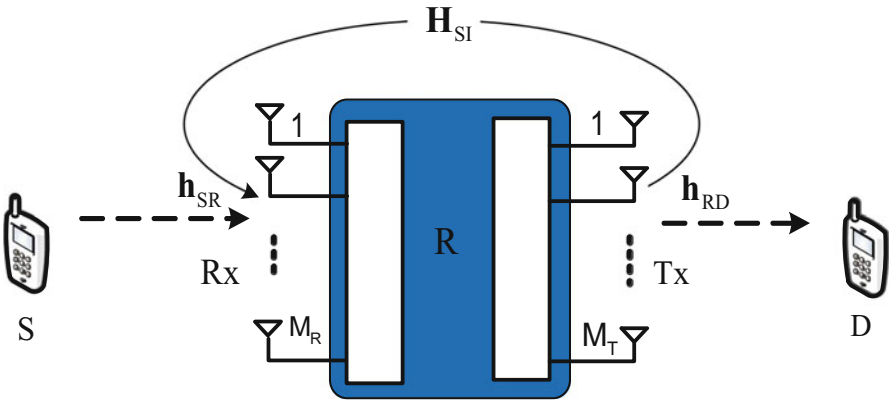

Fig. 2.4 FD wireless-powered relay system model

of the block time is devoted for energy harvesting and the remaining time, $(1-\alpha)T$, is used for information transmission. We assume that the channels in the two-hop system remain constant over the block time T and vary independently from one block to the other. Such a fading process is known as block fading in the literature. We denote the channel coefficient from S to R and from R to D by $\mathbf{h}_{SR} \in \mathbb{C}^{M_R \times 1}$ and $\mathbf{h}_{RD} \in \mathbb{C}^{1 \times M_T}$, respectively.

The relay uses the harvested energy during αT period for subsequent transmission to D. Therefore, the transmit power of R is given by

$$P_r = \kappa P_S \beta_1 \|\mathbf{h}_{SR}\|^2, \tag{2.18}$$

where P_S is the source transmit power and β_1 models the path loss effect in S-R channel.

At the information transmission phase, upon receiving source signal, R applies a linear combining vector $\mathbf{w}_r$, then forwards the estimated signal to D using the transmit beamforming vector $\mathbf{w}_t$. Hence, end to end SINR at D can be expressed as [44]

$$\gamma_{\mathsf{FD}} = \min\left(\frac{\bar{\gamma}_1 \beta_1 |\mathbf{w}_r^\dagger \mathbf{h}_{SR}|^2}{\kappa \bar{\gamma}_1 \beta_1 \|\mathbf{h}_{SR}\|^2 |\mathbf{w}_r^\dagger \mathbf{H}_{\mathsf{SI}} \mathbf{w}_t|^2 + 1}, \kappa \bar{\gamma}_2 \beta_1 \beta_2 \|\mathbf{h}_{SR}\|^2 |\mathbf{h}_{RD} \mathbf{w}_t|^2\right), \tag{2.19}$$

with $\bar{\gamma}_1 = \frac{P_S}{\sigma_R^2}$ and $\bar{\gamma}_2 = \frac{P_S}{\sigma_D^2}$ where σ_R^2 and σ_D^2 are the noise power at R and D, respectively, β_2 models the path loss effect for the R-D link, and $\mathbf{H}_{\mathsf{SI}} \in \mathbb{C}^{M_R \times M_T}$ represents the residual SI channel whose elements are modeled as circularly symmetric complex Gaussian $\mathscr{CN}(0, \sigma_{\mathsf{SI}}^2)$ RVs in line with the literature [3, 6]. Note that the SINR in (2.19) has a much more complicated form than the corresponding SINR in conventional relay networks having nodes with fixed power supplies, since

the signal received is subject to "double fading" due to channel fading during the energy harvesting and information transmission phases.

We now present the following optimization problem to maximize the instantaneous rate w.r.t. α, $\mathbf{w}_t$, and $\mathbf{w}_r$:

$$\max_{\|\mathbf{w}_r\|=\|\mathbf{w}_t\|=1,\,\alpha\in[0,1)} R(\alpha,\mathbf{w}_t,\mathbf{w}_r) = (1-\alpha)\log_2\left(1+\gamma_{\mathsf{FD}}\right). \tag{2.20}$$

2.3.2 Relay Beamforming Designs

The optimization problem (2.20) is non-convex and challenging to solve. To this end, we consider the beamforming design problem for a given α. In this case, (2.20) turns to a problem of maximizing the minimum of the first hop SINR and second-hop signal-to-noise ratio (SNR), which is expressed as

$$\max_{\|\mathbf{w}_r\|=\|\mathbf{w}_t\|=1} \min\left(\frac{\bar{\gamma}_1\beta_1|\mathbf{w}_r^\dagger\mathbf{h}_{SR}|^2}{\kappa\bar{\gamma}_1\beta_1\|\mathbf{h}_{SR}\|^2|\mathbf{w}_r^\dagger\mathbf{H}_{\mathsf{SI}}\mathbf{w}_t|^2+1}, \kappa\bar{\gamma}_2\beta_1\beta_2\|\mathbf{h}_{SR}\|^2|\mathbf{h}_{RD}\mathbf{w}_t|^2\right). \tag{2.21}$$

In the following subsections, we provide optimum as well as suboptimum schemes for solving (2.21). In the optimum approach, the problem of joint transmit and receive beamforming design is considered, whereas in the suboptimum schemes, different linear receiver/transmitter techniques are employed at R.

2.3.2.1 Optimum Scheme

The optimum scheme corresponds to finding $\mathbf{w}_r$ and $\mathbf{w}_t$ such that the end to end SINR is maximized. Since the second-hop SNR does not depend on $\mathbf{w}_r$, the first-hop SINR can be maximized w.r.t $\mathbf{w}_r$ by fixing $\mathbf{w}_t$. This optimization problem is a generalized Rayleigh ratio problem which is globally maximized when $\mathbf{w}_r = \frac{\mathbf{A}^{-1}\mathbf{h}_{SR}}{\|\mathbf{A}^{-1}\mathbf{h}_{SR}\|}$ where $\mathbf{A} = \left(\kappa\bar{\gamma}_1\beta_1\|\mathbf{h}_{SR}\|^2\mathbf{H}_{\mathsf{SI}}\mathbf{w}_t\mathbf{w}_t^\dagger\mathbf{H}_{\mathsf{SI}}^\dagger + \mathbf{I}\right)$. Accordingly, by substituting $\mathbf{w}_r$ into (2.21), the corresponding problem can be solved and the $\mathbf{w}_t^{\mathsf{OPT}}$ is given in [44, Proposition 1].

2.3.2.2 TZF Scheme

We now present some suboptimum beamforming solutions. One such scheme takes the advantage of the multiple transmit antennas to completely cancel the SI [58]. To ensure this is feasible, the number of the transmit antennas at relay should be greater than one, i.e., $M_T > 1$. In addition, maximal ratio combining (MRC) is

applied at the relay input, i.e., $\mathbf{w}_r^{\mathsf{MRC}} = \frac{\mathbf{h}_{SR}}{\|\mathbf{h}_{SR}\|}$. This solution is named as the transmit zero-forcing (TZF) scheme in [44]. After substituting $\mathbf{w}_r^{\mathsf{MRC}}$ into (2.21), the optimal transmit beamforming vector $\mathbf{w}_t$ is obtained by solving the following problem:

$$\max_{\|\mathbf{w}_t\|=1} \quad |\mathbf{h}_{RD}\mathbf{w}_t|^2, \quad \text{s.t.} \quad \mathbf{h}_{SR}^{\dagger}\mathbf{H}_{\mathsf{SI}}\mathbf{w}_t = 0. \tag{2.22}$$

From the ZF constraint in (2.22), we know that $\mathbf{w}_t$ lies in the null space of $\mathbf{h}_{SR}^{\dagger}\mathbf{H}_{\mathsf{SI}}$. Denoting $\mathbf{B} \triangleq \mathbf{I} - \frac{\mathbf{H}_{\mathsf{SI}}^{\dagger}\mathbf{h}_{SR}\mathbf{h}_{SR}^{\dagger}\mathbf{H}_{\mathsf{SI}}}{\|\mathbf{h}_{SR}^{\dagger}\mathbf{H}_{\mathsf{SI}}\|^2}$, we have $\mathbf{w}_t^{\mathsf{ZF}} = \frac{\mathbf{B}\mathbf{h}_{RD}^{\dagger}}{\|\mathbf{B}\mathbf{h}_{RD}^{\dagger}\|}$. Now, substituting the $\mathbf{w}_t^{\mathsf{ZF}}$ and $\mathbf{w}_r^{\mathsf{MRC}}$ into (2.19), the end-to-end SNR can be expressed as [44]

$$\gamma_{\mathsf{TZF}} = \frac{\bar{\gamma}_1\beta_1\|\mathbf{h}_{SR}\|^2}{(1-\alpha)} \min\left(1-\alpha, \frac{\bar{\gamma}_2}{\bar{\gamma}_1}\eta\alpha\beta_2\|\tilde{\mathbf{h}}_{RD}\|^2\right), \tag{2.23}$$

where $\tilde{\mathbf{h}}_{RD}$ is an $(M_T - 1) \times 1$ vector and follows the chi-square distribution with $2(M_T - 1)$ degrees-of-freedom.

2.3.2.3 RZF Scheme

As an alternative solution, the transmit beamforming vector can be set using the maximal ratio transmit (MRT) principle, i.e., $\mathbf{w}_t^{\mathsf{MRT}} = \frac{\mathbf{h}_{RD}^{\dagger}}{\|\mathbf{h}_{RD}\|}$, and $\mathbf{w}_r$ can be designed with the ZF criterion $\mathbf{w}_r^{\dagger}\mathbf{H}_{\mathsf{SI}}\mathbf{w}_t = 0$. This solution is named as the receive ZF (RZF) scheme in [44]. To ensure feasibility of RZF, R should be equipped with $M_R > 1$ receive antennas. Substituting the MRT solution for $\mathbf{w}_t$ into (2.21), the optimal receive beamforming vector $\mathbf{w}_r$ is the solution to the following problem:

$$\max_{\|\mathbf{w}_r\|=1} \quad |\mathbf{w}_r^{\dagger}\mathbf{h}_{SR}|^2 \quad \text{s.t.} \quad \mathbf{w}_r^{\dagger}\mathbf{H}_{\mathsf{SI}}\mathbf{h}_{RD}^{\dagger} = 0. \tag{2.24}$$

Using similar steps as in the TZF scheme, the vector $\mathbf{w}_r$ can be obtained as $\mathbf{w}_r^{\mathsf{ZF}} = \frac{\mathbf{D}\mathbf{h}_{SR}}{\|\mathbf{D}\mathbf{h}_{SR}\|}$, where $\mathbf{D} \triangleq \mathbf{I} - \frac{\mathbf{H}_{\mathsf{SI}}\mathbf{h}_{RD}^{\dagger}\mathbf{h}_{RD}\mathbf{H}_{\mathsf{SI}}^{\dagger}}{\|\mathbf{H}_{\mathsf{SI}}\mathbf{h}_{RD}\|^2}$ is the projection idempotent matrix with rank $(M_T - 1)$. Invoking (2.19), and using $\mathbf{w}_r^{\mathsf{ZF}}$ and $\mathbf{w}_t^{\mathsf{MRT}}$, the end-to-end SNR can be expressed as [44]

$$\gamma_{\mathsf{RZF}} = \min\left(\bar{\gamma}_1\beta_1\|\tilde{\mathbf{h}}_{SR}\|^2, \kappa\bar{\gamma}_2\beta_1\beta_1\|\mathbf{h}_{SR}\|^2\|\mathbf{h}_{RD}\|^2\right), \tag{2.25}$$

where $\tilde{\mathbf{h}}_{SR}$ is a $(M_R - 1) \times 1$ vector and follows the chi-square distribution with $2(M_R - 1)$ degrees-of-freedom.

2.3.2.4 MRC/MRT Scheme

As another suboptimal approach, principles of MRT and MRC can be employed where $\mathbf{w}_r$ and $\mathbf{w}_t$ are set to match the first hop and second hop channel, respectively. Hence, $\mathbf{w}_r^{\mathsf{MRC}} = \mathbf{h}_{SR}/\|\mathbf{h}_{SR}\|$ and $\mathbf{w}_t^{\mathsf{MRT}} = \mathbf{h}_{RD}^{\dagger}/\|\mathbf{h}_{RD}\|$. Accordingly, by substituting $\mathbf{w}_r^{\mathsf{MRC}}$ and $\mathbf{w}_t^{\mathsf{MRT}}$ into (2.19), the end-to-end SINR can be expressed as

$$\gamma_{\mathsf{MRC}} = \min\left(c_1\|\mathbf{h}_{SR}\|^2\left(\kappa\bar{\gamma}_1\beta_1\frac{|\mathbf{h}_{SR}^{\dagger}\mathbf{H}_{\mathsf{SI}}\mathbf{h}_{RD}^{\dagger}|^2}{\|\mathbf{h}_{RD}\|^2}+1\right)^{-1}, c_2\|\mathbf{h}_{SR}\|^2\|\mathbf{h}_{RD}\|^2\right), \tag{2.26}$$

where $c_1 = \bar{\gamma}_1\beta_1$ and $c_2 = \kappa\bar{\gamma}_2\beta_1\beta_2$. It is worthwhile to note that the optimum, TZF, and RZF schemes reduce to the MRC/MRT scheme in the absence of SI. Although the MRC/MRT scheme is not optimal in the presence of SI, it could be favored in situations where compatibility with HD systems is a concern. Note that the MRC/MRT scheme requires only the knowledge of $\mathbf{h}_{SR}$ and $\mathbf{h}_{RD}$, whereas the other three schemes require the knowledge of $\mathbf{h}_{SR}$, $\mathbf{h}_{RD}$, and $\mathbf{H}_{\mathsf{SI}}$.

2.3.3 Performance Analysis

In this subsection, we evaluate the throughput of the instantaneous transmission and delay-constrained transmission in the cases of optimum and suboptimum schemes.

2.3.3.1 Instantaneous Transmission

The instantaneous throughput of the considered FD wireless-powered relaying system can be computed as [38]

$$R_{\mathsf{I}}(\alpha) = (1-\alpha)\log_2(1+\gamma_{\mathsf{FD}}), \tag{2.27}$$

where γ_{FD} (2.19) is a function of α. This expression reveals an interesting trade-off between energy harvesting duration and the instantaneous throughput. A longer energy harvesting time increases the harvested energy and consequently the second hop SNR, however, decreases the available time for information transmission and vice-versa. Therefore, an appropriate system design can optimize the instantaneous throughput by adjusting α. The optimal α is obtained by solving

$$\alpha^* = \underset{0<\alpha<1}{\arg\max}\, R_{\mathsf{I}}(\alpha). \tag{2.28}$$

For a given end-to-end SINR or SNR of a particular scheme, $R_{\mathsf{I}}(\alpha)$ in (2.28) is a concave function of α and the optimized α^* can be obtained by solving the

equation $\frac{dR_1(\alpha)}{d\alpha} = 0$. For example, in case of the optimum scheme, by substituting the optimum $\mathbf{w}_t^{\mathsf{OPT}}$, the instantaneous throughput as a function of α is

$$R_1(\alpha) = (1-\alpha)\log_2\left(1+\bar{\gamma}_1\beta_1\|\mathbf{h}_{SR}\|^2 \min\left(1-\frac{\alpha b_1}{(1-\alpha)+\alpha b_2}, \frac{\alpha b_0}{1-\alpha}\right)\right), \tag{2.29}$$

where $b_0 = \frac{\bar{\gamma}_2}{\bar{\gamma}_1}\eta\beta_2|\mathbf{h}_{RD}\mathbf{w}_t^{\mathsf{OPT}}|^2$, $b_1 = \eta\bar{\gamma}_1\beta_1|\mathbf{h}_{SR}^{\dagger}\mathbf{H}_{\mathsf{SI}}\mathbf{w}_t^{\mathsf{OPT}}|^2$, and $b_2 = \eta\bar{\gamma}_1\beta_1\|\mathbf{h}_{SR}\|^2 \|\mathbf{H}_{\mathsf{SI}}\mathbf{w}_t^{\mathsf{OPT}}\|^2$. The optimization problem (2.28) can be solved by using the procedure described in [44]. Let $a_0 = \eta\bar{\gamma}_2\beta_1\beta_2\|\mathbf{h}_{SR}\|^2|\mathbf{h}_{RD}\mathbf{w}_t^{\mathsf{OPT}}|^2$. Then, the optimal value of α can be obtained as

$$\alpha^*_{\text{Opt}} = \begin{cases} \frac{e^{W\left(\frac{a_0-1}{e}\right)+1}-1}{a_0-1+e^{W\left(\frac{a_0-1}{e}\right)+1}}, & \text{if} \quad e^{W\left(\frac{a_0-1}{e}\right)+1} < \frac{a_0}{\alpha_0}+1; \\ \frac{1}{1+\alpha_0}, & \text{otherwise}, \end{cases} \tag{2.30}$$

where $\alpha_0 = \frac{2b_0b_2}{(b_2-b_1-b_0)+\sqrt{b_0^2+(b_2-b_1)^2+2b_0(b_1+b_2)}}$.

Furthermore, optimal α for the proposed suboptimum beamforming schemes can be obtained from (2.30) by replacing a_0 and α_0 from Table 2.2.

An important point to stress is that, in contrast to the suboptimum schemes, the obtained solution of $\mathbf{w}_t$ in the optimum scheme depends on α. As a consequence, joint optimization w.r.t. α and $\mathbf{w}_t$ is required. There are two ways to solve this joint optimization. The first way is to find $\mathbf{w}_t$ by following Proposition 1 and next performing a one-dimensional line search over $0 < \alpha < 1$. This guarantees the global optimum solutions for α and $\mathbf{w}_t$. Another way is to employ an iterative approach where each iteration step consists of a two-step optimization, i.e., optimizing $\mathbf{w}_t$ for a given α and vice-versa.

Figure 2.5 shows the instantaneous throughput versus the time portion α of the beamforming schemes for an arbitrary frame of block time T. In the simulations, we set the channel variances as $\beta_1 = d_1^{-\nu}$ and $\beta_2 = d_2^{-\nu}$, where d_1 and d_2 denote the distances between the S and R and between R and D, respectively and ν is the path loss exponent. As expected, the optimum scheme outperforms all suboptimum schemes on all TS values. In addition, simulation results, not shown in the figure to avoid clutter, reveal that the values of the optimal α decrease as either the number of

Table 2.2 Suboptimum beamforming schemes' parameters

Scheme	a_0	α_0
TZF	$\eta\bar{\gamma}_2\beta_1\beta_2\|\mathbf{h}_{SR}\|^2\|\mathbf{B}\mathbf{h}_{RD}\|^2$	$\eta\bar{\gamma}_1\bar{\gamma}_2\beta_2\|\mathbf{B}\mathbf{h}_{RD}\|^2$
RZF	$\eta\bar{\gamma}_2\beta_1\beta_2\|\mathbf{h}_{SR}\|^2\|\mathbf{h}_{RD}\|^2$	$\frac{\bar{\gamma}_2}{\bar{\gamma}_1}\eta\beta_2\frac{\|\mathbf{h}_{SR}\|^2\|\mathbf{h}_{RD}\|^2}{\|\mathbf{D}\mathbf{h}_{SR}\|^2}$
MRC/MRT	$\eta\bar{\gamma}_2\beta_1\beta_2\|\mathbf{h}_{SR}\|^2\|\mathbf{h}_{RD}\|^2$	$2\eta\bar{\gamma}_1\beta_1\frac{\|\mathbf{h}_{SR}^{\dagger}\mathbf{H}_{\mathsf{SI}}\mathbf{h}_{RD}^{\dagger}\|^2}{\|\mathbf{h}_{RD}\|^2}\Big/\left(\sqrt{1+\frac{4\beta_1\bar{\gamma}_1^2}{\beta_2\bar{\gamma}_2}\frac{\|\mathbf{h}_{SR}^{\dagger}\mathbf{H}_{\mathsf{SI}}\mathbf{h}_{RD}^{\dagger}\|^2}{\|\mathbf{h}_{RD}\|^4}}-1\right)$

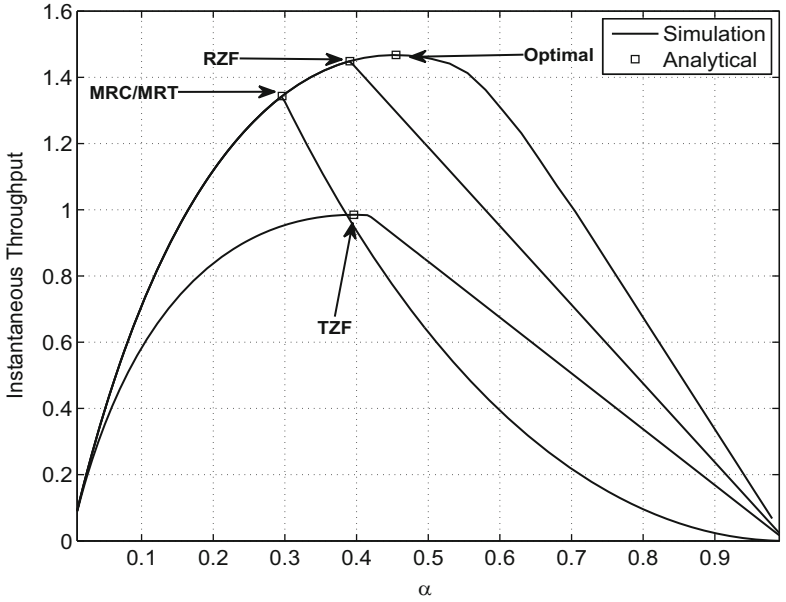

Fig. 2.5 Instantaneous throughput versus α ($M_T = M_R = 3$, $P_S = 20$ dBm, $d_1 = 20$, $d_2 = 10$ and $\nu = 3$)

relays' receive antennas or the sources' transmit power is increased. This is because in these cases the relay node can harvest the same amount of energy in a shorter time. Therefore, more time must be allocated to the information transmission phase in order to improve the throughput.

2.3.3.2 Delay-Constrained Transmission

Throughput of the delay-constrained transmission can be determined by evaluating the outage probability, P_{out}, at a fixed source transmission rate R_c bits/s/Hz where $R_c = \log_2(1 + \gamma_{\text{th}})$ and γ_{th} is the value of SNR for correct data detection at the destination [59]. Due to the time variation of the fading channel, outage events where the instantaneous channel capacity is below the source transmission rate may occur. Therefore, P_{out} can be written as

$$\mathsf{P}_{\text{out}} = \Pr(\gamma_{\text{FD}} < \gamma_{\text{th}}) = F_{\gamma_{\text{FD}}}(\gamma_{\text{th}}), \tag{2.31}$$

where $\gamma_{\text{th}} = 2^{R_c} - 1$. Given that the source is communicating R_c bits/sec/Hz and $(1 - \alpha)T$ is the effective communication time from S to D in the block time T seconds, the throughput, $R_{\text{D}}(\alpha)$, in delay-constrained transmission mode is given by [59]

$$R_{\text{D}}(\alpha) = (1 - \mathsf{P}_{\text{out}})R_c(1 - \alpha). \tag{2.32}$$

In order to determine the delay-constrained throughput, it is important to characterize the outage probability of each scheme. In the following, both exact and asymptotic expressions for the outage probability of the TZF, RZF, and MRC/MRT schemes are presented. We notice that derivation of the outage probability of the optimum scheme is difficult. Hence we have resorted to simulations for evaluating the delay-constrained throughput of the optimum scheme in Fig. 2.6.

According to (2.23), (2.25), and (2.31), the outage probability at D for TZF and RZF schemes can be expressed as [44]

$$\mathsf{P}_{\text{out}}^{\text{TZF}} = 1 - \frac{1}{\Gamma(M_R)} \int_{\frac{\gamma_{\text{th}}}{\bar{\gamma}_1\beta_1}}^{\infty} Q\left(M_T - 1, \frac{1}{\kappa\bar{\gamma}_2\beta_1\beta_2}\frac{\gamma_{\text{th}}}{x}\right) x^{M_R-1}\mathrm{e}^{-x}dx, \tag{2.33}$$

and

$$\mathsf{P}_{\text{out}}^{\text{RZF}} = 1 - Q\left(M_R, \frac{\gamma_{\text{th}}}{\bar{\gamma}_1\beta_1}\right) + \frac{1}{\Gamma(M_R)}\left(\int_{\frac{\gamma_{\text{th}}}{\bar{\gamma}_1\beta_1}}^{\infty} P\left(M_T, \frac{1}{\kappa\bar{\gamma}_2\beta_1\beta_2}\frac{\gamma_{\text{th}}}{x}\right) x^{M_R-1}\mathrm{e}^{-x}dx \right.$$
$$\left. + \left(\frac{\gamma_{\text{th}}}{\bar{\gamma}_1\beta_1}\right)^{M_R-1} \int_{\frac{\gamma_{\text{th}}}{\bar{\gamma}_1\beta_1}}^{\infty} Q\left(M_T, \frac{1}{\kappa\bar{\gamma}_2\beta_1\beta_2}\frac{\gamma_{\text{th}}}{x}\right)\mathrm{e}^{-x}dx\right), \tag{2.34}$$

respectively, where $Q(a,x) = \Gamma(a,x)/\Gamma(a)$ and $P(a,x) = \gamma(a,x)/\Gamma(a)$.

The outage probability analysis of the MRC/MRT scheme for arbitrary M_T and M_R appears to be cumbersome. Therefore, we only consider two special cases:

- Case (1) $M_T = 1, M_R \geq 1$
- Case (2) $M_T \geq 1, M_R = 1$

Statistics of the associated RVs in both of these special cases can be found. Therefore, using (2.26) and (2.31), outage probability of Cases 1 and 2 can be expressed as [44]

$$\mathsf{P}_{\text{out}}^{\text{MRC,1}} = 1 - \int_{\frac{\gamma_{\text{th}}}{\bar{\gamma}_1\beta_1}}^{\infty} G_{23}^{21}\left(\frac{1}{\kappa\bar{\gamma}_1\beta_1\sigma_{\text{SI}}^2}\left(\frac{c_1}{\gamma_{\text{th}}} - \frac{1}{x}\right) \middle| \begin{matrix} 1, M_R \\ 1, M_R, 0 \end{matrix}\right) \frac{x^{M_R-1}}{\Gamma(M_R)}\mathrm{e}^{-\left(x+\frac{\gamma_{\text{th}}}{c_2 x}\right)}dx, \tag{2.35}$$

and

$$\mathsf{P}_{\text{out}}^{\text{MRC,2}} = 1 - \int_{\frac{\gamma_{\text{th}}}{\bar{\gamma}_1\beta_1}}^{\infty} \left(1 - \mathrm{e}^{-\frac{1}{c_2 x}\left(\frac{c_1 x}{\gamma_{\text{th}}} - 1\right)}\right) Q\left(M_T, \frac{\gamma_{\text{th}}}{\kappa\bar{\gamma}_1\beta_1\sigma_{\text{SI}}^2 x}\right)\mathrm{e}^{-x}dx, \tag{2.36}$$

respectively. The integrals in (2.33)–(2.36) do not admit a closed-form solution, however, they can be evaluated numerically. To gain further insights, we now look into the high SNR regime and present simple approximations from [44]. These

expressions enable the characterization of the achievable diversity order of the TZF, RZF, and MRT/MRC schemes.

Proposition 2. *In the high SNR regime, i.e., $\bar{\gamma}_1, \bar{\gamma}_2 \to \infty$, the outage probability of the TZF scheme can be approximated as:* $\mathsf{P}_{\text{out}}^{\text{TZF}} \approx$

$$\begin{cases} \left(\frac{1}{\Gamma(M_R+1)} + \frac{1}{\Gamma(M_T-1)\Gamma(M_R)} \sum_{k=0}^{\infty} \frac{(-1)^{k+1}}{k!(k+M_T)} \left(\frac{\sigma_D^2}{\sigma_R^2} \frac{1}{\kappa\bar{\beta}_2} \right)^{M_T+k-1} \frac{1}{M_R-M_T-k+1} \right) \left(\frac{\gamma_{\text{th}}}{\bar{\gamma}_1\bar{\beta}_1} \right)^{M_R}, & \\ & M_T > M_R+1, \\ \frac{1}{\Gamma(M_R+1)} \left(1 + \frac{1}{\Gamma(M_R)} \left(\ln\left(\frac{\bar{\gamma}_1\bar{\beta}_1}{\gamma_{\text{th}}} \right) + \psi(1) \right) \left(\frac{\sigma_D^2}{\sigma_R^2} \frac{1}{\kappa\bar{\beta}_2} \right)^{M_R} \right) \left(\frac{\gamma_{\text{th}}}{\bar{\gamma}_1\bar{\beta}_1} \right)^{M_R}, & M_T = M_R+1, \\ \frac{\Gamma(M_R-M_T+1)}{\Gamma(M_T)\Gamma(M_R)} \left(\frac{1}{\kappa\bar{\beta}_2} \right)^{M_T-1} \left(\frac{\gamma_{\text{th}}}{\bar{\gamma}_2\bar{\beta}_1} \right)^{M_T-1}, & M_T < M_R+1. \end{cases} \tag{2.37}$$

By inspecting (2.37), we see that the TZF scheme achieves a diversity order of $\min(M_R, M_T - 1)$. This is intuitive since one degree-of-freedom is used for interference cancellation. Moreover, for the case $M_R + 1 = M_T$, $\mathsf{P}_{\text{out}}^{\text{TZF}}$ decays as $\bar{\gamma}_1^{-M_R} \ln(\bar{\gamma}_1)$ rather than $\bar{\gamma}_1^{-M_R}$ as in the conventional case with fixed power, which implies that in the energy harvesting case the slope of $\mathsf{P}_{\text{out}}^{\text{TZF}}$ converges much slowly.

Proposition 3. *In the high SNR regime, i.e., $\bar{\gamma}_1, \bar{\gamma}_2 \to \infty$, the outage probability of the RZF scheme can be approximated as*

$$\mathsf{P}_{\text{out}}^{\text{RZF}} \approx \begin{cases} \frac{1}{\Gamma(M_R)} \left(\frac{\gamma_{\text{th}}}{\bar{\gamma}_1\bar{\beta}_1} \right)^{M_R-1}, & M_R < M_T+1, \\ \frac{1}{\Gamma(M_R)} \left(1 + \frac{1}{\Gamma(M_T+1)} \left(\frac{\sigma_D^2}{\sigma_R^2} \frac{1}{\kappa\bar{\beta}_2} \right)^{M_T} \right) \left(\frac{\gamma_{\text{th}}}{\bar{\gamma}_1\bar{\beta}_1} \right)^{M_T}, & M_R = M_T+1, \\ \frac{\Gamma(M_R-M_T)}{\Gamma(M_R)\Gamma(M_T+1)} \left(\frac{1}{\kappa\bar{\beta}_2} \right)^{M_T} \left(\frac{\gamma_{\text{th}}}{\bar{\gamma}_2\bar{\beta}_1} \right)^{M_T}, & M_R > M_T+1. \end{cases} \tag{2.38}$$

Proposition 3 indicates that the RZF scheme achieves a diversity order of $\min(M_R - 1, M_T)$. This result is also intuitively satisfying since one degree-of-freedom should be allocated for SI cancellation at the receive side of R.

Proposition 4. *In the high SNR regime, i.e., $\bar{\gamma}_1, \bar{\gamma}_2 \to \infty$, with $M_T = 1$ the outage probability of the MRC/MRT scheme can be approximated as*

$$\mathsf{P}_{\text{out}}^{\text{MRC,1}} \approx 1 - \frac{2}{\Gamma(M_R)} G_{23}^{21} \left(\frac{1}{\kappa\sigma_{\text{SI}}^2\gamma_{\text{th}}} \,\middle|\, \begin{matrix} 1, M_R \\ 1, M_R, 0 \end{matrix} \right) \left(\frac{\gamma_{\text{th}}}{\kappa\bar{\gamma}_2\bar{\beta}_1\bar{\beta}_2} \right)^{\frac{M_R}{2}} K_{M_R} \left(2\sqrt{\frac{\gamma_{\text{th}}}{\kappa\bar{\gamma}_2\bar{\beta}_1\bar{\beta}_2}} \right). \tag{2.39}$$

Moreover, by applying a Bessel function approximation for small arguments, $K_\nu(x) \approx \frac{\Gamma(\nu)}{2} \left(\frac{x}{2} \right)^{-\nu}$, in (2.39) we can write

$$\mathsf{P}_{\text{out}}^{\text{MRC,1}} \to 1 - G_{23}^{21}\left(\frac{1}{\kappa\sigma_{\text{SI}}^2\gamma_{\text{th}}}\,\middle|\,\begin{matrix}1, M_R\\ 1, M_R, 0\end{matrix}\right). \tag{2.40}$$

Note that (2.40) presents the outage probability floor and indicates that the MRC/MRT scheme with $M_T = 1$ exhibits a zero-diversity order in presence of residual SI.

Proposition 5. *In the high SNR regime, i.e., $\bar{\gamma}_1, \bar{\gamma}_2 \to \infty$, with $M_R = 1$, the outage probability of the MRC/MRT scheme can be approximated as*

$$\mathsf{P}_{\text{out}}^{\text{MRC,2}} \approx 1 - \left(1 - \mathrm{e}^{-\frac{1}{\kappa\sigma_{\text{SI}}^2\gamma_{\text{th}}}}\right)\left(\mathrm{e}^{-\frac{\gamma_{\text{th}}}{\bar{\gamma}_1\beta_1}} - \frac{\gamma_{\text{th}}}{\bar{\gamma}_1\beta_1\Gamma(M_T)}\sum_{k=0}^{\infty}\frac{(-1)^k}{k!(M_T+k)}\right.$$
$$\left.\times\left(\frac{\bar{\gamma}_1}{\bar{\gamma}_2}\frac{1}{\kappa\beta_2}\right)^{M_T+k} E_{M_T+k}\left(\frac{\gamma_{\text{th}}}{\bar{\gamma}_1\beta_1}\right)\right). \tag{2.41}$$

At this point, it is important to determine the value of α that maximizes the throughput. We note that delay-constrained throughput should converge to the ceiling value of $R_c(1-\alpha)$ when $\mathsf{P}_{\text{out}} \to 0$. For each beamforming scheme we observe that P_{out} is a complicated function of α and it decreases as the value of α is increased. However, this will lead to the decrease of the term $(1-\alpha)$ at the same time. Therefore, an optimal value of α that maximizes the delay-constrained throughput exists and it can be found by solving the following optimization problem:

$$\alpha^* = \underset{0<\alpha<1}{\arg\max}\, R_{\mathsf{D}}(\alpha). \tag{2.42}$$

Given (2.33)–(2.36), the optimization problem in (2.42) does not admit closed-form solutions. However, the optimal α^* can be solved numerically. Figure 2.6 demonstrates the impact of optimal α on the delay-constrained throughput. The superior performance of the optimum scheme compared to suboptimal schemes is more pronounced especially between 0.4 and 0.8 values of α. The highest throughput with optimized α for the optimum, RZF, MRC/MRT, and TZF schemes are given by 0.6517, 0.6396, 0.5672, and 0.4824, respectively. Moreover, we see that each one of the TZF, RZF, and MRC/MRT schemes can surpass other schemes depending on the value of α. This observation reveals the existence of various design choices when performance-complexity trade-off becomes a design factor. It is also observed that all schemes achieve significant throughput gains as compared to the HD mode.

Simulations also show that as long as a beamforming scheme is capable of cancelling the SI, the delay-constrained throughput can be improved as either the number of relays' receive antennas or the sources' transmit power is increased. This is because, the amount of the harvested energy at the relay is increased and consequently the outage probability is decreased, i.e., $\mathsf{P}_{\text{out}} \to 0$. Therefore, the delay-constrained throughput tends to $R_{\mathsf{D}}(\alpha) \to R_c(1-\alpha)$ which approximately

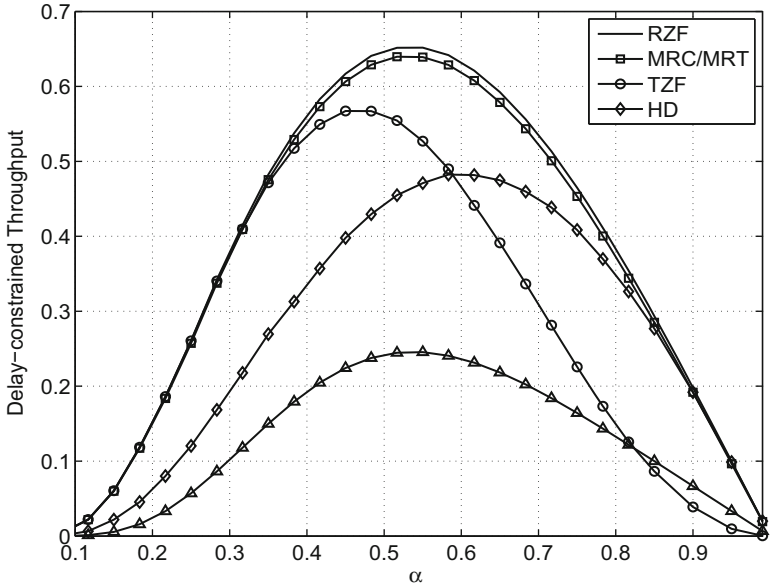

Fig. 2.6 Delay-constrained throughput of different schemes ($M_T = M_R = 3$, $P_S = 10$ dBm, $d_1 = 15$, $d_2 = 10$, $\eta = 0.5$, and $R_c = 2$)

deliver the highest throughput for some small values of the α. However, an excessive amount of harvested energy at R is not always advantageous. For example, in case of MRC/MRT scheme it is detrimental since it results in a strong irreducible SI effect at R.

2.4 Full-Duplex Information and Power Transfer with Hybrid AP

If a BS or an AP is empowered with FD operation, simultaneous uplink and downlink transmission among a set of users can be implemented. Thus, in addition to FD bi-directional and relay topologies, some papers have also considered the above scenario [45, 46, 60]. The gains that can be achieved with the help of the FD BS (or AP) topology are largely influenced by the residual SI at the BS (or AP) as well as the inter-user interference at downlink users due to uplink user transmissions. Moreover in multi-cell environments, compared to HD operation that employs time-division duplexing (TDD) or frequency-division duplexing, simultaneous uplink and downlink transmissions can cause different interference patterns [61]. Hence, in order to reap the spectral efficiency gains promised by the FD mode, systems based on the BS topology need to be carefully designed [62].

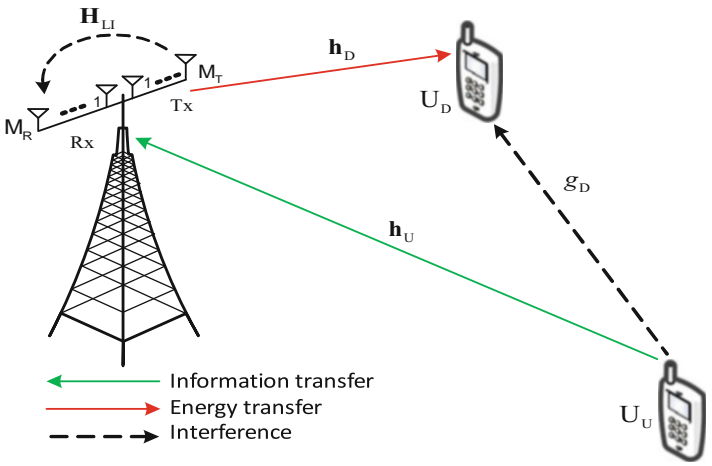

Fig. 2.7 FD hybrid data-and-energy transfer system

In the sequel, a design to maximize the rate-energy region of a FD system with one multi-antenna hybrid AP, one uplink user, and one energy harvester downlink user is presented.

2.4.1 System Model

Consider a FD system, as shown in Fig. 2.7, consisting of a hybrid AP, one uplink user (U_{U}), and one downlink user (U_{D}). Both U_{U} and U_{D} are equipped with a single antenna, while the AP is equipped with M_R receive antennas and M_T transmit antennas. The FD AP communicates with U_{U} in the uplink and transmits energy to U_{D} in the downlink at the same time over the same frequency band [45, 46]. Denote $\mathbf{h}_{\mathsf{U}} \in \mathbb{C}^{M_R \times 1}$ as the channel vector from the U_{U} to AP, $\mathbf{h}_{\mathsf{D}} \in \mathbb{C}^{M_T \times 1}$ as the channel vector from AP to the U_{D}, $\mathbf{H}_{\mathsf{SI}} \in \mathbb{C}^{M_R \times M_T}$ as the residual SI channel from transmit antennas to the receive antennas at FD AP, and g_{D} as the channel coefficient from U_{U} to U_{D}. The transmit and receive beamformers at the AP are $\mathbf{w}_t$ and $\mathbf{w}_r$, respectively.

Given the total transmit power P_{AP} at the AP, the harvested energy at the U_{D} is $E = \eta \left(P_{\mathsf{AP}} |\mathbf{h}_{\mathsf{D}}^{\dagger} \mathbf{w}_t|^2 + P_{\mathsf{U}} |g_{\mathsf{D}}|^2 \right)$ where P_{U} is the transmit power of U_{U}. Moreover, SINR at the FD AP can be expressed as

$$\gamma_{\mathsf{U}} = \frac{P_{\mathsf{U}} |\mathbf{w}_r^{\dagger} \mathbf{h}_{\mathsf{U}}|^2}{P_{\mathsf{AP}} |\mathbf{w}_r^{\dagger} \mathbf{H}_{\mathsf{SI}} \mathbf{w}_t|^2 + \|\mathbf{w}_r\|^2 \sigma_n^2}, \tag{2.43}$$

where σ_n^2 is the noise power at the AP.

Our objective is to maximize the uplink rate of U_{U} by jointly designing the transmit and receive beamformers at the AP, subject to an EH constraints. Thus, the following optimization problem is formulated as:

$$\begin{aligned} \max_{\|\mathbf{w}_r\|=\|\mathbf{w}_t\|=1} \quad & R_{\mathsf{U}} = \log_2\left(1+\frac{P_{\mathsf{U}}|\mathbf{w}_r^{\dagger}\mathbf{h}_{\mathsf{U}}|^2}{P_{\mathsf{AP}}|\mathbf{w}_r^{\dagger}\mathbf{H}_{\mathsf{SI}}\mathbf{w}_t|^2+\sigma_n^2}\right), \\ \text{s.t.} \quad & \eta\left(P_{\mathsf{AP}}|\mathbf{h}_{\mathsf{D}}^{\dagger}\mathbf{w}_t|^2+P_{\mathsf{U}}|g_{\mathsf{D}}|^2\right)\geq \bar{E}, \end{aligned} \tag{2.44}$$

where $\bar{E}$ denotes the minimum requirement of the harvested energy at the U_{D}.

2.4.2 *Precoding Design for Rate-Energy Maximization*

The joint optimization problem (2.44) can be solved by first optimizing over $\mathbf{w}_r$ while fixing $\mathbf{w}_t$. For a given $\mathbf{w}_t$ that satisfies the constraint in (2.44), the optimization problem w.r.t. $\mathbf{w}_r$ reduces to

$$f_{\text{re}} \triangleq \max_{\|\mathbf{w}_r\|=1} \frac{P_{\mathsf{U}}|\mathbf{w}_r^{\dagger}\mathbf{h}_{\mathsf{U}}|^2}{P_{\mathsf{AP}}|\mathbf{w}_r^{\dagger}\mathbf{H}_{\mathsf{SI}}\mathbf{w}_t|^2+\sigma_n^2}. \tag{2.45}$$

Define $\bar{\mathbf{A}} \triangleq [P_{\mathsf{AP}}\mathbf{H}_{\mathsf{SI}}\mathbf{w}_t\mathbf{w}_t^{\dagger}\mathbf{H}_{\mathsf{SI}}^{\dagger}+\sigma_n^2\mathbf{I}]$. The optimum $\mathbf{w}_r$ is given by

$$\mathbf{w}_r = \frac{\bar{\mathbf{A}}^{-1}\mathbf{h}_{\mathsf{U}}}{\|\bar{\mathbf{A}}^{-1}\mathbf{h}_{\mathsf{U}}\|}. \tag{2.46}$$

Substitution of $\mathbf{w}_r$ from (2.46) into (2.45) yields

$$\begin{aligned} f_{\text{re}} &= P_{\mathsf{U}}\mathbf{h}_{\mathsf{U}}^{\dagger}[P_{\mathsf{AP}}\mathbf{H}_{\mathsf{SI}}\mathbf{w}_t\mathbf{w}_t^{\dagger}\mathbf{H}_{\mathsf{SI}}^{\dagger}+\sigma_n^2\mathbf{I}]^{-1}\mathbf{h}_{\mathsf{U}} \\ &= \frac{P_{\mathsf{U}}}{\sigma_n^2}\left[\|\mathbf{h}_{\mathsf{U}}\|^2-\frac{P_{\mathsf{AP}}\mathbf{h}_{\mathsf{U}}^{\dagger}\mathbf{H}_{\mathsf{SI}}\mathbf{w}_t\mathbf{w}_t^{\dagger}\mathbf{H}_{\mathsf{SI}}^{\dagger}\mathbf{h}_{\mathsf{U}}}{\sigma_n^2+P_{\mathsf{AP}}\mathbf{w}_t\mathbf{H}_{\mathsf{SI}}^{\dagger}\mathbf{H}_{\mathsf{SI}}\mathbf{w}_t}\right], \end{aligned} \tag{2.47}$$

where the second expression is due to the application of Sherman–Morrison formula [30]. Consequently, the joint optimization (2.44) reduces to an optimization problem over $\mathbf{w}_t$, which is expressed as

$$\begin{aligned} \max_{\|\mathbf{w}_t\|=1} \quad & \log_2(1+f_{\text{re}}) \\ \text{s.t.} \quad & \eta\left(P_{\mathsf{AP}}|\mathbf{h}_{\mathsf{D}}^{\dagger}\mathbf{w}_t|^2+P_{\mathsf{U}}|g_{\mathsf{D}}|^2\right)\geq \bar{E}, \end{aligned} \tag{2.48}$$

which is equivalent to

$$\min_{\|\mathbf{w}_t\|=1} \quad \frac{\mathbf{h}_{\mathsf{U}}^{\dagger}\mathbf{H}_{\mathsf{SI}}\mathbf{w}_t\mathbf{w}_t^{\dagger}\mathbf{H}_{\mathsf{SI}}^{\dagger}\mathbf{h}_{\mathsf{U}}}{\sigma_n^2 + P_{\mathsf{AP}}\mathbf{w}_t\mathbf{H}_{\mathsf{SI}}^{\dagger}\mathbf{H}_{\mathsf{SI}}\mathbf{w}_t}$$
$$\text{s.t.} \quad |\mathbf{h}_{\mathsf{D}}^{\dagger}\mathbf{w}_t|^2 \geq \frac{1}{P_{\mathsf{AP}}}\left[\frac{\bar{E}}{\eta} - P_{\mathsf{U}}|g_{\mathsf{D}}|^2\right]. \tag{2.49}$$

The optimization problem (2.49) does not admit a closed-form solution for the optimum $\mathbf{w}_t$. Its numerical solution is attainable, however, (2.49) is not a convex problem. Introducing an auxiliary variable τ, a matrix variable $\mathbf{W}_t = \mathbf{w}_t\mathbf{w}_t^{\dagger}$, and relaxing the non-convex rank-one constraint on $\mathbf{W}_t$, (2.49) can be expressed as an SDR problem

$$\begin{aligned}
&\min_{\mathbf{W}_t,\tau} \quad \tau \\
&\text{s.t.} \quad \text{tr}\left(\mathbf{W}_t\left(\tau\left(\sigma_n^2\mathbf{I} + \mathbf{H}_{\mathsf{SI}}\mathbf{H}_{\mathsf{SI}}^{\dagger}\right) - \mathbf{H}_{\mathsf{SI}}^{\dagger}\mathbf{h}_{\mathsf{U}}\mathbf{h}_{\mathsf{U}}^{\dagger}\mathbf{H}_{\mathsf{SI}}\right)\right) \geq 0, \\
&\qquad \text{tr}\left(\mathbf{W}_t\mathbf{h}_{\mathsf{D}}\mathbf{h}_{\mathsf{D}}^{\dagger}\right) \geq \bar{c}, \\
&\qquad \text{tr}\left(\mathbf{W}_t\right) = 1, \ \mathbf{W}_t \succeq 0,
\end{aligned} \tag{2.50}$$

where $\bar{c} = \frac{1}{P_{\mathsf{AP}}}\left[\frac{\bar{E}}{\eta} - P_{\mathsf{U}}|g_{\mathsf{D}}|^2\right]$. Let $\mathbf{W}_t^*$ be an optimum solution in (2.49) for a given τ. Using similar arguments as in the case of (2.7), it can be shown that $\mathbf{W}_t^*$ is rank-one. The optimization (w.r.t. $\mathbf{W}_t$) has to be solved for all possible values of τ, where $\tau \in [0, \tau_{\max}]$, i.e., a grid search over τ is required.[1] However, the computational cost of solving (2.49) can be significantly reduced by solving it as a feasibility problem. In particular, it is clear that the minimum τ is the one for which the optimization problem (2.49) turns to be feasible. As such, the joint optimum solutions of τ and $\mathbf{W}_t$ can be determined using the following steps:

1. Define a fine grid of τ in steps of $\partial\tau$,
2. Solve (2.49) with the smallest τ, i.e., $\tau = 0$,
3. If feasible, stop and output τ and $\mathbf{W}_t$,
4. If not, repeat step (2) with the increment of $\partial\tau$.

As soon as the problem is feasible, the above iterative approach can be stopped and the optimum $\mathbf{w}_t$ is recovered from the eigenvalue decomposition of $\mathbf{W}_t$. In particular, since the optimum happens to be $\mathbf{W}_t$ rank-one, $\mathbf{w}_t$ is the eigenvector corresponding to the largest eigenvalue (also the only one non-zero eigenvalue) of $\mathbf{W}_t$.

[1] Although $\tau_{\max}$ can be analytically calculated, it is not required for solving (2.49).

In order to understand the gains of FD operation, a common practice adopted in the literature is to compare with HD mode. We compare the performance of FD and HD modes of operation at the hybrid AP under the so-called RF chain preserved condition.[2] In the HD mode of AP operation, hybrid AP employs orthogonal time slots to serve the uplink and downlink users. At the uplink we use MRC to combine the received signals and deploy MRT as the beamformer to transmit energy towards the downlink user. Without loss of any generality, we normalize T to 1 and devote $0 < \alpha^{\mathsf{HD}} \leq 1$ fraction of the block time for energy transfer and $(1 - \alpha^{\mathsf{HD}})$ for information transfer. For a fair comparison, the EH constraint of the downlink user in the HD mode is set as the harvested energy in the FD mode. Therefore, $\alpha^{\mathsf{HD}} = \frac{E}{\eta P_{\mathsf{AP}} \|\mathbf{h}_{\mathsf{D}}\|^2}$ and $R_{\mathsf{U}}^{\mathsf{HD}} = (1 - \alpha^{\mathsf{HD}}) \log_2 \left(1 + P_{\mathsf{U}} \|\mathbf{h}_{\mathsf{U}}\|^2 / \sigma_n^2\right)$.

Figure 2.8 shows rate-energy region with $M_R = 2$ and $M_T = 5$, when $P_{\mathsf{U}} = 10\,\text{dBm}$, $P_{\mathsf{AP}} = 40\,\text{dBm}$, and $\eta = 0.7$. We consider a scenario where a line-of-sight (LoS) link is present between the AP and the downlink user and for which the complex channel gain vector from the AP to downlink user can be represented by the Rician fading model as [63]

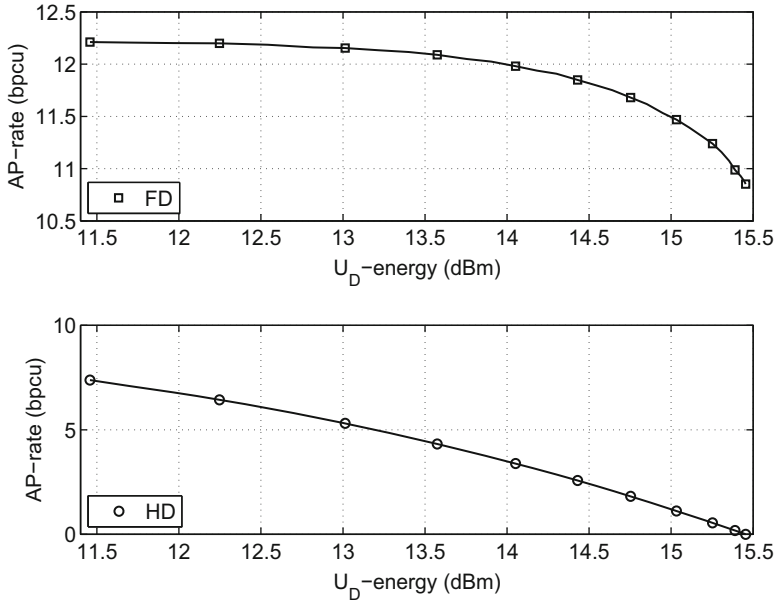

Fig. 2.8 Comparison of rate-energy regions with $M_R = 2$ and $M_T = 5$

[2]RF chains have a higher cost than antenna elements and therefore FD/HD studies based on RF chain preserved condition as compared to "antenna-preserved" condition have been widely used in the literature for fair comparison.

$$\mathbf{h}_{\mathsf{D}} = \sqrt{\frac{\beta K}{K+1}}\mathbf{h}_{\mathsf{D},d} + \sqrt{\frac{\beta}{K+1}}\mathbf{h}_{\mathsf{D},s}, \tag{2.51}$$

where $\mathbf{h}_{\mathsf{D},d}$ represents the LoS component, β denotes path loss effect, K is the Rician K-factor, and $\mathbf{h}_{\mathsf{D},s}$ denotes the scattered components of the channel. Furthermore, we utilize the far-field uniform linear antenna array model as in [63].

The EH constraint is varied from 0 dBm to $\bar{E}^{\max}$ which is obtained by applying MRT beamformer at the AP. We also assume that the distance between the AP and U_{D} is 10 meters and $K = 5$ dB. The curves in Fig. 2.8 show that the FD mode of operation can provide significant performance gains. For example, FD AP can provide a higher uplink rate as compared to the HD mode in all regions of the harvested energy. Moreover, the decrease in the uplink rate when the harvested energy varies from the minimum value to the maximum is more in HD. Under HD operation, the downlink user does not exploit the inter-user interference for energy harvesting, a high value of α^{HD} causes the uplink rate to be reduced.

2.5 Future Directions

Research community faces a number of challenges ahead for the design and deployment of FD wireless-powered systems. From a practical perspective these challenges can be categorized into several key areas as outlined below:

- **Full-duplex transceiver design:** Research on SI cancellation algorithm development is required to guarantee practical FD transceiver implementation with flexible energy harvesting capability. Research on SI mitigation techniques with low energy consumption is crucial since circuitry required in the cancellation step could drain harvested energy significantly. Further, nonlinear behavior of the energy harvesting circuit components needs to be captured accurately via new mathematical modeling. Such advances will offer new opportunities for system optimization. In order to test transceiver solutions, test-bed development needs to be undertaken as well.
- **Interference exploitation:** Traditionally in wireless system design, interference has been considered as a detrimental factor. However, in energy harvesting communications, interference can be exploited as an extra source of energy. A FD BS can simultaneously schedule the uplink and downlink transmission on the same resource block, and hence as compared to traditional HD systems, high interference conditions within the cell and from neighboring cells can be expected [62]. As of now, how such interference can be best exploited to improve the performance of FD wireless-powered systems is unknown. Therefore, it is worthwhile to conduct research on transmission schemes, scheduling and interference cancellation algorithms that can strike a good balance between harvested energy and performance.

- **MIMO implementation:** In the context of FD wireless-powered systems, MIMO techniques can be used for spatial-domain SI cancellation and to harvest more energy. However, often optimal solutions that maximize the rate-energy trade-off in FD wireless-powered systems are complex and require significant energy consumption for computation purposes. Hence, it is worth looking at low-complexity MIMO schemes suitable for efficient FD MIMO design. As an example, flexible and low-complexity MIMO architectures that dynamically adapt to the energy harvesting environment and assign different number of antennas for energy harvesting/information transfer seem an interesting direction to pursue.
- **MAC layer design:** While majority of research on FD so far have considered physical layer aspects, research work on MAC layer issues has been still on infancy. In particular, MAC layer operations from an energy consumption point are less understood. Significant research efforts must be dedicated to model FD MAC layer behavior and propose algorithms that can operate with minimum energy. Moreover, whenever possible, the design of cross-layer algorithms that can exploit information available at physical, MAC, and network layer should be promoted [64].
- **Co-existence issues with HD systems:** FD mode is capable of providing performance gains in terms of the throughput over HD mode in several cases. However, in other cases, such as under asymmetric traffic scenarios and high SNR conditions, HD model outperforms the FD mode. Several works have already proposed hybrid schemes, where the system could operate either in HD mode or FD mode. Advantages of switching between HD/FD in the context of wireless-powered communications are not well understood at present and investigations must be carried out to find whether such hybrid operation would be beneficial. In addition, future wireless networks will be mainly heterogeneous and both HD and FD nodes would operate. From a network perspective, the presence of HD nodes will create new opportunities for the efficient design of future FD wireless-powered systems.

2.6 Conclusions

In this chapter, we considered the application of FD in WPCNs under bi-directional, relay, and hybrid AP topologies. We first considered an N-antenna BS and a wireless-powered MS and characterized optimum and suboptimum schemes for optimizing bi-directional information rates between the BS and MS. The beamformer at the BS and the TS parameter was jointly optimized for both optimum and suboptimum schemes. Compared to the HD operation, a significant improvement in the BS-MS rate region can be observed. Then, we studied the instantaneous and delay-constrained throughput of a FD wireless-powered MIMO relay system. We considered optimum linear processing at the relay as well as several suboptimum schemes. Next, optimum transceiver design for SWIPT in a FD system with one

hybrid AP, one downlink energy user, and one uplink user was investigated. We jointly optimized the transmit and receiver beamformers at the AP to maximize the uplink rate subject to EH constraint at the downlink user. We showed how transmit and receiver beamformers at the AP, that maximize the uplink rate subject to EH constraint at the downlink user, can be designed. In all cases, results that are useful for evaluating the performance and extracting insights into the effects of key parameters, such as the antenna configuration, linear processing scheme, and TS parameters, on the performance were presented. In certain regimes, FD mode shows a better throughput as compared to the HD mode. Therefore, FD operation is a promising approach to design energy and spectrally efficient future wireless communication networks.

References

1. A. Sabharwal, P. Schniter, D. Guo, D.W. Bliss, S. Rangarajan, R. Wichman, In-band full-duplex wireless: challenges and opportunities. IEEE J. Sel. Areas Commun. **32**(9), 1637–1652 (2014)
2. Z. Zhang, K. Long, A.V. Vasilakos, L. Hanzo, Full-duplex wireless communications: challenges, solutions, and future research directions. Proc. IEEE **104**(7), 1369–1409 (2016)
3. J.I. Choi, M. Jain, K. Srinivasan, P. Levis, S. Katti, Achieving single channel, full duplex wireless communication, in *Proceedings of 16th International Conference on Mobile Computing and Networking (MobiCom'10)*, Chicago, IL, September (2010), pp. 1–12
4. M. Duarte, C. Dick, A. Sabharwal, Experiment-driven characterization of full-duplex wireless systems. IEEE Trans. Wirel. Commun. **11**(12), 4296–4307 (2012)
5. E. Aryafar, M.A. Khojastepour, K. Sundaresan, S. Rangarajan, M. Chiang, MIDU: enabling MIMO full duplex, in *Proceedings of 18th International Conference on Mobile Computing and Networking (MobiCom '12)*, New York, August (2012), pp. 257–268
6. T. Riihonen, S. Werner, R. Wichman, Hybrid full-duplex/half-duplex relaying with transmit power adaptation. IEEE Trans. Wirel. Commun. **10**(9), 3074–3085 (2011)
7. T. Riihonen, S. Werner, R. Wichman, Mitigation of loopback self-interference in full-duplex MIMO relays. IEEE Trans. Signal Process. **59**(12), 5983–5993 (2011)
8. S.S. Hong, J. Brand, J.I. Choi, M. Jain, J. Mehlman, S. Katti, P. Levis, Applications of self-interference cancellation in 5G and beyond. IEEE Commun. Mag. **52**(2), 114–121 (2014)
9. E. Everett, A. Sahai, A. Sabharwal, Passive self-interference suppression for full-duplex infrastructure nodes. IEEE Trans. Wirel. Commun. **13**(2), 680–694 (2014)
10. M. Heino, D. Korpi, T. Huusari, E. Antonio-Rodriguez, S. Venkatasubramanian, T. Riihonen, L. Anttila, C. Icheln, K. Haneda, R. Wichman, M. Valkama, Recent advances in antenna design and interference cancellation algorithms for in-band full duplex relays. IEEE Commun. Mag. **53**(5), 91–101 (2015)
11. European FP7 project DUPLO (full-duplex radios for local access) European commission - research: the seventh framework programme [Online]. Technical Report (2012). Available: http://www.fp7-duplo.eu/index.php/general-info
12. T. Riihonen, R. Wichman, Energy detection in full-duplex cognitive radios under residual self-interference, in *Proceedings of International Conference on Cognitive Radio Oriented Wireless Networks and Communications (CrownCom' 14)*, Oulu, June (2014), pp. 57–60
13. G. Zheng, I. Krikidis, J. Li, A.P. Petropulu, B.E. Ottersten, Improving physical layer secrecy using full-duplex jamming receivers. IEEE Trans. Signal Process. **61**(20), 4962–4974 (2013)
14. S. Priya, D.J. Inman, *Energy Harvesting Technologies* (Springer, Boston, MA, 2009)
15. X. Lu, P. Wang, D. Niyato, D.I. Kim, Z. Han, Wireless networks with RF energy harvesting: a contemporary survey. IEEE Commun. Surv. Tut. **17**(2), 757–789 (2015, Second quarter)

16. S. Ulukus, A. Yener, E. Erkip, O. Simeone, M. Zorzi, P. Grover, K. Huang, Energy harvesting wireless communications: a review of recent advances, IEEE J. Sel. Areas Commun. **33**(3), 360–381 (2015)
17. K. Huang, V.K.N. Lau, Enabling wireless power transfer in cellular networks: architecture, modeling and deployment. IEEE Trans. Wirel. Commun. **13**(2), 902–912 (2014)
18. S. Bi, C.K. Ho, R. Zhang, Wireless powered communication: opportunities and challenges. IEEE Commun. Mag. **53**(4), 117–125 (2015)
19. R. Zhang, C.K. Ho, MIMO broadcasting for simultaneous wireless information and power transfer. IEEE Trans. Wirel. Commun. **12**(5), 1989–2001 (2013)
20. K.J. Lee, H.B. Kong, H. Lee, S.R. Lee, I. Lee, Optimal beamforming designs for wireless information and power transfer in MISO interference channels. IEEE Trans. Wirel. Commun. **14**(9), 4810–4821 (2015)
21. E.S. Lo, D.W.K. Ng, R. Schober, Wireless information and power transfer: energy efficiency optimization in OFDMA systems. IEEE Trans. Wirel. Commun. **12**(12), 6352–6370 (2013)
22. H. Tabassum, E. Hossain, On the deployment of energy sources in wireless-powered cellular networks. IEEE Trans. Commun. **63**(9), 3391–3404 (2015)
23. B. Clerckx, E. Bayguzina, Waveform design for wireless power transfer. IEEE Trans. Signal Process. **64**(23), 6313–6328 (2016)
24. S. O'Driscoll, A.S.Y. Poon, T.H. Meng, Optimal frequency for wireless power transmission into dispersive tissue. IEEE Trans. Antennas Propag. **58**(5), 1739–1750 (2010)
25. W.C. Brown, The history of power transmission by radio waves. IEEE Trans. Microwave Theory Tech. **32**(9), 1230–1242 (1984)
26. L.R. Varshney, Transporting information and energy simultaneously, in *Proceedings of IEEE International Symposium on Information Theory (ISIT 2008)*, Toronto July (2008), pp. 1612–1616
27. Z. Ding, C. Zhong, D.W.K. Ng, M. Peng, H.A. Suraweera, R. Schober, H.V. Poor, Application of smart antenna technologies in simultaneous wireless information and power transfer. IEEE Commun. Mag. **53**(4), 86–93 (2015)
28. Y. Zeng, R. Zhang, Full-duplex wireless-powered relay with self-energy recycling. IEEE Wirel. Commun. Lett. **4**(2), 201–204 (2015)
29. M. Maso, C. Liu, C. Lee, T.Q.S. Quek, L.S. Cardoso, Energy-recycling full-duplex radios for next-generation networks. IEEE J. Sel. Areas Commun. **33**(12), 2948–2962 (2015)
30. M. Mohammadi, H.A. Suraweera, Y. Cao, I. Krikidis, C. Tellambura, Full-duplex radio for uplink/downlink wireless access with spatially random nodes. IEEE Trans. Commun. **63**(12), 5250–5266 (2015)
31. S. Goyal, C. Galiotto, N. Marchetti, S.S. Panwar, Throughput and coverage for a mixed full and half duplex small cell network, in *Proceedings of IEEE International Conference on Communications (ICC'16)*, Kuala Lumpur, May (2016), pp. 1–7
32. Y.L. Che, J. Xu, L. Duan, R. Zhang, Multiantenna wireless powered communication with cochannel energy and information transfer. IEEE Commun. Lett. **19**(12), 2266–2269 (2015)
33. Z. Hu, C. Yuan, F. Zhu, F. Gao, Weighted sum transmit power minimization for full-duplex system with SWIPT and self-energy recycling. IEEE Access. **4**, 4874–4881 (2016)
34. M. Gao, H.H. Chen, Y. Li, M. Shirvanimoghaddam, J. Shi, Full-duplex wireless-powered communication with antenna pair selection, in *Proceedings of IEEE Wireless Communications and Networking Conference (WCNC'15)*, New Orleans, LA, March (2015), pp. 693–698
35. A.A. Okandeji, M.R.A. Khandaker, K. Wong, Wireless information and power transfer in full-duplex communication systems, in *Proceedings of IEEE International Conference on Communications (ICC'16)*, Kuala Lumpur, May (2016), pp. 1–6
36. W. Mou, Y. Cai, W. Yang, W. Yang, X. Xu, J. Hu, Exploiting full duplex techniques for secure communication in SWIPT system, in *Proceedings of International Conference on Wireless Communications and Signal Processing (WCSP'15)*, Nanjing, October (2015), pp. 1–6
37. Y. Xiao, Z. Xiong, D. Niyato, Z. Han, L.A. DaSilva, Full-duplex machine-to-machine communication for wireless-powered internet-of-things, in *Proceedings of IEEE International Conference on Communications (ICC'16)*, Kuala Lumpur, May (2016), pp. 1–6

38. C. Zhong, H.A. Suraweera, G. Zheng, I. Krikidis, Z. Zhang, Wireless information and power transfer with full duplex relaying. IEEE Trans. Commun. **62**(10), 3447–3461 (2014)
39. S. Hu, Z. Ding, Q. Ni, Beamforming optimisation in energy harvesting cooperative full-duplex networks with self-energy recycling protocol. IET Commun. **10**(7), 848–853 (2016)
40. Z. Wen, X. Liu, N.C. Beaulieu, R. Wang, S. Wang, Joint source and relay beamforming design for full-duplex MIMO AF relay SWIPT systems. IEEE Commun. Lett. **20**(2), 320–323 (2016)
41. I. Krikidis, G. Zheng, B.E. Ottersten, Harvest-use cooperative networks with half/full-duplex relaying, in *Proceedings of IEEE Wireless Communications and Networking Conference (WCNC'13)*, Shanghai, April (2013), pp. 4256–4260
42. H. Liu, K.J. Kim, K.S. Kwak, H.V. Poor, Power splitting-based SWIPT with decode-and-forward full-duplex relaying. IEEE Trans. Wirel. Commun. **15**(11), 7561–7577 (2016)
43. T. Riihonen, L. Zhao, M. Vehkaperä, X. Wang, On the feasibility of full-duplex relaying powered by wireless energy transfer, in *Proceedings of IEEE Workshop on Signal Processing Advances in Wireless Communications (SPAWC'16)*, Edinburgh, July (2016), pp. 1–5
44. M. Mohammadi, B.K. Chalise, H.A. Suraweera, C. Zhong, G. Zheng, I. Krikidis, Throughput analysis and optimization of wireless-powered multiple antenna full-duplex relay systems. IEEE Trans. Commun. **64**(4), 1769–1785 (2016)
45. H. Ju, R. Zhang, Optimal resource allocation in full-duplex wireless-powered communication network. IEEE Trans. Commun. **62**(10), 3528–3540 (2014)
46. X. Kang, C.K. Ho, S. Sun, Full-duplex wireless-powered communication network with energy causality. IEEE Trans. Wirel. Commun. **14**(10), 5539–5551 (2015)
47. H. Kim, H. Lee, M. Ahn, H. Kong, I. Lee, Joint subcarrier and power allocation methods in full duplex wireless powered communication networks for OFDM systems. IEEE Trans. Wirel. Commun. **15**(7), 4745–4753 (2016)
48. S. Leng, D.W.K. Ng, N. Zlatanov, R. Schober, Multi-objective resource allocation in full-duplex SWIPT systems, in *Proceedings of IEEE International Conference on Communications (ICC'16)*, Kuala Lumpur, May (2016), pp. 1–7
49. V.-D. Nguyen, H.V. Nguyen, G.-M. Kang, H.M. Kim, O.-S. Shin, Sum rate maximization for full duplex wireless-powered communication networks, in *Proceedings of European Signal Processing Conference (EUSIPCO'16)*, Budapest (2016), pp. 798–802
50. Y. Wang, R. Sun, X. Wang, Transceiver design to maximize the weighted sum secrecy rate in full-duplex SWIPT systems. IEEE Signal Process. Lett. **23**(6), 883–887 (2016)
51. K. Yamazaki, Y. Sugiyama, Y. Kawahara, S. Saruwatari, T. Watanabe, Preliminary evaluation of simultaneous data and power transmission in the same frequency channel, in *Proceedings of IEEE Wireless Communications and Networking Conference (WCNC'15)*, New Orleans, LA, March (2015), pp. 1237–1242
52. R.M. Corless, G.H. Gonnet, D.E.G. Hare, D.J. Jeffrey, D.E. Knuth, On the Lambert W function. Adv. Comput. Math. **5**(4), 329–359 (1996)
53. I.S. Gradshteyn, I.M. Ryzhik, *Table of Integrals, Series and Products*, 7th edn. (Academic, San Diego, CA, 2007)
54. B.K. Chalise, H.A. Suraweera, G. Zheng, Throughput maximization for full-duplex energy harvesting MIMO communications, in *Proceedings of IEEE Workshop on Signal Processing Advances in Wireless Communications (SPAWC'16)*, Edinburgh, July (2016), pp. 1–5
55. B.K. Chalise, W. Ma, Y.D. Zhang, H.A. Suraweera, M.G. Amin, Optimum performance boundaries of OSTBC based AF-MIMO relay system with energy harvesting receiver. IEEE Trans. Signal Process. **61**(17), 4199–4213 (2013)
56. K. Long, A.V. Vasilakos, Z. Zhang, X. Chai, L. Hanzo, Full duplex techniques for 5G networks: self-interference cancellation, protocol design, and relay selection. IEEE Commun. Mag. **53**(5), 128–137 (2015)
57. R. Wichman, K. Pajukoski, E. Lahetkangas, R. Pitaval, O. Tirkkonen, E. Tiirola, Full-duplex self-backhauling for small-cell 5G networks. IEEE Wirel. Commun. **22**(5), 83–89 (2015)
58. H.A. Suraweera, I. Krikidis, G. Zheng, C. Yuen, P.J. Smith, Low-complexity end-to-end performance optimization in MIMO full-duplex relay systems. IEEE Trans. Wirel. Commun. **13**(2), 913–927 (2014)

59. A.A. Nasir, X. Zhou, S. Durrani, R.A. Kennedy, Relaying protocols for wireless energy harvesting and information processing. IEEE Trans. Wirel. Commun. **12**(7), 3622–3636 (2013)
60. H. Ahmadi, S. Narayanan, M.F. Flanagan, Simultaneous uplink/downlink transmission using full-duplex single-RF MIMO. IEEE Wirel. Commun. Lett. **5**(1), 88–91 (2016)
61. C. Psomas, M. Mohammadi, I. Krikidis, H.A. Suraweera, Impact of directionality on interference mitigation in full-duplex cellular networks. IEEE Trans. Wirel. Commun. **16**(1), 1536–1276 (2017)
62. S. Goyal, P. Liu, S.S. Panwar, R.A. DiFazio, R. Yang, E. Bala, Full duplex cellular systems: will doubling interference prevent doubling capacity? IEEE Commun. Mag. **53**(5), 121–127 (2015)
63. S. Kashyap, E. Björnson, E.G. Larsson, On the feasibility of wireless energy transfer using massive antenna arrays. IEEE Trans. Wirel. Commun. **15**(5), 3466–3480 (2016)
64. K.M. Thilina, H. Tabassum, E. Hossain, D.I. Kim, Medium access control design for full duplex wireless systems: challenges and approaches. IEEE Commun. Mag. **53**(5), 112–120 (2015)

Chapter 3
Multi-Objective Resource Allocation Optimization for SWIPT in Small-Cell Networks

Nafiseh Janatian, Ivan Stupia, and Luc Vandendorpe

3.1 Introduction

The rapid development of mobile internet and internet of things (IoTs) has given rise to a serious concern about the highly growing traffic and the support of a massive number of connected devices. Therefore, the energy storage, power management and increase of the battery life of these devices are major issues to be considered in realizing the upcoming networks successfully. While many energy efficient strategies aim at expanding the system's battery life by reducing the energy consumption, the others propose to recycle the ambient energy associated with the energy harvesting (EH) sources such as vibration, heat and electromagnetic waves. Among these different EH techniques, radiofrequency (RF) EH via RF electromagnetic waves is one of the most appealing techniques. In this context, the idea of using the same electromagnetic field for transferring both information and power to wireless devices, called simultaneous wireless information and power transfer (SWIPT) has recently attracted significant attention. It is predicted that SWIPT will become an essential part for many commercial and industrial wireless systems in the future, including the IoT, wireless sensor networks and small-cell networks [1].

The ideal SWIPT receiver is the one which is able to extract energy from the same signal as that used for information decoding (ID) [2]. However, this extraction is not possible with the current circuit designs, since the energy carried by the RF signal is lost during the ID process. Hence, a considerable effort has been devoted to investigate different practical SWIPT receiver architectures. These architectures can

N. Janatian (✉) • I. Stupia • L. Vandendorpe
Institute of Information and Communication Technologies, Electronics, and Applied Mathematics, Université catholique de Louvain, Louvain-la-Neuve, Belgium
e-mail: nafiseh.janatian@uclouvain.be; ivan.stupia@uclouvain.be; luc.vandendorpe@uclouvain.be

D.N.K. Jayakody et al. (eds.), *Wireless Information and Power Transfer: A New Paradigm for Green Communications*, DOI 10.1007/978-3-319-56669-6_3

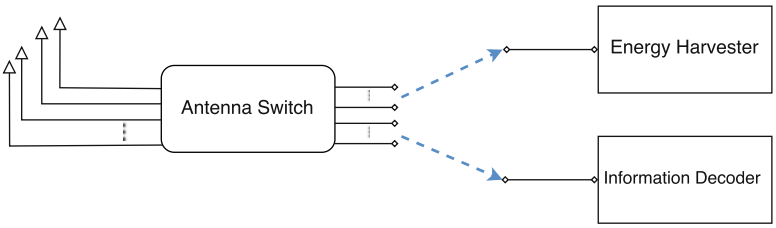

Fig. 3.1 Antenna switching SWIPT receiver

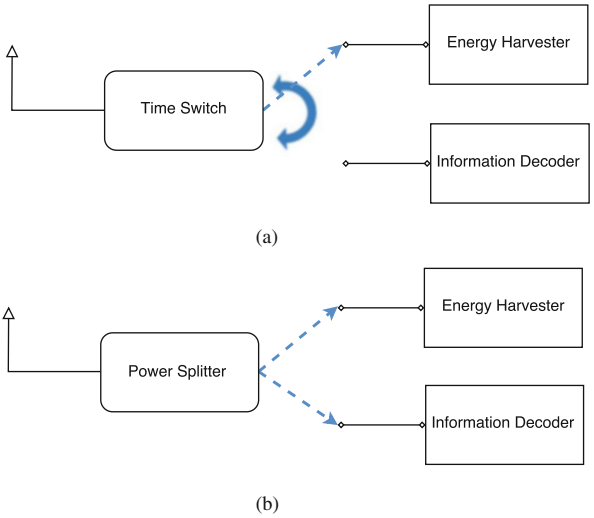

Fig. 3.2 Practical designs for the co-located SWIPT receiver. (**a**) Time switching (TS). (**b**) Power splitting (PS)

be classified into two groups of: parallel and co-located receivers [3]. In a parallel receiver architecture, also referred to as antenna switching, energy harvester and information receiver are equipped with independent antennas for EH and ID. As shown in Fig. 3.1, the antenna array is divided into two subsets, one for EH and the other for ID. In a co-located receiver architecture, the energy harvester and the information receiver share the same antennas. Two practical methods to design the co-located receiver architecture for SWIPT are time switching (TS) and power splitting (PS). As shown in Fig. 3.2a, in a TS design, each reception time frame is divided into two orthogonal time slots, one for ID and the other for EH and the receiver switches in time between EH and ID modes. However, in PS design the receiver splits the received signal into two streams of different power levels for EH and ID, as shown in Fig. 3.2b.

To realize SWIPT, the available resources such as transmit power, subcarriers and beamforming vectors should be allocated properly among both information and energy transfer functionalities. In [4–6], the authors address the problem of designing TS/PS SWIPT receivers in a point-to-point wireless environment to achieve

various trade-offs between wireless information transfer and EH. In multi-user environments, however, most of the researches focus on the power and subcarrier allocation among different users such that some criteria (throughput, harvested power, fairness, etc.) are met. Various policies have been proposed for single input-single output (SISO) and multiple input-single output (MISO) configurations in a multi-user downlink channel [7–12].

Resource allocation algorithm design aiming at maximization of the energy efficiency of data transmission in a SISO PS SWIPT multi-user system is considered in [7] with an orthogonal frequency division multiple access (OFDMA).

In MISO configuration, there exists an additional degree of freedom of beamforming vector optimization at the transmitter. In [11], a joint beamforming and PS ratio allocation scheme was designed to minimize the power cost under the constraints of throughput and harvested energy. The problem of joint power control and TS in MISO SWIPT systems by considering the long-term power consumption and heterogeneous quality of service (QoS) requirements for different types of traffics is also studied in [9]. In [10] resource allocation algorithm design for SWIPT is addressed in a multi-user coordinated multipoint (CoMP) network which includes multiple multi-antenna remote radio heads (RRHs) and separate single antenna EH and ID receivers. A MISO femtocell co-channel overlaid with a macro-cell is considered in [12] to exploit the advantages of SWIPT while promoting the energy efficiency. The femto base station sends information to ID femto users (FUs) and transfers energy to EH FUs simultaneously, and also suppresses its interference to macro users. A novel EH balancing technique for robust beamformers design in MISO SWIPT system is also proposed in [8] considering imperfect channel state information (CSI) at the transmitter.

SWIPT in multi-user MIMO interference channel is studied in [13, 14]. In [13] a MIMO interference channel with two transmitter–receiver pairs is considered. When both receivers are set in ID mode or EH mode, the achievable rate obtained with iterative water-filling and without CSI sharing is studied. Strategies are proposed for the mixed case of one ID receiver and one EH receiver, in order to maximize the energy transfer to the EH receiver and minimize the interference to the ID receiver. PS SWIPT in a multi-user MIMO interference channel scenario is also studied in [14]. The objective is to minimize the total transmit power of all transmitters by jointly designing the transmit beamformers, power splitters and receiver filters, subject to the signal-to-interference-plus-noise ratio (SINR) constraint for ID and the harvested power constraint for EH at each receiver.

In this chapter, we address SWIPT from the following points of view:

- First, based on the literature review conducted, most of the existing works in SWIPT consider single cell cases with one base station (BS) and single or multiple mobile users. In a multi-cell case the system becomes interference limited, since reuse of subcarriers from users in different cells produce interference that degrades the system performance in terms of throughput and spectral efficiency, particularly for cell edge users. In this perspective, important features such as inter-cell interference coordination (ICIC) and CoMP communication have been introduced for cellular communication networks. However, while interference

links are always harmful for information decoding, constructive interferences are useful for energy harvesting. This already shows the dualistic nature of interference in SWIPT networks. On the other hand, it is worth remarking that the signal strength of far-field RF transmission is greatly impaired by the path loss when the separation between the transmitter and the RF energy harvester increases. From an architectural point of view, a potential solution that could ensure ubiquitous SWIPT is the avoidance of the high signal attenuation due to path loss. This can be achieved, thanks to densification of network nodes. Therefore, the concept of ICIC relying on a cloud-based centralized digital processing can be the basis to SWIPT technologies ensuring large energy transfer efficiency and reduced costs. In this scenario, a large number of low-cost RRHs, also referred to as access points (APs), are randomly deployed and connected to the baseband unit (BBU) pool through the fronthaul links. This concept has generally been applied to macro-cells, i.e. large outdoor tower-based systems. However, it can also be applied to small-cells that provide distributed coverage across a large space such as a stadium, airport or office building. Such an architecture would permit an integrated control of power and data transfer while keeping the RF front ends relatively close to the associated devices.

- Second, we consider TS SWIPT technique, which is practically feasible and can be implemented using simple switches, while PS receivers require highly complex hardware due to the different power sensitivity levels of ID and EH parts in each receiver. In this perspective, it is worth mentioning that TS SWIPT receivers can be considered as a special case of dynamic PS SWIPT receivers with on–off power splitting factor. Hence, since realistic values of the ID and EH receivers' sensitivities may differ by more than 30dB, TS and dynamic PS SWIPT will have similar performance in practical scenarios.
- Third, existing SWIPT works have considered single objective optimization (SOO) framework to formulate the problem of resource allocation or beamforming optimization. Popular objectives are classical performance metrics such as sum rate/ throughput (to be maximized), or transmit power (to be minimized), or sum of energy harvested (to be maximized). However, SWIPT has a multi-objective nature, i.e. both throughput and the amount of harvested energy are desirable objectives in designing SWIPT systems. In SOO one of these objectives is selected as the sole objective while the others are considered as constraints. This approach assumes that one of the objectives is of dominating importance and also it requires prior knowledge about the accepted values of the constraints related to the other objectives. Therefore, the fundamental approach used in our study is the multi-objective optimization (MOO) which investigates the optimization of the vector of objectives, for nontrivial situations, where there is a conflict between objectives. This approach has been proposed lately for wireless information systems [15] and is only considered in [16, 17] very recently for a parallel SWIPT system which consists of a multi-antenna transmitter, a single-antenna information receiver and multiple EH receivers equipped with multiple antennas. In this scenario, the trade-off between the maximization of the energy

efficiency of information transmission and the maximization of the wireless power transfer efficiency is studied by means of resource allocation using an MOO framework.

3.2 System Model

We consider a small-cell network consisting of several APs which may overlay the existing macro-cell network as in Fig. 3.3. Small-cells are realized using multiple RRHs which are connected to a central BBU through the fronthaul links [18]. Macro BS and RRHs are equipped with multiple antennas and serve multiple single antenna users. We assume that each cell in Fig. 3.3 consists of N_{AP} APs which are equipped with $N_{A_j}, j = 1, \ldots, N_{\mathrm{AP}}$ antennas and serve N_{UE} single antenna user equipments (UEs). The term UE in this chapter refers to the broader range of devices from the ones directly used by the end-users to the autonomous sensors. The sets of all UEs and all APs are denoted by $\mathcal{N}_{\mathrm{UE}}$ and $\mathcal{N}_{\mathrm{AP}}$, respectively. Each user is assumed to be served by multiple transmitters but with different beamforming vectors. Therefore, the received signal in the ith UE can be modelled as:

$$y_i = \sum_{j=1}^{N_{\mathrm{AP}}} \boldsymbol{h}_{ij}^{\boldsymbol{H}} \sum_{l=1}^{N_{\mathrm{UE}}} \boldsymbol{x}_{lj} s_l + n_i, \tag{3.1}$$

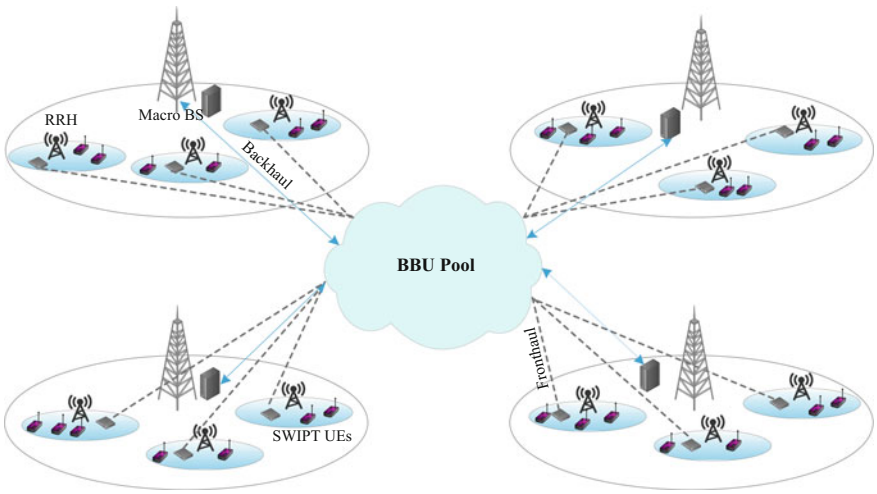

Fig. 3.3 Small-cell network with TS scheme in MISO SWIPT system

where $i, l \in \mathcal{N}_{\mathrm{UE}}, j \in \mathcal{N}_{\mathrm{AP}}$, s_l is the information symbol from APs to the lth UE which originates from independent Gaussian codebooks, $s_l \sim \mathscr{CN}(\mathbf{0}, 1)$ and $\boldsymbol{x_{lj}} \in \mathbb{C}^{N_{A_j} \times 1}$ is the beamforming vector from the jth AP to the lth UE. We assume quasi-static flat fading channel for all UEs and denote by $\boldsymbol{h_{ij}} \in \mathbb{C}^{N_{A_j} \times 1}$ the complex channel vector from the jth AP to the ith UE. Also $n_i \sim \mathscr{CN}(0, \sigma_i^2)$ is the circularly symmetric complex Gaussian receiver noise which includes the antenna noise and the ID processing noise in the ith user. According to (3.1), the achievable data rate R_i (bits/s/Hz) for the ith UE can be found from the following equation:

$$R_i = \log_2 \left(1 + \frac{\sum_{j=1}^{N_{\mathrm{AP}}} \mathrm{trace}(\boldsymbol{H_{ij}} \boldsymbol{X_{ij}})}{\sigma_i^2 + \sum_{j=1}^{N_{\mathrm{AP}}} \sum_{l=1, l \neq i}^{N_{\mathrm{UE}}} \mathrm{trace}(\boldsymbol{H_{ij}} \boldsymbol{X_{lj}})} \right), \tag{3.2}$$

where $\boldsymbol{X_{ij}} = \boldsymbol{x_{ij}} \boldsymbol{x_{ij}^H}$, $\boldsymbol{H_{ij}} = \boldsymbol{h_{ij}} \boldsymbol{h_{ij}^H}$ and therefore $\boldsymbol{X_{ij}}, \boldsymbol{H_{ij}} \in \mathbb{C}^{N_{A_j} \times N_{A_j}}$ are rank-one matrices for $i \in \mathcal{N}_{\mathrm{UE}}, j \in \mathcal{N}_{\mathrm{AP}}$. This information data rate is achieved by treating the interference as noise.

Besides, the received energy per channel use E_i (assuming normalized energy unit of Joule/(channel use) or W) in the ith UE is given by:

$$E_i = \sum_{j=1}^{N_{\mathrm{AP}}} \sum_{l=1}^{N_{\mathrm{UE}}} \mathrm{trace}(\boldsymbol{H_{ij}} \boldsymbol{X_{lj}}), \tag{3.3}$$

in which the antenna noise power is neglected. However, this amount of energy cannot be harvested in practice due to the technical issues of RF-to-DC energy conversion. The efficiency of the RF energy harvester depends on the efficiency of the antenna, the accuracy of the impedance matching between the antenna and the voltage multiplier, and the power efficiency of the voltage multiplier that converts the received RF signals to DC voltage [19].

In this scenario, the UEs are assumed to use TS design for implementing SWIPT. As stated before, in a TS scheme each reception time frame is divided into two orthogonal time slots, one for ID and the other for EH. Consequently, denoting by α_i the fraction of time devoted to ID in the ith UE, the average data rate in this scheme can be written as:

$$R_i^{\mathrm{TS}}(\boldsymbol{X}, \alpha_i) = \alpha_i R_i(\boldsymbol{X}), \tag{3.4}$$

where $R_i(\boldsymbol{X})$ can be found from (3.2). Also we have the following equation for the amount of harvested energy at the ith UE:

$$E_{h_i}^{\mathrm{TS}}(\boldsymbol{X}, \alpha_i) = (1 - \alpha_i) \eta_i E_i(\boldsymbol{X}), \tag{3.5}$$

in which $E_i(\boldsymbol{X})$ can be found from (3.3) and η_i denotes the energy harvesting efficiency factor of the ith UE.

3.3 Resource Allocation Optimization for TS SWIPT

In this section, we study the resource allocation optimization problem for our TS SWIPT system in a multi-objective manner. First we formulate the problem of designing the optimal transmit strategies $\boldsymbol{X} = [\boldsymbol{X}_{lj}]_{l\in\mathcal{N}_{\mathrm{UE}},j\in\mathcal{N}_{\mathrm{AP}}}$ and time switching ratios $\boldsymbol{\alpha} = [\alpha_l]_{l\in\mathcal{N}_{\mathrm{UE}}}$ jointly to maximize the performance of all users simultaneously and then we propose an algorithm based on the majorization–minimization approach [20] to solve this problem.

3.3.1 Problem Formulation

As mentioned earlier, the data rate and harvested energy are both desirable for each user in SWIPT scenarios. Therefore, in our problem formulation, we define the utility vector of the ith UE by $\boldsymbol{u}_i(\boldsymbol{X},\alpha_i) = [R_i^{\mathrm{TS}}(\boldsymbol{X},\alpha_i), E_{h_i}^{\mathrm{TS}}(\boldsymbol{X},\alpha_i)]$ which includes both the data rate and the harvested energy values of the ith TS SWIPT UE. Our optimization objective is then to maximize the utility vector of the whole system defined by $\boldsymbol{u}(\boldsymbol{X},\boldsymbol{\alpha}) = [\boldsymbol{u}_1(\boldsymbol{X},\alpha_1),\boldsymbol{u}_2(\boldsymbol{X},\alpha_2),\ldots,\boldsymbol{u}_{N_{\mathrm{UE}}}(\boldsymbol{X},\alpha_{N_{\mathrm{UE}}})]$ jointly via the multi-objective problem formulation. This problem can be written as:

$$\begin{aligned}
\underset{\boldsymbol{X},\boldsymbol{\alpha}}{\text{Maximize}} \quad & \boldsymbol{u}(\boldsymbol{X},\boldsymbol{\alpha}) \\
\text{subject to} \quad & (1)\ \sum_{j=1}^{N_{\mathrm{AP}}}\sum_{l=1}^{N_{\mathrm{UE}}} \mathrm{trace}(\boldsymbol{X}_{lj}) \le P_{\max} \\
& (2)\ \boldsymbol{X}_{lj} \succeq 0,\ \mathrm{Rank}(\boldsymbol{X}_{lj}) = 1,\ \forall l,j \\
& (3)\ \alpha_l \in [0,1],\ \forall l,
\end{aligned} \tag{3.6}$$

where constraint (1) denotes the average power constraint for APs across all transmitting antennas with upper limit of $P_{\max}$, constraint (2) considers the rank-one property of X_{lj}s and constraint (3) is due to definition of TS rates.

The design problem for the ideal SWIPT case in which energy is assumed to be extracted simultaneously while information decoding is the same as problem (3.6) but with utility vectors of $\boldsymbol{u}_i(\boldsymbol{X}) = [R_i(\boldsymbol{X}), \eta_i E_i(\boldsymbol{X})]$, where $R_i(\boldsymbol{X})$ and $E_i(\boldsymbol{X})$ can be found from (3.2) and (3.3), respectively. As already stated, this ideal receiver is not feasible in practice; however, for theoretical benchmarking, its performance can be used as an upper bound for the performance of the TS SWIPT.

3.3.2 Resource Allocation Algorithm

Our approach to solve problem (3.6) is to relax the rank constraints on X_{lj}s. It is proved in [21] that the optimal solution of the relaxed problem satisfies $\text{Rank}(\boldsymbol{X_{lj}}) = 1, \forall l \in \mathcal{N}_{\text{UE}}, \forall j \in \mathcal{N}_{\text{AP}}$. As the objectives in problem (3.6) are conflicting, this problem cannot be solved in a globally optimal way and the Pareto optimality of the resource allocation will be adopted as the optimality criterion. Pareto optimality is a state of allocating the resources in which none of the objectives can be improved without degrading the other objectives [22]. As there usually exists multiple Pareto optimal solutions for MOO problems, it is generally converted into a SOO problem involving possibly some parameters or additional constraints to compute each Pareto optimal point. This conversion is called scalarization and examples of it are the weighted sum, weighted product and the weighted Chebyshev methods [15].

To solve the relaxed version of MOO problem (3.6), we use the weighted Chebyshev method, which provides the complete Pareto optimal set by varying predefined preference parameters. The weighted Chebyshev goal function is

$$f_{\text{ch}}(.) = \underset{\boldsymbol{i} \in \mathcal{N}_{\text{UE}}, \boldsymbol{m}=\mathbf{1,2}}{\text{Minimum}} \frac{\boldsymbol{u}_i^{(m)}}{v_i^{(m)}}, \tag{3.7}$$

where $\boldsymbol{u}_i^{(m)}$ denotes the mth element of $\boldsymbol{u}_i(\boldsymbol{X}, \alpha_i)$ and $v_i^{(1)}, v_i^{(2)}$ $\forall i \in \mathcal{N}_{\text{UE}}$ are the predefined preference parameters that specify the priority of each objective. Therefore, introducing the new parameter λ, weighted Chebyshev scalarization is equivalent to the following problem:

$$\begin{aligned}
\underset{\boldsymbol{X}, \boldsymbol{\alpha}, \lambda}{\text{Maximize}} \quad & \lambda \\
\text{subject to} \quad & (1)\ \alpha_i R_i(\boldsymbol{X}) \geq \lambda v_i^{(1)},\ \forall i \\
& (2)\ (1-\alpha_i)\eta_i E_i(\boldsymbol{X}) \geq \lambda v_i^{(2)},\ \forall i \\
& (3)\ \sum_{j=1}^{N_{\text{AP}}} \sum_{l=1}^{N_{\text{UE}}} \text{trace}(\boldsymbol{X_{lj}}) \leq P_{\max} \\
& (4)\ \boldsymbol{X_{lj}} \succeq 0,\ \forall l, j \\
& (5)\ \alpha_i \in [0,1],\ \forall i,
\end{aligned} \tag{3.8}$$

The above problem is a non-convex semidefinite program (SDP) due to not only the coupled TS ratios and R_i, E_i in the first and second constraints but also the definition of $R_i(\boldsymbol{X})$ as presented in (3.2). Introducing the new variables R_i, E_i, I_i and β_i, problem (3.8) can be represented as:

$$
\begin{aligned}
\underset{\boldsymbol{X},\alpha_i,\beta_i,R_i,E_i,I_i,\lambda,\ \forall i}{\text{Maximize}} \quad & \lambda \\
\text{subject to} \quad & \text{(C1)}\ \alpha_i R_i \geq \lambda v_i^{(1)},\ \forall i \\
& \text{(C2)}\ \beta_i \eta_i E_i \geq \lambda v_i^{(2)},\ \forall i \\
& \text{(C3)}\ E_i = \sum_{j=1}^{N_{\text{AP}}} \sum_{l=1}^{N_{\text{UE}}} \text{trace}(\boldsymbol{H_{ij}} \boldsymbol{X_{lj}}),\ \forall i \\
& \text{(C4)}\ I_i = \sum_{j=1}^{N_{\text{AP}}} \sum_{l=1, l\neq i}^{N_{\text{UE}}} \text{trace}(\boldsymbol{H_{ij}} \boldsymbol{X_{lj}}),\ \forall i \\
& \text{(C5)}\ R_i = \log(E_i + \sigma_i^2) - \log(I_i + \sigma_i^2),\ \forall i \\
& \text{(C6)}\ \sum_{j=1}^{N_{\text{AP}}} \sum_{l=1}^{N_{\text{UE}}} \text{trace}(\boldsymbol{X_{lj}}) \leq P_{\max} \\
& \text{(C7)}\ \boldsymbol{X_{lj}} \succeq 0,\ \forall l, j \\
& \text{(C8)}\ \alpha_i + \beta_i = 1,\ \forall i \\
& \text{(C9)}\ \alpha_i \in [0, 1],
\end{aligned}
\tag{3.9}
$$

where E_i and I_i defined in (C3) and (C4) are the received energy and the interference level in the ith UE, respectively. Also (C5) is directly obtained from substituting the definition of E_i and I_i in the definition of R_i given by Eq. (3.2). It is shown in [21] that the constraint (C5) in problem (3.9) can be relaxed to ($\overline{\text{C5}}$) defined below:

$$
(\overline{\text{C5}})\ R_i \leq \log(E_i + \sigma_i^2) - \log(I_i + \sigma_i^2). \tag{3.10}
$$

We define $\hat{\lambda} = \log(\lambda)$, and use the monotonicity and concavity properties of the logarithm function to reformulate the above problem as below:

$$
\begin{aligned}
\underset{\boldsymbol{X},\alpha_i,\beta_i,R_i,E_i,I_i,\hat{\lambda},\ \forall i}{\text{Maximize}} \quad & \hat{\lambda} \\
\text{subject to} \quad & (\overline{\text{C1}})\ \log(\alpha_i) + \log(R_i) \geq \hat{\lambda} + \log(v_i^{(1)}) \\
& (\overline{\text{C2}})\ \log(\beta_i) + \log(\eta_i E_i) \geq \hat{\lambda} + \log(v_i^{(2)}) \\
& \text{(C3)–(C4)} \\
& (\overline{\text{C5}})\ R_i \leq \log(E_i + \sigma_i^2) - \log(I_i + \sigma_i^2) \\
& \text{(C6)–(C9)},
\end{aligned}
\tag{P}
$$

in which the nonconvexity of problem (3.9) is concentrated in inequality ($\overline{\text{C5}}$). Now problem (P) can be considered as a DC (difference of convex) programming

[23] since ($\overline{\text{C5}}$) is the difference of two convex functions ($R_i - \log(E_i + \sigma_i^2)$, $-\log(I_i + \sigma_i^2)$). Therefore, it can be solved using local optimization method of convex–concave procedure (CCP) [24]. CCP is a majorization–minimization algorithm [20] that solves DC programs as a sequence of convex programs by linearizing the concave part, $\log(I_i + \sigma_i^2)$, around the current iteration solution of I_i. To this end, we use the first order Taylor expansion and replace problem (P) in the kth step by the following subproblem:

$$
\begin{aligned}
\underset{\boldsymbol{X},\alpha_i,\beta_i,R_i,E_i,I_i,\hat{\lambda},\ \forall i}{\text{Maximize}} \quad & \hat{\lambda} \\
\text{subject to} \quad & (\overline{\text{C1}}), (\overline{\text{C2}}), (\text{C3})\text{–}(\text{C4}) \\
& (\overline{\text{C5}})\ R_i \leq \log(E_i + \sigma_i^2) - \left(\log(I_i^k + \sigma_i^2) + \frac{1}{I_i^k + \sigma_i^2}(I_i - I_i^k) \right) \\
& (\text{C6})\text{–}(\text{C9}).
\end{aligned}
\tag{P_k}
$$

This problem is a convex SDP and it can be solved by standard optimization techniques such as Interior-Point Method. In this paper, we have used the CVX package to solve (P_k). The linearization point is updated with each iteration until it satisfies the termination criterion as described in Algorithm 1. It can be easily verified that if I_i^k is the stationary point of subproblem (P_k), i.e. fulfilling the

Algorithm 1: CCP Algorithm for TS SWIPT

1: Define a step size $\gamma \in \mathbb{R}$ and a given tolerance $\varepsilon > 0$.
2: Initialize: choose a value for I_i^0 inside the convex set defined by (C1)-(C4), (C6)-(C9).
3: Set $k := 0$.
4: For the given I_i^k, solve the convex SDP of (P_k) to obtain the solution $\hat{I}_i(I_i^k)$.
5: **if** $\|\hat{I}_i(I_i^k) - I_i^k\| \leqslant \varepsilon$ **then**
6: stop.
7: **else**
8: update $I_i^k = I_i^k + \gamma(\hat{I}_i(I_i^k) - I_i^k)$.
9: update iteration, $k = k + 1$.
10: go back to line 4.
11: **end if**

KKT conditions of subproblem (P_k), it is also a stationary point of problem (P) [25]. The conditions under which the constrained CCP algorithm converges to a stationary point of the original problem are studied in [26] using Zangwill's global convergence theory [27] of iterative algorithms. These conditions are shown to be satisfied for Algorithm 1 in [21].

3.4 Numerical Results

In this section, we provide numerical results to demonstrate the performance of the proposed beamforming and TS algorithm in terms of harvested energy-data rate trade-off. We investigate the effect of different parameters on this trade-off to get a general overview for the practical design of the network.

3.4.1 Experimental Setup

We consider two small-cells as shown in Fig. 3.4, consisting of $N_{\text{AP}} = 2$ APs equipped with N_{A_1}, N_{A_2} antennas and N_{UE} TS SWIPT sensors. Sensors are distributed uniformly in a region bounded by two concentric circles with radius of $d_{\min}$ and $d_{\max}$. The distance of APs from each other is denoted by D as shown in Fig. 3.4. Transmission channel gains, $\boldsymbol{h}_{ij}, \forall i \in \mathcal{N}_{\text{UE}}, j = 1, 2$, depend on the location of sensors with respect to APs and the channel fading model. At each sensor location, channel gains are generated with Rayleigh fading and path loss exponent of 3. Noise powers are assumed to be $\sigma_i^2 = -90\,\text{dBm}$, $\forall i \in \mathcal{N}_{\text{UE}}$ and the maximum total power budget is set to $P_{\max} = 1\,\text{W}$. Parameter assumptions in this section (unless they are clearly stated with different values) are summarized in Table 3.1.

3.4.2 Discussion

In this section, we illustrate the Pareto boundary of TS and ideal SWIPT systems to investigate the trade-off between the harvested energy and the data rate. To plot the Pareto boundaries, we solve the optimization problems (3.6) using Algorithm 1 in several directions by changing the preference weights of $v_i^{(1)}, v_i^{(2)}, \forall i$. To have a general view of the Pareto boundary, we first consider a setup which includes

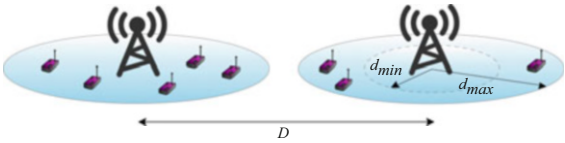

Fig. 3.4 Simulation scheme

Table 3.1 Parameter assumptions

Parameters	Specification	Parameters	Specification
N_{AP}	2	$P_{\max}$	1 W
$N_{A_1} = N_{A_2}$	2	$d_{\min}$	2 m
N_0	−150 dBm/Hz	$d_{\max}$	10 m
ΔW	1 MHz	Multipath exponent	3
D	20 m	Fading	Rayleigh
η_i	0.6	No. of channel realizations	100

two UEs served by two coordinated APs. The first UE is assumed to be a SWIPT sensor while the second UE is assumed to be an ID receiver such as smartphone. Therefore, we set $v_1^{(1)} = \theta_2\theta_1, v_1^{(2)} = \theta_2, v_2^{(1)} = \theta_1$ and search for the optimal solutions in different directions by changing the values of θ_1 and θ_2. In this setup, θ_1 changes the trade-off between the harvested energy and the data rate in the first UE and θ_2 changes the data rate preference between the first and second UE.

Figure 3.5 depicts the 3D Pareto boundary and its three 2D projections for one channel realization. As can be seen in Fig. 3.5a, the maximum harvested energy occurs when both the data rate of the first and second UEs are almost zero. By decreasing the amount of desired harvested energy, we can achieve higher data rates. In this scenario, the first UE (SWIPT sensor) desires high amount of harvested energy. Achieving high data rate is not required by this sensor while it is desired for the second UE. The desired trade-off is therefore the boundary marked in pink colour in Fig. 3.5d. The corresponding counterparts are also shown in Fig. 3.5b,c. To explain the behaviour of the Pareto boundary in this area, we study the performance in three different regions shown in Fig. 3.5d. At point A, we have the maximum data rate for the second UE, i.e. $R_2^{\text{TS}} = 33$ bits/s/Hz, $R_1^{\text{TS}} = 2$ bits/s/Hz and $E_1^{\text{TS}} = 0.08$ mW. At this point, the whole power is assigned to the AP which is closest to the second UE (it should be noted that we have assumed global power constraint for the APs in our system model). A small part of this power is only devoted to the sensor and therefore we will have such a low data rate and harvested energy in the first UE. By adapting the TS ratio of the sensor we can increase the harvested energy to a certain point B in which we have $E_1^{\text{TS}} = 0.5$ mW with the data rate of $R_1^{\text{TS}} = 1.8$ bits/s/Hz in this case. As a result while we are increasing the harvested energy, data rate of the second UE decreases only slightly to $R_2^{\text{TS}} = 30$ bits/s/Hz. However, to further increase the harvested energy, the beamformers should be aligned toward the first UE and this yields to an interference which suddenly decreases the data rate of the second UE to $R_2^{\text{TS}} = 10$ bits/s/Hz at point C. As a result, region 2 is the region in which both APs are active. In region 3, we are willing to harvest more energy and therefore the power will be assigned to the AP which is closer to the first UE. Therefore by transferring the power to the first AP and adapting the TS ratio we could harvest up to $E_1^{\text{TS}} = 0.9$ mW (point D).

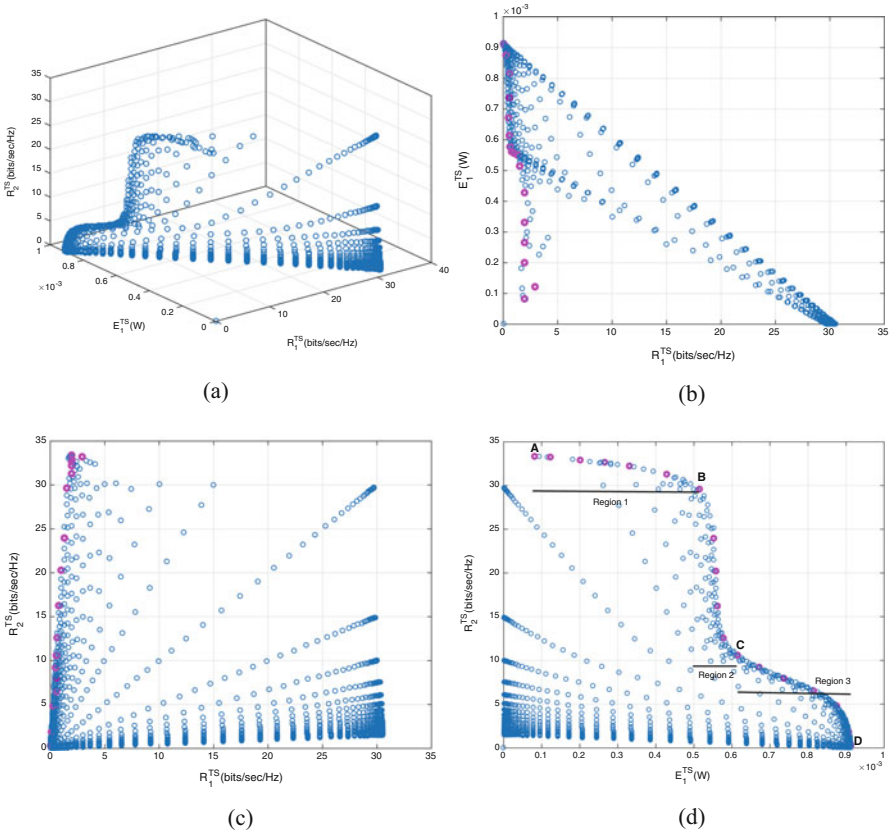

Fig. 3.5 3D Pareto boundary of TS SWIPT and its projections. (**a**) $R_1^{\mathrm{TS}}/E_1^{\mathrm{TS}}/R_2^{\mathrm{TS}}$. (**b**) $R_1^{\mathrm{TS}}/E_1^{\mathrm{TS}}$. (**c**) $R_1^{\mathrm{TS}}/R_2^{\mathrm{TS}}$. (**d**) $E_1^{\mathrm{TS}}/R_2^{\mathrm{TS}}$

Now we consider a symmetric setup which includes $N = \frac{N_{\mathrm{UE}}}{2} = 1$ UE with the same priority in each small-cell. Therefore we set $v_i^{(1)} = \theta_1, v_i^{(2)} = 1\ \forall i$ and search for the optimal solutions by changing the value of θ_1 only. Figure 3.6 shows the average Pareto boundary of the first TS SWIPT UE. As it can be seen, the average harvested energy is a monotonically decreasing function of the achievable data rate. This result shows that these two objectives are generally conflicting and any resource allocation algorithm that maximizes the harvested energy cannot maximize the data rate. In this plot, as the amount of harvested energy increases from 0.45 μW to 1.8 mW, the average data rate reduces from 29.13 to 0.2657 bits/s/Hz.

Pareto boundary of the infeasible ideal SWIPT is also shown in this figure as an upper bound. It can be observed that the maximum value of the harvested energy $E_{h_{\max}}$ and the achievable data rates $R_{\max}$ are the same for ideal and TS SWIPT. However, as expected, the minimum value of the harvested energy and the

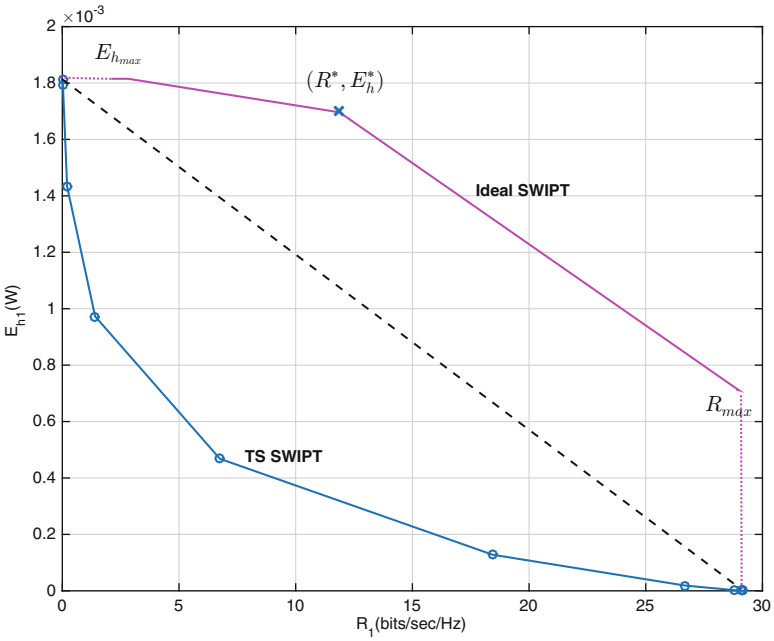

Fig. 3.6 Pareto boundary of TS SWIPT and ideal SWIPT

achievable data rates are not zero in this case since the ideal SWIPT is assumed to be able to harvest energy while decoding the information. It should be noticed that if the AP is able to change its beamforming vector for EH and ID, the optimal strategy would be to use the beamforming vectors related to the two extreme points of the ideal SWIPT Pareto boundary in each time slot. In this case, the optimal TS Pareto boundary would simply be the dashed linear line in Fig. 3.6. However, since in our scenario the same beamforming vector is used for EH and ID, the optimal TS Pareto boundary is the envelope of all linear lines connecting the projection of ideal Pareto boundary points (R^*, E_h^*) on two axes, i.e. $(0, E_h^*)$ and $(R^*, 0)$. Besides, as it is evident from Fig. 3.6, the Pareto boundary of TS SWIPT generated from the objectives in our problem formulation is non-convex. This is due to the multiple AP schemes and joint optimization of TS ratios and the beamforming vectors considered in this problem. In the following, we study the effect of the network parameters such as the number of UEs, distance of the APs from each other and the maximum possible distance of UEs from the APs on the Pareto boundary of the TS SWIPT UE.

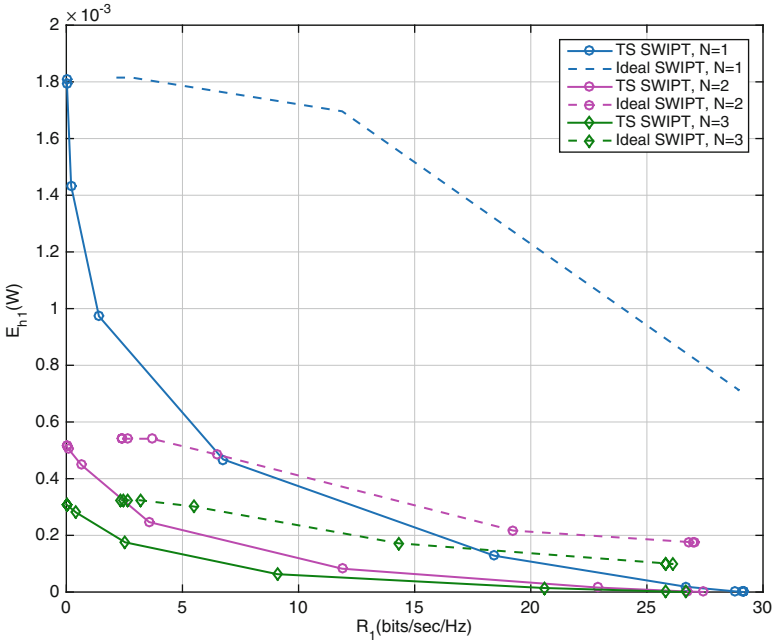

Fig. 3.7 Pareto boundary of TS SWIPT and ideal SWIPT

3.4.2.1 Effect of the Number of UEs

To study the effect of the number of UEs, we consider a symmetric setup which includes $N = \frac{N_{\text{UE}}}{2} = 1, 2, 3$ UEs in each small-cell with the same user preference weights as in previous plot. Figure 3.7 shows the Pareto boundary of the first TS SWIPT UE in this setup.

As can be seen, increasing the number of UEs highly affects the possible amount of harvestable energy at each UE, while the maximum data rate changes very slightly by increasing the number of UEs. For example, the maximum harvested energy in Fig. 3.7 reduces approximately from 1.8 mW to 0.5 mW and 0.3 mW by increasing the number of UEs at each small-cell from $N = 1$ to $N = 2$ and $N = 3$, respectively. This result is expectable, due to the fixed total power consumption assumption and the direct impact of transmit power on the received energy.

In Fig. 3.7 we have also plotted the Pareto boundaries of ideal SWIPT for $N = 1, 2, 3$ UEs in each small-cell. Comparing the results of ideal and TS SWIPT for different number of UEs shows that the harvested energy loss of TS SWIPT with respect to the ideal SWIPT for a fixed required data rate reduces with increasing the number of UEs. As can be seen in Fig. 3.7, to achieve $R_1 = 5$ bits/s/Hz in the first UE, we lose approximately 1 mW in TS SWIPT with respect to the ideal SWIPT in $N = 1$ UE per small-cell. However, this amount reduces to nearly 0.3 mW and 0.2 mW in $N = 2$ and $N = 3$, respectively.

3.4.2.2 Effect of the Distance D Between APs

The effect of multi-user interference on the harvested energy-data rate trade-off is shown in Fig. 3.8. In this figure, we have plotted the Pareto boundaries for the first UE for different AP distances of $D = 10, 15, 20$ m for two cases of $d_{\max} = 5, 10$ m. As can be seen in Fig. 3.8a, in $d_{\max} = 5$ m, the Pareto boundaries are quite close to each other for different values of D. The maximum harvested energy is slightly higher in $D = 10$ m because of the higher level of interference in this case. However, by increasing the demand for the data rate, this interference will degrade the performance. In the case of $d_{\max} = 10$ m, as plotted in Fig. 3.8b, Pareto boundaries for $D = 15, 20$ m are very close to each other. However, by decreasing the distance to $D = 10$ m the harvested energy increases in a fixed desired data rate. This is due to the fact that in higher $d_{\max}$s the probability of utilizing both APs increases while in lower $d_{\max}$s the UEs are mostly fed with their nearest AP.

3.4.2.3 Effect of Maximum UE Distance $d_{\max}$ from the AP

The effect of small-cell size is investigated in this section by plotting the Pareto boundaries for different maximum distance of UEs from the APs. Figure 3.9 shows the harvested energy-data rate trade-off for $N = 1$, $d_{\max} = 5, 7.5, 10$ m. As can be seen, by decreasing the maximum distance of the UEs from the AP, in the same number of UEs, the system can benefit from less path loss and harvest more energy. This superior performance is mostly seen in the region when harvested energy has a higher preference weight. By decreasing the $d_{\max}$ further to 5 m, the system can also benefit from less interference due to the farther distance of UEs in each cell from the AP of the other cell and therefore, this better performance can also be observed in the data-rate preference region.

3.4.2.4 Effect of Inter-User Trade-Off

To study the trade-off between users in different small-cells, we choose different preference weights for $N_{\text{UE}} = 2$ UEs by setting $v_1^2 = \theta_1\theta_2, v_1^2 = \theta_2$ and $v_2^1 = \theta_1, v_2^2 = 1$. As a result, the trade-off between harvested energy and data rate is changing with θ_1 for both UEs the same as previous plots, but the priority of the first UE is θ_2 times the second UE.

Figure 3.10a,b show the Pareto boundaries of these two UEs for $\theta_2 = 1, 5, 10, 15$. As can be seen, both UEs have the same Pareto boundaries for $\theta_2 = 1$. To benefit from better performance in the first UE, we increase the θ_2. It can be inferred from Fig. 3.10 that this superior performance is not achievable by only adapting the TS ratio. Consequently beamformers will be aligned toward the first UE by allocating more power to the first AP which results in increasing the $E_{h_1}^{\text{TS}}$ without increasing the interference on the first UE. Hence the maximum data rate and harvested energy

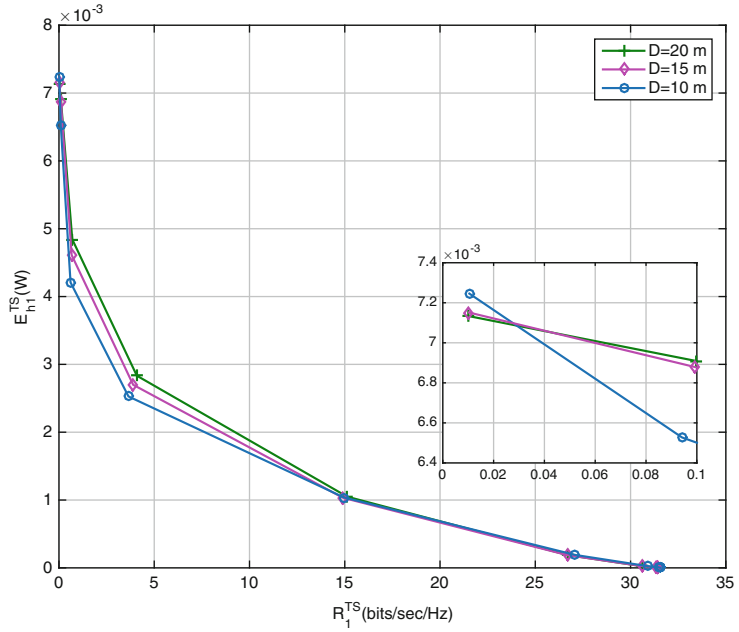

(a)

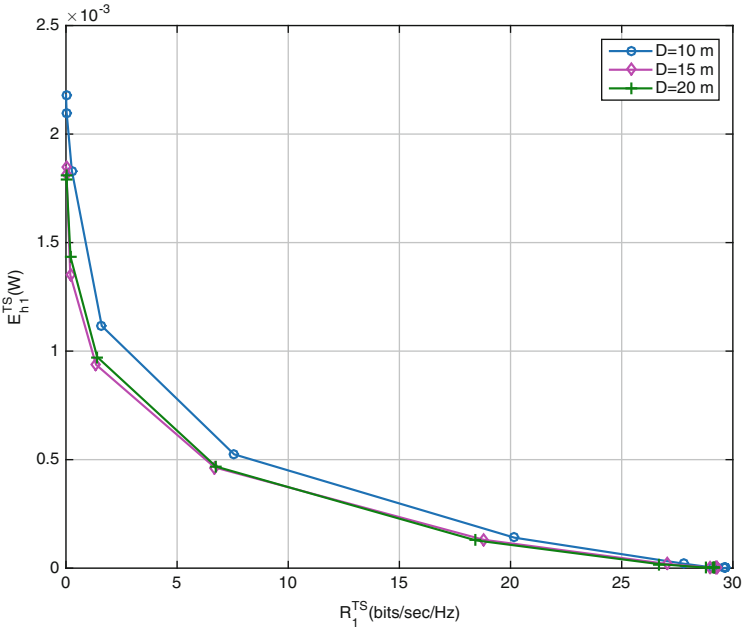

(b)

Fig. 3.8 Pareto boundary of TS SWIPT for different D and $d_{\max} = 5, 10\,\text{m}$. (**a**) $d_{\max} = 5\,\text{m}$. (**b**) $d_{\max} = 10\,\text{m}$

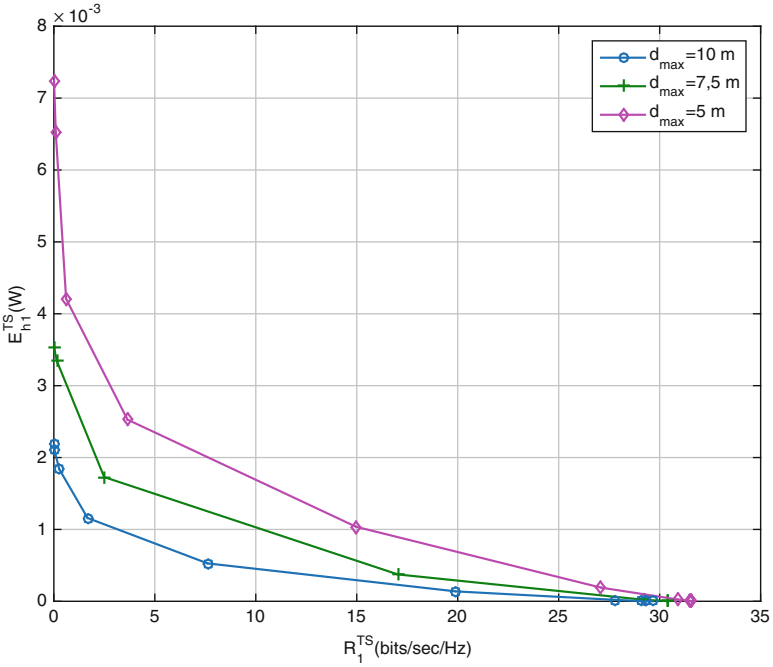

Fig. 3.9 Pareto boundary of TS SWIPT for different $d_{\max}$

both decrease in the second UE. Therefore, improving the performance of one user by increasing its preference weight will be at the expense of decreasing the performance of the other user drastically.

3.4.2.5 Effect of the TS Ratios α_i

In this section, we study the effect of the TS ratios on harvested energy-data rate trade-off. Specifically, we compare the Pareto boundaries of the optimal TS SWIPT with the Pareto boundaries of the TS SWIPT which uses fixed predefined switching rate. We consider a symmetric scenario with $N = 1$ and for the fixed switching rate case, we assume the same TS rate for both users. Figure 3.11 illustrates the Pareto boundaries for fixed switching rates of $\alpha_1 = 0.1, \ldots, 0.9$. As can be seen, for lower switching rates, we have higher maximum harvested energy and lower maximum achievable data rates. However, the optimal TS SWIPT leverages the best possible harvested energy and data rate by optimizing $\alpha_i, \forall i$ jointly with the beamforming strategy.

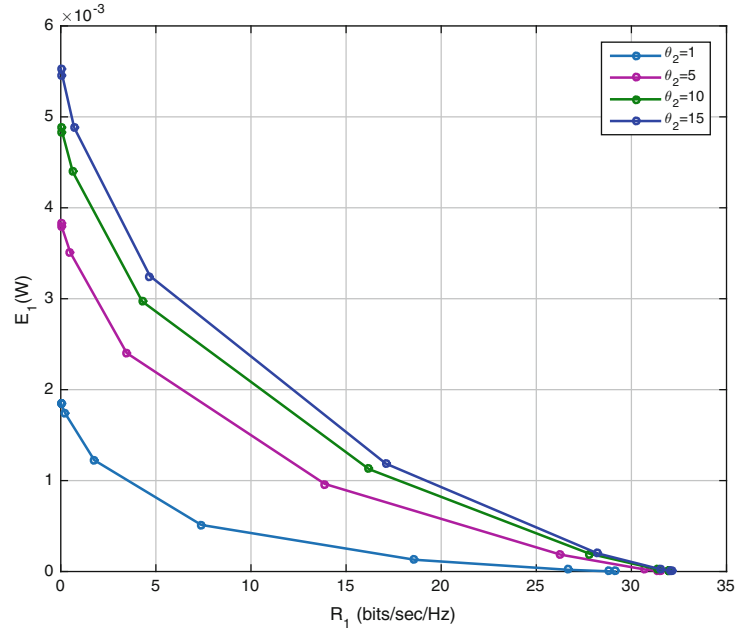

(a)

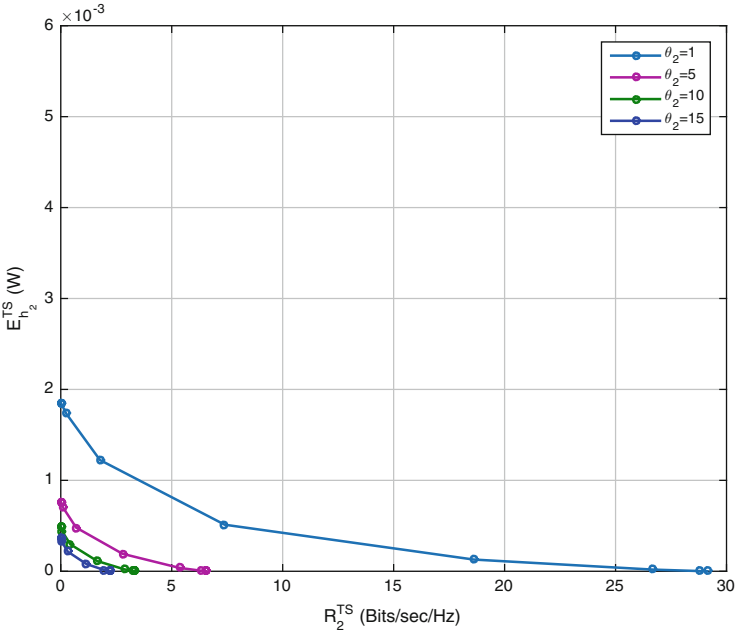

(b)

Fig. 3.10 Pareto boundary of (**a**) first and (**b**) second TS SWIPT UEs with different priorities

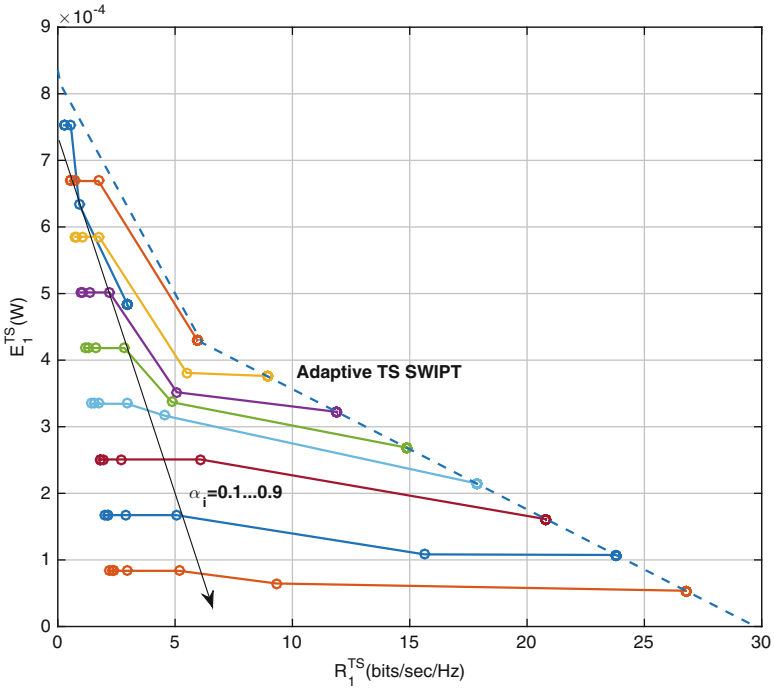

Fig. 3.11 Pareto boundary of TS SWIPT with fixed and adaptive TS ratios

3.5 Conclusion

In this chapter, we studied the resource allocation optimization for SWIPT in small-cell networks. We considered a small-cell network with MISO SWIPT system model and we addressed the problem of joint transmit beamforming and receiver time switching design in an MOO manner. The design problem was formulated as a non-convex MOO problem with the goal of maximizing the harvested energy and information data rates for all users simultaneously. The proposed MOO problem was scalarized employing the weighted Chebyshev method. This problem is a non-convex SDP which is relaxed and solved using convex–concave procedure based on the majorization–minimization algorithm. The trade-off between energy harvested and information data rate and the effect of network parameters on this trade-off was investigated by means of numerical results. The numerical results showed that:

- For TS SWIPT receiver, the energy performance loss with respect to ideal case increases when the number of UEs decreases.
- Interference is beneficial in case of low-rate devices operating in a very dense network.

- Cooperation among multiple transmitters can be used to drastically increase the achievable trade-off of one UE but the effect on the trade-off of other UEs could be detrimental.

In this work, we have considered perfect CSI. However, channel estimation is not possible during energy harvesting phase which may lead to out-dated CSI if the harvesting phase is too long. Reliability of CSI estimation also depends on TS ratio. Analysing this dependence and its associated trade-off which implies robust beamforming and SWIPT strategy can be considered as an interesting future work. Also generalization of this work can be applied in distributed massive MIMO scenario which has the potential to increase the harvested energy.

Acknowledgements The authors would like to thank IAP BESTCOM project funded by BELSPO, and the FNRS for the financial support.

References

1. S. Bi, C. Ho, R. Zhang, Wireless powered communication: opportunities and challenges. IEEE Commun. Mag. **53**(4), 117–125 (2015)
2. L.R. Varshney, Transporting information and energy simultaneously, in *IEEE International Symposium on Information Theory*, Auckland, December 2008
3. R. Zhang, C.K. Ho, MIMO broadcasting for simultaneous wireless information and power transfer. IEEE Trans. Wirel. Commun. **12**(5), 1989–2001 (2013)
4. L. Liu, R. Zhang, K.C. Chua, Wireless information transfer with opportunistic energy harvesting. IEEE Trans. Wirel. Commun. **12**(1), 288–300 (2013)
5. L. Liu, R. Zhang, K.C. Chua, Wireless information and power transfer: a dynamic power splitting approach. IEEE Trans. Commun. **61**(9), 3990–4001 (2013)
6. X. Zhou, Training-based SWIPT: optimal power splitting at the receiver. IEEE Trans. Veh. Technol. **64**(9), 4377–4382 (2015)
7. D.W.K. Ng, E.S. Lo, R. Schober, Wireless information and power transfer: energy efficiency optimization in OFDMA systems. IEEE Trans. Wirel. Commun. **12**(12), 6352–6370 (2013)
8. H. Zhang, K. Song, Y. Huang et al., Energy harvesting balancing technique for robust beamforming in multiuser MISO SWIPT system, in *Proceedings of IEEE International Conference on Wireless Communication and Signal Processing (WCSP)*, Hangzhou, October 2013
9. Q. Shi, L. Liu, W. Xu et al., Joint transmit beamforming and receive power splitting for MISO SWIPT systems. IEEE Trans. Wirel. Commun. **13**(6), 3269–3280 (2014)
10. D. Wing, K. Ng, R. Schober, Resource allocation for coordinated multipoint networks with wireless information and power transfer, in *IEEE Global Communications Conference*, Austin, TX, December 2014
11. Y. Dong, M. Hossain, J. Cheng, Joint power control and time switching for SWIPT systems with heterogeneous QoS requirements. IEEE Commun. Lett. **20**(2), 328–331 (2015)
12. M. Sheng, L. Wang, X. Wang et al., Energy efficient beamforming in MISO heterogeneous cellular networks with wireless information and power transfer. IEEE J. Sel. Areas Commun. **34**(4), 954–968 (2016)
13. J. Park, B. Clerckx, Joint wireless information and energy transfer in a two-user MIMO interference channel. IEEE Trans. Wirel. Commun. **12**(8), 4210–4221 (2013)
14. Z. Zong, H. Feng, F.R. Yu et al., Optimal transceiver design for SWIPT in *k*-user MIMO interference channels. IEEE Trans. Wirel. Commun. **15**(1), 430–445 (2016)

15. E. Bjornson, E.A. Jorswieck, M. Debbah et al., Multiobjective signal processing optimization: the way to balance conflicting metrics in 5G systems. IEEE Signal Process. Mag. **31**(6), 14–23 (2014)
16. S. Leng, D.W.K. Ng, N. Zlatanov et al., Multi-objective beamforming for energy-efficient SWIPT systems, in *IEEE International Conference on Communications (ICC)*, Kuala Lumpur, 22–27 May 2016
17. S. Leng, D.W.K. Ng, N. Zlatanov et al., Multi-objective resource allocation in full-duplex SWIPT systems (2015). arXiv preprint arXiv:1509.05959
18. M. Peng, Y. Li, J. Jiang et al., Heterogeneous cloud radio access networks: a new perspective for enhancing spectral and energy efficiencies. IEEE Trans. Wirel. Commun. **21**(6), 126–135 (2014)
19. X. Lu, P. Wang, D. Niyato, Wireless networks with RF energy harvesting: a contemporary survey. Commun. Surv. Tutorials **17**(2), 757–789 (2015)
20. D.R. Hunter, K. Lange, A tutorial on MM algorithms. Am. Stat. **58**(1), 30–37 (2004)
21. N. Janatian, I. Stupia, L. Vandendorpe, Joint MOO of transmit precoding and receiver design in a downlink time switching MISO SWIPT system (2016). arXiv preprint arXiv:1610.08290
22. P.M. Pardalos, A. Migdalas, L. Pitsoulis, Pareto optimality, game theory and equilibria, in *Pareto Optimality*, ed. by D.T. Luc (Springer Science & Business Media, New York, 2008), pp. 481–515
23. R.H.N. Thoai, Dc programming: an overview. J. Optim. Theory Appl. **193**(1), 1–43 (1999)
24. R.H. Tutuncu, K.C. Toh, M.J. Todd, Solving semidefinite-quadratic-linear programs using SDPT3. Math. Program. **95**(2), 189–217 (2003)
25. N. Janatian, I. Stupia, L. Vandendorpe, Joint multi-objective transmit precoding and receiver time switching design for MISO SWIPT systems, in *IEEE 17th International Workshop on Signal Processing Advances in Wireless Communications*, University of Edinburgh, July 2016
26. G.R. Lanckriet, B.K. Sriperumbudur, On the convergence of the concave-convex procedure. Adv. Neural Inf. Process. Syst. **22**, 1759–1767 (2009)
27. W.I. Zangwill, *Nonlinear Programming* (Prentice Hall, Englewood Cliffs, NJ, 1969)

Chapter 4
Harvesting Signal Power from Constructive Interference in Multiuser Downlinks

Christos Masouros

4.1 Introduction to Constructive Interference: Definitions, Examples, and Classification

Interference is traditionally considered as the major limitation in meeting the ever-increasing demands for transmission rates and quality of service (QoS) in current and future wireless communication systems. In multi-user and multi-access communications, interference is typically manifested in the communication channel, where signals of different links are superimposed. Particular effort has been placed on utilizing the channel's state information (CSI) to counteract its effects on transmission. It has been shown that in both time- and frequency-division duplex modes the CSI can be made known to the transmitter (a situation termed as CSIT). The a priori knowledge of interference is therefore not an uncommon situation and it is in fact readily available at the cellular base stations during downlink transmission, when CSIT combined with the knowledge of all data symbols intended for transmission can be used to predict the resulting interference between the symbols.

The seminal work of Costa in [1] has shown by information-theoretic analysis that in the cases where CSIT is available, known interference does not affect the capacity of the broadcast channel, which is therefore equivalent to the respective noise-only channel. In [1] it is also stressed that the optimum strategy to achieve this capacity would be to invest power not in cancelling interference, but rather in coding along interference. Nevertheless, the majority of existing transmission strategies attempt to eliminate, cancel, or pre-subtract interference. Indeed, a number of important technologies exist that make use of the channel knowledge to mitigate

C. Masouros (✉)
University College London, Torrington Place, London, UK
e-mail: chris.masouros@ieee.org

D.N.K. Jayakody et al. (eds.), *Wireless Information and Power Transfer: A New Paradigm for Green Communications*, DOI 10.1007/978-3-319-56669-6_4

or manage interference. Only recently, however, there has been a rising interest in making use of the interference power to enhance the useful signal [2, 3].

What justifies the traditional interference-cancellation approaches is that, from a statistical perspective, interference imposes a "random," noise-like perturbation to the transmitted information and introduces a variance to the received signal which on average hinders detection and deteriorates the resulting performance. By employing an instantaneous, as opposed to statistical, view of interference one can see that interference can contribute to the detection of the useful signal and in fact, act as a source of useful signal power. This phenomenon can be utilized in the CSIT-assisted downlink transmission and other known-interference scenarios where interference can be predicted, and its power can be harvested to improve the wireless link's performance. In modern systems where transmitted power is becoming a scarce resource and energy efficiency is becoming more and more central in the overall network design, the harvesting and use of signal power from interference which is inherent in the communication system provides an important source of green useful power for reliable signal detection.

4.1.1 Is All Interference Harmful? Examples and Definitions

To motivate the concept of interference exploitation, this section presents a qualitative analysis of instantaneous interference and explores the possibility of treating part of interference as constructive, as a step towards the design of innovative transmission schemes.

A trivial example of a two-user link is shown in Fig. 4.1a, where we define the desired symbol of user 1 as u_1 and the interfering symbol from user 2 as u_2. For simplicity, and without loss of generality, let us assume that these belong to a Binary Phase Shift Keying (BPSK) constellation and that $u_1 = 1, u_2 = -1$. For illustration purposes, ignore the noise at the receiver, and assume a lossless channel from the

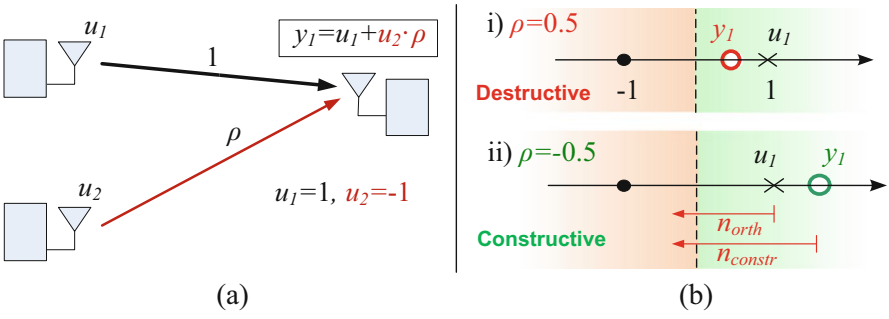

Fig. 4.1 The concept of constructive interference—a two-user example: (**a**) transmission scenario, (**b**) destructive (*i*) and constructive (*ii*) interference

intended transmitter to the receiver and an interfering channel represented by the coefficient ρ. Accordingly, the received signal can be expressed as

$$y_1 = u_1 + u_2 \cdot \rho, \tag{4.1}$$

where $u_2 \cdot \rho$ is the interference. Note that this model also corresponds to a multiple-input-single-output (MISO) transmission with a matched filtering receiver tuned to the channel of user 1, where the correlation between the two channels is ρ [4]. In Fig. 4.1b two distinct cases are shown, depicting the transmitted ($\times$) and received (o) symbols for user 1 on the BPSK constellation. In case (i) with $\rho = 0.5$ it can be seen from (4.1) that $y_1 = 0.5$. In this case, the destructive interference from user 2 has caused the received symbol of user 1 to move towards the decision threshold (denoted by the dashed line) in the BPSK constellation. The received power of user 1 has been reduced and its detection is prone to low-power noise. In case (ii), however, for $\rho = -0.5$, the system equation (4.1) yields $y_1 = 1.5$, and hence the interference from user 2 is constructive. The power received by user 1 has been augmented due to the interference from user 2 and now its detection is tolerant to noise n_{constr} of higher power compared to n_{orth} for the orthogonal transmission case without interference. It should be stressed that in both cases the transmit power for each user in this elementary example is equal to one. Note that, while the above example refers to a two-user transmission scenario for illustration purposes, the fundamental concept can be extended to more users, multipath transmission, inter-cell interference in a multi-cell environment, and other generic interference-limited systems.

Let us make the above observation more explicit, by looking at the geometrical representation in a two-user example with arbitrary channels. In Fig. 4.2 we show a scenario of two users with channels h_1 and h_2. One could think of this as a multiple-input-single-output (MISO) channel with two transmit antennas and one receive antenna. To focus the study on the interference between the two transmissions, in line with the above example, noise is also assumed to be zero here. In both subfigures, the axes depict the directions of the complex-valued channels, and $u_1 = 1, u_2 = -1$ like in the case above. The bold-lined arrow in each subfigure represents the received signal y and the purple arrows denote its projection to each

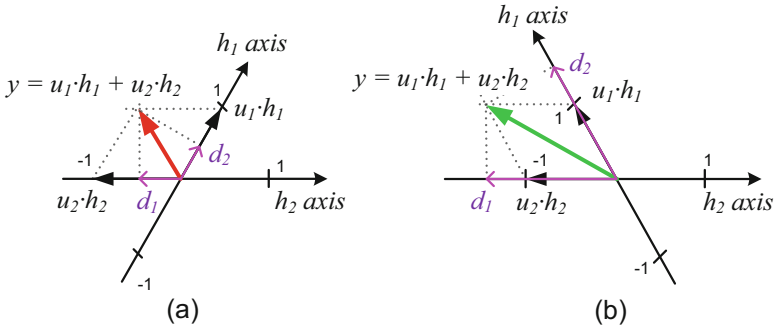

Fig. 4.2 Geometrical representations of interference scenarios: (**a**) destructive, (**b**) constructive

of the channel axes which represents the match-filtered symbols d_1, d_2 at the receiver before the decision stage. In the case of Fig. 4.2a, the two transmitted symbols add up destructively in the received signal y. Consequently, the projections d_1, d_2 of the received signal on the channel axes yield reduced symbol energy compared to the transmitted symbols u_1, u_2 and the detection is destructively affected by interference. In the case of Fig. 4.2b, however, the addition of the users' transmitted symbols yields a received signal which has higher amplitude compared to the destructive case. As a result, the detected symbols d_1, d_2 have higher amplitudes compared to the destructive case, and more importantly compared to the transmitted symbols u_1, u_2 themselves, which in a practical scenario and in the presence of noise translate to higher signal to noise ratios (SNRs).

Note that in both cases the amplitude of the transmitted symbols u_1, u_2 (and hence the transmitted power) is the same, and it is the interfering power that increases the received amplitude (hence the SNR) in the second case. Moreover, note that in the case where different combinations of symbols u_1, u_2 are transmitted, the configurations of Fig. 4.2a, b may result in constructive and destructive interference, respectively. In other words, a channel configuration that yields constructive interference for a specific symbol combination may result in destructive interference for other combinations and vice versa. It is clear from the above that the characterization of interference and its separation into constructive–destructive depends not only on the correlation of the transmission paths but also on the instantaneous symbol values.

4.1.2 Systematic Classification of Interference for Generic Constellations

To utilize the above observations and take advantage of constructive interference in a systematic way in practical scenarios, it is important to be able to classify interference into constructive and destructive systematically. Accordingly, here we discuss the mathematical classification of interference for a number of PSK and QAM constellations.

Let us first derive the mathematical classification criteria for PSK modulation. Figure 4.3a–c shows Monte Carlo generated received constellation points for different PSK modulations. These are represented by randomly positioned dots in the PSK constellations, centered around the nominal PSK constellation points. The red dots denote received signals corrupted by destructive interference while the green dots represent received symbols resulting from constructive interference. The generic criterion for constructive/destructive interference classification is as follows:

Constructive interference is that which yields received signals that have increased distances from the decision boundaries of the modulated-symbol constellation, with respect to the nominal constellation points.

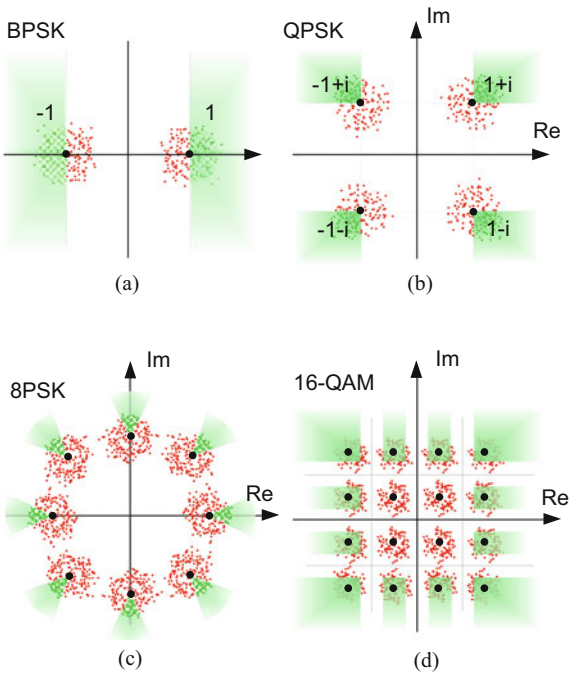

Fig. 4.3 Basic PSK and QAM constellations and constructive (*green*)–destructive (*red*) interference sectors

Note that this is a simplistic definition of constructive interference, where the comparison is made to the nominal constellation points. In the context of SNR optimization, we will see in Sect. 4.2.2 that the definition can be extended to arbitrary distances from the constellation's decision boundaries to reflect varying SNR and QoS requirements for the communication links. Based on the above definition, below we derive the mathematical criteria for constructive interference for BPSK, QPSK, and generic M-PSK modulation.

BPSK Let us take a closer look at Fig. 4.3a, and let us we define $u_i = e^{j\phi_i}$ as the PSK symbol of interest and y_i as the received signal without noise, for the ith user. Accordingly, the interference to the ith user can be found as $g_i = y_i - u_i$. For the BPSK modulation of Fig. 4.3a the desired user's signal $u_i \in \{-1, +1\}$, and therefore the decision boundary is the imaginary axis. Constructive interference pushes the received symbol away from the decision boundary, and therefore for $u_i = -1$ interference is constructive when its real part is negative, and for $u_i = 1$ interference is constructive when it's positive. Accordingly, for BPSK, interference is constructive when

$$\mathrm{Re}(u_i)\mathrm{Re}(g_i) \geq 0 \tag{4.2}$$

QPSK For quadrature-PSK (QPSK) modulation, since there are two decision boundaries (the real and imaginary axes) in the signal constellation, the above

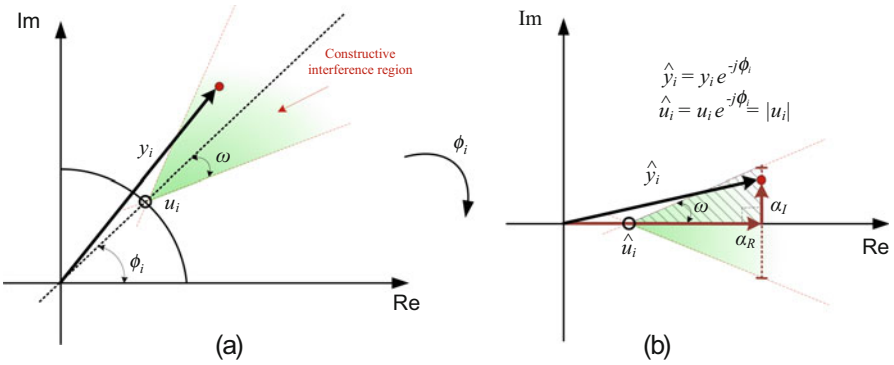

Fig. 4.4 Interference classification for M-PSK constellations

criterion has to be applied separately to the real and imaginary part of the received signal. Therefore, for QPSK, interference is constructive when

$$\mathrm{Re}(u_i)\mathrm{Re}(g_i) \geq 0 \;\&\; \mathrm{Im}(u_i)\mathrm{Im}(g_i) \geq 0 \tag{4.3}$$

Again, the received symbols that satisfy this requirement are shown in green color in Fig. 4.3b.

Interference Classification for *M*-PSK To obtain a more generic characterization of interference for M-PSK, let us observe the constellation example shown in the diagram of Fig. 4.4a, which focuses on one out of the M possible constellation points in the modulated-symbol constellation, namely the point with symbol phase ϕ_i. The constructive interference region denoted by the green shaded area spans an angle on each side of ϕ_i that depends on the order M of the modulation, and is defined by the parameter ω for which

$$\omega = \frac{\pi}{M} \tag{4.4}$$

To obtain a generic characterization irrespective of the specific constellation point studied, let us rotate our observation by $-\phi_i$ as shown in Fig. 4.4b, where

$$\hat{y}_i = y_i e^{-j\phi_i} \tag{4.5}$$

Applying the same transformation to the symbol of interest results in

$$\hat{u}_i = u_i e^{-j\phi_i} = |u_i| \tag{4.6}$$

i.e., we have now isolated the amplitude of the desired symbol. Let us also define $\alpha_R = \mathrm{Re}(\hat{y}_i)$ and $\alpha_I = \mathrm{Im}(\hat{y}_i)$, where clearly, α_R represents the amplitude of

the received constellation point due to constructive interference and α_I provides a measure of the angle shift from the phase of the original constellation point.

For constructive interference conditions to hold, it can be seen that α_R and α_I are allowed to grow infinitely, as long as their ratio is such that the received symbol is contained within the constructive area of the constellation, i.e., the green shaded area in Fig. 4.4b. Using basic geometry in the right triangle denoted by the diagonal stripes in the figure we have that, for the received symbol to fall inside the constructive interference region, α_I, α_R have to obey

$$|\alpha_I| \leq (\alpha_R - |u_i|) \tan \omega \tag{4.7}$$

In other words, for an M-PSK modulation for which the constellation points are normalized to unit power, the resulting interference is constructive when the received symbol (excluding noise) follows

$$\left|\mathrm{Re}(y_i e^{-j\phi_i})\right| \leq (\mathrm{Im}(y_i e^{-j\phi_i}) - 1) \tan \omega \tag{4.8}$$

where ϕ_i is the desired information and ω is the modulation-dependent parameter as defined above.

Analytical characterization criteria of the interference for B-, Q-, and higher order PSK modulation are further detailed in [5, 6]. We shall generalize the above to accommodate arbitrary SNR requirements in the beamforming optimization discussion of Sect. 4.2.2.

Constructive Interference in QAM Constellations It was shown in the previous section that there are benefits to be gained from utilizing interference in PSK-based communication systems. Notably, low order PSK appears in numerous scenarios in many communication standards [7]. Indeed BPSK and QPSK are favored in high interference scenarios where the achievable rates are limited due to the ill-conditioned nature of the channel or the density of the communication access points. Evidently, the more the interference, the more the gain from utilizing it as opposed to eliminating it. In a highly correlated or a densely populated multi-access channel conventional schemes would employ low order PSK modulation and invest most of their power in canceling the existing interference, so it is in these scenarios where it is expected to gain the most from exploiting interference.

For the completeness of the discussion, however, we must not omit situations where higher transmission rates are achievable, in which case higher order QAM would be used according to the communication standards. It is therefore reasonable to raise the following questions: "Can the above concept be applied to QAM constellations?," "How much benefit can be extracted from interference energy in these cases?". A first attempt to address these issues is presented in [8, 9] and more recently in [10–12]. To examine this, let us observe the 16-QAM constellation, shown in Fig. 4.3d. It can be seen that for the inner constellation points, since they are bounded by decision thresholds in all directions around them, the concept of constructive interference does not hold. Interference that shifts the received

inner constellation point away from one decision boundary pushes it closer to another decision boundary. However, for the outer constellation points there is still some space for constructive interference. Indeed for the points at the corners of the 16-QAM constellation the conditions are identical to the ones for the QPSK constellation points. Therefore, as shown in Fig. 4.3d the interference classification criteria for these points are similar to the ones discussed above. Moreover, for the outer constellation points in-between the corner points again there exists a margin of constructive interference as shown in Fig. 4.3d, strictly towards the directions away from the inner decision boundaries, as shown by the green shaded areas. Combining the above observations, we can design the constructive interference criteria for the example of 16-QAM defined by the alphabet $\mathscr{A} = \{\eta^r + i\eta^i | \eta^r, \eta^i \in \{\pm 1, \pm 3\}\}$ as [10]

$$\begin{aligned} \mathrm{Re}(u_i)\mathrm{Re}(g_i) \geq 0 \;\&\; \mathrm{Im}(u_i)\mathrm{Im}(g_i) \geq 0, &\quad \text{for } u_i \in \{\pm 3 \pm i3\} \\ \mathrm{Re}(u_i)\mathrm{Re}(g_i) \geq 0 \;\&\; \mathrm{Im}(g_i) = 0, &\quad \text{for } u_i \in \{\pm 3 \pm i\} \\ \mathrm{Re}(g_i) = 0 \;\&\; \mathrm{Im}(u_i)\mathrm{Im}(g_i) \geq 0, &\quad \text{for } u_i \in \{\pm 1 \pm i3\} \\ \emptyset, &\quad \text{for } u_i \in \{\pm 1 \pm i\} \end{aligned} \tag{4.9}$$

4.1.2.1 Decision-Boundary Adaptation

Notably, from the above discussion it follows that constructive interference does not apply for the inner constellation points of QAM constellations, which increase in population as the order of QAM modulation increases. However, further scope for accommodating constructive interference in QAM constellations can be provided by employing adaptive, channel-dependent, decision boundaries in the receive constellation. This concept is illustrated in Fig. 4.5. Based on a stochastic study of the

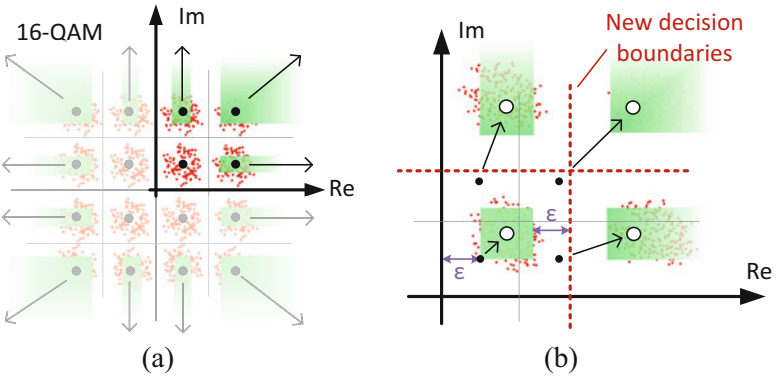

Fig. 4.5 Decision-boundary expansion for 16-QAM: (**a**) 16-QAM with fixed decision boundaries, (**b**) boundary expansion to accommodate constructive interference

power of constructive interference for a given communication scenario, one could envisage an expansion of the decision boundaries of the QAM constellation such that the whole constellation spreads to accommodate an expansion of the Euclidean distances between all constellation points. This would allow for additional constructive interference for all constellation points, including the inner points. The resulting effect is shown in Fig. 4.5b where the focus is on the top right quadrant of the 16-QAM constellation, and the black dots represent the original constellation points, while the circles represent the expanded constellation points. The distances from the constellation points to the decision boundaries in the original constellation are denoted as ε. It can be seen that the new constellation points can move within the green shaded areas, while maintaining an equal or greater minimum Euclidean distance ε from the new decision thresholds compared to the distance in the original constellation. Importantly, this allows for constructive interference power to be accommodated for the inner constellation points, that had no provision for constructive interference when employing fixed decision boundaries as in Fig. 4.5a.

These remarks indicate that, while the advantages of interference exploitation are more pronounced in systems using PSK modulation, there are still benefits to be gained in QAM-based systems. While initial efforts have been made towards this direction in [11], it is yet to be explored how to optimally expand the decision boundaries of QAM to accommodate interference, and how the above qualitative observations quantify in performance gain for the QAM constellations.

Early work carried out on simple precoding techniques that will be discussed in the following indicates that there are significant benefits to be derived by the above observations. The important feature is that these benefits are drawn not by increasing the transmitted power of the useful signals u_i, but rather by the reuse of interference energy that already exists in the communication system; a source of green signal energy that with conventional interference-cancellation techniques is left unexploited.

4.2 Constructive Interference in Multiuser Downlinks: Harvesting Useful Signal Power

To illustrate the usefulness of the above observations, we shall overview a number of techniques that exploit constructive interference superposition, focusing on the baseline scenario of single-cell multiuser downlink transmission. We note, however, that interference-exploitation approaches have also been developed for multi-cell scenarios in cognitive radio applications [13–16].

Accordingly, consider a multiuser MISO (MU-MISO) downlink that consists of a base station transmitter equipped with N_t antennas and K single-antenna receivers. For the case of the closed-form precoders of [5, 6, 8–11, 17–20], it is required that $N_t \geq K$. The above channel is modelled by

$$\mathbf{y} = \mathbf{H}\mathbf{x} + \mathbf{n}, \tag{4.10}$$

where $\mathbf{y} \in \mathbb{C}^{K\times 1}$ is the vector that models the received symbols in all receive antennas and $\mathbf{H} = [\mathbf{h}_1; \mathbf{h}_2; \ldots \mathbf{h}_K,] \in \mathbb{C}^{N_t \times K}$ is the channel matrix with $\mathbf{h}_k \in \mathbb{C}^{1\times N_t}$ denoting the channel vector to the kth user, with elements $h_{m,n}$ representing the complex-valued channel coefficient between the nth transmit antenna and the mth receive antenna. Furthermore, $\mathbf{x} \in \mathbb{C}^{N_t\times 1}$ is the vector of precoded transmit symbols that will be discussed in the following and $\mathbf{n} \in \mathbb{C}^{K\times 1} \sim \mathscr{CN}(0, \sigma^2\mathbf{I})$ is the additive white Gaussian noise (AWGN) at the receiver, with $\mathscr{CN}(\mu, \sigma^2)$ denoting the circularly symmetric complex Gaussian distribution associated with a mean of μ and a variance of σ^2.

4.2.1 Closed-Form Precoders, Linear and Non-linear

To accommodate constructive interference the precoding can be designed such that the signal received at the MUs allows for the existence of interference when this is constructive. The first applications of this concept were developed for code division multiple access (CDMA) communications [5, 17–19]. Since then, a number of closed-form precoders have been developed to accommodate constructive interference [6, 12, 20–26] in MU-MISO systems. A generic block diagram of the low-complexity precoding adaptations for a MU-MISO downlink is shown in Fig. 4.6. The essential additional components involve the symbol-by-symbol characterization of interference and the judicious precoding block.

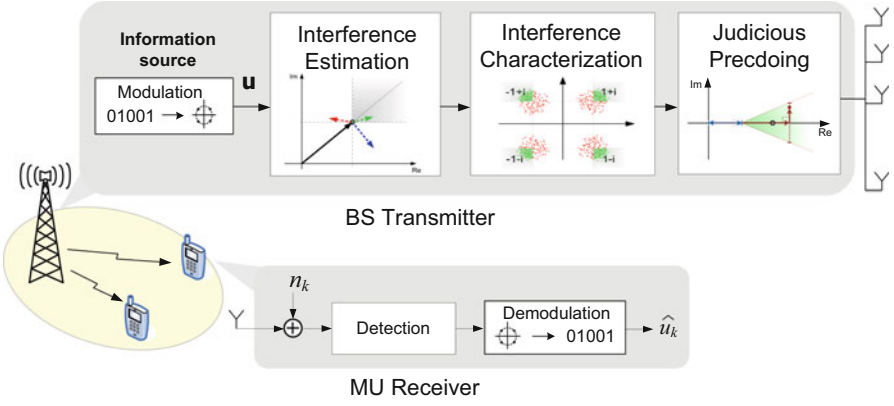

Fig. 4.6 A generic precoding block diagram for the exploitation of interference. Three distinct operations can be observed: interference estimation, interference characterization, and judicious precoding [3]

4.2.1.1 Closed-Form Linear Precoders

Early work such as the one in [6] has looked at adapting simple precoding techniques such as zero forcing (channel inversion) [27] to accommodate for constructive interference in MU-MISO downlinks. Here the main idea is to retain the correlation between the transmitted symbols when it yields constructive interference and eliminate the correlation when it results in destructive interference by means of zero-forcing (ZF) precoding. A further step towards transmitting along interference is shown in [20, 21] for the MU-MISO downlink. Instead of observing and characterizing the interference and zero forcing it accordingly, the precoder actively influences the interference by means of rotational precoding to yield constructive interference. In this case the useful signal benefits from all interfering signals' energy at every symbol period.

To exploit constructive interference the correlation rotation precoder of [20] carefully aligns interference so that it contributes constructively to the desired signal power. In brief, the transmit vectors of [20] follow the typical linear precoding form of

$$\mathbf{x} = \sqrt{\frac{P}{\beta}}\mathbf{W}\mathbf{u}, \tag{4.11}$$

where $\mathbf{u} \in \mathbb{C}^{K\times 1}$ is the modulated data vector, P is the transmit power budget. The precoding matrix $\mathbf{W} = [\mathbf{w}_1, \mathbf{w}_2, \ldots, \mathbf{w}_k] \in \mathbb{C}^{N_t\times K}$, with $\mathbf{w}_k \in \mathbb{C}^{N_t\times 1}$ denoting the beamforming vector for the kth user, is formed as

$$\mathbf{W} = \mathbf{H}^{\dagger}\mathbf{R}_{\phi}, \tag{4.12}$$

where $\mathbf{H}^{\dagger} = \mathbf{H}^H(\mathbf{H}\mathbf{H}^H)^{-1}$ is the Moore–Penrose generalized inverse of the channel matrix, and $\mathbf{R}_{\phi} = \mathbf{R} \odot \mathbf{Q}$, with $\odot$ denoting element-wise matrix multiplication, $\mathbf{R}_{\phi}$ representing the correlation rotation (CR) matrix. The CR matrix contains the elements of the channel correlation matrix $\mathbf{R} = \mathbf{H}\mathbf{H}^H$ rotated by the phase-only matrix $\mathbf{Q}$ with elements in the form $q_{k,l} = e^{j\Delta\phi_{k,l}}$ with

$$\Delta\phi_{k,l} = \angle u_k - \angle u_l\rho_{k,l}, \tag{4.13}$$

such that the resulting interference aligns constructively to the received signal. In (4.13) above, $\rho_{k,l}$ is the k,lth element of the channel correlation matrix $\mathbf{R}$, $\angle x$ denotes the phase of the complex number x. Finally, in (4.11) β is the scaling factor that constraints the average transmit power, and is given as

$$\beta = ||\mathbf{W}||^2 = \text{trace}(\mathbf{W}^H\mathbf{W}). \tag{4.14}$$

Notably, by letting $\mathbf{R}_{\phi} = \mathbf{I}_K$ the CR precoder reduces to the conventional zero-forcing (channel inversion) precoder. It can also be observed that the precoder

in (4.12) combines the channel-only dependent zero-forcing component $\mathbf{H}^{\dagger}$ with the symbol-by-symbol adaptive part in $\mathbf{R}_{\phi}$. By combining (4.10)–(4.12) it can be seen that this results in the following received symbol vector:

$$\mathbf{y} = \sqrt{\frac{P}{\beta}}\mathbf{R}_{\phi}\mathbf{u} + \mathbf{n}, \tag{4.15}$$

where by the definition of matrix $\mathbf{R}_{\phi}$ above, the signal contained in the component $\mathbf{R}_{\phi}\mathbf{u}$ benefits from constructive interference, and falls inside the constructive interference regions in the received constellations, as in Fig. 4.3.

4.2.1.2 Dirty Paper Non-linear Approaches

The capacity achieving alternative to low-complexity linear precoding is dirty paper coding (DPC). While optimal DPC has prohibitive complexity, low-complexity suboptimal approaches have been explored in the form of Tomlinson–Harashima Precoding (THP) [28] and Vector Perturbation (VP) [29]. Both the THP and VP families of techniques have been shown to benefit from harvesting useful signal power from interference.

Interference Optimized Tomlinson–Harashima Precoding THP transmission involves the pre-subtraction of interference at the transmitter in an iterative manner, by which the transmit symbol of the kth user is given as

$$x_k = \left[u_k - \sum_{l=1}^{k-1} b_{k,l} x_l \right] \mathrm{mod}_L \, , \, k \in [1, K] \tag{4.16}$$

where $b_{k,l}$ is the k,lth element of matrix $\mathbf{B}$, which is the equivalent channel matrix obtained after lower-triangularization, such that each user only sees interference from previously encoded users. u_k is the kth user's information data symbol, selected from an integer constellation $\mathscr{A} = \{\eta^r + i\eta^i | \eta^r, \eta^i \in \{\pm 1, \pm 3, \ldots \pm (\sqrt{M} - 1)\}\}$ where M is the constellation order. Accordingly, THP in (4.16) pre-subtracts from the desired symbol all interference from the previously encoded users. $[.]\mathrm{mod}_L$ denotes the modulo operation with base L, and is used to constrain the transmitted power [28]. Still, this modulo operation results in a transmit power for THP that is higher compared to uncoded transmission, a situation referred to as *Power Loss*.

A number of adaptations of THP have been developed such that interference is exploited to improve the interference pre-subtraction function of the THP encoder. Interference-optimized THP (IO-THP) in [30, 31] exploits the power of interference to reduce the abovementioned power loss. It uses an encoding strategy where the amplitude and phase of the useful signal for a number of users is optimized, within the constructive constellation sectors as shown in Fig. 4.3 and under an SNR

threshold, such that the resulting interference is better aligned to the symbols of interest. In this way the power required by THP encoding to subtract the interference (and therefore the transmitted power) is minimized, leading to a more power-efficient transmission. Accordingly, for IO-THP the data symbols for a subset $K_s \leq K$ users are scaled by the real-valued factors v_k^r, v_k^i as

$$\tilde{u}_k = v_k^r u_k^r + i v_k^r u_k^i, \; k \in [1, K_s] \tag{4.17}$$

where $u_k^r = \text{Re}(u_k), u_k^i = \text{Im}(u_k)$, and v_k^r, v_k^i are carefully optimized such that $\tilde{u}_k$ falls in the constructive area of the modulation constellation as discussed in the previous section and shown in Fig. 4.3. Thereafter, the typical THP pre-subtraction is applied to the modified data symbols as

$$\tilde{x}_k = \left[\tilde{u}_k - \sum_{l=1}^{k-1} b_{k,l} \tilde{x}_l(v^*) \right] \text{mod}_L, k \in [1, K] \tag{4.18}$$

where now the transmitted symbols $\tilde{x}_k$ are a function of the optimal scaling factors v^*. For the details of the optimization of the factors v_k^r, v_k^i the reader is referred to [30, 31]. By means of the above constructive symbol optimization, power is saved from the interference-cancellation operation and invested in the useful signal as a source of additional signal power.

An illustrative result of this effect is shown in Fig. 4.7 where the performance in terms of bit error rate (BER) is shown for a system with $N_t = 4, K = 4$ as a function of the transmit power in vector $\mathbf{x}$ expressed as the percentage of the power of the uncoded symbols in vector $\mathbf{u}$, for conventional THP and IO-THP with increasing numbers of prescaled users K_s. A trade-off between transmit power and performance can be obtained for IO-THP by varying the SNR threshold involved in the optimization of the pre-scaling factors [30, 31]. While in this chapter we skip the details of this trade-off, the main message in this result is that, by harvesting the interference energy in this scenario, IO-THP achieves a transmit power reduction down to $1/6$ of that for conventional THP, for the same BER performance.

Constructive Vector Perturbation Precoding Vector perturbation designates another family of non-linear precoders that employ a channel inversion precoding matrix and apply a perturbation on the transmitted symbols such that the signal content at the receiver is maximized. The transmitted signal is given by [29]

$$\mathbf{x} = \sqrt{\frac{P}{\beta}} \mathbf{H}^\dagger (\mathbf{u} + \tau \mathbf{l}^\star) \tag{4.19}$$

where

$$\beta = ||\mathbf{H}^\dagger (\mathbf{u} + \tau \mathbf{l}^\star)||^2 \tag{4.20}$$

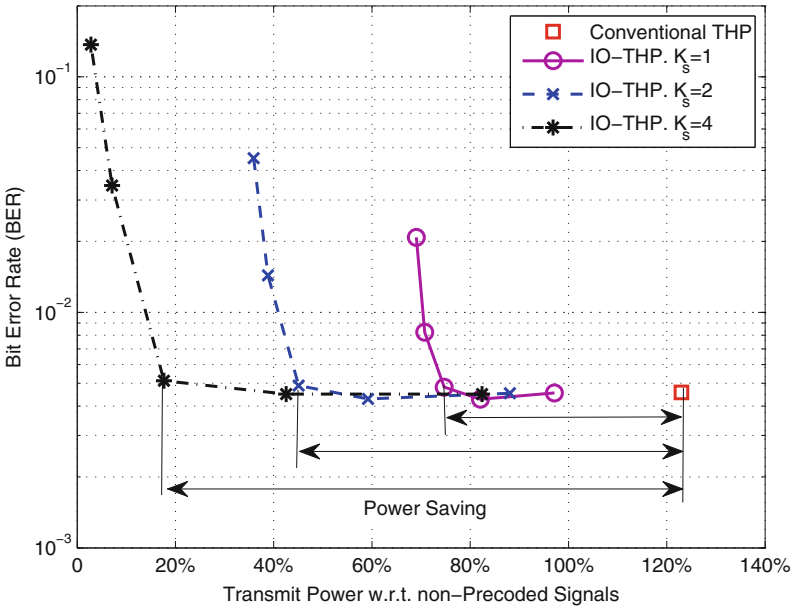

Fig. 4.7 BER versus transmit power for THP, and IO-THP. $N_t = K = 4$, QPSK, SNR $= 29$ dB [31]

is the transmit power scaling factor so that $||\mathbf{x}||^2 = P$ and $\mathbf{l}^\star \in \mathbb{C}^{M\times 1}$ is the selected perturbation vector with integer entries. Also $\tau = 2|c|_{\max} + \Delta$ where $|c|_{\max}$ is the absolute value of the constellation symbol with the maximum magnitude and Δ denotes the minimum Euclidean distance between constellation symbols. The idea here is that the perturbation vectors $\mathbf{l}^\star$ are introduced to increase the degrees of freedom in optimizing the resulting performance, and are later removed at the receiver by applying a modulo operation with base τ.

Accordingly, the perturbation vectors $\mathbf{l}^\star$ are chosen from an integer constellation $\mathbb{Z}^M + j\mathbb{Z}^M$ to maximize the signal component in the received symbols or equivalently minimize β and the resulting the noise amplification at the receiver, as

$$\mathbf{l}^\star = \arg \min_{\mathbf{l}\in\mathbb{Z}^M + j\mathbb{Z}^M} ||\mathbf{H}^\dagger(\mathbf{u} + \tau\mathbf{l})||^2 \tag{4.21}$$

This is typically an NP hard problem solved with sphere search techniques [32] that have complexity which grows exponentially with the number of users K.

To apply the concept of interference exploitation, the above optimization can be constrained to ensure that the perturbation vectors add up strictly constructively to the information symbols, so that the removal of perturbation is not necessary at the receiver and the receiver complexity can be drastically reduced. In particular, in the constructive vector perturbation approach of [33] the search space for the

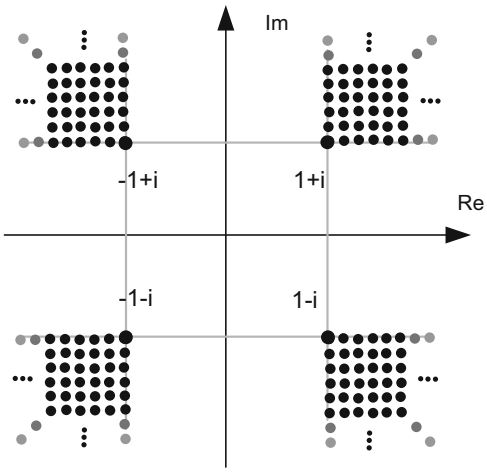

Fig. 4.8 Constructive perturbation lattice, QPSK example [30]

perturbation vectors is limited to the constructive areas in the symbol constellation. In other words the above optimization is modified (4.21) to

$$\mathbf{l}^{\star} = \arg \min_{\mathbf{l} \in \mathbb{A}^M} ||\mathbf{H}^{\dagger}(\mathbf{u} + \tau \mathbf{l})||^2 \tag{4.22}$$

where $\mathbb{A}^M$ is a lattice that only involves the constructive areas of the constellation as shown in Fig. 4.3. For the example of QPSK this constellation can be described as $\mathbb{A}^M = \left\{0, \varepsilon \left(m \cdot \text{sgn}\{\text{Re}(\mathbf{u})\} + n \cdot \text{sgn}\{\text{Im}(\mathbf{u})\}\right)\right\}$ where $m, n \in \{1, 2, 3 \ldots\}$, sgn$\{x\}$ denotes the sign of x and ε is an arbitrary constant, which results in the lattice shown in Fig. 4.8. The effect of this optimization is that, as the perturbed signals lie in the constructive areas of the constellation, there is no need to remove the perturbation at the receiver, which therefore alleviates the need to apply the $[.]\text{mod}_{\tau}$ operation at the receiver and the need to feed-forward the scaling factor β for receiver equalization. This further implies that there is no need for the perturbation quantities to take integer values, and in fact, it is shown in [33] that the perturbation operation can be transformed into a linear scaling operation in the form

$$\mathbf{x} = \sqrt{\frac{P}{\beta}} \mathbf{H}^{\dagger} \mathbf{S} \mathbf{u} \tag{4.23}$$

where $\mathbf{S}$ is a diagonal scaling matrix with elements s_i and $\beta = ||\mathbf{H}^{\dagger}\mathbf{S}\mathbf{u}||^2$. Accordingly, the perturbation search need not apply on an integer lattice $\mathbb{A}^M$ like the one in (4.21), (4.22), and can be extended to all points in the constructive regions of the symbols' constellation. By applying a lower-threshold s_t on the scaling factors so that a minimum QoS level is guaranteed, the perturbation search can be transformed into

$$\mathbf{S}^{\star} = \arg\min_{\mathbf{S}} ||\mathbf{H}^{\dagger}\mathbf{S}\mathbf{u}||^2$$
$$\text{s.t.} \quad s_i \geq s_t, \forall i \tag{4.24}$$

that can be solved with quadratic programming. As a result, it has been shown that this can offer up to an order of magnitude complexity reduction at the transmitter for a moderate MU-MISO downlink with $N_t = 10, K = 10$ [33].

4.2.2 *Beamforming Optimization for Constructive Interference*

The above early work on closed-form precoders has been the baseline for designing a number of optimum beamforming designs, specifically tailored for accommodating and maximizing constructive interference. These have built upon traditional optimization techniques that directly minimize the transmit power subject to quality of service (QoS) constraints—most commonly the signal-to-interference-plus-noise ratio (SINR)—for the MU-MISO downlink [34], where convex optimization strategies are typically pursued. Moreover, SINR balancing optimizations [35] are of interest, where the minimum achievable SINR is maximized, subject to a total transmit power constraint. In all these strategies, from a stochastic point of view and treating interference as harmful, the average SINR for the ith user is typically expressed as

$$\gamma_i = \frac{|\mathbf{h}_i\mathbf{w}_i|^2}{\sum_{k=1,k\neq i}|\mathbf{h}_i\mathbf{w}_k|^2 + N_0} \tag{4.25}$$

where $\mathbf{h}_i$ and $\mathbf{w}_i$ are the channel vector and the beamforming vector for the ith user, and N_0 is the noise spectral density.

Power Minimization The conventional power minimization precoder, treating all interference as harmful, aims to minimize the average transmit power subject to an SINR threshold Γ_i by formulating the optimization problem shown below [34]

$$\min_{\{\mathbf{w}_i\}} \sum_{i=1}^{K} \|\mathbf{w}_i\|^2 \tag{4.26}$$
$$\text{s.t.} \quad \frac{|\mathbf{h}_i\mathbf{w}_i|^2}{\sum_{k=1,k\neq i}|\mathbf{h}_i\mathbf{w}_k|^2 + N_0} \geq \Gamma_i, \forall i.$$

The above optimization is most commonly solved as a second-order cone programming (SOCP) problem or exploiting uplink/downlink duality [34].

SINR Balancing SINR balancing maximizes the minimum achievable SINR subject to a transmit power budget, in the form

$$\begin{aligned} \max_{\mathbf{w}_w} \quad & \Gamma_t \\ \text{s.t.} \quad & \frac{\|\mathbf{h}_i \mathbf{w}_i\|^2}{\sum_{k=1,k\neq i} \|\mathbf{h}_i \mathbf{w}_k\|^2 + N_0} \geq \Gamma_t, \forall i. \\ & \sum_{i=1}^{K} \|\mathbf{w}_i\|^2 \leq P \end{aligned} \tag{4.27}$$

where P denotes the total transmit power budget. We note that the above optimization is non-convex and the solution involves more complex iterative approaches [35].

4.2.2.1 Beamforming for Interference Exploitation

By harvesting useful signal power from constructive interference, recent works in the area of beamforming optimization [8, 36–39] have shown significant gains with respect to the above optimization. Specifically, it has been demonstrated that the transmit power required for a given QoS threshold can be drastically reduced in the power minimization problem, or equivalently the QoS obtained for a given transmit power can be drastically improved in the SINR balancing formulation. More recently, these beamforming strategies have been extended to the realm of hybrid analog-digital precoding, to exploit mutual coupling between the transmit antennas by means of tunable antenna loads [40].

Let us place our attention on how the beamforming optimization can be adapted to exploit constructive interference. As per the interference classification and discussion in Sect. 4.1.2, the optimizations in (4.26), (4.27) can be modified to take the constructive interference into account. This can be done by imposing interference constraints, not in terms of suppressing the stochastic interference, but rather optimizing instantaneous interference to contribute to the received signal power, thus providing a source for harvesting useful signal power. Indeed, for the case when interference has been aligned, by means of precoding vectors $\mathbf{w}_k$, to overlap constructively with the signal of interest, all interference in the received signal contributes constructively to the useful signal. Accordingly, it has been shown in [20] that in this case the instantaneous received SNR is given as

$$\gamma_i = \frac{\left|\mathbf{h}_i \sum_{k=1}^{K} \mathbf{w}_k u_k\right|^2}{N_0} \tag{4.28}$$

where all interference contributes in the useful received signal power.

Strict Phase Alignment Accordingly, and based on the classification criteria detailed in [5] and Fig. 4.3 for constructive interference, the first approach in this area in [36], focusing on PSK modulation in the form $u_i = e^{j\phi_i}$, introduced

a modified interference constraint in (4.26) where interference is constrained to strictly align to the phase of the useful signal. The power minimization problem was reformulated in [36] as

$$\begin{aligned} \min_{\{\mathbf{w}_i\}} \quad & \left\| \sum_{k=1}^{K} \mathbf{w}_k e^{j(\phi_k - \phi_i)} \right\|^2 \\ \text{s.t.} \quad & \angle \left(\mathbf{h}_i \sum_{k=1}^{K} \mathbf{w}_k u_k \right) = \angle(u_i), \forall i \\ & \text{Re} \left(\mathbf{h}_i \sum_{k=1}^{K} \mathbf{w}_k e^{j(\phi_k - \phi_i)} \right) \geq \sqrt{\Gamma_i N_0}, \forall i. \end{aligned} \tag{4.29}$$

Here clearly the transmit power is minimized on an instantaneous basis in the objective function, and the first set of constraints imposes that, for each user, the phase of interference is strictly constrained to equal the phase of the symbol of interest. The second set of constraints poses QoS constraints for each user, in the form of the SNR thresholds Γ_i which relate to the instantaneous SNR expression in (4.28).

We note the use of the sum of phase shifted (by the phase of the symbol of interest ϕ_i) interfering symbols plus the symbol of interest in the above expressions. This is in line with our analysis above in Sect. 4.1.2, and serves to isolate the received amplitude and phase shift in the symbol of interest due to interference. Note that the above two conditions contain K equations and K inequalities, while there are $2N_t \geq 2K$ real variables, so there are sufficient degrees of freedom to satisfy these two sets of constraints.

Phase Relaxation Still, it can be seen that due to the strict angle constraint, the formulation (4.29) is more constrained than the constructive interference regions in Fig. 4.3 where the strict phase constraints do not exist. To obtain a more relaxed optimization for M-PSK, we resort to the previous classification criteria in Sect. 4.1.2 which we extend to incorporate an arbitrary SNR constraint γ. With reference to Fig. 4.4, and using the beamforming vectors $\mathbf{w}_k$ the above-defined components of the phase rotated received symbols excluding interference can be rewritten as

$$\alpha_R = \text{Re} \left(\mathbf{h}_i \sum_{k=1}^{K} \mathbf{w}_k e^{j(\phi_k - \phi_i)} \right), \text{ and } \alpha_I = \text{Im} \left(\mathbf{h}_i \sum_{k=1}^{K} \mathbf{w}_k e^{j(\phi_k - \phi_i)} \right) \tag{4.30}$$

To extend the above discussion to the case where constructive interference is defined with respect to an SNR threshold—as opposed to the nominal constellation points—let us look at Fig. 4.9 where we have revisited the geometry of Fig. 4.4 by

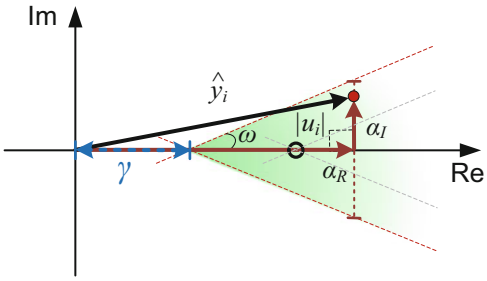

Fig. 4.9 Optimization region for beamforming for interference exploitation based on SNR threshold γ

introducing an SNR parameter $\gamma = \sqrt{\Gamma_i N_0}$, following the SNR expression (4.28). This gives rise to the constructive interference sector denoted by the green shaded sector in Fig. 4.9. By a similar process to that in Fig. 4.4 it can be seen that α_R and α_I are allowed to grow infinitely, as long as their ratio is such that the received symbol is contained within the constructive area of the constellation, i.e., the distances from the decision boundaries, as set by the SNR constraints Γ_i, are not violated. Accordingly, α_R, α_I have to follow

$$|\alpha_I| \leq \left(\alpha_R - \gamma\right) \tan \omega \tag{4.31}$$

As regards the constructive area in the constellation, with respect to (4.29), it can be seen that the angle of the received signal need not strictly align with the angle of the useful signal, as long as it falls within the constructive area of the constellation with a maximum phase shift of $\Delta\phi = \pm\pi/M$, for an M-PSK modulation. Accordingly, to relax the optimization, α_I is allowed to be non-zero as long as the resulting symbol lies within the constructive area of the constellation.

Power Minimization with Interference Exploitation Using (4.30), (4.31) we arrive at the power minimization problem presented in [37] as

$$\begin{aligned} &\min_{\{\mathbf{w}_i\}} \left\| \sum_{k=1}^{K} \mathbf{w}_k e^{j(\phi_k - \phi_i)} \right\|^2 \\ &\text{s.t.} \left| \text{Im}\left(\mathbf{h}_i \sum_{k=1}^{K} \mathbf{w}_k e^{j(\phi_k - \phi_i)} \right) \right| \leq \left(\text{Re}\left(\mathbf{h}_i \sum_{k=1}^{K} \mathbf{w}_k e^{j(\phi_k - \phi_i)} \right) - \sqrt{\Gamma_i N_0} \right) \tan \omega, \forall i \end{aligned} \tag{4.32}$$

It can be seen that the above optimization in (4.32) is more relaxed than the zero-angle-shift optimization (4.29), which results in a smaller minimum in the transmit power. Moreover, it contains a number of K inequalities which result in an increased feasibility region compared to the conventional optimization, as detailed

in [37]. Problem (4.32) is a standard second-order cone program (SOCP), thus can be optimally solved using numerical software.

SNR Balancing with Interference Exploitation The respective SNR balancing problem that allows interference exploitation can be designed in a similar fashion as

$$\begin{aligned} &\max_{\{\mathbf{w}_i\}} \ \Gamma_t \\ &\text{s.t.} \ \left| \text{Im}\left(\mathbf{h}_i \sum_{k=1}^{K} \mathbf{w}_k e^{j(\phi_k - \phi_i)} \right) \right| \leq \left(\text{Re}\left(\mathbf{h}_i \sum_{k=1}^{K} \mathbf{w}_k e^{j(\phi_k - \phi_i)} \right) - \sqrt{\Gamma_t N_0} \right) \tan\omega, \forall i \\ &\left\| \sum_{k=1}^{K} \mathbf{w}_k e^{j(\phi_k - \phi_i)} \right\|^2 \leq P \end{aligned} \tag{4.33}$$

Remarkably, the relaxed nature of the interference-exploitation beamforming problems leads to larger feasibility regions. To illustrate the extended feasibility region for the optimization problems (4.32), (4.33), Fig. 4.10 shows the feasibility probability of a $K = 4$ user system with respect to the number of transmit

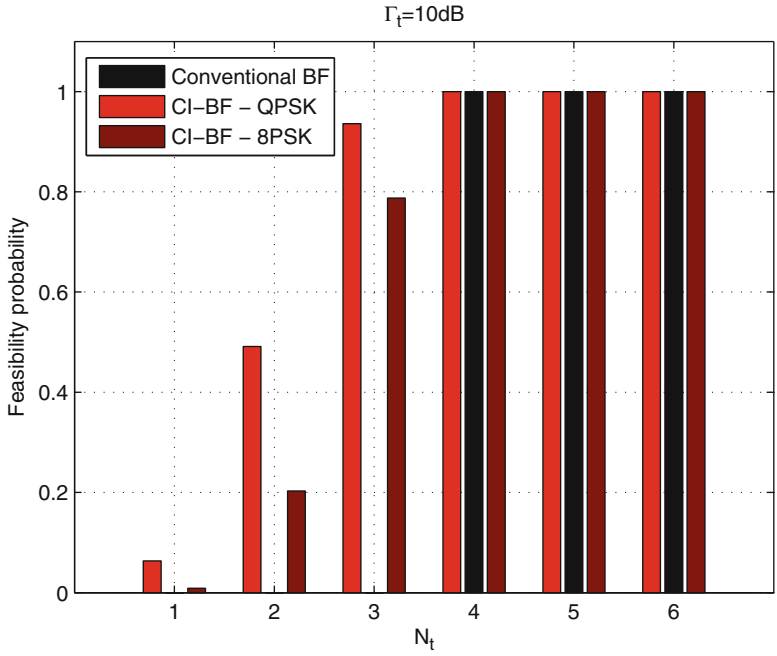

Fig. 4.10 Feasibility probability vs. N_t for conventional and interference-exploitation beamforming, $K = 4$, $\Gamma_t = 10$ dB [37]

antennas N_t. The comparison is between the conventional beamforming of (4.26) ("Conventional BF" in the legend) and the constructive interference beamforming of (4.32) ("CI-BF") for the cases of QPSK and 8PSK modulation. It can be seen that, while the conventional optimization is only feasible for $N_t \geq K$, the proposed can be feasible with non-zero probability for lower values of N_t. This observation could have a significant impact in the communication system design, where, by applying interference-exploitation principles, more users can be scheduled simultaneously in a given cell. Furthermore, it is important to note that the cell-edge users are more prone to interference. In a single cell scenario this would be naturally captured and exploited with the above interference-exploitation optimizations, given the channel characteristics. More importantly, regarding other-cell interference, this is the topic of multi-cell interference exploitation, which while captured to-date in CR applications [13–16], is a widely open research area in the context of interference exploitation.

Beamforming Optimizations for QAM Constellations While the above approaches are shown for PSK constellations, the works in [8, 9] and more recently in [10–12] have applied the interference-exploitation beamforming approaches to QAM and star-QAM modulations. This has been pursued by adapting the interference constraints in the beamforming optimizations according to the interference classification for QAM constellations outlined in Sect. 4.1.2 and in (4.9). The keen reader is referred to [10, 11] for detailed formulations of the corresponding optimizations.

Notably, all the above interference-exploitation optimizations allow for equivalent multicast formulations to be employed, which result in more efficient solvers with much reduced complexity, as detailed in [36, 37]. Still, it is clear that the interference-exploitation beamformers are data dependent and therefore require the optimization problem to be solved on a symbol-by-symbol basis. This therefore necessitates a closer look at the resulting complexity.

4.2.2.2 Notes on the Complexity of Interference-Exploitation Beamforming

To facilitate the complexity comparison, the main signal-processing operations for the conventional and the interference-exploitation beamforming approaches are illustrated in the block diagrams of Fig. 4.11a, b, respectively.

Transmit (Base Station) Complexity With the low-complexity multicasting simplifications derived in [36, 37] it has been shown that the complexity of solving the equivalent multicasting optimization problems of (4.32), (4.33) is greatly reduced. In fact, the complexity study found in [37] has shown that, due to the relaxed nature of the problem, computationally efficient gradient projection approaches can be developed that achieve a complexity of down to 15% w.r.t. conventional power minimization precoding, for each precoding optimization. More recent work in [39] relying on barrier-method solvers has further reduced the complexity down

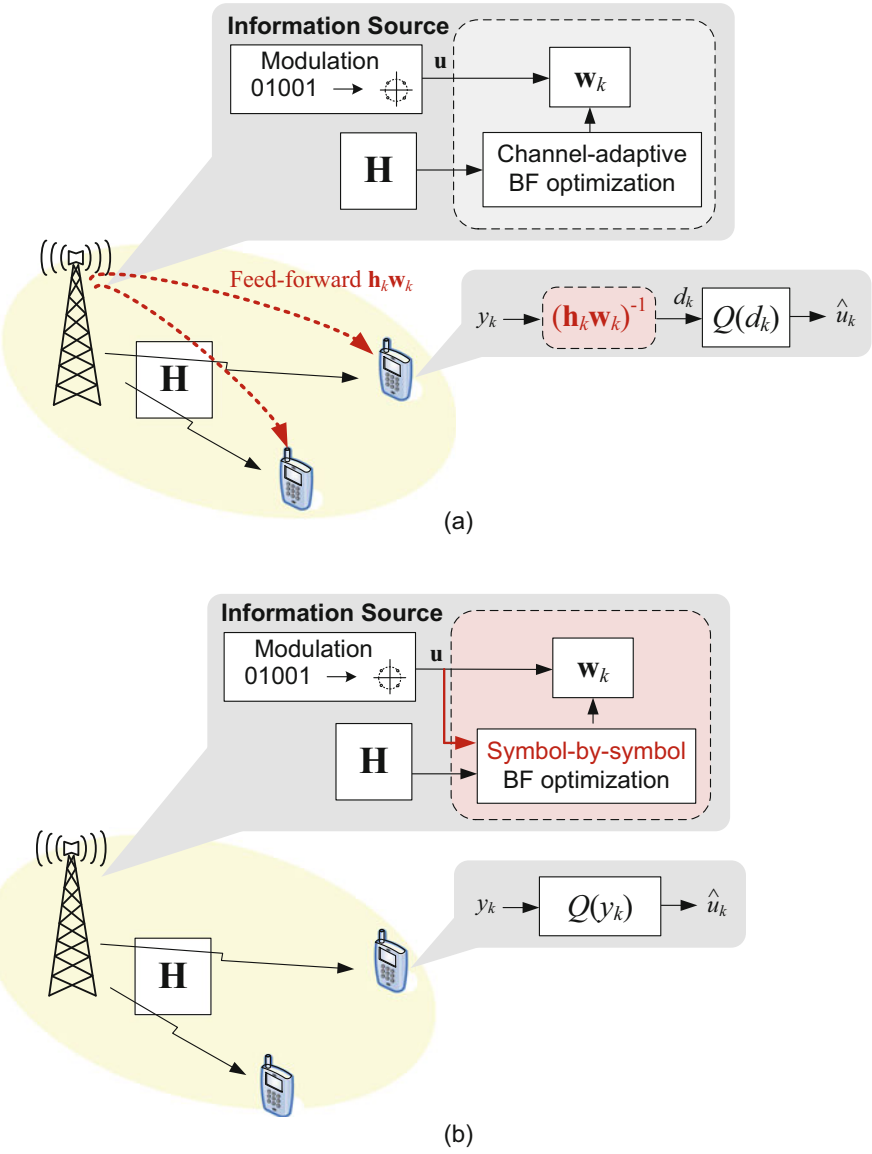

Fig. 4.11 Block diagram showing transmit and receive processing, (**a**) conventional beamforming optimization, (**b**) beamforming for interference exploitation

to 2% w.r.t. conventional beamforming. However, as the interference-exploitation beamforming optimizations need to be performed on a symbol-by-symbol basis (denoted in the red box in Fig. 4.11b), a frame-based complexity analysis is pertinent. For the example of an LTE Type 2 TDD frame with up to 112 downlink

symbol time slots [7], this translates to a doubling of complexity per frame of $112 \times 2\% = 224\%$ for the interference-exploitation schemes w.r.t. conventional precoding optimization. It is important to note that this complexity involves the base station (BS) transmitter, where computational resources are more accessible. At the same time, the complexity of the mobile units is drastically reduced as explained below. In addition, this complexity increase comes with significant power savings of, for example, up to 3 dB for a small scale MU-MISO downlink of $N_t = 4, K = 4$ [37].

Power Efficiency In fact, in terms of the ultimate metric of power efficiency at the transmitter, for an LTE base station the transmit power is typically measured on the order of 20 W, while the power consumption of the DSP processing is typically orders of magnitude lower. Since with the interference-exploitation beamformers show a halving of the transmit power at roughly double the DSP power w.r.t. to their conventional counterparts, the gains in the power efficiency by harvesting useful signal power form interference are therefore undeniable.

Receiver (Mobile Unit) Complexity Regarding the receive complexity, the proposed approaches provide significant benefits compared to conventional beamforming. Indeed, for conventional beamforming the MU receiver is required to equalize the composite channel $\mathbf{h}_i\mathbf{w}_i$ from (4.26), (4.27) as shown in the red box in Fig. 4.11a, in order to recover the data. This necessitates that the BS feed-forward the composite channel to each MU receiver for correct detection, denoted by the dashed red arrows in Fig. 4.11a. Clearly, this is subject to CSI quantization and detection errors, and introduces additional computational overheads at the MU receivers.

By contrast, as for the interference-exploitation approaches the received symbols lie at the constructive area of the constellation (see Fig. 4.3), there is no need for equalizing the composite channel $\mathbf{h}_i\mathbf{w}_i$ to recover the data symbols at the ith MU, and a simple decision stage suffices. Accordingly, the benefit of interference-exploitation approaches is that CSI is not required for detection at the MU, which allows for significant savings in the training time and computational overheads for signalling the beamformers to the MUs. It also makes these schemes immune to the quantization errors involved in the feed-forward of $\mathbf{h}_i\mathbf{w}_i$ for conventional beamforming. The resulting benefits are quantified in [15].

4.2.3 Resource Allocation for Interference Exploitation

The gains obtained by the above adaptations can be augmented by employing specifically tailored resource allocation techniques. To enhance the performance of the interference-exploitation schemes the goal of resource allocation would be, instead of allocating resources that inherently experience minimum interference, to optimize the interference between the resources according to QoS criteria.

This of course covers a vast area where resources can pertain to antenna selection, power allocation, sub-carrier allocation in OFDM, user association and scheduling,

and so on. In this subsection, we overview recent antenna selection [41–43] and power allocation [25] strategies developed to optimize and exploit constructive interference, while the same concept can be extended to alternative resources such as user scheduling [44], adaptive modulation [11], or specific power allocation for non-orthogonal multiple access (NOMA) [45] combined with interference exploitation. Building upon the power allocation work, we further look at constant envelope precoding (CEP) [46] where the CEP is optimized to exploit constructive interference under given per-antenna power budgets.

4.2.3.1 Antenna Selection

The antenna-selection techniques developed for interference exploitation build upon existing antenna-selection benchmark schemes, namely capacity maximization [47] and path gain selection [48].

Capacity Maximization Recent work in the area of large scale antenna systems [49] showed channel-capacity-based antenna selection can be performed by means of convex optimization, drastically reducing the complexity of previous techniques from the literature, such as the capacity maximization technique in [50]. Accordingly, the selection of N_s antennas out of the available N_t antennas at the transmitter is performed over the system sum-capacity, and the optimization problem is formulated as

$$\begin{aligned} \max_{\boldsymbol{\Delta}} \ & \log_2 \left[\det \left(\mathbf{I}_K + \zeta \mathbf{H}^H \boldsymbol{\Delta} \mathbf{H} \right) \right] \\ \text{s.t.} \ & \Delta_{n,n} \in [0,1], \\ & \textstyle\sum_{n=1}^{N} \Delta_{n,n} = N_s. \end{aligned} \tag{4.34}$$

where ζ is an SNR parameter and $\boldsymbol{\Delta}$ is an $N_t \times N_t$ selection matrix. In particular, $\boldsymbol{\Delta}$ is a real diagonal matrix, whose entries should be either null, i.e., $\Delta_{n,n} = 0$ if n is a non-selected antenna, or unitary, i.e., $\Delta_{n,n} = 1$ if n is an antenna selected for transmission. Since constraining the diagonal values of $\boldsymbol{\Delta}$ to be binary results in a non-convex formulation, a relaxation such that the elements of $\boldsymbol{\Delta}$ take values in between 0 and 1, i.e., $\Delta_{n,n} \in \{0, 1\}$ in the optimization (4.34) above is commonly adopted. With the above relaxation, the optimization problem becomes convex, and the final selection can be done by rounding the elements such that $\Delta_{n,n} \in [0, 1]$. This approach has been shown to achieve near-optimal performance in the large scale MIMO regime when compared to exhaustive search approaches [47].

Path Gain Selection A similar approach selects the subset of antennas whose path gains are higher, according to the following optimization:

$$\begin{aligned} \max_{\boldsymbol{\Delta}} \ & \mathbf{H}^H \boldsymbol{\Delta} \mathbf{H} \\ \text{s.t.} \ & \Delta_{n,n} \in \{0,1\}, \\ & \textstyle\sum_{n=1}^{N} \Delta_{n,n} = N_s. \end{aligned} \tag{4.35}$$

This form of selection has received a lot of attention due to its simplicity.

4.2.3.2 Antenna Selection for Interference Exploitation

Given the conditions for constructive interference reviewed in the previous sections, it is possible to identify new antenna-selection metrics that maximize constructive interference, thus optimally exploiting this important source of useful signal power.

Antenna Selection for Closed-Form Precoding Initial approaches were introduced in [41, 42] where the selection takes place for given closed-form precoding vectors $\mathbf{w}_k$ such as selective precoding (SP) [41], matched filtering (MF), or correlation rotation (CR) [42]. In the more recent work of [42], the problem was formulated as

$$\begin{aligned} \max_{\boldsymbol{\Delta}} \min_{i} \ & \left(\mathrm{Re}\left(\mathbf{h}_i \boldsymbol{\Delta} \textstyle\sum_{k=1}^{K} \mathbf{w}_k e^{j(\phi_k - \phi_i)} \right) \right) \tan\omega - \left| \mathrm{Im}\left(\mathbf{h}_i \boldsymbol{\Delta} \textstyle\sum_{k=1}^{K} \mathbf{w}_k e^{j(\phi_k - \phi_i)} \right) \right| \\ \text{s.t.} \ & \Delta_{n,n} \in \{0,1\}, \\ & \textstyle\sum_{n=1}^{N} \Delta_{n,n} = N_s. \end{aligned} \tag{4.36}$$

The above optimization selects the antenna subset that maximizes the minimum constructive interference amongst the users for a given set of $\mathbf{w}_k$ in the MU-MISO downlink. The above approach is most suitable for large scale antenna systems with a low-complexity MF precoder and with a sufficient number of transmit antennas that guarantee constructive interference for all users. A clear connection to the interference-exploitation beamforming optimizations in the previous section can be seen, with the addition of the selection matrix $\boldsymbol{\Delta}$, along with the antenna-selection constraints.

Joint Antenna Selection and Precoding Optimization Going one step further, the approach in [43] pursues a joint optimization of both the antenna subset and the precoding vectors, by formulating the problem as

$$\begin{aligned} \max_{\boldsymbol{\Delta}, \{\mathbf{w}_i\}} \min_{i} \ & \left(\mathrm{Re}\left(\mathbf{h}_i \boldsymbol{\Delta} \textstyle\sum_{k=1}^{K} \mathbf{w}_k e^{j(\phi_k - \phi_i)} \right) \right) \tan\omega - \left| \mathrm{Im}\left(\mathbf{h}_i \boldsymbol{\Delta} \textstyle\sum_{k=1}^{K} \mathbf{w}_k e^{j(\phi_k - \phi_i)} \right) \right| \\ \text{s.t.} \ & \Delta_{n,n} \in \{0,1\}, \\ & \textstyle\sum_{n=1}^{N} \Delta_{n,n} = N_s, \\ & \left\| \textstyle\sum_{k=1}^{K} \mathbf{w}_k e^{j(\phi_k - \phi_i)} \right\|^2 \leq P. \end{aligned} \tag{4.37}$$

As we can see, the above formulation is designed to jointly optimize the antenna selection by means of $\boldsymbol{\Delta}$, together with the precoding vectors $\mathbf{w}_i$. The joint optimization allows us to fully exploit the resulting constructive interference, and can be solved using mixed integer programming techniques [51].

Successive Optimization To reduce the optimization complexity, the above problem can be decomposed into two sub-problems and solved with a successive optimization approach. In [43] first a subset selection is performed by solving the following optimization problem based on the antenna cross-correlations $\mathbf{h}_i\mathbf{h}_k^H$:

$$\begin{aligned} &\max_{\boldsymbol{\Delta}} \min_{i} \left(\mathrm{Re}\left(\mathbf{H}^H\boldsymbol{\Delta}\mathbf{H}e^{j\boldsymbol{\phi}-\phi_i}\right)\right)\tan\omega - \left|\mathrm{Im}\left(\mathbf{H}^H\boldsymbol{\Delta}\mathbf{H}e^{j\boldsymbol{\phi}-\phi_i}\right)\right| \\ &\text{s.t.} \quad \Delta_{n,n} \in \{0,1\}, \\ &\qquad \textstyle\sum_{n=1}^{N} \Delta_{n,n} = N_s. \end{aligned} \tag{4.38}$$

where $\boldsymbol{\phi} = [\phi_1, \phi_2, \ldots, \phi_i]^T$. It can be observed that the above bears resemblance to the path gain selection of (4.35), but with a modified objective function, specifically tailored for constructive interference. Then, for the selected subset of antennas corresponding to the channel matrix $\tilde{\mathbf{H}} = [\tilde{\mathbf{h}}_1; \tilde{\mathbf{h}}_2; \ldots; \tilde{\mathbf{h}}_K]$, the optimal precoding vectors $\mathbf{w}_k$ are computed by solving the following problem:

$$\begin{aligned} &\max_{\{\mathbf{w}_i\}} \min_{i} \left(\mathrm{Re}\left(\tilde{\mathbf{h}}_i \textstyle\sum_{k=1}^{K} \mathbf{w}_k e^{j(\phi_k-\phi_i)}\right)\right)\tan\omega - \left|\mathrm{Im}\left(\tilde{\mathbf{h}}_i \textstyle\sum_{k=1}^{K} \mathbf{w}_k e^{j(\phi_k-\phi_i)}\right)\right| \\ &\text{s.t.} \quad \left\|\textstyle\sum_{k=1}^{K} \mathbf{w}_k e^{j(\phi_k-\phi_i)}\right\|^2 \leq P. \end{aligned} \tag{4.39}$$

which is now a function of $\mathbf{w}_i$ only. Both max–min optimizations in (4.38), (4.39) are convex and can be solved using an auxiliary threshold variable as, for example, in (4.27). It has been shown in [43] that the successive optimization approach in (4.38), (4.39) performs within 0.5 dB of the joint optimization approach of (4.37), at a significantly reduced complexity, down to $1/6$ of the joint optimization complexity for a large scale system with $N_t = 128, K = 5$. It can be observed in the relevant works that both beamforming and antenna selection for interference exploitation provide significant performance benefits. Whether the former or the latter are dominant in a practical scenario is subject to the size of the system and the number of auxiliary antennas.

4.2.3.3 Power Allocation for Constructive Interference Maximization

Power allocation approaches in the area of interference exploitation have mainly focused on the closed-form precoders of Sect. 4.2.1. Firstly, it is important to note that, contrary to conventional zero-forcing precoding, the precoders in [12, 20–25] do not obtain uniform performance across all users. This is because the power of

constructive interference received may vary from user to user. Building on this observation, an interesting power allocation approach in [25], designed for CR precoding, optimizes the power allocation amongst the users such that the worst user's SNR is maximized. First it is shown that the user with the worst SNR is the one that experiences the minimum constructive interference, which for CR is measured by the parameter

$$c_i = \sum_{k=1}^{K} |\rho_{i,k}| \tag{4.40}$$

where $\rho_{i,k}$ is the i,kth element of the channel correlation matrix as defined in Sect. 4.2.1. Accordingly, the per-user power p_i is determined by solving the following optimization:

$$\begin{aligned} &\max_{\{p_i\}} \min_i \; c_i^2 p_i \\ &\text{s.t.} \qquad \sum_i p_i = P_T, 0 \le p_i \end{aligned} \tag{4.41}$$

where P_T is the total transmit power budget. It can be seen that the above power allocation ensures the same SINR to all users, which constitutes an SINR balancing approach.

4.2.3.4 Constructive Constant Envelope Precoding

Constant envelope precoding (CEP), where the amplitude of the transmitted symbols remains unchanged, has received particular attention recently due to its suitability for large scale antenna systems envisaged for 5G implementations.

Building on the above power allocation discussion, and given a per-antenna transmit power budget P_n for the nth transmit antenna, CEP forms the transmitted symbol from the nth antenna of the BS as [52]

$$x_n = \sqrt{P_n} e^{j\theta_n}, \tag{4.42}$$

where θ_n represents the precoding phase of the CEP signal. It is clear that the transmitted symbols have a constant envelope of $\sqrt{P_n}$ with phase-only variation. For notational simplicity, let us assume that all transmit antennas obey $P_n = \frac{1}{N_t}, \forall n \in \{1, \ldots, N_t\}$, in which case we can write

$$\mathbf{x} = \frac{1}{\sqrt{N_t}} e^{j\boldsymbol{\theta}}, \tag{4.43}$$

where $\boldsymbol{\theta} = [\theta_1, \theta_2, \ldots, \theta_{N_t}]^T$. Accordingly CEP aims at minimizing the interference as [52]

$$\begin{aligned} &\min_{\boldsymbol{\theta}} \sum_{m=1}^{M} \left| \tfrac{1}{\sqrt{N_t}} \mathbf{h}_m e^{j\boldsymbol{\theta}} - u_m \right|^2 \\ &\text{s.t. } |\theta_n| \leq \pi, \forall n \in \{1, \ldots, N_t\}, \end{aligned} \tag{4.44}$$

where, unlike the transmit symbols x_n, the information symbols u_n can be taken from a constellation with either constant or non-constant envelope. The above optimization represents a non-convex non-linear least squares (NLS) problem, subject to local minima. The optimization problem (4.44) was first solved in [52] with a gradient descent (GD) based approach, and further improved in [53] with a direct application of the cross-entropy method [54].

Constructive CEP Exploiting the concept of constructive interference in Sect. 4.1.2, it is possible to define a new optimization problem that maximizes the constructive interference, while employing phase-only transmit symbols. Accordingly, in [46] the CEP optimization problem was defined for PSK symbols $u_i = e^{j\phi_i}$ as

$$\begin{aligned} &\max_{\boldsymbol{\theta}} \quad \min_{i} \left\{ \mathrm{Re}\left(\tfrac{1}{\sqrt{N_t}} \mathbf{h}_i e^{j(\boldsymbol{\theta} - \phi_i)} \right) \tan\omega - \left| \mathrm{Im}\left(\tfrac{1}{\sqrt{N_t}} \mathbf{h}_i e^{j(\boldsymbol{\theta} - \phi_i)} \right) \right| \right\} \\ &\text{subjectto } |\theta_n| \leq \pi, \forall n \in \{1, \ldots, N\}. \end{aligned} \tag{4.45}$$

In line with its conventional counterpart in [52], the formulation in (4.45) is clearly non-convex, but can be efficiently solved via the cross-entropy method. It is demonstrated in [46] that the constructive CEP approach, by harvesting useful signal power from constructive interference, provides significant performance benefits compared to conventional CEP approaches. For the example of a large scale system with $N_t = 64, K = 12$, power gains of more than 5 dB were demonstrated in [46].

4.3 Constructive Interference for Harvesting Both Radiated Power and Useful Signal Power

The recent research attention on energy harvesting from RF signals, the motivator behind this Book, has been stimulated from the fact that radiated energy can provide a useful source of wireless power. Complimentary to the discussion above where interfering energy is harvested as a source of useful signal power, recent works focus on the beamforming optimization where part of the signal is used for decoding and

part of it is harvested as wireless power, giving rise to the concept of simultaneous wireless information and power transfer (SWIPT) [55–57].

4.3.1 Constructive Interference in SWIPT

In the majority of SWIPT approaches, while interference is harvested as useful energy for powering the receiver's electronic components, in terms of signal detection interference is still treated as a harmful effect. In this section, we show that, by means of the constructive interference concept, interference can be harvested both as a source of wireless power *and* a source of useful signal power.

4.3.1.1 Conventional Beamforming for SWIPT

Beamforming approaches for SWIPT are based on the premise that part of the received signal is used for information decoding, while the rest of the signal power is used for energy harvesting at the receiver. When the receiver has only one antenna from which to both harvest energy and decode information, two practical receiver structures for SWIPT termed as "time switching" (TS) and "power splitting" (PS), are typically employed to separate the received signal for decoding information and harvesting energy [55]. For illustration reasons, at this point we focus on the PS approach, while the discussion in this section is trivially applicable to the TS approach.

A block diagram of the PS approach is shown in Fig. 4.12a, where it can be seen that a portion P_i of the received signal is used for decoding the signal, while the rest ($P_H = 1 - P_i$) is used for energy harvesting. In the figure, z_i models the noise from the signal conversion from RF to baseband.

Treating interference as harmful, the received SINR for user i is given by

$$\Gamma_i^{\text{con}} = \frac{|\mathbf{h}_i \mathbf{w}_i|^2}{\sum\limits_{k=1, k\neq i}^{K} |\mathbf{h}_i \mathbf{w}_k|^2 + N_0 + \frac{N_C}{P_i}}, \tag{4.46}$$

where N_C is the spectral density of the conversion noise z_i.

Similarly the harvested energy is typically expressed following the model in Fig. 4.12a as:

$$P_i^{\text{con}} = (1 - P_i) \left(\sum_{k=1}^{K} |\mathbf{h}_i \mathbf{w}_k|^2 + N_0 \right). \tag{4.47}$$

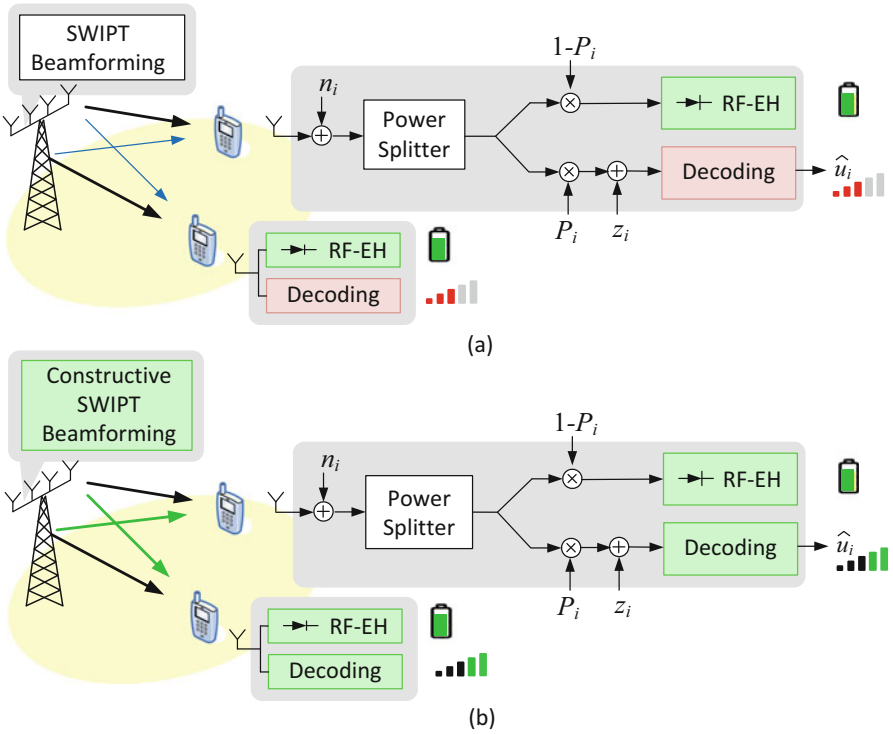

Fig. 4.12 Block diagram showing the power splitting SWIPT approach at the receiver with (**a**) SWIPT beamforming, (**b**) constructive SWIPT beamforming

Consequently, the power minimization problem with both QoS and EH constraints is formulated as

$$\begin{aligned} &\min_{\{\mathbf{w}_i, P_i\}} \sum_{i=1}^{K} \|\mathbf{w}_i\|^2 \\ &\text{s.t.} \quad \frac{|\mathbf{h}_i \mathbf{w}_i|^2}{\sum\limits_{k=1, k\neq i}^{K} |\mathbf{h}_i \mathbf{w}_k|^2 + N_0 + \frac{N_C}{P_i}} \geq \Gamma_i, \\ &\qquad (1 - P_i)\left(\sum_{k=1}^{K} |\mathbf{h}_i \mathbf{w}_k|^2 + N_0\right) \geq E_i, \; 0 < P_i < 1, \forall i. \end{aligned} \tag{4.48}$$

It is easy to see that formulation (4.48) is non-convex and hence challenging to solve. Semidefinite programming relaxation is usually employed to solve the optimization [58]. It is evident in the above optimization that, while interference is treated as useful for energy harvesting, is still treated as harmful for information

decoding, as it reduces the SINR at the receiver. This is demonstrated in Fig. 4.12a by the red shaded decoding part. Accordingly, the beamformer tries to constrain the interference in the decoding part of the received power, to secure a QoS level.

4.3.2 Interference-Exploitation Beamforming for SWIPT

Clearly, like in the beamforming optimizations of Sect. 4.2.2, there is scope to modify the optimization constraints such that constructive interference is harvested both as a source of RF energy and a source of useful signal energy. By adapting the beamforming optimizations in (4.32), (4.33) to the new transmission model as per Fig. 4.12 and including the EH constraint, it is straightforward to see that the interference-exploitation SWIPT beamforming optimization can be written as

$$\begin{aligned}
&\min_{\{\mathbf{w}_i\}} \left\| \sum_{k=1}^{K} \mathbf{w}_k e^{j(\phi_k-\phi_i)} \right\|^2 \\
&\text{s.t.} \left| \text{Im}\left(\mathbf{h}_i \sum_{k=1}^{K} \mathbf{w}_k e^{j(\phi_k-\phi_i)} \right) \right| \leq \left(\text{Re}\left(\mathbf{h}_i \sum_{k=1}^{K} \mathbf{w}_k e^{j(\phi_k-\phi_i)} \right) - \sqrt{\Gamma_i \left(N_0 + \frac{N_C}{P_i} \right)} \right) \tan\omega, \\
&\quad \left| \mathbf{h}_i \sum_{k=1}^{K} \mathbf{w}_k e^{j(\phi_k-\phi_i)} \right| \geq \sqrt{\frac{E_i}{1-P_i}}, 0 < P_i < 1, \forall i
\end{aligned} \tag{4.49}$$

The problem (4.49) is nontrivial to solve because of the non-convex constraint $\left|\mathbf{h}_i \sum_{k=1}^{K} \mathbf{w}_k e^{j(\phi_k-\phi_i)}\right| \geq \sqrt{\frac{E_i}{1-P_i}}$. A number of SOCP bounds have been derived in [59] to obtain the beamforming vectors $\mathbf{w}_k$.

It is clear here that interference now provides a source of both RF power for harvesting and useful signal power for decoding, as demonstrated in Fig. 4.12b. The above approach has been shown to offer power gains of more than 15 dB compared to conventional SWIPT beamforming in an $N_t = 4, K = 4$ MU-MISO system.

4.3.3 Open Problems and Research Directions

The above sections have overviewed work carried out in the area of interference exploitation, that has received recent attention in the context of harvesting interfering power for energy efficient wireless transmission. While a body of work has already focused on exploiting wireless interference in a number of scenarios and under various approaches, the topic is quite broad, with wide potential in revisiting

existing interference-cancellation approaches in interference-limited transmission scenarios. Accordingly, there are numerous open problems in the area.

Information Theory An important pillar of research that is widely open in the interference-exploitation research to date is that of communication-theoretic analysis and optimization. To this date, the fundamental extent of the potential benefits from constructive interference is unknown, as there is a lack of information-theoretic studies to provide performance benchmarks for the scenarios of interest. The main limitation here is the fact that, as interference exploitation is modulation dependent, Shannonian analysis and capacity calculations that assume Gaussian signals cannot be applied. Instead modulation-dependent analysis is required, building on the more complex finite-constellation approaches [60]. The development of such an analysis would, however, provide a benchmark against which to measure the performance of existing approaches, and more importantly, pave the way for optimizing practical approaches for interference exploitation towards achieving the theoretically optimal.

CSI Robustness and Asynchronous Interference It could be suggested that interference-exploitation approaches may be more sensitive to CSI errors and asynchronicity, since they heavily depend on the careful superposition of the interfering signals. While initial studies on CSI-robust techniques have disproved this [26, 37], the analytical study of the effects of CSI errors and asynchronicity, and the design of robust techniques specifically tailored for interference exploitation is still an open topic in the literature. Given that practical systems operate with various forms of CSI quantization and errors, and are subject to asynchronicity this provides a very pragmatic research direction.

Multi-Level Modulation Initial work on the application of the concept of constructive interference for multi-level modulation such as QAM and star-QAM has been ongoing [8–11], primarily designing the optimization constraints for beamforming to accommodate constructive interference. It is yet to be explored, however, how to adaptively adjust the decision boundaries in the multi-level constellations to further benefit from constructive interference, as discussed in Sect. 4.1.2. This entails both signal-processing algorithms and analytical work to study the extent of the required constellation expansion, and how to optimally benefit for such an approach.

Advanced Scenarios and Applications Finally, the application of the concept of this chapter to more advanced scenarios is still widely open. While initial work has been ongoing related to multi-cell transmission [13–16] and to energy harvesting communications [59] as detailed above, both these areas are open to contributions in their various scenarios and existing solutions. Other exciting applications as, for example, the exploitation of self-interference in full-duplex communications, the application of this concept to emerging wireless paradigms such as distributed antenna systems, Cloud–RAN transmissions, amongst many others, are still untouched territory that provide grounds for future research directions.

In the coming generations of wireless networks where power efficiency will play a dominant role, harvesting energy from interference, both as RF power and as useful signal power, is a critical enabling solution. The abovementioned concept of constructive interference and the identified open problems provide scope for fruitful research for the years to come.

Acknowledgements The author would like to thank the researchers in the Department of Electrical and Electronic Engineering in University College London, Pierluigi Amadori, Adrian Garcia Rodriguez, and Ka Lung Law for the helpful discussions and assistance in developing the content of this chapter.

The financial support from the Royal Academy of Engineering, UK is gratefully acknowledged.

References

1. M. Costa, Writing on dirty paper. IEEE Trans. Inf. Theory **IT-29**, 439–441 (1983)
2. G. Zheng, I. Krikidis, C. Masouros, S. Timotheou, D.A. Toumpakaris, Z. Ding, Rethinking the role of interference in wireless networks. IEEE Commun. Mag. **52**(11), 152–158 (2014)
3. C. Masouros, T. Ratnarajah, M. Sellathurai, C. Papadias, A. Shukla, Known interference in the cellular downlink: a performance limiting factor or a source of green signal power? IEEE Commun. Mag. **51**(10), 162–171 (2013)
4. D.N.C. Tse, P. Viswanath, *Fundamentals of Wireless Communications* (Cambridge University Press, Cambridge, 2005)
5. C. Masouros, E. Alsusa, Soft linear precoding for the downlink of DS/CDMA communication systems. IEEE Trans. Veh. Technol. **59**(1), 203–215 (2010)
6. C. Masouros, E. Alsusa, Dynamic linear precoding for the exploitation of known interference in mimo broadcast systems. IEEE Trans. Wirel. Commun. **8**(3), 1396–1404 (2009)
7. 3GPP TS 36.211, V8.2.0 (2008-03), Release 8 Evolved Universal Terrestrial Radio Access (E-UTRA); Physical Channels and Modulation
8. F. Keskin, J. Hahn, P.W. Baier, Minimum energy soft precoding. Electron. Lett. **43**(6), 55–56 (2007)
9. M. Li, C. Liu, S.V. Hanly, Transmitter optimization for the network mimo downlink with finite-alphabet and QoS constraints, in *AusCTW* Adelaide, 2013
10. M. Alodeh, S. Chatzinotas, B. Ottersten, Constructive interference through symbol level precoding for multi-level modulation, in *2015 IEEE Global Communications Conference (GLOBECOM)*, San Diego, CA, 2015
11. M. Alodeh, S. Chatzinotas, B. Ottersten, Symbol-level multiuser MISO precoding for multi-level adaptive modulation: a multicast view (2016). arXiv preprint arXiv:1601.02788
12. D. Kwon, W. Yeo, D.K. Kim, A new precoding scheme for constructive superposition of interfering signals in multiuser MIMO systems. IEEE Commun. Lett. **18**(11), 2047–2050 (2014)
13. F. Khan, C. Masouros, T. Ratnarajah, Interference driven linear precoding in multiuser MISO downlink cognitive radio network. IEEE Trans. Veh. Technol. **61**(6), 2531–2543 (2012).
14. C. Masouros, T. Ratnarajah, Interference as a source of green signal power in cognitive relay assisted co-existing MIMO wireless transmissions. IEEE Trans. Commun. **60**(2), 525–536 (2012)
15. K.L. Law, C. Masouros, M. Pesavento, Transmit beamforming for interference exploitation in the underlay cognitive radio Z-channel. IEEE Trans. Signal Process. (submitted). Available on https://arxiv.org/abs/1606.06504

16. M. Alodeh, S. Chatzinotas, B. Ottersten, Symbol based precoding in the downlink of cognitive MISO channel, in *Proceedings of CROWNCOM* (2015)
17. C. Masouros, E. Alsusa, Two-stage transmitter precoding based on data-driven code hopping and partial zero forcing beamforming for MC-CDMA communications. IEEE Trans. Wirel. Commun. **8**(7), 3634–3645 (2009)
18. C. Masouros, E. Alsusa, Interference exploitation using adaptive code allocation for the downlink of precoded MC-CDMA systems. IET J. Commun. **2**(9), 1118–1130 (2008). doi:10.1049/iet-com:20070628
19. E. Alsusa, C. Masouros, Adaptive code allocation for interference management on the downlink of DS-CDMA systems. IEEE Trans. Wirel. Commun. **7**(7), 2420–2424 (2008). doi:10.1109/TWC.2008.061043
20. C. Masouros, Correlation rotation linear precoding for MIMO broadcast communications. IEEE Trans. Signal. Process. **59**(1), 252–262 (2011)
21. S.M. Razavi, T. Ratnarajah, C. Masouros, Transmit-power efficient linear precoding utilizing known interference for the multiantenna downlink. IEEE Trans. Veh. Technol. **63**(9), 4383–4394 (2014)
22. S.M. Razavi, T. Ratnarajah, Adaptively regularized phase alignment precoding for multiuser multiantenna downlink. IEEE Trans. Veh. Technol. **64**(10), 4863–4869 (2015)
23. M.-J. Qi, Y.-C. Wu, Correlation rotation precoding algorithm based on criterion of minimum mean square error. J. Comput. Appl. **1**, 037 (2012)
24. X.M. Yang, Y. Xiong, Linear precoding with known interference for MIMO broadcast channels. Electron. Lett. **47**(13), 778–780 (2011)
25. Z.J. Liu, J.L. Wang, D.C. Sun K.C. Yi, Unified SER performance analysis and improvement for multiuser MIMO downlink with correlation rotation linear precoding. IEEE Trans. Wirel. Commun **12**(4), 1678–1685 (2013)
26. D. Kwon, H.S. Kang, D.K. Kim, Robust interference exploitation-based precoding scheme with quantized CSIT. IEEE Commun. Lett. **20**(4), 780–783 (2016)
27. C.B. Peel, B.M. Hochwald, A.L. Swindlehurst, A vector-perturbation technique for near-capacity multiantenna multiuser communication-part I: channel inversion and regularization. IEEE Trans. Commun. **53**(1), 195–202 (2005)
28. C. Windpassinger, R. Fischer, T. Vencel, J. Huber, Precoding in multiantenna and multiuser communications, IEEE Trans. on Wireless Comms. **3**(4), 1305–1316 (2004)
29. C.B. Peel, B.M. Hochwald, A.L. Swindlehurst, A vector-perturbation technique for near-capacity multiantenna multiuser communication-part II: perturbation. IEEE Trans. Commun. **53**(3), 537–544 (2005)
30. C. Masouros, M. Sellathurai, T. Ratnarajah, Interference optimization for transmit power reduction in Tomlinson-Harashima precoded MIMO downlinks. IEEE Trans. Signal Process. **60**(5), 2470–2481 (2012)
31. A. Garcia, C. Masouros, Power-efficient Tomlinson-Harashima precoding for the downlink of multi-user MISO systems. IEEE Trans. Commun. **62**(6), 1884–1896 (2014)
32. E. Agrell, T. Eriksson, A. Vardy, K. Zeger, Closest point search in lattices. IEEE Trans. Inf. Theory **48**(8), 2201–2214 (2002)
33. C. Masouros, M. Sellathurai, T. Ratnarajah, Vector perturbation based on symbol scaling for limited feedback MISO downlinks. IEEE Trans. Signal Process. **62**(3), 562–571 (2014)
34. M. Bengtsson, B. Ottersten, Optimal and suboptimal transmit beamforming, in *Handbook of Antennas in Wireless Communications*, ed. by L. Godara, ch. 18 (CRC, Boca Raton, FL, 2001)
35. M. Schubert, H. Boche, Solution of the multi-user downlink beamforming problem with individual SINR constraints. IEEE Trans. Veh. Technol. **53**(1), 18–28 (2004)
36. M. Alodeh, S. Chatzinotas, B. Ottersten, Constructive multiuser interference in symbol level precoding for the MISO downlink channel. IEEE Trans. Signal Process. **63**(9), 2239–2252 (2015)

37. C. Masouros, G. Zheng, Exploiting known interference as green signal power for downlink beamforming optimization. IEEE Trans. Signal Process. **63**(14), 3668–3680 (2015)
38. M. Alodeh, S. Chatzinotas, B. Ottersten, Energy-efficient symbol-level precoding in multiuser MISO based on relaxed detection region. IEEE Trans. Wirel. Commun. **15**(5), 3755–3767 (2016)
39. K.L. Law, C. Masouros, K.K. Wong, G. Zheng, Constructive interference exploitation for QoS-based downlink beamforming optimization. IEEE Trans. Signal Process. (in press)
40. A. Li, C. Masouros, Exploiting constructive mutual coupling in P2P MIMO by analog-digital phase alignment. IEEE Trans. Wirel. Commun. **16**(3), 1948–1962 (2017)
41. C. Masouros, E. Alsusa, Transmit antenna selection for partial linear precoding MIMO schemes. IET Electron. Lett. **45**(14), 736–737 (2009)
42. P.V. Amadori and C. Masouros, interference driven antenna selection for massive multi-user MIMO. IEEE Trans. Veh. Technol. **65**(8), 5944–5958 (2016)
43. P.V. Amadori, C. Masouros, Large scale antenna selection for interference exploitation. IEEE Trans. Commun. (in press)
44. M. Alodeh, S. Chatzinotas, B. Ottersten, Data aware user selection in the cognitive downlink MISO precoding systems, in *IEEE International Symposium on Signal Processing and Information Technology (ISSPIT)*, December 2013. Invited paper
45. Z. Ding, Z. Yang, P. Fan, H.V. Poor, On the performance of non-orthogonal multiple access in 5G systems with randomly deployed users. IEEE Signal Process. Lett. **21**(12), 1501–1505 (2014)
46. P.V. Amadori, C. Masouros, Constant envelope precoding by interference exploitation in phase shift keying-modulated multiuser transmission. IEEE Trans Wirel. Commun. **16**(1), 538–550 (2017)
47. X. Gao, O. Edfors, F. Tufvesson, E.G. Larsson, Massive MIMO in real propagation environments: do all antennas contribute equally? IEEE Trans. Commun. **63**(11), 3917–3928 (2015)
48. Z. Chen, J. Yuan, B. Vucetic, Z. Zhou, Performance of Alamouti scheme with transmit antenna selection, in *IEEE International Symposium on Personal, Indoor and Mobile Radio Communications*, vol. 2 (2004), pp. 1135–1141
49. F. Rusek, D. Persson, B.K. Lau, E. Larsson, T. Marzetta, O. Edfors, F. Tufvesson, Scaling up MIMO: opportunities and challenges with very large arrays. IEEE Signal Process. Mag. **30**(1), 40–60 (2013)
50. A. Gorokhov, D. Gore, A. Paulraj, Receive antenna selection for MIMO spatial multiplexing: theory and algorithms. IEEE Trans. Signal Process. **51**(11), 2796–2807 (2003)
51. Y. Cheng, M. Pesavento, Joint discrete rate adaptation and downlink beamforming using mixed integer conic programming. IEEE Trans. Signal Process. **63**(7), 1750–1764 (2015)
52. S.K. Mohammed, E.G. Larsson, Per-antenna constant envelope precoding for large multi-user MIMO systems. IEEE Trans. Commun. **61**(3), 1059–1071 (2013)
53. J.C. Chen, C.K. Wen, K.K. Wong, Improved constant envelope multiuser precoding for massive MIMO systems. IEEE Commun. Lett. **18**(8), 1311–1314 (2014)
54. P.T. De Boer, D.P. Kroese, S. Mannor, R.Y. Rubinstein, A tutorial on the cross-entropy method. Ann. Oper. Res. **134**(1), 19–67 (2005)
55. R. Zhang, C.K. Ho, MIMO broadcasting for simultaneous wireless information and power transfer. IEEE Trans. Wirel. Commun. **12**(5), 1989–2001 (2013)
56. G. Zhu, C. Zhong, H.A. Suraweera, G.K. Karagiannidis, Z. Zhang, T.A. Tsiftsis, Wireless information and power transfer in relay systems with multiple antennas and interference. IEEE Trans. Commun. **63**, 1400–1418 (2015)
57. Y. Zeng, R. Zhang, Full-duplex wireless-powered relay with self-energy recycling. IEEE Wirel. Commun. Lett. **4**(2), 201–204 (2015)

58. S. Timotheou, I. Krikidis, G. Zheng, B. Ottersten, Beamforming for MISO interference channels with QoS and RF energy transfer. IEEE Trans. Wirel. Commun. **13**(5), 2646–2658 (2014)
59. S. Timotheou, G. Zheng, C. Masouros, I. Krikidis, Exploiting constructive interference for simultaneous wireless information and power transfer in multiuser downlink systems. IEEE JSAC Spec. Issue Green Commun. Netw. Second Issue **34**(5), 1772–1784 (2016)
60. W. He, C.N. Georghiades, Computing the capacity of a MIMO fading channel under PSK signaling. IEEE Trans. Inform. Theory **51**(5), 1794–1803 (2005)

Chapter 5
Energy Harvesting for Wireless Relaying Systems

Yunfei Chen

5.1 Introduction

In wireless communications, the destination node may be too far away from the source node, or it may be obstructed from the source node, such that direct communications between them are not possible. In this case, idle nodes between them can be used to form a relaying link [1, 2]. Even when direct communications between source and destination are available, idle nodes can still be used to provide extra links. Thus, in wireless relaying, the relaying nodes forward signals from the source to the destination to extend network coverage or to achieve diversity gain.

However, one of the main problems of existing wireless relaying systems is that the relaying node has to consume its own energy to perform the relaying operation. This discourages idle nodes from taking part in relaying, especially when they operate on batteries and hence have a limited lifetime. Energy harvesting can solve this problem by allowing the relaying node to harvest wireless energy from the source and to use the harvested energy for relaying. Thus, this chapter investigates energy harvesting wireless relaying. Figure 5.1 compares the conventional wireless relaying with energy harvesting relaying. One sees that their main difference is that energy harvesting relaying has an extra energy link between source and relay so that the source can transfer energy to the relay wirelessly.

There are two main relaying protocols: amplify-and-forward (AF) and decode-and-forward (DF) [3, 4]. In AF, the signal from the source is amplified and then forwarded to the destination without any further processing. The amplification and forwarding operations will consume energy. In DF, the signal from the source

Y. Chen (✉)
University of Warwick, Coventry CV4 7AL, UK
e-mail: yunfei.chen@warwick.ac.uk

D.N.K. Jayakody et al. (eds.), *Wireless Information and Power Transfer: A New Paradigm for Green Communications*, DOI 10.1007/978-3-319-56669-6_5

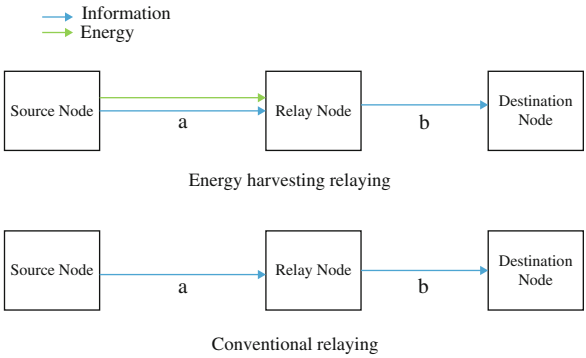

Fig. 5.1 Comparison of conventional and energy harvesting relaying

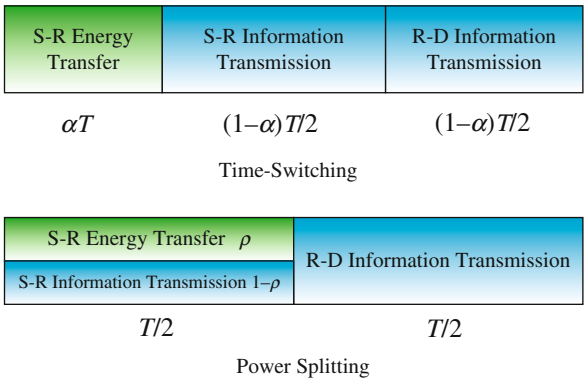

Fig. 5.2 TS and PS strategies for wireless relaying

is first decoded and then re-encoded before being forwarded to the destination. The decoding, encoding and forwarding operations will also consume energy. The AF protocol is simpler than the DF protocol by performing a straightforward amplification without any decoding but its performance is usually poorer than the DF protocol due to the amplified noise.

On the other hand, there are two main energy harvesting strategies: time-switching (TS) and power-splitting (PS) [5]. In TS, a dedicated harvesting time is allocated for energy harvesting. This simplifies the hardware requirement but the dedicated harvesting time reduces the throughput or achievable rate of the system. In PS, no dedicated harvesting time is allocated but a portion of the received power is split for energy harvesting. This strategy keeps the throughput of the system but increases the hardware requirement, as a power splitter is not trivial in the implementation. Figure 5.2 compares the TS and PS strategies. In this figure, T is the total transmission time in wireless relaying, α is the so-called TS coefficient that determines how much time will be dedicated for harvesting, and ρ is the so-called PS factor that determines how much of the received power should be split for harvesting.

In this chapter, we consider both TS and PS for AF and DF protocols. For simplicity, we only consider a three-node relaying system, where the signal is

transmitted from the source to the relay and then forwarded to the destination, without a direct link between source and destination. Each node is also half-duplex and has a single antenna.

5.2 Energy Harvesting DF Relaying Without Interference

5.2.1 Introduction

In this section, we show the performance of energy harvesting DF relaying without interference. As mentioned before, DF normally offers better performance than AF and thus, it is preferred in applications that emphasize performances. On the other hand, compared with TS, the PS scheme does not require any dedicated harvesting time. Thus, PS normally has higher throughput. Considering these, in this section, the performance of DF using PS will be studied.

Several previous works on DF relaying using energy harvesting exist. For example, reference [6] used stochastic geometry theories to study the effect of random location on the outage probability of DF using PS. Reference [7] studied the approximate ergodic capacity of DF using both TS and PS. Reference [8] considered interference for DF relaying using TS. Reference [9] compared full-duplex and half-duplex DF relaying systems using TS. This was extended to the multiple antenna case in [10]. All of them assumed Rayleigh fading channels. There were no results on bit error rate (BER) either.

In this section, the exact BER and throughput performances of DF using PS will be studied for Nakagami-m fading channels. Two different transmission scenarios will be considered: instantaneous transmission with known channel state information and delay- or error-tolerant transmission with averaged error rate or throughput. For each scenario, exact analytical expressions for the end-to-end BER and throughput will be derived. These expressions will then be used to study the optimum PS factor, a key parameter for energy harvesting relaying. Design guidance on energy harvesting relaying will be provided based on the study.

As mentioned before, we consider a three-node DF relaying system using PS but without a direct link. From Fig. 5.2, the source transmits a signal to the relay in the first phase. The relay splits this signal into two parts: one part for energy harvesting and one part for information decoding. The decoded information is then encoded again and forwarded to the destination using the harvested energy. Thus, the part of the received signal at the relay for information decoding is

$$y_k^r = \sqrt{(1-\rho)P_S}hs + \sqrt{1-\rho}n_k^{\mathrm{ra}} + n_k^{\mathrm{rc}}. \tag{5.1}$$

In the above equation, P_S is the transmitted power of the source, ρ is the PS factor to be optimized, h is the Nakagami-m fading gain of the source-to-relay link, s is the transmitted binary phase shift keying (BPSK) bit such that $s = +1$ and $s = -1$

with equal probabilities, n_k^{ra} is the k-th sample of the noise from the antenna and n_k^{rc} is the k-th sample of the noise from the RF-to-baseband conversion, assumed to be additive white Gaussian noise (AWGN) with mean zero and variance σ_{ra}^2 and σ_{rc}^2, respectively, and the fading power $|h|^2$ is Gamma distributed with $f_{|h|^2}(x) = \left(\frac{m_1}{\Omega_1}\right)^{m_1} \frac{x^{m_1-1}}{\Gamma(m_1)} e^{-\frac{m_1}{\Omega_1}x}, x > 0$, m_1 is the Nakagami m parameter, Ω_1 is the average fading power of the source-to-relay link and $\Gamma(\cdot)$ is the complete Gamma function [11, Eq. (8.310.1)].

The other part of the received signal for energy harvesting can give the harvested energy $E_h = \eta\rho P_S|h|^2\frac{T}{2}$ so that the transmission power of the relay is $P_r = \frac{E_h}{T/2} = \eta\rho P_S|h|^2$, where η is the conversion efficiency of the energy harvester used. Using the harvested energy calculated, one has the received signal at the destination as

$$y_k^d = \sqrt{P_r}g\hat{s} + n_k^{\text{da}} + n_k^{\text{dc}} \tag{5.2}$$

where P_r is the transmission power of the relay given before, g is the Nakagami-m fading gain of the relay-to-destination link, $\hat{s}$ is the data decision of the BPSK bit made and transmitted by the relay, and n_k^{da} and n_k^{dc} are the antenna noise and the conversion noise, respectively. In this case, $|g|^2$ is Gamma distributed $f_{|g|^2}(x) = \left(\frac{m_2}{\Omega_2}\right)^{m_2} \frac{x^{m_2-1}}{\Gamma(m_2)} e^{-\frac{m_2}{\Omega_2}x}, x > 0$, where m_2 is the Nakagami m parameter and Ω_2 is the average fading power of the relay-to-destination link. Also, n_k^{da} and n_k^{dc} are AWGN with mean zero and variance σ_{da}^2 and σ_{dc}^2, respectively.

5.2.2 BER

Using (5.1) and (5.2), the BERs of the S-R and R-D links are derived as $\text{BER}_r = \frac{1}{2}\text{erfc}(\sqrt{\gamma_1})$ and $\text{BER}_d = \frac{1}{2}\text{erfc}(\sqrt{\gamma_2})$, respectively, where $\gamma_1 = \frac{(1-\rho)P_S|h|^2}{(1-\rho)\sigma_{\text{ra}}^2+\sigma_{\text{rc}}^2}$ is defined as the instantaneous signal-to-noise ratio (SNR) of the S-R link, $\gamma_2 = \frac{\eta\rho P_S|h|^2|g|^2}{\sigma_{\text{da}}^2+\sigma_{\text{dc}}^2}$ is defined as the instantaneous SNR of the R-D link, and $\text{erfc}(\cdot)$ is the complementary error function [11, Eq. (8.250.4)].

For instantaneous transmission, h and g are known through channel estimation. Thus, the end-to-end BER of the whole relaying link can be derived as $\text{BER} = \text{BER}_r(1-\text{BER}_d) + \text{BER}_d(1-\text{BER}_r)$ or

$$\begin{aligned}\text{BER} = {} & \frac{1}{2}\text{erfc}\left(\sqrt{\frac{(1-\rho)P_S|h|^2}{(1-\rho)\sigma_{\text{ra}}^2+\sigma_{\text{rc}}^2}}\right) + \frac{1}{2}\text{erfc}\left(\sqrt{\frac{\eta\rho P_S|h|^2|g|^2}{\sigma_{\text{da}}^2+\sigma_{\text{dc}}^2}}\right) \\ & -\frac{1}{2}\text{erfc}\left(\sqrt{\frac{(1-\rho)P_S|h|^2}{(1-\rho)\sigma_{\text{ra}}^2+\sigma_{\text{rc}}^2}}\right)\text{erfc}\left(\sqrt{\frac{\eta\rho P_S|h|^2|g|^2}{\sigma_{\text{da}}^2+\sigma_{\text{dc}}^2}}\right).\end{aligned} \tag{5.3}$$

One sees that, when the hop SNRs are large, the third term in (5.3) is much smaller than the first two terms and may be ignored. In this case, when the value of ρ increases, the first term in (5.3) increases while the second term in (5.3) decreases. Thus, there exists an optimum value of ρ that minimizes the BER. This optimum value can be derived using standard mathematical manipulations of first-order differentiation but there is no closed-form expression for the optimum value of ρ.

For error-tolerant transmission, the average end-to-end BER can be calculated as

$$\bar{\text{BER}} = \int_0^\infty \int_0^\infty \left[\frac{1}{2}\text{erfc}\left(\sqrt{\frac{(1-\rho)P_S x}{(1-\rho)\sigma_{\text{ra}}^2 + \sigma_{\text{rc}}^2}}\right) + \frac{1}{2}\text{erfc}\left(\sqrt{\frac{\eta\rho P_S xy}{\sigma_{\text{da}}^2 + \sigma_{\text{dc}}^2}}\right) - \frac{1}{2}\text{erfc}\left(\sqrt{\frac{(1-\rho)P_S x}{(1-\rho)\sigma_{\text{ra}}^2 + \sigma_{\text{rc}}^2}}\right)\text{erfc}\left(\sqrt{\frac{\eta\rho P_S xy}{\sigma_{\text{da}}^2 + \sigma_{\text{dc}}^2}}\right)\right] f_{|h|^2}(x) f_{|g|^2}(y)\,dxdy. \tag{5.4}$$

5.2.3 Throughput

Similarly, the throughput of the S-R and R-D can be derived from the received signals as $C_r = \ln(1+\gamma_1)$ and $C_d = \ln(1+\gamma_2)$, respectively.

For instantaneous transmission, the fading channel gains are known. Using them, the end-to-end throughput of the DF relaying system can be derived as

$$C = \min\{C_r, C_d\} = \ln\left(1 + \min\left\{\frac{(1-\rho)P_S|h|^2}{(1-\rho)\sigma_{\text{ra}}^2 + \sigma_{\text{rc}}^2}, \frac{\eta\rho P_S|h|^2|g|^2}{\sigma_{\text{da}}^2 + \sigma_{\text{dc}}^2}\right\}\right). \tag{5.5}$$

This throughput also has an optimum value of ρ. The optimum value of ρ can be derived as $\rho_{\text{opt}}^C = \frac{(\sigma_{\text{da}}^2+\sigma_{\text{dc}}^2+\eta|g|^2\sigma_{\text{rc}}^2+\eta|g|^2\sigma_{\text{ra}}^2)-\sqrt{\Delta}}{2\eta|g|^2\sigma_{\text{ra}}^2}$, where $\Delta = [\eta|g|^2\sigma_{\text{rc}}^2]^2 + 2(\eta|g|^2\sigma_{\text{rc}}^2)(\sigma_{\text{da}}^2+\sigma_{\text{dc}}^2+\eta|g|^2\sigma_{\text{ra}}^2) + (\sigma_{\text{da}}^2+\sigma_{\text{dc}}^2-\eta|g|^2\sigma_{\text{ra}}^2)^2$. One sees that this optimum ρ does not depend on $|h|^2$. As well, when $\frac{|g|^2}{\sigma_{\text{da}}^2+\sigma_{\text{dc}}^2}$ is large and goes to infinity, ρ_{opt}^C approaches zero.

For delay-tolerant transmission, the ergodic throughput is obtained by averaging it over the channel gains such that only the channel statistics are needed. Using this, the ergodic capacity can be calculated as

$$\bar{C} = \int_0^\infty \int_0^\infty \ln\left(1 + \min\left\{\frac{(1-\rho)P_S x}{(1-\rho)\sigma_{\text{ra}}^2 + \sigma_{\text{rc}}^2}, \frac{\eta\rho P_S xy}{\sigma_{\text{da}}^2 + \sigma_{\text{dc}}^2}\right\}\right) f_{|h|^2}(x) f_{|g|^2}(y)\,dxdy. \tag{5.6}$$

The ergodic throughput in [7] and [8] are approximate expressions, since [8] and [7] interchanged the order of integration and logarithm or the order of logarithm and the minimum function, while mathematically they are not interchangeable due to the non-linearity of the logarithm operation. The integration in (5.6) may be simplified by using special functions but no closed-form expressions can be derived due to its complexity.

5.2.4 Numerical Results

In this case, numerical examples of the BER and throughput in different scenarios will be presented. Without loss of generality, in the examples, we set $P_S = 1$, $\sigma_{\text{ra}}^2 = \sigma_{\text{rc}}^2 = \sigma_{\text{da}}^2 = \sigma_{\text{dc}}^2 = 1$, while $|h|^2$ and $|g|^2$ in the instantaneous transmission change with $\beta_1 = \frac{|h|^2}{\sigma_{\text{ra}}^2+\sigma_{\text{rc}}^2}$ and $\beta_2 = \frac{|g|^2}{\sigma_{\text{da}}^2+\sigma_{\text{dc}}^2}$ and Ω_1 and Ω_2 in the delay- and error-tolerant transmissions change with $\beta_1 = \frac{\Omega_1}{\sigma_{\text{ra}}^2+\sigma_{\text{rc}}^2}$ and $\beta_2 = \frac{\Omega_2}{\sigma_{\text{da}}^2+\sigma_{\text{dc}}^2}$. The values of β_1 and β_2 indicate how good the source-to-relay and relay-to-destination links are.

Figure 5.3 shows the maximum throughput using the optimized ρ for different values of β_1 and β_2. When β_1 is fixed in the legend, the X-axis corresponds to β_2, and when β_2 is fixed in the legend, the X-axis corresponds to β_1. In this case, one

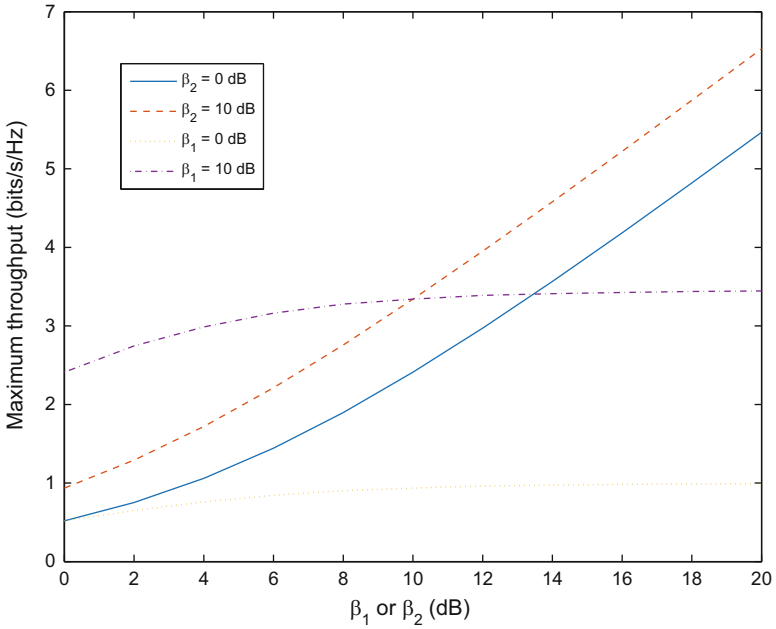

Fig. 5.3 Maximum throughput using optimum ρ vs. β_1 or β_2 when $\eta = 0.3$ in instantaneous transmission

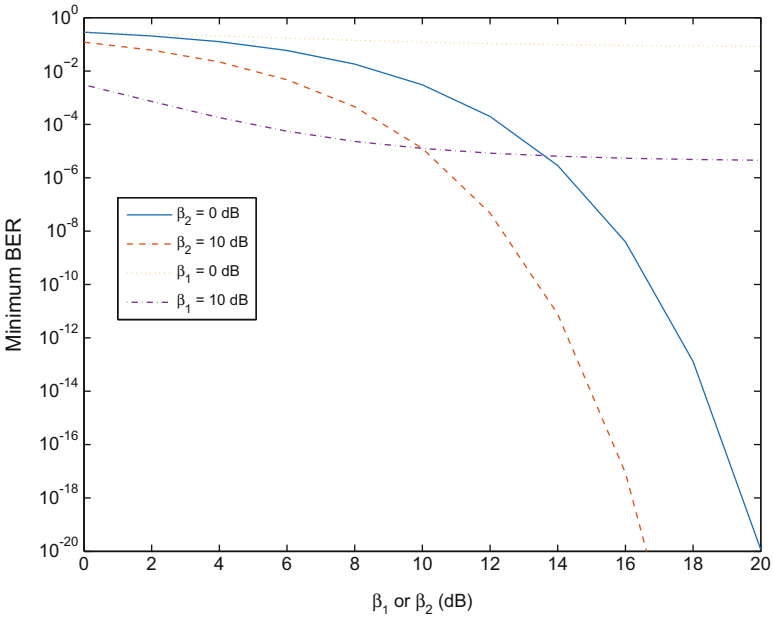

Fig. 5.4 Minimum BER using optimum ρ vs. β_1 or β_2 when $\eta = 0.3$ in instantaneous transmission

sees that the optimized throughput increases significantly with β_1, when β_2 is fixed to 0 and 10 dB, while the optimized throughput remains almost the same when β_2 increases and β_1 is fixed to 0 and 10 dB. Thus, the throughput is more sensitive to β_1. Figure 5.4 shows the minimum BER using the optimized ρ for different values of β_1 and β_2. Similarly, the BER is more sensitive to β_1 than to β_2. This indicates that the S-R link is more important than the R-D link in this case, as expected, as the S-R link not only determines the throughput or BER at the relay, but also determines the throughput or BER at the destination, via the harvested power.

Figure 5.5 shows the optimized value of ρ used to calculate the maximum throughput in Fig. 5.3. When β_2 is fixed to 0 dB or 10 dB, the optimum ρ does not change when β_1 increases. This agrees with the discussion before that the optimum ρ does not depend on $|h|^2$. When β_1 is fixed to 0 dB or 10 dB, the optimum ρ decreases with an increasing β_2, as less power needs to be harvested when the channel condition of the relay-to-destination link improves, under the same other conditions. Figure 5.6 gives the optimum ρ used to calculate the minimum BER in Fig. 5.4. Again, in general, the optimum ρ is more sensitive to β_2 than to β_1.

Figure 5.7 gives the optimized ρ for the maximum throughput for different β_1 and β_2 in delay- or error-tolerant transmission. It is interesting to note that in this case, when β_2 is fixed to 0 dB or 10 dB, the optimum ρ increases very slowly with β_1, very close to a constant as in the instantaneous transmission. However, the optimum ρ does decrease when β_2 increases, for fixed β_1. This implies to us

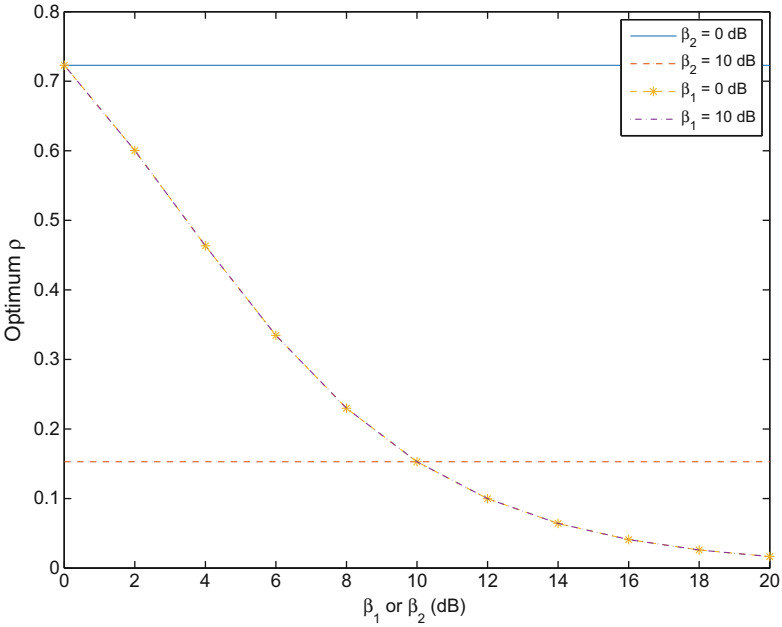

Fig. 5.5 The optimum ρ vs. β_1 or β_2 when $\eta = 0.3$ to achieve the maximum throughput in instantaneous transmission

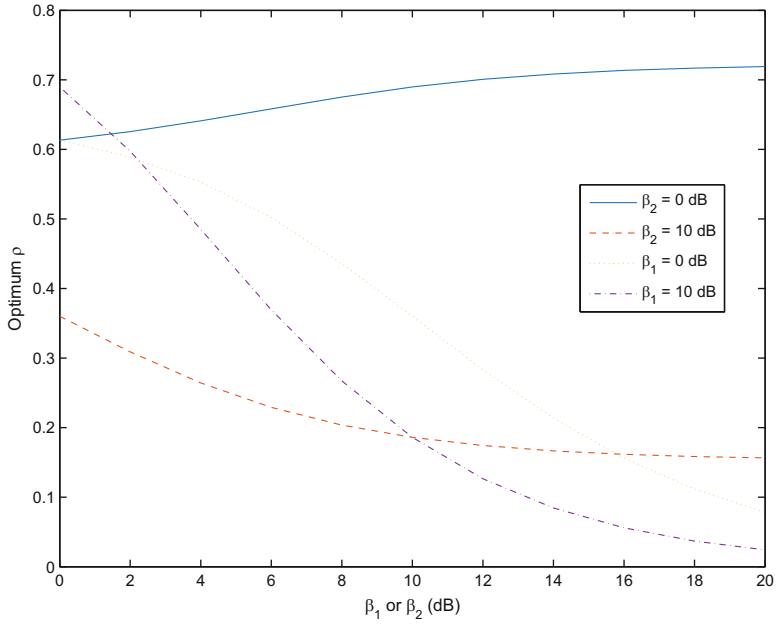

Fig. 5.6 The optimum ρ vs. β_1 or β_2 when $\eta = 0.3$ to achieve the minimum BER in instantaneous transmission

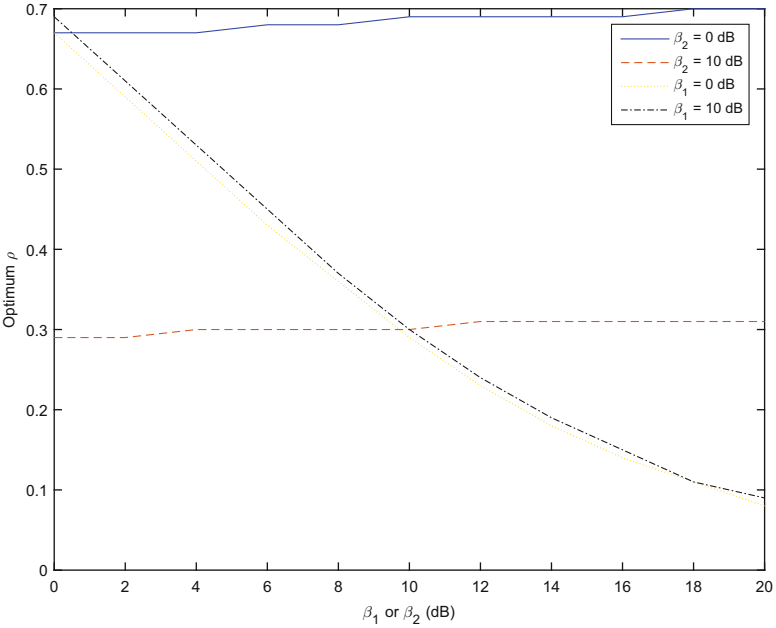

Fig. 5.7 The optimum ρ vs. β_1 or β_2 when $m_1 = m_2 = 2$ and $\eta = 0.3$ for the maximum throughput in delay-tolerant transmission

that in delay-tolerant transmission, the R-D link is more important than the S-R link. Figure 5.8 gives the optimum ρ for the minimum BER for different β_1 and β_2 in delay- or error-tolerant transmission. In this case, this optimum value changes significantly in most curves when β_1 or β_2 increase or decrease.

5.2.5 *Conclusion*

In this section, the throughput and BER expressions for DF relaying using PS have been analysed for Nakagami-m fading channels in two different transmission scenarios. Numerical results have shown that there does exist an optimum value of the PS factor in all the cases considered. For instantaneous transmission, the optimum value of ρ for maximum throughput does not depend on β_1 in this case. For delay- or error-tolerant transmissions, the relaying performance is less sensitive to η too. In addition, the optimum ρ that achieves maximum throughput is insensitive to β_1, while the optimum ρ for minimum BER is sensitive to both β_1 and β_2.

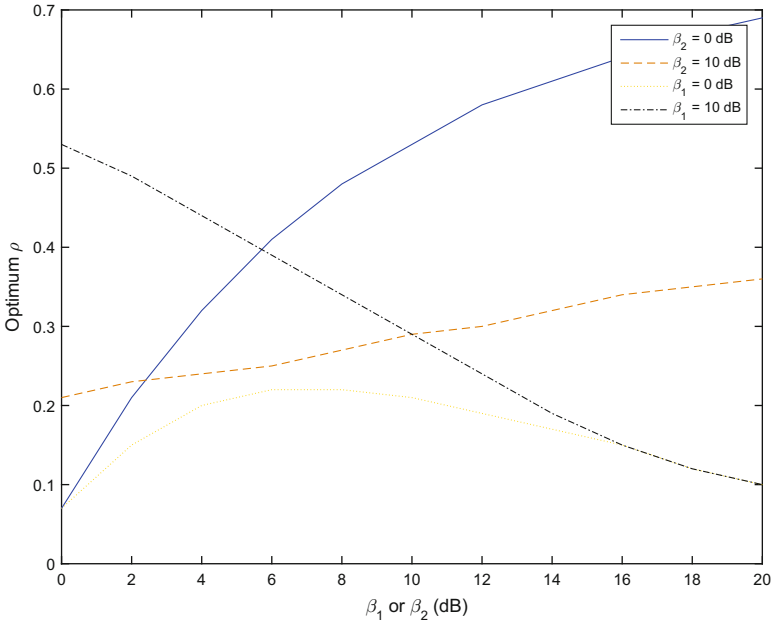

Fig. 5.8 The optimum ρ vs. β_1 or β_2 when $m_1 = m_2 = 2$ and $\eta = 0.3$ for the minimum BER in error-tolerant transmission

5.3 Energy Harvesting AF Relaying with Interference

5.3.1 Introduction

The AF protocol does not perform as well as the DF protocol but is simpler than the DF protocol. So it will be useful for applications where complexity is limited. Also, in a practical network, the relaying process may be subject to interference caused by other transmitters in the network. In this section, we will study the performance of energy harvesting AF relaying with interference. Again, we consider the PS scheme.

Some previous works on energy harvesting AF relaying exist. For example, reference [12] studied two energy harvesting AF schemes using PS and TS. Reference [13] studied a harvest-use structure, where the relay does not have energy storage capability and has to use the harvested energy immediately after it is harvested, for the optimal trade-off between harvesting time and relaying time. Reference [14] studied the optimal power allocation for energy harvesting AF, where relays can harvest energies from multiple source nodes and the total harvested energy was then allocated for transmissions of signals to different destinations. All these works consider Rayleigh fading. They did not consider the effect of interference either.

To provide more insights on various aspects of AF relaying using PS, in this section, the performance of AF relaying using PS is analysed by deriving the outage probability and the throughput in Nakagami-m fading channels, when both the relay and the destination suffer from interference. Both fixed-gain relaying and variable-gain AF relaying are studied. Using the derived expressions, the effects of different system parameters on the system performance are examined.

Again, consider a three-node system without a direct link between source and destination. For PS, a fraction of the received signal is harvested without any dedicated harvesting time. Thus, the transmission from the source to the relay takes $\frac{T}{2}$ seconds and the received information signal at the relay is given by

$$y_k^r = \sqrt{(1-\rho)P_s}ha + \sqrt{1-\rho}\sum_{i=1}^{N}\sqrt{P_i}h_i a_i + \sqrt{1-\rho}n_k^{\mathrm{ra}} + n_k^{\mathrm{rc}} \tag{5.7}$$

where N is the number of interfering sources at the relay, P_i is the transmission power of the i-th interferer, h_i is the fading gain from the i-th interferer to the considered relay, a_i is the transmitted BPSK bit of the i-th interferer and all the other symbols are defined as before. We assume Nakagami-m fading such that $|h_i|^2$, $i = 1, 2, \ldots, N$, are Gamma distributed with $f_{|h_i|^2}(x) = \left(\frac{m_{I1}}{\Omega_{I1}}\right)^{m_{I1}} \frac{x^{m_{I1}-1}}{\Gamma(m_{I1})} e^{-\frac{m_{I1}}{\Omega_{I1}}x}, x > 0$, where m_{I1} and Ω_{I1} are the m parameter and the average fading power from the interferer to the relay, respectively. They are assumed to be independent and identically distributed. Then, the harvested energy is given by $E_h = \eta\rho(P_s|h|^2 + \sum_{i=1}^{N} P_i|h_i|^2)\frac{T}{2}$.

Using the harvested energy, the received information is amplified and forwarded. The received signal at the destination is given by

$$y_k^d = \sqrt{P_r}agy_k^r + \sum_{j=1}^{N}\sqrt{Q_j}g_j b_j + n_k^{\mathrm{da}} + n_k^{\mathrm{dc}} \tag{5.8}$$

where $P_r = \frac{E_h}{T/2} = \eta\rho(P_s|h|^2 + \sum_{i=1}^{N} P_i|h_i|^2)$, Q_j is the transmission power of the j-th interferer to the destination, g_j is the fading gain from the j-th interferer to the destination, b_j is the transmitted BPSK bit of the j-th interferer and all other symbols are defined as before. The amplification factor depends on the method of AF relaying [15–17]. In fixed-gain relaying, a is a constant and without loss of generality, $a = 1$. In variable-gain relaying, one has $a = \frac{1}{\sqrt{(1-\rho)P_S|h|^2 + (1-\rho)\sigma_{\mathrm{ra}}^2 + \sigma_{\mathrm{rc}}^2}}$. We again assume Nakagami-m fading such that $|g_j|^2, j = 1, 2, \ldots, N$, are Gamma distributed with $f_{|g_j|^2}(x) = \left(\frac{m_{I2}}{\Omega_{I2}}\right)^{m_{I2}} \frac{x^{m_{I2}-1}}{\Gamma(m_{I2})} e^{-\frac{m_{I2}}{\Omega_{I2}}x}, x > 0$, where m_{I2} and Ω_{I2} are the m parameter and the average fading power in the link from the j-th interferer to the destination, respectively.

5.3.2 Outage

The outage probability is defined as the probability that the SINR is below a certain threshold γ_0 as $P_{\text{out}} = Pr\{\gamma < \gamma_0\}$. Denote $\gamma_2 = \frac{|g|^2}{\sum_{j=1}^{N} Q_j|g_j|^2+\sigma_{\text{da}}^2+\sigma_{\text{dc}}^2}$ and $\gamma_3 = \frac{|h|^2}{\sum_{i=1}^{N} P_i|h_i|^2+\sigma_{\text{ra}}^2+\sigma_{\text{rc}}^2/(1-\rho)}$. Using (5.8), the end-to-end signal-to-interference-plus-noise ratio (SINR) can be derived as

$$\gamma = \frac{P_S a^2 \gamma_2 \gamma_3}{a^2\gamma_2 + \frac{1}{\eta\rho[(1-\rho)\sum_{i=1}^{N} P_i|h_i|^2+(1-\rho)\sigma_{\text{ra}}^2+\sigma_{\text{rc}}^2](P_S|h|^2+\sum_{i=1}^{N} P_i|h_i|^2)}}. \tag{5.9}$$

Compared with the end-to-end SINR for the conventional relaying, the end-to-end SINR for energy harvesting relaying has an additional term of $(P_S|h|^2 + \sum_{i=1}^{N} P_i|h_i|^2)$ multiplied with the second term in the denominator, which has caused complexity.

The outage probability for fixed-gain relaying using PS can be derived as

$$\begin{aligned} P_{\text{out}}^{\text{PS-FG}} = 1 - &\left(\frac{m_{I1}}{P_{I1}\Omega_{I1}}\right)^{Nm_{I1}} \left(\frac{m_1}{P_S\Omega_1}\right)^{m_1} \left(\frac{m_{I2}}{Q_{I2}\Omega_{I2}}\right)^{Nm_{I2}} \frac{1}{\Gamma(Nm_{I1})\Gamma(m_1)\Gamma(Nm_{I2})} \\ &\sum_{l=0}^{m_2-1}\sum_{l'=0}^{l} \frac{(m_2/\Omega_2)^l \binom{l'}{l} (\sigma_{\text{da}}^2+\sigma_{\text{dc}}^2)^{l-l'}(Nm_{I2}+l'-1)!}{l!} \\ &\cdot \int_0^{\infty}\int_{\gamma_0 z+\gamma_0\sigma_{\text{ra}}^2+\gamma_0\sigma_{\text{rc}}^2/(1-\rho)}^{\infty} e^{-\frac{m_2(\sigma_{\text{da}}^2+\sigma_{\text{dc}}^2)}{\Omega_2}X_{PS-FG}(y,z)-\frac{m_1}{P_S\Omega_1}y-\frac{m_{I1}}{P_{I1}\Omega_{I1}}z} \\ &\cdot \frac{(X_{PS-FG}(y,z))^l y^{m_1-1} z^{Nm_{I1}-1}}{\left(\frac{m_{I2}}{Q_{I2}\Omega_{I2}}+\frac{m_2 X_{\text{PS-FG}}(y,z)}{\Omega_2}\right)^{Nm_{I2}+l'}} dydz. \end{aligned} \tag{5.10}$$

where $X_{PS-FG}(y,z) = \frac{\gamma_0}{\eta\rho(1-\rho)}\frac{1}{(y+z)}\frac{1}{(y-\gamma_0 z-\gamma_0\sigma_{ra}^2-\gamma_0\sigma_{rc}^2/(1-\rho))}$.

Similarly, if variable-gain relaying is used, the outage probability is derived as

$$\begin{aligned} P_{\text{out}}^{\text{PS-VG}} = 1 - &\left(\frac{m_{I1}}{P_{I1}\Omega_{I1}}\right)^{Nm_{I1}} \left(\frac{m_1}{P_S\Omega_1}\right)^{m_1} \left(\frac{m_{I2}}{Q_{I2}\Omega_{I2}}\right)^{Nm_{I2}} \frac{1}{\Gamma(Nm_{I1})\Gamma(m_1)\Gamma(Nm_{I2})} \\ &\sum_{l=0}^{m_2-1}\sum_{l'=0}^{l} \frac{(m_2/\Omega_2)^l \binom{l'}{l} (\sigma_{\text{da}}^2+\sigma_{\text{dc}}^2)^{l-l'}(Nm_{I2}+l'-1)!}{l!} \\ &\cdot \int_0^{\infty}\int_{\gamma_0 z+\gamma_0\sigma_{\text{ra}}^2+\gamma_0\sigma_{\text{rc}}^2/(1-\rho)}^{\infty} e^{-\frac{m_2(\sigma_{\text{da}}^2+\sigma_{\text{dc}}^2)}{\Omega_2}X_{PS-VG}(y,z)-\frac{m_1}{P_S\Omega_1}y-\frac{m_{I1}}{P_{I1}\Omega_{I1}}z} \\ &\cdot \frac{(X_{\text{PS-VG}}(y,z))^l y^{m_1-1} z^{Nm_{I1}-1}}{\left(\frac{m_{I2}}{Q_{I2}\Omega_{I2}}+\frac{m_2 X_{\text{PS-VG}}(y,z)}{\Omega_2}\right)^{Nm_{I2}+l'}} dydz \end{aligned} \tag{5.11}$$

where $X_{\mathrm{PS-VG}}(y,z) = \frac{\gamma_0}{\eta\rho(1-\rho)} \frac{(1-\rho)y+(1-\rho)\sigma_{\mathrm{ra}}^2+\sigma_{\mathrm{rc}}^2}{(y+z)(y-\gamma_0 Z_1-\gamma_0\sigma_{\mathrm{ra}}^2-\gamma_0\sigma_{\mathrm{rc}}^2/(1-\rho))}$. The detailed derivation can be found in [18].

5.3.3 Throughput

Let R be a fixed transmission rate that the source needs to satisfy such that $R = \log_2(1+\gamma_0)$. Then, one has $\gamma_0 = 2^R - 1$. For PS, the throughput can be derived as

$$\tau = (1 - P_{\mathrm{out}})R\frac{T/2}{T} = \frac{R}{2}(1 - P_{\mathrm{out}}) \tag{5.12}$$

Using $P_{\mathrm{out}}^{\mathrm{PS-FG}}$ in (5.10) and $P_{\mathrm{out}}^{\mathrm{PS-VG}}$ in (5.11) to replace P_{out} in (5.12), the throughput for energy harvesting relaying using PS can be derived.

5.3.4 Numerical Results

In this subsection, the effects of some important system parameters are examined by showing relevant numerical examples. In these examples, we set $\sigma_{\mathrm{ra}}^2 = \sigma_{\mathrm{rc}}^2 = \sigma_{\mathrm{da}}^2 = \sigma_{\mathrm{dc}}^2 = 1$, $P_S = P_{I1} = Q_{I2} = \Omega_{I1} = \Omega_{I2} = 1$, while Ω_1 and Ω_2 vary with the average SINR of the source-to-relay link and the average SINR of the relay-to-destination link defined as $\Delta_1 = \frac{\Omega_1}{NP_{I1}\Omega_{I1}+\sigma_{\mathrm{ra}}^2+\sigma_{\mathrm{rc}}^2}$ and $\Delta_2 = \frac{\Omega_2}{NQ_{I2}\Omega_{I2}+\sigma_{\mathrm{ra}}^2+\sigma_{\mathrm{rc}}^2}$, respectively.

Figures 5.9, 5.10, 5.11, 5.12, 5.13 show the throughput of energy harvesting relaying using PS versus ρ under different conditions. In these cases considered, the throughput always increases and the rate of increase becomes small, when the value of ρ increases. When $\rho = 0.8$, the throughput is very close to the maximum it can be, indicating that there is greater flexibility in the choice of ρ. Also, the sensitivity of the throughput to ρ is small, as the value of throughput ranges between 0.9 and 1 in most cases in Figs. 5.9, 5.10, 5.11, 5.12, 5.13. One also sees from these figures that fixed-gain relaying has larger throughput than variable-gain relaying, the throughput increases when η increases, N decreases, R increases, the SINR increases or the m parameter increases. The throughput is more sensitive to N, R, Δ_1 and m_1 than to η, Δ_2 and the relaying method.

5.3.5 Conclusion

The performance of energy harvesting AF relaying has been evaluated in terms of the outage and the throughput for Nakagami-m fading with interference. Using these results, the effects of the PS factor ρ, the conversion efficiency of harvester η, the number of interferers N, the required fixed transmission rate R, the SINR of different hops and the m parameter on the throughput performance have been examined.

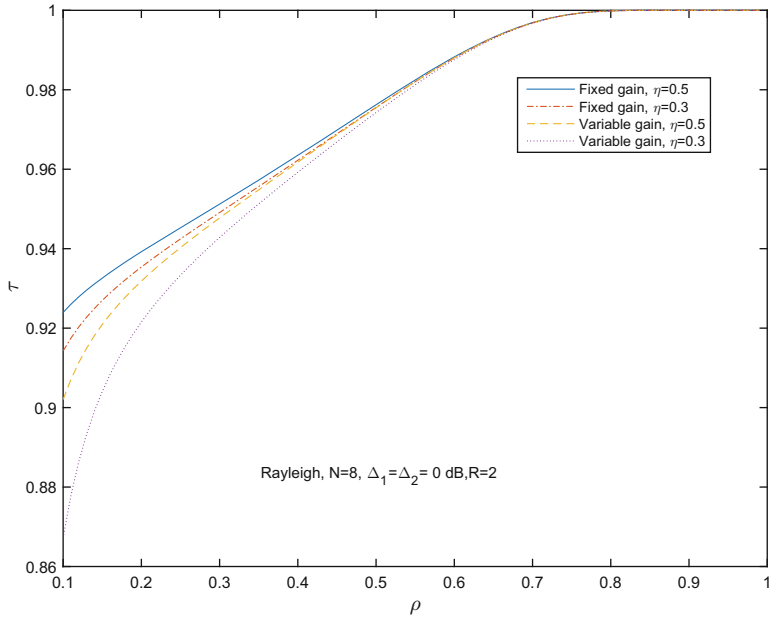

Fig. 5.9 Throughput vs. ρ for different values of η using PS energy harvesting when $N = 8$, $\Delta_1 = \Delta_2 = 0$ dB, $R = 2$ bits/s/Hz in Rayleigh fading channels

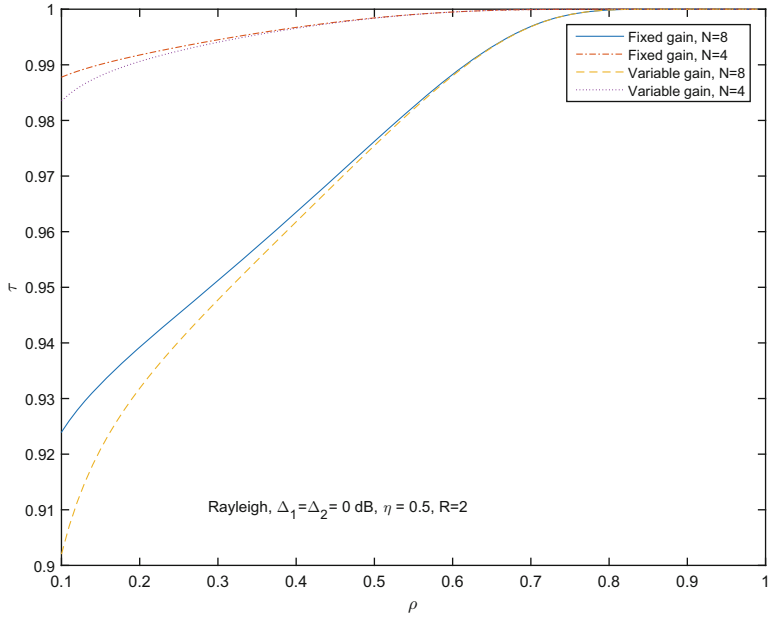

Fig. 5.10 Throughput vs. ρ for different values of N using PS energy harvesting when $\eta = 0.5$, $\Delta_1 = \Delta_2 = 0$ dB, $R = 2$ bits/s/Hz in Rayleigh fading channels

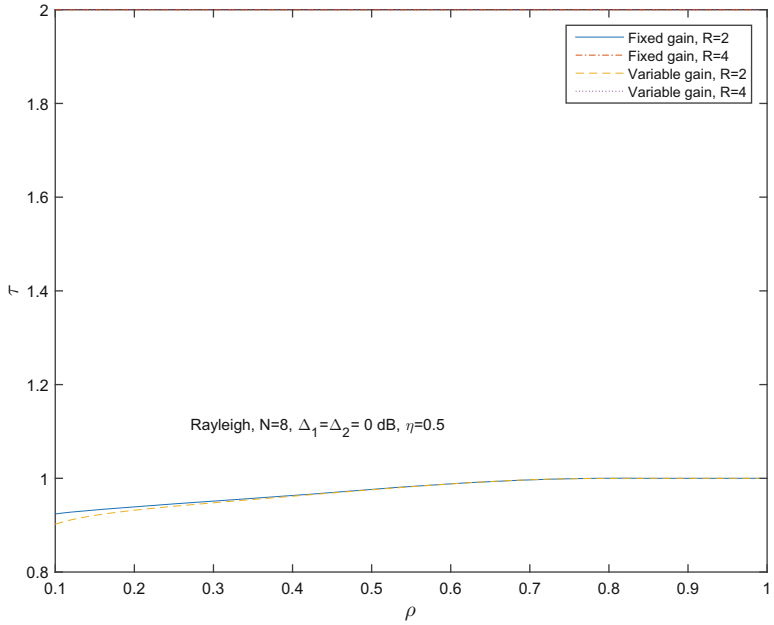

Fig. 5.11 Throughput vs. ρ for different values of R using PS energy harvesting when $N = 8$, $\Delta_1 = \Delta_2 = 0\,\text{dB}$, $\eta = 0.5$ in Rayleigh fading channels

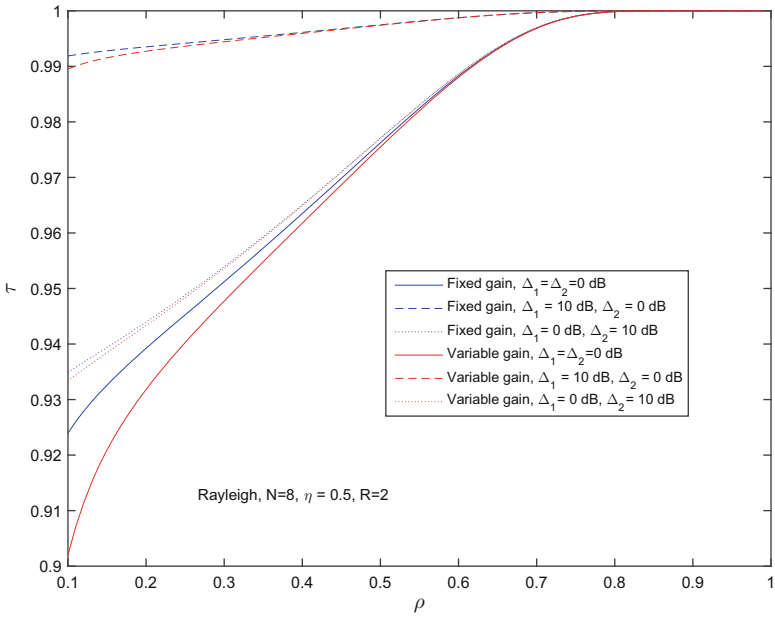

Fig. 5.12 Throughput vs. ρ for different values of Δ_1 and Δ_2 using PS energy harvesting when $N = 8$, $\eta = 0.5$, $R = 2$ bits/s/Hz in Rayleigh fading channels

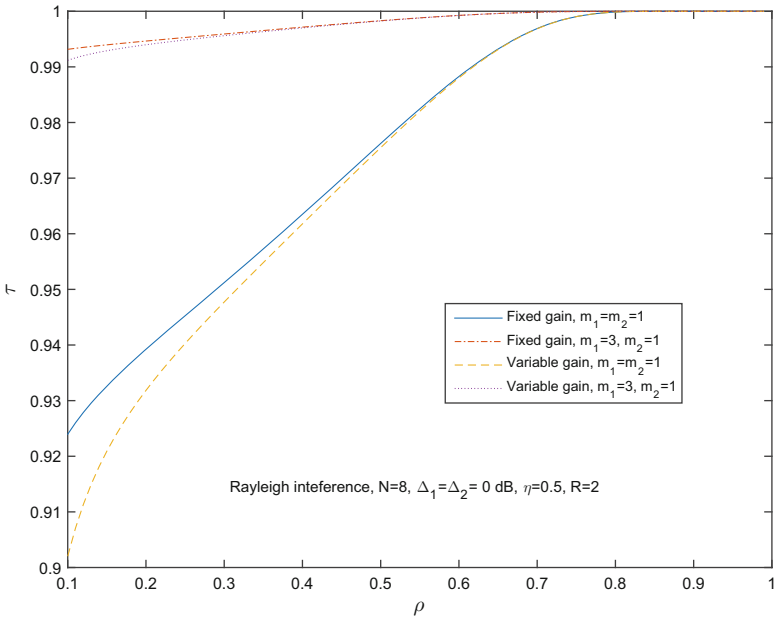

Fig. 5.13 Throughput vs. ρ for different values of m_1 using PS energy harvesting when $N = 8$, $\Delta_1 = \Delta_2 = 0$ dB, $R = 2$ bits/s/Hz, $\eta = 0.5$ and other channels suffer from Rayleigh fading

Numerical results show that PS is not sensitive to energy harvesting and that the throughput is more sensitive to N, R, Δ_1 and m_1 than to η, Δ_2 and the relaying method. Using these results, one can choose appropriate parameters for different application environments.

5.4 Design of New Energy Harvesting Relaying Protocol

5.4.1 Introduction

The above two sections and most previous works on energy harvesting relaying in the literature [6–14] have assumed energy harvesting relaying where the source transfers wireless energy to the relay in the first phase of broadcasting. More specifically, the conventional energy harvesting relaying protocol has two phases. In the first broadcasting phase, the source transmits signal to the relay for energy harvesting as well as information delivery. In the second relaying phase, the relay uses the harvested energy to forward the signal to the destination. This protocol provides an effective solution to energy harvesting relaying. However, note that in the second relaying phase when the relay uses the harvested energy to forward the signal, the signal is still broadcast by the relay to the destination. Thus, the conventional energy harvesting protocol can be further improved by allowing the

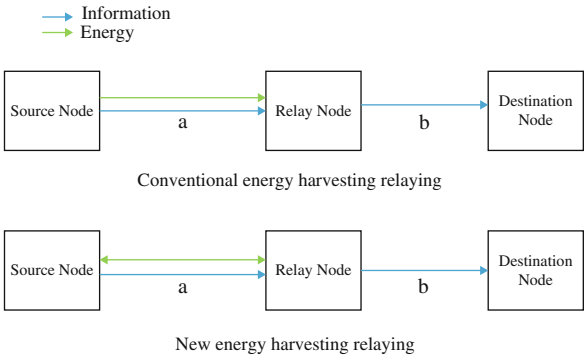

Fig. 5.14 Comparison of conventional energy harvesting relaying and new energy harvesting relaying

source to harvest energy from the relay transmitting in the second relaying phase to maximize the energy use. Figure 5.14 compares the conventional energy harvesting relaying with the new energy harvesting relaying schemes. One sees that in the new schemes the relay harvests energy from the source in the broadcasting phase and the source harvests energy from the relay in the relaying phase. In the conventional scheme, only the relay harvests energy from the source in the broadcasting phase.

In this work, we will study the performance of the new energy harvesting relaying protocol using AF as an example, where in the relaying phase, the relay transmits information to the destination while the source harvests energy from this transmission. In this case, we consider both TS and PS energy harvesting schemes. Before we move on to the analysis, a few assumptions need to be laid out. Again, consider a three-node relaying system without direct link between the source and the destination. Assume that both the source and the relay are equipped with energy harvesters. To illustrate the performance gain of the new protocol, we consider static AWGN channels without fading but with large-scale path loss. Also, assume that there are E_t joules of total energy initially available at the source and that the whole relaying transmission takes T seconds that includes broadcasting, relaying and energy harvesting. The system works as follows.

For TS, the relay receives energy from the source for αT seconds followed by information reception from the source for $\frac{1-\alpha}{2}T$ seconds, in the first broadcasting phase. The received signal at the relay can be given by

$$y_k^r = \sqrt{P_s}\frac{h}{\sqrt{d_{\text{sr}}^m}}a + n_k^{\text{ra}} + n_k^{\text{rc}} \tag{5.13}$$

where d_{sr} is the distance between source and relay, m is the path loss exponent and all the other symbols are defined as before. Thus, compared with the signals we used before, we have stated the large-scale path loss explicitly as d_{sr}^m. Using this received signal, the first period of time is used for energy harvesting to give the harvested energy at the relay as $E_{\text{hr}} = \eta P_s \frac{h^2}{d_{\text{sr}}^m}\alpha T$.

In the second relaying phase, the relay node will forward the signal from the source to the destination for $\frac{1-\alpha}{2}T$ seconds and the received signal at the destination can be given by

$$y_k^d = \frac{g}{\sqrt{d_{\mathrm{rd}}^m}}\sqrt{P_r}dy_k^r + n_k^{\mathrm{da}} + n_k^{\mathrm{dc}} \tag{5.14}$$

where d_{rd} is the distance between relay and destination, $P_r = \frac{E_{\mathrm{hr}}}{\frac{1-\alpha}{2}T} = \frac{2\alpha\eta}{1-\alpha}P_s\frac{h^2}{d_{\mathrm{sr}}^m}$ is the transmission power of the relay, dy_k^r is the normalized transmitted signal, normalized with respect to the average power of y_k^r as $d = \frac{1}{\sqrt{P_s\frac{h^2}{d_{\mathrm{sr}}^m}+\sigma_{\mathrm{ra}}^2+\sigma_{\mathrm{rc}}^2}}$.

Unlike the conventional energy harvesting relaying protocol, in the new protocol, the source also harvests energy from the signal transmitted by the relay. Thus, during the second relaying phase, the received signal at the source is given by

$$y_k^s = \frac{h}{\sqrt{d_{\mathrm{sr}}^m}}\sqrt{P_r}dy_k^r + n_k^{\mathrm{sa}} \tag{5.15}$$

where we have used the channel reciprocity such that the channel gain h and the distance d_{sr} do not change for the S-R or R-S links and n_k^{sa} is the AWGN at the source. In this case, the harvested energy at the source is $E_{\mathrm{hs}} = \eta\frac{P_rP_sd^2h^4}{d_{\mathrm{sr}}^{2m}}\cdot\frac{(1-\alpha)T}{2}$. This equals to $E_{\mathrm{hs}} = \eta^2\alpha\frac{P_s^2(h^2/d_{\mathrm{sr}}^m)^3T}{P_sh^2/d_{\mathrm{sr}}^m+\sigma_{\mathrm{ra}}^2+\sigma_{\mathrm{rc}}^2}$.

For PS, since there is no dedicated harvesting time, in this case, the source first transmits the signal to the relay for $\frac{T}{2}$ seconds, part of which is received at the relay for information decoding as

$$y_k^r = \sqrt{(1-\rho)P_s}\frac{h}{\sqrt{d_{\mathrm{sr}}^m}}a + \sqrt{1-\rho}n_k^{\mathrm{ra}} + n_k^{\mathrm{rc}} \tag{5.16}$$

and part of which is harvested by the relay as $E_{\mathrm{hr}} = \eta\rho P_s\frac{h^2}{d_{\mathrm{sr}}^m}\frac{T}{2}$. All the symbols are defined as before.

In the second relaying phase, the relay will use its harvested energy to forward the received signal. Then, the received signal at the destination becomes

$$y_k^d = \frac{g}{\sqrt{d_{\mathrm{rd}}^m}}\sqrt{P_r}dy_k^r + n_k^{\mathrm{da}} + n_k^{\mathrm{dc}} \tag{5.17}$$

where in this case $P_r = \frac{E_{\mathrm{hr}}}{T/2} = \eta\rho P_s\frac{h^2}{d_{\mathrm{sr}}^m}$.

Also, unlike the conventional relaying protocol, in the second relaying phase of the new protocol, the source needs to harvest energy from the signal transmitted by the relay so its received signal is

$$y_k^s = \frac{h}{\sqrt{d_{\mathrm{sr}}^m}}\sqrt{P_r}dy_k^r + n_k^{\mathrm{sa}} \tag{5.18}$$

and the harvested energy from this received signal is derived as $E_{\text{hs}} = \eta^2\rho(1-\rho)\frac{P_s^2(h^2/d_{\text{sr}}^m)^3T/2}{P_s h^2/d_{\text{sr}}^m+\sigma_{\text{ra}}^2+\sigma_{\text{rc}}^2}$. Next, we consider two strategies of using this newly harvested energy. In the first strategy, all the harvested energies at the source node during different relaying transmissions will be stored until all the transmissions are finished. The stored energy is then used to conduct more relaying transmissions. In the second strategy, instead of storing all harvested energy until all the relaying transmissions are finished, the harvested energy will be used immediately in the next relaying transmission to increase its transmission power and therefore its transmission rate. This strategy has the advantages of requiring smaller energy storage at the source node as well as improving the quality of each relay transmission.

5.4.2 Conventional Protocol

For the conventional TS relaying protocol, the source transmits the signal for a duration of $\alpha T + \frac{1-\alpha}{2}T$ with a transmission power of P_s, where the first part is the dedicated energy transfer time and the second part is the extra information transmission time. Thus, each relaying transmission will assume an energy of $E_i = \left[\alpha T + \frac{1-\alpha}{2}T\right]P_s$. Thus, given a total energy of E_t at the beginning, the total number of relaying transmissions the source can perform using the conventional TS relaying protocol can be calculated as $K_{\text{TS}}^{\text{Con}} = \frac{E_t}{E_i} = \frac{E_t}{P_s T}\frac{2}{1+\alpha}$.

For TS, the end-to-end signal-to-noise ratio (SNR) can be derived using the received signal expression as $\gamma_{\text{TS}} = \frac{P_s\gamma_d\gamma_r a^2}{\gamma_d d^2+\frac{(1-\alpha)d_{\text{sr}}^m}{2\alpha\eta P_s h^2(\sigma_{\text{rc}}^2+\sigma_{\text{ra}}^2)}}$, where $\gamma_d = \frac{g^2}{d_{\text{rd}}^m(\sigma_{\text{da}}^2+\sigma_{\text{dc}}^2)}$ and $\gamma_r = \frac{h^2}{d_{\text{sr}}^m(\sigma_{\text{ra}}^2+\sigma_{\text{rc}}^2)}$ are the hop SNRs similar to before but with large-scale path loss now. Thus, the total transmission rate or throughput in all relaying transmissions can be shown as

$$C_{\text{TS}}^{\text{Con}} = K_{\text{TS}}^{\text{Cov}} \cdot \log_2(1+\gamma_{\text{TS}})\frac{1-\alpha}{2}. \tag{5.19}$$

The calculation for PS is very similar. In the conventional PS relaying protocol, each relay transmission consumes an energy of $E_i = \frac{T}{2}P_s$ and thus, given the initial energy of E_t, the total number of relaying transmissions is then $K_{\text{PS}}^{\text{Con}} = \frac{2E_t}{P_s T}$.

Also, for PS, the end-to-end SNR can be derived as $\gamma_{\text{PS}} = \frac{P_s\gamma_d\gamma_p a^2}{\gamma_d d^2+\frac{d_{\text{sr}}^m}{(1-\rho)[\sigma_{\text{ra}}^2+\sigma_{\text{rc}}^2/(1-\rho)]\eta\rho P_s h^2}}$, where $\gamma_p = \frac{h^2}{d_{\text{sr}}^m[\sigma_{\text{ra}}^2+\sigma_{\text{rc}}^2/(1-\rho)]}$ and other symbols are defined as before. Finally, the total transmission rate or throughput of all relaying transmissions using the conventional PS relaying protocol is

$$C_{\text{PS}}^{\text{Con}} = \frac{K_{\text{PS}}^{\text{Con}}}{2}\log_2(1+\gamma_{\text{PS}}). \tag{5.20}$$

5.4.3 First Strategy of Using New Energy

Consider the first strategy where the harvested energies at the source will be stored until all relaying transmissions are finished. Then, they will be used to transmit more data. In this case, the new total number of relaying transmissions can be derived as $K_{\mathrm{TS}}^{\mathrm{New}} = \left[\frac{E_t/(P_s T)}{\frac{1+\alpha}{2} - \eta^2 \alpha \frac{P_s^2 (h^2/d_{\mathrm{sr}}^m)^3 T}{P_s h^2/d_{\mathrm{sr}}^m + \sigma_{\mathrm{ra}}^2 + \sigma_{\mathrm{rc}}^2}} \right]$, where $[\cdot]$ is the rounding function to get an integer and $\frac{1+\alpha}{2} > \eta^2 \alpha \frac{P_s^2 (h^2/d_{\mathrm{sr}}^m)^3 T}{P_s h^2/d_{\mathrm{sr}}^m + \sigma_{\mathrm{ra}}^2 + \sigma_{\mathrm{rc}}^2}$ which is always the case as the harvested energy is positive. Thus, since the number of relaying transmissions is increased while the throughput for each transmission is the same as conventional scheme, one has the total throughput in the first strategy as

$$C_{\mathrm{TS}}^{\mathrm{New1}} = K_{\mathrm{TS}}^{\mathrm{New}} \cdot \log_2(1 + \gamma_{\mathrm{TS}}) \frac{1-\alpha}{2}. \tag{5.21}$$

For PS, the derivation is similar. The new number of total relaying transmissions using PS is calculated as $K_{\mathrm{PS}}^{\mathrm{New}} = \left[\frac{2E_t/(P_s T)}{1 - \eta^2 \rho(1-\rho) \frac{P_s^2 (h^2/d_{\mathrm{sr}}^m)^3 T/2}{P_s h^2/d_{\mathrm{sr}}^m + \sigma_{\mathrm{ra}}^2 + \sigma_{\mathrm{rc}}^2}} \right]$, where $1 > \eta^2 \rho(1-\rho) \frac{P_s^2 (h^2/d_{\mathrm{sr}}^m)^3 T/2}{P_s h^2/d_{\mathrm{sr}}^m + \sigma_{\mathrm{ra}}^2 + \sigma_{\mathrm{rc}}^2}$ and thus one has the new total throughput as

$$C_{\mathrm{PS}}^{\mathrm{New1}} = \frac{K_{\mathrm{PS}}^{\mathrm{New}}}{2} \log_2(1 + \gamma_{\mathrm{PS}}). \tag{5.22}$$

5.4.4 Second Strategy of Using New Energy

Consider the second strategy. In this case, the extra energy harvested by the source will be used in the next relaying transmission to save battery capacity. Because of this, an iterative process is used as

$$\begin{aligned}
P_s^{(i+1)} &= \frac{E_t/K_{\mathrm{TS}}^{\mathrm{Con}} + E_{\mathrm{hs}}^{(i)}}{T} \frac{2}{1+\alpha} \\
\gamma_{\mathrm{TS}}^{i+1} &= \frac{P_s^{(i+1)} \gamma_d \gamma_r}{\gamma_d + \frac{(1-\alpha) d_{\mathrm{sr}}^m (P_s^{(i+1)} \frac{h^2}{d_{\mathrm{sr}}^m} + \sigma_{\mathrm{ra}}^2 + \sigma_{\mathrm{rc}}^2)}{2\alpha\eta P_s^{(i+1)} h^2 (\sigma_{\mathrm{ra}}^2 + \sigma_{\mathrm{rc}}^2)}} \\
E_{\mathrm{hs}}^{(i+1)} &= \eta^2 \alpha \frac{(P_s^{(i)})^2 (h^2/d_{\mathrm{sr}}^m)^3 T}{P_s^{(i)} h^2/d_{\mathrm{sr}}^m + \sigma_{\mathrm{ra}}^2 + \sigma_{\mathrm{rc}}^2}.
\end{aligned} \tag{5.23}$$

where $i = 1, 2, \ldots, K_{\text{TS}}^{\text{Con}}$ denote the i-th transmission, $E_{\text{hs}}^1 = 0$ and $P_s^1 = P_s$ as the initial conditions. Thus, the new total throughput is derived as

$$C_{\text{TS}}^{\text{New2}} = \sum_{i=1}^{K_{\text{TS}}^{\text{Con}}} \log_2(1 + \gamma_{\text{TS}}^{(i)}) \frac{1-\alpha}{2}. \tag{5.24}$$

For PS, one has

$$\begin{aligned} P_s^{(i+1)} &= \frac{2(E_t/K_{\text{PS}}^{\text{Con}} + E_{\text{hs}}^{(i)})}{T} \\ \gamma_{\text{PS}}^{i+1} &= \frac{P_s^{(i+1)} \gamma_d \gamma_p}{\gamma_d + \frac{d_{\text{sr}}^m (P_s^{(i+1)} \frac{h^2}{d_{\text{sr}}^m} + \sigma_{\text{ra}}^2 + \sigma_{\text{rc}}^2)}{[(1-\rho)\sigma_{\text{ra}}^2 + \sigma_{\text{rc}}^2]\eta\rho P_s^{(i+1)} h^2}} \\ E_{\text{hs}}^{(i+1)} &= \eta^2 \rho(1-\rho) \frac{(P_s^{(i)})^2 (h^2/d_{\text{sr}}^m)^3 T/2}{P_s^{(i)} h^2/d_{\text{sr}}^m + \sigma_{\text{ra}}^2 + \sigma_{\text{rc}}^2}. \end{aligned} \tag{5.25}$$

and the new total throughput is therefore

$$C_{\text{PS}}^{\text{New2}} = \sum_{i=1}^{K_{\text{PS}}^{\text{Con}}} \log_2(1 + \gamma_{\text{PS}}^{(i)}) \frac{1}{2}. \tag{5.26}$$

5.4.5 Numerical Results

In this subsection, numerical examples are given to show the performance of the new protocol, where the values of α and ρ are calculated by maximizing the throughput of a single transmission $\log_2(1+\gamma_{\text{TS}})\frac{1-\alpha}{2}$ or $\log_2(1+\gamma_{\text{PS}})\frac{1}{2}$, respectively. For fixed h, the value of $\frac{h^2}{d_{\text{sr}}^m}$ is determined by d_{sr}. Thus, in the following, we examine the effects of P_s, η, d_{sr} and $\sigma_{\text{ra}}^2 + \sigma_{\text{rc}}^2$ on the performance gain. Other parameters are set as $E_t = 100\,\text{J}$, $T = 1\,\text{s}$, $\sigma_{\text{ra}}^2 = \sigma_{\text{rc}}^2 = \sigma_{\text{da}}^2 = \sigma_{\text{dc}}^2 = \sigma^2$, $m = 2.7$ and $h = g = 1$. These parameters can be changed to evaluate more conditions. The path loss exponent $m = 2.7$ corresponds to an urban cellular environment [19]. The channel gains $h = g = 1$ is chosen such that the operating SNR will be from 10 to 20 dB without path loss, when σ^2 is from 0.01 to 0.1 as examined in this work. The choices of distances are for illustration purpose only. The performance gain examined in the following figures is calculated as the difference between the total throughput of new and conventional protocols normalized by that of the conventional protocol.

Figure 5.15 shows the performance gain vs. P_s. Several observations can be made. First, since the gain is always positive, the new protocol outperforms the

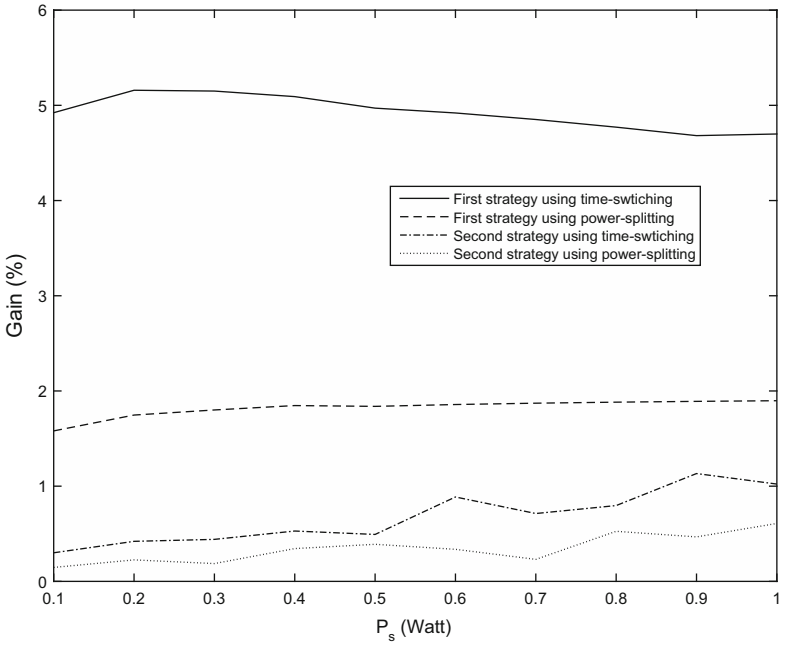

Fig. 5.15 Performance gain vs. P_s when $d_{\mathrm{sr}} = 1.2\,\mathrm{m}$, $d_{\mathrm{rd}} = 1.2\,\mathrm{m}$, $\eta = 0.5$ and $\sigma^2 = 0.01$

conventional protocol, as expected, as the source node harvests extra energy in the relaying phase. Second, the new protocol using the first strategy has a larger performance gain than that using the second strategy at the cost of requiring a larger capacity for energy storage. Third, the TS energy harvesting has a larger gain than the PS energy harvesting, as PS normally harvests less energy than TS.

Figure 5.16 shows the gain vs. η. One sees that the performance gain increases when η increases. Figure 5.17 shows the gain vs. d_{sr}. In this case, the performance gain decreases when d_{sr} increases. Also, compared with Fig. 5.16, the rate of change in Fig. 5.17 is much higher than that in Fig. 5.16. Again, the first strategy using TS has the largest gain. Figure 5.18 shows the gain vs. σ^2. In this case, the gain increases when σ^2 increases, except when the first strategy is used with PS.

5.4.6 Conclusion

From this section, one concludes that the distance d_{sr} has the largest effect on the performance gain, followed by the conversion efficiency η. To increase the performance gain of the new protocol, one needs to choose a large η or a small d_{sr}. Also, TS is preferred to PS, as it produces larger gains. Note that the above

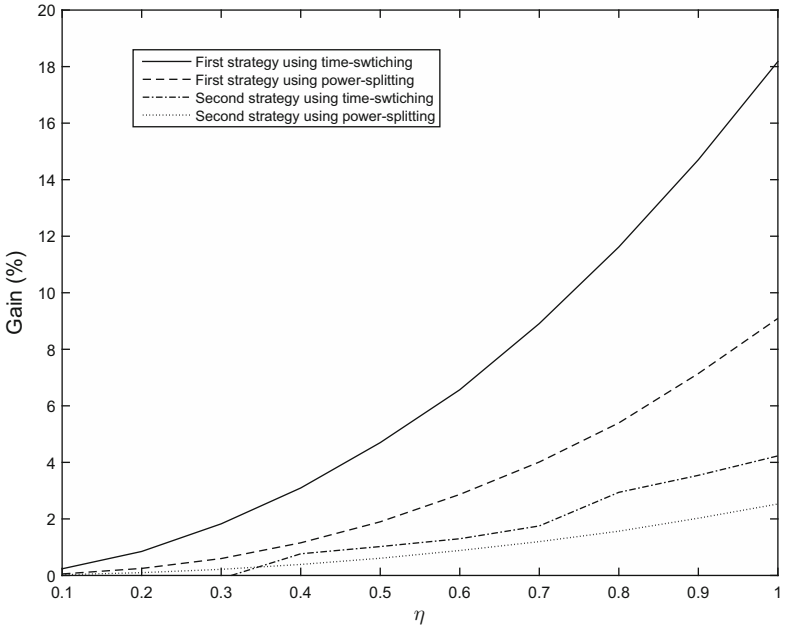

Fig. 5.16 Performance gain vs. η when $P_s = 1\,\text{W}$, $d_{\text{sr}} = 1.2\,\text{m}$, $d_{\text{rd}} = 1.2\,\text{m}$ and $\sigma^2 = 0.01$

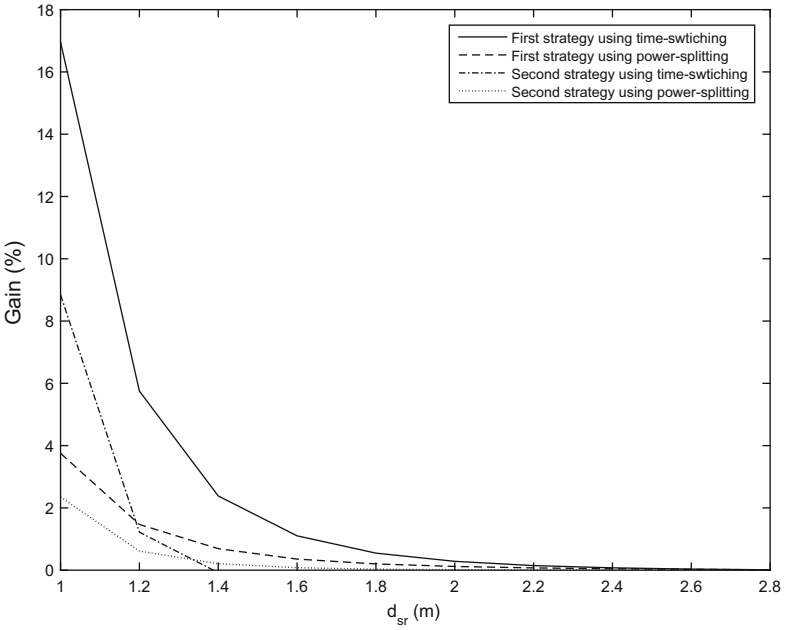

Fig. 5.17 Performance gain vs. d_{sr} when $P_s = 1\,\text{W}$, $d_{\text{rd}} = 3 - d_{\text{sr}}$, $\eta = 0.5$ and $\sigma^2 = 0.01$

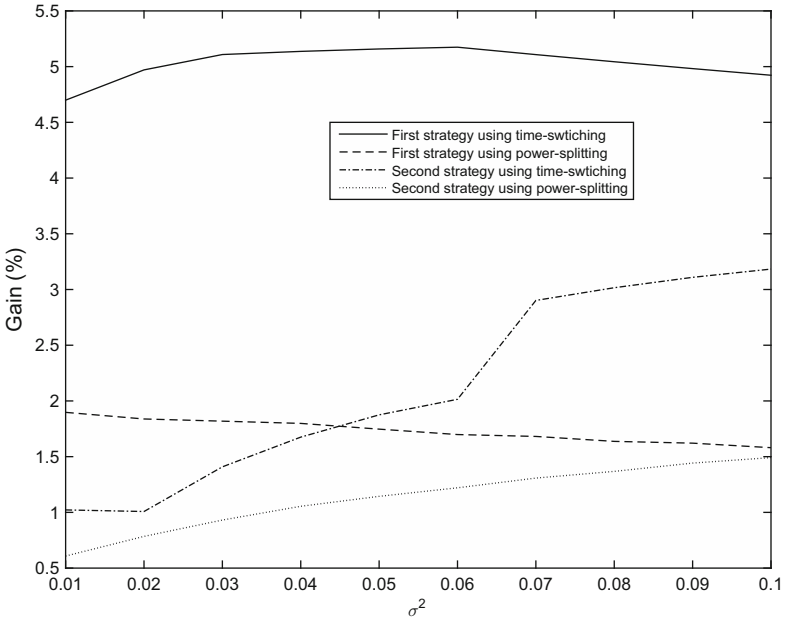

Fig. 5.18 Performance gain vs. σ^2 when $P_s = 1\,\text{W}$, $d_{\text{sr}} = 1.2\,\text{m}$, $d_{\text{rd}} = 1.2\,\text{m}$ and $\eta = 0.5$

result considers a static AWGN channel for simplicity. For fading channels, channel estimation can be performed for each transmission [20] and the estimated channel information can then be used at the source node for rate adaptation.

5.5 Channel Estimation in Energy Harvesting Relaying

5.5.1 Introduction

Channel estimation is an important part of wireless relaying, as the destination needs the channel gains for signal demodulation and the relay may also need the channel gains for variable-gain amplification. There are a few existing works on channel estimation for relaying. For example, reference [21] discussed several linear minimum mean squared error (LMMSE) estimators for the cascaded channel coefficient as the product of the channel coefficient in the source-to-relay link and that in the relay-to-destination. Reference [22] proposed a new least squares (LS) estimator and reference [23] proposed a minimum mean squared error (MMSE) estimator, for the cascaded channel coefficient. References [24] and [25] proposed pilot-based moment-based (MB) estimators and maximum likelihood (ML) methods for the individual channel powers.

The previous sections analysed and proposed energy harvesting relaying schemes. In these schemes, the energy is mainly harvested for data transmission or data symbol forwarding in the relaying phase. Similar to data transmission, in pilot-based channel estimation, pilot symbols need to be transmitted or forwarded by the relay. Without energy harvesting, this transmission will bring a huge burden to the relay in terms of energy consumption and thus, will also discourage idle nodes from participating in relaying. Thus, it is important to adopt energy harvesting in the channel estimation of wireless relaying.

In this section, new pilot-based channel estimators for AF relaying are proposed. The pilots are sent using energy harvested from the source. Channel estimation is performed only using these pilots multiplexed in the time domain with the data symbols for single-carrier systems. Both TS and PS are considered. We propose several new estimation schemes using the approximate ML method. In Schemes 1 and 2, the relay harvests energy from pilots sent by the source and then uses this energy to forward pilots from the source as well as transmit its own pilots to the destination. In Schemes 3 and 4, the relay harvests energy from pilots sent by the source and also uses these pilots to estimate the source-to-relay link. Then, the harvested energy is used to transmit its own pilot to the destination to estimate the relay-to-destination link. Again, consider a three-node system without direct link. Assume that a total of K pilots are used in all schemes for energy harvesting and channel estimation. Each pilot occupies a time duration of T_p.

5.5.2 Scheme One

In Scheme 1, the relay harvests energy from the source using TS and then uses the harvested energy to forward pilots from the source as well as transmit its own pilots to the destination.

First, the source sends I pilots to the relay for energy harvesting. The received signal at the relay is given by

$$y_i^{(r-\mathrm{eh})} = \sqrt{P_s}h + n_i^{(r-\mathrm{eh})} \tag{5.27}$$

where $i = 1, 2, \ldots, I$, $n_i^{(r-\mathrm{eh})}$ is the AWGN with mean zero and variance $2\sigma_r^2$, and other symbols are defined as before. All the noise in this paper is assumed circularly symmetric. Using (5.27), the harvested energy is $E_h = \eta P_s |h|^2 I T_p$.

Second, the source sends another J_1 pilots to the relay, which will be forwarded to the destination for channel estimation. The received signal at the destination is

$$y_{j_1}^{(d-s)} = \sqrt{P_r} g a y_{j_1}^{(r-\mathrm{ce})} + n_{j_1}^{(d-s)}, \tag{5.28}$$

where $y_{j_1}^{(r-\mathrm{ce})} = \sqrt{P_s}h + n_{j_1}^{(r-\mathrm{ce})}$ is the forwarded pilot symbol, $j_1 = 1, 2, \ldots, J_1$, $n_{j_1}^{(r-\mathrm{ce})}$ is the AWGN at the relay with mean zero and variance $2\sigma_r^2$, and $n_{j_1}^{(d-s)}$ is the

AWGN at the destination with mean zero and variance $2\sigma_d^2$. In Scheme 1, since the relay does not perform channel estimation, fixed-gain relaying can be used such that one can set a as a constant for simplicity [15, 17].

Finally, in addition to forwarding J_1 pilots from the source, the relay also uses the harvested energy to transmit J_2 pilots of its own to the destination, giving

$$y_{j_2}^{(d-r)} = \sqrt{P_r} g + n_{j_2}^{(d-r)} \tag{5.29}$$

where $j_2 = 1, 2, \ldots, J_2$, $n_{j_2}^{(d-r)}$ is the AWGN at the destination during this transmission and is again complex Gaussian with mean zero and variance $2\sigma_d^2$. Using the harvested energy, since the relay has to forward J_1 pilots from the source and transmit J_2 pilots of its own, the transmission power of the relay can be written as $P_r = \frac{E_h}{JT_p} = \eta P_s |h|^2 \frac{I}{J}$, where $J = J_1 + J_2$.

The ML estimators can be derived as follows. Denote $G_y = \sqrt{\eta \frac{I}{J} P_s} |h| g$. Using the ML method, one log-likelihood function can be derived as $llf_1 = -J_2 \ln(2\pi\sigma_d^2) - \frac{1}{2\sigma_d^2} \sum_{j_2=1}^{J_2} |y_{d-r}^{(j_2)} - G_y|^2$. Thus, by differentiating llf_1 with respect to G_y, setting the derivative to zero and solving the equation for G_y, the ML estimate of G_y can be derived as

$$\hat{G}_y = \frac{1}{J_2} \sum_{j_2=1}^{J_2} y_{d-r}^{(j_2)} = \sqrt{\eta \frac{I}{J} P_s} |\hat{h}| \hat{g}. \tag{5.30}$$

Also, denote $H_y = \sqrt{P_s} h$. Using the ML method, another log-likelihood function can be derived as $llf_2 = -J_1 \ln(2\pi(1 + |G_y|^2 a^2)\sigma_d^2) - \frac{1}{2(1+|G_y|^2 a^2)\sigma_d^2} \sum_{j_1=1}^{J_1} |y_{d-s}^{(j_1)} - G_y H_y a|^2$. By differentiating llf_2 with respect to H_y, setting the derivative to zero and solving the equation for H_y, the ML estimate of H_y can be derived as

$$\hat{H}_y = \frac{1}{J_1 \hat{G}_y a} \sum_{j_1=1}^{J_1} y_{d-s}^{(j_1)} = \sqrt{P_s} \hat{h}. \tag{5.31}$$

The invariance principle of ML estimation states that a function of ML estimate is the ML estimate of that function [26]. Using this principle, the ML estimates of g and h can be derived by solving (5.30) and (5.31) for $\hat{g}$ and $\hat{h}$, which gives

$$\hat{g}_1 = \frac{\frac{1}{J_2} \sum_{j_2=1}^{J_2} y_{d-r}^{(j_2)} | \frac{1}{J_2} \sum_{j_2=1}^{J_2} y_{d-r}^{(j_2)}|}{\frac{1}{a} \sqrt{\eta \frac{I}{J}} | \frac{1}{J_1} \sum_{j_1=1}^{J_1} y_{d-s}^{(j_1)}|} \tag{5.32}$$

$$\hat{h}_1 = \frac{1}{\sqrt{P_s} a} \frac{\frac{1}{J_1} \sum_{j_1=1}^{J_1} y_{d-s}^{(j_1)}}{\frac{1}{J_2} \sum_{j_2=1}^{J_2} y_{d-r}^{(j_2)}} \tag{5.33}$$

These ML estimators are approximate estimators because the exact ML estimators should be obtained by multiplying llf_1 with llf_2 and using the joint function for estimation. However, this renders complicated nonlinear functions of g and h and hence, it is not used here. Since both $y_{d-s}^{(j_1)}$ and $y_{d-r}^{(j_2)}$ are samples received at the destination, the relay does not perform channel estimation. This reduces the complexity at the relay.

5.5.3 Scheme 2

Scheme 2 is similar to Scheme 1, except that the energy is harvested using PS. First, the source sends K_1 pilots to the relay. Part of the received signal at the relay is used for channel estimation as $z_{k_1}^{(r-\text{ce})} = \sqrt{(1-\rho)P_s}h + n_{k_1}^{(r-\text{ce})}$, which is forwarded to the destination to give

$$z_{k_1}^{(d-s)} = \sqrt{P_r}gaz_{k_1}^{(r-\text{ce})} + n_{k_1}^{(d-s)} \tag{5.34}$$

where $k_1 = 1, 2, \ldots, K_1$ index the pilots from the source, ρ is the PS factor, $n_{k_1}^{(r-\text{ce})}$ and $n_{k_1}^{(d-s)}$ are the AWGN with means zero and variances $2\sigma_r^2$ and $2\sigma_d^2$, respectively. The other part of the received power at the relay is harvested as $E_h = \eta\rho P_s|h|^2K_1T_p$.

Second, the relay also transmits K_2 its own pilots to the destination such that the received signal at the destination is

$$z_{k_2}^{(d-r)} = \sqrt{P_r}g + n_{k_2}^{(d-r)} \tag{5.35}$$

where $k_2 = 1, 2, \ldots, K_2$ and $n_{k_2}^{(d-r)}$ is the AWGN with mean zero and variance $2\sigma_d^2$. Since the relay forwards K_1 pilots from the source and transmits K_2 pilots of its own, a total of $K = K_1 + K_2$ pilots will be sent to the destination such that $P_r = \frac{E_h}{KT_p} = \eta\rho P_s|h|^2\frac{K_1}{K}$.

The ML estimators are derived as follows. Denote $G_z = \sqrt{\eta\rho P_s\frac{K_1}{K}}|h|g$ and $H_z = \sqrt{(1-\rho)P_s}h$. Similar to before, using the samples and the ML method, the ML estimate of G_z can be derived as $\hat{G}_z = \frac{1}{K_2}\sum_{k_2=1}^{K_2} z_{d-r}^{(k_2)} = \sqrt{\eta\rho P_s\frac{K_1}{K}}|\hat{h}|\hat{g}$ and using the samples and the ML method, the ML estimate of H_z can be derived as $\hat{H}_z = \frac{1}{K_1\hat{G}_z a}\sum_{k_1=1}^{K_1} z_{d-s}^{(k_1)} = \sqrt{(1-\rho)P_s}\hat{h}$. Using the invariance principle, the ML estimators for g and h can be obtained as

$$\hat{g}_2 = \frac{a\sqrt{1-\rho}}{\sqrt{\eta\rho\frac{K_1}{K}}}\frac{\frac{1}{K_2}\sum_{k_2=1}^{K_2} z_{d-r}^{(k_2)}|\frac{1}{K_2}\sum_{k_2=1}^{K_2} z_{d-r}^{(k_2)}|}{|\frac{1}{K_1}\sum_{k_1=1}^{K_1} z_{d-s}^{(k_1)}|} \tag{5.36}$$

and

$$\hat{h}_2 = \frac{1}{\sqrt{(1-\rho)P_s a}} \frac{\frac{1}{K_1}\sum_{k_1=1}^{K_1} z_{d-s}^{(k_1)}}{\frac{1}{K_2}\sum_{k_2=1}^{K_2} z_{d-r}^{(k_2)}} \tag{5.37}$$

respectively. Again, only the destination needs to perform channel estimation to reduce complexity at the relay.

5.5.4 Scheme 3

In Scheme 3, first, the source sends J_1 pilots to the relay such that the received signal at the relay is

$$u_{j_1}^{(r-\text{ce})} = \sqrt{P_s}h + n_{j_1}^{(r-\text{ce})} \tag{5.38}$$

where $j_1 = 1, 2, \ldots, J_1$ and $n_{j_1}^{(r-\text{ce})}$ is the AWGN with mean zero and variance $2\sigma_r^2$. Second, the source sends I pilots to the relay for energy harvesting. The harvested energy is $E_h = \eta P_s |h|^2 I T_p$. Finally, the relay uses the harvested energy to transmit J_2 pilots of its own to the destination. The transmission power of the relay is $P_r = \frac{E_h}{J_2 T_p} = \eta P_s |h|^2 \frac{I}{J_2}$ and the received signal at the destination is

$$u_{j_2}^{(d-r)} = \sqrt{\eta P_s \frac{I}{J_2}}|h|g + n_{j_2}^{(d-r)} \tag{5.39}$$

where $j_2 = 1, 2, \ldots, J_2$. In the above, $n_{j_1}^{(r-\text{ce})}$ and $n_{j_2}^{(d-r)}$ are again circularly symmetric AWGN with means zero and variances $2\sigma_r^2$ and $2\sigma_d^2$, respectively.

The ML estimators can also be derived. Using (5.38), since there is only one unknown parameter in the log-likelihood function, the ML estimator for h can be easily derived. Also, denote $G_u = \sqrt{\eta P_s \frac{I}{J_2}}|h|g$. Using (5.39), the ML estimate of G_u can be derived as $\hat{G}_u = \frac{1}{J_2}\sum_{j_2=1}^{J_2} u_{d-r}^{(j_2)} = \sqrt{\eta P_s \frac{I}{J_2}}|\hat{h}|\hat{g}$. Then, using the invariance principle, the ML estimators are

$$\hat{g}_3 = \frac{\frac{1}{J_2}\sum_{j_2=1}^{J_2} u_{d-r}^{(j_2)}}{\sqrt{\eta \frac{I}{J_2}}|\frac{1}{J_1}\sum_{j_1=1}^{J_1} u_{r-\text{ce}}^{(j_1)}|} \tag{5.40}$$

and

$$\hat{h}_3 = \frac{1}{\sqrt{P_s}} \frac{1}{J_1} \sum_{j_1=1}^{J_1} u_{r-\text{ce}}^{(j_1)}. \tag{5.41}$$

Note that, in this scheme, the relay estimates h and its estimate has to be sent to the destination via control channels for the estimation of g at the destination. Thus, this scheme is more complicated than Schemes 1 and 2.

5.5.5 Scheme 4

Scheme 4 is similar to Scheme 3, except that the relay uses PS to harvest energy. First, the source sends K_1 pilots to the relay, part of which is received for channel estimation as

$$v_{k_1}^{(r-\mathrm{ce})} = \sqrt{(1-\rho)P_s}h + n_{k_1}^{(r-\mathrm{ce})} \tag{5.42}$$

for $k_1 = 1, 2, \ldots, K_1$ and part of which is harvested with $E_h = \eta\rho P_s|h|^2 K_1 T_p$. Second, the relay uses the harvested energy to transmit K_2 pilots of its own such that the received signal at the destination is

$$v_{k_2}^{(d-r)} = \sqrt{\eta\rho P_s \frac{K_1}{K_2}}|h|g + n_{k_2}^{(d-r)} \tag{5.43}$$

for $k_2 = 1, 2, \ldots, K_2$. Note that $n_{k_1}^{(r-\mathrm{ce})}$ and $n_{k_2}^{(d-r)}$ are also circularly symmetric AWGN with means zero and variances $2\sigma_r^2$ and $2\sigma_d^2$, respectively.

Using (5.42) and (5.43), the ML estimators for g and h can be derived in a similar way as

$$\hat{g}_4 = \frac{\frac{1}{K_2}\sum_{k_2=1}^{K_2} v_{d-r}^{(k_2)}}{\sqrt{\eta\frac{K_1}{K_2}\frac{\rho}{1-\rho}}\left|\frac{1}{K_1}\sum_{k_1=1}^{K_1} v_{r-\mathrm{ce}}^{(k_1)}\right|} \tag{5.44}$$

and

$$\hat{h}_4 = \frac{1}{\sqrt{(1-\rho)P_s}}\frac{1}{K_1}\sum_{k_1=1}^{K_1} v_{r-\mathrm{ce}}^{(k_1)}. \tag{5.45}$$

5.5.6 Numerical Results

In this section, the new estimators will be examined. We set $\eta = 0.5$, $P_s = 1$, $K = 100$ and $2\sigma_r^2 = 2\sigma_d^2 = 2$. Define $\gamma_g = \frac{|g|^2}{2\sigma_d^2}$, $\gamma_h = \frac{|h|^2}{2\sigma_r^2}$. The values of g and h will change with γ_g and γ_h and their real and imaginary parts equal to each other. The normalized mean squared error (MSE) is defined as $\frac{1}{R|g|^2}\sum_{r=1}^{R}|\hat{g}_r - g|^2$,

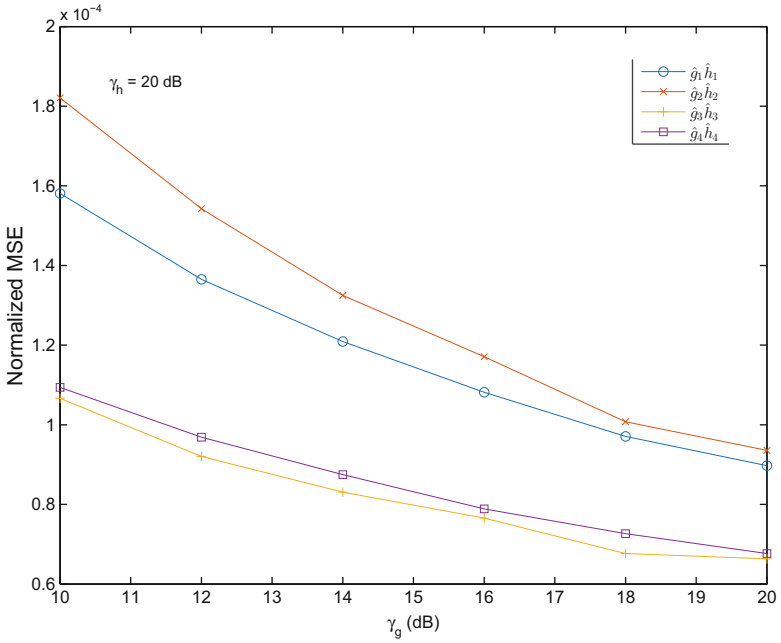

Fig. 5.19 Minimum normalized MSE of $\hat{g}\hat{h}$ vs. γ_g for different schemes

$\frac{1}{R|h|^2}\sum_{r=1}^{R}|\hat{h}_r - h|^2$, $\frac{1}{R|gh|^2}\sum_{r=1}^{R}|\hat{g}_r\hat{h}_r - gh|^2$ for $\hat{g}$, $\hat{h}$ and $\hat{g}\hat{h}$, respectively, where R is the total number of simulation runs and $\hat{g}_r$ and $\hat{h}_r$ are the channel estimates in the r-th run.

Figures 5.19 and 5.20 compare the estimators in terms of their minimum normalized MSEs of $\hat{g}\hat{h}$ achieved by performing exhaustive searches over the relevant parameters. One sees that Schemes 3 and 4 have the best performances, and Schemes 1 and 2 have the worst performance. Also, TS is better than PS in most cases.

5.5.7 Conclusion

New pilot-based ML estimators for AF relaying have been proposed by using harvested energy to transmit or forward pilots. Numerical results have been presented to show their performances. It is concluded that the two schemes that perform channel estimation only at the destination are the simplest but have the worst performances in terms of MSE. Note that the proposed estimators use pilots only, similar to some previous works. No data symbols are available for energy harvesting in the estimation. One could extend this scheme to blind or semi-blind estimation, where energy can also be harvested from data symbols.

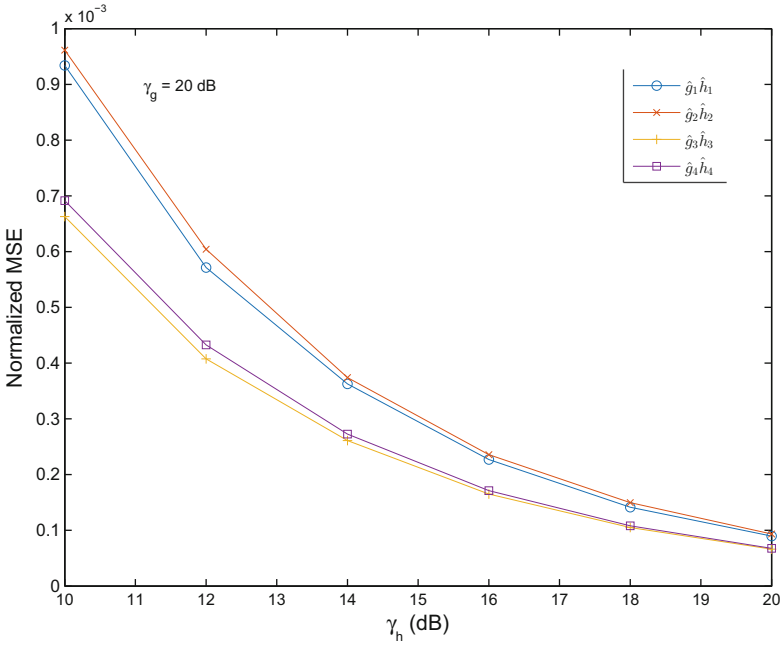

Fig. 5.20 Minimum normalized MSE of $\hat{g}\hat{h}$ vs. γ_h for different schemes

5.6 Summary

In this chapter, the performance of wireless powered relaying has been analysed in the absence or presence of co-channel interference. The analysis has shown the benefit of using energy harvesting or wireless power to reduce the energy consumption at the relay. Moreover, new energy harvesting relaying protocols have been designed to improve the system energy efficiency further. As an important part of wireless relaying, channel estimation in the context of energy harvesting has also been studied and several new channel estimators have been proposed. Owing to the many benefits offered by wireless power, energy harvesting relaying has seen wider use in emerging applications, such as massive multiple-input-multiple-output [27]. Also, in addition to the schemes discussed in this chapter, there are quite a few works focusing on the optimal use of the harvested energy in the relaying process [28, 29]. Finally, the above results only consider the case when the direct link between source and destination does not exist. It may be possible to extend these results to the case when the direct link exists. For example, in Sect. 5.2.2, assuming that the direct link is independent of the relaying link, the overall BER may be modified by combining (3) with the BER of the direct link, depending on the decision fusion rules. Also, in Sect. 5.2.3, assuming selection combining, the throughput of the relaying link in (5) can be combined with the throughput of the direct link. However, for Sect. 5.3, this extension may be difficult.

References

1. M. Peng, Y. Liu, D. Wei, W. Wang, H.-H. Chen, Hierarchical cooperative relay based heterogeneous networks. IEEE Wirel. Commun. **18**, 48–56 (2011)
2. B. Zhou, H. Hu, S.-Q. Huang, H.-H. Chen, Intracluster device-to-device relay algorithm with optimal resource allocation. IEEE Trans. Veh. Technol. **62**, 2315–2326 (2013)
3. J.N. Laneman, G.W. Wornell, Energy-efficient antenna sharing and relaying for wireless networks, in *Proceedings of 2000 IEEE Wireless Communication Networking Conference (WCNC)*, Chicago, vol. 1, March (2000), pp. 7–12
4. J.N. Laneman, D.N.C. Tse, G.W. Wornell, Cooperative diversity in wireless networks: efficient protocols and outage behaviors. IEEE Trans. Inf. Theory **50**, 3062–3080 (2004)
5. R. Zhang, C.K. Ho, MIMO broadcasting for simultaneous wireless information and power transfer. IEEE Trans. Wirel. Commun. **12**(5), 1989–2001 (2013)
6. Z. Ding, I. Krikidis, B. Sharif, H.V. Poor, Wireless information and power transfer in cooperative networks with spatially random relays. IEEE Trans. Wirel. Commun. **13**, 4440–4453 (2014)
7. A.A. Nasir, X. Zhou, S. Durrani, R.A. Kennedy, Throughput and ergodic capacity of wireless energy harvesting based DF relaying network, in *Proceedings of IEEE ICC 2014*, pp. 4066–4071, Sydney, June (2014)
8. Y. Gu, S. Aissa, Interference aided energy harvesting in decode-and-forward relaying systems, in *Proceedings of IEEE ICC 2014*, pp. 5378–5382, Sydney, June (2014)
9. H.A. Suraweera, G. Zheng, I. Krikidis, Z. Zhang, Wireless information and power transfer with full duplex relaying. IEEE Trans. Commun. **62**, 3447–3461 (2014)
10. M. Mohammadi, B.K. Chalise, H.A. Suraweera, C. Zhong, G. Zheng, I. Krikidis, Throughput analysis and optimization of wireless-powered multiple antenna full-duplex relay systems. IEEE Trans. Commun. **64**, 1769–1785 (2016)
11. I.S. Gradshteyn, I.M Ryzhik, *Table of Integrals, Series and Products*, 7th edn. (Academic, London, 2007)
12. A.A. Nasir, X. Zhou, S. Durrani, R.A. Kennedy, Relaying protocols for wireless energy harvesting and information processing. IEEE Trans. Wirel. Commun. **12**, 3622–3636 (2013)
13. I. Krikidis, G. Zhang, B. Ottersten, Harvest-use cooperative networks with half/full-duplex relaying, in *Proceedings of WCNC'13*, pp. 4256–4260 (2013)
14. Z. Ding, S.M. Perlaza, I. Esnaola, H.V. Poor, Power allocation strategies in energy harvesting wireless cooperative networks. IEEE Trans. Wirel. Commun. **13**, 846–860 (2014)
15. M.O. Hasna, M.-S. Alouini, A performance study of dual-hop transmissions with fixed gain relays. IEEE Trans. Wirel. Commun. **3**, 1963–1968 (2004)
16. G.K. Karagiannidis, Performance bounds of multihop wireless communications with blind relays over generalized fading channels. IEEE Trans. Wirel. Commun. **5**, 498–503 (2006)
17. M. Di Renzo, F. Graziosi, F. Santucci, A comprehensive framework for performance analysis of dual-hop cooperative wireless systems with fixed-gain relays over generalized fading channels. IEEE Trans. Wirel. Commun. **8**, 5060–5074 (2009)
18. Y. Chen, Energy-harvesting AF relaying in the presence of interference and Nakagami-m fading. IEEE Trans. Wirel. Commun. **15**, 1008–1017 (2016)
19. H. Meyr, M. Moeneclaey, S.A. Fechtel, *Digital Communication Receivers, Synchronization, Channel Estimation, and Signal Processing* (Wiley, New York, 1998)
20. F.H. Khan, Y. Chen, M.-S. Alouini, Novel receivers for AF relaying with distributed STBC using cascaded and disintegrated channel estimation. IEEE Trans. Wirel. Commun. **11**, 1370–1379 (2012)
21. C.S. Patel, G.L. Stuber, Channel estimation for amplify and forward relay based cooperation diversity systems. IEEE Trans. Wirel. Commun. **6**, 2348–2356 (2007)
22. P. Lioliou, M. Viberg, M. Coldrey, Efficient channel estimation techniques for amplify and forward relaying systems. IEEE Trans. Commun. **60**, 3150–3155 (2012)

23. F. Gao, T. Cui, A. Nallanathan, On channel estimation and optimal training design for amplify and forward relay networks. IEEE Trans. Wirel. Commun. **7**, 1907–1916 (2008)
24. H. Yomo, E. de Carvalho, A CSI estimation method for wireless relay networks. IEEE Commun. Lett. **11**, 480–482 (2007)
25. N. Aerts, M. Moeneclaey, Pilot-based ML estimation in amplify-and-forward cooperative networks, in *Proceedings of IEEE WCNC 2012*, Shanghai (2012), pp. 1044–1048
26. S. Kay, *Fundamentals of Statistical Signal Processing: Estimation Theory* (Prentice Hall, London, 1993)
27. G. Amarasuriya, E.G. Larsson, H.V. Poor, Wireless information and power transfer in multiway massive MIMO relay networks. IEEE Trans. Wirel. Commun. **15**, 3837–3855 (2016)
28. A. Rajaram, D.N.K. Jayakody, V. Skachek, Store-then-cooperate: energy harvesting scheme in cooperative relay networks, in *Proceedings of 13th International Symposium on Wireless Communication Systems (ISWCS'16)*, Poznan, Sept 2016
29. H. Chen, Y. Li, J.L. Rebelatto, B.F. Uchoa-Filho, B. Vucetic, Harvest-then-cooperate: wireless-powered cooperative communications. IEEE Trans. Signal Process. **63**(7), 1700–1711 (2015)

Chapter 6
Multi-Scale Energy Harvesting

Weisi Guo, Yansha Deng, Arumugam Nallanathan, Bin Li, and Chenglin Zhao

6.1 Introduction

One of the key trends over the past half a century has been that technology is getting smaller, faster, cheaper, and more powerful every day. In terms of computing technology, the key components have become 100-times smaller each decade. For example, the ENIAC computer (1956) used to fill a warehouse, and its equivalent compute power now sits inside a musical greeting card at the price of $4. Standard smartphones today have more computing power than the personal computers (PCs) of a decade ago. Today, this miniaturization trend continues in the form of personal wearables that can perform many of the functions of smartphones and pads of yesteryear. Smaller devices not only enable a greater number of them in any given space, but also enable mobility and personalization. It is envisaged that device miniaturization will lead to over 50 billion devices connected to the Internet, forming a large part of the Internet-of-Things (IoT) paradigm. The consequence is that devices are getting closer to the human body and integrating and interacting with our lifestyles. Inevitably, as device dimensions reduce to microns, they are able to be inserted inside our body to achieve precision sensing, communications, and actuation; potentially transforming health-care. In fact, the Internet of Nano Things (IoNTs) has been named as one of the top ten emerging technologies by the World Economic Forum in 2016.

W. Guo (✉)
University of Warwick, Coventry, UK
e-mail: weisi.guo@warwick.ac.uk

Y. Deng • A. Nallanathan
Kings College London, London, UK

B. Li • C. Zhao
Beijing University of Posts and Telecommunications (BUPT), Beijing Shi, China

D.N.K. Jayakody et al. (eds.), *Wireless Information and Power Transfer: A New Paradigm for Green Communications*, DOI 10.1007/978-3-319-56669-6_6

The energy efficiency of systems in general determines its operational sustainability. For small devices, removing the power-tether is an important mobility enabler. Such devices today include sensor motes, radio frequency (RF) tags, and wearable computers. When there is limited recharging or energy storage capability, ad-hoc harvesting of energy is a crucial technology for a variety of systems. These devices need to harvest energy from alternative sources such as natural environment or even intercepting ambient wireless signals. Energy harvesting techniques not only prolong operational life-time of such devices and reduce their infrastructure dependency, but also allow devices to be deployed in any location deemed desirable and be mobile. Harvesting energy from high frequency electromagnetic radiation (i.e., visible band) has been most widely used in photovoltaic cells, but requires direct sunlight which may not always be readily available when devices are embedded inside or in the shadow of objects. Consequently, energy harvesting from low frequency information transmissions (i.e., radio band) have been proposed as an alternative.

A variety of wireless systems and devices that transmit across multiple distance scales fit this profile, from relatively power-hungry macro-base stations (BSs) deployed in remote regions, to nano-scale sensors in vivo environments (i.e., embedded sensors that monitor wound healing status). The wide range of devices transverse multiple device length scales and communicate across distance scales that vary by up to 9 orders of magnitude (from km to microns). Yet, it remains unclear what set of energy harvesting technologies are suitable for the different dimension and distance scales, as well as diverse operating environments. RF energy harvesting solutions have recently been proposed as an alternative [1], especially for low-power devices such as sensor motes in urban and semi-urban environments [2, 3]. The concept has been around since the 1970s [4]. For example, it has been shown experimentally that the power delivered at a location that is 20 km away from a 150 kW TV transmitter or within 30 m from a cellular BS [5] is typically in the order of 0.1 mW [6, 7]. Recent advances in this area have shown that energy - efficient transmitters can be entirely powered by RF energy harvesting devices, which use cognitive methods to sense fruitful primary-network spectrum bands for targeted energy harvesting [8] or sensing traffic patterns for targeted deployment of nodes [9], and simultaneous wireless information and power transfer is possible (SWIPT) [10, 11]. Given knowledge of the location of a RF energy source, a receive antenna array can be appropriately configured to further improve energy harvesting efficiency. However, little is known about the peak power or reliable energy level that can be harvested from multiple transmitters of different radio networks (e.g., cellular base stations, Wi-Fi access points, and mobile handsets).

This chapter will review state-of-the-art technologies that allow multi-scale wireless devices to simultaneous harvest energy and transmit data, especially from a number of different wireless signal sources. The chapter will be organized into different technology dimension scales, and focus on both the fundamental scientific principles and opportunities and the engineering challenges. The key sections are listed as follows:

1. Macro-/Meso-scale energy harvesting for small devices such as RFID tags. The focus will be on the potential of crowd harvesting from multiple radio transmissions in complex urban environments.
2. Micro-/Nano-scale energy harvesting for nano devices such as drug delivery robots and embedded health monitoring devices. The focus will be on information and energy bearing bio-molecules and drawing inspiration from equivalent biological processes.

We now present the detailed outline of each of the aforementioned sections.

6.2 Macro-/Meso-Scale Energy Harvesting

Current cellular and long-distance wireless systems are relatively large in dimension and consume significant power (i.e., each antenna element can consume up to 600 W [12]). There are already efforts to reduce the power consumption of wireless infrastructures such as macro-/metro-BSs. In certain rural areas that lack reliable and sufficient electricity coverage, energy harvesting from solar radiation is possible [13]. Certainly this is an active area of research for cellular network vendors such as Alcatel-Lucent. The challenge lies in optimizing data transmission and sleep mode in the face of an unreliable energy source with the aid of energy storage [14]. On a smaller scale, femto-BSs and other small-cell technologies (i.e., wireless relays), which are often deployed in areas that require coverage compensation and may not have access to electricity in the immediate vicinity, are likely to demand 10–100 W of power. As such, indoor optical wireless systems have been proposed to transfer power to small cells at night time [15]. Nonetheless, it remains challenging to power a large wireless system using entirely energy harvesting. Several realistic problems related to obstacles that obstruct the energy beams and unexpected high traffic demand can lead to unacceptable levels of service outage.

Smaller meso-scale systems are likely to demand a significantly lower level of power, varying from 1 mW to 1 W. As such, harvesting energy from wireless transmissions becomes possible. This section will examine the potential of crowd harvesting energy from all neighbouring transmissions with particular emphasis on large-scale network modeling and theoretical bounds under full and variable traffic patterns.

6.2.1 Crowd Energy Harvesting

6.2.1.1 Background

Over the past decade, increased urbanization and growing demands for wireless data have led to a dramatic increase in the number and density of wireless transmitters in

cities. The global cellular infrastructures constituted more than four million macro-BSs and served more than seven billion active user equipments (UEs) in 2013. Moreover, public and privately owned Wi-Fi access points (APs) in developed cities have reached the density of over 350/km^2, with top metropolitan cities reaching over 700/km^2. With IoT devices equipped with wireless capabilities, it is expected the number of wireless devices will exceed 50 billion by 2020.

Despite the growing density of RF transmitters in urban areas, doubts remain with regard to the amount of RF energy that they can provide over a period of time. Whilst the increase in transmitter density will undoubtedly increase the amount of RF energy available in urban environments, a few challenges in large-scale reliable RF energy harvesting are undeniable. As shown in Fig. 6.1, some of these challenges are: (1) the random nature of RF transmitter locations, (2) stochastic elements in the RF propagation channel, and (3) variations in spectrum utilization due to varying data traffic patterns (i.e., sensors may only transmit data occasionally), all of which need to be carefully considered in the design of an efficient RF energy harvesting system. For example, the fluctuating harvested energy due to channel

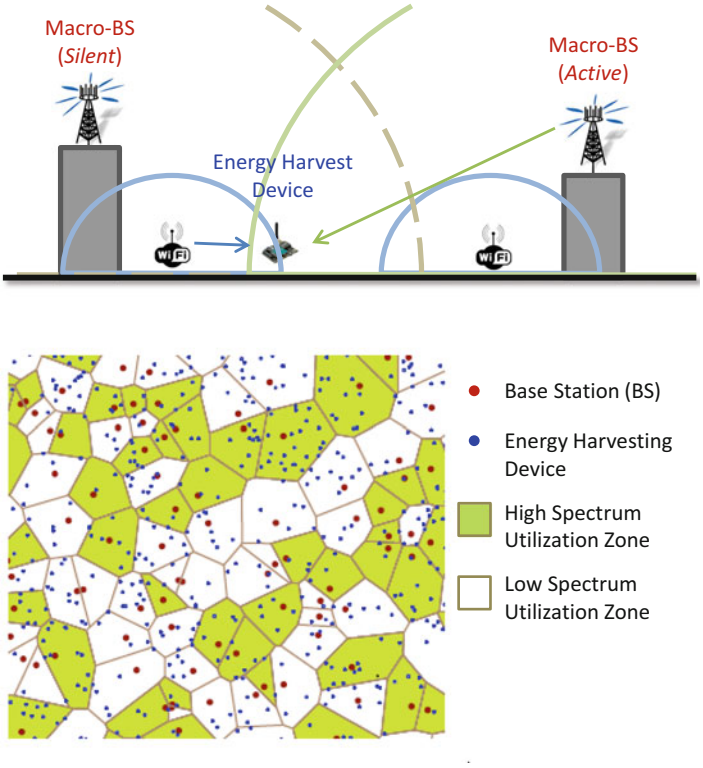

Fig. 6.1 Illustration of large-scale RF energy harvesting by multiple RF transmitters. On any particular spectrum band, the transmitter may or may not be transmitting, depending on the local traffic load

fading and node movements needs to be converted into constant DC voltage using a capacitor. However, longer-term stable energy harvesting is harder to predict and more difficult to compensate for. Understanding the long-term energy harvesting reliability is important for energy aware transmission protocols and for devices that have a limited battery capacity [16].

6.2.1.2 Hardware

Energy harvesting of electromagnetic radiation is most widely used by photovoltaic cells. However, direct sunlight is not always readily available. RF harvesting solutions have been proposed as an alternative [6, 17, 18]. By amalgamating multiple radio signals, RF energy harvesting has the greatest potential in urban areas, where there is an abundance of wireless communication devices from multiple Radio-Access-Technologies (RATs). Due to stochastic signal strength variations, the fluctuating harvested power can be converted into constant DC voltage using a capacitor. Recently, it has been shown that the power delivered is typically in the order of 0.1 mW at a location that is 20 km away from a 150 kW TV transmitter [7], or within a short range of 30 m from a cellular BS [5]. Several commercial devices exist with reasonably low sensitivity (i.e., −11 dBm of the P2110 Powerharvester) and significantly higher sensitivities are needed to harvest from a wider variety of RF signals. Even with improved energy harvesting circuits, little is known about the power lever that can be delivered in RF bands other than the TV channels and when devices attempt to harvest from the increasingly densely deployed BSs, Wi-Fi hotspots, and even mobile handsets. Due to stochastic variations in RF signal strength and traffic load (for example, BS traffic is notoriously stochastic [19]), the harvested power level fluctuates over time and needs to be converted into constant DC voltage using a capacitor. However, long-term stability is harder to predict and more difficult to compensate for. Existing performance tests have focused on specific scenarios: *single dominant link* (e.g., transmission from a nearby TV-station) [6], or field tests in a small experimental area, typically without considering the effects of: *multi-path*, *shadowing*, *traffic load*, and *mobility* [20].

6.2.1.3 Modeling Crowd Energy Harvesting Potential

Considering energy harvesting from a large number of fixed RF transmitters, it is possible to calculate the specific pathloss for each channel and predict the energy harvesting performance. The computational complexity grows linearly with the number of energy harvesting devices. If there is a lack of perfect knowledge of transmitters' locations, e.g., private Wi-Fi APs and mobile phones, predicting the energy harvesting performance becomes impractical if not impossible. Therefore, an accurate statistical notion of the available ambient RF energy as a function of the wireless networks interested and the associated propagation environment is needed. Stochastic geometry studies random spatial patterns, formed by spatial point

processes. The underlying principle is that the locations of network transmitters are random in nature, but their density and mutual distances follow certain statistical distributions. This knowledge can be used to create tractable statistical frameworks for analysing the performance of wireless networks [21]. In order for the results to be accurate, the spatial distribution of the network nodes must be derived from empirical cell location data. In this section, we offer a review of the spatial distributions of cellular macro-BSs and present new data and spatial distributions for femto-BSs and Wi-Fi APs.

In order to estimate the energy received from a large number of RF transmitters, one needs to know the probability distribution of the distance between the kth nearest RF transmitter and the energy harvesting device. In the literature, two independent sets of macro-BS data and mathematical proofs have produced the same spatial distribution of macro-BSs [22, 23]. The probability density function (pdf) of the distance r between the energy harvesting device at an arbitrary location and the kth nearest macro-BS is given by

$$f_{\mathrm{BS},R_k}(r;k) = \frac{2(\Lambda\pi)^k}{(k-1)!} r^{2k-1} e^{-\Lambda\pi r^2}, \quad k \geqslant 1, \tag{6.1}$$

where Λ is the average spatial density of macro-BSs in an area where the signal power is high enough to be considered. Such an area is approximately $4\,\mathrm{km}^2$ for urban environments concerning macro-BSs. The $k = 1$ case (i.e., the nearest macro-BS), which follows a Rayleigh distribution, is most commonly considered in wireless communications.

In recent years, femto-BSs are being deployed with increasing densities in urban areas. Empirical data obtained has shown that the spatial distribution of the kth nearest femto-BS is identical to that of macro-BSs. That is to say, despite the tedious multi-variable optimization for cellular network planning, macro- and femto-BSs are in fact randomly deployed with the spatial distribution of the kth nearest BS given by (6.1). In the literature, Poisson cluster processes (PCPs) such as the Matern and Thomas cluster processes have been utilized for modeling ad-hoc and small-cell networks [24], but there is a lack of evidence base for such PCP-based modeling.

Wi-Fi APs are deployed in a fundamentally different way to cellular BSs. Their higher density,[1] possibly different spatial distribution, and higher traffic load may yield a different prospect in terms of energy harvesting. Note that the vast majority of Wi-Fi APs are owned by private residential or individual business entities, as opposed to network operators, and both the density and number of Wi-Fi APs change over time. Therefore, the locations of Wi-Fi APs are not exactly known. Whilst certain efforts have been made to locate Wi-Fi APs using directional spectrum sensing approaches [25], a more systematic approach is to infer Wi-Fi APs' locations and density through residential and business census data.

[1] In urban areas, the deployment density of Wi-Fi APs has grown over the past decade to 400–1000 APs per square km.

By assigning a Wi-Fi AP to each residential or business registration address, one can infer the approximate locations of Wi-Fi APs. Based on this data, two discoveries were made [11]: (1) the density distribution of Wi-Fi APs is a log-normal distributed cluster process, commonly found in the ions of materials [26], and that (2) the pdf of the distance between a random point in space and the kth nearest Wi-Fi AP follows the Gamma distribution, i.e., $f_{\text{Wi}-\text{Fi},R_k}(r;k) \sim \Gamma(k,\theta)$, where θ is the scale parameter. What remains undiscovered is the precise distribution of Wi-Fi APs in terms of the scale parameter θ, and the precise spatial distribution of mobile UEs.

6.2.1.4 Full Spectrum Utilization Upper-Bound Analysis

In this section, we consider the aggregated RF power density (Watts per Hz) over a bandwidth of B and from an area with an average transmitter density of Λ. We first assume that all transmitters are transmitting across the whole spectrum available and emit with the maximum allowable power spectrum density on all frequency bands, and hence this is an upper-bound analysis. Leveraging the spatial distributions of RF transmitters found in the previous section, the total *average received RF power* from K RF transmitters is given by

$$P^*_{\text{rx}}(\alpha,\lambda) = B\sum_{k=1}^{K}\int_0^{+\infty} P_{\text{tx}}\lambda r_k^{-\alpha} f_{R_k}(r_k;k)\,\mathrm{d}r_k, \tag{6.2}$$

where P_{tx} is the transmit power, λ is the frequency dependent pathloss constant, α is the pathloss distance exponent, and $f_{R_k}(r_k;k)$ is given in (6.1).

As an example, let us consider the aggregate harvested power P_{rx} for a deployment of macro-BSs that follow the spatial distribution given by (6.1). By integrating (6.2), the total power harvested is found to have the following scaling relationships:

- Linearly proportional to the transmit power: $P^*_{\text{rx}} \propto P_{\text{tx}}$;
- Exponentially proportional to the cell density: $P^*_{\text{rx}} \propto (\Lambda)^{1+\frac{\alpha}{2}}$.

Alternative spatial distributions of RF transmitters are likely to yield different solutions.

A key question at this stage of the analysis is: given that transmitters further away are unlikely to contribute much more power, what is the power difference between harvesting from only the closest transmitter and crowd harvesting? Based on both simulation and the analytical expression in (6.2), the latter can harvest approximately 5–10% more power than the former. Note that this considers only *power*. When *energy* is considered, one also needs to take into account spectrum utilization over time. The reliability of crowd harvesting energy over time will improve dramatically over targeting just a single transmitter.

6.2.1.5 Variable Spectrum Utilization Analysis

In the previous section we have studied the upper-bound to the amount of power that can be harvested from a number of RF transmitters. In order to estimate the harvestable RF energy, it is important to consider the spectrum utilization over time for each RF transmitter. Spectrum utilization depends on the traffic load of each transmitter. Unlike TV channels, which are fewer in number and broadcast over long periods, cellular and Wi-Fi network nodes transmit on demand and the demands can fluctuate in unpredictable temporal and spatial patterns.

Over the past decade, wireless network traffic has shifted from mainly circuit-switched call traffic to packet-switched data traffic dominated. Whilst voice call traffic is well understood, data traffic arrival and departure patterns are much more diversified and unpredictable over time and geographical locations. In this subsection, we leverage the statistical attributes of real 3G HSPA data from a European city's 3G network [27]. Two key observations have been made in all cellular network areas used for traffic data collection:

1. The mean traffic R_k at the kth BS is related to the mean capacity of the BS. In other words, given that each BS has the same bandwidth, cells having superior propagation conditions emit greater energy. The relationship between the traffic and the BS capacity C_k is approximately logarithmic, i.e., $R_k \sim \log_{10} C_k$ [27].
2. The pdf of the traffic load L_k at the kth BS is exponentially distributed, i.e., $f_{L_k} \sim \exp(\tau)$, whereby the rate of decay τ is the same for each cell and varies slowly with time (e.g., hours in a day, and days in a week) [19].

Given knowledge of the statistical properties of data traffic, one can infer the spectrum utilization pattern at each BS as a ratio of the traffic and the peak capacity of the BS, i.e., $L_k = \frac{R_k}{C_k}$. Given that each of the K BSs is independent and identically distributed in space and in spectrum utilization, the pdf of the power density (Watts per Hz) harvested from the sum of all K RF transmitters is the K-fold continuous convolution of the traffic load pdf and the inverse of the received power upper-bound from (6.2):

$$f_{P_{\text{rx}}} = \bigotimes_{k=1}^{K} f_{L_k} / P^*_{\text{rx}}. \tag{6.3}$$

The cumulative distribution function (CDF) of harvested power density (Watts per Hz) shows the reliability of harvestable power density at any given instance in time, where the main variation is derived from the spectrum utilization pattern. By aggregating the CDF over both the frequency bands and time, we can obtain the total expected RF energy that is harvestable.

6.2.2 Case Study: Central London

6.2.2.1 Above Ground

In this section, we consider a central London case study area detailed in [28] that is of 9 km wide and 5 km long. It covers Hyde Park, parts of the Thames River, and major tourism hotspots such as Trafalgar Square, Piccadilly Circus, the Parliament, China Town, London Eye, and Oxford Street. Multiple RATs are included: (1) 4G Cellular Macro-BS Downlink (50 MHz); (2) 4G Cellular UE Uplink (20 MHz); (3) Wi-Fi AP Downlink (20 MHz); and (4) TV Broadcast (100 MHz). The main parameters of the case study are given in Table 6.1.

Table 6.2 shows the mean peak power for different RATs on the per 20 MHz band level, with the whole spectrum available to each RAT. This was a study conducted in [28]. It can be seen that the greatest opportunity for power harvesting lies in the Wi-Fi and TV broadcast RATs. In fact, given that the network traffic on Wi-Fi and TV is typically higher than that of the cellular RAT, it is advisable to focus energy harvesting in these bands, at least before femto-BSs are more widely deployed. By comparing with existing test observations that 100 μW can be achieved at a 20 km distance from a 150 kW TV station [7] or within 30 m from a cellular BS [5], we can see that in general the mean energy harvestable is approximately 5–10 times lower than the special cases tested in [5, 7]. This is primarily due to the log-normal shadow fading considered in our model, as well as the non-line-of-sight (NLOS) positioning of the energy harvesting devices with respect to the RF transmitters.

Due to the small number and fixed locations of TV masts, their energy harvesting potential has been well analysed. We now focus on the effect of Wi-Fi APs' density, number of spectrum bands, and the shadow fading variance on the power harvesting effectiveness. Figure 6.2 shows the simulated aggregate power available to harvest for various Wi-Fi hotspot densities and number of bands available (each band having a bandwidth of 20 MHz). In the simulations, a number of cellular and TV bands are also in operation, with static parameter values set to the peak values shown in Table 6.1. The simulation results show that for a high Wi-Fi density (1000/km^2), the ambient RF power available is in the order of μW, depending on the number of spectrum bands.

Figure 6.3 shows the simulated aggregate power available to harvest versus various Wi-Fi hotspot densities and log-normal shadow fading variance. We can see that when log-normal shadow fading is considered, the average RF power available for harvesting degrades log-linearly with the shadowing variance. In realistic channel conditions, the shadow fading variance can be up to $\sigma^2 = 9$ dB [29]. Compared to the case with no shadow fading, the RF power available for harvesting is lowered by 9 dB for the 3 dB shadow fading variance, and 35 dB for the 6 dB shadow fading variance. *Accordingly, in order to achieve a good RF energy harvesting performance, the devices need to be deployed at locations that experience a shadow fading variance of no greater than 3 dB.*

Table 6.1 London simulation case study parameters

Parameters	Symbol and value
Case study environment	
Geographic area	Central London, 45 km^2
Energy harvester location	Uniform random
No. of energy harvesters	500
Duration of study	2 week period
Propagation model	3GPP urban micro [29]
Pathloss constant	λ, 10^{-4}
Pathloss distance exponent	α, 2–4
Channel fading	Rayleigh
Shadow fading	Log-normal (3 dB variance)
Traffic and spectrum	
Spectrum utilization pdf	f_{L_k}
User arrival pdf	Poisson
Data traffic pdf	Log-normal
Traffic time sample	15 min
4G cellular RAT	
Total no. of macro-BSs	96
Macro-BS density	$\Lambda_{\text{macro}-\text{BS}}$, 2/$km^2$
Macro-BS distribution	Uniform random [22]
Macro-BS transmit power	$P_{\text{tx, macro}-\text{BS}}$, 40 W
Total no. of UE	700,000
UE density	Λ_{UE}, 15,500/km^2
UE distribution	Uniform random (assumed)
UE transmit power	$P_{\text{tx, UE}}$, 0.1 W
Total no. of Wi-Fi APs	45,000
Wi-Fi AP density	$\Lambda_{\text{Wi}-\text{Fi}}$, 1000/$km^2$
Wi-Fi AP distribution	Log-normal cluster based
Wi-Fi AP transmit power	$P_{\text{tx, Wi}-\text{Fi}}$, 1 W
Total no. of TV masts	4–5
TV mast density	Λ_{TV}, 0.1/km^2
TV mast distribution	Fixed
TV mast transmit power	$P_{\text{tx, TV}}$, 1000 kW

As shown previously in (6.3), the energy harvested depends on the convolution between the peak power available for harvesting and the pdf of the spectrum utilization level. The peak power value given by (6.2) is largely determined by the spatial distribution and density of RF transmitters, as well as the propagation environment itself. We have shown that the harvested power value can be improved by 5–10% through crowd harvesting as compared to harvesting from the closest transmitter only. Moreover, the spectrum usage can be dynamic and in the event that the closest transmitter is not transmitting, crowd energy harvesting shines. When

Table 6.2 London case study results with different RATs [28]

RAT	*Peak power per band* (μW/sqm)
Cellular downlink	0.3
UE uplink	1
Wi-Fi downlink	5
TV broadcast	1.2
RAT	*Peak power* (μW/sqm)
Cellular downlink (50 MHz)	0.6
UE uplink (20 MHz)	1
Wi-Fi downlink (20 MHz)	5
TV broadcast (100 MHz)	6
RAT	*Aggregate daily energy*
Cellular downlink (50 MHz)	5 mJ/sqm
UE uplink (20 MHz)	4.2 mJ/sqm
Wi-Fi downlink (20 MHz) 8	0.13 J/sqm
TV broadcast (100 MHz)	0.5 J/sqm

Peak power and aggregate daily energy harvested averaged across all devices over a 2 week period

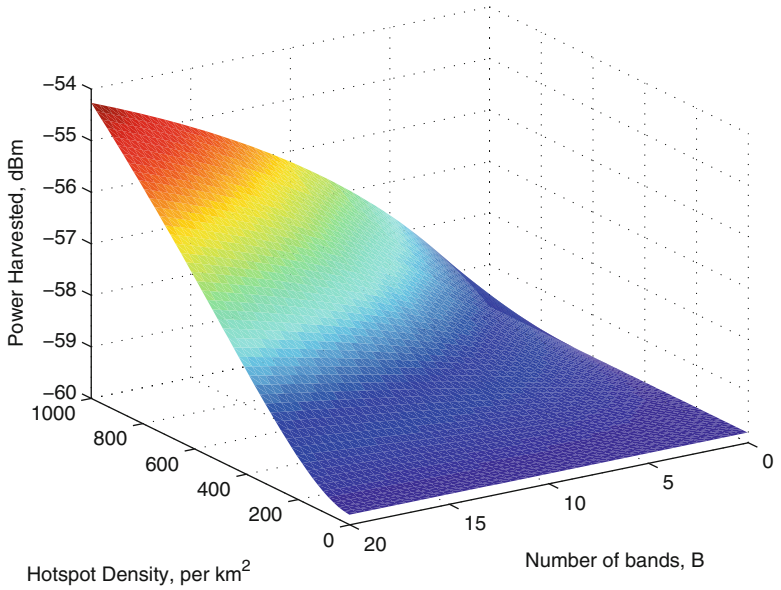

Fig. 6.2 Simulated aggregate power available to harvest for various Wi-Fi hotspot densities and number of bands available

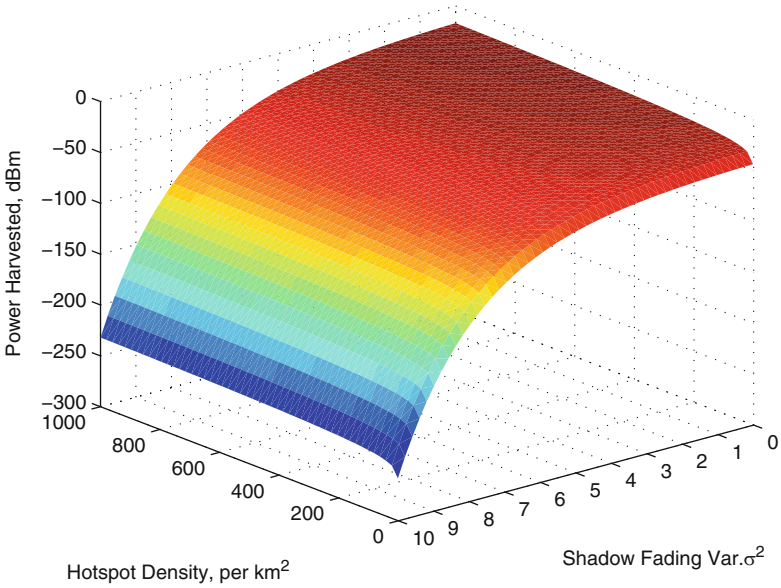

Fig. 6.3 Simulated aggregate power available to harvest for various Wi-Fi hotspot densities and shadow fading variances (dB)

the investigation factors in the variational spectrum utilization, it is apparent that the total energy harvested from all ambient RF transmitters will produce a fixed 5% of improved reliability in energy delivery per second over that from the strongest transmitter. For a fixed reliability demand (i.e., deliver at least a certain power level for at least 30% of the time), the power harvested has improved from 4 μW (harvesting from the closest transmitter only) to 8.5 μW (crowd harvesting), an improvement of over 100%. This is primarily down to exploiting diverse variations in spectrum utilization at different transmitters by harvesting energy from a diverse range of radio sources. The aggregate daily energy harvested (averaged across all devices) is given in Table 6.2. It shows that Wi-Fi and TV broadcast remain the most promising bands to harvest because of their wider bandwidth and greater spectrum utilization due to higher traffic.

6.2.2.2 Below Ground

Table 6.3 shows a different study conducted for central London detailed in [2] for underground stations. The study uses real measurement data across from 400 MHz to 2.5 GHz to test the average and peak received power density. The results show that GSM900 and GSM1800 and 3G all have similar high energy harvesting potential, whilst Wi-Fi and DTV remain significantly weaker (by approximately

Table 6.3 London underground case study results with different RATs [2]

RAT	Average power (μW/sqm)	Peak power
Cellular downlink (75 MHz)	840	64 mW/sqm
UE uplink (75 MHz)	5	200 μW/sqm
Wi-Fi downlink (100 MHz)	1.8	60 μW/sqm
TV broadcast (140 MHz)	8.9	4.6 mW/sqm

Average power density and maximum power density

20 dBm/sqcm). These results seem to indicate that in reality BSs are a far better source of energy harvesting than DTV and Wi-Fi, possibly because of the nature of the embedded underground environment.

6.2.3 Optimization for Crowd Harvesting

We have so far reviewed the potential of crowd harvesting across different RATs, which is attractive, especially in the TV bands (LoS) and Wi-Fi bands (NLoS). However, what remains unclear is how a relay system, where the nodes are sufficiently apart (and hence have different energy harvesting potentials), can collaborate to achieve optimal relaying performance. In this section we discuss node collaboration and transmission scheduling for crowd harvesting [11]. It has been revealed that the correlation distance of the traffic density is less than 80 m in urban areas [30], indicating that the RF energy harvesting process may follow similar spatial correlation. Two nodes that are more than 100 m apart tend to have almost independent energy harvesting processes, and thus node collaboration can be performed to exploit the independent relationship between energy profiles, e.g., to achieve energy harvesting diversity gains.

First we illustrate the benefit of node collaboration via combining the SWIPT and ambient energy harvesting, in order to compensate for the possible energy shortage. Assuming that the source can harvest more ambient RF energy than the relay node, the energy harvesting phase can be split further into two parts: (1) source-to-relay energy delivery, and (2) ambient RF energy harvesting at relay. Note that the source can make use of the time when the relay forwards the message, to harvest additional ambient RF energy. Furthermore, for the scenario where the nodes have no SWIPT structure or have some common information to the same destination, for example, the multiple relays in the second hop of a relaying transmission, or multiple sensors that sense the same target and need to deliver the sensing results to the sink. In this case, collaborative transmission can be used to address the uneven energy arrival rates. As a simple example, a transmission frame can be divided into two subframes. In the first subframe, only one of the nodes can be scheduled to transmit in the conventional way. In the second subframe, multiple nodes can perform simultaneous joint transmission (JT) to the destination with distributed beamforming. To this end,

the frame division portion and the node scheduling should be jointly optimized, taking into account the ESI of all nodes. For both cases, to get the optimal system parameters, practical online algorithms should be designed based on the prediction of the mobile traffic that generates the crowd EH source. One can model the mobile traffic variation with Markovian model, of which the transition probabilities can be trained based on real data [11], and then MDP policy iteration will provide the optimal transmission scheduling and system parameters. To reduce the complexity of MDP, one can do conventional optimization on a per-frame basis, with the energy arrivals and channel conditions of several future frames as known, given the traffic prediction precision is high.

6.2.4 Summary and Discussion

Most existing work on energy harvesting has focused on the hardware design of energy harvesting devices. Field tests of those devices are typically in LoS with a nearby BS or TV mast. Whilst the results are beneficial, they reveal very little about how such devices will perform when mass deployed in an urban environment. In an urban mass deployment, the energy harvesting devices may need to be at locations to serve a purpose (e.g., to sense the pollution level at a specific location) and there is very little flexibility in alternative locations. Such locations are likely to be in NLoS from RF transmitters, and far away from powerful TV mast transmitters. Crowd energy harvesting can leverage the growing density of BSs, Wi-Fi APs, and mobile UEs. However, an analytical framework backed up by empirical data has been absent thus far. This review paper has shown that stochastic geometry has the potential to provide a upper-bound to the power available to harvest (6.2), provided that we know the spatial distribution of the transmitters. Further understanding of the traffic patterns can yield insight into the spectrum usage level. By convolving the upper-bound of the power from multiple transmissions with the spectrum utilization probability function, the reliability distribution of energy harvesting from multiple sources can be found (6.3).

What the preliminary study has shown can be summarized as:

- The upper-bound power available for harvesting scales linearly with transmit power, and exponentially with the transmitter density. This is sensitive to both the pathloss distance exponent and the spatial distribution of the transmitters. Harvesting power from multiple sources offers a 5–10% improvement over harvesting from only the closest source.
- The reliability of the energy available for harvesting depends on the upper-bound power, as well as the traffic pattern. The pdf of the spectrum utilization typically follows a log-normal distribution. Harvesting energy from multiple sources offers greater diversity, which translates into a 5% improvement in reliability and 100% improvement of energy level as compared to harvesting from the closest source.

There remains plenty of further work to be carried out, including large-scale field trials, finding accurate spatial distributions for transmitters of different RATs, as well as their traffic load distributions. Whilst TV and cellular networks are relatively well understood, Wi-Fi and mobile UEs are not. Yet, it is the Wi-Fi APs and mobile UEs that could potentially grow the fastest in terms of transmitter density, and their cluster-like spatial distributions offer the greatest prospect of improving crowd RF energy harvesting.

6.3 Micro-/Nano-Scale Energy Harvesting

6.3.1 Introduction

Today, micro-electronic devices can perform comparable operations to analog electronic machines that used to occupy a factory floor. One consequence of increasing device miniaturization is that we can now carry, wear, and embed advanced machinery on or inside ourselves. As the technology for mobile and wearable devices matures, research focus has now shifted towards embedded devices for health monitoring. Whilst macro-scale implantable devices (i.e., pacemakers) can trace its origin back to late 1950s, a new generation of micro-scale sensors can monitor a variety of physical and biochemical states (i.e., wound recovery, hormone levels) in the human body are being developed.

Nano-machines or nano-robotics define a broad number of devices comprised of components that are close to the scale of a nanometre. Nano-machines have a variety of applications that range from precision drug delivery, real-time sensing, and controlling cell dynamics. Nanotechnology in this context has emerged greatly in the early state (theoretical designs and simulated performance testing, with a few in vitro and in vivo tests), although there are still some limitations for further development. Currently, nano-machines lack the ability to communicate with each other, limiting their potential to perform coordinated tasks. For example, coordinated and controlled (via light, pH, swelling/shrinkage, etc.) drug delivery can maximize the therapeutic range and minimize toxicity and ineffectiveness. Being able to achieve nano-scale communications will herald a new era of nano-medicine: connecting a plethora of nano-sensors and realizing a key component in the Internet of Bio-Nano things (IoBNT) paradigm [31].

IoBNT systems are an essential component of nano-medicine, which promises to revolutionize health-care. The demand for precision medicine such as nano-machines operating in vivo environments is immense (current market valued at $100 billion with a 14% CAGR). One example application area is coordinated drug delivery. Today, poor drug delivery effectiveness costs the world $ billions and exposes patients to the risk of high toxicity. Normal delivery of drugs through the digestion and blood stream causes a long exposure to toxicity across a wide range of cells. In effect, the therapeutic range is small and waste is high.

Coordinated drug deliveries by mechanical and chemically triggered processes are sensitive to the unpredictable in vivo environment, and do not achieve coordination between devices. Coordinated drug delivery by a swarm of nano-machines that can coordinate a simultaneous payload release can improve the therapeutic range and decrease toxicity risk and waste. Wireless communication between such robots and the outside world is necessary for the purposes of command and control, and monitoring. Yet, wireless communication is extraordinarily challenging at the nano-scale in fluidic in vivo environments, i.e., small device dimension limits electromagnetic waves to be at the lossy THz band. On the other hand, cells use molecular signaling. Drawing an inspiration from these processes, researchers have set out to design functional bioengineering sub-systems (i.e., remote controlled DNA-circuits and bacteria systems [32]), as well as molecular communication sub-systems [33]. In converting theoretical designs into practice, recent progress in building macro-scale prototypes [34, 35] has allowed researchers to test various signal detection and diversity schemes. Despite this progress at the macro-scale, there remains no viable pathway to downscale the testbeds to the nano-scale (Fig. 6.4).

6.3.1.1 Challenges with Wireless Energy Efficiency

In the previous section, we reviewed the growing focus on increasing the energy efficiency of both mobile and fixed wireless systems. Whilst we have built up a good understanding of power consumption mechanisms in terrestrial mobile networks, we still lack understanding in how nano-machines can communicate in an energy efficient manner. As communications and energy is vital for coordination and control of any system, so too will they be for nano-machines. It is envisaged that nano-scale communications will be critical to nano-machines that seek to coordinate tasks such as in vivo drug delivery and surgery [31]. Whilst many meso- and macro-scale in vivo medical devices (i.e., pacemaker) are battery powered, nano-batteries (50 μm [36]) are still significantly larger or of the same dimension as

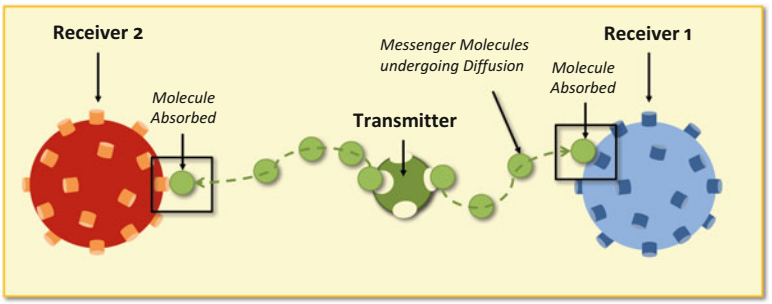

Fig. 6.4 Illustration of molecular communications via diffusion (MCvD) with a single emitter and multiple absorbing receivers

their nano-machine counter-parts. Therefore, charging batteries using externally generated acoustic [37] and electromagnetic radiation is not always viable and furthermore, nano-machines can be embedded in vivo areas that are either sensitive to radiation or difficult for radiation to penetrate. As such, energy harvesting from the nano-machines' locality is needed, i.e., the energy source should be near the nano-machine. Over the past decade, there is increasing interest to harvest energy from communication signals and achieve simultaneous wireless information and power transfer (SWIPT). In this chapter, we draw on our understanding of energy consumption and harvesting knowledge in current wireless systems to better understand nano-scale communications and exploit opportunities.

6.3.1.2 Challenges with Wave-Based Systems

The traditional practices of wireless planning with known coverage areas and propagation environments start to breakdown at the micro- and nano-scales. Communication systems in complex biological environments must be: bio-compatible, low-power consumption, low complexity, small dimension, and achieve reliable signaling in a fluid environment with complex cell/tissue obstacles. Such constraints are challenging for both EM-based THz systems and nano-acoustic systems. Current electricity and wave-based information delivery cannot downscale to the nano-scale whilst retaining the required level of propagation robustness and energy efficiency in vivo fluidic environments.

6.3.2 Molecular Communication via Diffusion

For centuries, scientists have known that molecular signaling underpins biological processes across multiple distance scales: from microscopic cell regulation to long range insect signaling. Inspired by the abundant use of molecules in biological signaling, Molecular communication via diffusion (MCvD) utilizes *molecular signal* (i.e., a chemical pulse) as an alternative carrier for information [33]. MCvD avoids the limitations of wave generation and propagation, and allows the signal to both persist and propagate to areas that are difficult to reach [38, 39]. The information in MCvD can be repetitive signaling from a limited alphabet, which is common in biological systems; or generic information from a rich alphabet, which is more common in human interaction. Historically, molecular-based signaling between animals has been observed since the ancient times, and more explicit arguments relating signaling success and natural selection were articulated by Darwin in 1871 [40]. It is only in the last decade or so that molecular communication from a telecommunications and information theory perspective has been explored [41]. Primarily, this has been due to the rise in demand from nano-scale engineering

(e.g., communication between swarms of nano-robots for targeted drug delivery [42]) and also the demand for industrial sensing in adverse environments. In both of these cases, the local environment can be adverse to the efficient propagation of electromagnetic (EM) wave signals.

Intense interest in molecular signaling between external bodies began over two decades ago, the scientific community paid particular interest to the pulse modulation techniques used by moths to attract mating partners [43]. Over the last decade, observations showed that chemical signals were encoded and decoded both in the time- and spatial-domains to assist homing and message delivery [44], and the moth's antenna system has been successfully reverse-engineered using biochemical sensors [45]. A more generalized communication system capable of transmitting any alpha-numeric message was later devised and built [34], linking the aforementioned bioengineering research with the field of telecommunication. In recent years, a growing body of significant molecular communication research has been devoted to a wide range of channel modeling [46] and telecommunication system design [47–49], information theory [50, 51], sensor and circuit design [45, 52], as well as biological system modeling [53, 54]. Furthermore, information theorists have become interested in the achievable reliable information rate of the random walk channel [50]. This led to various channel models been constructed, including and not limited to the capacity of a delay-time modulated channel [51].

With the advent of IoBNT systems in nano-medicine, there is an urgent need to connect various elements and sub-systems together to perform coordinated action. Yet, engineers simply do not know how to design and build nano-scale communication systems that can operate reliably and efficiently in vivo environments over long durations. Existing work in molecular communications has extended earlier understanding of chemical signals to transmit continuous information (i.e., a sequence of distinctive data packets, as opposed to repetitive data). As such, challenges in encoding and transmission strategies that relate to inter-packet chemical interference arise, which are exasperated by the stochastic nature of molecular diffusion channels.

6.3.3 Biological Communication and Energy Harvesting Systems

In biology, chemical signaling using molecules exchanges information and energy. In this subsection, we review some of the chemical signaling mechanisms in the communications context. In particular, we focus on biological cell signaling, which is essential to organized behaviour in multi-cellular organisms. A human body contains 100 trillion cells that coordinate actions through chemical signaling. Whilst the distances in cell signaling are typically small, hormone signals can transverse over long distances (i.e., several metres in the blood stream). A mixture of reception models exist. For example, signal receptors exist both within the cell

cytoplasm and on the surface of the cell membrane. Cell surface receptors often use secondary messengers to transmit an amplified signal to the cytoplasm. Adjacent cells often form direct passages that link their cytoplasms, permitting the passage of messengers.

6.3.3.1 Intra- and Inter-Cell Signaling

A variety of chemical macromolecules are used for signaling, including but not limited to peptides, proteins, dissolved gases, amino acids, nucleotides, steroids, and other lipids. Cell receptors are designed only to react to certain chemical signals, whilst ignoring the large volume and diversity of other signals. Receptor proteins have unique shapes that fit the shape of a specific signal molecule. Binding with the right signal will produce a response within the cell. *Intra-cell* signaling only affects a single cell and is divided into two categories. Intracrine occurs within the cell, binding to receptors inside the cell's cytoplasm and is used to regulate intracellular events. Autocrine signaling also affects the host cell, but the chemical messenger is ejected out of the cell and binds to the surface receptors of the cell. *Inter-cell* signaling affects a secondary cell or cells. Inter-cell signaling occurs across multiple distance scales, from a few microns (adjacent cells), to a metre (across the human body). Juxtacrine signaling is a contact dependent signaling process that allows chemical messengers to transverse via a ligand, junction, or matrix to another attached cell (see Fig. 6.5a). Longer distance cell-to-cell communications is called paracrine signaling. Here, cells eject molecular messengers that diffuse to a local cell, a few hundred microns away (see Fig. 6.5b). Longer distance diffusion communications occurs across the body between gland cells. This is known as endocrine signaling. The gland cells excrete hormones that use the circulatory system to be carried to target organ cells (see Fig. 6.5c).

The diffusive nature of endocrine signaling means that distant communications is slow. The nervous system provides rapid communication between distant cells and this is called *synaptic signaling*. Fiber extensions of nerve cells release neurotransmitters (chemical messengers) from their tips close to the target cells via the synaptic gap (see Fig. 6.5d). In addition to the aforementioned four techniques, some signals perform autocrine signaling, where it secrets signals for the sole purpose of binding to its own receptors, reinforcing developmental changes.

6.3.3.2 GABA Re-Uptake Mechanism

Energy harvesting using signaling molecules is common in biology at the cellular level. One such biological example that utilizes two types of molecules is the GABA re-uptake mechanism at the synaptic cleft. Glial cell absorbs/harvests GABA molecules and converts them to glutamine for utilizing at the signaling mechanisms

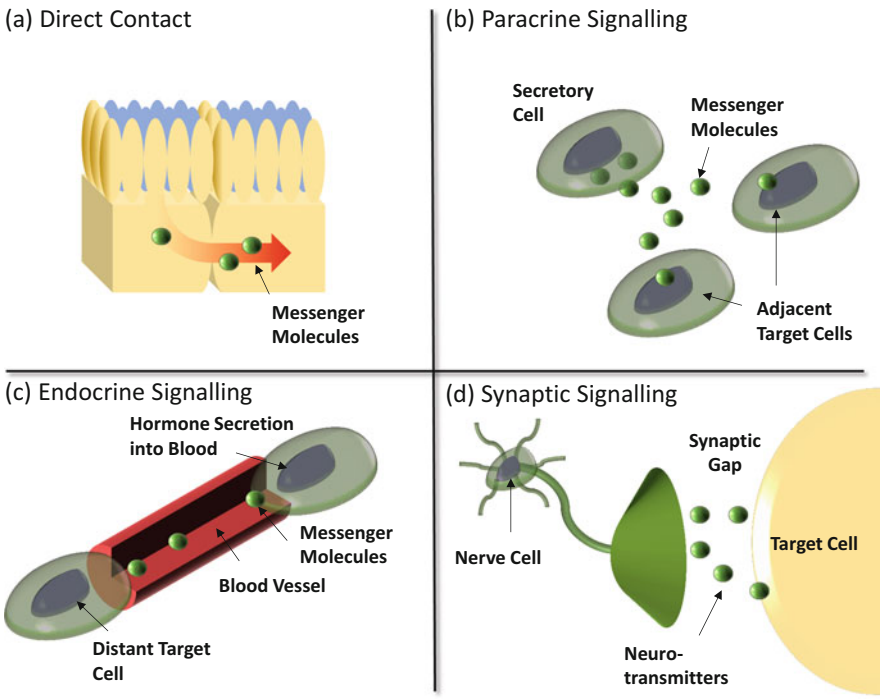

Fig. 6.5 Four kinds of cell signaling: (**a**) Juxtacrine signaling—cells in direct contact with each other send signals across junctions. (**b**) Paracrine signaling—secretions from one cell have an effect only on cells in the immediate area. (**c**) Endocrine signaling—hormones are released into the circulatory system, which carries them to the target cells. (**d**) Synaptic signaling—transmission of signal molecules (neurotransmitters) from a neuron over a small synaptic gap to the target cell

of presynaptic region. Type A molecule generated by the source is absorbed and converted to type B molecule inside the receiving node to be utilized in another subsequent signaling mechanism. The γ-Aminobutyric acid (GABA) metabolism and uptake is widely distributed across almost all regions of mammalian brain. GABA is constructed by glutamate via enzymatic reaction with glutamic acid decarboxylase (GAD) in the presynaptic neuron cell, which is then released as a neurotransmitter for sending signal to both neighbour Glia cells and postsynaptic neuron cells via GABA transporters (GATs). In this example, the presynaptic neuron cell acts as the source to emit the GABA as type A molecule, and Glia cell acts as the molecule harvesting node, and emit glutamine as type B molecule in response to the electrical charge polarization caused by GABA. This example of molecular signaling and simultaneous molecule harvesting demonstrates the dual usage of signaling molecules in biology.

6.3.4 Nano-Scale Energy Models

Almost all nano-scale systems have biological equivalents, which lends us an opportunity to better understand the energy levels involved. Biochemical processes in a cell are performed by molecular machines (mostly protein based). Molecular machine building blocks are constructed from single to multiple molecules. These building blocks are generally divided between passive mechanisms (i.e., switches react to a chemical stimulant) and active mechanisms (i.e., actuators consume energy to perform an action) [55]. Unlike macroscopic machines, molecular machines operate at energy scales close to the thermal energy, i.e., kT, where k is Boltzmann's constant and T is the temperature. Many of the motor actions are driven by non-equilibrium thermodynamics, converting force (i.e., chemical potential) into flux (motor movement, chemical flow). This process is known as free energy transduction. There are many examples of molecular motors in action, such as the muscle myosin, which is a motor that causes muscle contraction by converting ATP (chemical fuel) into mechanical work (i.e., for ATP hydrolysis the energy is $20kT \approx 4$ zJ).

6.3.5 Nano-Scale Propagation Models

The power expenditure model of a generic wireless system can be approximately modularized into a number of contributing components. In this paper, the authors focus on the propagation layer of consumption (including the data modulation, amplification, antenna loss, and propagation effects). The overhead consumption due to signal processing and cooling elements are left for future discussions. The main factors are: (1) the receiver antenna gain with radius R, (2) the free-space propagation loss λ, (3) the transmitter efficiency (i.e., power amplifier efficiency μ or chemical synthesis cost ϕ), (4) absorption loss τ (also known as transmittance), and the (5) the circuit power consumption. In general, the received electromagnetic (EM) power (P_{Rx}) or molecular number (N_{Rx}) is a small fraction of the total power extracted by the transmitter P_{Total}:

$$\begin{aligned} \frac{P_{\mathrm{Rx}}}{P_{\mathrm{Total}}} &\propto \mu \times \tau \left(\frac{R^2}{d^{\alpha}}\right) \quad \text{for EM} \\ \frac{N_{\mathrm{Rx}}}{P_{\mathrm{Total}}} &\propto \frac{1}{\phi(n_{\mathrm{Tx}}-1)} \times \left(\frac{R}{d+R}\right) \quad \text{for MCvD: } t \to \infty, \end{aligned} \tag{6.4}$$

assuming that the communication circuit power is relatively small in a nano-machine. Like RF communications, there is an energy efficiency factor for generating N_{Tx} molecules for transmission. This is related to the number of basic chemical

components per molecule n_{Tx} and the energy cost to bind or synthesize them ϕ [56, 57]. We now explain the reasoning and details of the efficiency equations given in Eq. (6.4) in the rest of the section.

6.3.5.1 THz Electromagnetic (EM) Communications

We first examine the EM communications case. One can see that the best achievable efficiency in Eq. (6.4) is limited by $d^{-\alpha}$ for EM and limited by $\tau d^{-\alpha}$ for THz nanoscale communications (where $\tau \propto \exp(-kfd)$). The absorption loss τ is log-linear proportional to absorption coefficient k, which depends on the chemical composition of the medium and is typically 1×10^{-5} for air and $1-3$ for water at $f = 0-10$ THz [58]. To illustrate the aforementioned reasoning, we show an illustration of radio wave versus molecular propagation in Fig. 6.6. In the (a) subplot, an isotropic EM

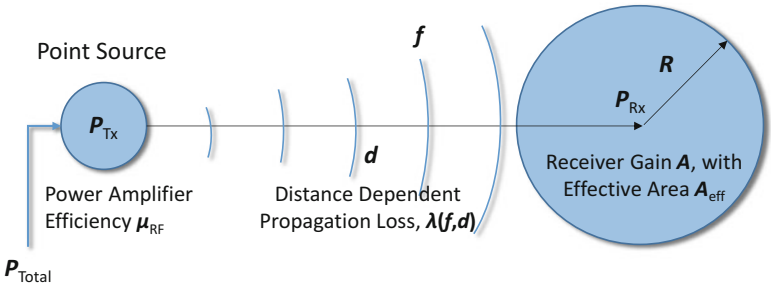

(a) Radio Frequency (RF) Channel

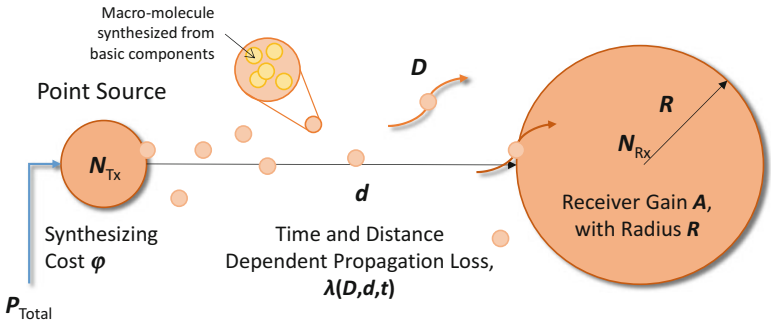

(b) Molecular Communication via Diffusion (MCvD) Channel

Fig. 6.6 Illustration of power loss in transmitting signals in (**a**) electromagnetic (EM) wave communications, and (**b**) Molecular communications via diffusion (MCvD)

antenna transmits to a receiver antenna with an effective area $A_{\text{eff}} \propto (fR)^2$, and the resulting received power after propagating a distance of d is $\mu_{\text{EM}} \frac{R^2}{d^{-\alpha}}$, where the value of μ_{EM} is typically 10–30% for EM systems [59].

6.3.5.2 Molecular Communication via Diffusion

MCvD, on the other hand, relies on message bearing molecules to freely diffuse from the transmitter to the receiver. We do not consider the base energy cost of physical matter (i.e., the molecules) as matter is not lost in the communication process. We do consider the energy cost of creating specific chemical compounds, as well as the energy benefits of restructuring the compound. In general, MCvD involves messenger molecules performing a random walk motion across the communication channel through collision interaction and a diffusion gradient. For each emitted molecule, there is a finite probability that it will reach the intended receiver. The power in the system at any given time instance is proportional to the number of molecules. Whilst the stochastic process is intuitively unreliable and requires a transmission time that is orders of magnitude longer than wave propagation, these deficiencies can be mitigated by communicating at very small distances (microns) or with the aid of strong ambient flow. For a basic random walk process, consider (as in Fig. 6.6b) a point emitter that transmits N_{Tx} molecules. The full absorption receiver, will capture N_{Rx} molecules given by Yilmaz [46]:

$$N_{\text{Rx}} = N_{\text{Tx}} h_c, \quad h_c = \left(\frac{R}{d+R}\right) \frac{d}{\sqrt{4\pi D t^3}} e^{\frac{-d^2}{4Dt}}, \tag{6.5}$$

where h_c is known as the *first passage time* density distribution.

The resulting expected number of received molecules up to time $t = T$ is $N_{\text{Tx}} F_c$, where $F_c = \frac{R}{d+R} \text{erfc}(\frac{d}{\sqrt{4DT}})$. This converges to N_{Tx} for 1-dimensional (1-D) space and $N_{\text{Tx}} \frac{R}{d+R}$ for 3-D space as $t \to \infty$ [60]. This means the full harvest of all transmitted molecules is possible in certain conditions, independent of the transmission distance. Naturally, the reality is that molecules will have a half life and not all data bearing molecules can be harvested. Reactions with other chemicals (i.e., enzymes) in the environment can reduce the effectiveness of energy harvesting in MCvD over time [61]. Yet, the potential to capture the vast majority of the transmitted molecules due to the random walk nature of propagation demonstrates the potential of MCvD over wave-based transmission. As with EM communications, there is a cost to produce the N_{Tx} molecules at the source in the first place. This can be shown to be [57]: $P_{\text{Total}} = \phi(n_{\text{Tx}} - 1)N_{\text{Tx}}$, where ϕ is the synthesizing cost of bonding n_{Tx} amino acids per transmitted molecule.

Comparing MCvD with EM propagation at the macro-scale to draw similar levels of performance (see Fig. 6.7), the received EM power is $\propto d^{-\alpha}$, where α typically varies between 2 and 4. On the other hand, the received molecules from MCvD can asymptotically be $\propto d^{-1}$, and at best independent of d in 1-D space, provided

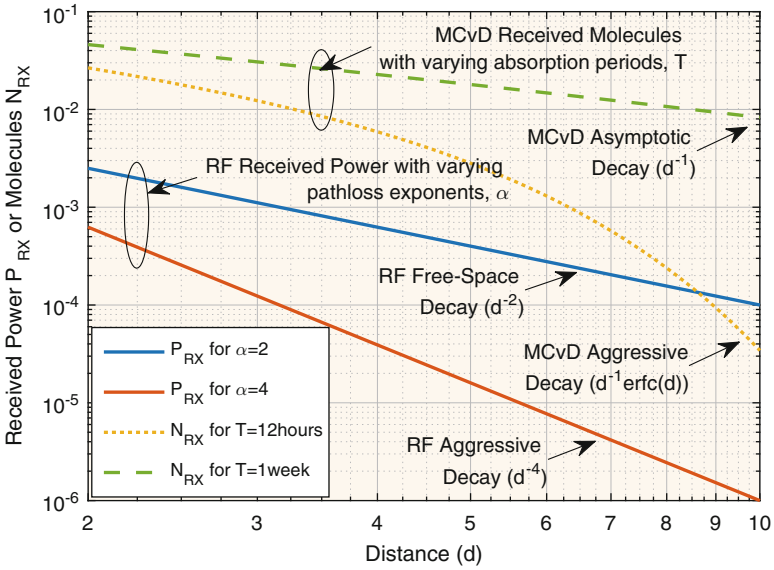

Fig. 6.7 Plot of received EM power (P_{Rx}) or MCvD molecules (N_{Rx}) for different transmission distances (d). The results show that MCvD can achieve asymptotic distance-dependent power decay at the rate of $\propto d^{-1}$, which is superior to all EM scenarios. Modeling parameters: mass diffusivity (water molecules in air) $D = 0.28\,\text{cm}^2/\text{s}$, EM frequency 5 GHz with parabolic receiver antenna $A_{\text{eff}} = 0.56\,\pi\text{R}^2$, and receiver radius of $R = 10\,\text{cm}$

the receiver is willing to wait for a long time $t \to \infty$. Yet, the long waiting time is not as ridiculous as it may appear for the following two reasons. Firstly, the rate of diffusion is in reality accelerated by ambient air flow (i.e., convection currents) or shortened to a few milliseconds at the nano-scale. Secondly, when one transmits a continuous stream of symbols, the power emitted for the first symbol will be recovered by the N-th symbol's time (when N is large). Hence, there are no incurred delays to power or energy recovery in MCvD, provided a long stream of information symbols are transmitted (Fig. 6.8).

Several aspects of the previously reviewed biological processes can inspire engineers to design energy efficient communication systems at the nano-scale. As mentioned previously, the GABA is constructed by glutamate via enzymatic reaction with glutamic acid decarboxylase (GAD) in the presynaptic neuron cell, which is then released as a neurotransmitter for sending signal to both neighbour Glia cells and postsynaptic neuron cells via GABA transporters (GATs). In this example, the presynaptic neuron cell acts as the source to emit the GABA as type A molecule, and Glia cell acts as the relay, and emit glutamine as type B molecule in response to the electrical charge polarization caused by GABA. Note that the energy harvesting relay can also be engineered in cell by using genetic circuits with chemical reaction promoted by certain catalyst. The idea of using biological circuits for engineering transmitter and receiver in molecular communication system has already been studied.

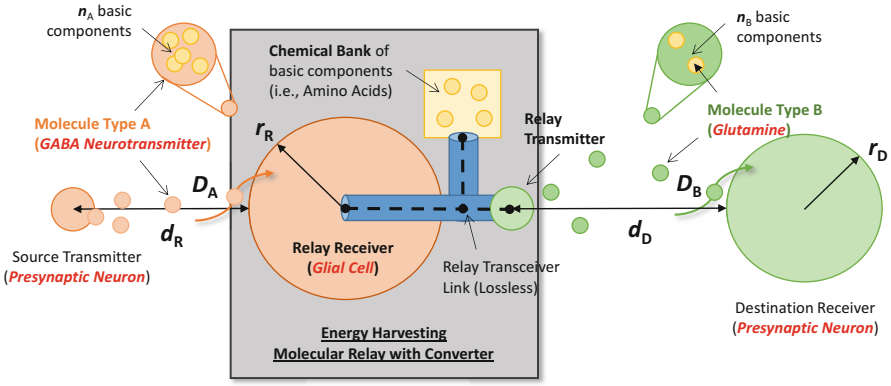

Fig. 6.8 Illustration of molecular relay communications with simultaneous energy harvesting. The mechanism is similar to the GABA biological mechanism in recycling molecules and converting molecular types through fragmentation and synthesis

6.3.6 *Molecular Crowd Harvesting*

As shown previously, despite the growing density of RF transmissions across multiple spectrum bands, the amount of energy available to harvest is dominated by the closest high power link. The rapid loss in RF energy due to transmission distance limits the potential for crowd harvesting, and unless all the transmitters are spaced equal distant to the receiver, crowd harvesting energy from N transmitters is not significantly superior to receiving energy from the nearest transmitter. For MCvD systems, as mentioned in Sect. 6.2, the energy of molecules does not obey the propagation laws of waves. Instead of experiencing a hostile $\propto d^{-\alpha}$ rate of energy decay, molecular numbers (or energy) decay $\propto d^{-1}$. Therefore, the potential to harvest energy from a field of transmitters is far greater for MCvD than for RF communications. If one assumes that the molecular transmitters are randomly and uniformly distributed according to a Poisson Point Process (PPP) or Poisson Cluster Process (PCP), one can leverage on existing stochastic geometry techniques [62] to find the expected molecular energy. This typically involves understanding the general distance distribution $f_D(d, n)$ from the energy harvesting node to the n-th nearest transmitter node [63].

Figure 6.9 shows a simulation of crowd harvesting energy from a formation of nodes distributed according to a modified Thomas PCP. Subplot (a) shows an instant snap-shot of the PCP formation of nodes with an energy harvesting receiver at the centre. Subplot (b) shows a scatter and box plot of the percentage of energy harvested for MCvD and RF transmissions. The results show that RF energy harvesting is far more sensitive to the density of transmitter nodes than MCvD energy harvesting. The random walk nature of molecular propagation means that the distance distribution (i.e., $f_D(d, n)$) is not a key consideration in crowd harvesting, whereas it is for RF systems. This demonstrates the potential for crowd harvesting in

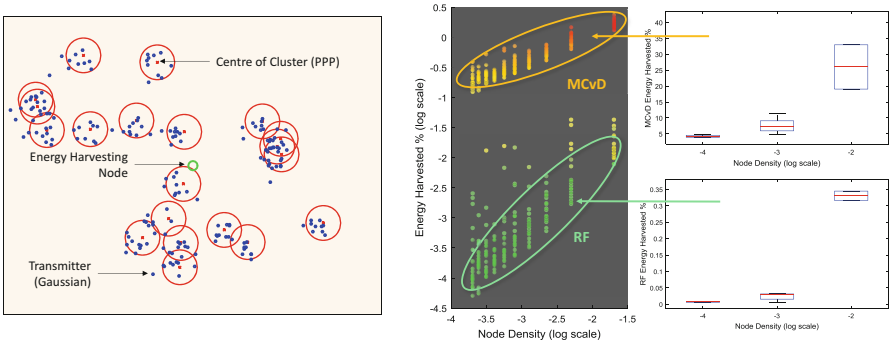

(a) Transmitters Distributed in a Modified Thomas PCP

(b) Scatter and Box Plot of Energy Harvested for Node Densities

Fig. 6.9 Crowd harvesting energy from a formation of nodes distributed according to a Thomas PCP. Subplot (**a**) shows an instant snap-shot of the PCP formation of nodes with an energy harvesting receiver at the centre. Subplot (**b**) shows a scatter and box plot of the percentage of energy harvested for MCvD and RF transmissions as a function of node density (per m^2). Modeling parameters: a variable modeling area radius 0.1–1 km, 20 clusters each with 10 nodes 2D Gaussian distributed with s.d. 30 m, mass diffusivity $D = 79.5\,\mu m^2/s$, pathloss exponent $\alpha = 2$, transmit power $P_{Tx} = 1$ W, transmit molecule $N_{Tx} = 1$, and receiver radius of $R = 1$ m

molecular systems, which can achieve 2–5 dB improvement in harvesting efficiency compared to RF systems in a similar setting, with the highest relative gain at low node densities.

6.4 Conclusions and Future Work

The performance of communication systems is fundamentally limited by the loss of energy through propagation and circuit inefficiencies. In this chapter, we have shown that it is possible to achieve ultra-low energy communications across different device size and transmission distance scales.

At the macro-scale, we have reviewed recent progress in simultaneous energy and information transfer for large-scale networks. It can greatly reduce the use of battery power and increase the availability and reliability for relaying. Through a case study, we show that it is better to harvest energy from TV bands in LoS channels and ambient Wi-Fi signals in NLoS conditions. Furthermore, we have discussed the optimization of transmissions in crowd harvesting, especially with the use of node collaboration.

At the nano-scale, we show that while the energy of waves will inevitably decay as a function of transmission distance and time, the energy in molecules does not. In fact, over time, the molecular receiver has an opportunity to recover some, if not all of the molecular energy transmitted. Inspired by the GABA metabolism system in nature, which fragments and reassembles molecules, we discuss a number of communication systems. For point-to-point links, we found that given sufficient time, the energy harvested can be fully recovered in 1-D channels and scales with

d^{-1} in 3-D channels. This fundamentally improves over wave-systems that have a free-space upper-bound of d^{-2}. For more complex systems, we designed two relay systems that can achieve high energy harvesting efficiency (12–25% at the relay). For parallel channels, we found that molecular communications offer superior energy harvesting scaling with node density (2–5 dB gain) and are significantly less sensitive to the spatial distribution of nodes. Regarding the information capacity, the generalized capacity remains to be discovered, but capacity limits for specific modulation schemes exist and are beyond the scope of this paper. In summary, chemically manipulation to improve energy efficiency of information transmission is something that has no parallel in radio frequency communications. What currently remains beyond engineering capabilities is the ability to build such biological functionalists into realistic systems. Nonetheless, the preliminary results in this article indicate that the potential for simultaneous molecular information and energy transfer (SMIET) is immense and further cross-discipline research is needed to transform theory to reality.

References

1. S. Bi, C. Ho, R. Zhang, Wireless powered communication: opportunities and challenges. IEEE Commun. Mag. **53**(4), 117–125 (2015)
2. M. Pinuela, P. Mitcheson, S. Lucyszyn, Ambient RF energy harvesting in urban and semi urban environments. IEEE Trans. Microwave Theory Tech. **61**(7), 2715–2726 (2013)
3. F. Iannello, O. Simeone, U. Spagnolini, Medium access control protocols for wireless sensor networks with energy harvesting. IEEE J. Sel. Areas Commun. **60**(5), 1381–1389 (2012)
4. W. Brown, The history of power transmission by radio waves. IEEE Trans. Microwave Theory Tech. **32**, 1230–1242 (1984)
5. B. Han, R. Nielsen, C. Papadias, R. Prasad, Radio frequency energy harvesting for long lifetime wireless sensor networks, in *International Symposium on Wireless Personal Multimedia Communications* (2013), pp. 1–5
6. T. Ajmal, D. Jazani, B. Allen, Design of a compact RF energy harvester for wireless sensor networks, in *IEEE Conference on Wireless Sensor Systems*, June (2012), pp. 1–5
7. T. Ajmal, V. Dyo, B. Allen, D. Jazani, I. Ivanov, Design and optimisation of compact RF energy harvesting device for smart applications. Electron. Lett. **50**(2), 111–113 (2014)
8. S. Lee, R. Zhang, K. Huang, Opportunistic wireless energy harvesting in cognitive radio networks. IEEE Trans. Wirel. Commun. **12**, 4788–4799, (2013)
9. W. Guo, S. Wang, Mobile crowd-sensing wireless activity with measured interference power. IEEE Wirel. Commun. Lett. **2**, 539–542 (2013)
10. I. Krikidis, Simultaneous information and energy transfer in large-scale networks with/without relaying. IEEE Trans. Commun. **62**, 900–912 (2014)
11. W. Guo, S. Zhou, Y. Chen, S. Wang, X. Chu, Z. Niu, Simultaneous information and energy flow for IoT relay systems with crowd harvesting. IEEE Commun. Mag. **54**(11), 143–149 (2016)
12. EARTH, WP2.D2.3: energy efficiency analysis of the reference systems. Energy Aware Radio and Network Technologies (EARTH), Technical Report, December (2010)
13. S. Zaidi, A. Afzal, M. Hafeez, D. McLernon, M. Ghogho, Solar energy empowered cognitive metro cellular networks. IEEE Commun. Mag. **53**(7), 70–77 (2015)
14. O. Ozel, K. Shahzad, S. Ulukus, Optimal energy allocation for energy harvesting transmitters with hybrid energy storage and processing cost. IEEE Trans. Signal Process. **62**(12), 3232–3245 (2014)

15. J. Fakidis, S. Videv, S. Kucera, H. Claussen, H. Haas, Indoor optical wireless power transfer to small cells at nighttime. IEEE J. Lightwave Technol. **34**(13), 3236–3258 (2016)
16. O. Ozel, K. Tutuncuoglu, J. Yang, S. Ulukus, A. Yenner, Transmission with energy harvesting nodes in fading wireless channels: optimal policies. IEEE J. Sel. Areas Commun. **29**(8), 1732–1743 (2011)
17. T. Le, K. Mayaram, T. Fiez, Efficient far-field radio frequency energy harvesting for passively powered sensor networks. IEEE J. Solid-State Circuits **43**(5), 1287–1302 (2008)
18. D. Pavone, A. Buonanno, M. D'Urso, F.G.D. Corte, Design considerations for radio frequency energy harvesting devices. Prog. Electromagn. Res. B **45**, 19–35 (2012)
19. E. Nan, X. Chu, W. Guo, J. Zhang, User data traffic analysis for 3G cellular networks, in *IEEE International ICST Conference on Communications and Networking in China*, August (2013), pp. 468–472
20. U. Olgun, C. Chen, J.L. Volakis, Investigation of rectenna array configurations for enhanced RF power harvesting. IEEE Antennas Wirel. Propag. Lett. **10**, 262–265 (2011)
21. M. Haenggi, *Stochastic Geometry for Wireless Networks* (Cambridge University Press, Cambridge, 2012)
22. S. Wang, W. Guo, M. McDonnell, Distance distributions for real cellular networks, in *IEEE Conference on Computer Communications (INFOCOM)* (2014), pp. 181–182
23. M. Haenggi, On distances in uniformly random networks. IEEE Trans. Inf. Theory **51**, 3584–3586 (2005)
24. R. Ganti, M. Haenggi, Interference and outage in clustered wireless ad hoc networks. IEEE Trans. Inf. Theory **55**(9), 4067–4086 (2009)
25. S. Kumar, E. Hamed, D. Katabi, L.E. Li, LTE radio analytics made easy and accessible, in *ACM Special Interest Group on Data Communication (SIGCOMM)*, August (2014), pp. 1–12
26. I. Pocsik, Lognormal distribution as the natural statistics of cluster systems. Eur. Phys. J. D At. Mol. Opt. Plasma Phys. **20**(1), 395–397 (1991)
27. M. Laner, P. Svoboda, S. Schwarz, M. Rupp, Users in cells: a data traffic analysis, in *IEEE Wireless Communications and Networking Conference (WCNC)*, April (2012), pp. 3063–3068
28. W. Guo, S. Wang, Radio-frequency energy harvesting potential: a stochastic analysis. Trans. Emerg. Telecommun. Technol. **24**, 453–457 (2013)
29. 3GPP, TR36.814 V9.0.0: further advancements for E-UTRA physical layer aspects (Release 9), 3GPP. Technical Report, March (2010)
30. D. Lee, S. Zhou, X. Zhong, Z. Niu, X. Zhou, H. Zhang, Spatial modeling of the traffic density in cellular networks. IEEE Wirel. Commun. **21**(1), 80–88 (2014)
31. I.F. Akyildiz, M. Pierobon, S. Balasubramaniam, Y. Koucheryavy, The internet of bio-nano things. IEEE Commun. Mag. **53**(3), 32–40 (2015)
32. D. Piraner, M. Abedi, B. Moser, A. Lee-Gosselin, M. Shapiro, Tunable thermal bioswitches for in vivo control of microbial therapeutics. Nat. Chem. Biol. **13**(1), 75–80 (2016)
33. N. Farsad, H. B. Yilmaz, A. Eckford, C.-B. Chae, W. Guo, A comprehensive survey of recent advancements in molecular communication. IEEE Commun. Surv. Tutorials **18**(3), 1887–1919 (2016)
34. N. Farsad, W. Guo, A. Eckford, Tabletop molecular communication: text messages through chemical signals. PLoS ONE **8**, e82935 (2013)
35. B. Koo, C. Lee, H. Yilmaz, N. Farsad, A. Eckford, C. Chae, Molecular MIMO: from theory to prototype. IEEE J. Sel. Areas Commun. **34**(3), 600–614 (2016)
36. S. Gowda, A. Reddy, X. Zhan, P. Ajayan, Building energy storage device on a single nanowire. ACS Nano Lett. **11**(8), 3329–3333 (2011)
37. M. Donohoe, S. Balasubramaniam, B. Jennings, J.M. Jornet, Powering in-body nanosensors with ultrasounds. IEEE Trans. Nanotechnol. **15**(2), 151–154 (2016)
38. S. Qiu, W. Guo, S. Wang, N. Farsad, A. Eckford, A molecular communication link for monitoring in confined environments, in *IEEE International Conference on Communications (ICC) - Workshops*, June (2014), pp. 718–723
39. W. Guo, C. Mias, N. Farsad, J.L. Wu, Molecular versus electromagnetic wave propagation loss in macro-scale environments. IEEE Trans. Mol. Biol. Multiscale Commun. (T-MBMC) **1**(1), 18–25 (2015)

40. T.D. Wyatt, Fifty years of pheromones. Nature **457**, 262–263 (2009)
41. T. Nakano, A. Eckford, T. Haraguchi, *Molecular Communication* (Cambridge University Press, Cambridge, 2013)
42. S. Chandrasekaran, D. Hougen, Swarm intelligence for cooperation of bio-nano robots using quorum sensing, in *IEEE Bio Micro and Nanosystems Conference*, January (2006), p. 141
43. A. Mafra-Neto R.T. Carde, Fine-scale structure of pheromone plumes modulates upwind orientation of flying moths. Nature **369**, 142–144 (1994)
44. P. Knusel, M. Carlsson, B. Hansson, T. Pearce, P. Verschure, Time and space are complementary encoding dimensions in the moth antennal lobe. Comput. Neural Syst. **18**, 35–62 (2007)
45. M. Cole, Z. Racz, J. Gardner, T. Pearce, A novel biomimetic infochemical communication technology: from insects to robots, in *IEEE Sensors* (2012), pp. 1–4
46. H.B. Yilmaz, A.C. Heren, T. Tugcu, C.-B. Chae, Three-dimensional channel characteristics for molecular communications with an absorbing receiver. IEEE Commun. Lett. **18**(6),929–930 (2014)
47. I.F. Akyildiz, F. Brunetti, C. Blazquez, Nanonetworks: a new communication paradigm. Elsevier Comput. Netw. **52**, 2260–2279 (2008)
48. I. Llatser, A. Cabellos-Aparicio, M. Pierobon, Detection techniques for diffusion-based molecular communication. IEEE J. Sel. Areas Commun. **31**(12), 726–734 (2013)
49. L. Felicetti, M. Femminella, G. Reali, T. Nakano, A.V. Vasilakos, TCP-like molecular communications. IEEE J. Sel. Areas Commun. **32**(12), 2354–2367 (2014)
50. B. Atakan, O. Akan, An information theoretical approach for molecular communication, in *IEEE Bionetics Conference*, December (2007), pp. 33–40
51. K. Srinivas, A. Eckford, R. Adve, Molecular communication in fluid media: the additive inverse Gaussian noise channel. IEEE Trans. Inf. Theory **8**, 4678–4692 (2012)
52. M. Pierobon, I.F. Akyildiz, A physical end-to-end model for molecular communication in nanonetworks. IEEE J. Sel. Areas Commun. **28**(4), 602–611 (2010)
53. S. Hiyama, Y. Moritani, T. Suda, R. Egashira, A. Enomoto, M. Moore, T. Nakano, Molecular communication, in *Technical Proceedings of the 2005 NSTI Nanotechnology Conference and Trade Show*, vol. 3 (2005), pp. 391–394
54. P. Lio, S. Balasubramaniam, Opportunistic routing through conjugation in bacteria communication nanonetwork. Elsevier Nano Commun. Netw. **3**, 36–45 (2012)
55. A. Coskun, M. Banaszak, R. Astumian, J. Stoddart, B. Grybowski, Great expectations: can artificial molecular machines deliver on their promise. Chem. Soc. Rev. **41**(1), 19–30 (2012)
56. T. Furubayashi, T. Nakano, A. Eckford, Y. Okaie, T. Yomo, Packet fragmentation and reassembly in molecular communication. IEEE Trans. Nanobiosci. **15**, 284–288 (2016)
57. M.S. Kuran, H.B. Yilmaz, T. Tugcu, B.O. Edis, Energy model for communication via diffusion in nanonetworks. Nano Commun. Netw. **1**(2), 86–95 (2010)
58. J. Jornet, I. Akyildiz, Channel modeling and capacity analysis for electromagnetic wireless nanonetworks in the terahertz band. IEEE Trans. Wirel. Commun. **10**(10), 3211–3221 (2011)
59. G. Auer, V. Giannini, C. Desset, I. Godor, P. Skillermark, M. Olsson, M. Imran, D. Sabella, M. Gonzalez, O. Blume, A. Fehske, How much energy is needed to run a wireless network? IEEE Commun. Mag. **18**(5), 40–49 (2011)
60. Y. Deng, W. Guo, A. Noel, M. Elkashlan, A. Nallanathan, Enabling energy efficient molecular communication via molecule energy transfer. IEEE Commun. Lett. **21**(2), 254–257 (2016)
61. A. Noel, K.C. Cheung, R. Schober, Improving receiver performance of diffusive molecular communication with enzymes. IEEE Trans. NanoBiosci. **13**(1), 31–43 (2014)
62. S. Akbar, Y. Deng, A. Nallanathan, M. Elkashlan, Downlink and uplink transmission in K-tier heterogeneous cellular network with simultaneous wireless information and power transfer, in *IEEE Global Communications Conference (GLOBECOM)*, 2015
63. W. Guo, Y. Deng, H.B. Yilmaz, N. Farsad, M. Elkashlan, C.-B. Chae, A. Eckford, A. Nallanathan, SMIET: simultaneous molecular information and energy transfer. IEEE Wirel. Commun. (2017, to appear)

Part II
Energy Harvesting Protocols For Wireless Sensor and Related Areas

Chapter 7
RF Energy Harvesting Networks: Existing Techniques and Hardware Technology

Fahira Sangare and Zhu Han

7.1 Introduction

Radio frequency (RF) is any of the electromagnetic wave frequencies that lie in the range extending from below 3 kHz to about 300 GHz, and that include the frequencies used for communications or radar signals [115]. The radio spectrum is bounded on the lower limit by low frequency signals like sound and on the higher limit by signals such as visible light, as shown in Fig. 7.1.

RF signals can be primarily generated from two sources: dedicated and ambient. The former can be deployed to provide energy when predictable supply is expected, usually from license-free frequency bands of radio spectrum. The latter refer to RF transmitters originally not intended for energy transfer, such as TV towers, radio towers, and Wi-Fi routers. The continuous miniaturization of electronics has led to an increasing interest in ever more tiny wireless autonomous sensor systems. This, in turn, has led to the need for low-power electronics and alternatives to battery power. Of the different methods that exist for scavenging energy (e.g., solar, wind, vibration, and thermal), RF energy is seen as an attractive possibility.

This introductory chapter provides a basic understanding of RF energy harvesting (RFEH) techniques. Starting with a brief explanation of existing wireless power transfer techniques in Sect. 7.2, we explain the advantages of RFEH over other techniques, then describe the underlying electronics hardware design of an RFEH system from the power source (e.g., dedicated and ambient) to the energy scavenger components. Sections 7.3 and 7.4 present the design considerations, current

This work is partially supported by US NSF CPS-1646607, ECCS-1547201, CCF-1456921, CNS-1443917, and ECCS-1405121.

F. Sangare (✉) • Z. Han
University of Houston, Houston, TX 77004, USA
e-mail: fsangare@uh.edu; fahira@gmail.com; zhan2@central.uh.edu

D.N.K. Jayakody et al. (eds.), *Wireless Information and Power Transfer: A New Paradigm for Green Communications*, DOI 10.1007/978-3-319-56669-6_7

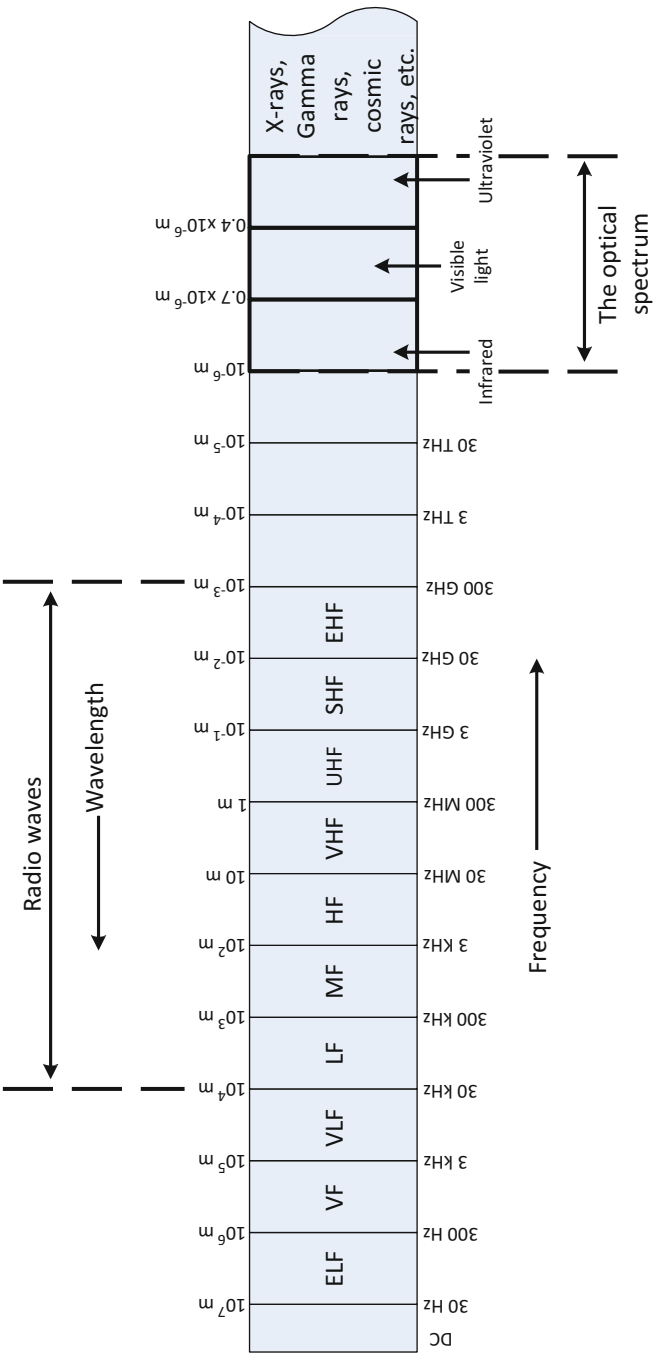

Fig. 7.1 Electromagnetic spectrum

state-of-the-art applications and commercially available products for dedicated and ambient sources, respectively, and finally expand to future applications and challenges ahead. We finally provide a brief summary in Sect. 7.5.

7.2 RF Energy Harvesting Techniques

RFEH, also referred to as RF energy scavenging, is one of the main wireless energy transfer (WET) techniques. The other methods are inductive coupling, magnetic resonance coupling, and capacitive coupling. In the following originally subsections, we survey and compare these three transfer methods, then focus on RFEH systems.

7.2.1 Overview of RF Energy Harvesting

7.2.1.1 Wireless Power Transfer Techniques

The development of wireless charging technologies is advancing toward two major directions: radiative wireless charging (or RF-based) and non-radiative wireless charging (or coupling-based) such as inductive, magnetic resonance, and capacitive. Inductive coupling [60] is based on magnetic coupling that delivers electrical energy between two coils tuned to resonate at the same frequency. The electric power is carried through the magnetic field between the coils. Magnetic resonance coupling [92] utilizes evanescent-wave coupling to generate and transfer electrical energy between two resonators. The resonator is formed by adding a capacitance on an induction coil. Both these techniques are near-field wireless transmissions featured with high power density and conversion efficiency. The power transmission efficiency depends on the coupling coefficient, which further relies on the distance between two coils/resonators. The power strength is attenuated according to the cube of the reciprocal of the distance (60 dB per decade of the distance) [122, 197], which results in limited transfer. Besides, both inductive and resonance couplings require calibration and alignment of coils/resonators at transmitters and receivers sides. Therefore, they are not suitable for mobile and remote replenishment or charging.

On the other hand, in capacitive power transfer (CPT), the electric field is confined between conductive plates, alleviating the need for magnetic flux guiding and shielding components that add bulk and cost to inductive solutions [85]. Although CPT is developing quickly, it is perceived as only suitable for low-power levels over short transfer distances, and it is limited in range to short gap distances (i.e., <1 mm) [25]. Furthermore, the realizable amount of coupling capacitance is restrained by the available area of the device, imposing a challenging design constraint.

In contrast, RF energy transfer has no such limitation. As the radiative electromagnetic wave cannot retroact upon the antenna that generated it at a distance of above $\lambda/2\pi$ [71], RF energy transfer can be regarded as a far-field energy transfer technique. The idea to use electromagnetic radiation for power transfer was pioneered by Nicolas Tesla in the end of the nineteenth century by conducting experiments on microwave technology. In 1931, he demonstrated the principle by wirelessly powering a light bulb located 5 m away from a power source of 15 kW in New York. It was until 1964, when W.C. Brown, who is regarded as the principal engineer of practical wireless charging, realized the conversion of microwaves to electricity through a rectenna [15]. In powering a model helicopter, Brown demonstrated the practicality of microwave power transfer. During the past decade, with the advancement in complementary metal-oxide-semiconductor (CMOS) circuit design, higher circuit density, and efficient energy storage, low-power transfer for powering wireless sensors began to attract increasing attention. Table 7.1 shows a comparison of the four main WET techniques.

Table 7.1 Contents of the wireless energy transfer (WET) techniques

WET technique	Field region	Propagation	Effective distance	Efficiency	Applications
RF energy transfer	Far field	Radiative	Typically from several meters to several kilometers (depends on distance, frequency, and sensitivity of the harvester)	0.4% at −40 dBm, >18.2% at −20 dBm, and >50% at −5 dBm input power, respectively [116]	Wireless sensor networks [132], wireless body networks [226]
Resonant inductive coupling	Near field	Non-radiative	From a few millimeters to a few centimeters	From 5.81 to 57.2% when frequency varies from 16.2 to 508 kHz	RFID tags, smart cards, electric vehicle [64, 129], cell phone charging [153], and inductive toothbrush [181]
Magnetic resonance coupling	Near field	Non-radiative	From a few centimeters to a few meters	From >90 to >30% with distance from 0.75 to 2.25 m [209].	PHEV charging [82], cellular phone [211]
Capacitive coupling	Near field	Non-radiative	Less than a millimeter	From 90 to 40% for air gaps varying from 0.1 to 1 mm [25].	Electric vehicle [26], contactless USB [205], rotating machinery [109]

7.2.1.2 Radiative RF Power Transfer

Radiative far-field wireless power transfer utilizes diffused RF/microwave as a medium to carry energy. Under idealized conditions, the received energy is governed by the *Friis' free space equation*:

$$p_r = G_t G_r \left(\frac{\lambda}{4\pi d}\right)^2 p_t, \tag{7.1}$$

where p_r is the received RF power, d the distance between the receiver and the source power p_t, G_t the source antenna gain, G_r the receiver antenna gain, and λ the wavelength of the carrier frequency.

Friis' equation is accurate for long-distance transmission such as satellite communications when there is negligible atmospheric absorption. However, these ideal conditions are almost never achieved in ordinary terrestrial communications due to obstructions, absorption, reflection, and more particularly in the case of wireless rechargeable sensor networks, to polarization loss and effects of power rectification and conversion. Therefore, empirical adjustments are sometimes necessary [159]. A more general form of average received power can be estimated as follows:

$$p_r \propto G_t G_r \left(\frac{\lambda}{d}\right)^n p_t. \tag{7.2}$$

However, to get useful results, further adjustments are usually necessary resulting in much more complex relations, such the Hata Model for Urban Areas [52].

Radiative RF power transfer can be further sorted into directive RF power beamforming (radiated toward a direction) and nondirective RF power transfer (radiated isotropically) [147]. For point-to-point transmission, beamforming transmits electromagnetic waves [225] and can improve the power transmission efficiency. However, the limitation of beamforming lies in the fact that the charger needs to know the exact location of the energy receiver. Due to the obvious limitation of this technique, RF wireless charging is usually realized through nondirective radiation.

7.2.1.3 RF Energy Harvesting System

An RFEH system consists of the following three elements:

- An RF energy source,
- An RF energy harvester, and
- A load used for the application.

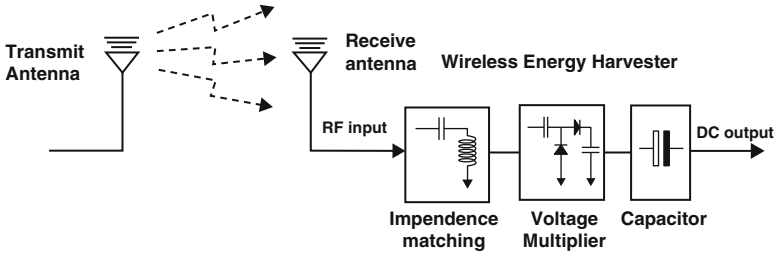

Fig. 7.2 RF energy harvesting (RFEH) system [108]

Figure 7.2 illustrates the block diagram of a typical RF energy harvester made of an antenna, an impedance matching circuit, a rectifier/filtering circuit, a voltage multiplier or boost converter, and a power management module that may include an energy storage unit. Each element of the system is described in the next sections.

7.2.2 RF Energy Sources: Dedicated Vs. Ambient

Unlike energy scavenging from environmental sources such as solar, wind, thermal, or kinetic energy, radiative radio-frequency must provide controllable, steady, and stable power over distance for the energy harvesters. For example, in a fixed RFEH Network, the harvested energy is predictable and relatively stable over time due to fixed distance [208].

RF energy can be generated and captured from two origins: intentional or dedicated RF sources, and unintentional or ambient RF sources. The former can be deployed to provide energy when predictable supply is expected, usually from license-free frequency bands of the radio spectrum. The latter refer to RF transmitters originally not intended for energy transfer, such as TV or radio towers, and Wi-Fi routers.

7.2.2.1 Dedicated RF Sources

Dedicated RF sources can be deployed to transmit in the license-free ISM frequency bands. However, these sources may incur high costs. Moreover, ISM-bands output power is limited by regulations, such as the FCC and the general ISM regulations, out of safety and health concerns related to radiations [66]. For example, in the 915 MHz ISM band, the maximum allowed power is 4 W [46]. Even at this highest setting, the received power at a moderate distance of 20 m is attenuated down to only 10 μW. Due to these restrictions, several dedicated RF sources may need to be set up in order to meet user's demand. Power beacons (PB) [63], which are stations deployed in an existing cellular network for recharging sensors and mobile devices,

illustrate such scenario by creating direct line-of-sight (LOS) links to mobiles. Sharp energy beams formed at PBs aim to counteract propagation loss and reduce power consumption of mobile devices, enabling close-to-free-space power transfer [56].

As the RFEH process with dedicated origin is fully controllable, it is suitable to support applications with QoS constraints. These sources can also be mobile, to travel and transfer power to rechargeable wireless network nodes. In [40–42, 103], different transmission schemes for mobile RF power transmitters are investigated for replenishing wireless sensor networks (WSNs).

7.2.2.2 Ambient RF Sources

Ambient RF sources refer to transmitters not intended for energy transfer. This energy is essentially free. Their transmission powers vary significantly, from around 10^6 W for TV tower, 10 W for cellular systems, to about 0.1 W for mobile devices and Wi-Fi systems. These sources can further be split into static and dynamic sources.

- Static ambient RF sources: provide relatively stable and foreseeable power over time, such as TV and radio towers. However, there could be long-term and short-term fluctuations due to service schedule (e.g., TV and radio) and fading, respectively. Their power density is usually very small. As a result, a high-gain antenna for many frequency bands and a rectifier designed for wideband spectrum should be considered. In [48], the performance analysis of a sensor powered by static ambient RF sources is performed using a stochastic geometry approach. An interesting finding is that when the distribution of RF sources exhibits stronger repulsion, larger RFEH rate can be achieved at the sensor.
- Dynamic ambient RF sources: work periodically or use time-varying transmit power (e.g., a Wi-Fi access point and licensed users in a cognitive radio network (CRN)). The energy collected from these sources has to be adaptive and possibly intelligent to search for harvesting opportunities in a certain frequency range. The study in [97] is an example of energy harvesting from dynamic ambient RF sources in a CRN. A secondary user can harvest RF energy from nearby transmitting primary users and transmit data when it is sufficiently far from primary users, or when the nearby primary users are idle.

7.2.3 General Architecture of an RF Energy Harvester

Most of the RF energy harvester circuit implementations use semiconductor-based rectifying elements to convert RF to DC power thanks to their low cost and small form factor. The semiconductors are either bridges of discrete components such as Schottky diodes or integrated circuits (ICs) based on CMOS technology with diode-connected transistors. Schottky diodes are regularly chosen when large amounts of

power are required, such as in space Solar Power Station (SPS) systems. Examples of Schottky diodes implementation of RF rectifiers are shown in Table 7.2, which include Avago Technologies' HSMS [10] and Skyworks' SMS [176] families of surface mount microwave detector diodes. On the other hand, CMOS technology is employed at low power because of lower parasitic values and customizable rectifiers that significantly increase the harvester efficiency. Furthermore, digital logic can be incorporated onto the same die [198]. Table 7.2 shows the circuit performance of some up-to-date designs.

Literature characterizes energy harvesting circuits from two different metrics: efficiency and sensitivity. Efficiency can be expressed as a total energy harvesting circuit efficiency or a power-conversion efficiency, while sensitivity is defined as the minimum power necessary to power an IC [198]. The efficiency of the energy scavenger depends on the performance and type of antenna, the accuracy of the impedance matching between antenna and load, and the power efficiency of the rectifier and voltage multiplier. On the other hand, sensitivity depends on the semiconductor technology used and the application, as different sensors and protocols may cause an increase in sensitivity value.

Table 7.2 RFEH circuits performance comparison [208]

Literature	Minimum RF input power	Peak conversion efficiency	Frequency	Rectifier element
Kocer and Flynn [86]	−19.58 dBm @ 1 V	10.90% @ −12 dBm	450 MHz	0.25 μm CMOS
Yi et al. [215]	N/A	26.50% @ −11 dBm	900 MHz	0.18 μm CMOS
Mandal and Sarpeshkar [110]	−17.70 dBm @ 0.8 V	37% @ −18.7 dBm	970 MHz	0.18 μm CMOS
Shameli et al. [166]	−14.10 dBm @ 1 V	N/A	920 MHz	0.18 μm CMOS
Le et al. [94]	−22.60 dBm @ 1 V	30% @ −8 dBm	906 MHz	0.25 μm CMOS
Yao et al. [213]	−14.70 dBm @ 1.5 V	15.76% @ −12.7 dBm	900 MHz	0.35 μm CMOS
Salter et al. [156]	−25.50 dBm @ 1 V	N/A	2.2 GHz	130 nm CMOS
Vera et al. [199]	N/A	42.1% @ −10 dBm	2.45 GHz	SMS 7630
Papotto et al. [138]	−24 dBm (4 μW) @ 1 V	11% @ −15 dBm	915 MHz	90 nm CMOS
Seunghyun and Wentzloff [160]	−32 dBm @ 1 V	N/A	915 MHz	130 nm CMOS

(continued)

Table 7.2 RFEH circuits performance comparison [208]

Literature	Minimum RF input power	Peak conversion efficiency	Frequency	Rectifier element
Masuch et al. [112]	N/A	22.70% @ −3 dBm	2.4 GHz	130 nm CMOS
Scorcioni et al. [161]	−17 dBm @ 2 V	60% @ −3 dBm	868 MHz	0.13 μm CMOS
Taris et al. [188]	−22.50 dBm @ 0.2 V −11 dBm @ 1.08 V	N/A	900 MHz	HSMS-2852
Sun et al. [184]	−3.20 dBm @ 1 V	83% @ −1 dBm	2.45 GHz	HSMS-2852
Karolak et al. [75]	−21 dBm @ 1.45 V −21 dBm @ 1.43 V	65.20% @ −21 dBm 64% @ −21 dBm	900 MHz 2.4 GHz	13 nm CMOS
Roberg et al. [155]	40 dBm @ 30 V	85% @ 40 dBm	2.45 GHz	SMS-7630
Nintanavongsa et al. [130]	−10 dBm @ 1 V	10% @ −10 dBm	915 MHz	HSMS-2852
Franciscatto et al. [49]	0 dBm @ 1.2 V	10.9% 70.40% @ 0 dBm	2.45 GHz	HSMS-2852
Scorcioni et al. [163]	−16 dBm @ 2 V	58% @ −3 dBm	868 MHz	130 nm CMOS
Stoopman et al. [178]	−26.30 dBm @ 1 V	31.50% @ −15 dBm	868 MHz	90 nm CMOS
Wang and Mortazawi [204]	−39 dBm @ 2.5 V	N/A	AM freq	N/A
Thierry et al. [194]	−10 dBm @ 2.2 V −20 dBm @ 0.4 V	N/A	900 MHz 2.4 GHz	HSHS-2852
Nimo et al. [128]	−30 dBm @ 1.9 V	55% @ −30 dBm	13.56 MHz	HSMS-286B
Alam et al. [3]	−15 dBm @ 0.55 V	N/A	2.45 GHz	HSMS-2850
S. Agrawal et al. (2014)	−10 dBm @ 1.3 V	75% @ −10 dBm	900 MHz	HSMS-2852
Stoopman et al. [179]	−27 dBm @ 1 V	40% @ −17 dBm	868 MHz	90 nm CMOS

7.2.3.1 Antenna Module

The antenna is the first stage of an RFEH and is responsible for capturing sufficient signals that would further be converted into voltage. The main parameters to consider in designing such an antenna are the size, gain, and the frequency it is tuned to. The average received input RF power P_{RF} depends on the input power density S and the antenna's aperture A_{real} (equivalent area which intercepted the incident power density), expressed as follows:

$$P_{RF} = S \times A_{real}. \tag{7.3}$$

When a receiving antenna intercepts incident electromagnetic waves, a voltage V_{oc} is induced across its terminals. To a generator feeding a transmitting antenna, the

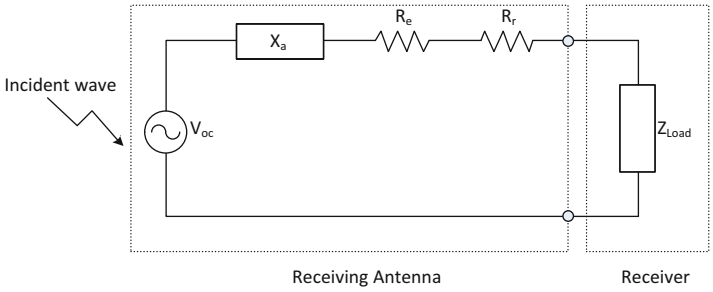

Fig. 7.3 Antenna equivalent circuit

antenna appears as a load. In the same manner, the receiver circuitry connected to a receiving antenna's output terminal will appear as a load impedance. The electrical model of an antenna can be represented by an equivalent circuit as in Fig. 7.3, where X_a is the antenna reactance, R_l the loss resistance (related to the material used), R_r the wave radiation resistance, and Z_{load} the input impedance of the receiver.

The antenna impedance Z_a is given by:

$$Z_a = (R_l + R_r) + jX_a = R_a + jX_a. \tag{7.4}$$

Common values of Z_a are 300 Ω (closed dipole antenna), 75 Ω (open dipole antenna), and 50 Ω (wireless systems). The antenna reactance X_a depends on the antenna structure; it is usually inductive for a loop antenna and capacitive for a patch antenna [140]. Various antenna types for electromagnetic energy harvesting have recently been proposed: dipole [2], Yagi-Uda [78, 185], microstrip [7, 172], monopole [51, 221], loop [95, 133], patch (coplanar, L-shape, U-shape, E-shape, start shape, circular, or square) [154], bow tie [23, 121], and spiral antenna [28]. For a detailed comparison of existing antenna structures, readers can refer to [222].

A trade-off exists between antenna size and performance, hence the main design challenge is to obtain high conversion efficiency. For example, in order to increase the conversion efficiency, several broadband antennas, large antenna arrays, and circularly polarized antennas are encountered in the existing literature:

1. Broadband antennas receive relatively high power of high frequency (on order of 1 GHz) from various sources [126, 200, 214, 216, 220].
2. Antenna arrays increase incident power delivered to the diode for rectification. It is an effective mean of increasing the receiving power but a trade-off arises between the antenna size and the radiation gain [11].
3. Circularly polarized antennas offer power reception with less polarization mismatch.

The antenna module can be designed to work on either single frequency or multiple frequency bands, in which the application can harvest from a single or multiple sources simultaneously. Research efforts have been made for narrow-band

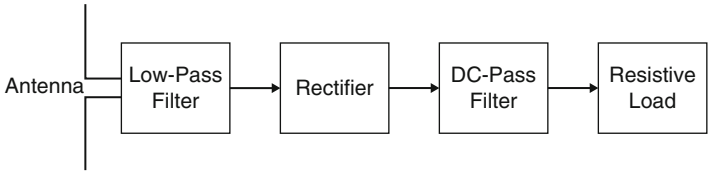

Fig. 7.4 Block diagram of a rectenna

antenna (typically from several to tens of MHz) designs in a single band [3, 8, 9], in dual bands [6, 99, 223] as well as in triple bands [30, 79, 111]. The antenna module can also include a rectifying circuit, as detailed in the next subsection (Fig. 7.4).

Rectenna

A rectenna is a particular type of antenna that rectifies incoming electromagnetic waves into DC current [170]. Over the last century, the development of rectennas for wireless power transmission and SPS transmission [169] has achieved great success in implementing specific functions and applications as diverse as Radio Identification (RFID) tagging systems, WLANs, WiMax, cognitive radio systems, and wireless body area networks (WBAN).

There are two approaches to achieve high conversion efficiency with rectennas. The first option is to collect the maximum power and deliver it to the rectifying diode, and the second one is to suppress the harmonics generated by the diode that reradiate from the antenna as the power lost. Among various types of antenna used in rectennas, microstrip antennas, and especially patch, are gaining popularity in wireless applications owing to their low profile, light weight, simple, and inexpensive to manufacture using modern printed-circuit technology. The other reason for the wide use of patch antenna is their versatility in terms of resonant frequency, polarization, pattern, and impedance when particular patch shape and mode are chosen [170].

7.2.3.2 Impedance Matching

Following the antenna in an RF energy harvester, the impedance matching network performs impedance transformation to assure maximum power delivery by reducing the transmission loss from antenna to rectifier, and increasing the voltage gain at the rectifier input [1].

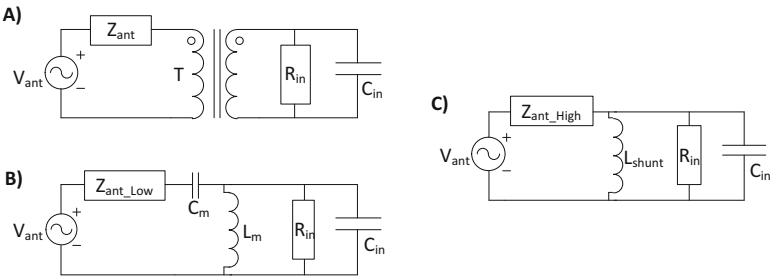

Fig. 7.5 Matching circuits: (**a**) transformer, (**b**) shunt inductor, and (**c**) LC network [143]

A matching network is a resonator circuit operating at the designed frequency and is usually made with reactive components such as coils and capacitors that are not dissipative. Several topologies of matching circuits exist; three main ones widely used are shown in Fig. 7.5.

Maximum power transfer can also be realized when the impedance at the antenna output and the impedance of the load are conjugates of each other, thus eliminating the need of an impedance matching network. However, many energy harvesting circuits are made up with nonlinear devices such as diodes, thus exhibiting a nonlinearity. This implies that the impedance of the energy harvesting circuit varies with the amount of power received by the antenna [130]. For example in [47], a method to dynamically maximize the delivered power from an RF source to a receiving antenna is proposed using a finite number of discrete capacitors. The control of the dynamic impedance matching is assigned to a Control Unit that runs an algorithm to estimate the input power of the circuit and then set the capacitance with the best value in the impedance matching network.

7.2.3.3 Rectification and Filtering

The function of a rectifier is to convert the AC current induced in the antenna by received RF signals into a DC voltage. Two topologies for signal rectification exist:

1. Half-wave rectification: either the positive or negative half of the AC wave is passed, while the other half is blocked. Rectifiers yield a unidirectional but pulsating direct current; and
2. Full-wave rectification: converts the whole of the input waveform to one of constant polarity (positive or negative) at its output. Full-wave rectification converts both polarities of the input waveform to pulsating DC (direct current) and yields a higher average output voltage.

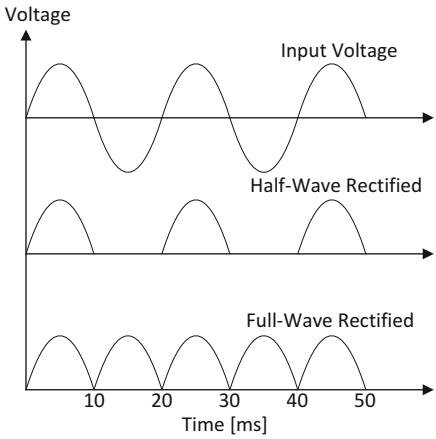

Fig. 7.6 Half-wave and full-wave rectification

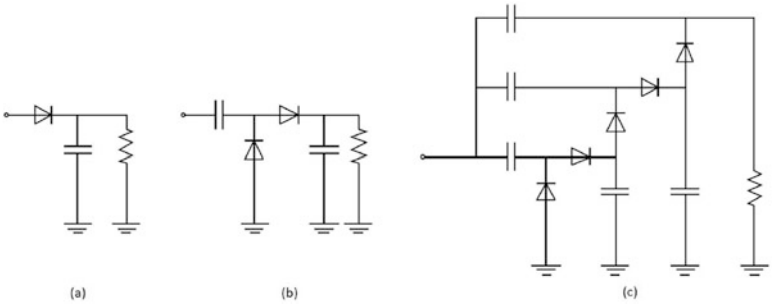

Fig. 7.7 Types of rectifiers circuits: (**a**) Basic rectifier, (**b**) voltage double, and (**c**) voltage multiplier

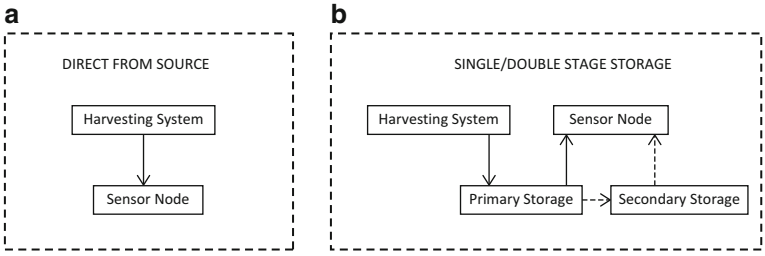

Fig. 7.8 Energy harvesting architectures with and without storage capability [183]. (**a**) Harvest–use, (**b**) Harvest–store–use

Half-wave rectifiers produce far more ripple than full-wave rectifiers, and much more filtering is needed to eliminate harmonics of the AC frequency from the output (Figs. 7.6, 7.7, and 7.8).

As mentioned in Sect. 7.2.3.1, a single diode in a serial configuration that also acts as a half-wave rectifier is the most common rectifying circuit. Generally, higher

Table 7.3 Comparison of rectifier circuits

Rectifier type	Structure	Topology
Basic (single-stage) rectifier	Single diode connected in series with a load. A capacitor may be added as a filter to smoothen the ripple in the output	Half-wave or full-wave
Voltage doubler	Rectifies the full-wave peak-to-peak voltage of the incoming AC signal using two stages to approximately double up the DC voltage	Full-wave. Villard circuit (single shunt), Greinacher circuit (dual diode), bridge (Delon) circuit [29, 88], and Dickson charge pump
Voltage multiplier	Multistage rectifier to further increase the voltage using a network of capacitors and diodes	Full-wave. Cockcorft–Walton circuit [83, 86], multiplier resonant [68, 145], Villance multiplier [127], and boost converter [87]

conversion efficiency can be achieved by diodes with lower built-in voltage such as Schottky diodes. CMOS technology can be deployed as an alternative to diodes. In [93, 175, 217], floating-gate devices were designed to passively reduce the threshold voltage of the rectifier circuit. Furthermore, the floating-gate rectifier technique allows the threshold of the rectifier circuits to be programmed and optimized to operate over a wide range of output current.

When the received power is not high enough, the rectifier input needs to be amplified in order to power the circuit. In these cases, a rectifier circuit that includes a multiplier may be used. There exist three main options of rectifier circuit designs: basic rectifier using a single diode and capacitor, voltage doubler with two diodes and capacitors, and voltage multiplier. Table 7.3 shows a comparison of the rectifiers.

The RF signal source and received power dictate the type of rectification circuit to implement. Different values of DC voltage could be obtained with the same circuit but different RF sources. The multiplier is usually formed by different stages, each with diodes and capacitors. The higher the number of stages, the higher the voltage output. However, because diode loss increases with the stage number, the system efficiency is affected [140]. The measure to quantify the effect of the multiplier is its efficiency η_{rect}, which depends on input power P_{inrect} and output power P_{outrect}.

$$\eta_{\text{rect}} = \frac{P_{\text{outrect}}}{P_{\text{inrect}}}. \tag{7.5}$$

7.2.3.4 Power Management Module

The power management module decides whether to store the electricity obtained from the scavenger or to use it for the application immediately. It can adopt two methods to control the incoming energy flow: harvest–store–use and harvest–use.

The harvest–store–use method is the conventional architecture in most energy harvesting systems. Here, the network node is equipped with an energy storage device (battery or supercapacitor) that stores the converted electricity. Whenever the collected energy is greater than the node's consumption, it is stored for future use [219]. The storage component itself may be single-stage (primary) or double-stage (primary and secondary). Secondary storage is a backup storage for situations when the primary storage is exhausted [69]. However, harvest–store–use method suffers from several issues that will be described in Sect. 7.2.3.5.

In the harvest–use method, the harvested energy is directly used to power the application or network node with no need of storage and voltage converter [96]. Therefore, for a network node to operate normally, the converted electricity has to constantly exceed its minimum energy demand. Otherwise, the node will be disabled. Some energy management techniques for harvest–use such as *energy neutral operation* that adjusts the duty cycle of operation to the predicted rate of harvest, *time-switching approach* where a sensor node harvests energy for a percentage of time frame and transmits data for the rest of the time, and *converter-less operation* to provide almost constant voltage directly to the target device without using a voltage converter were proposed in [74, 171], and in [96], respectively.

In both schemes, the aim is to create a balanced energy management between the RF source and the load in order to avoid energy deficiency in a network. Most of the power management efforts in the literature mainly focus toward efficient node's energy consumption. The aim is to use algorithms, which take into account the limited RF energy supply constraints as well as to develop applications with minimum energy consumption. Some strategies include duty cycling [168], energy driven [22], adaptive sensing rate [120], event driven [158], data compression [119], data prediction [12], mobility based [210], and fuzzy control [5].

7.2.3.5 Energy Storage

Energy storage is of paramount importance in energy harvesting. Depending on the level and duration of storage, proper technique has to be selected. There are several technologies that vary in properties such as capacity, energy density, power density, number of charge cycles, leakage, equivalent series resistance (ESR), lifetime, temperature effects, etc. Because of these wide variations, it is important to understand the differences between technologies and choose a storage device that is well-suited for a given application [150].

For example, in traditional RFEH networks, it is common practice to use rechargeable batteries for repositing energy owing to their high-energy density, which is the energy extracted per unit volume (volumetric: Wh/l) or mass (gravimetric: Wh/kg). In contrast, power density is extracted from a battery per unit volume (W/l) or mass (W/kg) and mainly depends on the internal impedance of the battery. Some batteries are specially designed to promote power density through reduced internal impedance. Batteries designed to improve power density have less energy

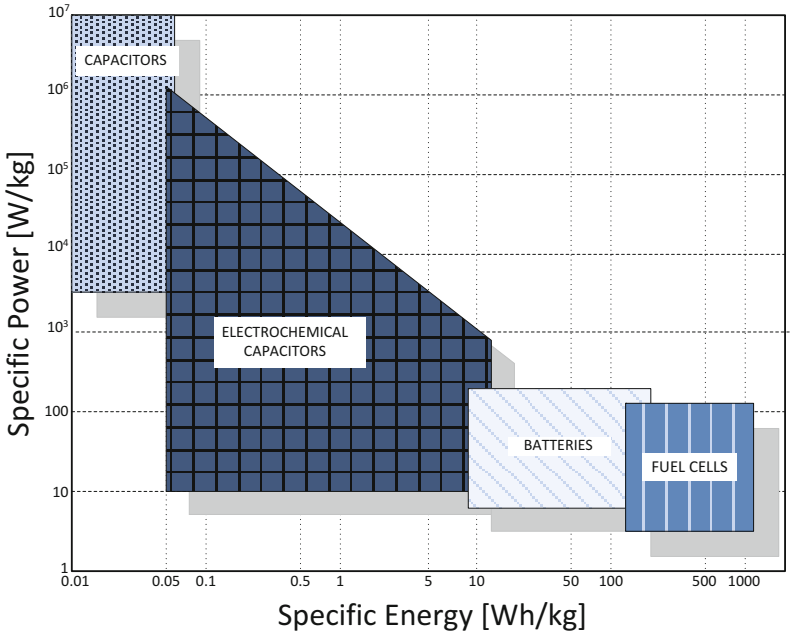

Fig. 7.9 Power density vs energy density (Ragone plot) of energy storage units [39]

density for the same battery size (and vice versa). Figure 7.9 shows a generic graph of the power density versus the energy density of storage units. As noticed in the figure, power density decreases with increasing energy density.

There are essentially two devices known for storing harvested RF energy: supercapacitors and batteries. In this section, we discuss their general properties (Fig. 7.10).

Batteries

Batteries extract electrical power from a chemical reaction. They comprise of one or more basic electrochemical units known as cells, which are connected in series or in parallel to obtain the desired voltage and capacity. Each cell contains a negative electrode (anode), a positive electrode (cathode), and an ionic conductor (electrolyte). The anode and cathode are physically isolated by the electrolyte which provides the medium for charge transfer (via ions) inside the cell.

The most common rechargeable batteries for autonomous low-cost, low-power wireless sensors are Nickel Cadmium (NiCd), Nickel metal hydride (NiMH), and Lithium based (Li-ion or Li polymer). The performance of these batteries systems is compared in Fig. 7.11.

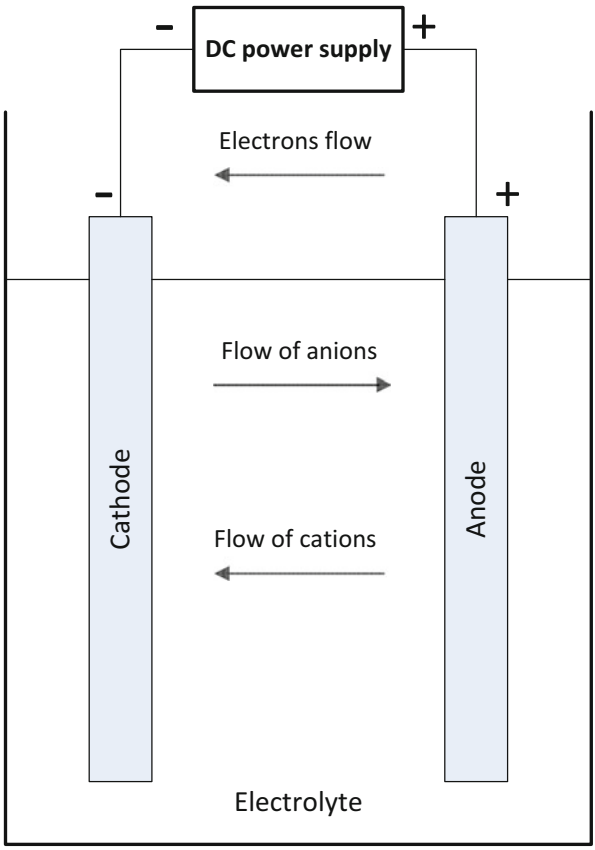

Fig. 7.10 Electrochemical cell at discharge [101]

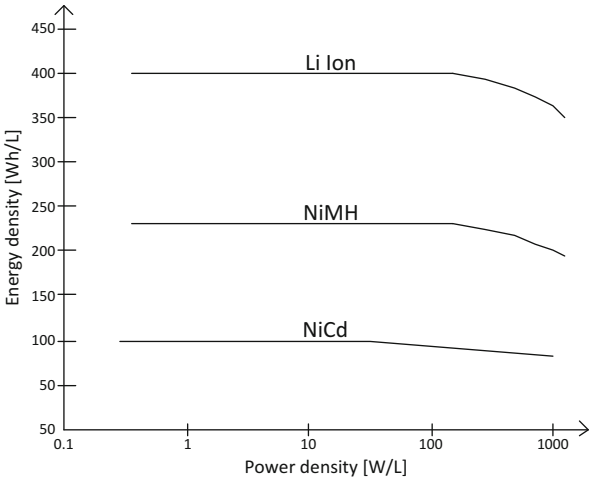

Fig. 7.11 Comparison of rechargeable 14500 Li-ion, AA-size NiMH, and NiCd batteries at 20 °C [101]

1. NiCd batteries use nickel hydroxide $Ni(OH)_2$ for the cathode, Cd as the anode, and an alkaline Potassium hydroxide (KOH) electrolyte. Their small size and high discharge capacity made them suitable for portable tools and other consumer applications. In addition, their cells, with nominal potential of 1.2 V, are sealed and utilize a recombinant system [37] to prevent electrolyte loss and extend the useful life. Once the battery of choice for low-power products, they have lost market share to NiMH and Li-ion batteries which have superior energy density and performance characteristics.
2. The components of NiMH batteries include a cathode of nickel hydroxide, an anode of Hydrogen absorbing alloys, and a KOH electrolyte, which are collectively more benign than the active chemicals used in rival Lithium batteries. Their cell voltage is 1.2 V. The cells operating temperature range has been extended to over 100 °C, far exceeding the range currently achievable by Lithium cells. However, they suffer from high discharge rate and much lower energy density.
3. Typical Lithium-ion cells use Carbon for their anode and Lithium Cobalt dioxide or a Lithium Manganese compound as the cathode. The electrolyte is usually based on a Lithium salt in an organic solvent. Cell voltage is typically 4.2 V. They have many attractive performance advantages which make them ideal for low-power applications such as mobile phones, laptops, cameras, sensors, and other consumer electronic products; and as well as higher power applications such as automotive and standby power.

Internal impedance in batteries depends on factors such as cell size and construction, number of connected cells, chemistry, wiring, and contact type [17]. Manufacturers datasheet often provide discharge profile graphs as well as AC impedance plots at a specific frequency. However, the data found in these plots are not sufficient to predict a battery's voltage behavior under pulsed loads, such as that of WSNs. Thus, the prediction of the transient response of the supply voltage of low-power sensors requires a suitable electrical model like the Min and Rincon-Mora model [20]. Such representation can be useful for predicting the runtime of autonomous sensors and estimating the useful lifetime of the battery.

Many of today's WSNs rely on batteries as the primary power source. Batteries are frequently cited as the primary limiting factor in the lifetime of WSNs. Due to the limited number of recharge cycles and their inability to hold full charge for long duration, batteries often require replacement after 1–2 years. Such recurring maintenance cost is very expensive or prohibitive for thousands of deeply embedded nodes, which may also be spread out in remote locations. In both cases, the battery is the primary limiting factor to operating maintenance-free for several years at nontrivial data rates [173]. In addition to their low-power density and tendency to leak, explode, or fail abruptly, batteries are losing favor among researchers [150]. Removing the battery altogether and storing energy solely in a supercapacitor is now an alternative option for achieving longer life operation.

Supercapacitors

Supercapacitors are not only an excellent compromise between "electronic" or "dielectric" capacitors (such as ceramic and tantalum) and rechargeable batteries but are also a valuable technology for providing a unique combination of characteristics, particularly very high-energy, power, and capacitance densities. They have been found to be a good choice of energy storage for several reasons. As shown in the Ragone plot of Fig. 7.9, supercapacitors are placed between capacitors and batteries, indicating that they have the advantage of power density higher than batteries as well as energy density higher than ordinary capacitors [89]. They do not undergo irreversible chemical reactions, thus tolerate many more charge and discharge cycles [123]. They exhibit much longer lifetime than batteries with minimal environmental impact, accept and deliver charge much faster, with less complex charging circuitry [206].

Supercapacitors are governed by the same basic principles as conventional capacitors. However, they incorporate electrodes with larger surface areas and much thinner dielectrics between the electrodes [57], which lead to increase in both capacitance C and energy E as seen in the following equations:

$$C = \frac{Q}{V}, \tag{7.6}$$

where Q is the stored positive charge and V the applied voltage;

$$E = \epsilon_0 \times \epsilon_r \times A \times D, \tag{7.7}$$

where ϵ_0 is the dielectric constant (or permittivity) of free space, ϵ_r the dielectric constant of the insulating material between the electrodes, A the surface area of each electrode, and D the distance between the electrodes.

A block diagram of supercapacitors is given in Fig. 7.12. Various schematics of supercapacitors have been proposed through equivalent circuit models such as the RC model, the parallel-branch model, the transmission-line model, the multibranch model, and the multistage ladder model [118, 167].

Based upon current R&D trends, supercapacitors can be divided into three general classes: electrochemical double-layer capacitors, pseudocapacitors, and hybrid capacitors. A graphical taxonomy of the different classes and subclasses of supercapacitors is presented in Fig. 7.13.

The main criteria for selecting a supercapacitor are the values of capacitance, leakage current, and ESR. Since the amount of energy to be accumulated depends on the capacitance value, the larger it is, the higher the amount of energy to be gained. However, it has been found that supercapacitors with larger capacitance undergo larger losses in stored energy due to leakage [212], which is the current required to keep a capacitor charged at the rated voltage [124] for 72 h. Thus a supercapacitor with large capacitance will not only take longer to charge but also discharge faster. This implies that the number of operations that could be performed at a particular

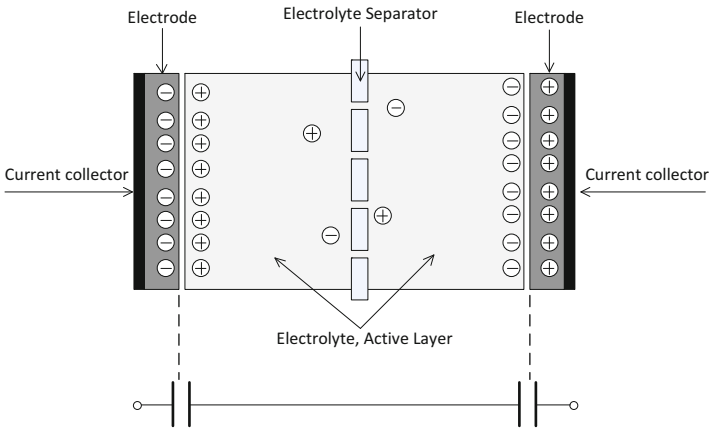

Fig. 7.12 Schematic of an electrochemical double-layer capacitor

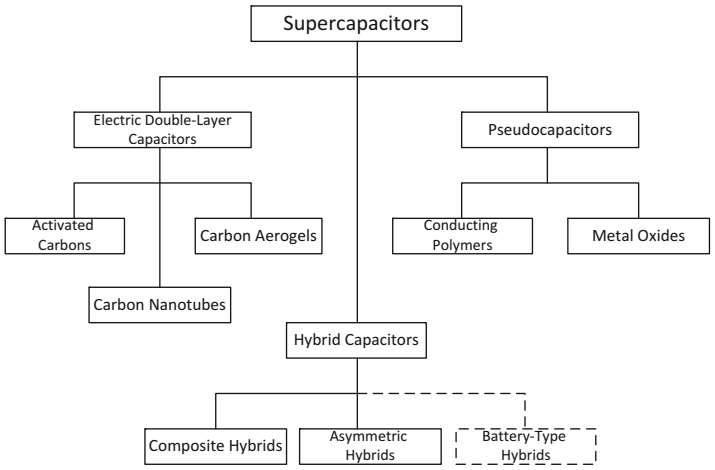

Fig. 7.13 Taxonomy of supercapacitors [57]

rate would be less than the number of operations that could be performed by a lower capacitance value, at the same rate. This could lead to scenarios where the rate at which a node performs operations has to be increased in order to be comparable to a low capacitance storage device. On the other hand, a small capacitance would not be adequate to store enough energy. Hence, it is wise to choose an appropriate value based on the application's requirements or on the rate of collected energy [18].

The major drawback of supercapacitors is their reported high leakage (also referred to as self-discharge), which has been shown to increase exponentially with terminal voltage (energy stored) [114], or to internal charge redistribution [113]. Some researchers suggest that loss of charging efficiency due to internal charge distribution can be partially offset if the supercapacitor undergoes more

than three cycles of a fixed pattern of charging [16]. However, others suggest that leakage is higher in supercapacitors that go through frequent charge cycles [113]. Another disadvantage is their ESR that prevents from achieving power densities closer to theoretical limits. Thus, determining how to lower the ESR of supercapacitors is becoming an important area of research. Several methods for reducing the ESR have already been developed, including polishing the surface of the current collector, chemically bonding the electrode to the current collector, and using colloidal thin-film suspensions [57]. Finally, elevated temperatures have a direct effect on supercapacitors ESR and consequently on their lifetime. While measurements indicate that supercapacitor lifetime degrades by a factor of 2 with a 10 °C rise in temperature [90], it has also been shown that the temperature of supercapacitor banks increases exponentially after being charged for a given duration of time at constant current [24].

Hybrid Storage

In certain scenarios, it is not advisable to use batteries in energy harvesting applications because of their internal impedance. Similarly, drawbacks in supercapacitors such as high leakage are not found in batteries. Thus, when an application requires high power density as well as high-energy density, it is possible to employ a mixture of both devices. Storage units comprising of a battery and a supercapacitor operating in tandem are known as *hybrid systems*.

There are extensive works done with hybrid-storage units to prolong the runtime and life extension of storage units under pulsed load [34, 61, 69, 177]. However, their advantages have not been thoroughly assessed and tested in low-power WSNs which operate with pulsed load currents in the order of tens of milliamperes. In [142], a comprehensive theoretical analysis provides design guidelines for choosing a supercapacitor in parallel with a battery. The analysis was supported by experiments comparing the performance between two low-capacity batteries and their hybrid-storage unit counterparts when using an electronic load as a pulsed current sink. It was proven that the hybrid-storage units always achieved a higher runtime and the sensor node runtime was extended by 16%.

Likewise, in [187], a hybrid system was further optimized by adding a DC–DC converter coupled with a supercapacitor to extend the battery autonomy of ultralow power WSNs with minimal operating voltage of 2.1 V or less. The basic idea was to supply power to the sensor node from the supercapacitor with the DC–DC converter disabled, and enabling it on demand for efficiently recharging the supercapacitor. Several tests were conducted with two low ESR supercapacitors, yielding a battery autonomy extension of at least 19%.

7.3 Dedicated RF Energy Harvesting Applications and Products

Dedicated RFEH systems, also referred to as "RF power-on-demand" or "anticipated" power sources, consist of a power source or charger that intentionally utilizes license-free ISM bands to transmit power, and a receiver that captures the transmitted signals to convert to a DC voltage in order to operate. This can be achieved either via directive RF power beamforming or via nondirective RF power transmission. Therefore, the transmitter can consist of either a fixed device or a mobile device that periodically moves and transfers RF energy to network nodes [210]. The transmitter also may or may not be oriented toward a receiver, i.e., with LOS or not. Similarly, the receiving device may or may not be mobile. Applications of RF power-on-demand systems include WSNs, WBANs in the healthcare industry, and RFID tags. Additionally, RFEH can be used to provide charging capability for a wide variety of low-power mobile devices such as electronic watches, MP3 players, wireless keyboard, and mouse, as most of them consume only microwatts to milliwatts range of power.

WSNs are by far the most widely used applications of RF-powered energy scavenging. A variety of wirelessly powered sensors have been reported or proposed in the past decade for monitoring data such as temperature, conductivity, vibration, humidity, luminosity, etc. Sensing in adverse conditions, such as in toxic manufacturing, would benefit from maintenance-free wireless sensors that gather typically low-duty cycle data. Furthermore, there are a lot of practical opportunities for low-cost residential and commercial building sensors with no need of battery replacements for knowing environmental parameters such as occupancy, humidity, temperature, light level, water level, air flow in pipes, air quality, appliance activity, etc. Examples of WSNs powered with anticipated RF sources can be found in [4, 33, 44, 139, 141]. In [77, 134, 164], multi-hop RF-powered WSNs are demonstrated through experiments.

In the healthcare industry, many existing implanted devices are powered inductively, which requires proximity of the powering device to the patient and is often uncomfortable. Recently, it has been shown that loosely coupled coils at farther range can be effective for powering cardiac implants [152]. Some implanted devices could benefit from far-field powering, e.g., during the night when the person is confined to the bedroom, which can increase the battery life and time between surgical battery replacements. Thus, low-power medical devices can achieve real-time work-on-demand power from anticipated RF sources, which further enables a battery-free circuit with reduced size. Examples of body device implementations can be found in [148, 174, 207].

Finally, another application that has caught intensive research investigation is RFID, widely used for identification, tracking, and inventory management [230]. As depicted in Fig. 7.14, these devices can be classified based upon the presence or absence of radio transmitter or battery [32]:

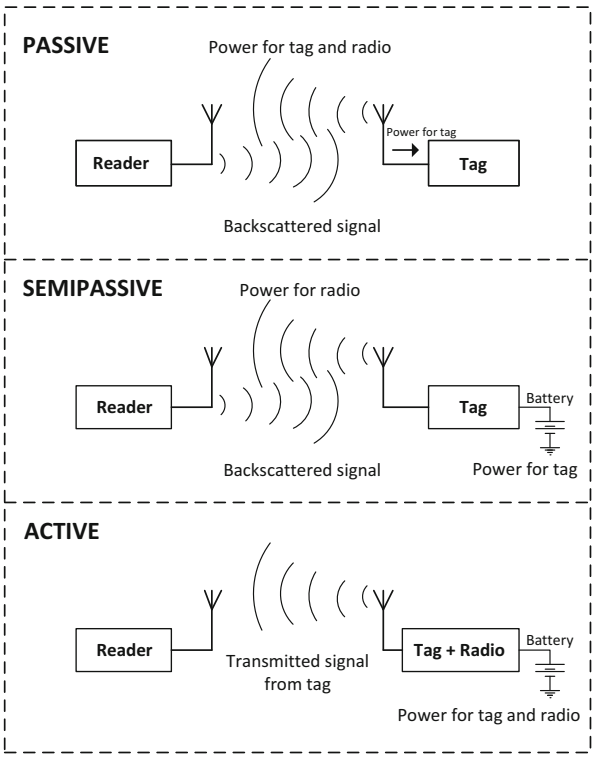

Fig. 7.14 Classification of Radio Identification (RFID) systems [32]

1. Passive tags: with no independent source of electrical power to drive the circuitry, they have no radio transmitter of their own and rely instead on the received power from a reader to be turned on as well as sending information through amplitude modulation (AM). In exchange to their simplicity, small size, and low cost, their read range is very short and limited, and their computational power is minimal.
2. Semi-passive tags: also known as battery-assisted passive tags, they incorporate a battery to power their circuitry but still use backscattered communications [58] for uplink communications, also via AM modulation. They are typically used in automobile tolling applications. The trade-off is their increase in size, cost, and maintenance requirements.
3. Active tags: configured as conventional bidirectional communication devices, they include both an internal power source and a conventional transmitter tuned to specific frequency channels via frequency-division multiplexing (FDM) in the presence of other tags. They naturally suffer from the same trade-offs as their semi-passive counterparts.

Recent developments in low-power circuit and energy harvesting technology can extend the lifetime and operation range of conventional RFID tags. Instead of relying on the readers to activate their circuits passively, RFID tags can harvest RF

energy and perform communication actively [104]. Consequently, RFID technology is evolving from simple passive tags to smart tags with newly introduced features such as sensing, on-tag data processing, and intelligent power management [135]. Research progress has covered the designs of RFID tags with energy harvesting in rectenna [62], rectifier [73], RF-to-DC converter [161], charge pump [27], and power harvester [19]. Despite the stellar advancement made in the RFID technology, several issues such as reliability, security, speed of communications, and evolution to a global standard still need to be addressed appropriately.

In the rest of the section, we present the major considerations to take when designing a dedicated RFEH system, describe some prototype implementations as well as commercial products, and finally expand with potential future applications.

7.3.1 Design Considerations

Depending on the electromagnetic transmission model, the energy source and receivers must be designed and possibly adapted for maximum efficiency. This includes selecting and assessing the frequency range to transmit, the adequate antenna type, the power limitations and management, and the storage technologies.

7.3.1.1 RF Energy Source Design Constraints

Most anticipated RF power sources transmit in one of the common ISM bands (center frequencies of 433 MHz, 915 MHz, 2.4 GHz, or 5.8 GHz). These bands however do not allow for high power transmissions as they are limited by government regulatory bodies such as the FCC [46] in the USA due to concerns over interference, safety, and health. For example, in the 915 MHz band, the maximum threshold is 4 W. Even at the highest setting, the received power at a moderate distance of 20 m is attenuated down to only 10 μW [208]. Due to this limitation, several dedicated RF sources may need to be deployed to meet the user demand.

Proper selection of the antenna is crucial. Several parameters must be taken into account such as radiation pattern, gain, power rating, size, distance between transmitting antenna and receiving antenna, etc. Radiation pattern depends on the type of antenna selected. Most antennas show a pattern of "lobes" or maxima of radiation. In a directive antenna, shown in Fig. 7.15, the largest lobe in the desired direction of propagation is called *main lobe*. The other lobes are called *side lobes* and usually represent radiation in unwanted directions. On the other hand, in the radiation pattern of a simple omnidirectional antenna, the antenna is at the center of the "donut" or *torus*. Radial distance from the center represents the power radiated in that direction. Common types of low-gain omnidirectional antennas are the whip antenna, vertically oriented dipole antenna, horizontal loop antenna, and the halo antenna.

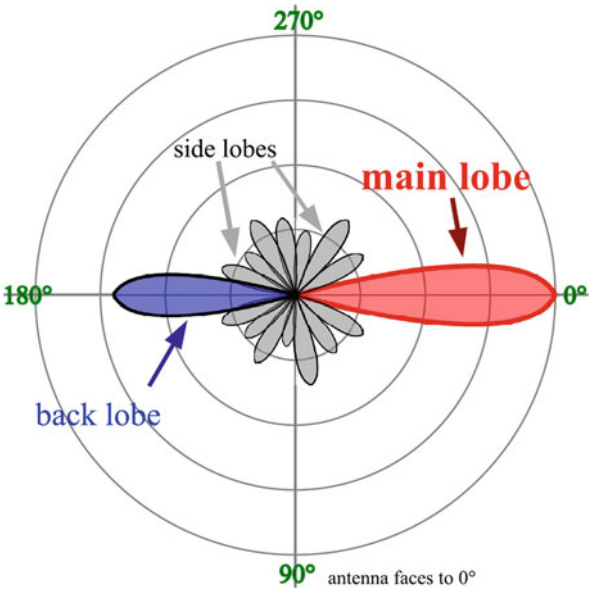

Fig. 7.15 Antenna radiation patterns [196]

The antenna gain is not a mere amplification of the RF signal, but rather a measure of the focus of the signal (degree of directivity of the antenna's radiation pattern). Hence, a high-gain antenna will radiate most of its power in a particular direction, while a low-gain antenna will radiate over a wider angle.

7.3.1.2 RF Energy Harvester Design

The antenna selection of the energy harvester should be identical to the one used by the RF source. Because antenna efficiency is related to the frequency, dedicated RF energy harvester usually has an antenna with small bandwidth, in contrast with ambient RFEH where a wideband receiver antenna can be used to capture signals from multiple sources or multiple frequency bands.

Good matching circuits are essential to achieve maximum power and improve efficiency. For financial reasons, RFID tags and WSNs use shunt inductors and LC networks as matching networks instead of transformers [140]. Moreover, it is recommended for high impedance antennas like dipole antennas to use parallel coils [143], whereas small impedance antennas may employ LC networks for ambient RFEH (e.g., Wi-Fi antenna), or when the available power is low [93].

Choice of rectification circuits depends on the strength of the RF signal and power received, since different values of DC voltage could be obtained with the same circuit and different RF sources. When the distance from the RF source is far and the received power is not high enough, the rectifier input needs to be amplified in order to power the circuit (most WSNs and RFID tags require at least 3.3 V).

The power management design is rendered easier to accomplish for a dedicated energy transmitter, thanks to a predictable and stable power transmission. Similarly, more energy is expected to be stored within a shorter period of time than in ambient RFEH, thus requiring sufficient storage capability.

7.3.2 Commercial Products

Besides the well-known RFID systems, there exist few commercial products for RF wireless power transfer aimed for WSNs and WBANs. In this subsection, we introduce some manufacturers and their products.

7.3.2.1 Powercast Corp.

Built in 2003, Powercast Corp. [149] brings remote, wireless power capability to micro-power devices such as wireless sensors, data loggers, and active RFID tags. The company's energy scavenging technology provides wireless power by converting electromagnetic signals into a DC power, thus reducing or eliminating battery replacement by trickle charging rechargeable batteries, or using supercapacitors and thin-film energy cells. Their products address existing and future markets by providing a full suite of FCC approved products:

- Powerharvesters receivers: chips that harvest directive or ambient RF energy and convert to DC power. These chips include the P1110 Powerharvester Receiver (short-range, higher power), the P2110B Powerharvester Receiver (long range), and the PCC110 or PCC210 chipsets (for OEM volume applications).
- Powercaster transmitter TX91501: provides a reliable source of 915 MHz wireless energy to power, over a distance, devices equipped with Powerharvester receivers. It comes in two versions that output either 1 or 3 W equivalent isotropically radiated power (EIRP) with a transmitter ID broadcast.

In addition, the company supplies development kits and evaluation boards to enable simple and fast testing and prototyping with RF-based wireless power technology. Figure 7.16 shows the *P2110-EVAL-01 lifetime power energy harvesting development kit for wireless sensors*.

7.3.2.2 Texas Instruments

A more renowned company, Texas Instruments [189], introduced in December 2014 its new family of sensor transducers designated *RF430FRL15XH*. The devices are the first sensor transducers designed to operate over the traditional 13.56 MHz radio spectrum and powered by scavenging energy from a nearby NFC-enabled reader or smartphone. It is advertised to be implemented in applications ranging from

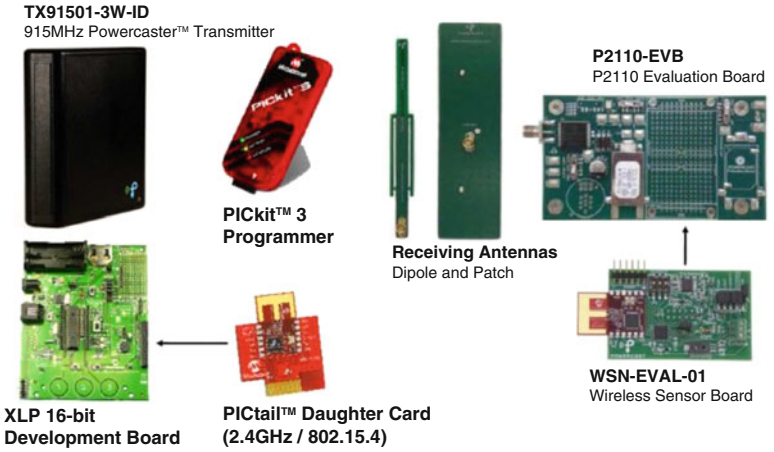

Fig. 7.16 Lifetime power energy harvesting development kit for wireless sensors [149]

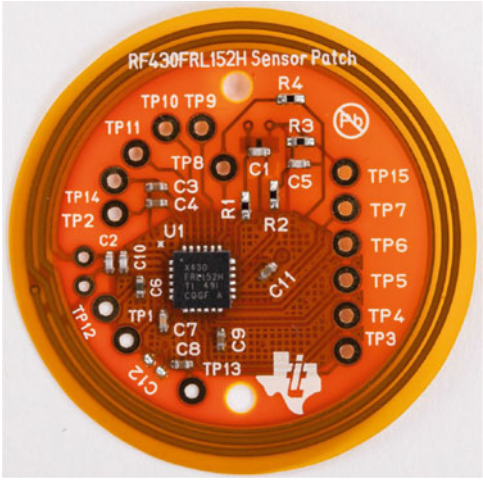

Fig. 7.17 Battery-less NFC/RFID temperature sensing patch

medical, health and fitness, and industrial where instantaneous measurements are required and a battery is not feasible or desired. Connections to power via other options such as battery or USB are also offered as an alternative. An evaluation board, *RF430FRL152HEVM*, is available for purchase to evaluate the key features of the device and some sensor measurements. Application report *SLOA212A* demonstrates the implementation of a single chip NFC/RFID field powered temperature sensor system with the *RF430FRL152H*, illustrated in Fig. 7.17.

7.3.2.3 Energous Corp.

Silicon Valley startup Energous Corp. [38] is developing a new technology called *WattUp*. Its transmitters deliver energy to devices via microwave beams: small antennas embedded in speakers, televisions, and dedicated router-size boxes that can direct wireless power to toys, lights, and mobile phones over several meters distance. WattUp's sophisticated localization and beamforming technology allows multiple RF antennas to emit low-power, 5.8 GHz beams along different paths that converge in a "pocket" around the targeted device to reach the receiving antenna, even not in direct LOS. Energous claims that a *WattUp* transmitter is capable of delivering microwaves up to four devices simultaneously. The amount of power the beams deliver is dependent on distance: 4 W within 1.5 m, 2 W within 3 m, and 1 W within 4.6 m. The company says that its eventual goal is 25% end-to-end efficiency of the system for integration into near-market consumer devices.

7.3.2.4 Ossia Inc.

Energous has a competitor in Ossia Inc., based in Washington, which is also developing an RF power delivery system named *Cota*. The *Cota* system uses a Wi-Fi-like signal designed to charge many devices simultaneously, stationary or moving, using their patented smart antenna technique. The company asserts that at an effective radius of 10 m, a single Cota charging station can feed rechargeable battery-operated devices in every room of an average home or office suite. Under license from Ossia, consumer electronics manufacturers will be able to include Cota receivers in new products and have the opportunity to build their own branded transmitters.

7.3.2.5 Farsens S.L.

Farsens S.L. [45] is a Spanish company based in San Sebastian that has developed a wide range of wireless and battery-free RFID sensor tags. Its UHF RFID ICs harvest energy from the RF field created by commercial RFID readers and use that power to drive sensors, actuators, or other electronics effectively creating battery-free devices from a distance as far as 1.5 m. It also offers development platforms to create one's own wireless and battery-free sensors.

7.3.2.6 Texzon Technologies, LLC.

On a much larger scale, Texzon Technologies LLC. [191] in Texas introduced a novel wireless power transmission system concept at the 2016 IEEE symposium for Wireless and Microwave circuits, which is capable of transferring megawatts of power. They intend to revolutionize the current electrical power distribution systems

by switching to a global wireless scheme utilizing a Zenneck surface wave [144] between optimally sited power generation facilities and local distribution grids and microgrids. This wireless power system will employ a "transmitter probe" located near a power generation plant, to launch a Zenneck carrier wave. Receiver antennas will be positioned appropriately around the world to receive the signal and download the power into a local microgrid or conventional grid architecture. The company claims that the consequential RF exposure levels are more than ten times lower than the FCC, OSHA [193] and ANSI [192] recommended limits.

7.3.3 Future Directions

7.3.3.1 RF Energy Harvesting and Aerial Vehicles

Since the demonstration by W.C. Brown and Raytheon company of a model helicopter powered via microwaves in the early 1960s [15], various similar research in microwave-powered airplanes took off. Strassner and Chang summarize in [180] the historical milestones achieved in the USA as well as internationally. The present day desire to remotely power unmanned aerial vehicles (UAVs) or drones [36] continues to serve as the main driving force behind current advancements being made in RFEH, particularly in rectenna array components [43]. The use of UAVs for communication and surveillance is seen as a huge potential, especially in the military. Future uses for RFEH include powering probes from space stations into deep space, and robots to enter perilous environments like nuclear contaminated areas.

7.3.3.2 Simultaneous Wireless Information and Power Transfer

This book chapter focuses on energy transmission via electromagnetic waves. Even so, the prime application of RF signals is for wireless communications. Hence, since RF signals carry energy as well as information, theoretically energy harvesting and information transfer can also be performed from the same signal input. This is referred to as the simultaneous wireless information and power transfer (SWIPT) [228] concept. It allows the information receiver and energy harvester to share the same antenna or antenna array. Figure 7.18 displays the corresponding receiver architecture for SWIPT. Wireless information is modulated on the amplitude and phase of RF waves, while WET is carried out through far-field radiation.

The traditional information receiver architecture designed for information reception may not be optimal for SWIPT because information reception and RFEH work on very different power sensitivities (e.g., −10 dBm for energy harvesters versus −50 dBm for information receivers) [224]. This inspired the research efforts in devising receivers for RF power/information receivers. Currently, there are four typical types of receiver architectures [208]:

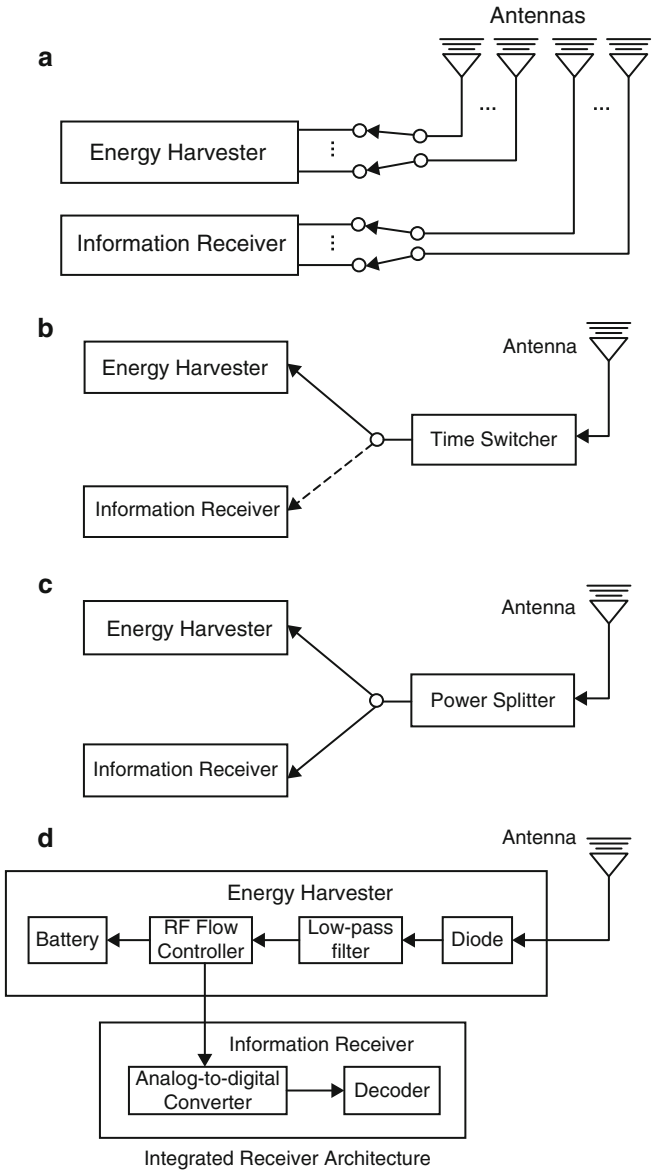

Fig. 7.18 Receiver architecture designs for RF-powered information receiver [208]: (**a**) Separated receiver architecture; (**b**) time-switching architecture; (**c**) power-splitting architecture; and (**d**) integrated receiver architecture

- Separated receiver architecture, also known as antenna-switching: equips an energy harvester and information receiver with independent antenna(s) so that they observe different channels.

- co-located receiver architecture: categorized into time-switching and power-splitting models, it allows a power harvester and an information receiver to share the same antenna(s) so that they observe the same channel(s).
- Integrated receiver architecture: implementation of RF-to-baseband conversion for information decoding is integrated with the RFEH via the rectifier circuit.
- Ideal receiver architecture: assumes that the receiver is able to extract the RF energy from the same signals used for information decoding.

The studies in [228] show that when the circuit power consumption is relatively small compared to the received signal power, the integrated receiver architecture outperforms the co-located receiver architecture at high harvested energy region, whereas the co-located receiver architecture is superior at low harvested energy region. However, when the circuit power consumption is high, the integrated receiver architecture performs better. They also mentioned that for a system without minimum harvested energy requirement, the integrated receiver achieves higher information rate than that of the separated receiver at short transmission distances.

The above study and other related publications [21, 125] assume a linear energy harvesting model where the RF to DC conversion efficiency does not depend on the input power level. In practice however, there is a nonlinear relationship between input and output as described in [54, 94, 198]. In [14], a practical nonlinear model and corresponding resource allocation algorithm was proposed for SWIPT networks, unveiling a greater performance gain over traditional linear models.

A key concern for both wireless information and energy transfer is the decay in efficiency with the increase of transmission distance due to propagation path loss. Such problem is especially severe in a single-antenna transmitter that generates omnidirectional radiations. This low energy transfer efficiency calls for advanced multi-antenna and signal processing techniques such as beamforming [31, 91, 107].

7.3.3.3 Beamforming

Point-to-point transmission of RF waves is referred to as power beamforming [224]; its sharpness improves with the number of transmit antennas. In RFEH networks, beamforming designs have been explored to steer the RF signals toward the target receivers with different information and/or energy harvesting requirements. Figure 7.19 shows the SWIPT beamforming general model.

The knowledge of channel state information (CSI) plays an important role in beamforming performance optimization. To accurately estimate a channel state, a significant overhead (e.g., time) can be incurred at a receiver. Normally, the longer the time for channel state estimation, the more accurate CSI becomes. However, it may result in reduced time for transmission, and also less amount of collected energy. As a result, an optimization of RF energy transfer or SWIPT entails a trade-off between data transmission and channel state estimation duration [208].

Distributed Energy Beamforming enables a cluster of distributed energy sources to cooperatively emulate an antenna array by transmitting RF energy simultaneously in the same direction to an intended harvester for better diversity gains. The potential

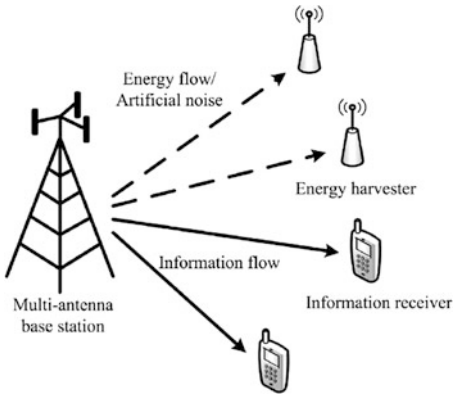

Fig. 7.19 A general model for simultaneous wireless information and power transfer (SWIPT) beamforming system [208]

energy gains are expected to be the same as from information beamforming. However, challenges arise in the implementation, e.g., time synchronization among energy sources and coordination of distributed carriers in phase and frequency so that signals can be combined constructively at the receiver side [208].

7.4 Ambient RF Energy Harvesting Applications and Products

The obvious appeal of harvesting ambient RF energy over dedicated power transmission is the utilization of "free" energy generated by radio transmitters such as radio (AM and FM) towers, TV towers, cellular phone towers, and Wi-Fi routers. Similar to dedicated RFEH applications, in ambient RFEH, the most popular research attention is found on WSNs [100, 147] and WBAN [13, 70]. Other than the above popular applications, devices powered by ambient RF energy is also attracting increasing research attention. For example, in [68], the authors present a design of an RF circuit that enables continuous charging of mobile devices especially in urban areas where the density of ambient RF sources is high. Liu et al. [102] demonstrate that an information rate of 1 kbps can be achieved between two prototype devices powered by ambient RF signals, at the distance of up to 75 and 45 cm for outdoors and indoors, respectively.

Additionally, RFEH can be used to provide charging capability for a wide variety of low-power mobile electronic devices as most of them consume only microwatts to milliwatts range of power. Existing literature has also presented many implementations of battery-free devices powered by ambient energy such as mobile electronic devices, electronic watches, MP3 players, wireless keyboard, and mouse from Wi-Fi [136, 186], GSM [53, 146] and Digital Television (DTV) bands [79, 81]. Furthermore, in [105], a novel approach to embed systems in clothes is presented.

In the following subsections, we explore the constraints and requirements for the development of an ambient RFEH system, the current research orientations and finally conclude with some novel applications.

7.4.1 Design Considerations

As ambient RF levels are lower than those provided by an anticipated source, the availability of the RF power, the efficiency of the harvesting system, and its minimum startup power are of critical importance. In order to assess the feasibility of deploying ambient harvesters, the available RF power needs to be evaluated in different locations. Such measurements, in conjunction with knowledge on harvester performance, can then be used to determine the locations at which RF harvester powered devices can be successfully deployed.

7.4.1.1 Power Density Measurements

The surface power density (or specific power) is the amount of power per unit area, usually expressed in W/m^2. The input RF power density measured by a spectrum analyzer is calculated summing all the spectral peaks across the band. These levels provide a snapshot of source availability at the time and location of the measurement [146]. Several RF spectral surveys, which measure ambient RF power levels from sources such as television and mobile phone base stations, were undertaken with spectrum analyzers in unknown measurement locations and with no regard of the conditions that might affect the evaluation (e.g., outdoor, indoor, street, bus, etc.) [59, 201]. In order to demonstrate the feasibility for implementing ambient RFEH, a rigorous spectral survey must be taken first, indicating the exact time/location, and the associated RF bands with sufficient input power density levels for harvesting. Also, appropriate equipment to measure the electric field strength should be selected, such as an RF analyzer and a calibrated antenna.

The Effective Radiated Power (ERP) is the transmitter power delivered to the antenna multiplied by the directivity or gain of the antenna [46]. Since high-gain antennas direct most of the energy toward the horizon and not toward the ground, high ERP transmission systems such as used for UHF-TV broadcast tend to have less ground level field intensity near the station than FM radio broadcast systems with lower ERP and gain values. In urban areas, available RF energy in areas close to transmission towers provides an opportunity to harvest that energy. Some of the most prominent sources are AM radio transmission (540–1700 kHz, maximum ERP of 50 KW), FM radio transmission (88–108 MHz, maximum ERP of 100 KW), TV transmission (180–220 MHz, ERP from 3 KW for low-power VHF to 1000 KW for full-power UHF), cellular and Personal Communications Services (PCS) transmission (824–896 and 1850–1990 MHz, up to 500 W per channel), Wi-Fi (2.45 or 5.8 GHz, transmit power around 100 mW), and mobile phones (transmit

Table 7.4 RF power density

Band name	Frequency	Distance to base station	Power density	Applications
AM station	540 MHz	from 5 to 10 km	from 0.159 to 0.04 mW/m^2	Radio [229]
GSM-900	950 MHz	from 25 to 100 m	from 1.0 to 0.1 mW/m^2	Phone [201]
GSM-1800	1747.5 MHz	from 25 to 100 m	from 1.0 to 0.1 mW/m^2	Phone [201]
UMTS-2100	2110 MHz	from 11.8 to 150 m	from 2 to 0.2 mW/m^2	Phone (3G) [185]
WLAN	2.4 GHz	7 and 12 m	1 and 0.1 $\mu W/m^2$, respectively	WLAN [201]

power of 1–2 W). Cellular towers can be used as a continuous source of renewable energy as they transmit 24 h. Table 7.4 summarizes some examples of power density measurements in an urban environment.

7.4.1.2 Antenna and Circuit Design

Once the RF power density levels for harvesting are known, antennas can now be fabricated. As discussed in Sect. 7.2.3, rectennas are the most common designs mentioned in the existing literature. A well-designed rectenna should ideally be capable of harvesting energy across an entire band, and thus it is important to calculate the total band power. Furthermore, the antenna needs to match the impedance of the rectifying device over a range of input power levels to optimize efficiency. Other requirements for the antenna include the fact that they must be omnidirectional and dual-linear polarized since the exact location of the transmitter is assumed to be unknown and the propagation environment includes scattering.

In addition, proper power management technique must be selected (e.g., harvest–store–use or harvest–use). In the case of harvest–store–use, the DC output of the converted signals should not be directly connected to the storage device to avoid discharging under some conditions [147]. Monitoring of the available stored energy, the received DC power, the power management circuit control, the sensor data collection, and duty cycle, etc., are necessary functions that need to be accomplished at the lowest possible potency. There are a number of very low-power microcontrollers on the market, and some of their parameters like clock speeds can be adjusted to reduce the power in different modes of operation.

Finally, energy storage could use supercapacitors or various types of rechargeable batteries. If there is not enough energy captured, sensor data cannot be transmitted and there is a danger of damaging the storage device. Therefore, the available rectified RF power and the available energy stored should be monitored in a closed-loop system allowing for adaptive adjustment of the data transmission duty cycle.

7.4.1.3 Multiband RF Energy Harvesting and Hybrid Systems

Most early research on RF energy scavenger designs focus on a single frequency band [8, 50]. Lately, there have been design implementations of dual-band [131], triple-band [72], and multiband antenna designs [146]. Due to relatively low-power density and availability of ambient RF sources, it is highly advisable for a harvester to capture signals over a large number of frequency bands to ensure continuous and steady voltage for sensors operation.

A multiband harvester may have one antenna and circuit to harvest each frequency band separately, then store the overall DC power in a single device. However, this configuration needs many antennas, thus increasing the overall costs, weight, and size of the harvesting system. To overcome this problem, a possible solution is to use only one ultrawide band or multiband antenna. In this case, adequate matching networks must be constructed to overcome the nonlinearity of the diodes with respect to both frequency and RF power input. An alternative was presented in [141], where rectifying circuits tuned at different frequencies were connected in series, allowing better rectification and DC-combining efficiency. Unfortunately, this architecture would not identify the optimum load in terms of harvested DC power since the input of each rectifier circuit changed with the frequency of the signal.

One of the first commercial applications of multiband ambient RFEH was pioneered with Freevolt, a trademark of Drayson Technologies Ltd [35]. It is branded as a new innovative technology that provides power for low energy Internet of Things (IoT) devices by scavenging power from wireless and broadcast networks such as 2G, 3G, 4G, Wi-Fi, and DTV. The approach was implemented in the CleanSpace Tag, a personal air quality pollution sensor. It claims no interference with the data connectivity and does not require any increase in transmission power.

The use of ambient RFEH for WSNs depends on the application, the distance to the base station, the frequency, the distance between nodes, etc. Table 7.5 depicts the commercial requirements of existing sensor network nodes. The results deduced from Tables 7.2 and 7.5 indicate that energy solely harvested from the ambiance is typically insufficient as a primary power source of WSNs. Hence, it may be combined with other energy harvesting sources. As an example, for outdoor applications, when the base station is far from the nodes, RFEH can be combined with photovoltaic [98], or even piezoelectric [76] sources. In a similar way, for human body sensors, it can be associated with other sources such as thermal or vibration [140]. These types of dual harvesting systems are called “hybrid energy harvesting systems.”

7.4.2 Hardware Implementation and Future Directions

Harvesting energy from the ambient environment is a promising field that opens the door to many different applications, the bulk of which relates to sensing nodes.

Table 7.5 Comparison of power consumption of some selected sensor network nodes [229]

Operating conditions	Crossbow MICAz	Waspmote	Intel IMote2	Jennic JN5139
Radio standard	IEEE 802.15.4 ZigBee	IEEE 802.15.4/ZigBee	IEEE 802.15.4	IEEE 802.15.4/ZigBee
Typical range	100 m outdoor, 30 m indoor	500 m	30 m	1000 m
Data rate	250 kbps	250 kpps	250 kbps	250 kbps
Sleep mode	15 μA	62 μA	390 μA	2.8 μA
Processor consumption	8 mA active mode	9 mA	31–53 mA	2.7 + 0.325 mA/MHz
Transmission	17.4 mA (+0 dBm)	50.26 mA	44 mA	34 mA (+3 dBm)
Reception	19.7 mA	49.56 mA	44 mA	34 mA
Supply voltage (min)	2.7 V	3.3 V	3.2 V	2.7 V
Average power	2.8 mW	1 mW	12 mW	3 mW

While several concepts of energy harvesting through RF signals have been proposed mainly in the academia, a commercial product that works solely on energy harvested from thin air has yet to be offered. In the following paragraphs, we survey the latest achievements in ambient RFEH and future directions.

7.4.2.1 Harvesting from Cell Towers

There are 4 GSM frequency bands operating in the world, with 850 and 1900 MHz in America, and 900 and 1800 MHz in the rest of the world [65]. The aggregated power density over some GSM frequency bands is shown in Table 7.4. Most publications focus on the proof of concept rather than on a viable option for energy replenishment. Some examples of DC power scavenged from cellular towers radiations are in [8, 53, 76]. However, it remains that energy scavenging from cellular towers still suffers from very low efficiency and long duty cycle.

7.4.2.2 Digital Television Band Energy Harvesting

Cellular base transceiver stations and TV broadcast represent the most promising ambient RF sources due to their high transmit power (e.g., TV) and ubiquity in urban environments. Collecting energy from DTV signals was first investigated by Intel [157] in 2009, where 60 μW of power was harvested at a distance of 4 km from a broadcasting TV station. Other practical examples of DTV band energy harvesting can be found in [78, 84, 132, 168, 202].

7.4.2.3 Wi-Fi Energy Harvesting

With the ubiquity of Wi-Fi signals in urban environments and the fact that it operates mainly in the crowded 2.45 GHz band (same with RFID, cordless phones, Bluetooth, ZigBee, etc.), harvesting energy from Wi-Fi has become a hot topic. Wi-Fi transmission operates in "bursts," i.e., a router emits power only when it is sending data packets to a host, with a typical power of 100 mW at short range. Thus, while a harvester can capture power during transmission, the power leaks during silent periods, limiting the minimum voltage requirement needed to turn on a sensor. Many prototype implementation of devices operating on Wi-Fi energy were demonstrated in the academia [72, 136, 186] but are yet to match the efficiency and effectiveness of a dedicated source. Nevertheless, the research and development divisions of companies like Samsung, Intel, Qualcomm, and Texas Instruments are currently hard at work trying to make harvesting from ambient Wi-Fi signals a reality.

7.4.2.4 Cognitive Radio

A CRN powered with RF energy can provide a spectrum and energy-efficient solution for wireless networking [106]. The idea of utilizing electromagnetic signals from primary transmitters to power secondary devices was initially proposed in [97]. In an RF-powered CRN, the scavenging capability allows secondary users to gain and store energy from nearby transmissions (of primary users). Then, the secondary users can transmit data when far away from primary users or when nearby primary users are idle. Thus, they must not only identify spectrum availabilities for opportunistic data transmission but also explore for occupied spectrum channels to harvest energy [208].

Figure 7.20 shows a general network architecture for RF-powered CRNs. There are three zones associated with the primary user: energy harvesting, transmission, and inference zones. In the harvesting zone, a secondary user can receive RF energy from a primary user on transmission. The transmission zone refers to the communication coverage of the primary user; if the secondary user is still in the harvesting zone, he can scavenge power from the primary user. If the latter occupies the channels, then the secondary user cannot transmit data if he is in the interference zone.

Cognitive radio consists of four main functions to support intelligent and efficient dynamic spectrum access:

1. Spectrum sensing: to detect the activities of primary users accurately
2. Spectrum access: to access spectrum while protecting primary users from collision and to provide fair and efficient sharing of available spectrum
3. Spectrum management: to achieve high spectrum utilization for both communication and RFEH by performing channel selection
4. Spectrum handoff: to switch a secondary user from one channel to another

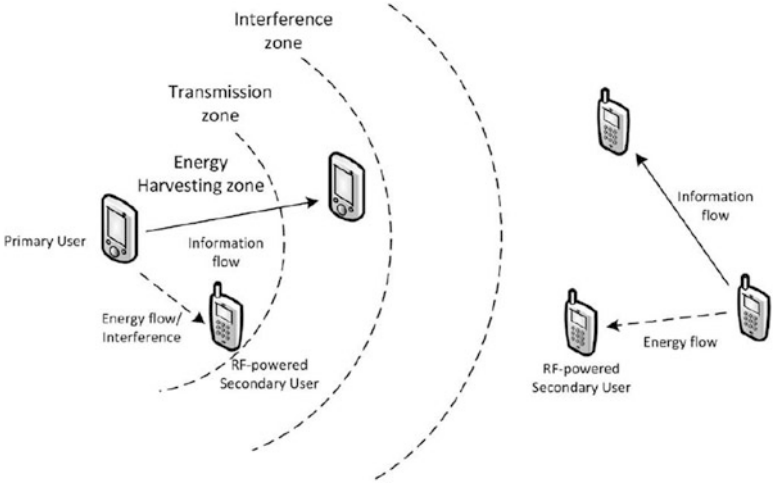

Fig. 7.20 A general network architecture of RF-powered cognitive radio networks (CRNs)[208]

Detailed research issues in the RF-powered CRN related to these four functions can be found in survey paper [208].

7.5 Summary

Energy harvesting from radiative wireless charging is a promising field that opens the door to many different applications, the bulk of which relates to sensing nodes. It enables wire-free operation, simple scalability, low-cost setup and maintenance, reliable, controllable, and environmentally friendly solution for networks placement. The energy can be scavenged either from dedicated or from ambient transmitters. Dedicated sources can be deployed where a stable and predictable amount of power to meet user's demand is expected, while ambient sources are transmitters not primarily intended for this purpose, thus granting freely available signals in the environment. Harvesting energy from the latter is very challenging, given the amount of energy density available ($0.04–2\,\mathrm{mW/m^2}$), whatever the transmitter type may be.

This chapter surveyed the general architecture of a harvester from both anticipated and ambient RF origins, in order to meet the future demand for self-powered devices. All the subsystems of the harvester were discussed: antenna design, matching circuit, rectifier, power management, and energy storage. In addition, potential RF signals scavenging applications and techniques beyond wireless sensor nodes power were explored, such as long-distance electrical power distribution, SWIPT, beamforming, and cognitive radio. While several concepts of energy harvesting through RF signals have been proposed mainly in the academia, it remains that very

few products are commercially available in the market. With the ubiquitousness of the IoT, Wi-Fi signals, which work in the 2.4 GHz/5 GHz band, are gaining lots of research interests. Currently, the research and development divisions of companies like Samsung, Intel, Qualcomm, and Texas Instruments are hard at work trying to make harvesting from Wi-Fi signal and other ambient sources a reality. The first to market with a viable solution will create huge amounts of goodwill.

References

1. S. Agrawal, S. Pandey, J. Singh, P.N. Kondekar, An efficient RF energy harvester with tuned matching circuit, in *VLSI Design and Test* (Springer, Berlin, 2013), pp. 138–145
2. A. Alaeldine, M. Latrach, H. Raggad, Z. Sayegh, Design and optimization of a GSM printed dipole antenna for energy harvesting applications, in *2011 IEEE International Symposium on Antennas and Propagation (APSURSI)* (2011), pp. 1780–1783. doi:10.1109/APS.2011.5996840
3. S.B. Alam, M.S. Ullah, S. Moury, Design of a low power 2.45 GHz RF energy harvesting circuit for rectenna, in *Proceedings of the IEEE ICIEV, Dhaka, Bangladesh* (2013), pp. 1-4
4. A. Al-Khayari, H. Al-Khayari, S. Al-Nabhani, M.M. Bait-Suwailam, Z. Nadir, Design of an enhanced RF energy harvesting system for wireless sensors, in *2013 7th IEEE GCC Conference and Exhibition (GCC)* (2013), pp. 479–482. doi:10.1109/IEEEGCC.2013.6705826
5. F.A. Aoudia, M. Gautier, O. Berder, Fuzzy power management for energy harvesting wireless sensor nodes, in *IEEE International Conference on Communications (ICC16)* (2016), pp. 1–6. doi:10.1109/ICC.2016.7510767
6. H. Arai, M. Chomora, M. Yoshida, A voltage-boosting antenna for RF energy harvesting, in *IEEE Antenna Technology (iWAT), 2012 IEEE International Workshop* (2012), pp. 169–172. doi:10.1109/IWAT.2012.6178638
7. M. Arrawatia, M.S. Baghini, G. Kumar, RF energy harvesting system at 2.67 and 5.8 GHz, in *2010 Asia-Pacific Microwave Conference* (2010), pp. 900–903
8. M. Arrawatia, M.S. Baghini, G. Kumar, RF energy harvesting system from cell towers in 900MHz band, in *2011 IEEE National Conference in Communications (NCC)* (2011), pp. 1–5. doi:10.1109/NCC.2011.5734733
9. M. Arsalan, M.H. Ouda, L. Marnat, T.J. Ahmad, A. Shamim, K.N. Salama, A 5.2 GHz, 0.5 mW RF powered wireless sensor with dual on-chip antennas for implantable intraocular pressure monitoring, in *2013 IEEE Microwave MTT-S International Microwave Symposium Digest (IMS)* (2013), pp. 1–4. doi:10.1109/MWSYM.2013.6697639
10. Avago Technologies, http://www.avagotech.com/. Cited 30 Dec 2016
11. N.P. Basta, E.A. Falkenstein, Z. Popovic, Bow-tie rectenna arrays, in *2015 IEEE Wireless Power Transfer Conference (WPTC)* (2015), pp. 1–4. doi:10.1109/WPT.2015.7140158
12. A. Bogliolo, V. Freschi, E. Lattanzi, A.L. Murphy, U. Raza, Towards a true energetically sustainable WSN: a case study with prediction-based data collection and a wake-up receiver, in *Proceedings of the 9th IEEE International Symposium on Industrial Embedded Systems (SIES)* (2014), pp. 21–28. doi:10.1109/SIES.2014.6871181
13. L.M. Borges, N. Barroca, H.M. Saraiva, J. Tavares, P.T. Gouveia, F.J. Velez, C. Loss, R. Salvado, P. Pinho, R. Gonçalves, N.B. Carvalho, Design and evaluation of multi-band RF energy harvesting circuits and antennas for WSNs, in *2014 21st International Conference on Telecommunications (ICT)* (2014), pp. 308–312. doi:10.1109/ICT.2014.6845129
14. E. Boshkovska, D.W. Ng, N. Zlatanov, R. Schober, Practical non-linear energy harvesting model and resource allocation for SWIPT systems. IEEE Commun. Lett. **19**(12), 2082–2085 (2015). doi:10.1109/LCOMM.2015.2478460

15. W.C. Brown, R.H. George, N.I. Heenan, R.C. Wonson, Microwave to dc converter. US Patent 3,434,678, https://www.google.com/patents/US3434678.GooglePatents (1969). Cited 30 Dec 2016
16. D. Brunelli, C. Moser, L. Thiele, L. Benini, Design of a solar-harvesting circuit for batteryless embedded systems. IEEE Trans. Circuits Syst. Regul. Pap. **56**(11), 2519–2528 (2009). doi:10.1109/TCSI.2009.2015690
17. I. Buchman, *Batteries in a Portable World: A Handbook on Rechargeable Batteries for Non-engineers*, 3rd edn. (Cadex Electronics Inc., Richmond, 2011)
18. R. Chai, Y. Zhang, A practical supercapacitor model for power management in wireless sensor nodes. IEEE Trans. Power Electron. **30**(12), 6720–6730 (2015). doi:10.1109/TPEL.2014.2387113
19. A. Chasin, V. Volskiy, M. Libois, M. Ameys, M. Nag, M. Rockele, K. Myny, S. Steudel, S. Schols, G.A. Vandenbosch, W. de Raedt, Integrated UHF a-IGZO energy harvester for passive RFID tags, in *2013 IEEE International Electron Devices Meeting* (2013), pp. 11–3. doi:10.1109/IEDM.2013.6724608
20. M. Chen, G.A. Rincon-Mora, Accurate electrical battery model capable of predicting runtime and IV performance. IEEE Trans. Energy Convers. **21**(2), 504–511 (2006). doi:10.1109/TEC.2006.874229
21. X. Chen, X. Wang, X. Chen, Energy-efficient optimization for wireless information and power transfer in large-scale MIMO systems employing energy beamforming, IEEE Wireless Commun. Lett. **2**(6), 667–670 (2013). doi:10.1109/WCL.2013.092813.130514
22. J.F. Christmann, E. Beigné, C. Condemine, J. Willemin, C. Piguet, Energy harvesting and power management for autonomous sensor nodes, in *Design Automation Conference (DAC)* (2012), pp. 1049–1054. doi:10.1145/2228360.2228550
23. F. Congedo, G. Monti, L. Tarricone, M. Cannarile, Broadband bowtie antenna for RF energy scavenging applications, in *Proceedings of the 5th European Conference on Antennas and Propagation (EUCAP)* (2011), pp. 335–337
24. A.B. Cultura, Z.M. Salameh, Performance evaluation of a supercapacitor module for energy storage applications, in *Power and Energy Society General Meeting-Conversion and Delivery of Electrical Energy in the 21st Century* (2008), pp. 1–7. doi:10.1109/PES.2008.4596322
25. J. Dai, D.C. Ludois, A survey of wireless power transfer and a critical comparison of inductive and capacitive coupling for small gap applications. IEEE Trans. Power Electron. **30**(11), 6017–6029 (2015). doi:10.1109/TPEL.2015.2415253
26. J. Dai, D.C. Ludois, Capacitive power transfer through a conformal bumper for electric vehicle charging. IEEE J. Emerging Sel. Top. Power Electron. **4**(3), 1015–1025 (2015). doi:10.1109/JESTPE.2015.2505622
27. D. De Donno, L. Catarinucci, L. Tarricone, An UHF RFID energy-harvesting system enhanced by a DC-DC charge pump in silicon-on-insulator technology. IEEE Microwave Wireless Compon. Lett. **23**(6), 315–317 (2013). doi:10.1109/LMWC.2013.2258002
28. K.K.A. Devi, S. Sadasivam, Design of a 377 ohms patch antenna for ambient RF energy harvesting at downlink frequency of GSM 900, in *The 17th Asia Pacific Conference on Communications (APCC)* (2011), pp. 492–495. doi:10.1109/APCC.2011.6152859
29. K.K. Devi, S. Sadasivam, N.M. Din, C.K. Chakrabarthy, Design of a 377Ω patch antenna for ambient RF energy harvesting at downlink frequency of GSM 900, in *The 17th Asia Pacific Conference on Communications* (2011), pp. 492–495. doi:10.1109/APCC.2011.6152859
30. Y. Ding, T. Arslan, A triple bands printed inverted-F antenna for mobile RF energy scavenging, in *2014 Loughborough Antennas and Propagation Conference (LAPC)* (2014), pp. 218–221. doi:10.1109/LAPC.2014.6996362
31. Z. Ding, C. Zhong, D.W. Ng, M. Peng, H.A. Suraweera, R. Schober, H.V. Poor, Application of smart antenna technologies in simultaneous wireless information and power transfer. IEEE Commun. Mag. **53**(4), 86–93 (2015). doi:10.1109/MCOM.2015.7081080
32. D.M. Dobkin, *The RF in RFID: Passive UHF RFID in Practice* (Newnes, Boston, 2008)

33. D. Dondi, S. Scorcioni, A. Bertacchini, L. Larcher, P. Pavan, An autonomous wireless sensor network device powered by a RF energy harvesting system, in *38th Annual Conference on IEEE Industrial Electronics Society (IECON)* (2012), pp. 2557–2562. doi:10.1109/IECON.2012.6388696
34. R.A. Dougal, S. Liu, R.E. White, Power and life extension of battery-ultracapacitor hybrids. IEEE Trans. Compon. Packag. Technol. **25**(1), 120–131 (2002). doi:10.1109/6144.991184
35. Drayson Technologies Ltd., http://draysontechnologies.com/. Cited 30 Dec 2016
36. S. Dunbar, F. Wenzl, C. Hack, R. Hafeza, H. Esfeer, F. Defay, S. Prothin, D. Bajon, Z. Popovic, Wireless far-field charging of a micro-UAV, in *2015 IEEE Wireless Power Transfer Conference (WPTC)* (2015), pp. 1–4. doi:10.1109/WPT.2015.7140154
37. Electropaedia, http://www.mpoweruk.com/. Cited 30 Dec 2016
38. Energous Corp., http://www.energous.com/. Cited 30 Dec 2016
39. Energy Storage Technologies, http://www.cap-xx.com/resource/energy-storage-technologies/. Cited 30 Dec 2016
40. M. Erol-Kantarci, H.T. Mouftah, DRIFT: differentiated RF power transmission for wireless sensor network deployment in the smart grid, in *2012 IEEE Globecom Workshops* (2012), pp. 1491–1495. doi:10.1109/GLOCOMW.2012.6477806
41. M. Erol-Kantarci, H.T. Mouftah, Mission-aware placement of RF-based power transmitters in wireless sensor networks, in *2012 IEEE Symposium on Computers and Communications (ISCC)* (2012), pp. 12–17. doi:10.1109/ISCC.2012.6249261
42. M. Erol-Kantarci, H.T. Mouftah, Suresense: sustainable wireless rechargeable sensor networks for the smart grid. IEEE Wirel. Commun. **19**(3), 30–36 (2012). doi:10.1109/MWC.2012.6231157
43. J. Estrada, I. Ramos, A. Narayan, A. Keith, Z. Popovic, RF energy harvester in the proximity of an aircraft radar altimeter, in *2016 IEEE Wireless Power Transfer Conference (WPTC)* (2016), pp. 1–4. doi:10.1109/WPT.2016.7498824
44. K.M. Farinholt, G. Park, C.R. Farrar, RF energy transmission for a low-power wireless impedance sensor node. IEEE Sensors J. **9**(7), 793–800 (2009). doi:10.1109/JSEN.2009.2022536
45. S.L. Farsens, http://www.farsens.com/. Cited 30 Dec 2016
46. Federal Communications Commission, FCC Rules and Regulations Part 15 Section 247 (15.247). Operation within the bands 902–928 MHz, 2400–2483.5 MHz, and 5725–5850 MHz, Technical Report (2014)
47. C. Felini, M. Merenda, F.G. Della Corte, Dynamic impedance matching network for RF energy harvesting systems, in *2014 IEEE RFID Technology and Applications Conference (RFID-TA)* (2014), pp. 86–90. doi:10.1109/RFID-TA.2014.6934206
48. I. Flint, X. Lu, N. Privault, D. Niyato, P. Wang, Performance analysis of ambient RF energy harvesting: a stochastic geometry approach, in *2014 IEEE Global Communications Conference* (2014), pp. 1448–1453. doi:10.1109/GLOCOM.2014.7037012
49. B.R. Franciscatto, V. Freitas, J.M. Duchamp, C. Defay, T.P. Vuong, High-efficiency rectifier circuit at 2.45 GHz for low-input-power RF energy harvesting, in *Proceedings of the IEEE EuMC, Nuremberg, Germany* (2013), pp. 507–510
50. A. Georgiadis, G.V. Andia, A. Collado, Rectenna design and optimization using reciprocity theory and harmonic balance analysis for electromagnetic (EM) energy harvesting. IEEE Antennas Wirel. Propag. Lett. **9**, 444–446 (2010). doi:10.1109/LAWP.2010.2050131
51. S. Ghosh, S.K. Ghosh, A. Chakrabarty, Design of RF energy harvesting system for wireless sensor node using circularly polarized monopole antenna: RF energy harvesting system for WSN node using circularly polarized antenna, in *9th International Conference on Industrial and Information Systems (ICIIS)* (2014), pp. 1–6. doi:10.1109/ICIINFS.2014.7036513
52. A. Goldsmith, *Wireless Communications*, 1st edn. (Cambridge University Press, New York, 2005)
53. W.M. Gunathilaka, H.G. Dinesh, G.G. Gunasekara, K.M. Narampanawe, J.V. Wijayakulasooriya, Ambient radio frequency energy harvesting, in *2012 IEEE 7th International Conference on Industrial and Information Systems (ICIIS)* (2012), pp. 1–5. doi:10.1109/ICIInfS.2012.6304789

54. J. Guo, X Zhu, An improved analytical model for RF-DC conversion efficiency in microwave rectifiers, in *2012 IEEE/MTT-S International Microwave Symposium Digest* (2012), pp. 1–3. doi:10.1109/MWSYM.2012.6259492
55. S. Guo, C. Wang, Y. Yang, Joint mobile data gathering and energy provisioning in wireless rechargeable sensor networks. IEEE Trans. Mob. Comput. **13**(12), 2836–2852 (2014). doi:10.1109/TMC.2014.2307332
56. J. Guo, S. Durrani, X. Zhou, H. Yanikomeroglu, Outage probability of ad hoc networks with wireless information and power transfer. IEEE Wirel. Commun. Lett. **4**(4), 409–412 (2015). doi:10.1109/LWC.2015.2427163
57. M.S. Halper, M.S. Ellenbogen, *Supercapacitors: A Brief Overview* (The MITRE Corporation, McLean, 2006)
58. K. Han, K. Huang, Wirelessly powered backscatter communication networks: modeling, coverage and capacity (2016). arXiv preprint arXiv:1605.05875
59. T.H. Haumann, U. Munzenberg, W.O. Maes, P.E. Sierck, P. Kostarakis, HF-Radiation levels of GSM cellular phone towers in residential areas, in *2nd International Workshop on Biological Effects of EMFS*, vol.1 (2002), pp. 327–333
60. S.L. Ho, J. Wang, W.N. Fu, M. Sun, A comparative study between novel witricity and traditional inductive magnetic coupling in wireless charging. IEEE Trans. **47**(5), 1522–1525 (2011). doi:10.1109/TMAG.2010.2091495
61. C.E. Holland, J.W. Weidner, R.A. Dougal, R.E. White, Experimental characterization of hybrid power systems under pulse current loads. J. Power Sources **109**(1), 32–37 (2002). doi:10.1016/S0378-7753(02)00044-7
62. S.S. Hong, R. Ibrahim, M.M. Khir, H. Daud, M.A. Zakariya, Rectenna architecture based energy harvester for low power RFID application, in *2012 4th International Conference on Intelligent and Advanced Systems (ICIAS)*, vol. 1 (2012), pp. 382–387. doi:10.1109/ICIAS.2012.6306223
63. K. Huang, V.K. Lau, Enabling wireless power transfer in cellular networks: architecture, modeling and deployment. IEEE Trans. Wirel. Commun. **13**(2), 902–912 (2014). doi:10.1109/TWC.2013.122313.130727
64. J. Huh, S.W. Lee, W.Y. Lee, G.H. Cho, C.T. Rim, Narrow-width inductive power transfer system for online electrical vehicles. IEEE IEEE Trans. Power Electron. **26**(12), 3666–3679 (2011). doi:10.1109/TPEL.2011.2160972
65. A. Huurdeman, *The Worldwide History of Telecommunications* (Wiley, New York, 2003)
66. Institute of Electrical and Electronics Engineers (IEEE), IEEE standard for safety levels with respect to human exposure to radio frequency electromagnetic fields, 3 kHz to 300 GHz. IEEE C95.1-2005 (2005)
67. International Telecommunication Union, http://www.itu.int. Cited 30 Dec 2016
68. H. Jabbar, Y.S. Song, T.T. Jeong, RF energy harvesting system and circuits for charging of mobile devices. IEEE Trans. Consum. Electron. **56**(1), 247–253 (2010). doi:10.1109/TCE.2010.5439152
69. X. Jiang, J. Polastre, D. Culler, Perpetual environmentally powered sensor networks, in *IPSN 2005 Fourth International Symposium on Information Processing in Sensor Networks* (2005), pp. 463–468. doi:10.1109/IPSN.2005.1440974
70. L. Jianying, D. Fang, Z. Yichen, Y. Xin, C. Lulu, Z. Panpan, W. Mengjun, Bending effects on a flexible Yagi-Uda antenna for wireless body area network, in *2016 Asia-Pacific International Symposium on Electromagnetic Compatibility (APEMC)*, vol. 1 (2016), pp. 1001–1003. doi:10.1109/APEMC.2016.7522928
71. R.C. Johnson, H.A. Ecker, J.S. Hollis, Determination of far-field antenna patterns from near-field measurements. Proc IEEE **61**(12), 1668–1694 (1973). doi:10.1109/PROC.1973.9358
72. E.A. Kadir, A.P. Hu, M. Biglari-Abhari, K.C. Aw, Indoor WiFi energy harvester with multiple antenna for low-power wireless applications, in *2014 IEEE 23rd International Symposium on Industrial Electronics (ISIE)* (2014), pp. 526–530. doi:10.1109/ISIE.2014.6864668

73. P. Kamalinejad, K. Keikhosravy, S. Mirabbasi, V.C. Leung, An efficiency enhancement technique for CMOS rectifiers with low start-up voltage for UHF RFID tags, in *2013 International Green Computing Conference (IGCC)* (2013), pp. 1–6. doi:10.1109/IGCC.2013.6604483
74. A. Kansal, J. Hsu, S. Zahedi, M.B. Srivastava, Power management in energy harvesting sensor networks. ACM Trans. Embed. Comput. Syst. (TECS) **6**(4) (2007). doi:10.1145/1274858.1274870
75. D. Karolak, T. Taris, Y. Deval, J.B. Begueret, A. Mariano, Design comparison of low-power rectifiers dedicated to RF energy harvesting, in *Proceedings of the IEEE ICECS, Seville, Spain* (2012), pp. 524–527
76. B.G. Karthik, S. Shivaraman, V. Aditya, Wi-Pie: energy harvesting in mobile electronic devices, in *2011 IEEE Global Humanitarian Technology Conference (GHTC)* (2011), pp. 398–401. doi:10.1109/GHTC.2011.43
77. K. Kaushik, D. Mishra, S. De, S. Basagni, W. Heinzelman, K. Chowdhury, S. Jana, Experimental demonstration of multi-hop RF energy transfer, in *2013 IEEE 24th Annual International Symposium on Personal, Indoor, and Mobile Radio Communications (PIMRC)* (2013), pp. 538–542. doi:10.1109/PIMRC.2013.6666195
78. S. Keyrouz, H.J. Visser, A.G. Tijhuis, Ambient RF energy harvesting from DTV stations, in *2012 Loughborough Antennas and Propagation Conference (LAPC)* (2012), pp. 1–4. doi:10.1109/LAPC.2012.6403012
79. S. Keyrouz, H.J. Visser, A.G. Tijhuis, Multi-band simultaneous radio frequency energy harvesting, in *2013 7th European Conference on Antennas and Propagation (EuCAP)* (2013), pp. 3058–3061
80. J.A. Khan, H.K. Qureshi, A. Iqbal, Energy management in wireless sensor networks: a survey. Comput. Electr. Eng. **41**, 159–176 (2015). doi:10.1016/j.compeleceng.2014.06.009
81. S. Kim, R. Vyas, J. Bito, K. Niotaki, A. Collado, A. Georgiadis, M.M. Tentzeris, Ambient RF energy-harvesting technologies for self-sustainable standalone wireless sensor platforms. Proc. IEEE **102**(11), 1649–66 (2014). doi:10.1109/JPROC.2014.2357031
82. H. Kim, C. Song, J. Kim, D.H. Jung, E. Song, S. Kim, J. Kim, Design of magnetic shielding for reduction of magnetic near field from wireless power transfer system for electric vehicle, in *2014 International Symposium on Electromagnetic Compatibility* (2014), pp. 53–58. doi:10.1109/EMCEurope.2014.6930876
83. H. Kitayoshi, K. Sawaya, Long range passive RFID-tag for sensor networks, in *2005 IEEE 62nd Vehicular Technology Conference (VTC)*, vol. 4 (2005), pp. 2696–2700. doi:10.1109/VETECF.2005.1559038
84. S. Kitazawa, H. Ban, K. Kobayashi, Energy harvesting from ambient RF sources, in *IEEE MTT-S International Microwave Workshop Series on Innovative Wireless Power Transmission: Technologies, Systems, and Applications (IMWS)* (2012), pp. 39–42. doi:10.1109/IMWS.2012.6215815
85. M. Kline, I. Izyumin, B. Boser, S. Sanders, Capacitive power transfer for contactless charging, in *2011 Twenty-Sixth Annual IEEE Applied Power Electronics Conference and Exposition (APEC)* (2011), pp. 1398–1404. doi:10.1109/APEC.2011.5744775
86. F. Kocer, M.P. Flynn, A new transponder architecture with on chip ADC for long-range telemetry applications. IEEE J. Solid-State Circuits **41**(5), 1142–1148 (2006)
87. F. Kocer, M.P. Flynn, An RF-powered, wireless CMOS temperature sensor. IEEE Sensor J. **6**(3), 557–564 (2006). doi:10.1109/JSEN.2006.874457
88. A. Kordzadeh, F. Hojjat-Kashani, A new reduced size microstrip patch antenna with fractal shaped defects. Prog. Electromagn. Res. B (PIER B) **11**, 29–37 (2009). doi:10.2528/PIERB08100501
89. R. Kotz, M. Carlen, Principles and applications of electrochemical capacitors. Electrochim. Acta **45**(15), 2483–2498 (2000). doi:10.1016/S0013-4686(00)00354-6
90. R. Kötz, M. Hahn, R. Gallay, Temperature behavior and impedance fundamentals of supercapacitors. J. Power Sources **154**(2), 550–555 (2006). doi:10.1016/J.JPOWSOUR.2005.10.048

91. I. Krikidis, S. Timotheou, S. Nikolaou, G. Zheng, D.W. Ng, R. Schober, Simultaneous wireless information and power transfer in modern communication systems. IEEE Commun. Mag. **52**(11), 104–110 (2014). doi:10.1109/MCOM.2014.6957150
92. A. Kurs, A. Karalis, R. Moffatt, J.D. Joannopoulos, P. Fisher, M. Soljacic, Wireless power transfer via strongly coupled magnetic resonances. Science **317**(5834), 83–86 (2007). doi:10.1126/science.1143254
93. T.T. Le, Efficient power conversion interface circuits for energy harvesting applications, Doctorate Thesis, Oregon State University, USA (2008)
94. T. Le, K. Mayaram, T. Fiez, Efficient far-field radio frequency energy harvesting for passively powered sensor networks. IEEE J. Solid-State Circuits **43**(5), 1287–1302 (2008)
95. H. Le, N. Fong, H.C. Luong, RF energy harvesting circuit with on-chip antenna for biomedical applications, in *2010 Third International Conference on Communications and Electronics (ICCE)* (2010), pp. 115–117. doi:10.1109/ICCE.2010.5670693
96. H.G. Lee, N. Chang, Powering the IoT: storage-less and converter-less energy harvesting, in *The 20th Asia and South Pacific Design Automation Conference* (2015), pp. 124–129. doi:10.1109/ASPDAC.2015.7058992
97. S. Lee, R. Zhang, K. Huang, Opportunistic wireless energy harvesting in cognitive radio networks. IEEE Trans. Wirel. Commun. **12**(9), 4788–4799 (2013). doi:10.1109/TWC.2013.072613.130323
98. S. Lemey, F. Declercq, H. Rogier, Textile antennas as hybrid energy-harvesting platforms. Proc. IEEE **102**(11), 1833–1857 (2014). doi:10.1109/JPROC.2014.2355872
99. B. Li, X. Shao, N. Shahshahan, N. Goldsman, T. Salter, G.M. Metze, An antenna co-design dual band RF energy harvester. IEEE Trans. Circuits Syst. Regul. Pap. **60**(12), 3256–66 (2013). doi:10.1109/TCSI.2013.2264712
100. T.B. Lim, N.M. Lee, B.K. Poh, Feasibility study on ambient RF energy harvesting for wireless sensor network, in *2013 IEEE MTT-S International Microwave Workshop Series on RF and Wireless Technologies for Biomedical and Healthcare Applications (IMWS-BIO)* (2013), pp. 1–3. doi:10.1109/IMWS-BIO.2013.6756226
101. D. Linden, T.B. Reddy, *Handbook of Batteries*, 3rd edn. (McGraw-Hill, New York, 2001) USA
102. V. Liu, A. Parks, V. Talla, S. Gollakota, D. Wetherall, J.R. Smith, Ambient backscatter: wireless communication out of thin air. ACM SIGCOMM Comput. Commun. Rev. **43**(4), 39–50 (2013). doi:10.1145/2486001.2486015
103. W. Liu, X. Zhou, S. Durrani, H. Mehrpouyan, S.D. Blostein, Energy harvesting wireless sensor networks: delay analysis considering energy costs of sensing and transmission. IEEE Trans. Wirel. Commun. **15**(7), 4635–4650 (2016). doi:10.1109/TWC.2016.2543216
104. W. Liu, K. Huang, X. Zhou, S. Durrani, Full-duplex backscatter interference networks based on time-hopping spreading spectrum (2016). arXiv preprint arXiv:1609.00062
105. C. Loss, R. Gon, C. Lopes, R. Salvado, P. Pinho, Textile antenna for RF energy harvesting fully embedded in clothing, in *2016 10th European Conference on Antennas and Propagation (EuCAP)* (2016), pp. 1–4. doi:10.1109/EuCAP.2016.7481721
106. X. Lu, P. Wang, D. Niyato, E. Hossain, Dynamic spectrum access in cognitive radio networks with RF energy harvesting. IEEE Wirel. Commun. **21**(3), 102–110 (2014). doi:10.1109/MWC.2014.6845054
107. X. Lu, P. Wang, D. Niyato, Z. Han, Resource allocation in wireless networks with RF energy harvesting and transfer. IEEE Network **29**(6), 68–75 (2015). doi:10.1109/MNET.2015.7340427
108. X. Lu, P. Wang, D. Niyato, D.I. Kim, Z. Han, Wireless charging technologies: Fundamentals, standards, and network applications. IEEE Commun. Surv. Tutorials **18**(2), 1413–1452 (2015). doi:10.1109/COMST.2015.2499783
109. D.C. Ludois, J. Reed, M. Erickson, Aerodynamic fluid bearings for capacitive power transfer and rotating machinery, in *IEEE Energy Conversion Congress and Exposition (ECCE)* (2012), pp. 1932–1937. doi:10.1109/ECCE.2012.6342576

110. S. Mandal, R. Sarpeshkar, Low-power CMOS rectifier design for RFID applications. IEEE Trans. Circuits Syst. I **54**(6), 1177–1188 (2007)
111. D. Masotti, A. Costanzo, S. Adami, Design and realization of a wearable multi-frequency RF energy harvesting system, in *Proceedings of the 5th European Conference on Antennas and Propagation (EuCAP)* (2011), pp. 517–520
112. J. Masuch, M. Delgado-Restituto, D. Milosevic, P. Baltus, An RF-to-DC energy harvester for co-integration in a low-power 2.4 GHz transceiver frontend, in *Proceedings of the IEEE ISCAS, Seoul, Korea* (2012), pp. 680–683
113. G.V. Merrett, A.S. Weddell, Supercapacitor leakage in energy-harvesting sensor nodes: fact or fiction? in *Networked Sensing Systems (INSS)* (2012), pp. 1–5. doi:10.1109/INSS.2012.6240581
114. G.V. Merrett, A.S. Weddell, A.P. Lewis, N.R. Harris, B.M. Al-Hashimi, N.M. White, An empirical energy model for supercapacitor powered wireless sensor nodes, in *2008 Proceedings of 17th International Conference on Computer Communications and Networks* (2008), pp. 1–6. doi:10.1109/ICCCN.2008.ECP.34
115. Merriam-Webster, Definition of radio frequency, in *Encyclopedia Britannica*, http://www.merriam-webster.com/dictionary/radiofrequency (2016). Cited 30 Dec 2016
116. C. Mikeka, H. Arai, Design issues in radio frequency energy harvesting system, in *Sustainable Energy Harvesting Technologies - Past, Present and Future*, ed. by K.T. Yen (INTECH Open Access Publisher, Rijeka, 2011). doi:10.5772/945
117. C. Mikeka, H. Arai, A. Georgiadis, A. Collado, DTV band micropower RF energy-harvesting circuit architecture and performance analysis, in *IEEE International Conference on RFID-Technologies and Applications (RFID-TA)* (2011), pp. 561–567. doi:10.1109/RFID-TA.2011.6068601
118. S. Moayedi, F. Cingoz, A. Davoudi, Accelerated simulation of high-fidelity models of supercapacitors using waveform relaxation techniques. IEEE Trans. Power Electron. **28**(11), 4903–4909 (2013). doi:10.1109/TPEL.2013.2250522
119. M.I. Mohamed, W.Y. Wu, M. Moniri, Adaptive data compression for energy harvesting wireless sensor nodes, in *10th IEEE International Conference on Networking, Sensing and Control (ICNSC)* (2013), pp. 633–638. doi:10.1109/ICNSC.2013.6548812
120. C. Moser, L. Thiele, D. Brunelli, L. Benini, Adaptive power management for environmentally powered systems. IEEE Trans. Comput. **59**(4), 478–491 (2010). doi:10.1109/TC.2009.158
121. M. Mrnka, Z. Raida, J. Grosinger, Wide-band dielectric resonator antennas for RF energy harvesting, in *2015 Conference on Microwave Techniques (COMITE)* (2015), pp. 1–4. doi:10.1109/COMITE.2015.7120313
122. J.O. Mur-Miranda, G. Fanti, Y. Feng, K. Omanakuttan, R. Ongie, A. Setjoadi, N. Sharpe, Wireless power transfer using weakly coupled magnetostatic resonators, in *Proc. IEEE ECCE*, Atlanta, GA, USA (2010), pp. 4179–4186. doi:10.1109/ECCE.2010.5617728
123. D.B. Murray, J.G. Hayes, Cycle testing of supercapacitors for long-life robust applications. IEEE Trans. Power Electron. **30**(5), 2505–2516 (2015). doi:10.1109/TPEL.2014.2373368
124. Nesscap Co., http://www.nesscap.com/. Cited 30 Dec 2016
125. D.W. Ng, E.S. Lo, R. Schober, Wireless information and power transfer: Energy efficiency optimization in OFDMA systems. IEEE Trans. Wirel. Commun. **12**(12), 6352–6370 (2013). doi:10.1109/TWC.2013.103113.130470
126. A. Nimo, D. Grgic, L.M. Reindl, Ambient electromagnetic wireless energy harvesting using multiband planar antenna, in *9th International Multi-Conference on Systems, Signals and Devices (SSD)* (2012), pp. 1–6. doi:10.1109/SSD.2012.6198036
127. A. Nimo, D. Grgic, L.M. Reindl, Impedance optimization of wireless electromagnetic energy harvester for maximum output efficiency at μW input power, in *International Society for Optics and Photonics (SPIE) Smart Structures and Materials Nondestructive Evaluation and Health Monitoring* (2012), vol. 8341. doi:10.1117/12.914778
128. A. Nimo, D. Grgic, T. Ungan, L.M. Reindl, A new family of passive wireless RF harvesters based on R-C-Quartz oscillators, in *Proceedings of the IEEE EuMC, Nuremberg, German* (2013), pp. 511–514

129. P. Ning, J.M. Miller, O.C. Onar, C.P. White, A compact wireless charging system for electric vehicles, in *2013 IEEE Energy Conversion Congress and Exposition* (2013), pp. 3629–3634. doi:10.1109/ECCE.2013.6647179
130. P. Nintanavongsa, U. Muncuk, D.R. Lewis, K.R. Chowdhury, Design optimization and implementation for RF energy harvesting circuits. IEEE J. Emerging Sel. Topics Circuits Syst. **2**(1), 24–33 (2012)
131. P. Nintanavongsa, M.Y. Naderi, K.R. Chowdhury, A dual-band wireless energy transfer protocol for heterogeneous sensor networks powered by RF energy harvesting, in *2013 International Conference on Computer Science and Engineering Conference (ICSEC)* (2013), pp. 387–392. doi:10.1109/ICSEC.2013.6694814
132. H. Nishimoto, Y. Kawahara, T. Asami, Prototype implementation of ambient RF energy harvesting wireless sensor networks, in 2010 IEEE Sensors (2010), pp. 1282–1287. doi:10.1109/ICSENS.2010.5690588
133. A. Noguchi, H. Arai, Small loop rectenna for RF energy harvesting, in *2013 Asia-Pacific Microwave Conference Proceedings (APMC)* (2013), pp. 86–88. doi:10.1109/APMC.2013.6695199
134. J.P. Olds, W.K. Seah, Design of an active radio frequency powered multi-hop wireless sensor network, in *2012 7th IEEE Conference on Industrial Electronics and Applications (ICIEA)* (2012), pp. 1721–1726. doi:10.1109/ICIEA.2012.6361003
135. U. Olgun, C.C. Chen, J.L. Volakis, Low-profile planar rectenna for batteryless RFID sensors, in *2010 IEEE Antennas and Propagation Society International Symposium* (2010), pp. 1–4. doi:10.1109/APS.2010.5562220
136. U. Olgun, C.C. Chen, J.L. Volakis, Efficient ambient WiFi energy harvesting technology and its applications, in *2012 IEEE International Symposium on Antennas and Propagation* (2012), pp. 1–2. doi:10.1109/APS.2012.6349384
137. Ossia Inc., http://www.ossia.com/. Cited 30 Dec 2016
138. G. Papotto, F. Carrara, G. Palmisano, A 90-nm CMOS threshold compensated RF energy harvester. IEEE J. Solid-State Circuits **46**(9), 1985–1997 (2011)
139. G. Papotto, F. Carrara, A. Finocchiaro, G. Palmisano, A 90-nm CMOS 5-Mbps crystal-less RF-powered transceiver for wireless sensor network nodes. IEEE J. Solid State Circuits **49**(2), 335–346 (2014). doi:10.1109/JSSC.2013.2285371
140. A.M. Pareja, A. Bakkali, J. Pelegri-Sebastia, T. Sogorb, V. Llario, A Bou, Radio frequency energy harvesting - sources and techniques, in *Renewable Energy - Utilisation and System Integration*, ed. by C. Wenping (INTECH Open Access Publisher, Rijeka, 2016). doi:10.5772/61722
141. D. Pavone, A. Buonanno, M. D'Urso, F. Della Corte, Design considerations for radio frequency energy harvesting devices. Prog. Electromagn. Res. B **45**, 19–35 (2012). doi:10.2528/PIERB12062901
142. M. Penella, F.M. Gasulla, Runtime extension of low-power wireless sensor nodes using hybrid-storage units. IEEE Trans. Instrum. Meas. **59**(4), 857–865 (2010). doi:10.1109/TIM.2009.2026603
143. M.T. Penella-Lopez, M. Gasulla-Forner, *Powering Autonomous Sensors: An Integral Approach with Focus on Solar and RF Energy Harvesting* (Springer, Dordrecht, 2011). doi:10.1007/978-94-007-1573-8
144. G. Peterson, The application of electromagnetic surface waves to wireless energy transfer, in *2015 IEEE Wireless Power Transfer Conference (WPTC)* (2015), pp. 1–4. doi:10.1109/WPT.2015.7139133
145. M. Pinuela, P.D. Mitchenson, S. Lucyszyn, Analysis of scalable rectenna configurations for harvesting high frequency electromagnetic ambient radiation, in *International Conference on Micro and Nanotechnology for Power Generation and Energy Conversion Applications* (2010), pp. 41–44
146. M. Pinuela, P.D. Mitcheson, S. Lucyszyn, Ambient RF energy harvesting in urban and semi-urban environments. IEEE Trans. Microwave Theory Tech. **61**(7), 2715–2726 (2013). doi:10.1109/TMTT.2013.2262687

147. Z. Popovic, Cut the cord: low-power far-field wireless powering. IEEE Microw. Mag. **14**(2), 55–62 (2013). doi:10.1109/MMM.2012.2234638
148. Z. Popovic, P. Momenroodaki, R. Scheeler, Toward wearable wireless thermometers for internal body temperature measurements. IEEE Commun. Mag. **52**(10), 118–25 (2014). doi:10.1109/MCOM.2014.6917412
149. Powercast Corp., http://www.powercastco.com/. Cited 30 Dec 2016
150. R.V. Prasad, S. Devasenapathy, V.S. Rao, J. Vazifehdan, Reincarnation in the ambiance: Devices and networks with energy harvesting. IEEE Commun. Surv. Tutorials **16**(1), 195–213 (2013). doi:10.1109/SURV.2013.062613.00235
151. D.V. Ragone, Review of battery systems for electrically powered vehicles. SAE Technical Paper (1968). doi:10.4271/680453
152. S. Rao, J.C. Chiao, Body electric: wireless power transfer for implant applications. IEEE Microw. Mag. **16**(2), 54–64 (2015). doi:10.1109/MMM.2014.2377586
153. RAV Power, Datasheet for Qi-enabled charger, http://www.ravpower.com/qi-wireless-charger-black.html. Cited 30 Dec 2016
154. V. Rizzoli, G. Bichicchi, A. Costanzo, F. Donzelli, D. Masotti, CAD of multi-resonator rectenna for micro-power generation, in *2009 European microwave conference (EuMC)* (2009), pp. 1684–1687
155. M. Roberg, T. Reveyrand, I. Ramos, E.A. Falkenstein, Z. Popovic, High-efficiency harmonically terminated diode and transistor rectifiers. IEEE Trans. Microw. Theory Tech. **60**(12), 4043–4052 (2012)
156. T. Salter, K. Choi, M. Peckerar, G. Metze, RF energy scavenging system utilizing switched capacitor DC-DC converter. Electron. Lett. **45**(7), 374–376 (2009)
157. A. Sample, J.R. Smith, Experimental results with two wireless power transfer systems, in *2009 IEEE Radio and Wireless Symposium* (2009), pp. 16–18. doi:10.1109/RWS.2009.4957273
158. F. Sangare, A. Arab, M. Pan, L. Qian, S.K. Khator, Z. Han, RF energy harvesting for WSNs via dynamic control of unmanned vehicle charging, in *IEEE Wireless Communications and Networking Conference (WCNC)* (2015), pp. 1291–1296. doi:10.1109/WCNC.2015.7127655
159. F. Sangare, Y. Xiao, D. Niyato, Z. Han, Mobile charging in wireless-powered sensor networks: optimal scheduling and experimental implementation. IEEE Trans. Veh. Technol. (TVT) (2016, to appear)
160. O.H. Seunghyun, D.D. Wentzloff, A -32 dBm sensitivity RF power harvester in 130 nm CMOS, in *Proceedings of the IEEE RFIC, Montreal, QC, USA* (2012), pp. 483–486
161. S. Scorcioni, L. Larcher, A. Bertacchini, Optimized CMOS RF-DC converters for remote wireless powering of RFID applications, in *2012 IEEE International Conference on RFID* (2012), pp. 47–53. doi:10.1109/RFID.2012.6193055
162. S. Scorcioni, A. Bertacchini, L. Larcher, A 868 MHz CMOS RFDC power converter with -17 dBm input power sensitivity and efficiency higher than 40% over 14 dB input power range, in *Proceedings of the IEEE ESSCIRC, Bordeaux, France* (2012), pp. 109–112
163. S. Scorcioni, L. Larcher, A. Bertacchini, L. Vincetti, M. Maini, An integrated RF energy harvester for UHF wireless powering applications, in *Proceedings of the IEEE WPT, Perugia, Italy* (2013), pp. 92–95
164. W.K. Seah, J.P. Olds, Data delivery scheme for wireless sensor network powered by RF energy harvesting, in *2013 IEEE Wireless Communications and Networking Conference (WCNC)* (2013), pp. 1498–1503. doi:10.1109/WCNC.2013.6554785
165. W.K. Seah, Z.A. Eu, H.P. Tan, Wireless sensor networks powered by ambient energy harvesting (WSN-HEAP)- survey and challenges, in *1st International Conference on Wireless Communication, Vehicular Technology, Information Theory and Aerospace and Electronic Systems Technology (Wireless VITAE)* (2009), pp. 1–5. doi:10.1109/WIRELESSVITAE.2009.5172411
166. A. Shameli, A. Safarian, A. Rofougaran, M. Rofougaran, F.D. Flaviis, Power harvester design for passive UHF RFID tag using a voltage boosting technique. IEEE Trans. Microwave Theory Tech. **55**(6), 1089–1097 (2007)

167. L. Shi, M.L. Crow, Comparison of ultracapacitor electric circuit models, in *Power and Energy Society General Meeting - Conversion and Delivery of Electrical Energy in the 21st Century* (2008), pp. 1–6. doi:10.1109/PES.2008.4596576
168. R. Shigeta, T. Sasaki, D.M. Quan, Y. Kawahara, R.J. Vyas, M.M. Tentzeris, T. Asami, Ambient RF energy harvesting sensor device with capacitor-leakage-aware duty cycle control. IEEE Sensors J. **13**(8), 2973–2983 (2013). doi:10.1109/JSEN.2013.2264931
169. N. Shinohara, S. Kawasaki, Recent wireless power transmission technologies in Japan for space solar power station/satellite, in *2009 IEEE Radio and Wireless Symposium* (2009), pp. 13–15. doi:10.1109/RWS.2009.4957272
170. S. Shrestha, S.K. Noh, D.Y. Choi, Comparative study of antenna designs for RF energy harvesting. Int. J. Antennas Propag. **2013**, 1–10 (2013). http://dx.doi.org/10.1155/2013/385260
171. A.M. Siddiqui, L. Musavian, Q. Ni, Energy efficiency optimization with energy harvesting using harvest-use approach, in *IEEE International Conference on Communication Workshop (ICCW)* (2015), pp. 1982–1987. doi:10.1109/ICCW.2015.7247471
172. Z.W. Sim, R. Shuttleworth, B. Grieve, Investigation of PCB microstrip patch receiving antenna for outdoor RF energy harvesting in wireless sensor networks, in *2009 Loughborough Antennas and Propagation Conference (LAPC)* (2009), pp. 129–132. doi:10.1109/LAPC.2009.5352525
173. F.I. Simjee, P.H. Chou, Efficient charging of supercapacitors for extended lifetime of wireless sensor nodes. IEEE Trans. Power Electron. **23**(3), 1526–1536 (2014). doi:10.1109/TPEL.2008.921078
174. V. Sivaji, D.K. Bhatia, S. Prasad, Novel technique for sleep apnea monitoring, in *2015 IEEE 12th International Conference on Wearable and Implantable Body Sensor Networks (BSN)* (2015), pp. 1–5. doi:10.1109/BSN.2015.7299418
175. A. Sivaramakrishnan, K.J. Jegadishkumar, A highly efficient power management system for charging mobile phones using RF energy harvesting. Int. J. Inf. Technol. Convergence Services (IJITCS) **1**(5), 21–30 (2011). doi:10.5121/ijitcs.2011.1503
176. Skyworks Inc., http://www.skyworksinc.com/. Cited 30 Dec 2016
177. T.A. Smith, J.P. Mars, G.A. Turner, Using supercapacitors to improve battery performance, in *Power Electronics Specialists Conference* (2002), pp. 124–128. doi:10.1109/PSEC.2002.1023857
178. M. Stoopman, S. Keyrouz, H.J. Visser, K. Philips, W.A. Serdijn, A self-calibrating RF energy harvester generating 1 V at -26.3 dBm, in *Proceedings of the IEEE Symposium VLSIC, Kyoto, Japan* (2013), pp. 226–227
179. M. Stoopman, S. Keyrouz, H.J. Visser, K. Philips, W.A. Serdijn, Co-design of a CMOS rectifier and small loop antenna for highly sensitive RF energy harvesters. IEEE J. Solid-State Circuits **49**(3), 622–634 (2014)
180. B. Strassner, K. Chang, Microwave power transmission: Historical milestones and system components. Proc. IEEE **101**(6), 1379–1396 (2013). doi:10.1109/JPROC.2013.2246132
181. M. Stratmann, P. Trawinski, Rechargeable toothbrushes with charging stations. Braun GmbH, US Patent 6,798,169, https://www.google.com/patents/US6798169.GooglePatents (2004). Cited 30 Dec 2016
182. W.L. Stutzman, G.A. Thiele, *Antenna Theory and Design*, 3rd edn. (Wiley, New York, 2012)
183. S. Sudevalayam, P. Kulkarni, Energy harvesting sensor nodes: Survey and implications. IEEE Commun. Surv. Tutorials **13**(3), 443–461 (2011). doi:10.1109/SURV.2011.060710.00094
184. H. Sun, Y. Guo, M. He, Z. Zhong, Design of a high-efficiency 2.45-GHz rectenna for low-input-power energy harvesting. IEEE Antennas Wirel. Propag. Lett. **11**, 929–932 (2012)
185. H. Sun, Y.X. Guo, M. He, Z. Zhong, A dual-band rectenna using broadband Yagi antenna array for ambient RF power harvesting. IEEE Antennas Wirel. Propag. Lett. **12**, 918–921 (2013). doi:10.1109/LAWP.2013.2272873
186. V. Talla, B. Kellogg, B. Ransford, S. Naderiparizi, S. Gollakota, J.R. Smith, Powering the next billion devices with Wi-Fi (2015). arXiv: 1505.06815

187. M. Tanevski, A. Boegli, P.A. Farine, Power supply energy optimization for ultra low-power wireless sensor nodes, in *Sensors Applications Symposium (SAS)* (2013), pp. 176–181. doi:10.1109/SAS.2013.6493581
188. T. Taris, V. Vigneras, L. Fadel, A 900 MHz RF energy harvesting module, in *Proceedings of the IEEE 10th International NEWCAS, Montreal, QC, USA* (2012), pp. 445–448
189. Texas Instruments Corp., http://www.ti.com/. Cited 30 Dec 2016
190. Texas Instruments Inc., ISM-band and short range device regulatory compliance overview, http://www.ti.com/lit/an/swra048/swra048.pdf. Cited 30 Dec 2016
191. Texzon Technologies, LLC., http://www.texzontechnologies.com/. Cited 30 Dec 2016
192. The American National Standard Institute, https://www.ansi.org/. Cited 30 Dec 2016
193. The Occupational Safety and Health Administration, https://www.osha.gov/. Cited 30 Dec 2016
194. T. Thierry, F. Ludivine, O. Laurent, V. Valerie, COTS-based modules for far-field radio frequency energy harvesting at 900 MHz and 2.4 GHz, in *Proceedings of the IEEE International NEWCAS, Paris, France* (2013), pp. 1–4
195. J.P. Thomas, M.A. Qidwai, J.C. Kellogg, Energy scavenging for small-unmanned systems. J. Power Sources **159**(2), 1494–1509 (2006)
196. Timothy Truckle (Own work), https://commons.wikimedia.org/wiki/File:Sidelobes_en.svg. Cited 30 Dec 2016
197. UPM Rafsec, Tutorial overview of inductively coupled RFID systems, Tampere, Finland, http://www.rafsec.com/rfidsystems.pdf (2003). Cited 30 Dec 2016
198. C.R. Valenta, G.D. Durgin, Harvesting wireless power: Survey of energy-harvester conversion efficiency in far-field, wireless power transfer systems. IEEE Microw. Mag. **15**(4), 108–120 (2014). doi:10.1109/MMM.2014.2309499
199. G.A. Vera, A. Georgiadis, A. Collado, S. Via, Design of a 2.45 GHz rectenna for electromagnetic (EM) energy scavenging, in *Proceedings of the IEEE Radio Wireless Symposium, New Orleans, LA, USA* (2010), pp. 61–64
200. L. Vincetti, M. Maini, E. Pinotti, L. Larcher, S. Scorcioni, A. Bertacchini, D. Grossi, A. Tacchini, Broadband printed antenna for radiofrequency energy harvesting, in *2012 International Conference on Electromagnetics in Advanced Applications (ICEAA)* (2012), pp. 814–816. doi:10.1109/ICEAA.2012.6328744
201. H.J. Visser, A.C. Reniers, J.A. Theeuwes, Ambient RF energy scavenging: GSM and WLAN power density measurements, in *38th European Microwave Conference (EuMC)* (2008), pp. 721–724. doi:10.1109/EUMC.2008.4751554
202. R.J. Vyas, H. Nishimoto, M.M. Tentzeris, Y. Kawahara, T. Asami, A battery-less, energy harvesting device for long range scavenging of wireless power from terrestrial TV broadcasts, in *IEEE MTT-S International Microwave Symposium Digest (MTT)* (2012), pp. 1–3. doi:10.1109/MWSYM.2012.6259708
203. R.J. Vyas, B.S. Cook, Y. Kawahara, M.M. Tentzeris, E-WEHP: a batteryless embedded sensor-platform wirelessly powered from ambient digital-TV signals. IEEE Trans. Microwave Theory Tech. **61**(6), 2491–2505 (2013). doi:10.1109/TMTT.2013.2258168
204. X. Wang, A. Mortazawi, High sensitivity RF energy harvesting from AM broadcasting stations for civilian infrastructure degradation monitoring, in *Proceedings of the IEEE IWS, Beijing, China* (2013), pp. 1–3
205. K. Wang, S. Sanders, Contactless USB – a capacitive power and bidirectional data transfer system, in *2014 IEEE Applied Power Electronics Conference and Exposition (APEC)* (2014), pp. 1342–1347. doi:10.1109/APEC.2014.6803481
206. N. Williard, D. Baek, J.W. Park, B.O. Choi, M. Osterman, M. Pecht, A life model for supercapacitors. IEEE Trans. Device Mater. Reliability **15**(4), 519–528 (2015). doi:10.1109/TDMR.2015.2479466
207. L. Xia, J. Cheng, N.E. Glover, P. Chiang, 0.56 V, −20 dBm RF-powered, multi-node wireless body area network system-on-a-chip with harvesting-efficiency tracking loop. IEEE J. Solid State Circuits **49**(6), 1345–1355 (2014). doi:10.1109/JSSC.2014.2305074

208. L. Xiao, P. Wang, D. Niyato, D. Kim, Z. Han, Wireless networks with RF energy harvesting: a contemporary survey. IEEE Commun. Surv. Tutorials **17**(2), 757–789 (2015). doi:10.1109/COMST.2014.2368999
209. L. Xie, Y. Shi, Y.T. Hou, A. Lou, Wireless power transfer and applications to sensor networks. IEEE Wirel. Commun. **20**(4), 140–145 (2013). doi:10.1109/MWC.2013.6590061
210. L. Xie, Y. Shi, Y.T. Hou, W. Lou, H.D. Sherali, H. Zhou, S.F. Midkiff, A mobile platform for wireless charging and data collection in sensor networks. IEEE J. Sel. Areas Commun. **33**(8), 1521–1533 (2015). doi:10.1109/JSAC.2015.2391631
211. L. Xie, Y. Shi, Y.T. Hou, W. Lou, H.D. Sherali, S.F. Midkiff, Multi-node wireless energy charging in sensor networks. IEEE/ACM Trans. Networking (TON) **23**(2), 437–450 (2015). doi:10.1109/TNET.2014.2303979
212. H. Yang, Y. Zhang, Analysis of supercapacitor energy loss for power management in environmentally powered wireless sensor nodes. IEEE Trans. Power Electron. **28**(11), 5391–5403 (2013). doi:10.1109/TPEL.2013.2238683
213. Y. Yao, W. Jie, S. Yin, F.F. Dai, A fully integrated 900-MHz passive RFID transponder front end with novel zero-threshold RF-DC rectifier. IEEE Trans. Ind. Electron. **56**(7), 2317–2325 (2009)
214. D. Yi, T. Arslan, Broadband differential antenna for full-wave RF energy scavenging system, in *2013 Loughborough Antennas and Propagation Conference (LAPC)* (2013), pp. 325–328. doi:10.1109/LAPC.2013.6711912
215. J. Yi, W.H. Ki, C.Y. Tsui, Analysis and design strategy of UHF micro-Power CMOS rectifiers for micro-sensor and RFID applications. IEEE Trans. Circuits Syst. I **54**(1), 153–166 (2007)
216. D. Yi, T. Arslan, A. Hamilton, Broadband antenna for RF energy scavenging system, in *2012 Loughborough Antennas and Propagation Conference (LAPC)* (2012), pp. 1–4. doi:10.1109/LAPC.2012.6403034
217. F. Yuan, *CMOS Circuits for Passive Wireless Microsystems* (Springer, New York, 2011). doi:10.1007/978-1-4419-7680-2
218. F. Yuan, K.Q. Zhang, S. Jin, H. Zhu, A harvest-use-store mode for energy harvesting communication systems with optimal power policy, in *2014 IEEE International Conference on Communications (ICC)* (2014), pp. 5366–5371. doi:10.1109/ICC.2014.6884174
219. F. Yuan, Q.T. Zhang, S. Jin, H. Zhu, Optimal harvest-use-store strategy for energy harvesting wireless systems. IEEE Trans. Wirel. Commun. **14**(2), 698–710 (2015). doi:10.1109/TWC.2014.2358215
220. N.A. Zainuddin, Z. Zakaria, M.N. Husain, B.M. Derus, M.A. Aziz, M.A. Mutalib, M.A. Othman, Design of wideband antenna for RF energy harvesting system, in *2013 3rd International Conference on Instrumentation, Communications, Information Technology, and Biomedical Engineering (ICICI-BME)* (2013), pp. 162–166. doi:10.1109/ICICI-BME.2013.6698485
221. Z. Zakaria, N.A. Zainuddin, M.A. Aziz, M.N. Husain, M.A. Mutalib, A parametric study on dual-band meander line monopole antenna for RF energy harvesting, in *2013 IEEE International Conference on RFID-Technologies and Applications (RFID-TA)* (2013), pp. 1–5. doi:10.1109/RFID-TA.2013.6694523
222. Z. Zakaria, N.A. Zainuddin, M.N. Husain, M.Z. Aziz, M.A. Mutalib, A.R. Othman, Current developments of RF energy harvesting system for wireless sensor networks. Adv. Inf. Sci. Serv. Sci. **5**(11), 328–338 (2013). doi:10.4156/AISS.vol5.issue11.39
223. Z. Zakaria, N.A. Zainuddin, M.A. Aziz, M.N. Husain, M.A. Mutalib, Dual-band monopole antenna for energy harvesting system, in *2013 IEEE Symposium on Wireless Technology and Applications (ISWTA)* (2013), pp. 225–229. doi:10.1109/ISWTA.2013.6688775
224. R. Zhang, C.K. Ho, MIMO broadcasting for simultaneous wireless information and power transfer. IEEE Trans. Wirel. Commun. **12**(5), 1989–2001 (2013). doi:10.1109/TWC.2013.031813.120224
225. R. Zhang, C.K. Ho, MIMO broadcasting for simultaneous wireless information and power transfer. IEEE Trans. Wirel. Commun. **12**(5), 1989–2001 (2013). doi:10.1109/GLOCOMW.2014.7063588

226. X. Zhang, H. Jiang, L. Zhang, C. Zhang, Z. Wang, X. Chen An energy-efficient ASIC for wireless body sensor networks in medical applications. IEEE Trans. Biomed. Circuits Syst. **4**(1), 11–8 (2010). doi:10.1109/TBCAS.2009.2031627
227. J. Zhang, Y. Huang, P. Cao, A wideband cross dipole rectenna for RF wireless harvesting, in *2013 7th European Conference on Antennas and Propagation (EuCAP)* (2013), pp. 3063–3067
228. X. Zhou, R. Zhang, C.K. Ho, Wireless information and power transfer: Architecture design and rate-energy tradeoff. IEEE Trans. Commun. **61**(11), 4754–4767 (2012). doi:10.1109/TCOMM.2013.13.120855
229. A.M. Zungeru, L.M. Ang, S. Prabaharan, K.P. Seng, Radio frequency energy harvesting and management for wireless sensor networks, in *Green Mobile Devices and Networks: Energy Optimization and Scavenging Techniques*, ed. by G.-M. Muntean, M. Venkataraman (CRC Press, Boca Raton, 2012), pp. 341–368. doi:10.1201/b10081-16
230. Y. Zuo, Survivable RFID systems: Issues, challenges, and techniques. IEEE Trans. Syst. Man Cybern. Part C Appl. Rev. **40**(4), 406–418 (2010). doi:10.1109/TSMCC.2010.2043949

Chapter 8
Wireless Powered Sensor Networks

Wanchun Liu, Salman Durrani, and Xiangyun Zhou

8.1 Wireless Sensor Networks

The first wireless sensor network (WSN) was originally invented by the United States Military in the 1950s to detect and track Soviet submarines [1]. The network, which consisted of acoustic sensors, was distributed in the Atlantic and Pacific oceans. In the 1980s, the United States Defense Advanced Research Projects Agency (DARPA) started the distributed sensor network program which boosted the civilian and scientific research on WSNs. Thanks to the advances in semiconductor, networking and material science technologies in the past a few decades, the ubiquitous deployment of large-scale WSNs has finally come true. The state-of-the-art WSNs have many applications such as micro-climates measurement on farms, habitat monitoring, volcano monitoring, structural monitoring, vehicle tracking, human presence detection in homes and offices, electrical/gas/water metering.

For instance, consider the applications of WSNs in Australia as an example [2]. In South Australia, WSNs have been widely used to monitor the growing of grapes. Sensors measure the temperature, light, wind speed, humidity, and soil moisture and provide information for analysis, in order to optimize plant growth and prevent crop loss. In Victoria, a wireless sensor network of 100 nodes was deployed over

This work was supported by the Australian Research Council's Discovery Project Funding Scheme (Project number DP140101133).

W. Liu (✉) • X. Zhou
Research School of Engineering, The Australian National University,
Canberra 2601, ACT, Australia
e-mail: wanchun.liu@anu.edu.au; xiangyun.zhou@anu.edu.au

S. Durrani
College of Engineering and Computer Science, The Australian National University,
Canberra, Aust Capital Terr, Australia
e-mail: salman.durrani@anu.edu.au

D.N.K. Jayakody et al. (eds.), *Wireless Information and Power Transfer: A New Paradigm for Green Communications*, DOI 10.1007/978-3-319-56669-6_8

a 1 km square region of forest in the Dandenong Ranges. The network monitors in real-time, a range of environmental parameters to improve situational awareness, such as the event of bush fires. In Melbourne, in order to solve the noise pollution problem, a WSN has been deployed across the central business district to measure sound level. A noise map of the city is generated by the data collected from the sensors, which is then used to manage noisy areas. In Sydney, WSNs are deployed to detect and indicate where open parking is located in the city streets to reduce traffic congestion.

The future Internet-of-Things (IoT), which is going to connect tens of billions of low-complexity wireless devices such as sensors and wearable computing devices, can be treated as a advanced evolution of WSN. The IoT will enable new applications such as smart cities, home automation, and e-healthcare. One of the most important implementation challenge of the IoT is that the finite battery capacity sensor nodes have a limited lifetime and thus require regular battery replacements [3]. This kind of battery replacement for massive number of IoT nodes is difficult or even infeasible as many sensors are deployed in hazardous environments or hidden in walls, furniture, and even in human bodies.

One immediate solution is to use large batteries for longer lifetimes, however, the increased size, weight, and cost may not be affordable for the massive number of sensors. Another solution is to adopt low power hardware, but at the cost of lesser computation ability and lower transmission ranges. To effectively address the finite node lifetime problem, an alternative technique, i.e., energy harvesting powered WSN is the most promising solution.

8.2 Energy Harvesting Wireless Sensor Networks

Generally speaking, energy harvesting (EH) means harvesting energy from the ambient environment such as solar, wind and thermal energy, or other energy sources such as foot strike, finger strokes, and body heat, and converting it to electrical power/energy. In theory, a sensor node can be powered perpetually as long as the harvested energy source is continuously available. Figure 8.1 illustrates the basic architecture of an EH WSN, which consists of multiple sensors and one sink. The sensors are able to harvests energy from a solar panel and may also harvests energy from other energy sources such as RF signals emitted by power beacons or base stations (which will be discussed in the next subsection).

More precisely, an EH sensor consists of six modules which are illustrated in Fig. 8.2: a micro-controller (not included in the figure for brevity), EH module, battery, sensing modulo, transmitter(and receiver), and data buffer. The sensor first needs to convert the ambient energy arrival into a direct current (DC) signal by the EH module, which is then used to charge the battery of the sensor. Powered by the harvested energy, the sensing module senses its relevant parameters and saves the sensed data into the data buffer, and the transmitter transmits the sensed data to the sink.

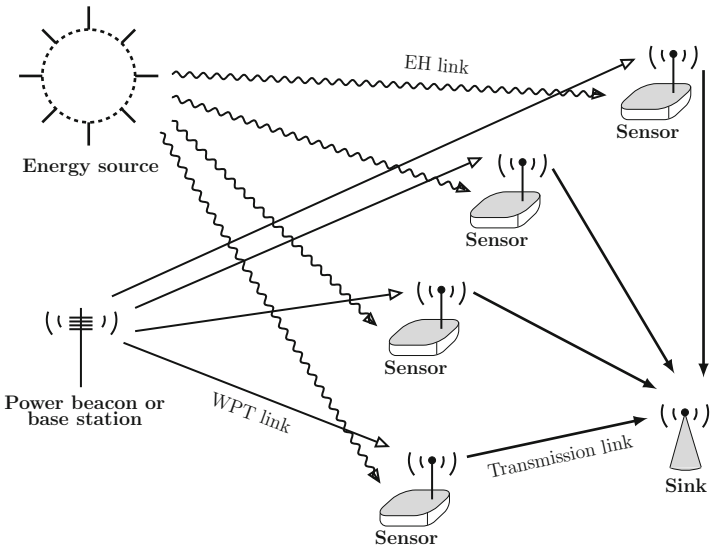

Fig. 8.1 Illustration of EH WSN

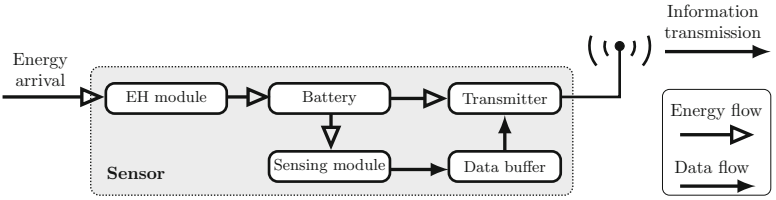

Fig. 8.2 Illustration of the components of a wireless sensor node

Table 8.1 Environmental energy harvesting power (reproduced from [5])

Source	Average harvested energy
Solar panel	15 mW/cm^2
Light (indoor)	10–100 μW/cm^2
Airflow	0.4–1 mW/cm^3
Vibrations	200–380 μW/cm^3
Thermoelectric	40–60 μW/cm^2
Piezoelectric	100–330 μW/cm^3

The EH rate of different energy sources are listed in Table 8.1. It is straightforward to see that EH from a solar panel can provide the highest EH rate. In addition, solar energy is the most easily accessible energy source and there are lots of existing WSN applications based on it. For example, the outdoor multi-target tracking networks [4], such as the zebra tracking and the turtle habitat monitoring networks in the USA.

8.2.1 WSN Power Consumptions

There are three main energy costs in wireless sensors, which are summarized in [5] as

1. Energy cost of RF transmission and reception. This is the energy consumption of the RF components of the transmitter (and also the receiver), such as the mixer and the analog to digital converter (ADC).
2. Energy cost of information sensing and processing. This is the energy consumption of the sensor chip and the ADC of the sensing module.
3. Energy cost of other basic processing while being active. This is the energy consumption of the micro-controller of the wireless sensor node. The processing unit, which is generally associated with a small storage unit, performs tasks, processes data, and controls the functionality of other components in the sensor node.

The power consumptions for processing, sensing, and transmission/reception for most commonly used WSN nodes are summarized in Tables 8.2, 8.3, and 8.4, respectively. In Table 8.2, we list two micro-controllers PXA271 and ATmega 128/L, which are used in WSN nodes Inote2 and MicaZ, respectively. We also include three micro-controllers of TI's low voltage low power series. Comparing TI's MSP430F2132 with ATmel's ATmega 128/L, we see that the active power consumption is significantly reduced. In Table 8.3, we list six sensor chips with the functions of dual-axis accelerometer, three-axis accelerometer, pressure sensing, light sensing, temperature sensing, and thermopile sensing. We see that the power consumption of different types of sensors varies greatly. In Table 8.4, we list six commonly used 2.4 GHz Low Power Transceiver for the IEEE 802.15.4 standard. Comparing TI's CC2502 with Freescale's MC1321, it is easy to see that MC1321's power consumption is almost doubled compared to CC2502 in the receive mode, while the transmit power consumption is almost the same.

We see that the energy cost of processing and sensing is much smaller compared to the energy cost of transmission, and this is the reason why majority of the current work on EH WSNs has considered only the energy cost of transmission, while ignoring the energy cost of processing and sensing [6, 7].

However, the IoT will require various more complicated sensing functions, such as charge coupled device (CCD) or complementary metal oxide semiconductor (CMOS) image sensors that adopt array sensing, and high-rate and high-resolution acoustic and seismic sensors [8] (and the references therein). The energy cost of sensing in this scenario can actually be higher than the energy cost of transmission. Moreover, as an emerging low power communication technique, backscatter communication [9], which does not have any active RF components and relies on passive RF signal reflection, has an ultra low power consumption roughly within a μW level when active for transmissions [10, 11]. Therefore, in these application scenarios, power consumptions for sensing are comparable to or even much higher

Table 8.2 Processor consumption

Features	PXA271	ATmega 128/L	TMS320c5535	MSP430BT5190	MSP430F2132
Manufacturer	CPU	MCU	DSP	MCU	MCU
Company	Intel	Atmel	TI	TI	TI
Voltage supply	3 V	5 V	1.05 V	3 V	2.2 V
CPU frequency	13 MHz	12 MHz	50 MHz	20 MHz	1 M
Active mode power	44.2 mW	125 mW	7.5 mW	9 mW (RAM program execution)	0.55 mW
Standby mode power	1.72 mW (idle 8.5 mW)	8.5 mW	0.26 mW	3.6 μW	1.54 μW
Wake up time	<0.6 ms	<1.5 ms	> 30.5 μs	<5 μs	<1 μs
Start time (from power down)	<136.65 ms	>4.12 ms	>8 ms	<0.15 ms	<2 ms
Notions	Used by Imote2 (High-performance wireless sensor network node)	Used by commercial off-the-shelf sensor plat form such as, MicaZ, Mica2	TI low voltage low power series	TI low voltage low power series	TI low voltage low power series

Table 8.3 Sensor consumption

Features	ADXL202JE	ADXL345	MS5534AM	TSL2550D	PGA309-ht	LMP91051
Manufacturer	Analog devices	Analog devices	Intersema	TAOS	TI	TI
Function	Dual-axis accelerometer	Three-axis accelerometer	Barometric pressure sensor	Ambient light sensor	Temperature and pressure sense	Thermopile sensor
Voltage supply	3.5 V	2.5 V	3 V	3.3 V	3 V	3.3 V
Active mode power	1.75 mW	58 μW	3 mW	1 mW	3.6 mW	11.88 mW
Standby mode power	< 0.084 mW	0.25 μW	0.01 mW	< 0.03 mW	0	0.247 mW
Data conversion time	2 ms	> 0.3 ms	< 35 ms	400 ms	< 0.2 ms	<10 μs
Begin to sleep	–	1.4 ms	–	–	0	2 μs
Wake up time	–	1.4 ms	–	1 s	0	1 ms

Table 8.4 Transceiver consumption (reproduced from [5])

Features	CC2520	CC2430	CC2590	JN5139	MC1321	EM1250
Manufacturer	TI	TI	TI	Jennic	Freescale	Ember
Radio frequency (GHz)	2.4	2.4	2.4	2.4	2.4	2.4
Bit rate (kbps)	250	250	250	250	250	250
Supply voltage (V)	1.8–3.8	2.0–3.6	2.2–3.6	2.2–3.7	2.0–3.4	2.1–3.6
Sleep current (μA)	1	0.5	0.1	0.2	1	1
Rx current (mA)	18.5	27	3.4	34	37	29
Tx current min (mA)	16.2(−18 dBm)	–	–	–	20.9(−28 dBm)	19(−32 dBm)
Tx current max (mA)	33.6 (5 dBm)	27 (0 dBm)	22.1 (12 dBm)	35 (3 dBm)	30 (0 dBm)	33 (5 dBm)

than that of transmission/reception. The first study is [12] that considers a WSN energy allocation problem taken into account both the sensing and transmission power consumptions.

8.2.2 EH Models

In order to evaluate the performance of EH-based communications, we need to model the EH process first. Most of the studies have modeled EH processes as a time-discrete process or a block-by-block process, due to the fact that sensors, in practice, operate in a time-block-based manner, i.e., transmission and sensing tasks are processed in one or several time blocks. In other words, we care about how much energy is harvested in different EH time blocks, rather than the entire time-continuous energy harvesting process within each of the block. In general, the harvested energy in each EH block could either remain constant or change from block to block. These EH fluctuations in time-domain are characterized by the coherent time. The coherence time is the time interval (i.e., the number of EH time blocks) within which the harvested energy does not change much.

There are three EH models listed below, as illustrated in Fig. 8.3.

1. Deterministic EH Model. Deterministic energy arrival is the most simple EH model. It is a proper model when the coherence time of the EH process is much larger than the duration of the entire communication session, such as EH by solar panel on clear days. Since the deterministic EH model is very simple, it is commonly adopted to evaluate the performance of EH-based WSN communications [13–15].
2. Non-Causal EH Model. Non-causal EH model is an ideal EH model that the future EH process is entirely known at the beginning of transmission. If the non-causal EH information is known at a node, it can adopt the optimal energy scheduling strategy and achieves the maximum communication performance. Therefore, non-causal EH model is useful to provide a performance upper bound.
3. Random EH Models. The most popular EH model in the recent years is the random EH model in which the EH process is regarded as random processes. In general, random EH process can be treated as a casual EH model. They are divided into two categories:

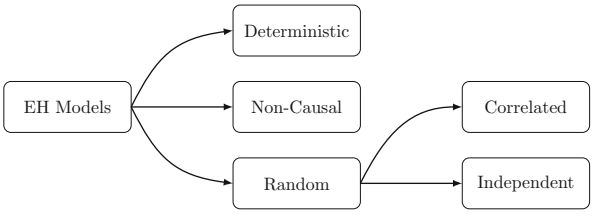

Fig. 8.3 Classification of EH models

a. Correlated EH process is an EH process that the harvested energy in the current time block, which is a random variable, is related to the harvested energy in the previous time blocks, i.e., a Markov EH model [6, 7, 16]. For example, in [17, 18], the EH process is modeled as an ON–OFF two-state a first-order discrete-time Markov process, where the harvested energy during an ON block is constant while there is no energy harvested in OFF blocks.
b. Independent EH process is an EH process that the harvested energy in the current time block is independent to the harvested energy in the previous time blocks, i.e., an i.i.d. EH model. For the i.i.d. energy arrival model, the available harvested energy in each time block follows i.i.d. continuous distribution [19–21]. In [21, 22], Bernoulli i.i.d. discrete EH process is considered.

8.2.3 Design and Performance Analysis

Most of the EH WSN design problems can be treated as energy/power scheduling/management problems under dynamic EH processes. If the allocated power usage in one time block is very high, an energy outage may happen in the next few time blocks in which the EH rate is very low and cannot support the relevant power consumptions, and thus causes performance losses. While if the allocated power usage is very low in one time block, an energy overflow may happen in the next a few time blocks in which the EH rate is very high and a finite battery cannot store all the available energy, and thus causes a waste of energy. Therefore, it is very important to carefully design the power scheduling protocols.

The power scheduling problem has basically two scenarios: offline and online, corresponding to non-causal and causal EH processes, respectively. The design targets of the power scheduling problems are mostly focused on average transmission throughput maximization during a certain time duration and transmission completion time minimization, and average delay minimization, such as [23–25], respectively. The required constraints of the optimization problems include the energy causality, i.e., not using energy in the future, and the battery capacity.

For the offline optimization problems, where the full knowledge of both the energy state information and the transmission channel state information are known before the beginning of transmission, when both the object function is a concave and the constraints are convex, the optimal power scheduling strategy can be found by solving Karush–Kuhn–Tucker conditions [23]. However, most of the EH power scheduling problems are not convex, and in this case, optimal (deterministic) dynamic programming policy and greedy policy are helpful [26]. The approach in the optimal dynamic programming policy is to break an optimization problem into sub-problems and then recursively find the optimal solutions to the sub-problems. The greedy policy also first breaks down the problem into sub-problems, but then it simply picks optimal choices for each sub-problem as the solution. However, such locally optimal (i.e., greedy) choices may result in a bad global solution. On the

other hand, the greedy policy has a much lower computation and space complexity compared to the optimal dynamic programming policy and usually provides an acceptable sub-optimal solution in some scenarios.

For the online optimization problems, the optimization only accounts for partial or full statistical knowledge of the EH and transmission channel fading dynamic processes, and the problem is usually solved as an online optimal power control problem. The most commonly used method is the stochastic dynamic programming [26, 27]. Formally, the stochastic dynamic policy has the same components as the deterministic one. The only difference is that for the stochastic dynamic programming, when evaluating each sub-problem, the long-term effect caused by the adopted strategy should be taken into account.

8.3 Wireless Power Transfer and Wireless Sensor Networks

Leveraging the far-field radiative properties of electromagnetic waves, wireless receivers are able to harvest energy remotely from RF signals radiated by RF signal emitters. This simple invention has been known long (a century ago) before the recent excitement about WPT. WPT techniques are considered popular because of the following two properties:

1. Wireless, which enables conveniently powering large-scale ubiquitous nodes without battery replacements or specific conventional EH sources, particularly for implanted in-body sensors. In other words, WPT technologies have the potential to make people's life truly wire free.
2. RF signals carry both energy and information at the same time, which enables wireless power and information transfer at the same time.

Compared to conventional EH techniques, WPT has another two advantages:

1. WPT is more controllable and does not rely on environmental EH sources.
2. RF EH devices, i.e., rectifier-based simple passive components, are suitable for large-scale WSNs and IoT nodes. This is in contrast to: solar-energy-based node is equipped with heavy solar panel, vibration-energy-based node is equipped with relatively complex mechanical construction, thermal-energy-based node is equipped with relatively large area thermoelectric generators, wind-energy-based node is equipped with big size wind turbine.

A summary of some of the industry studies about the available harvested RF power is listed in Table 8.5. Compared with the EH rate provided by the conventional ambient EH methods shown in Table 8.1, we see that the EH rate of the WPT techniques in general is much lower and decays rapidly with the distance with the RF signal emitter. This is the main problem of WPT. However, for low power WSNs, WPT is viable and an attractive solution.

Table 8.5 Wireless power transfer experimental data [28]

Source	Source power	Distance	Amount of energy harvested (μW)
Isotropic RF transmitter	4 W	15 m	5.5
Isotropic RF transmitter	1.78 W	25 m	2.3
Isotropic RF transmitter	1.78 W	27 m	2
TX91501 powercaster transmitter	3 W	5 m	189
TX91501 powercaster transmitter	3 W	11 m	1
Tokyo TV tower	48 kW	6.3 km	0.1–0.25
KING-TV tower (Seattle)	960 kW	4.1 km	60
KING-TV tower (Seattle)	960 kW	10.4 km	≥15.8

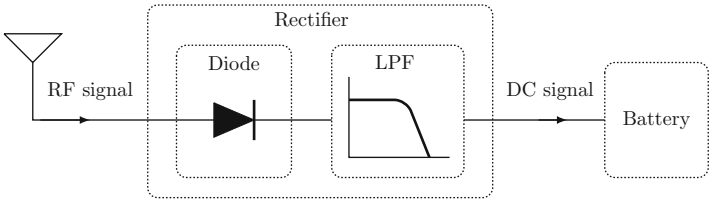

Fig. 8.4 Illustration of an RF-EH device

The architecture of a WPT-based wireless sensor is almost the same with an EH wireless sensor, as illustrated in Fig. 8.2. The only difference is that the EH module is replaced with an RF-DC converter, which is further discussed below.

8.3.1 RF-DC Converter

As mentioned above, an RF-EH device converting an RF signal to DC signal via a rectifier architecture is quite simple. It consists of a Schottky diode and a low pass filter (LPF), as illustrated in Fig. 8.4. To accurately measure how much available RF power captured by the antenna can be harvested, a proper model is required for the non-linear power conversion property introduced by the Schottky diode.

The I-V curve of a Schottky diode is illustrated in Fig. 8.5a, and it shows that only the positive part of the receive signal that is beyond a certain threshold can be harvested. The harvested power increases monotonically from zero when the receive signal power increases and is larger than the threshold. More precisely, the non-truncated part of the non-linear model can be written as

$$I = I_s \left(e^{\gamma V} - 1 \right), \tag{8.1}$$

where I_s is the saturation current, V is the voltage drop across the diode, and γ is the reciprocal of the thermal voltage.

Although the model (8.1) is precise, it is not tractable for general analysis. In [29], the authors take a Taylor expansion of the exponential function in (8.1), and

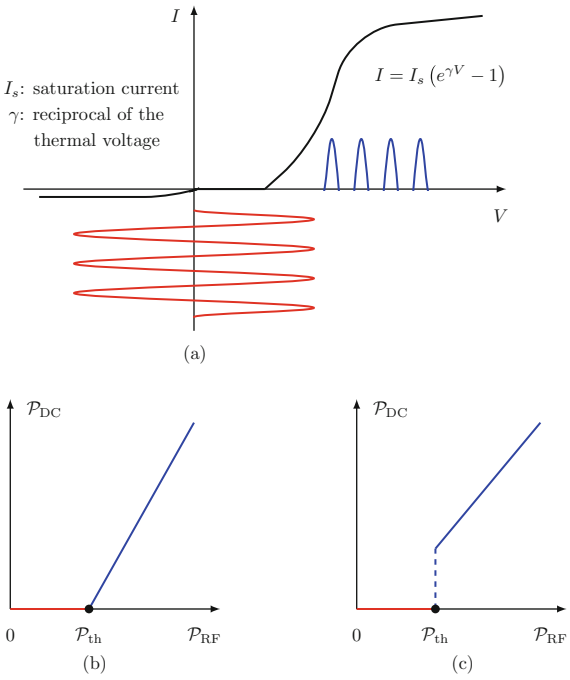

Fig. 8.5 Illustration of the models for RF-DC converter. (**a**) Accurate non-linear behavior of the Schottky diode. (**b**) Near-practical approximation. (**c**) Ideal approximation

the optimal waveform design is considered based on the simplified model. In [30], in order to better capture the truncated property of the Schottky diode, a non-linear model is considered as

$$\mathscr{P}_{\mathrm{DC}} = \frac{M}{1 + \exp\left(-a\left(\mathscr{P}_{\mathrm{RF}} - b\right)\right)}, \tag{8.2}$$

where M, a, b are the constant diode parameters, and $\mathscr{P}_{\mathrm{RF}}$ and $\mathscr{P}_{\mathrm{DC}}$ are the input RF power and the output DC power, respectively. Then an optimal resource allocation problem is considered for a multi-user simultaneous wireless information and power transfer system based on the non-linear model.

There are another two commonly considered simplified models for RF-DC power conversion, as illustrated in Fig. 8.5a,b.

1. For the near-practical model (Fig. 8.5b), the converted DC power is assumed to increase linearly with the received RF power only if it passes a threshold [31, 32].
2. For the ideal model (Fig. 8.5c), the converted DC power is assumed to be proportional to the RF power only if it is beyond the threshold [33, 34].

8.3.2 Network Model for WPT

There are three network models for WPT.

1. WPT only network, where energy transfer is in the downlink. In [35], the authors proposed a power beacon-based hybrid cellular network. In the network, mobile users are wirelessly powered by randomly deployed power beacons, which enables mobile users to have a much longer lifetime without battery replacement.

   Different scenarios such as single-/multi-user, relays, multi-carrier have been considered with WPT [29, 33, 36–41].

   In [33], wirelessly power transfer from a multi-antenna PB to single/multiple energy receivers is studied, where the optimal WPT strategy are obtained. In [36], a system consisting of a single power beacon and multiple energy receivers was considered, where the energy receiver can only do one-bit feedback. The optimal channel learning algorithm was also proposed for such a WPT system. In [37], the distributed WPT system with limited-feedback was studied, where a distributed channel learning method was proposed. In [38], WPT-based sensor networks were considered, where a large-scale sensor network is powered by randomly deployed power beacons. The sensor-active probability was also studied.

   In [39], the multiple power beacon placement problem was considered. The location of the power beacons was optimized which maximized the WPT powered communication network. In [40] and [41], WPT-based single- and bi-directional relay networks were considered, respectively, where the relay is wirelessly powered by the transmitter for relaying the information to the destination. The maximal throughput of such a relay networks was derived.

   In [29], WPT with multi-carrier waveform was considered, where waveform optimization method was proposed.
2. Simultaneous wireless information and power transfer (SWIPT) network, where energy and information are transferred simultaneously in the downlink by leveraging the property that RF signal carries both information and energy. In [33], the authors first proposed a practical SWIPT system, where the receiver can obtain information and energy simultaneously from the received signal by using a time-switching or power-splitting method, as illustrated in Fig. 8.6.

   For the time-switching-based SWIPT receiver, the RF antenna periodically switches between an information receiver and an energy receiver for information detection and energy harvesting, respectively. In this way, the SWIPT receiver is able to detect information for a certain percentage of time, and harvest energy in the rest of the time. For the power-splitting-based SWIPT receiver, the received RF signal is first split into two streams by a passive power splitter, and then one signal is sent to the information receiver and the other signal is sent to the energy receiver.

   SWIPT for a multi(MISO) broadcast channel was investigated in [42]. SWIPT in OFDM-based systems were further investigated in [43, 44]. Such systems are important, since 4G systems are based on OFDM. In [43], downlink

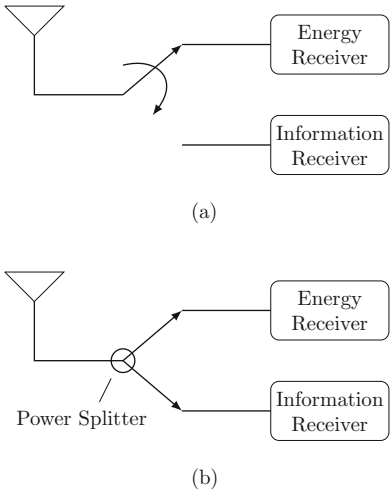

Fig. 8.6 SWIPT receivers. (**a**) Time-switching receiver. (**b**) Power-splitting receiver

OFDM-SWIPT in a multi-user system was studied, where the optimal resource allocation problem was solved. In [44], the resource allocation problem of an OFDM cellular system, which performs downlink SWIPT and uplink information transmission, was comprehensively studied.

3. Wireless powered communication network (WPCN), where energy is transferred in the downlink and information is transferred in the uplink. In [45], the authors first proposed the WPCN network model. In this network, mobile users harvest RF energy emitted by a base station, and transmit information to the base station when it has harvested enough energy. The WPCN is particularly useful in wireless sensor networks, since wireless sensors usually have very low downlink data rate but high uplink data rate, e.g., updating the sensed information to the sink.

8.3.3 WPT-Based WSN Transmission Protocols

Unlike traditional battery-operated communications, the available harvested RF power to the wirelessly powered nodes is time-variant due to the WPT channel fading. To smooth out the WPT channel randomness effect, the harvested RF energy is stored in an energy buffer, i.e., a battery or a super-capacitor, and there are two kinds of WSN transmission protocols that rely on the stored battery energy:

1. Harvest-use protocol, where the harvested energy in one time block is assumed to be used entirely within the same block. The harvest-use protocol can be adopted by WSNs with small battery storage [19, 33, 34, 45, 46], where the harvested energy should be used immediately, otherwise, the battery energy overflow occurs and leads to communication performance losses. On the other hand, the

performance analysis of harvest-use protocol-based WSNs is often tractable, which is hence adopted by many research studies. Therefore, the performance of a harvest-use protocol-based WSN can be treated as a lower bound of that obtained by an optimal transmission protocol.

2. Harvest-store-use protocol, where the harvested energy in one time block can be stored for future use. Since the harvested energy does not need to be consumed entirely, the harvest-store-use protocol provides a better transmission performance compared with the harvest-use protocol. The harvest-store-use protocol is adopted by WSNs with large battery storage [47–49]. In this case, the sensors do not need to use all the available energy at each time block, and thus can better utilize the available harvested energy and schedule its power consumption to improve the communication performance. In theory, in order to achieve a globally optimal performance of transmission, a sensor can adaptively change the transmit power in each time block depending on the current energy storage and the length of data queue. However, most of the WPT-based WSNs are simple devices, which require low-complexity protocols that do not allow adaptively changing the transmit power. Therefore, the widely adopted harvest-store-use protocol is a threshold-based protocol, which transmits with a constant power within a time block as long as there is sufficient energy for the transmission [47–49].

8.3.4 Performance Analysis

There is one important metric for each of the WPT network, SWIPT network, and WPCN, as shown below.

WPT efficiency is considered in WPT only networks, which is defined as

$$\eta_{\text{WPT}} = \frac{\mathscr{P}_{tx}}{\mathscr{P}_{rx}}, \tag{8.3}$$

where $\mathscr{P}_{tx}$ and $\mathscr{P}_{rx}$ are the transmit signal power and the harvested signal power at the transmitter and the receiver, respectively. WPT efficiently indicates the quality of a WPT protocol design, such as channel training-based energy transfer [50, 51], and multi-antenna energy beamforming [36, 37, 52].

Rate-energy region is considered in SWIPT networks, which is the boundary of all the achievable tradeoff for maximal information rate versus energy transfer [33, 34]. A large rate-energy region means the SWIPT network is more capable for simultaneously harvesting RF energy and detecting information, or the performance losses on information detection due to the RF energy harvesting is smaller.

Uplink throughput is the key metric for a WPCN. WPCNs encounter a doubly near-far problem due to the fact that a far sensor from the sink, which receives less wireless energy than a nearer sensor in the downlink, has to transmit with more power in the uplink to achieve the same reliable information transmission

rate [45]. Therefore, in order to achieve a better uplink throughput of a WSN, we need to properly design the downlink WPT and the uplink information transmission protocols. A time-division-multiple-access-based uplink–downlink user scheduling is proposed in [45].

8.4 Design Challenges

8.4.1 Sensor Power Consumption

Besides modeling the EH process, to accurately analyze the EH powered sensor behavior, we need an accurate model for sensor's energy costs. As discussed in the previous section, there are three main energy costs for a wireless sensors, and particularly, the energy costs of sensing and transmission/reception dominate the overall energy consumption.

Therefore, for a status monitoring WSN, we need to taken into account both the energy costs of sensing and transmission when analyze the performance of status monitoring.

8.4.2 The Age of Information

The recent internet-of-things brings ubiquitous wireless sensors together, which monitor environmental data and update them to the users. In this status monitoring application, we need the sensors to update their monitored status as timely as possible. The conventional metric to measure the timeliness of a WSN is update cycle, which measures the time elapsed from one status update at the sink to the next [48]. Update cycle captures how frequently the status information is updated at the user. For example, if the average update cycle of a WSN is 10 s, then we can expect that the status updates successfully at the user every 10 s. However, from the 10 s update cycle, we cannot see when the status was originally generated. For example, when a successful status is received/updated at the user, the status could be collected 9 s ago, which is not a fresh status, or 1 s ago, which is a fresh status. Measuring the freshness of the updated status has long been desirable, but it is only recently that it have been seriously considered and modeled in [53–55], and named as update age.

Since both the update frequency and freshness are related to determine how timely a status monitoring WSN is, we need both the update cycle and update age to accurately measure the timeliness of the status monitoring WSN. It was first proposed in a recent study [48] that using update cycle together with update age brings a comprehensive measure of the timeliness of a status monitoring WSN. The idea is simple that since update age and update cycle are complementary to each

other, i.e., update cycle does not reflect the update freshness at the sink whereas update age does not reflect the update frequency, the best way to evaluate the performance of a status monitoring WSN is to jointly utilize both of them.

8.5 WPT-WSN: Delay Analysis Considering Energy Costs of Sensing and Transmission

8.5.1 System Model

We consider a status monitoring scenario where a wirelessly powered sensor periodically transmits its sensed status information to a sink, as illustrated in Fig. 8.1. The sensor is able to harvest RF energy from a nearby power beacon. To complete the status monitoring task, the sensor has two main functions, i.e., sensing and transmission, each having individual energy cost. Before performing either sensing or transmission, the sensor first needs to spend a certain amount of time on EH. The harvested energy is stored in a half-duplex battery, which cannot charge and discharge at the same time [19]. Because the commercial battery capacity typically ranges from joules to thousands of joules [4], and the available harvested energy per second is only a few millijoules, as shown in Table 8.5, we assume that the battery has a sufficient capacity such that the amount of energy stored in the battery never reaches its maximum capacity.

We adopt a block-wise operation following the state-of-the-art EH sensor design practice [56]. Specifically, we assume that one sensing operation or one transmission is performed in one time block of duration T seconds, and sensing and transmission cannot occur within a same time block. In general, a sensor may spend different amounts of time on one sensing operation and one packet transmission [8]. Thus, in future study, the assumed protocol and analysis can be generalized to different sensing and transmission time durations. At the beginning of each block, the sensor makes a decision to perform either energy harvesting, sensing, or transmission depending on the current battery energy storage. Before the discussion of such sensing and transmission protocol, firstly, we need the following definitions of three types of time blocks:

1. Energy harvesting block (EHB): The sensor harvests RF energy and stores the energy in its battery. We consider that the wireless channel between the power beacon and the sensor suffers from independent and identically distributed (i.i.d.) block Rayleigh fading. In general, Rayleigh fading channel is commonly considered in the scenario where there is no line-of-sight, and there are sufficient scatters between the transmitter and the receiver. Note that if there is line-of-sight between the power beacon and the sensor, Rician or Nakagami fading channel model should be adopted, which is further studied in [48].

With the i.i.d. Rayleigh fading channel assumption for the WPT link, the harvested energy in each EHB follows the same exponential distribution and changes independently from block to block. Thus, we refer to the energy arrival process as exponential energy arrival process. The average EH rate is ρ Joules per block.

2. Sensing Block (SB): The sensor samples the environmental status information, and then processes and packs the sensed information into a data packet. The energy cost in a SB is denoted by $\mathscr{E}_{\mathrm{SB}}$ Joules.
3. Transmission Block (TB): The sensor transmits the data packet, which was generated from the last sensing operation, to the sink with energy cost $\mathscr{E}_{\mathrm{TB}}$ Joules, i.e., the transmit power is $\mathscr{P}_{\mathrm{TB}} = \mathscr{E}_{\mathrm{TB}}/T$. To indicate successful packet reception, the sink sends a one-bit feedback signal to the sensor after each TB. Note that the time and energy consumed for receiving the feedback signal at the sensor is negligible as compared to its packet transmission time. If the transmission is successful, we have a successful transmission block (STB); otherwise, we have a failed transmission block (FTB).

   The transmission outage, i.e., the probability of a TB being a FTB, is denoted by P_{out}. We assume that a transmission outage from the sensor to the sink occurs when the SNR at the sink γ is lower than SNR threshold $\gamma_0 = 40\,\mathrm{dB}$ [57]. The outage probability is

$$P_{\mathrm{out}} = \Pr\{\gamma < \gamma_0\}. \tag{8.4}$$

   The SNR at the sink is defined as [58]

$$\gamma = \frac{|h|^2 \mathscr{P}_{\mathrm{tx}}}{\Gamma d^{\lambda} \sigma^2}, \tag{8.5}$$

   where h is the sensor-sink transmission channel fading gain, Γ is a path loss factor which is assumed to be one [31] for simplicity, σ^2 is the noise power at the sink, d is the distance between the sensor and the sink, and λ is the path loss exponent.

   Also we assume that h is block-wise Rayleigh fading. Using (8.5), the transmission outage probability can be written as

$$P_{\mathrm{out}} = 1 - \exp\left(-\frac{d^{\lambda}\sigma^2\gamma_0}{\mathscr{P}_{\mathrm{tx}}}\right). \tag{8.6}$$

8.5.2 Sensing and Transmission Protocol

The time-varying EH process results in randomness in the delay for performing sensing and transmission. To properly design a sensing and transmission protocol for a status monitoring WSN, two issues need to be considered.

The first issue is about when to perform sensing. Considering the energy cost of sensing, it is necessary to harvest sufficient energy, $\mathscr{E}_{\mathrm{SB}}$, before a sensing operation. However, it is not a good choice to perform sensing as soon as the harvested energy reaches $\mathscr{E}_{\mathrm{SB}}$. Because there may not be sufficient energy left for transmission after the sensing operation, a certain amount of time for EH is required to prepare for transmission which results in unnecessary delay and makes the sensed status less timely. Therefore, to avoid such delays and make the update timely, we define the condition for the sensing operation to be when the harvested energy in the battery exceeds $\mathscr{E}_{\mathrm{SB}} + \mathscr{E}_{\mathrm{TB}}$. In this way, a transmission of sensed status information occurs immediately after the sensing operation (i.e., a SB is always followed by a TB).

The second issue is about whether we need a retransmission when a failed transmission (i.e., a FTB) occurs. Considering the energy cost of sensing, it is necessary to perform retransmission(s) if the first TB after a SB is failed, rather than drop the packet and perform the next sensing operation. However, an arbitrary number of retransmissions that make a status-information-containing packet to be eventually received by the sink should be prevented. This is because a very long retransmission process would make the updated status very untimely at the sink. Therefore, we impose a time window for retransmissions to control the delay caused by retransmissions. We denote W as the maximum number of time blocks after a SB, within which transmission and retransmission(s) of the currently sensed information can take place. Specifically, the *time window for retransmissions* is $W - 1$ time blocks, due to the fact that the first transmission always happens immediately after the SB.

We present the sensing and transmission protocol as follows, and the flowchart of the protocol is illustrated in Fig. 8.7.

(a) First, several EHBs are required to harvest enough energy, $\mathscr{E}_{\mathrm{SB}} + \mathscr{E}_{\mathrm{TB}}$, and then a SB and a TB occur immediately.
(b) If the TB is a STB, i.e., the transmission in the TB is successful, in order to prepare for the next sensing period, the sensor attempts to harvest energy, which may take several EHBs, until the battery energy exceeds $\mathscr{E}_{\mathrm{SB}} + \mathscr{E}_{\mathrm{TB}}$ again.
(c) If the TB is a FTB, i.e., the transmission in the TB fails, in order to prepare for a retransmission, the sensor has to go back to harvesting energy, which may take several EHBs, until the battery energy exceeds $\mathscr{E}_{\mathrm{TB}}$.
(d) Retransmission may occur several times until either one of the two conditions is met: (1) The sensed information is successfully transmitted to the sink, i.e., a STB finally occurs, or (2) the time window for retransmissions $W-1$ is reached but no STB occurs. Then, the data packet at the sensor is dropped, no matter successful retransmission or not, and the sensor goes back to harvesting energy for a new sensing operation.

An illustration of the sensing and transmission protocol with $W = 6$ is shown in Fig. 8.8. From the example, we see that two EHB occur first, after which the battery energy exceeds $\mathscr{E}_{\mathrm{SB}} + \mathscr{E}_{\mathrm{TB}}$, and then a SB together with a TB occurs. Although the TB is a FTB, after two retransmissions, a STB occurs. Then, after three EH

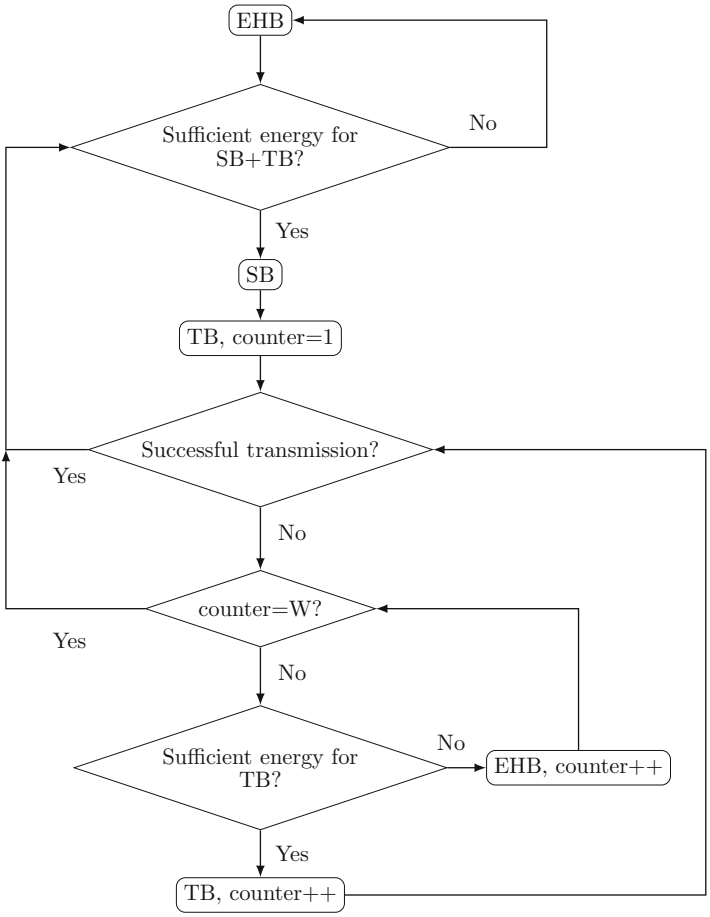

Fig. 8.7 Flowchart of the protocol

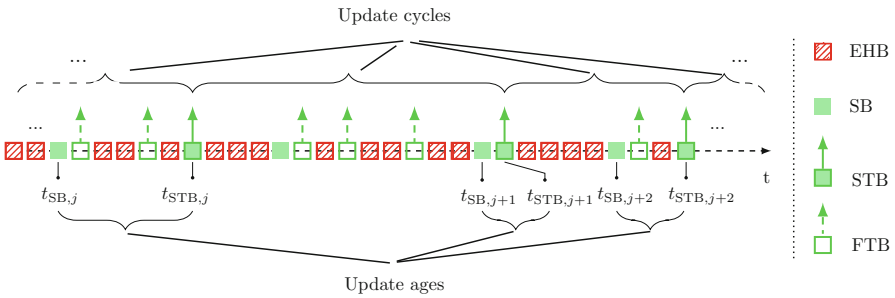

Fig. 8.8 Illustration of the sensing and transmission protocol, and the update cycle and update age

blocks, a new SB occurs, after which, however, a STB never occurs within 6 time blocks. Therefore, the sensed packet has to be dropped. In other words, the sensed information in the second SB is not able to be received by the sink.

The time indices shown in Fig. 8.8 will be defined in the following section.

8.5.3 Delay Related Metrics

As discussed in Sect. 8.4.2, to completely capture the timeliness of the status monitoring WSN, we need both the update cycle and the update age metrics. Recall that update age measures the time taken from when information is obtained by the sensor to when the sensed information is successfully transmitted to the sink, i.e., how timely the updated information at the sink is, and update cycle measures the time duration between two consecutive successful transmissions, i.e., how frequently the information at the sink is updated. Thus, both the metrics are important for measuring the timeliness of the status monitoring WSN.

As shown in Fig. 8.8, for the ease of describing the two metrics, $t_{\mathrm{STB},j}$ is used to denote the block index for the jth STB during the entire sensing and transmission operation. Since each STB corresponds to a SB that generates the status information contained in the STB, $t_{\mathrm{SB},j}$ is used to denote the block index for the SB in which the sensed information is transmitted in the jth STB.

The two delay related metrics, expressed in terms of the number of time blocks, are formally defined in the following.

Definition 1 (Update Age). For the jth STB, the update age is given by the number of time blocks from $t_{\mathrm{SB},j}$ to $t_{\mathrm{STB},j}$ (shown in Fig. 8.8). The jth update age is

$$T_{\mathrm{UA},j} = t_{\mathrm{STB},j} - t_{\mathrm{SB},j},\ j = 1, 2, 3, \ldots. \tag{8.7}$$

Remark 1. Conditioned on a successful status-information-containing packet reception at the sink, the update age measures the time elapsed from the generation of the packet at the sensor to the successful reception of the packet at the sink. A larger update age implies that a more outdated status is received by the sink. However, the update age does not capture the delay that caused by dropped data packets, and hence is not able to reflect the update frequency at the sink.

Definition 2 (Update Cycle). For the jth STB, the update cycle is given by the number of time blocks from $t_{\mathrm{STB},j-1}$ to $t_{\mathrm{STB},j}$ (shown in Fig. 8.8). The jth update cycle is

$$T_{\mathrm{UC},j} = t_{\mathrm{STB},j+1} - t_{\mathrm{STB},j},\ j = 1, 2, 3, \ldots. \tag{8.8}$$

Remark 2. The update cycle measures the time elapsed from one successful status update at the sink to the next, which takes into account the delay due to dropped data packets. However, the update cycle is not able to measure the update freshness at the sink, i.e., the time duration from the generation of a packet to its successful reception at the sink.

Therefore, update age and update cycle complement each other, and they jointly capture the update freshness and frequency. Using both the metrics provides comprehensive measure of the performance of a status monitoring WSN.

8.5.3.1 Modeling Update Age and Update Cycle as i.i.d. Random Variables

To study the steady-state behavior of the update age and the update cycle during the sensing and transmission process, we need the following lemma first.

Lemma 1. For an exponential energy arrival process, the steady-state distribution of the energy level after each TB has pdf

$$g(\varepsilon) = \frac{1}{\rho} e^{-\frac{\varepsilon}{\rho}}, \tag{8.9}$$

where ρ is the average harvested energy.

Proof. This proof is identical to [59, Lemma 1]. We repeat some of the details here for sake of completeness.

Because the harvested energy in each EHB is an exponentially distributed random variable with parameter ρ, as we have mentioned in Sect. 8.5.1, the energy accumulation process by consecutive EHBs can be treated as a Poisson process [60]. Using the memorylessness property of the Poisson process [60, p. 134], conditioned on that the available energy is higher than any given threshold value, the amount of energy exceeding that threshold has the same distribution with the harvested energy in each time block, i.e., Eq. (8.9). This completes the proof of Lemma 1.

From the definitions of the update age and the update cycle, $T_{\mathrm{UA},j}$ and $T_{\mathrm{UC},j}$ only depend on (1) the available energy after the first TB following a SB, and (2) the random EH process after the TB. Since the steady-state distribution after each TB is the same (i.e., Lemma 1) and the EH process is a steady-state process (i.e., the i.i.d. exponential energy arrival process), both $T_{\mathrm{UA},j}$ and $T_{\mathrm{UC},j}$ have steady-state distributions. For convenience, we remove subscript j for T_{UA} and T_{UC} in (8.7) and (8.8), respectively.

8.5.4 Delay Analysis

We present the analytical results of the update age and the update cycle in this section.

8.5.4.1 Update Age and Update Cycle

Theorem 1. *For an exponential energy arrival process, average update age is given by*

$$\bar{T}_{\mathrm{UA}} = \frac{(1-P_{\mathrm{out}})}{P_{\mathrm{suc}}}\left(1+\sum_{l=2}^{W} l \sum_{n=2}^{l} (P_{\mathrm{out}})^{n-1}\,\mathrm{Pois}\left(l-n,(n-1)\mathscr{E}_{\mathrm{TB}}/\rho\right)\right) \tag{8.10}$$

where

$$P_{\mathrm{suc}} = 1-P_{\mathrm{out}}+(1-P_{\mathrm{out}})\sum_{l=2}^{W}\sum_{n=2}^{l}(P_{\mathrm{out}})^{n-1}\,\mathrm{Pois}\left(l-n,(n-1)\mathscr{E}_{\mathrm{TB}}/\rho\right). \tag{8.11}$$

From Theorem 1, the average update age is independent with the energy cost of sensing.

Theorem 2. *For an exponential energy arrival process, average update cycle is given by*

$$\bar{T}_{\mathrm{UC}} = \frac{1-P_{\mathrm{suc}}}{P_{\mathrm{suc}}}\left(\frac{\mathscr{E}_{\mathrm{SB}}}{\rho}+\bar{V}+W+1\right)+\frac{\mathscr{E}_{\mathrm{SB}}+\mathscr{E}_{\mathrm{TB}}}{\rho}+\bar{T}_{\mathrm{UA}}+1, \tag{8.12}$$

where $\bar{T}_{\mathrm{UA}}$ *and* P_{suc} *are given in* (8.10) *and* (8.11)*, and*

$$\begin{aligned}\bar{V} = {} & \frac{P_{\mathrm{out}}}{1-P_{\mathrm{suc}}}\left(\frac{\mathscr{E}_{\mathrm{TB}}}{\rho}-\sum_{i=0}^{W-2} i\,\mathrm{Pois}\left(i,\frac{\mathscr{E}_{\mathrm{TB}}}{\rho}\right)-(W-1)\left(1-\sum_{i=0}^{W-2}\mathrm{Pois}\left(i,\frac{\mathscr{E}_{\mathrm{TB}}}{\rho}\right)\right)\right)\\ & +\frac{1}{1-P_{\mathrm{suc}}}\times\sum_{l=2}^{W}\sum_{n=2}^{l}(P_{\mathrm{out}})^{n}\,\mathrm{Pois}\left(l-n,(n-1)\frac{\mathscr{E}_{\mathrm{TB}}}{\rho}\right)\Phi_l,\end{aligned} \tag{8.13}$$

where

$$\Phi_l \triangleq \left(\frac{\mathscr{E}_{\mathrm{TB}}}{\rho}-\sum_{i=0}^{W-l-1} i\,\mathrm{Pois}\left(i,\frac{\mathscr{E}_{\mathrm{TB}}}{\rho}\right)-(W-l)\left(1-\sum_{i=0}^{W-l-1}\mathrm{Pois}\left(i,\frac{\mathscr{E}_{\mathrm{TB}}}{\rho}\right)\right)\right). \tag{8.14}$$

Proof. See Appendix F of [48].

From Theorem 2, the average update cycle depends on both the energy cost of sensing and transmission.

8.5.4.2 Asymptotic Update Age and Update Cycle

We also present the asymptotic update age and update cycle when the retransmission window $W-1$ is sufficiently large.

Corollary 1. *For an exponential energy arrival process, $\bar{T}_{\mathrm{UA}}$ increases with W, and as W gets large, the asymptotic $\bar{T}_{\mathrm{UA}}$ is given by*

$$\lim_{W\to\infty} \bar{T}_{\mathrm{UA}} = 1 + \frac{P_{\mathrm{out}}}{1-P_{\mathrm{out}}}\left(\frac{\mathscr{E}_{\mathrm{TB}}}{\rho}+1\right). \tag{8.15}$$

Proof. See Appendix G of [48].

Corollary 2. *For an exponential energy arrival process, $\bar{T}_{\mathrm{UC}}$ decreases with W, and as W grows large, the asymptotic $\bar{T}_{\mathrm{UC}}$ is given by*

$$\lim_{W\to\infty} \bar{T}_{\mathrm{UC}} = 2 + \frac{\mathscr{E}_{\mathrm{SB}}+\mathscr{E}_{\mathrm{TB}}}{\rho} + \frac{P_{\mathrm{out}}}{1-P_{\mathrm{out}}}\left(\frac{\mathscr{E}_{\mathrm{TB}}}{\rho}+1\right). \tag{8.16}$$

Proof. See Appendix G of [48].

8.5.4.3 Numerical Results

In this section, we present numerical results for the update age and update cycle. We set the distance between the sensor and the sink as $d = 90\,\mathrm{m}$. This is because the typical outdoor range for a wireless sensor is from 75 to 100 m [61]. Also we set the path loss exponent for the sensor-sink transmission link as $\lambda = 3$ [31]. The noise power at the sink is $\sigma^2 = -100\,\mathrm{dBm}$ [40]. The duration of a time block is $T = 5\,\mathrm{ms}$[14]. The average harvested power is 10 mW [62], i.e., average harvested energy per time block, $\rho = 50\,\mu\mathrm{J}$. The RF-DC sensitivity level is $-20\,\mathrm{dBm}$ [28]. Unless otherwise stated, (1) we set the power consumption in each TB, $\mathscr{P}_{\mathrm{TB}} = 40\,\mathrm{mW}$, i.e., $\mathscr{E}_{\mathrm{TB}} = 200\,\mu\mathrm{J}$. Note that this includes RF circuit consumption (main consumption) and the actual RF transmit power $\mathscr{P}_{\mathrm{tx}} = -5\,\mathrm{dBm}$[1] and (2) we set the power consumption in each SB as $\mathscr{P}_{\mathrm{SB}} = 45\,\mathrm{mW}$[8], i.e., $\mathscr{E}_{\mathrm{SB}} = 225\,\mu\mathrm{J}$. In the following calculations, power and SNR related quantities use a linear scale.

Assuming the SNR threshold $\gamma = 40\,\mathrm{dB}$ [57], we apply (8.6) to Theorems 1–2 and Corollaries 1–2, we compute the expressions of average and the asymptotic values of T_{UA} and T_{UC}.

Pmfs of Update Age and Update Cycle Figure 8.9 plots the pmfs of update cycle, T_{UC}, and update age, T_{UA}, for the exponential energy arrival process, respectively. The results are plotted using Monte Carlo simulation method with 10^9 points. We

[1]The values we chose for $\mathscr{P}_{\mathrm{TB}}$ and $\mathscr{P}_{\mathrm{tx}}$ are typical for commercial sensor platforms, such as MICAz [61].

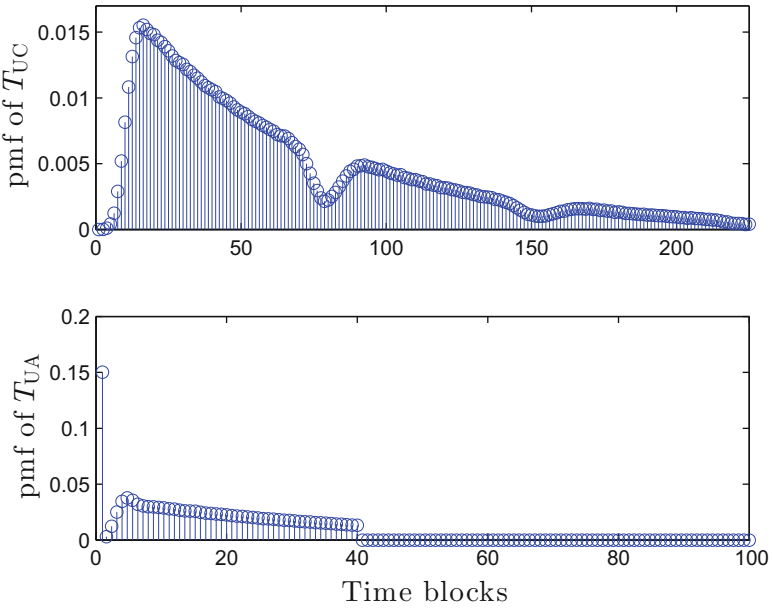

Fig. 8.9 Pmfs for T_{UC} and T_{UA}

set $W = 40$, i.e., the time window for retransmissions is $W - 1 = 39$ time blocks. We see that the pmfs in general cannot be modeled by commonly used pmfs, such as Poison distribution.

In the following figures, i.e., Figs. 8.7 and 8.8, we only present the numerical results for the average update age and the average update cycle, which have been presented in Corollaries 1–2.

Average Update Age and Average Update Cycle Figure 8.10 shows the average update age, $\bar{T}_{\mathrm{UA}}$, and the average update cycle, $\bar{T}_{\mathrm{UC}}$, for different W, i.e., different retransmission window, $W - 1$. The results are generated using Theorems 1 and 2 and Corollaries 1 and 2, respectively. We can see that as the time window for retransmissions increases, the average update age increases monotonically and approaches its asymptotic value given by Corollary 1, while the average update cycle decreases monotonically and approaches its analytical lower bound given by Corollary 2. Also we see that with a larger retransmission window $W-1$, the updated status is in general less fresh, but the update frequency is higher.

Effect of Energy Cost of Sensing on Average Update Cycle We illustrate the effect of energy cost of sensing on average update cycle. Figure 8.11 shows the average update age, $\bar{T}_{\mathrm{UA}}$, and the average update cycle, $\bar{T}_{\mathrm{UC}}$, versus W, with different energy cost of sensing, $\mathscr{P}_{\mathrm{SB}}T$. The results are generated using Theorems 1 and 2. The figure shows that the average update age increases with W, which is consistent with Fig. 8.10, but it does not change with the energy cost of sensing, i.e., *the update*

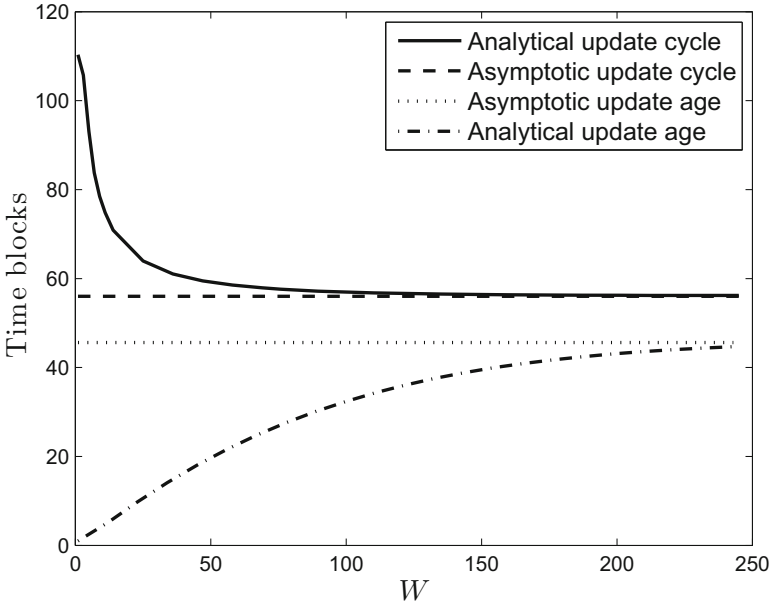

Fig. 8.10 $\bar{T}_{\mathrm{UA}}$ and $\bar{T}_{\mathrm{UC}}$, versus W

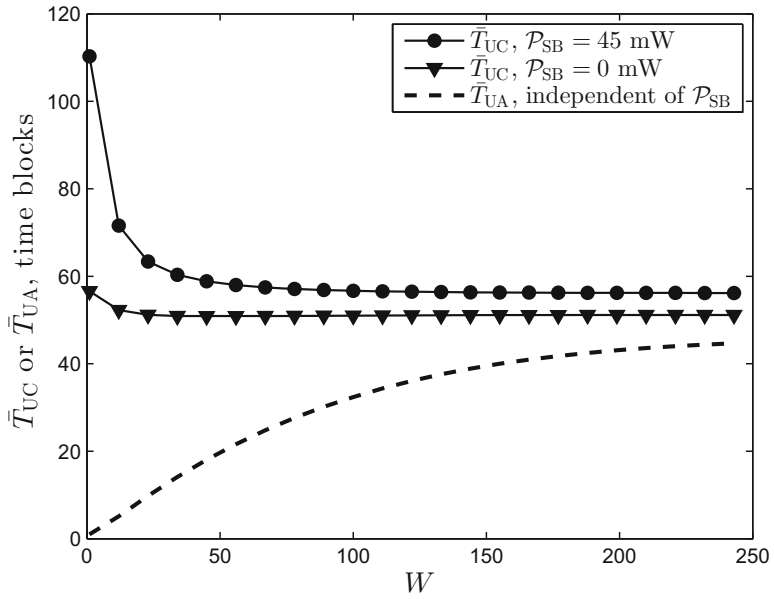

Fig. 8.11 $\bar{T}_{\mathrm{UC}}$ and $\bar{T}_{\mathrm{UA}}$ versus W for different sensing power, $\mathscr{P}_{\mathrm{SB}}$

age does not rely on the energy cost of sensing. This is because the update age is the delay after a SB, and is independent with the energy cost of sensing. We can see that for a fixed value of W, e.g., $W = 50$, the average update cycle increases as the sensing power consumption increases from 0 to 45 mW, i.e., *the higher the energy cost of sensing the larger update cycle.* This is because during an update cycle several SB occurs, and the higher energy cost of sensing the more EHBs within the update cycle. We can see that $\bar{T}_{\mathrm{UC}}$ is almost constant around the value of 52 and does not vary much with W, i.e., the effect retransmission window on the average update cycle is limited when the energy cost of sensing is ignored.

Summary

In this chapter, we have discussed the basic architecture of EH-based WSNs and wireless power transfer-based WSNs. We have highlighted the advantage and suitability of wireless power transfer-based WSNs, and discussed the associated design challenges. We have presented a novel solution to one of the challenges, related to the timeliness of the status monitoring WSNs, i.e., update cycle and update age. Moreover, we have presented a framework of analysis for both the update cycle and the update age, which takes into account both the energy cost of sensing and transmission.

References

1. K. Sohraby, D. Minoli, T. Znati, *Wireless Sensor Networks: Technology, Protocols, and Applications* (Wiley, New York, 2007)
2. M. Connectivity, The monitored World - a local perspective (2015). [Online]. Available: https://blog.m2mconnectivity.com.au/2015/09/07/the-monitored-world-a-local-perspective/
3. H. Yetgin, K.T.K. Cheung, M. El-Hajjar, L. Hanzo, A survey of network lifetime maximization techniques. IEEE Commun. Surv. Tutorials. (2017). Accepted
4. S. Sudevalayam, P. Kulkarni, Energy harvesting sensor nodes: survey and implications. IEEE Commun. Surv. Tutorials **13**(3), 443–461, Third Quarter (2011)
5. V. Gungor, G. Hancke, Industrial wireless sensor networks: challenges, design principles, and technical approaches. IEEE Trans. Ind. Electron. **56**(10), 4258–4265 (2009)
6. D. Niyato, E. Hossain, A. Fallahi, Sleep and wakeup strategies in solar-powered wireless sensor/mesh networks: performance analysis and optimization. IEEE Trans. Mob. Comput. **6**(2), 221–236 (2007)
7. J. Lei, R. Yates, L. Greenstein, A generic model for optimizing single-hop transmission policy of replenishable sensors. IEEE Trans. Wirel. Commun. **8**(2), 547–551 (2009)
8. V. Raghunathan, S. Ganeriwal, M. Srivastava, Emerging techniques for long lived wireless sensor networks. IEEE Commun. Mag. **44**(4), 108–114 (2006)
9. W. Liu, K. Huang, X. Zhou, S. Durrani, Backscatter communications for internet-of-things: theory and applications. ArXiv e-prints (2017). [Online]. Available: https://arxiv.org/abs/1701.07588

10. C. Boyer, S. Roy, Backscatter communication and RFID: coding, energy, and MIMO analysis. IEEE Trans. Commun. **62**(3), 770–785 (2014)
11. W. Liu, K. Huang, X. Zhou, S. Durrani, Full-duplex backscatter interference networks based on time-hopping spreading spectrum. IEEE Trans. Wirel. Commun. (2017, to appear)
12. S. Mao, M.H. Cheung, V. Wong, Joint energy allocation for sensing and transmission in rechargeable wireless sensor networks. IEEE Trans. Veh. Technol. **63**(6), 2862–2875 (2014)
13. H. Mahdavi-Doost, R. Yates, Energy harvesting receivers: finite battery capacity, in *Proceedings of IEEE ISIT*, July (2013), pp. 1799–1803
14. Z.A. Eu, H.-P. Tan, W.K. Seah, Design and performance analysis of MAC schemes for wireless sensor networks powered by ambient energy harvesting. Ad Hoc Netw. **9**(3), 300–323 (2011)
15. C. Huang, R. Zhang, S. Cui, Throughput maximization for the Gaussian relay channel with energy harvesting constraints. IEEE J. Sel. Areas Commun. **31**(8), 1469–1479 (2013)
16. C.K. Ho, R. Zhang, Optimal energy allocation for wireless communications with energy harvesting constraints. IEEE Trans. Signal Process. **60**(9), 4808–4818 (2012)
17. A. Seyedi, B. Sikdar, Energy efficient transmission strategies for body sensor networks with energy harvesting. IEEE Trans. Commun. **58**(7), 2116–2126 (2010)
18. S. Zhang, A. Seyedi, B. Sikdar, An analytical approach to the design of energy harvesting wireless sensor nodes. IEEE Trans. Wirel. Commun. **12**(8), 4010–4024 (2013)
19. S. Luo, R. Zhang, T.J. Lim, Optimal save-then-transmit protocol for energy harvesting wireless transmitters. IEEE Trans. Wirel. Commun. **12**(3), 1196–1207 (2013)
20. R. Morsi, D. Michalopoulos, R. Schober, On-off transmission policy for wireless powered communication with energy storage, in *Proceedings of Asilomar*, November (2014), pp. 1676–1682
21. Y. Dong, F. Farnia, A. Ozgur, Near optimal energy control and approximate capacity of energy harvesting communication. IEEE J. Sel. Areas Commun. **33**(3), 540–557 (2015)
22. N. Michelusi, L. Badia, M. Zorzi, Optimal transmission policies for energy harvesting devices with limited state-of-charge knowledge. IEEE Trans. Commun. **62**(11), 3969–3982 (2014)
23. O. Ozel, K. Tutuncuoglu, J. Yang, S. Ulukus, A. Yener, Transmission with energy harvesting nodes in fading wireless channels: optimal policies. IEEE J. Sel. Areas Commun. **29**(8), 1732–1743 (2011)
24. J. Yang, S. Ulukus, Transmission completion time minimization in an energy harvesting system, in *Proceedings of CISS*, March (2010), pp. 1–6
25. J. Yang, S. Ulukus, Delay-minimal transmission for energy constrained wireless communications, in *Proceedings of IEEE ICC*, May (2008), pp. 3531–3535
26. Y. Mao, G. Yu, Z. Zhang, On the optimal transmission policy in hybrid energy supply wireless communication systems. IEEE Trans. Wirel. Commun. **13**(11), 6422–6430 (2014)
27. N. Michelusi, M. Zorzi, Optimal random multiaccess in energy harvesting wireless sensor networks, in *Proceedings of IEEE ICC*, June (2013), pp. 463–468
28. X. Lu, P. Wang, D. Niyato, D.I. Kim, Z. Han, Wireless networks with RF energy harvesting: a contemporary survey. IEEE Commun. Surv. Tutorials **17**(2), 757–789, Second Quarter (2015)
29. B. Clerckx, E. Bayguzina, Waveform design for wireless power transfer. IEEE Trans. Signal Process. **64**(23), 6313–6328 (2016)
30. E. Boshkovska, D.W.K. Ng, N. Zlatanov, R. Schober, Practical non-linear energy harvesting model and resource allocation for SWIPT systems. IEEE Commun. Lett. **19**(12), 2082–2085 (2015)
31. T. Wu, H.-C. Yang, On the performance of overlaid wireless sensor transmission with RF energy harvesting. IEEE J. Sel. Areas Commun. **33**(8), 1693–1705 (2015)
32. W. Liu, X. Zhou, S. Durrani, P. Popovski, SWIPT with practical modulation and RF energy harvesting sensitivity, in *Proceedings of ICC*, May (2016), pp. 1–7
33. R. Zhang, C.K. Ho, MIMO broadcasting for simultaneous wireless information and power transfer. IEEE Trans. Wirel. Commun. **12**(5), 1989–2001 (2013)
34. X. Zhou, R. Zhang, C.K. Ho, Wireless information and power transfer: architecture design and rate-energy tradeoff. IEEE Trans. Commun. **61**(11), 4754–4767 (2013)
35. K. Huang, V.K.N. Lau, Enabling wireless power transfer in cellular networks: architecture, modeling and deployment. IEEE Trans. Wirel. Commun. **13**(2), 902–912 (2014)

36. J. Xu, R. Zhang, Energy beamforming with one-bit feedback. IEEE Trans. Signal Process. **62**(20), 5370–5381 (2014)
37. S. Lee, R. Zhang, Distributed energy beamforming with one-bit feedback, in *Proceedings of IEEE WCNC*, April (2016), pp. 1–6
38. Z. Wang, L. Duan, R. Zhang, Adaptively directional wireless power transfer for large-scale sensor networks. IEEE J. Sel. Areas Commun. **34**(5), 1785–1800 (2016)
39. S. Bi, R. Zhang, Placement optimization of energy and information access points in wireless powered communication networks. IEEE Trans. Wirel. Commun. **15**(3), 2351–2364 (2016)
40. A.A. Nasir, X. Zhou, S. Durrani, R.A. Kennedy, Wireless-powered relays in cooperative communications: time-switching relaying protocols and throughput analysis. IEEE Trans. Commun. **63**(5), 1607–1622 (2015)
41. Y. Zeng, H. Chen, R. Zhang, Bidirectional wireless information and power transfer with a helping relay. IEEE Commun. Lett. **20**(5), 862–865 (2016)
42. S. Luo, J. Xu, T.J. Lim, R. Zhang, Capacity region of MISO broadcast channel for simultaneous wireless information and power transfer. IEEE Trans. Commun. **63**(10), 3856–3868 (2015)
43. X. Zhou, C.K. Ho, R. Zhang, Wireless information and power transfer in multiuser OFDM systems. IEEE Trans. Wirel. Commun. **13**(4), 2282–2294 (2014)
44. K. Huang, E. Larsson, Simultaneous information and power transfer for broadband wireless systems. IEEE Trans. Signal Process. **61**(23), 5972–5986 (2013)
45. H. Ju, R. Zhang, Throughput maximization in wireless powered communication networks. IEEE Trans. Wirel. Commun. **13**(1), 418–428 (2014)
46. I. Krikidis, Simultaneous information and energy transfer in large-scale networks with/without relaying. IEEE Trans. Commun. **62**(3), 900–912 (2014)
47. W. Liu, X. Zhou, S. Durrani, P. Popovski, Secure communication with a wireless-powered friendly jammer. IEEE Trans. Wirel. Commun. **15**(1), 401–415 (2016)
48. W. Liu, X. Zhou, S. Durrani, H. Mehrpouyan, S.D. Blostein, Energy harvesting wireless sensor networks: delay analysis considering energy costs of sensing and transmission. IEEE Trans. Wirel. Commun. **15**(7), 4635–4650 (2016)
49. A. Nasir, X. Zhou, S. Durrani, R. Kennedy, Wireless-powered relays in cooperative communications: time-switching relaying protocols and throughput analysis. IEEE Trans. Commun. **63**(5), 1607–1622 (2015)
50. Y. Zeng, R. Zhang, Optimized training design for wireless energy transfer. IEEE Trans. Commun. **63**(2), 536–550 (2015)
51. Y. Zeng, R. Zhang, Optimized training for net energy maximization in multi-antenna wireless energy transfer over frequency-selective channel. IEEE Trans. Commun. **63**(6), 2360–2373 (2015)
52. J. Xu, R. Zhang, A general design framework for MIMO wireless energy transfer with limited feedback. IEEE Trans. Signal Process. **64**(10), 2475–2488 (2016)
53. M. Costa, M. Codreanu, A. Ephremides, Age of information with packet management, in *Proceedings of ISIT*, June (2014), pp. 1583–1587
54. S. Kaul, R. Yates, M. Gruteser, Real-time status: How often should one update? in *Proceedings of IEEE INFOCOM*, March (2012), pp. 2731–2735
55. Y. Sun, E. Uysal-Biyikoglu, R. Yates, C.E. Koksal, N.B. Shroff, Update or wait: how to keep your data fresh, in *Proceedings of IEEE INFOCOM*, April (2016), pp. 1–9
56. P. Lee, Z.A. Eu, M. Han, H. Tan, Empirical modeling of a solar-powered energy harvesting wireless sensor node for time-slotted operation, in *Proceedings of IEEE WCNC*, March (2011), pp. 179–184
57. Z. Ding, S. Perlaza, I. Esnaola, H.V. Poor, Power allocation strategies in energy harvesting wireless cooperative networks. IEEE Trans. Wirel. Commun. **13**(2), 846–860 (2014)
58. A.J. Goldsmith, *Wireless Communications* (Cambridge University Press, New York, 2005)

59. W. Liu, X. Zhou, S. Durrani, H. Mehrpouyan, S.D. Blostein, Performance of wireless-powered sensor transmission considering energy cost of sensing, in *Proceedings of IEEE GLOBECOM*, December (2015), pp. 1–7
60. R. Durrett, *Probability: Theory and Examples* (Cambridge University Press, Cambridge, 2010)
61. MICAz, Crossbow Technology (2006). [Online]. Available: http://www.openautomation.net/uploadsproductos/micaz-datasheet.pdf
62. F. Zhang, V. Lau, Closed-form delay-optimal power control for energy harvesting wireless system with finite energy storage. IEEE Trans. Signal Process. **62**(21), 5706–5715 (2014)

Chapter 9
Spectrum and Energy Harvesting Protocols for Wireless Sensor Nodes

Mansi Peer and Vivek Ashok Bohara

9.1 Introduction

Recently industry analysts predicted that by the year 2020, 50 billion devices will be connected to mobile network worldwide. The large scale integration of devices to a network is the result of the move towards a smarter planet. The goal is to generate and process data with minimal human intervention and create an Internet of Things (IoT). With emerging 5G wireless networks researchers are anticipating to unlock the potential of IoT. 5G networks are envisioned to bring together different wireless technologies paving a way for heterogeneous networks that can accommodate diverse devices. These devices may have varied applications, for instance, they may be wireless sensors used for monitoring temperature, pressure or stress, or actuators which can be used to remotely control devices or make adjustments in real time. These sensor nodes may be a part of body area network used for monitoring body vitals. In particular, these devices with sensing abilities form a wireless sensor network (WSN). There are two major concerns in the deployment of large scale WSN given as follows:

- **Energy inefficiency**: Energy consumption by the sensor nodes has been identified as one of the primary concerns. Further, most of the sensor nodes are deployed in hostile or inaccessible environment where replacing the batteries or providing stable energy source may not be feasible. The battery disposal also has a serious impact on the global carbon emission levels. It contributes significantly to global warming and causes concern for the environment.

M. Peer (✉) • V.A. Bohara
Wirocomm Research Group, Indraprastha Institute of Information Technology (IIIT), Delhi, India
e-mail: mansip@iiitd.ac.in; vivek.b@iiitd.ac.in

D.N.K. Jayakody et al. (eds.), *Wireless Information and Power Transfer: A New Paradigm for Green Communications*, DOI 10.1007/978-3-319-56669-6_9

- **Spectrum Under-Utilization**: Apart from above, recent frequency spectrum measurements have shown that although most of the spectrum band is allocated under license, the spectrum usage is very low. The unprecedented increase in the number of nodes has prompted researchers to come out with ways to better utilize this limited resource.

Recently, significant amount of interest has been shown by the scientific research community into the domain of radio frequency (RF) energy harvesting as a means of "green and nonpolluting source of energy." The ubiquitous presence of ambient RF sources like cellular towers, mobile phones, WiFi routers, television, and radio transmitters in a humanized environment make the option of charging low-power sensors by means of RF energy harvesting more feasible. RF energy unlike solar or wind is more predictable as it is less dependent of the time of the day, weather/geographical location, etc. and can be effectively provided on demand. Inductive coupling and magnetic resonance coupling are also other methods of wireless energy transfer (WET) which involve resonating of coils tuned at a particular frequency, however, there are two major limitations with this approach. First, the power is attenuated according to the cube of distance which restricts the power transfer distance. Second, it requires the calibration and alignment of resonators/coils which makes it difficult for mobile and remote charging [1]. Further, not only does a RF signal carry information but energy too, so information transmission and power transfer can occur simultaneously.

The spectral inefficiency problem in WSN can be alleviated by techniques such as cooperative spectrum sharing (CSS) which facilitate spectrum sharing between users, thus eliminating the need for dedicated spectrum band for sensor nodes. CSS can work well for sensor networks as the wireless sensor nodes do not need to send the data all the time, therefore providing a dedicated spectrum to sensor networks is not an economically viable approach.

9.1.1 Related Work

Most of the recent work in the field of RF energy harvesting has involved cooperative relaying [2–4]. In [2], authors have proposed two energy harvesting relaying protocols, namely the time switching-based relaying (TSR) protocol, where the energy constrained amplify and forward (AF) relay node switches between the energy harvesting and information decoding modes, and power splitting-based relaying (PSR) protocol, where a fraction of power received at relay is devoted to energy harvesting and rest of the power is utilized for information decoding. In both the protocols, the relays were assumed to be half-duplex. In [3] energy harvesting protocol was extended to full-duplex relays so that energy harvesting and information transmission from relay to primary destination occurs simultaneously that ensures uninterrupted information transmission. The energy stored in the battery can be used for further transmissions at relay.

Energy harvesting techniques have also been employed to complement cognitive radio networks. In a cognitive radio framework, two set of users, namely primary and secondary users are allowed to co-exist in the same frequency band. Primary user, also termed as licensed user, has a license to operate on a particular frequency band. Secondary user, also termed as cognitive user or unlicensed user, accesses the licensed band of primary user without degrading the performance of primary user. Furthermore, by incorporating RF energy harvesting techniques, secondary/cognitive user can be made self-sustaining. For instance, in [5], a model has been proposed where low-power mobile nodes in the secondary networks called the secondary transmitters (STs) harvest energy from the RF transmissions of the primary transmitters (PTs). In this framework, STs can operate in any of the following three modes: harvesting mode, transmitting mode, or idle mode. In the harvesting mode a ST lying in the harvesting zone of an active PT harvests energy from PT's transmissions, and in transmission mode a ST lying outside the guard zones of all the active PTs is able to transmit its information. When in idle mode neither harvesting nor transmission takes place.

Most of the above works on energy harvesting were based on underlay protocol wherein the performance of ST is limited by amount of interference acceptable at PR. Furthermore they did not consider cooperative spectrum sharing protocols. We believe that the cooperative and cognitive techniques are complementary to each other and thus by modeling ST as an energy constrained cooperative relay, performances of both primary and secondary systems can be enhanced simultaneously. In our previous work [6], we had proposed a two phase cognitive relaying protocol wherein secondary user, characterized as a self-sustaining energy constrained sensor node, harvests energy from the primary signal transmission based on PSR protocol. Further, it utilizes the harvested energy to assist the primary user to achieve the target rate of communication in exchange for access to primary's spectrum. Similarly [7] focus on the information and energy cooperation in cooperative cognitive radio networks.

9.1.2 Chapter Outline

This chapter tackles the problem of energy consumption by incorporating the technique of radio frequency (RF) energy harvesting in the sensor nodes. Specifically, in this chapter we use the approach of simultaneous energy harvesting and spectrum access to alleviate the major concerns of wireless sensor nodes such as limited power and spectrum. In the course of this chapter we come up with a hybrid time switching and power splitting spectrum sharing protocol to improve primary user's outage performance and provide spectrum access to secondary user. Later, we add the concept of optimal sensor node selection for forwarding primary user's information using the already proposed hybrid protocol. It is to be noted that in this chapter the wireless sensor nodes are considered to be in a cognitive cooperative relaying setup.

9.2 A Hybrid Spectrum Sharing Protocol for Energy Harvesting Sensor Nodes

In this section we have proposed a hybrid time switching and power splitting spectrum sharing protocol [15] that not only improves the energy efficiency but also leads to better spectrum utilization. Unlike [6], in the proposed work we incorporate unequal division of time between the two phases. Our results show that for each value of fraction of total harvested power used for transmission of primary signal there exists an optimal value of fraction of block time over which if energy is harvested results in minimum primary outage. Further, harvesting energy for the optimal amount of time maximizes the overall throughput. In [6], it is assumed that if ST fails in decoding the primary signal in phase 1, it will keep silent and there will be no secondary spectrum access. However, in the proposed work if ST fails in decoding primary signal in phase 1, it will transmit the secondary signal in phase 2. This will improve the performance of secondary system. In comparison to [5] where the performance of secondary node is limited by amount of interference acceptable at PR, in our proposed scheme we have allocated a dedicated fraction of block duration for secondary spectrum access. This will help the secondary node to maintain its own QoS.

9.2.1 Proposed System Model and System Performance Analysis

9.2.1.1 System Model

We have considered a cooperative spectrum sharing system [8] which consists of two source–destination pairs. One is primary transmitter–primary receiver (PT–PR) and other is secondary transmitter–secondary receiver (ST–SR) corresponding to the primary and secondary systems, respectively, as shown in Fig. 9.1. We assume that direct communication between PT and PR is not possible due to limitation of transmission range, fading, obstacles, etc. [2]. In this scenario PT needs the cooperation of a secondary node ST, which will act as a decode and forward (DF) relay,[1] to transmit from PT to PR. Moreover, ST, which is a sensor node, has no power of its own and will be powered wirelessly by harvesting energy from the PT–ST transmission. The block transmission time T is divided into two phases of duration αT and $(1-\alpha)T$. In phase 1, during αT time, PT broadcasts its information signal x_p which will be received at ST and SR. The total power, P, received at ST during phase 1 will be divided between energy harvesting and information decoding using PSR protocol.

[1] Interested readers may refer to [9] for details on control signaling involved between the primary and secondary system.

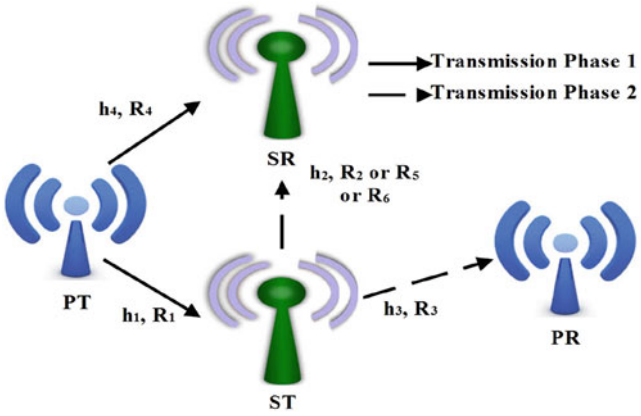

Fig. 9.1 System model

The channel between each pair of transmitter and receiver is assumed to be frequency non-selective Rayleigh slow fading channel. The channel coefficients corresponding to PT–ST, ST–SR, ST–PR, and PT–SR links are h_1, h_2, h_3, and h_4, respectively. We have $h_i \sim \mathscr{CN}(0, d_i^{-v}), i = 1, 2, 3, 4$, where v is the path loss exponent and d_i is the distance between the respective transmitter and receiver. The channel gain $\beta_i = |h_i|^2$ is exponentially distributed and is denoted as $\beta_i \sim \mathscr{E}(d_i^v)$, where d_i^{-v} is the mean of the distribution. The transmit power at PT is denoted as P_p. The signal received at jth node in kth phase is denoted as y_{jk}, where $j = 1, 2, 3$ for ST, SR, PR, respectively and $k = 1, 2$ for phase 1 and phase 2, respectively. In phase 1, signal received at ST from PT is given by

$$y_{11} = \sqrt{P_p} h_1 x_p + n_a, \tag{9.1}$$

where $n_a \sim \mathscr{CN}(0, \sigma_a^2)$ is the AWGN noise received at ST. As power splitting protocol is used at ST, γP and $(1 - \gamma)P$ power is made available to the energy harvesting and information receiver branches of the ST node, respectively, where $0 \leq \gamma \leq 1$. We have assumed that the power required for processing is negligible compared to transmission power at ST [2]. So, the signal received at energy harvester is given by

$$\sqrt{\gamma} y_{11} = \sqrt{\gamma P_p} h_1 x_p + \sqrt{\gamma} n_a. \tag{9.2}$$

Energy harvested in time αT is given by

$$E_h = \eta \gamma P_p |h_1|^2 \alpha T, \tag{9.3}$$

where $\eta\epsilon$ (0,1] is the conversion efficiency of the RF to DC conversion circuitry used. Power extracted from the harvested energy is the transmit power available at ST node and will be given by

$$P_h = \frac{E_h}{(1-\alpha)T} = \frac{\eta\gamma P_p |h_1|^2 \alpha}{(1-\alpha)}. \tag{9.4}$$

The signal received at information receiver of ST is given by

$$\sqrt{(1-\gamma)}y_{11} = \sqrt{(1-\gamma)P_p}h_1 x_p + \sqrt{(1-\gamma)}n_a + n_c, \tag{9.5}$$

where $n_c \sim \mathscr{CN}(0, \sigma_c^2)$ is the sampled AWGN due to RF to baseband signal conversion. From (9.5), the total AWGN variance at ST is given by $\sigma^2 = (1-\gamma)\sigma_a^2 + \sigma_c^2$.

Rate achievable at ST will be

$$R_1 = \alpha \log_2(1 + \text{SNR}_1), \tag{9.6}$$

where $\text{SNR}_1 = \frac{(1-\gamma)P_p|h_1|^2}{\sigma^2}$.

Signal received at SR is given by

$$y_{21} = \sqrt{P_p}h_4 x_p + n_{\text{SR}}, \tag{9.7}$$

where $n_{\text{SR}} \sim \mathscr{CN}(0, \sigma^2)$ is the AWGN noise added at SR.

Rate achievable at SR in phase 1 is given by

$$R_4 = \alpha \log_2\left(1 + \frac{P_p|h_4|^2}{\sigma^2}\right). \tag{9.8}$$

In transmission phase 2, three scenarios are possible depending on whether ST and/or SR are able to successfully decode PT's information in phase 1. The three cases are as follows:

- **Case 1** In this case both ST and SR decode PT's information. ST transmits signals x_p and x_s with ρP_h and $(1-\rho)P_h$ power, respectively, where $\rho\epsilon$ (0,1). Signal received at PR is given by

$$y_{32} = \sqrt{\rho P_h}h_3 x_p + \sqrt{(1-\rho)P_h}h_3 x_s + n_{\text{PR}}, \tag{9.9}$$

  where $n_{\text{PR}} \sim \mathscr{CN}(0, \sigma^2)$ is the AWGN noise added at PR. Signal received at SR is given by

$$y_{22} = \sqrt{(1-\rho)P_h}h_2 x_s + \sqrt{\rho P_h}h_2 x_p + n_{\text{SR}}. \tag{9.10}$$

Rate achievable at PR is given by

$$R_3 = (1-\alpha)\log_2\left(1+\frac{\rho P_h|h_3|^2}{(1-\rho)P_h|h_3|^2+\sigma^2}\right). \tag{9.11}$$

Rate achievable at SR, conditioned on successful decoding of x_p at ST and SR is given by

$$R_2 = (1-\alpha)\log_2\left(1+\frac{(1-\rho)P_h|h_2|^2}{\sigma^2}\right). \tag{9.12}$$

- **Case 2** In case 2, ST is unable to decode x_p with target rate in phase 1. So, complete harvested power at secondary node is used for secondary transmission and the signal received at SR in phase 2 is given by

$$y_{22} = \sqrt{P_h}h_2x_s + n_{\text{SR}}. \tag{9.13}$$

Hence, rate achievable at SR is given by

$$R_5 = (1-\alpha)\log_2\left(1+\frac{P_h|h_2|^2}{\sigma^2}\right). \tag{9.14}$$

- **Case 3** In case 3, ST successfully decodes x_p, however, SR fails to decode it. Hence, the primary signal present in the combined signal transmitted by ST will create interference at SR. So, the rate achievable at SR in phase 2 will be given by:

$$R_6 = (1-\alpha)\log_2\left(1+\frac{(1-\rho)P_h|h_2|^2}{\rho P_h|h_2|^2+\sigma^2}\right). \tag{9.15}$$

9.2.1.2 Outage Probability Analysis of Primary System

The outage at primary system will occur if any of the PT–ST and ST–PR links fail in achieving the target rate of communication, i.e., R_{pt}. Therefore, outage at PR is given by

$$P_{oP} = P[\min(R_1, R_3) < R_{\text{pt}}] = 1 - P[R_1 > R_{\text{pt}}]P[R_3 > R_{\text{pt}}]. \tag{9.16}$$

If any of the two links fail (this explains the use of minimum operator) then the overall primary transmission will be in outage. Using (9.6),

$$P[R_1 > R_{\text{pt}}] = 1 - P\left[|h_1|^2 < \frac{t}{m(1-\gamma)}\right] = e^{\frac{-d_1^{\eta}t}{m(1-\gamma)}}, \tag{9.17}$$

where $t = 2^{R_{\text{pt}}/\alpha} - 1$ and $m = \frac{P_p}{\sigma^2}$. Similarly,

$$P[R_3 > R_{\text{pt}}] = P\left[\frac{\rho\, P_h|h_3|^2}{(1-\rho)P_h|h_3|^2 + \sigma^2} > (2^{\frac{R_{\text{pt}}}{1-\alpha}} - 1)\right]. \tag{9.18}$$

Using (9.4)

$$P[R_3 > R_{\text{pt}}] = P[b|h_3|^2|h_1|^2 > a], \tag{9.19}$$

where $a = \frac{\sigma^2(1-\alpha)(2^{R_{\text{pt}}/(1-\alpha)}-1)}{\eta\gamma P_p \alpha}$, $b = \rho - (2^{R_{\text{pt}}/(1-\alpha)} - 1)(1-\rho)$. This b can be either positive or negative. Hence,

$$P[R_3 > R_{\text{pt}}] = \begin{cases} P[|h_3|^2|h_1|^2 > \frac{a}{b}], & \alpha < 1-\delta \\ P[|h_3|^2|h_1|^2 < \frac{a}{b}] = 0, & \text{otherwise}, \end{cases} \tag{9.20}$$

where $\delta = \frac{R_{\text{pt}}}{\log_2(1+\frac{\rho}{1-\rho})}$.

The second equality in (9.20) can be explained by the fact that the probability of $|h_3|^2|h_1|^2$ being less than a negative number is 0. The first term in (9.20) involves product of two independent exponentially distributed random variables. This can be determined as

$$P[R_3 > R_{\text{pt}}] = \begin{cases} \int_0^\infty f_{|h_1|^2}(x) P[|h_3|^2 > \frac{a}{bx}]dx, & \alpha < 1-\delta \\ 0, & \text{otherwise}. \end{cases} \tag{9.21}$$

Further for $\alpha < 1-\delta$, using the form $\int_0^\infty e^{-\frac{\beta}{4x}-\theta x}dx = \sqrt{\frac{\beta}{\theta}}K_1(\sqrt{\beta\theta})$ [10], where $K_1(.)$ is the modified first order Bessel function of second kind, we obtain

$$\begin{aligned} P[R_3 > R_{\text{pt}}] &= \frac{1}{d_1^{-v}} \int_0^\infty e^{-\frac{x}{d_1^{-v}}} . e^{-\frac{a}{bxd_3^{-v}}} dx \\ &= \sqrt{\frac{4a}{bd_1^{-v}d_3^{-v}}} K_1\left(\sqrt{\frac{4a}{bd_1^{-v}d_3^{-v}}}\right). \end{aligned} \tag{9.22}$$

The closed form expression for the outage probability of the primary system is given by

$$P_{oP} = \begin{cases} 1 - \phi u K_1(u), & \alpha < 1-\delta \\ 1, & \text{otherwise} \end{cases} \tag{9.23}$$

where $\phi = e^{\frac{-d_1^v t}{m(1-\gamma)}}$, $u = \sqrt{\frac{4a}{bd_1^{-v}d_3^{-v}}}$.

9.2.1.3 Outage Probability Analysis of Secondary System

The secondary system will be able to achieve the target rate, i.e., R_{st} for the three cases considered earlier with certain probability associated with each one of them as determined below:

1. PT–ST, PT–SR, and ST–SR links successfully achieve the target rates R_{pt}, R_{pt}, and R_{st}, respectively.

$$P_{s1} = P[R_1 > R_{\text{pt}}]P[R_4 > R_{\text{pt}}]P[R_2 > R_{\text{st}}]. \tag{9.24}$$

2. PT–ST link fails to achieve the target rate but ST–SR link achieves the rate R_{st}.

$$P_{s2} = P[R_1 < R_{\text{pt}}]P[R_5 > R_{\text{st}}]. \tag{9.25}$$

3. PT–SR link fails to obtain the target rate. However, PT–ST and ST–SR links achieve the rate R_{pt} and R_{st}, respectively.

$$P_{s3} = P[R_1 > R_{\text{pt}}]P[R_4 < R_{\text{pt}}]P[R_6 > R_{\text{st}}]. \tag{9.26}$$

Hence by combining all the above cases, the secondary system outage probability can be given as

$$\begin{aligned} P_{oS} = 1-(&P[R_1 > R_{\text{pt}}]P[R_4 > R_{\text{pt}}]P[R_2 > R_{\text{st}}]+P[R_1 < R_{\text{pt}}]P[R_5 > R_{\text{st}}] \\ &+ P[R_1 > R_{\text{pt}}]P[R_4 < R_{\text{pt}}]P[R_6 > R_{\text{st}}]), \end{aligned} \tag{9.27}$$

where

$$P[R_4 > R_{\text{pt}}] = P\left[|h_4|^2 > \left(\frac{\left(2^{\frac{R_{\text{pt}}}{\alpha}} - 1\right)\sigma^2}{P_p}\right)\right] = e^{\frac{-d_4^{\nu} t}{m}}, \tag{9.28}$$

$$P[R_2 > R_{\text{st}}] = P\left[\frac{(1-\rho)\, P_h |h_2|^2}{\sigma^2} > \left(2^{\frac{R_{\text{st}}}{1-\alpha}} - 1\right)\right]. \tag{9.29}$$

Using (9.4)

$$P[R_2 > R_{\text{st}}] = P[|h_2|^2 |h_1|^2 > c], \tag{9.30}$$

$$Pr[R_5 > R_{\text{st}}] = P\left[|h_2|^2 |h_1|^2 > d\right], \tag{9.31}$$

where $c = \frac{\sigma^2(1-\alpha)(2^{R_{st}/(1-\alpha)}-1)}{\eta\gamma P_p \alpha(1-\rho)}$ and $d = \frac{\sigma^2(1-\alpha)(2^{R_{st}/(1-\alpha)}-1)}{\eta\gamma P_p \alpha}$.

$$P[R_6 > R_{st}] = P\left[|h_2|^2|h_1|^2 > \frac{d}{e}\right], \tag{9.32}$$

where $e = (1-\rho) - \rho(2^{\frac{R_{st}}{1-\alpha}} - 1)$.

The terms in (9.30)–(9.32) can be found similar to (9.21). So,

$$P[R_2 > R_{st}] = \sqrt{\frac{4c}{d_1^{-v} d_2^{-v}}} K_1\left(\sqrt{\frac{4c}{d_1^{-v} d_2^{-v}}}\right), \tag{9.33}$$

$$P[R_5 > R_{st}] = \sqrt{\frac{4d}{d_1^{-v} d_2^{-v}}} K_1\left(\sqrt{\frac{4d}{d_1^{-v} d_2^{-v}}}\right), \tag{9.34}$$

$$P[R_6 > R_{st}] = \begin{cases} \sqrt{\frac{4d}{ed_1^{-v} d_2^{-v}}} K_1\left(\sqrt{\frac{4d}{ed_1^{-v} d_2^{-v}}}\right), & \alpha < 1-\mu \\ 0, & \text{otherwise,} \end{cases} \tag{9.35}$$

where $\mu = \frac{R_{st}}{\log_2(\frac{1}{\rho})}$.

The closed form expression for the outage probability of the secondary system obtained by substituting (9.17), (9.28), (9.33), (9.34), and (9.35) in (9.27) is given by

$$P_{oS} = \begin{cases} 1 - \left(\phi e^{\frac{-d_4^v t}{m}} wK_1(w) + (1-\phi) yK_1(y) + \left(1 - e^{\frac{-d_4^v t}{m}}\right) \phi zK_1(z)\right), & \alpha < 1-\mu \\ 1 - \left(\phi e^{\frac{-d_4^v t}{m}} wK_1(w) + (1-\phi) yK_1(y)\right), & \text{otherwise,} \end{cases} \tag{9.36}$$

where $w = \sqrt{\frac{4c}{d_1^{-v} d_2^{-v}}}$, $y = \sqrt{\frac{4d}{d_1^{-v} d_2^{-v}}}$ and $z = \sqrt{\frac{4d}{ed_1^{-v} d_2^{-v}}}$.

9.2.2 Simulation and Results

In this section, we present the plots of primary and secondary system outages. The distances between PT–ST, ST–PR, PT–SR, and ST–SR are v m, (50-v)m, 10 m, (v-10) m, respectively, where 50 m is the distance between the PT–PR link and ST is assumed to be placed between PT and PR. The remaining parameters are given in Table 9.1.

Table 9.1 Simulation parameters

Parameter	σ^2	η	γ	P_p	υ	Target rate
Value	−90 dBm	0.8	0.75	30 dBm	3	$R_{\text{pt}} = R_{\text{st}} = 1$

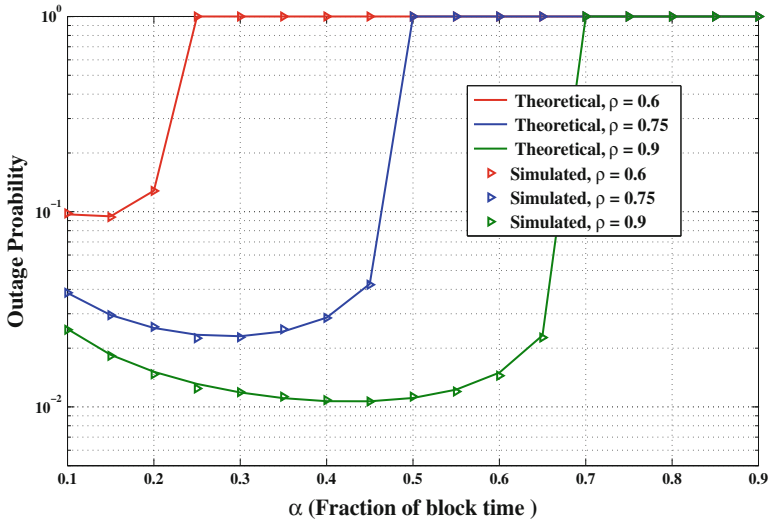

Fig. 9.2 Plot of primary outage probability against α for $\rho = 0.6, 0.75, 0.9$, $\nu = 30$ m, $\eta = 0.8$, and $\gamma = 0.75$

Figures 9.2 and 9.3 show the plots of primary and secondary system outages with respect to α for $\rho = 0.6, 0.75, 0.9$. From the figures it is quite apparent that the primary outage decreases with increase in α. This can be explained as follows. As α increases, more energy is harvested at ST which results in better performance of ST–PR link. However, after a certain value of α, corresponding to each ρ, there is an abrupt increase in primary outage. Since there is no direct link between PT and PR so when the ST–PR link becomes a failure, primary outage increases to 1. This can also be verified from (9.23). Further, secondary system outage at first decreases and later on increases with increase in α. The initial drop is due to the reason as stated for the primary case that is the increased amount of harvested energy at ST. The increase in the secondary outage occurs at higher values of α because as α increases further, the fraction of time available for transmission in phase 2 reduces.

Now, consider Fig. 9.4 which plots the primary and secondary outages with respect to PT–ST distance, i.e., ν. As can be seen from Fig. 9.4, primary outage at first increases and later on decreases with respect to PT–ST distance. As ν increases ST moves away from PT and that leads to the PT–ST link outage. Hence, the overall primary outage sees an increase. However, as ST moves away further from PT, it gets closer to PR. So, ST–PR link outage decreases and overall primary outage becomes low. In the secondary system case the amount of energy harvested

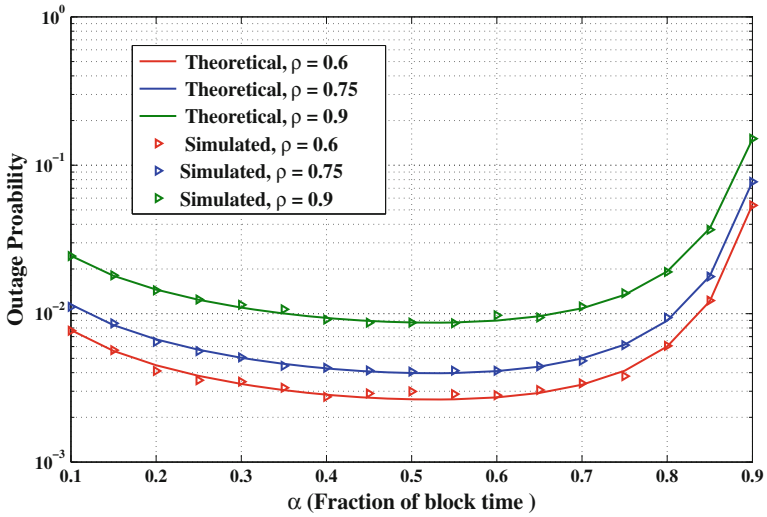

Fig. 9.3 Plot of secondary outage probability against α for $\rho = 0.6, 0.75, 0.9$, $\nu = 30$ m, $\eta = 0.8$, and $\gamma = 0.75$

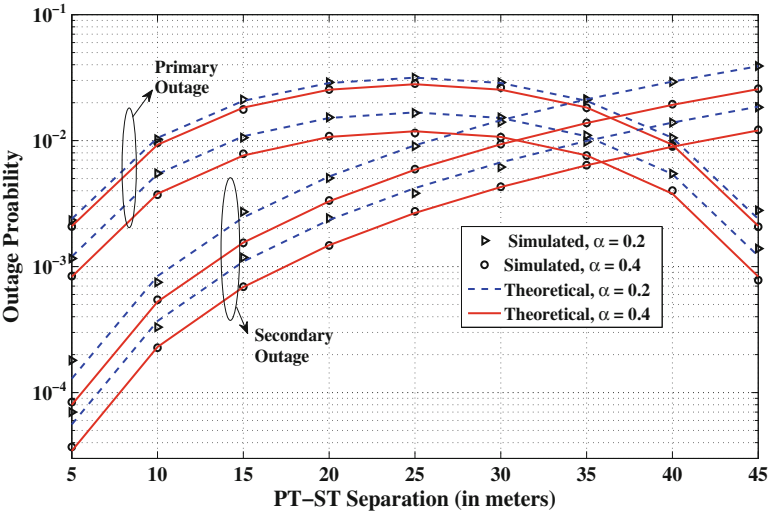

Fig. 9.4 Plot of primary and secondary outage probabilities against the PT–ST separation for $\alpha = 0.2, 0.4$ and $\rho = 0.75, 0.9$, $\eta = 0.8$, and $\gamma = 0.75$

becomes a predominant factor for determining the outage because as ν increases ST is anyway moving away from SR. As the ST moves away from PT less amount of energy is harvested and hence outage performance of the secondary system degrades. Figure 9.5 shows the dependence of primary and secondary outages on

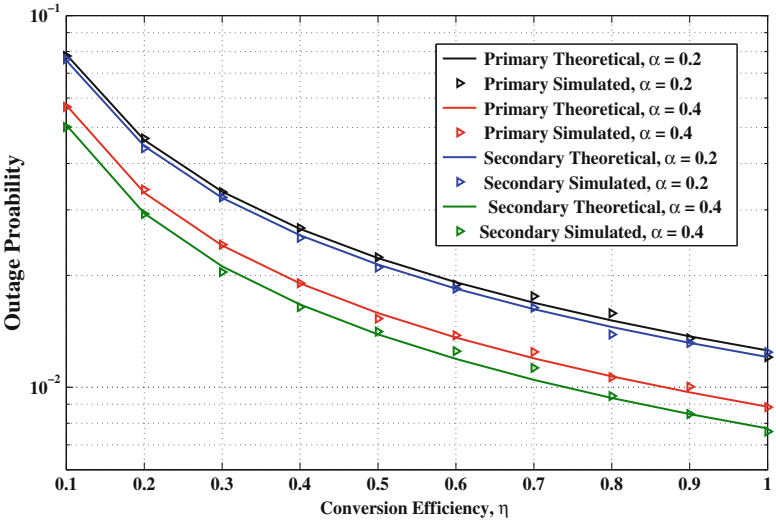

Fig. 9.5 Plot of primary and secondary outage probabilities against conversion efficiency for $\rho = 0.9, \alpha = 0.2, 0.4, \nu = 30\,\text{m}$, and $\gamma = 0.75$

the conversion efficiency, η, of the RF circuitry at ST. As η increases the primary and secondary outage decreases because greater amount of energy is harvested at ST which will improve the link performance.

9.3 Multiple Energy Harvesting Sensor Nodes Using Hybrid Spectrum Sharing Protocol

This section deals with a cooperative cognitive radio network wherein multiple energy harvesting sensor nodes in the secondary system are considered. In recent years work is being done in bringing together the complementary techniques of CSS and energy harvesting (EH) as it is beneficial for creating a standalone secondary system which is capable of meeting its energy and spectrum requirements using primary's resources [6, 11]. In the previous section we combined both CSS and EH to enhance the performance of primary and secondary systems. The performance of the system can be further enhanced by integrating the concept of optimal selection.

The limitation of the framework in [6, 8] is that SU remains silent if it is not decoding PU's information and in [12] the use of two different SU puts a constraint on the level of transmission power to avoid interference. In the proposed scheme we alleviate the above drawbacks by utilizing a hybrid energy harvesting and spectrum sharing protocol wherein the best node among multiple sensor nodes is selected to forward the information of primary system. As a consequence, since the

orthogonal channel (channel corresponding to the best node)[2] is required for PU's information transmission same diversity order as the cooperative diversity using multiple orthogonal channels [13]. In addition to the above we have employed a hybrid power splitting and time switching protocol where an optimal time duration is obtained during which if energy is harvested we will achieve the best QoS for the primary system.

The main contributions are summarized as follows:

- The selection process is robust in the sense that it makes joint use of both the channel conditions and the amount of energy harvested in a CSS scenario thus giving a better performance compared to [14].
- The node selection procedure is such that the node with maximum achievable rate is selected that is also capable of supporting secondary's transmission.
- The results obtained show that the value of fraction of power allocated for energy harvesting and information decoding at the nodes play a significant role in primary and secondary outage performance.
- Unlike [11] we have used optimal sensor node selection and have shown that the outage performance of the primary system is improved by increasing the number of sensor nodes in the secondary network. Further, the outage performance is also limited by the value of fraction of power allocated for primary and secondary transmissions.

We have also extended this work further. The Sect. 9.3.3 aims at giving an insight into the fact that how there is a trade-off between the power consumption at the BS and the number of sensor nodes present in the WSN to achieve a desired primary system performance.

9.3.1 Proposed System Model and Performance Analysis

9.3.1.1 System Model

The proposed system model consists of base station BS, a primary cellular user CU, N number of sensor nodes (secondary transmitters or STs), and one central monitoring station or SR as shown in Fig. 9.6. The channel between each pair of transmitter and receiver is assumed to be Rayleigh flat fading and is denoted by h_{i1} for BS–ST$_i$ link, h_{i2} for ST$_i$–CU link, h_{i3} for ST$_i$–SR link, h_4 for BS–SR link, where $i = 1, 2, 3 \ldots .N$. Here, $h_{ij} \sim \mathscr{CN}(0, d_{ij}^{-v})$ and $h_4 \sim \mathscr{CN}(0, d_4^{-v})$ where v is the path loss exponent, d_{ij} and d_4 is the distance between the respective transmitter and receiver and $j = 1, 2, 3$ for BS, CU, and SR, respectively. The channel gains $\beta_{ij} = |h_{ij}|^2$ and $\beta_4 = |h_4|^2$ are exponentially distributed and are denoted as $\beta_{ij} \sim \mathscr{E}(d_{ij}^v)$ and $\beta_4 \sim \mathscr{E}(d_4^v)$, respectively , where d_{ij}^{-v}, d_4^{-v} are the mean of the distribution.

[2]We have considered that direct link fails.

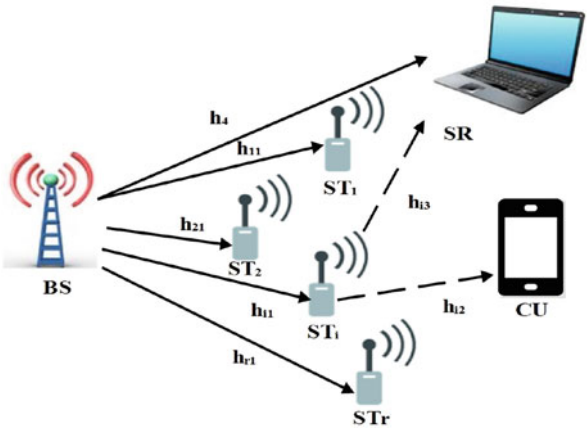

Fig. 9.6 System model where ST_i is the best relay

Further it is assumed that h_{ij} are independent and identically distributed (i.i.d.) $\forall i, j$. Hence, $d_1 = d_{i1}$, $d_2 = d_{i2}$, and $d_3 = d_{i3} \forall i$. The AWGN at each receiver is denoted as $n \sim \mathscr{CN}(0, \sigma^2)$. The signal received at ST_i, CU, SR in kth phase is denoted as $y^k_{ST_i}$, y^k_2, and y^k_3, respectively.

We assume that there is no direct link between BS and CU [2], hence BS requires the assistance of the secondary user for transmission of the primary information x_p to CU. It is worth noting that BS constantly monitors the channel conditions and gathers all the necessary CSI for selecting the best sensor node. After this BS broadcasts the message which includes the information of selected node and also the mode in which the selected node has to operate. The node selection process is carried out as given in Algorithm 1. The cases mentioned in the algorithm have been discussed later in the paper.

On the selected sensor node energy harvesting follows a hybrid power splitting and time switching protocol. The total transmission time T is divided into αT and $(1 - \alpha)T$, respectively, where α is the time switching factor. The power allocated for energy harvesting and information decoding is γP_i and $(1 - \gamma)P_i$, respectively, where P_i is the power received at ST_i and $0 \leq \gamma \leq 1$ is the power splitting factor.

In phase 1, BS broadcasts its signal x_p with a transmit power P_p. The signal received at ST_i from BS is given by

$$y^1_{ST_i} = \sqrt{P_p} h_{i1} x_p + n. \tag{9.37}$$

The signal received at the energy harvester branch of ST_i will be

$$\sqrt{\gamma} y^1_{ST_i} = \sqrt{\gamma P_p} h_{i1} x_p + \sqrt{\gamma} n. \tag{9.38}$$

Hence the energy harvested at each ST_i in time αT can be given by

$$E_{hi} = \eta \gamma P_p |h_{i1}|^2 \alpha T, \tag{9.39}$$

Algorithm 1: Selection procedure

Let R_i be the rate achievable at ST_i in phase 1, R_{pt} is the primary target rate and $R_i^{'}$ be the rate achievable at CU when ST_i is transmitting x_p and x_s with ρP_h and (1-ρ)P_h power respectively, where P_h is the harvested power. Also, R_{SR} is the rate achievable at SR in phase 1.

for $i = 1:1:N$ **do**
  if $R_i > R_{pt}$ **then**
    Select ST_i.
  end if
  $i \leftarrow i + 1$
end for
Create a decoding set D of the selected nodes.
if $D = \emptyset$ **then**
  case 1
else
  if $\max_i [R_i^{'}] > R_{pt}$ **then**
    Select the node from D for transmission of combination of x_p and x_s in phase 2.
    if $R_{SR} > R_{pt}$ **then**
      case 2
    else
      case 3
    end if
  else
    case 4
  end if
end if

where $\eta \epsilon$ (0,1] is the conversion efficiency of the RF to DC conversion circuitry used. The transmission power available at the energy harvesting sensor node is given by

$$P_{hi} = \frac{E_{hi}}{(1-\alpha)T} = \frac{\eta\gamma P_p |h_{i1}|^2 \alpha}{(1-\alpha)}. \tag{9.40}$$

The signal received at information receiver of each ST_i is given by

$$\sqrt{(1-\gamma)}y_{st_i}^1 = \sqrt{(1-\gamma)P_p}h_{i1}x_p + n. \tag{9.41}$$

Hence the rate achievable at ST_i will be

$$R_i = \alpha \log_2(1 + \text{SNR}_i), \tag{9.42}$$

where $\text{SNR}_i = \frac{(1-\gamma)P_p|h_{i1}|^2}{\sigma^2}$.

Similarly, signal received at SR in phase 1 will be

$$y_{31} = \sqrt{P_p} h_4 x_p + n. \tag{9.43}$$

Hence the rate achievable at SR in phase 1 will be

$$R_{\mathrm{SR}} = \alpha \log_2 \left(1 + \frac{P_p |h_4|^2}{\sigma^2}\right). \tag{9.44}$$

For phase 2 transmission, four cases are possible and they are illustrated in Table 9.2. The four cases signify the possible achievable rates for ST_b–SR link depending on the channel conditions and amount of energy harvested.

9.3.1.2 Outage Analysis of Primary System

The probability that no ST_i is able to decode x_p in phase 1 is given by

$$P_1 = P[R_1 < R_{\mathrm{pt}}] P[R_2 < R_{\mathrm{pt}}] \ldots\ldots P[R_N < R_{\mathrm{pt}}], \tag{9.45}$$

It is assumed that each ST_i is equidistant from BS and CU. Hence,

$$P_1 = \left(P[R_1 < R_{\mathrm{pt}}]\right)^N = \left(1 - e^{\frac{-d_1^v t}{m(1-\gamma)}}\right)^N, \tag{9.46}$$

where $t = (2^{\frac{R_{\mathrm{pt}}}{\alpha}} - 1)$ and $m = \frac{P_p}{\sigma^2}$.

The probability that at least one of the sensor nodes decode x_p will be

$$P_1' = 1 - P_1. \tag{9.47}$$

Thus the outage for the primary system can be given as (assuming k nodes have successfully decoded x_p)

$$P_{oP} = P_1 + P_1' P_2, \tag{9.48}$$

where

$$P_2 = \left[\sum_{k=1}^{N} \binom{N}{k} p^{N-k} (1-p)^k P[\max(R_1' \ldots R_k') < R_{\mathrm{pt}}]\right], \tag{9.49}$$

$$R_i' = (1-\alpha) \log_2 \left(1 + \frac{\rho P_h |h_{i2}|^2}{(1-\rho) P_h |h_{i2}|^2 + \sigma^2}\right). \tag{9.50}$$

$$P[\max(R_1' \ldots R_k') < R_{\mathrm{pt}}] = \begin{cases} \left[1 - uK_1(u)\right]^k, & \alpha < 1 - \delta \\ 1, & \text{otherwise,} \end{cases} \tag{9.51}$$

Table 9.2 Table containing the details of the four possible cases in phase 2

Case	Condition	Signal received at SR	Rate achievable corresponding to ST_b–SR link
Case 1	(a) Decoding set D is empty	$y_3^2 = \sqrt{P_h} h_{b3} x_s + n$	$R_{b3} = (1-\alpha)\log_2\left(1 + \frac{P_h \lvert h_{b3}\rvert^2}{\sigma^2}\right)$
	(b) Sensor node achieving maximum rate at SR corresponding to x_s transmission is selected		
Case 2	(a) Decoding set D is nonempty	$y_3^{2'} = \sqrt{(1-\rho)P_h} h_{b3} x_s + \sqrt{\rho P_h} h_{b3} x_p + n$	$R'_{b3} = (1-\alpha)\log_2\left(1 + \frac{(1-\rho)P_h \lvert h_{b3}\rvert^2}{\sigma^2}\right)$
	(b) A sensor node in D meets the criterion $\max_i[R'_i] > R_{\text{pt}}$		
	(c) SR decodes x_p successfully in phase 1		
Case 3	(a) Decoding set D is nonempty	$y_3^{2''} = \sqrt{(1-\rho)P_h} h_{b3} x_s + \sqrt{\rho P_h} h_{b3} x_p + n$	$R''_{b3} = (1-\alpha)\log_2\left(1 + \frac{(1-\rho)P_h \lvert h_{b3}\rvert^2}{\rho P_h \lvert h_{b3}\rvert^2 + \sigma^2}\right)$
	(b) A sensor node in D meets the criterion $\max_i[R'_i] > R_{\text{pt}}$		
	(c) SR unsuccessful in decoding x_p in phase 1		
Case 4	(a) Decoding set D is nonempty	$y_3^{2'''} = \sqrt{P_h} h_{b3} x_s + n$	$R'''_{b3} = (1-\alpha)\log_2\left(1 + \frac{P_h \lvert h_{b3}\rvert^2}{\sigma^2}\right)$
	(b) No node in D meets the criterion $\max_i[R'_i] > R_{\text{pt}}$		
	(c) A sensor node in D achieving maximum rate at SR corresponding to x_s transmission is selected		

Note: ST_b denotes the selected sensor node. h_{b3} denotes the channel coefficient of the link between selected node and SR. P_h is the power harvested at the selected node

where $u = \sqrt{\frac{4a}{bd_1^{-v}d_2^{-v}}}$, $a = \frac{\sigma^2(1-\alpha)(2^{R_{\rm pt}/(1-\alpha)}-1)}{\eta\gamma P_p\alpha}$, $b = \rho - (2^{R_{\rm pt}/(1-\alpha)} - 1)(1-\rho)$, $\delta = \frac{R_{\rm pt}}{\log_2(1+\frac{\rho}{1-\rho})}$ and $K_1(.)$ is the modified first order Bessel function of second kind.

The closed form expression for primary outage obtained on substituting (9.49)–(9.51) in (9.47) will be given by

$$P_{oP} = \begin{cases} P_1 + P_1' \left[\sum_{k=1}^{N} \binom{N}{k} p^{N-k}(1-p)^k w^k\right], & \alpha < 1-\delta \\ P_1 + P_1' \left[\sum_{k=1}^{N} \binom{N}{k} p^{N-k}(1-p)^k\right] = 1, & \text{otherwise,} \end{cases} \tag{9.52}$$

where $w = \left[1 - uK_1(u)\right]$ and $p = \left(1 - e^{\frac{-d_1^v t}{m(1-\gamma)}}\right)$.

9.3.1.3 Secondary System

The outage of the secondary system can be obtained by combining the four cases mentioned in Table 9.1,

$$\begin{aligned} P_{oS} &= P_1 P[\max(R_{13} \ldots . R_{N3}) < R_{\rm st}] + P_1'[1-P_2]P[R_{b3}' < R_{\rm st}]P[R_{\rm SR} > R_{\rm pt}] \\ &\quad + P_1'[1-P_2]P[R_{b3}'' < R_{\rm st}]P[R_{\rm SR} < R_{\rm pt}] \\ &\quad + P_1' P_2 \left[\sum_{k=1}^{N} \binom{N}{k} p^{N-k}(1-p)^k P[\max(R_{13} \ldots R_{k3}) < R_{\rm st}]\right], \end{aligned} \tag{9.53}$$

where $R_{\rm st}$ is the secondary target rate and R_{i3} is the rate corresponding to ST_i-SR link when only secondary signal is transmitted by ST_i. Further,

$$P[R_{b3}' < R_{\rm st}] = \left[1 - vK_1(v)\right], \tag{9.54}$$

where $v = \sqrt{\frac{4c}{d_1^{-v}d_3^{-v}}}$ and $c = \frac{\sigma^2(1-\alpha)(2^{R_{\rm st}/(1-\alpha)}-1)}{\eta\gamma P_p\alpha(1-\rho)}$.

$$P\left[\max(R_{13}R_{23} \ldots . R_{i3}) < R_{\rm st}\right] = \left[1 - yK_1(y)\right]^i. \tag{9.55}$$

$$P[R_{b3}'' < R_{\rm st}] = \begin{cases} 1 - zK_1(z), & \alpha < 1-\mu \\ 1, & \text{otherwise,} \end{cases} \tag{9.56}$$

where $\mu = \frac{R_{st}}{log_2\left(\frac{1}{\rho}\right)}$, $y = \sqrt{\frac{4d}{d_1^{-v}d_3^{-v}}}$ $z = \sqrt{\frac{4d}{ed_1^{-v}d_3^{-v}}}$, $d = \frac{\sigma^2(1-\alpha)(2^{R_{st}/(1-\alpha)}-1)}{\eta\gamma P_p\alpha}$ and $e = (1-\rho) - \rho\left(2^{\frac{R_{st}}{1-\alpha}} - 1\right)$.

$$P[R_{SR} > Rpt] = e^{\frac{-d_4^v t}{m}}. \tag{9.57}$$

By substituting (9.46), (9.51), (9.54), (9.55), (9.56), and (9.57) in (9.53) we get (9.58)

$$P_{oS}= \begin{cases} P_1Q^N+P_1'(1-P_{21})R\phi+P_1'(1-P_{21})T(1-\phi)+ \\ P_1'P_{21}\left[\sum_{k=1}^{N}\binom{N}{k}p^{N-k}(1-p)^kQ^k\right], & \alpha < 1-\delta \text{ and } \alpha < 1-\mu \\ P_1Q^N+P_1')(1-P_{21})R\phi+P_1'(1-P_{21})(1-\phi)+ \\ P_1'P_{21}\left[\sum_{k=1}^{N}\binom{N}{k}p^{N-k}(1-p)^kQ^k\right], & \alpha < 1-\delta \text{ and } \alpha \geq 1-\mu \\ P_1Q^N+P_1'(1-P_{22})R\phi + P_1'(1-P_{22})T(1-\phi)+ \\ P_1'P_{22}\left[\sum_{k=1}^{N}\binom{N}{k}p^{N-k}(1-p)^kQ^k\right], & \alpha \geq 1-\delta \text{ and } \alpha < 1-\mu \\ P_1Q^N+P_1'(1-P_{22})R\phi+P_1'(1-P_{22})(1-\phi)+ \\ P_1'P_{22}\left[\sum_{k=1}^{N}\binom{N}{k}p^{N-k}(1-p)^kQ^k\right], & \alpha \geq 1-\delta \text{ and } \alpha \geq 1-\mu, \end{cases} \tag{9.58}$$

where $Q = \left[1 - yK_1(y)\right]$, $R = \left[1 - vK_1(v)\right]$, $T = \left[\sum_{k=1}^{N}\binom{N}{k}p^{N-k}(1-p)^kw^k\right]$, $P_{21}=P_1+P_1'\left[\sum_{k=1}^{N}\binom{N}{k}p^{N-k}(1-p)^kw^k\right]$, $P_{22}=P_1+P_1'\left[\sum_{k=1}^{N}\binom{N}{k}p^{N-k}(1-p)^k\right]$ and $\phi = e^{\frac{-d_4^v t}{m}}$.

9.3.2 Simulation and Results

This section presents the study of the effect of various system parameters such as α, ρ, and N on the outage performance of the primary and secondary system. Each ST_i is assumed to be equidistant from BS and CU. BS, CU, and SR are assumed to be collinear. The distances between BS–ST_i, ST_i–SR, BS–SR, and ST_i–CU are 30, 20, 10, 20 m, respectively, where distance between the BS–CU link is 50 m. The remaining simulation parameters are given in Table 9.3.

Table 9.3 Simulation parameters

Parameter	σ^2	η	γ	P_p	v
Value	−90 dBm	0.8	0.75	10 dBm	3

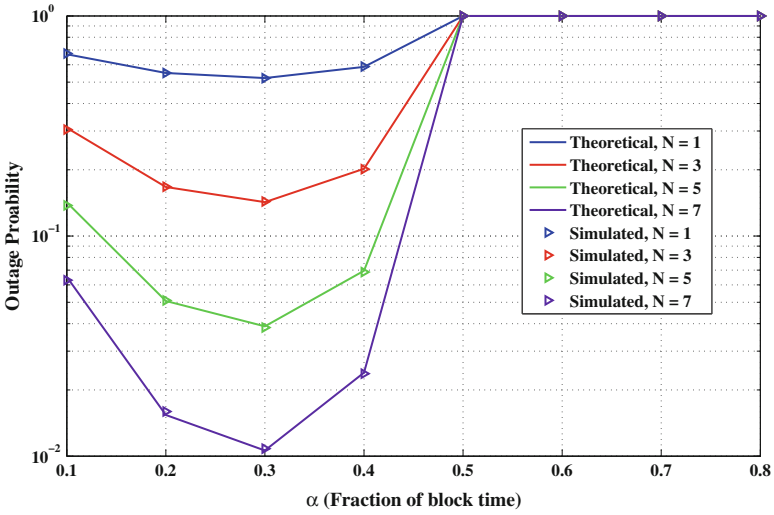

Fig. 9.7 Plot showing the outage probability of primary system with respect to α for $N = 1, 3, 5, 7$

Figure 9.7 shows the variation in the outage probability for a primary system with respect to α for $\rho = 0.75$. It is quite obvious that with the increase in the number of sensor nodes there is a performance improvement because the decoding probability of x_p in phase 1 increases (9.45). Further, corresponding to each value of ρ there is a value of α beyond which the increase in N has no impact on the outage performance of primary system. This can be explained as follows. Since there is no direct link between BS and CU so when ST_i-CU link becomes a failure $\forall ST_i \epsilon D$, primary outage increases to 1. This can also be verified from (9.52).

Figure 9.8 depicts the variation in the outage probability for a secondary system with respect to α for $\rho = 0.75$. Similar to primary system, with the increase in the number of sensor nodes the outage probability for secondary system decreases. This is due to the fact the proposed scheme selects the node which has the maximum harvested energy. Hence with an increase in number of nodes there is more probability that the selected node will have sufficient harvested energy to relay the information of secondary system, x_s, with less outage.

9.3.3 Power Reduction Using Multiple Sensor Nodes

In this subsection we have done an extended study on the multiple sensor node system model considered previously in Sect. 9.3.1. The prime difference is the inclusion of the direct link between BS and CU, unlike Sect. 9.3.1. In a network setup where the direct link is in operational mode the number of the sensor nodes

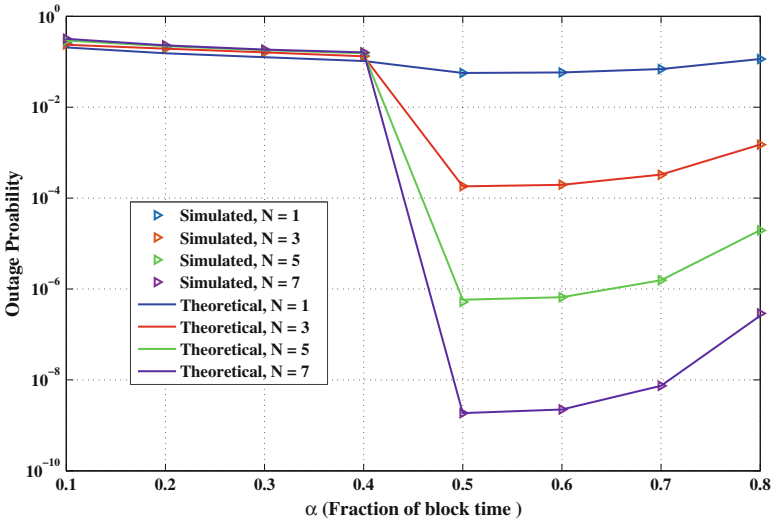

Fig. 9.8 Plot showing the outage probability of secondary system with respect to α for $N = 1, 3, 5, 7$

assisting the forwarding of BS's data and power level at the BS will be the deciding factors for selection of the direct link or the WSN for the primary information transmission, which is the focus of this section. We observed that given the provision to expand the WSN by incorporating more number of sensor nodes the WSN assisted primary transmission will outperform the direct link system configuration at much lower power levels, hence saving big on energy. There can be a case where the WSN expansion is not feasible then the direct link configuration will do a better job.

9.3.3.1 Performance Analysis

The system model is the same as shown in Fig. 9.6. An additional link between BS and CU is considered and the channel is denoted by h_d. We have $h_d \sim \mathscr{CN}(0, d_d^{-v})$ and $\beta_d = |h_d|^2$ where d_d is the distance between BS and CU. For making an unbiased comparison between the direct and relayed transmission we have taken the time of direct transmission equal to the time αT meant for EH and information decoding at the best sensor node. So the rate achievable corresponding to the direct link is given by

$$R_d = \alpha \log_2 \left(1 + \frac{P_p |h_d|^2}{\sigma^2}\right) \tag{9.59}$$

Hence, the outage probability of the BS–CU link can be calculated as

$$P[R_d > R_{\text{pt}}] = e^{\frac{-d_{dt}^{v}}{m}} \tag{9.60}$$

The rest of the outage analysis for the primary and secondary systems will remain the same as determined in Sect. 9.3.1.

9.3.3.2 Simulation and Results

This section highlights how the power at the BS and the values of ρ, N affects the outage probability of the primary and secondary system. All the simulation parameters have been kept same as before and we have kept $\alpha = 0.5$.

Figure 9.9 demonstrates that by varying the power level at BS different QoS can be obtained for primary system which is also impacted by the number of the sensor nodes in WSN. The plot also compares the performance with the direct transmission and the various crossover points corresponding to each value of senor nodes can be seen. The crossover points are reached earlier, i.e., at a lower power value for higher number of sensor nodes. The increase in the number of sensor nodes renders to greater probability of selection of a more energy efficient node for data forwarding that results in power reduction.

In Fig. 9.10 we have plotted the outage probability against the number of sensor nodes at $P_p = 5$, 10, and 15 dBm. As expected with the increase in number of

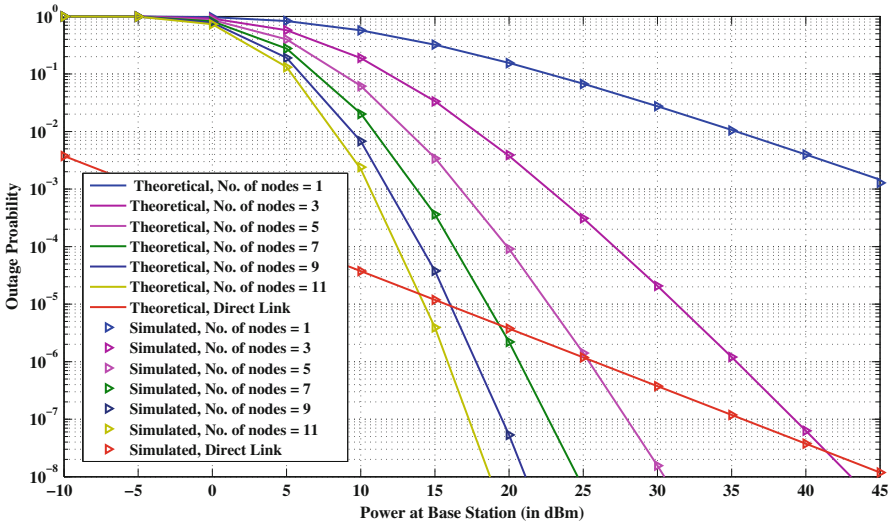

Fig. 9.9 Plot showing the primary outage probability against the power at base station (BS) for $N = 1, 3, 5, 7, 9$, and 11

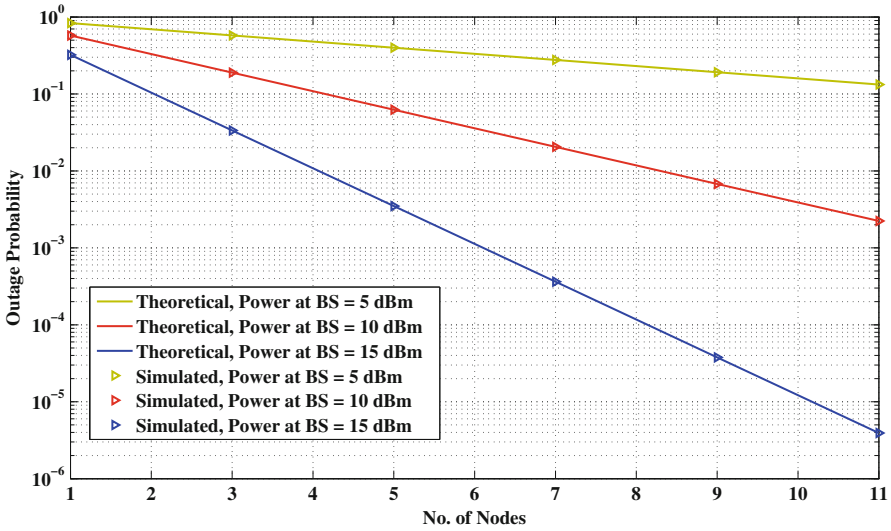

Fig. 9.10 Plot showing the primary outage probability against the number of sensor nodes in WSN

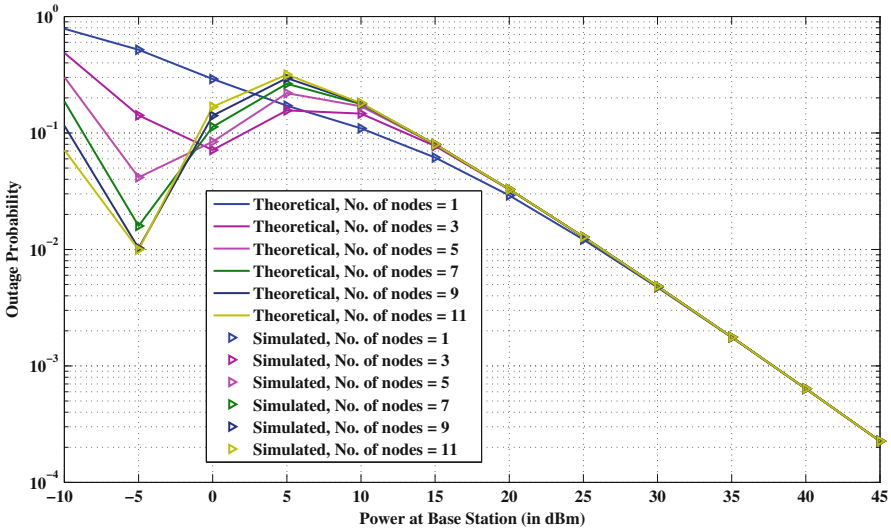

Fig. 9.11 Plot showing the secondary outage probability against the power at base station (BS) for $N = 1, 3, 5, 7, 9$, and 11

sensor nodes the outage performance is enhanced. In Fig. 9.11 we observe that the secondary system outage probability decreases, then transits to a higher outage value as power level at BS goes up and then again decreases. This is because of the fact that at lower power the sensor nodes will not harvest enough energy so the

probability of only secondary signal transmission increases. Hence, the secondary outage probability shows an improvement. But as the power level reaches a certain level the probability of composite signal transmission sees a rise which results in relatively higher secondary outage. Finally, as explained in the case of primary plot with further increase in power the secondary performance gets better. Further, it is to be noted as the power level gets higher the increase in sensor nodes has no impact on secondary outage. The explanation being that the increase will further improve primary performance hence providing no significant improvement for secondary transmission.

9.4 Summary and Future Direction

Energy harvesting and cooperative spectrum sharing techniques when employed together can solve the energy and spectrum requirement problems of wireless sensor nodes. In this chapter we proposed hybrid energy harvesting and cooperative spectrum sharing protocols which not only alleviates the energy and spectrum requirements of wireless sensor nodes but also results in significant performance improvement. We showed that for each value of α there exists an optimal value of fraction of block time over which if energy is harvested it will result in minimum primary outage.

The optimal selection of the sensor node is imperative. This has been the focus of the Sect. 9.3 of the chapter. We studied in detail the algorithm behind the selection procedure and the different factors that impact the node selection. The results showed the enhancement in primary and secondary system performance obtained.

This work can be extended to a scheme wherein the block duration of T is divided into αT for information decoding and energy harvesting at ST. $\beta(1-\alpha)T$ duration is used for primary transmission. The factor β is decided upon the EH capability of ST. If transmission power available at ST is high, less time will be taken to achieve preset value of primary's rate (or to meet the preset requirement of QoS). Hence, remaining time can be allocated for secondary transmission.

References

1. X. Lu, P. Wang, D. Niyato, D.I. Kim, Z. Han, Wireless networks with RF energy harvesting: a contemporary survey. IEEE Commun. Surv. Tutorials **17**(2), 757–789 (2015, Second quarter)
2. A. Nasir, X. Zhou, S. Durrani, R. Kennedy, Relaying protocols for wireless energy harvesting and information processing. IEEE Trans. Wirel. Commun. **12**(7), 3622–3636 (2013)
3. Y. Zeng, R. Zhang, Full-duplex wireless-powered relay with self-energy recycling. IEEE Wirel. Commun. Lett. **4**(2), 201–204 (2015)
4. A. Nasir, X. Zhou, S. Durrani, R. Kennedy, Wireless-powered relays in cooperative communications: time-switching relaying protocols and throughput analysis. IEEE Trans. Commun. **63**(5), 1607–1622 (2015)

5. S. Lee, R. Zhang, K. Huang, Opportunistic wireless energy harvesting in cognitive radio networks. IEEE Trans. Wirel. Commun. **12**(9), 4788–4799 (2013)
6. N. Jain, V. Bohara, Energy harvesting and spectrum sharing protocol for wireless sensor networks. IEEE Wirel. Commun. Lett. **4**(6), 697–700 (2015)
7. G. Zheng, Z. Ho, E.A. Jorswieck, B. Ottersten, Information and energy cooperation in cognitive radio networks. IEEE Trans. Signal Process. **62**(9), 2290–2303 (2014)
8. Y. Han, A. Pandharipande, S.H. Ting, Cooperative decode-and-forward relaying for secondary spectrum access. IEEE Trans. Wirel. Commun. **8**(10), 4945–4950 (2009)
9. V. Bohara, S.H. Ting, Y. Han, A. Pandharipande, Interference-free overlay cognitive radio network based on cooperative space time coding. in *Proceedings of the Fifth International Conference on Cognitive Radio Oriented Wireless Networks Communications (CROWNCOM)*, June 2010
10. I.S. Gradshteyn I.M. Ryzhik, *Table of Integrals, Series, and Products*, 7th edn. (Academic Press, Amsterdam, 2007)
11. C. Zhai, J. Liu, L. Zheng, Relay based spectrum sharing with secondary users powered by wireless energy harvesting. IEEE Trans. Commun. **64**, 1875–1887 (2016)
12. Y. Han, S.H. Ting, A. Pandharipande, Cooperative spectrum sharing protocol with secondary user selection. IEEE Trans. Wirel. Commun. **9**(9), 2914–2923 (2010)
13. S. Ikki, M. Ahmed, Performance analysis of adaptive decode-and-forward cooperative diversity networks with best-relay selection. IEEE Trans. Commun. **58**(1), 68–72 (2010)
14. Y.-H. Lee, K.-H. Liu, Battery-aware relay selection for energy-harvesting relays with energy storage, in *2015 IEEE 26th Annual International Symposium on Personal, Indoor, and Mobile Radio Communications (PIMRC)*, Aug (2015), pp. 1786–1791
15. M. Peer, N. Jain, V.A. Bohara, A hybrid spectrum sharing protocol for energy harvesting wireless sensor nodes, in *IEEE 17th International Workshop on Signal Processing Advances in Wireless Communications (SPAWC)*, July (2016), pp. 1–6

Chapter 10
Efficient Wireless Power Transfer Maximization Algorithms in the Vector Model

Ioannis Katsidimas, Sotiris Nikoletseas, Theofanis P. Raptis, and Christoforos Raptopoulos

10.1 Introduction

Wireless Power Transfer (WPT) has recently become a commercially viable option in various wireless systems due to the reliability of continuous power supply and the convenience provided by the fact that no static (wired) network connections are needed between the devices. The efficiency of the various technological alternatives is increasing every year. Current fast-charging protocols achieve up to 84% efficiency for WPT up to distances of 15 m [22], while at the same time keeping thermal dissipation significantly low [23]. A WPT enabled system consists of several wireless transmitter and receiver devices. A *wireless transmitter (charger)* is a device that has a dedicated power source with significant power supply and can transfer power wirelessly to receivers. A *receiver (node)* is a device that is powered by harvesting the radio frequency energy from the chargers. A receiver is usually an electronic device that is needed to perform a specific task in the wireless system, for example a sensor mote in a wireless sensor network. Systems of wireless devices have to operate under increasing demands of power in order to sustain various computational and communication tasks. For this reason, the efficient and distributed cooperation of the transmitters and receivers towards achieving an effective power allocation in the system is a crucial task.

I. Katsidimas (✉) • S. Nikoletseas • C. Raptopoulos
Department of Computer Engineering and Informatics, University of Patras, Computer Technology Institute and Press Diophantus, Patra, Greece
e-mail: ikatsidima@ceid.upatras.gr; nikole@cti.gr; raptopox@ceid.upatras.gr

T.P. Raptis
Institute for Informatics and Telematics, National Research Council, Pisa, Italy
e-mail: theofanis.raptis@iit.cnr.it

D.N.K. Jayakody et al. (eds.), *Wireless Information and Power Transfer: A New Paradigm for Green Communications*, DOI 10.1007/978-3-319-56669-6_10

Our Contribution While considerable research efforts have been invested into power management in wireless systems, most of the models studied in the literature neglect key features of electromagnetic fields. As a result, such models are unable to explain various phenomena occurring in real applications (e.g., cancellation and superadditive charging effects; see Sect. 10.3), yielding some algorithmic solutions impractical. In view of the above, our contribution in this chapter is the following:

- We algorithmically study a more realistic model for WPT at far-field region in wireless systems, which was nicely initiated in [17]. In particular, this is *a "vector" model* that takes into account *the superposition* of electromagnetic fields created by independent wireless transmitters, as well as fundamental properties of the superposition of waves from physics. To the best of our knowledge, this is the first algorithmic study of a vector model for WPT.
- We define *two new computational problems* for the efficient utilization of power resources in a wireless system consisting of a family of transmitters $\mathscr{C}$ and a family of receivers $\mathscr{R}$. In particular, we first consider the problem `MAX-POWER` of finding a configuration (set of operation levels) for transmitters that *maximizes the total power* received by $\mathscr{R}$. Second, we consider the problem `MAX-`k`MIN-GUARANTEE` of finding a configuration that maximizes *the minimum cumulative power*[1] *among all the sets of k receivers*.
- We formulate `MAX-POWER` as a *quadratic program* and we prove that we can find an optimal solution efficiently by presenting *a family of distributed algorithms* using different levels of knowledge of the system. We prove that these algorithms run in pseudopolynomial time, but we experimentally show that they are quite faster in practice.
- We design and experimentally evaluate *three efficient heuristics* for `MAX-`k`MIN-GUARANTEE` that provide good approximations of the optimal solution. The first heuristic is a generalization of our algorithmic solution to `MAX-POWER`, while the second samples a few representative k-sets of receivers and then solves the problem considering only those sets. Finally, our third heuristic is a hybrid of the previous two ideas and we show that it outperforms both in typical deployments of transmitters and receivers on the plane.

A preliminary version of this work [8] was appeared in the proceedings of the 18th International Conference on Distributed Computing and Networking (ICDCN 2017).

10.2 Related Work

WPT methods in large-scale networked systems have attracted much attention from researchers worldwide. The reader can find comprehensive reviews of the relevant literature in [11, 12, 26], and [10]. Also, the book [20] is the first systematic

[1]The cumulative power for a set of nodes is the aggregate received power by the nodes of a set from all the operational chargers.

exposition on the domain of wireless energy transfer in ad hoc communication networks. Several works study applications in sensor networks [1, 6, 25] and wireless distributed systems [13, 19], UAVs [5, 14]. Different to all those works, in this chapter we investigate a static setting, where transmitter and receiver locations are predefined and stationary, and there are no mobile elements in the system.

There have been some works on closely related themes to this chapter, which investigate different aspects of the WPT process. In [27], given a set of candidate locations for placing chargers, the authors provide a charger placement and a corresponding power allocation to maximize the charging quality, subject to a power budget. In a recent paper [18], a subset of the authors of this chapter study the Low Radiation Efficient Charging Problem, in which we optimize the amount of useful energy transferred from chargers to nodes (under constraints on the maximum level of imposed electromagnetic radiation). In a similar setting, the authors in [3] consider the Safe Charging with Adjustable Power (SCAPE) problem for adjusting the power of chargers to maximize the charging utility of devices, while assuring that electromagnetic intensity at any location in the field does not exceed a given threshold. It is worth noting that, even though all the above works nicely demonstrate the gains of carefully distributing the power in a wireless setting, they use one-dimensional models, which fall short of capturing various intricate aspects of WPT.

Wireless transfer of energy through directed radio frequency waves has the potential to realize perennially operating sensor nodes by replenishing the energy contained in the limited on-board battery. However, the high power energy transfer from energy transmitters interferes with data communication, limiting the coexistence of these functions. In [15], the authors provide an experimental study to quantify the rate of charging, packet loss due to interference, and suitable ranges for charging and data communication of the energy transmitters. They also explore how the placement and relative distances of multiple energy transmitters affect the charging process, demonstrating constructive and destructive energy aggregation at the sensor nodes. Finally, the authors investigate the impact of the separation in frequency between data and energy transmissions, as well as among multiple concurrent energy transmissions. Their results aim at providing insights on radio frequency-based energy harvesting wireless sensor networks for enhanced protocol design and network planning.

Furthermore, in [17], they formulate the location-dependent power harvesting rates in generalized 2D and 3D placement of multiple (RF) energy transmitters for recharging the nodes of a wireless sensor network. In particular, they study the distributions of total available and harvested power over the entire network. They then provide closed matrix forms of harvestable power at any given point in space due to the action of concurrent energy transfer from multiple energy transmitters, explicitly considering constructive and destructive interference of the transmitted energy signals. The authors also analyze the performance of energy transfer in the network through power outage probability, interference, and harvested voltage as a function of the wireless energy received from the energy transmitters. The results reveal that the network wide received power and interference power from concurrent

energy transfers exhibit Log-Normal distributions, and the harvested voltage over the network follows a Rayleigh distribution.

In [24], the authors investigate the impact of wireless charging technology on sensor network deployments and routing arrangements, formalize the deployment and routing problem, prove it as $\mathscr{NP}$-complete, develop heuristic algorithms to solve the problem, and evaluate the performance of the solutions through extensive simulations.

In [4], the authors introduce a scheme for improving the transmission power of nodes to bound end to end delay. They provide an algorithm for finding the minimal sleep latency from a node to a sink by increasing the minimal number of nodes whose transmission power improved. For bounding the end to end delay from the source node to the sink, the authors propose an end to end delay maintenance solution and demonstrate its efficiency in provide end to end delay guarantees in rechargeable wireless sensor networks.

Finally, in [16, 21], through an experimental study, the authors first demonstrate how the placement, the chosen frequency, and number of the RF energy transmitters affect the sensor charging time. These studies are then used to design a MAC protocol called RF-MAC that optimizes energy delivery to desirous sensor nodes on request.

10.3 The Charging Model

In a recent paper [17], the authors considered a model for the superposition of electromagnetic fields created by independent wireless energy sources, which takes into account fundamental properties of the superposition of waves from physics. The model of [17] goes beyond (in fact, it is a generalization of) the one-dimensional abstraction suggested by Friis' formula[2] for the power received by one antenna under idealized conditions given another antenna some distance away. In particular, the *electric field* created by an energy transmitter (charger) C, operating at full capacity, at a receiver R at distance $d = \text{dist}(C, R)$ is a two-dimensional vector given by

$$\mathbf{E}(C,R) \stackrel{\text{def}}{=} \beta \cdot \frac{1}{d} \cdot e^{-j\frac{2\pi}{\lambda}d} = \beta \cdot \frac{1}{d} \cdot \begin{bmatrix} \cos\left(\frac{2\pi}{\lambda}d\right) \\ \sin\left(\frac{2\pi}{\lambda}d\right) \end{bmatrix}, \tag{10.1}$$

[2]Given two antennas, the ratio of power available at the input of the receiving antenna, P_r, to output power to the transmitting antenna, P_t, is given by $\frac{P_r}{P_t} = G_t G_r (\frac{\lambda}{4\pi R})^2$ where G_t and G_r are the antenna gains (with respect to an isotropic radiator) of the transmitting and receiving antennas, respectively, λ is the wavelength, and R is the distance between the antennas.

where λ depends on the frequency at which the transmitter operates, and β is a constant that depends on the hardware of the transmitter and the environment.[3]

The main point of the charging model of [17], which also sets it apart from other (less realistic, but more tractable) models in the wireless charging literature, is that the total electric field created by a family of energy transmitters $\mathscr{C}$ at a receiver R is the *superposition (vector-sum)* of their individual electric fields, that is,

$$\mathbf{E}(\mathscr{C}, R) \stackrel{\text{def}}{=} \sum_{C \in \mathscr{C}} \mathbf{E}(C, R). \tag{10.2}$$

Furthermore, the total available *power* at the receiver R is given by

$$P(\mathscr{C}, R) = \gamma \cdot \|\mathbf{E}(\mathscr{C}, R)\|^2, \tag{10.3}$$

where $\|\cdot\|$ denotes the length (2-norm) of the vector. The constant γ depends on the hardware of the transmitter, the hardware of the receiver, and the RF-to-DC conversion efficiency.

It is worth noting that the above model arises naturally from fundamental properties of the superposition of energy fields and has been shown to be more realistic than other one-dimensional models that have been used in the past and can capture *superadditive* and *cancellation* effects [7, 9, 15]. To fix ideas and to demystify the above definitions, we present the following fictitious example: Assume that there are two transmitters C_1 and C_2 placed at points $(0, 0)$ and $(2, 0)$ in the two-dimensional plane. First, consider a receiver R placed at $(1, 0)$. Assume also, for the sake of clarity, that all constants in the above model are set to 1, i.e., $\lambda = \beta = \gamma = 1$. When only one of the two transmitters is operational, the power received by R is $P(C_1, R) = P(C_2, R) = \|\mathbf{E}(C_1, R)\|^2 = \|\mathbf{E}(C_2, R)\|^2 = \left(\frac{1}{\text{dist}(C_1,R)}\right)^2 = 1$. On the other hand, if both transmitters are operational, the power received by R is given by Eq. (10.2), that is,

$$P(\{C_1, C_2\}, R) = \|\mathbf{E}(C_1, R) + \mathbf{E}(C_2, R)\|^2.$$

Furthermore, it is not hard to see that, since R is equidistant from either C_1 or C_2, the vectors $\mathbf{E}(C_1, R)$ and $\mathbf{E}(C_2, R)$ point to the same direction. Therefore, $P(\{C_1, C_2\}, R) = 4P(C_1, R) = 2(P(C_1, R) + P(C_2, R)) = 4$. Notice then that the power received by R when both transmitters are operational is larger than the sum of the powers it receives when only one of the transmitters is operational; this is the so-called superadditive effect and is visible in local maxima in the curve shown in Fig. 10.1b.

[3] In fact, the exact formula used in [17] for the electric field is $\mathbf{E}(C, R) \stackrel{\text{def}}{=} \sqrt{\frac{Z_0 G_C P_C}{4\pi d^2}} \cdot e^{-j\frac{2\pi}{\lambda}d}$, where Z_0 is a physical constant indicating the wave-impedance of a plane wave in free space, G_C is the gain, and P_C is the output power of the transmitter. In this chapter, without loss of generality of our algorithmic solutions, we assume that all wireless transmitters and receivers are identical, thus the aforementioned parameters are the same for each charger.

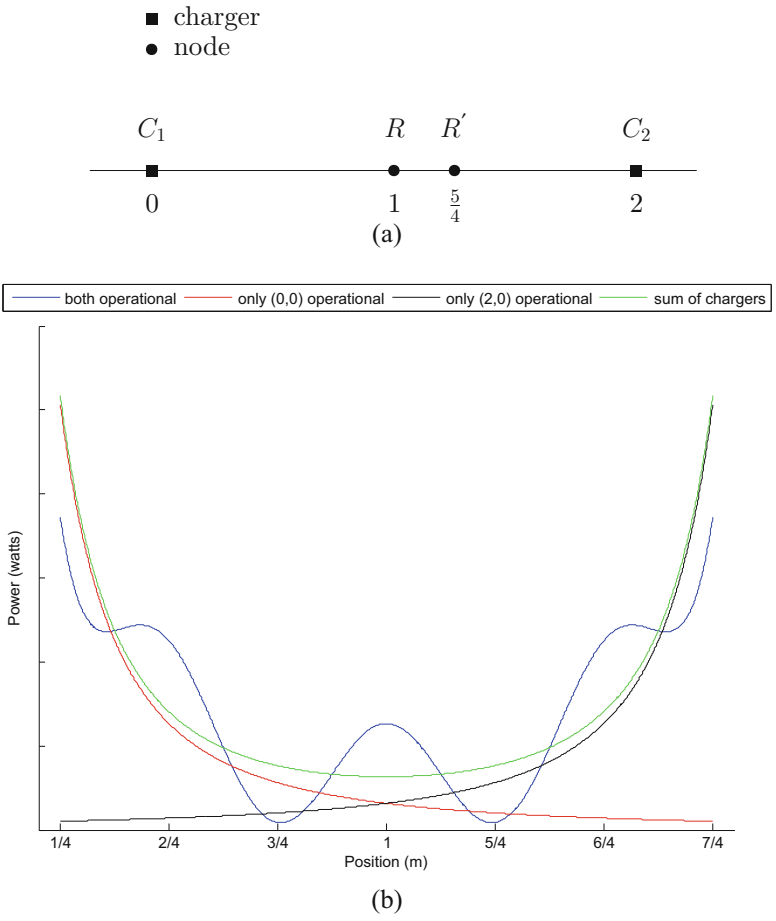

Fig. 10.1 Example showing the superadditive and cancelation effects. (**a**) Chargers' and nodes' placement on a straight line at points $(0, 0)$, $(0, 2)$, and $(0, 1)$, $(0, \frac{5}{4})$, respectively. (**b**) The power distribution between the two chargers. *Different curves* represent different operation levels of the chargers

Second, consider a receiver R' placed at $\left(\frac{5}{4}, 0\right)$. Then by Eq. (10.1), $\mathbf{E}(C_1, R') = \frac{4}{5} \cdot \begin{bmatrix} 0 \\ 1 \end{bmatrix}$, and also $\mathbf{E}(C_2, R') = \frac{4}{3} \cdot \begin{bmatrix} 0 \\ -1 \end{bmatrix}$. By Eq. (10.2), the power received by R' when both transmitters are operational is $P(\{C_1, C_2\}, R') = \left(\frac{8}{15}\right)^2 \approx 0.28$. Notice then that the power received by R' when both transmitters are operational is much less than $\min\{P(C_1, R'), P(C_2, R')\} = \left(\frac{4}{5}\right)^2 \approx 0.64$; this is the so-called cancellation effect and is visible in local minima in the curve shown in Fig. 10.1b.

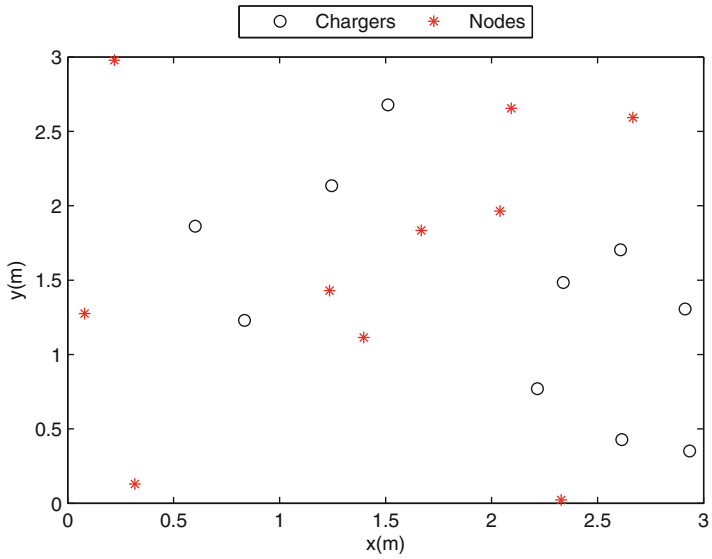

Fig. 10.2 Chargers' and nodes' deployment for the simulation

In view of our discussion in this chapter, it is worth noting that, even in the above toy example, it is nontrivial to provide a closed formula for the point in the line between the two chargers where the received power is maximized.

We also conducted a simple simulation in a 3 m $\times$ 3 m plane with 10 chargers and 10 nodes, randomly deployed in the field (Fig. 10.2). The parameters of this simulation are the same with those mentioned in Sect. 10.7. In this simulation, we present the results of two different configurations. As the scalar model suggests, we turn on all the chargers to get the maximum cumulative received power which is valued to 0.217 W (the evaluation is done with respect to the vector model). On the other hand, a better configuration with respect to the vector model turns on all the chargers except of the two at position $(2.2165, 0.7708)$ and $(2.9343, 0.3512)$. That configuration returns 0.230 W of cumulative received power in the network. Therefore, the claim of the toy example holds also for a more general case.

Finally, to further verify the vector model, we present the experiment, described in the technical report of [9]. In this experiment, the distance between the node and charger 1 is fixed to 0.3 m while the distance between the node and charger 2 varies from 0.4 m to 1.1 m in increments of 0.1 m. The results are presented in Table 10.1, where the second and third rows record the received power when either charger 1 or charger 2 is turned on. The fourth row records the actual power measured when both chargers are turned on. The next two rows give the results for each of the two models we compare. Observe that the vector model approaches the actual measurements of row three better than the scalar model. This can be verified from the last two rows, which present the relative error of each model.

Table 10.1 Charging power of two chargers

Harvesting power (mW)/Distance to charger 2 (m)	0.4	0.5	0.6	0.7	0.8	0.9	1.0	1.1
Charger 1	6.48	6.48	6.48	6.48	6.48	6.48	6.48	6.48
Charger 2	3.21	1.92	1.96	0.09	0.71	0.33	0.35	0.06
Charger 1 and charger 2	3.57	2.05	3.47	7.78	2.11	1.32	9.04	6.04
Scalar model (Friis)	9.69	8.40	8.44	6.57	7.19	6.81	6.83	6.54
Vector model	6.21	5.11	8.19	6.58	5.77	6.62	6.74	6.42
Relative error of scalar model (Friis)	6.12	6.35	4.97	−1.21	5.08	5.49	−2.21	0.14
Relative error of vector model	2.64	3.06	4.72	−1.2	3.66	5.3	−2.3	0.02

10.3.1 A Basic Assumption

A necessary condition that is required in Friis' formula, and by extension in the above model, is that the wireless transmitter and receiver need to be at distance at least λ (not in the near-field region). In fact, for transmitters to receivers distances less than λ, more complex laws apply but we do not consider them here as they are beyond the algorithmic focus of the paper. A similar constraint also holds for the power received by receivers that are very close to each other. In particular, if receivers R, R' are closer than $\frac{\lambda}{2\pi}$ apart, then the power received by each receiver no longer follows Friis' law. This was to be expected, since otherwise we could have wireless transmitters of bounded capabilities that could theoretically provide infinite power (e.g., by placing receivers arbitrarily close to each other and to the transmitter).

In this chapter, we consider algorithmic problems related to power guarantees with respect to a fixed deployment of a family $\mathscr{C}$ of wireless transmitters and a family $\mathscr{R}$ of receivers. To avoid confusion, we will assume that any placement of chargers and receivers satisfies the above *placement constraints*. In particular: (a) For each charger $C \in \mathscr{C}$ and receiver $R \in \mathscr{R}$, we have $\text{dist}(C, R) \geq \lambda$ and (b) for any pair of receivers $R, R' \in \mathscr{R}$, we have $\text{dist}(R, R') \geq \frac{\lambda}{2\pi}$.

We finally note that, since $\frac{\lambda}{2\pi}$ is usually smaller than a few centimeters, in practical situations, the above placement constraints will not be restrictive, as the nontrivial volume of any transmitting or receiving device guarantees that transmitters and chargers are far enough from each other.

10.4 Problem Definition

Consider a system consisting of a family $\mathscr{C}$ of identical wireless chargers and a family $\mathscr{R}$ of identical wireless receivers (nodes). For each charger $C \in \mathscr{C}$, we denote by $\mathbf{x}_C \in [0, 1]$ a variable that determines the level of operation of C. We assume that the chargers are able to operate at a level of operation between 0 and 100%. x equal

to 1 means that C is fully operational (i.e., operates at 100% capacity), while x equal to 0 means that C is nonoperational (operates at 0%). Clearly, we must have $x \in [0, 1]$. In particular, generalizing Eq. (10.1), the electric field vector created by C at the location of a receiver R, when the former operates at level $\mathbf{x}_C$ is given by $\mathbf{x}_C \cdot \mathbf{E}(C, R) = \mathbf{x}_C \cdot \beta \cdot \frac{1}{\text{dist}(C,R)} \cdot e^{-j\frac{2\pi}{\lambda}\text{dist}(C,R)}$.

We will refer to the vector $\mathbf{x} \in [0, 1]^{\mathscr{T}}$ as the *configuration* of the chargers in the system. Slightly abusing notation, we will denote by $\mathscr{C}(\mathbf{x})$ a family of chargers that operate according to configuration $\mathbf{x}$.

We initially consider the following problem:

Definition 1 (MAX-POWER). Given a family of chargers $\mathscr{C}$ and family of receivers $\mathscr{R}$ that satisfy the placement constraints of Sect. 10.3.1, find a configuration for the chargers that maximizes the total power to $\mathscr{R}$. That is, find $\mathbf{x}^*$ such that

$$\mathbf{x}^* \in \arg \max_{\mathbf{x} \in [0,1]^{\mathscr{C}}} P(\mathscr{C}(\mathbf{x}), \mathscr{R}), \tag{10.4}$$

where $P(\mathscr{C}(\mathbf{x}), \mathscr{R}) = \sum_{R \in \mathscr{R}} P(\mathscr{C}(\mathbf{x}), R)$.

We will denote by $\binom{\mathscr{R}}{k}$ the family of all subsets of $\mathscr{R}$ containing k nodes. In this chapter, we also study the following generalization of MAX-POWER, which finds a configuration that provides a minimum charging guarantee among all k-sets of nodes:

Definition 2 (MAX-kMIN-GUARANTEE). Given a family of chargers $\mathscr{C}$ and a family of receivers $\mathscr{R}$ that satisfy the placement constraints of Sect. 10.3.1, find a configuration for the chargers that maximizes the minimum cumulative power among all subsets of $\mathscr{R}$ of size k. That is, find $\mathbf{x}^*$ such that

$$\mathbf{x}^* \in \arg \max_{\mathbf{x} \in [0,1]^{\mathscr{C}}} \min_{A \in \binom{\mathscr{R}}{k}} P(\mathscr{C}(\mathbf{x}), A), \tag{10.5}$$

where $P(\mathscr{C}(\mathbf{x}), A) = \sum_{R \in A} P(\mathscr{C}(\mathbf{x}), R)$.

10.5 Maximum Total Power

In this section, we present an efficient algorithm for MAX-POWER. For simplicity, consider a family of wireless chargers $\mathscr{C} = \{C_1, \ldots, C_m\}$, where $m = |\mathscr{C}|$, and a family of receivers $\mathscr{R} = \{R_1, \ldots, R_n\}$, where $n = |\mathscr{R}|$. Let also $\mathbf{x} \in [0, 1]^m$ be the configuration of the chargers, where $\mathbf{x}_j$ is the level of operation of charger $C_j, j \in [m]$.

We first show that the MAX-POWER problem can be expressed as a quadratic program. To this end, for each $R \in \mathscr{R}$, define $\mathbf{Q}^{(R)}$ be a $2 \times m$ matrix whose j-th column is the two-dimensional vector of the electric field created from C_j at R, i.e., $\mathbf{Q}^{(R)}_{:,j} = \sqrt{\gamma} \cdot \mathbf{E}(C_j, R)$, for each $j \in [m]$. Notice now that we can write the power harvested by the receiver R as follows:

$$
\begin{aligned}
P(\mathscr{C}(\mathbf{x}), R) &= \gamma \|\mathbf{E}(\mathscr{C}(\mathbf{x}), R)\|^2 \\
&= \gamma \left\| \sum_{C \in \mathscr{C}} \mathbf{x}_C \mathbf{E}(C, R) \right\|^2 \\
&= \left(\sum_{C \in \mathscr{C}} \mathbf{x}_C \sqrt{\gamma} \mathbf{E}(C, R) \right)^T \left(\sum_{C \in \mathscr{C}} \mathbf{x}_C \sqrt{\gamma} \mathbf{E}(C, R) \right) \\
&= (\mathbf{Q}^{(R)} \mathbf{x})^T \mathbf{Q}^{(R)} \mathbf{x},
\end{aligned}
$$

where $(\cdot)^T$ denotes the transpose of a matrix or vector. Therefore, setting $\mathbf{H} \stackrel{\text{def}}{=} \sum_{R \in \mathscr{R}} \left(\mathbf{Q}^{(R)}\right)^T \mathbf{Q}^{(R)}$, the solution to `MAX-POWER` is given by

$$
\mathbf{x}^* \in \arg \max_{\mathbf{x} \in [0,1]^m} \mathbf{x}^T \mathbf{H} \mathbf{x}. \tag{10.6}
$$

It is worth noting that, in general, the maximization of a quadratic form is a non-convex quadratic program (even when $\mathbf{H}$ is positive semi-definite, which is the case here), hence cannot be solved in polynomial time. Nevertheless, by taking into account several properties and the special form of our problem, we are able to provide an efficient algorithm for `MAX-POWER`.

We first need the following elementary lemma that considerably reduces the size of the search space.

Lemma 1. *If $\mathbf{x}^*$ is an optimal solution to `MAX-POWER`, then $\mathbf{x}^* \in \{0,1\}^m$. In particular, there exists an optimal solution to `MAX-POWER` in which each charger either operates at full capacity or not at all.*

Proof. Let $\mathbf{y} \in [0,1]^m$ be such that
(a) $\mathbf{y} \in \arg\max_{\mathbf{x} \in [0,1]^m} \mathbf{x}^T \mathbf{H} \mathbf{x}$ (i.e., it is an optimal solution to `MAX-POWER`) and (b) $\mathbf{y}$ has the minimum number of elements that are neither 0 nor 1; let also k be the number of such elements, i.e., $k \stackrel{\text{def}}{=} |\{i : \mathbf{y}_i \notin \{0,1\}\}|$. If $k = 0$, then there is nothing to prove, so we will assume for the sake of contradiction that $k > 0$. Let j be an index such that $\mathbf{y}_j \notin \{0,1\}$ and define vectors $\mathbf{y}^{(0)}$ and $\mathbf{y}^{(1)}$ that are equal to $\mathbf{y}$ everywhere, except on position j, where $\mathbf{y}_j^{(0)} = 0$ and $\mathbf{y}_j^{(1)} = 1$. Notice now that, by the optimality and minimality assumptions on $\mathbf{y}$, we have that $\mathbf{y}^T \mathbf{H} \mathbf{y} > \left(\mathbf{y}^{(0)}\right)^T \mathbf{H} \mathbf{y}^{(0)}$ and $\mathbf{y}^T \mathbf{H} \mathbf{y} > \left(\mathbf{y}^{(1)}\right)^T \mathbf{H} \mathbf{y}^{(1)}$.

On the other hand, for $z \in (0,1)$, define the vector $\mathbf{y}^{(z)} \stackrel{\text{def}}{=} (1-z)\mathbf{y}^{(0)} + z\mathbf{y}^{(1)}$. In particular, $\mathbf{y}^{(z)}$ is the m-dimensional vector that is equal to $\mathbf{y}$ everywhere, except on position j, where $\mathbf{y}_j^{(z)} = z$. Consider now the function $f(z) = \left(\mathbf{y}^{(z)}\right)^T \mathbf{H} \mathbf{y}^{(z)}$. Notice that $f(z)$ is a single variable polynomial of degree 2, and it is a simple

matter of calculus to show that its second derivative satisfies $\frac{d^2f}{dz^2} = \mathbf{H}_{j,j} = \sum_{R\in\mathscr{R}} \gamma \|\mathbf{E}(C_j,R)\|^2 = P(C_j,\mathscr{R})$, which is strictly positive. But this implies that $f(z) < \max\{f(0),f(1)\}$, for all $z \in (0,1)$. However, this is a contradiction, since we have already established that, by assumption, $f(\mathbf{y}_j) = \mathbf{y}^T\mathbf{H}\mathbf{y} > \max\{\left(\mathbf{y}^{(0)}\right)^T \mathbf{H}\mathbf{y}^{(0)}, \left(\mathbf{y}^{(1)}\right)^T \mathbf{H}\mathbf{y}^{(1)}\} = \max\{f(0),f(1)\}$. We conclude that in any optimal solution to MAX-POWER each charger either operates at full capacity or not at all. □

We now prove a useful property of global maxima of the objective function $\mathbf{x}^T\mathbf{H}\mathbf{x}$ in $[0,1]^m$. The proof uses properties of positive semi-definite (PSD) matrices (see [2] for an introduction to PSD matrices and their properties). We note here that Lemma 1 and Theorem 1 below imply that any local maxima of the objective function $P(\mathscr{C}(\mathbf{x}),R) = (\mathbf{Q}\mathbf{x})^T\mathbf{Q}\mathbf{x}$ are also global maxima that belong to $\{0,1\}^m$. In particular, this means that the gradient descent method can be used to find a global maximum (i.e., an optimal solution to MAX-POWER). Nevertheless, in our experimental evaluation, we used a pseudopolynomial distributed algorithm for computing the *exact* optimum configuration for MAX-POWER, which is quite fast in practice. We present this algorithm later in this section.

Theorem 1. *A configuration* $\mathbf{x}^* \in \{0,1\}^m$ *is an optimal solution to* MAX-POWER *if and only if* $P(\mathscr{C}(\mathbf{x}^*),\mathscr{R}) \geq P(\mathscr{C}(\mathbf{y}),\mathscr{R})$, *for each* $\mathbf{y}$ *that comes from* $\mathbf{x}$ *by setting exactly one of its coordinates to either 0 or 1.*

Proof. For a configuration $\mathbf{x} \in \{0,1\}^m$ and for all $j \in [m]$ and $a \in \{0,1\}$, define $\mathbf{x}^{(j,a)} \stackrel{\text{def}}{=} \mathbf{x} + (a - \mathbf{x}_j)\mathbf{e}_j$, where $\mathbf{e}_j$ is the j-th vector in the standard basis of $\mathbf{R}^m$. Notice that $\mathbf{x}^{(j,1)}$ (respectively, $\mathbf{x}^{(j,0)}$) is the configuration that is identical to $\mathbf{x}$, with the only difference that charger j operates at full capacity (respectively, does not operate).

Clearly, if $\mathbf{x}^*$ is an optimal solution, then $P(\mathscr{C}(\mathbf{x}^*),\mathscr{R}) \geq P(\mathscr{C}(\mathbf{x}^{*(j,a)}),\mathscr{R})$, for any $j \in [m]$ and $a \in \{0,1\}$. Therefore, it remains to prove the "only if" part of the Theorem. To this end, let $\mathbf{x}^*$ be such that $P(\mathscr{C}(\mathbf{x}^*),\mathscr{R}) \geq P(\mathscr{C}(\mathbf{x}^{*(j,a)}),\mathscr{R})$, for any $j \in [m]$ and $a \in \{0,1\}$, and assume for the sake of contradiction that there is a configuration $\mathbf{z}$ such that $P(\mathscr{C}(\mathbf{x}^*),\mathscr{R}) < P(\mathscr{C}(\mathbf{z}),\mathscr{R})$.

By Lemma 1, we only need to consider configurations in $\{0,1\}^m$. Therefore, assume that $\mathbf{x}^* \in \{0,1\}^m$ and $\mathbf{z} = \mathbf{x}^* + \sum_{j=1}^m a_j\mathbf{e}_j = \mathbf{x}^* + \mathbf{a}$, for some $\mathbf{a} \in \{-1,0,1\}^m$, such that $\mathbf{z}^T\mathbf{H}\mathbf{z} = P(\mathscr{C}(\mathbf{z}),\mathscr{R}) > P(\mathscr{C}(\mathbf{x}),\mathscr{R}) = \mathbf{x}^{*T}\mathbf{H}\mathbf{x}^*$.

Note that, since $\mathbf{H}$ is symmetric, for any $j \in [m]$ we have $\mathbf{e}_j^T\mathbf{H}\mathbf{x}^* = \mathbf{x}^{*T}\mathbf{H}\mathbf{e}_j$, and so

$$(\mathbf{x}^* + a_j\mathbf{e}_j)^T\mathbf{H}(\mathbf{x}^* + a_j\mathbf{e}_j) = \mathbf{x}^{*T}\mathbf{H}\mathbf{x}^* + 2a_j\mathbf{e}_j^T\mathbf{H}\mathbf{x}^* + a_j^2\mathbf{H}_{j,j}. \tag{10.7}$$

Rearranging, and using the assumption that $P(\mathscr{C}(\mathbf{x}^*),\mathscr{R}) \geq P(\mathscr{C}(\mathbf{x}^* + a_j\mathbf{e}_j),\mathscr{R})$, we get

$$2a_j\mathbf{e}_j^T\mathbf{H}\mathbf{x}^* + a_j^2\mathbf{H}_{j,j} \leq 0, \tag{10.8}$$

for any $j \in [m]$. By a similar computation, we have

$$\begin{aligned}\mathbf{z}^T\mathbf{H}\mathbf{z} &= \mathbf{x}^{*T}\mathbf{H}\mathbf{x}^* + 2\mathbf{a}^T\mathbf{H}\mathbf{x}^* + \mathbf{a}^T\mathbf{H}\mathbf{a} \\ &= \mathbf{x}^{*T}\mathbf{H}\mathbf{x}^* + \sum_{j=1}^{m} 2a_j\mathbf{e}_j^T\mathbf{H}\mathbf{x} + \mathbf{a}^T\mathbf{H}\mathbf{a}. \end{aligned} \tag{10.9}$$

Summing (10.8) over all $j \in [m]$ and substituting in (10.9), we get

$$\mathbf{z}^T\mathbf{H}\mathbf{z} - \mathbf{x}^{*T}\mathbf{H}\mathbf{x}^* \leq -\sum_{j=1}^{m} a_j^2\mathbf{H}_{j,j} + \mathbf{a}^T\mathbf{H}\mathbf{a}. \tag{10.10}$$

It is now a simple matter of algebra to show that the right-hand side of the above inequality is nonpositive. Indeed, let $\mathbf{H}'$ be the $m' \times m'$ principal submatrix of $\mathbf{H}$ corresponding to rows (and columns) j for which $a_j \neq 0$ (in particular, m' is the number of nonzero elements of $\mathbf{a}$). Clearly, since $\mathbf{H}$ is PSD, then so is $\mathbf{H}'$. Let $\lambda'_1 \geq \cdots \geq \lambda'_{m'} \geq 0$ and $\mathbf{v}'_1, \ldots, \mathbf{v}'_{m'}$ be the eigenvalues and eigenvectors of $\mathbf{H}'$. Now notice that $\sum_{j=1}^{m} a_j^2\mathbf{H}_{j,j} = \sum_{j=1}^{m'} a_j^2\mathbf{H}'_{j,j} = \mathrm{tr}(\mathbf{H}') = \sum_{j=1}^{m'} \lambda'_j$, where $\mathrm{tr}(\mathbf{H}')$ is the trace of $\mathbf{H}'$ and we have used the fact that the trace of a matrix is equal to the sum of its eigenvalues. Finally, since $\mathbf{a}$ is an orthonormal rotation of the vector $\sum_{j=1}^{m'} \mathbf{v}'_j$, we have $\mathbf{a}^T\mathbf{H}\mathbf{a} = \sum_{j=1}^{m'} \lambda'_j$.

In view of the above, by inequality (10.10), we get that $\mathbf{z}^T\mathbf{H}\mathbf{z} - \mathbf{x}^{*T}\mathbf{H}\mathbf{x}^* \leq 0$, which is a contradiction. Therefore, we conclude that if $P(\mathscr{C}(\mathbf{x}^*), \mathscr{R}) \geq P(\mathscr{C}(\mathbf{x}^{*(j,a)}), \mathscr{R})$, for any $j \in [m]$ and $a \in \{0, 1\}$, then $\mathbf{x}^*$ is an optimal solution. □

Lemma 1 and Theorem 1 suggest that the following distributed algorithm (which we call `IterativeMaxPower`) can be used to find an *exact* optimum configuration for `MAX-POWER`: Initially, we begin from an arbitrary configuration in $\{0, 1\}^m$. In each subsequent step, we parse the set of chargers in order to find a charger $C \in \mathscr{C}$ such that the total power received by R can be increased by flipping the operation level of C (e.g., if C operates at full capacity, it checks whether the received power is increased if it is not operational). The algorithm terminates if there is no such charger C.

For a given placement of a family $\mathscr{C}$ of chargers and a family $\mathscr{R}$ of receivers, define $\delta(\mathscr{C}, \mathscr{R}) \stackrel{\text{def}}{=} \min\{|P(\mathscr{C}(\mathbf{x}), \mathscr{R}) - P(\mathscr{C}(\mathbf{x}^{j,a}), \mathscr{R})| : \mathbf{x} \in \{0, 1\}^m, a \in \{0, 1\}, j \in [m]\}$. In particular, $\delta(\mathscr{C}, \mathscr{R})$ is the minimal increment in the total received power that can be incurred by a single iteration of `IterativeMaxPower`. In addition, notice that every such iteration takes $O(m^3)$ time. Finally, given that the chargers and receivers satisfy the placement constraints of Sect. 10.3.1, a crude upper bound for the maximum total power is $nm^2\gamma\beta^2\frac{4\pi^2}{\lambda^2} = O(nm^2)$. Therefore, we have the following:

Theorem 2. *Given a family $\mathscr{C}$ of m chargers and a family $\mathscr{R}$ of n receivers that satisfy the placement constraints of Sect. 10.3.1, Algorithm* `IterativeMaxPower` *finds an optimal solution of* `MAX-POWER` *in $O\left(\frac{1}{\delta(\mathscr{C},\mathscr{R})}nm^5\right)$.*

Algorithm 1: `IterativeMaxPower`

Input : $dist, \mathscr{R}, \mathscr{C}, communication\_range$
Output: $\mathbf{x}$

begin
  $\mathbf{x} \in \{0,1\}^m$ is a random initial charger configuration;
  while $\exists C_j \in \mathscr{C} : P(\mathscr{C}(\mathbf{x}), \mathscr{R}) < P(\mathscr{C}(\mathbf{x}^{(j,a)}), \mathscr{R}),\ a \in \{0,1\}$ **do**
    choose randomly a charger $C_j \in \mathscr{C}$;
    $\mathscr{R}_{C_j} = 0$;
    foreach $R \in \mathscr{R}$ **do**
      if $dist(C_j, R) \leq communication range$ **then**
        $\mathscr{R}_{C_j} = \mathscr{R}_{C_j} \cup R$
        //at this point C_j communicates with R and receives $\mathbf{E}(\mathscr{C}(\mathbf{x}), R)$;
      end if
    end foreach
    $\mathbf{x}_{C_j} = \arg\max_{a \in \{0,1\}} P(\mathscr{C}(\mathbf{x}^{(j,a)}), \mathscr{R}_{C_j})$;
  end while
  return $\mathbf{x}$;
end

Note In our experiments, we implemented `IterativeMaxPower` using different levels of knowledge of the wireless system. In particular, we define the *communication range* of a charger as the maximum radius of the disc area within which it can send and receive *messages* from nodes. Hence, a transmitter ignores any node that is outside its communication range. Whenever a charger C_j communicates with a node R, the latter sends to C_j the energy field vector $\mathbf{E}(\mathscr{C}(\mathbf{x}), R)$, where $\mathbf{x}$ is the configuration at the time when the communication took place. This information is enough for the charger to compute $P(\mathscr{C}(\mathbf{x}^{(j,a)}), R)$, for each $a \in \{0,1\}$, since $P(\mathscr{C}(\mathbf{x}^{(j,a)}), R) = \gamma \|\mathbf{E}(\mathscr{C}(\mathbf{x}), R) + (a - \mathbf{x}_j)\mathbf{E}(C_j, R)\|^2$. By using the above, it is easy to compute $P(\mathscr{C}(\mathbf{x}^{(j,a)}), \mathscr{R}_{C_j})$ for each $a \in \{0,1\}$, where $\mathscr{R}_{C_j} \subseteq \mathscr{R}$ includes the nodes in the communication range of the charger C_j. The pseudocode of `IterativeMaxPower` can be found in Algorithm 1 that simulates the distributed process in order to have an output.

10.6 Maximum k-Minimum Guarantee

In this section, we present our algorithmic solutions to `MAX-`k`MIN-GUARANTEE`. This is more general than `MAX-POWER` and, even though we believe that it is computationally hard, we were unable to prove this formally. It is worth noting that the hardness of this problem does not lie in the computation of the minimum power among all k-set of receivers for a given configuration $\mathbf{x}$. It is not hard to see that this quantity is equal to the sum of powers of nodes having the k minimum powers.

On the other hand, exhaustive search algorithms do not work in the general case. In particular, Lemma 1 does not apply, as we show in the following example in which it is established that fractional operation power level of the transmitters can achieve better performance than $x \in \{0,1\}^m$. Assume again that there are

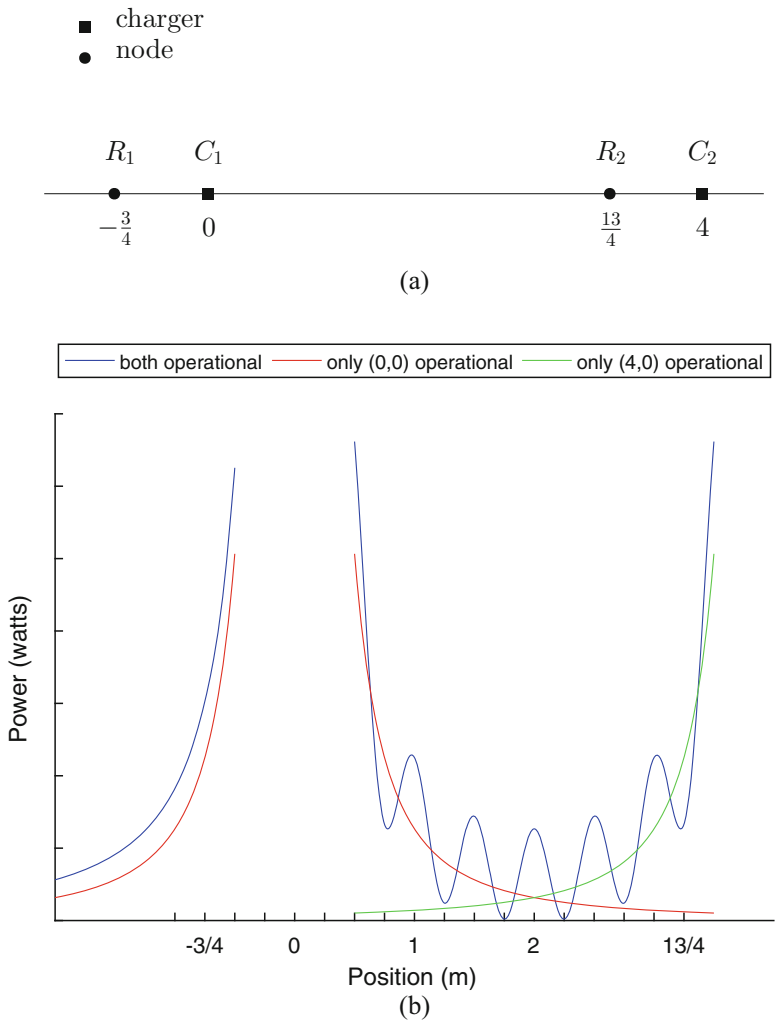

Fig. 10.3 Counterexample for fractional operation level of the chargers in MAX-kMIN-GUARANTEE problem. (**a**) Chargers' and nodes' placement on a straight line at points $(0, 0)$, $(0, 4)$ and $(0, -\frac{3}{4})$, $(0, \frac{13}{4})$, respectively. (**b**) The power distribution in the straight line from the two chargers. *Different curves* represent different operation levels of the chargers

two transmitters C_1 and C_2 placed at points $(0, 0)$ and $(4, 0)$ and two receivers R_1 at $(-\frac{3}{4}, 0)$ and R_2 at $(\frac{13}{4}, 0)$, respectively (see Fig. 10.3a). Also, assume that all constants in the above model are set to 1, i.e., $\lambda = \beta = \gamma = 1$. Figure 10.3b demonstrates the example on how the fractional operation level of C_1 can increase the $\min\{P(\{C_1, C_2\}, \{R_1\}), P(\{C_1, C_2\}, \{R_2\})\}$. So, if $x \in \{0, 1\}^2$, there are three operation cases (obviously when both chargers are closed is excluded). Firstly, if only C_1 is on, then $P(C_1, R_1) = (\frac{4}{3})^2 = 1.77$ and $P(C_1, R_2) = (\frac{4}{13})^2 = 0.094$. On

the other hand if C_2 is only on, the $\min\{P(C_2, R_1), P(C_2, R_2)\} = (\frac{1}{4})^2 = 0.0625$. In the final case, where $x_{C_1} = x_{C_2} = 1$, the power at the points is $P(\{C_1, C_2\}, R_1) = (\frac{4}{3} + \frac{4}{19})^2 = 2.38$ and $P(\{C_1, C_2\}, R_2) = (\frac{4}{3} - \frac{4}{13})^2 = 1.025$. Clearly if the power from R_1 is reduced by a small amount e, then $P(\{C_1, C_2\}, R_2)$ achieves a better minimum and at the same time $P(\{C_1, C_2\}, R_1)$ remains high.

In view of the above hardness indications, we consider a relaxation of `MAX-`k`MIN-GUARANTEE` in which we are only interested in optimal configurations in $\{0, 1\}^m$, i.e., configurations in which each charger is either full operational or does not operate.

Optimal Configuration in $\{0, 1\}^m$ We consider the following exhaustive search solution, which we use as a measure of comparison for our heuristics. In particular, *Optimal Algorithm (OPT)* uses brute force to find an optimal solution. Due to its high time complexity $O(2^m)$, it is not practical when the problem size tends to grow. OPT can serve as a performance upper bound when benchmarking our algorithms.

Algorithm 2 crushingly searches (without taking anything into consideration) among all the possible configurations of the chargers the one that maximizes the cumulative power of the k-set of nodes with the least power received.

Greedy Algorithm (GRE) The algorithm initiates from a random configuration which through an iterative process improves. The algorithm's decision for the chargers' operation level is the one that contributes more to the cumulative received power of the k-set that consist of the nodes with the least power received. Although the heuristic disambiguation can sometimes perform badly, it may yield locally optimal solution that approximates the global optimum in reasonable time. Clearly, time complexity depends on the number the algorithm checks to calibrate the chargers.

Algorithm 2: Brute-force (OPT)

```
   Input  : dist, ℛ, 𝒞, k
   Output: x^OPT
 1 begin
 2     maxpowerofkset = 0;
 3     foreach x ∈ {0,1}^m do
 4         foreach R ∈ ℛ do
 5             p(R) = P(𝒞(x), R);
 6         end foreach
 7         sort(p, asc);
 8         if (Σ_{i=1}^{k} p(i) ≥ maxpowerofkset) then
 9             maxpowerofkset = Σ_{i=1}^{k} p(i);
10             x^OPT = x;
11         end if
12     end foreach
13     return x^OPT;
14 end
```

Algorithm 3: Greedy (GRE)

Input : $dist, \mathscr{R}, \mathscr{C}, k$
Output: Chargers configuration

begin
  choose an arbitrary $\mathbf{x} \in \{0,1\}^m$;
  $y =$ *a random chargers sequence*;
  for $i = 1 \rightarrow length(y)$ **do**
    foreach $R \in \mathscr{R}$ **do**
      $\mathbf{p1}(R) = P(\mathscr{C}(\mathbf{x}^{(y(i),1)}), R)$;
      $\mathbf{p0}(R) = P(\mathscr{C}(\mathbf{x}^{(y(i),0)}), R)$;
    end foreach
    $sort(\mathbf{p1}, asc)$;
    $sort(\mathbf{p0}, asc)$;
    if $(\sum_{j=1}^{k} \mathbf{p0}(j) \leq \sum_{j=1}^{k} \mathbf{p1}(j))$ **then**
      $\mathbf{x}_{y(i)} = 1$;
    else
      $\mathbf{x}_{y(i)} = 0$;
    end if
  end for
  return x
end

Algorithm 3 tries to find an optimal solution after a number of iterations. In each step, it randomly chooses a charger $y(i)$, computes the power received from each node R, and stores them in the vector **p1** when $y(i)$ is activated and at vector **p0** when it is deactivated. Subsequently, GRE measures the cumulative received power of the k nodes that receive the less power from **p1** and **p0**, respectively. The operation level that is providing the larger amount of cumulative received power will be the algorithm's choice for the current step.

Sampling Algorithm (SAM) Instead of going through all possible solutions extensively as the Brute-force algorithm does, and in order to avoid the greedy approach and its disadvantages, we propose a sampling heuristic. It randomly samples σ k-sets of nodes and aims to maximize the cumulative received power of all possible k-sets with the configuration that will come up from the sample. In this way, the algorithm overcomes the threat of a locally optimal solution but due to the random grouping, it does not take into account the nodes that form the k-set with the least received power.

Algorithm 4 consists of two phases. During the first phase, it randomly chooses σ k-sets of nodes and finds their optimal chargers configuration $\mathbf{x}^i : i \in [1, \sigma]$ via Algorithm 1. The second phase is iterative. Within each iteration, it chooses a charger $perm(j)$ from a random permutation ($perm$) of the chargers set and measures the cumulative received power of each k-set that belongs to the sample when the charger is activated and when it is not. Then, it sums the gain when the charger is activated ($gain1$) and compares it with the gain when it is closed ($gain0$). The operation level with the larger sum of gain is decided as the final operation level

Algorithm 4: Sampling (SAM)

Input : $dist, \mathscr{R}, \mathscr{C}, k$
Output: $\mathbf{x}$

begin
  choose randomly σ k-sets of nodes $\{k_1, k_2, \ldots, k_\sigma\}$;
  for $i = 1 \rightarrow \sigma$ **do**
    $\mathbf{x^i} =$ `IterativeMaxPower`$(dist, k_i, \mathscr{C}, open)$;
  end for
  $perm =$ *a random permutation of chargers*;
  for $j = 1 \rightarrow m$ **do**
    $gain0 = 0$;
    $gain1 = 0$;
    for $i = 1 \rightarrow \sigma$ **do**
      $\mathbf{p0}(i) = P(\mathscr{C}(\mathbf{x^i}^{((perm(j),0)}), k_i)$;
      $\mathbf{p1}(i) = P(\mathscr{C}(\mathbf{x^i}^{((perm(j),1)}), k_i)$;
      if $(\mathbf{p1}(i) \leq \mathbf{p0}(i))$ **then**
        $gain0 = gain0 + \mathbf{p0}(i) - \mathbf{p1}(i)$;
      else
        $gain1 = gain1 + \mathbf{p1}(i) - \mathbf{p0}(i)$;
      end if
    end for
    if $(gain1 \leq gain0)$ **then**
      $\forall\, i \in [\sigma], \mathbf{x}^i_{perm(j)} = 0$;
    else
      $\forall\, i \in [\sigma], \mathbf{x}^i_{perm(j)} = 1$;
    end if
  end for
  return any $\mathbf{x}^i : i \in [\sigma]$
end

of the charger. Thus, at the end of the process the σ k-sets share the same chargers configuration. Finally, the configuration of the sampled k-sets is SAM's output.

Fusion Algorithm (FUS) Our last algorithm tries to combine the advantages of the previous ones and at the same time to restrict their weaknesses. FUS initiates by having the best chargers configuration for each node individually. Step by step it changes the operation level of one charger at the time. This way, the algorithm fuses the n different configurations to one with respect to the received power sum of the k nodes with the least power. FUS takes into consideration the received power for each node separately and aims to keep it as high as possible.

Algorithm 5 consists of two phases. During the first phase, it finds the optimal chargers configuration $\mathbf{x}^R$ via Algorithm 1 for each node R individually. During the second phase, it proceeds iteratively. Within each iteration, it chooses a charger $perm(j)$ from a random permutation of the chargers set and measures the power of each node when it is activated and when it is not. Those power values are stored in two vectors, **p1** and **p0**, respectively. In the sequel, it sums the k nodes with the

Algorithm 5: Fusion (FUS)

Input : $dist, \mathscr{R}, \mathscr{C}, k$
Output: Chargers configuration

begin
  //find optimal configuration for each node;
  foreach $R \in \mathscr{R}$ **do**
    $\mathbf{x}^R = \texttt{IterativeMaxPower}(dist, R, \mathscr{C}, open)$;
  end foreach
  $perm = a\ random\ permutation\ of\ chargers$;
  for $j = 1 \rightarrow m$ **do**
    foreach $R \in \mathscr{R}$ **do**
      $\mathbf{p0}(R) = P(\mathscr{C}(\mathbf{x}^{R((perm(j),0)}), R)$;
      $\mathbf{p1}(R) = P(\mathscr{C}(\mathbf{x}^{R((perm(j),1)}), R)$;
    end foreach
    $sort(\mathbf{p1}, asc)$;
    $sort(\mathbf{p0}, asc)$;
    if $(\sum_{i=1}^{k} \mathbf{p1}(i) \leq \sum_{i=1}^{k} \mathbf{p0}(i))$ **then**
      $\forall R \in \mathscr{R},\ \mathbf{x}^R_{perm(j)} = 0$;
    else
      $\forall R \in \mathscr{R},\ \mathbf{x}^R_{perm(j)} = 1$;
    end if
  end for
  return any $\mathbf{x}^R : R \in \mathscr{R}$
end

Table 10.2 Summary table

Algorithm	Assumption	Knowledge	Running time	Performance
Greedy	Initiate from a random configuration for chargers	Checks all the nodes of the network	Fast	Low
Sampling	Initiate with σ different configuration, optimal for each sample	Checks only the nodes of the sample	Average	Low for small k, Average
Fusion	Initiate with n different configuration, optimal for each node	Checks all the nodes of the network	Slow	High

least power for each operation level and compares them. The operation level of the charger with the larger sum will be chosen. That way FUS changes the charger's operation level to the one that has the less negative impact on the k-set with the least received power that has risen. At the end of the algorithm, all the nodes share the same chargers configuration. In Table 10.2 you can find a list of advantages and limitations for each algorithm.

10.7 Evaluation

We conducted simulations in order to evaluate our methods and reveal insights of the proposed design performance, using Matlab R2016a. The system that we consider for the performance evaluation consists of chargers and nodes randomly deployed in a square field of 10 m × 10 m. Each charger delivers to the transmit antenna power equal to 2 W and it has 2 dbi gain, while the gain of the receiver's antenna is 1 dbi. The number of chargers and nodes is set to 15 and 200, respectively, and all the experiments run on the same system where the wavelength is 29 cm. Figure 10.4a depicts an instance of the deployment. For statistical smoothness, we conducted each simulation 100 times. Even though the statistical analysis of the findings demonstrates very high concentration around the mean, in the following simulation results we also depict the confidence intervals. Actually, we provide the confidence intervals for 20 repetitions, in order to demonstrate an earlier convergence.

In this section, we provide our simulation results on three performance metrics: (a) cumulative power fuelled into the system, (b) communication overhead (the number of messages that has been sent or received from nodes), and (c) power balance (the variation of power among nodes).

Cumulative Power In general, as the communication range of the chargers grows, the distributed Algorithm 1 achieves a near optimal solution. Figure 10.4b depicts the cumulative received power by the nodes by varying the communication range of the chargers over time (for 90 rounds). In each round, a charger is chosen randomly and decides on its operation level.

We can see that the cumulative power with the open communication range never decreases over time like the others do. This is because every charger has global knowledge of the power exchange in the system. Indeed, when a charger has limited communication range, then its choice serves the nodes in the communication range that covers, but for the rest of the nodes the result might be negative. On the other hand, at the first steps of the distributed algorithm, choices made from chargers with short communication range can benefit temporarily the cumulative power for the next steps, but in the end, the one with the global knowledge will perform better.

We also observe that when the communication range is 1 m we achieve a near optimal solution. The reason behind this is that the received power of the nodes far from the charger is reduced due to distance and they do not contribute that much to the cumulative received power. The confidence intervals which are presented in the Fig. 10.4c show a high concentration around the mean. As the time passes, Algorithm 1 has higher concentration around the mean and without overlaps unlike at the first steps.

As mentioned before, it is impractical to run OPT because it uses brute-force approach. For this reason, we use the same experimental setup with a small number of chargers as above for comparing GRE, SAM, and FUS with OPT. Figure 10.4a shows the corresponding deployment.

We are also interested in the impact of the number k. Figure 10.5a depicts the cumulative power of the k nodes with the least power over various k. An interesting observation is that SAM does not perform much better than GRE for low k. On the

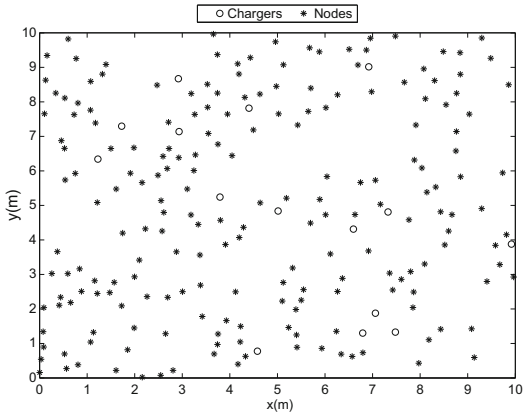

(a)

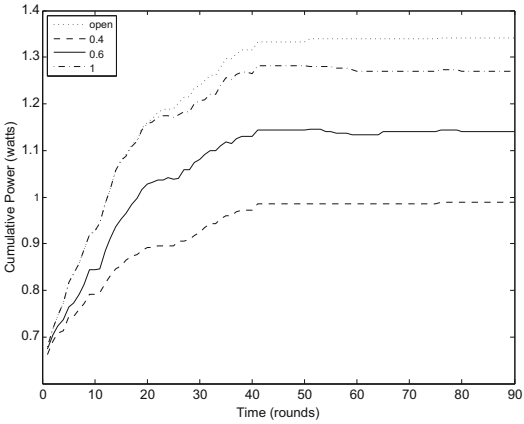

(b)

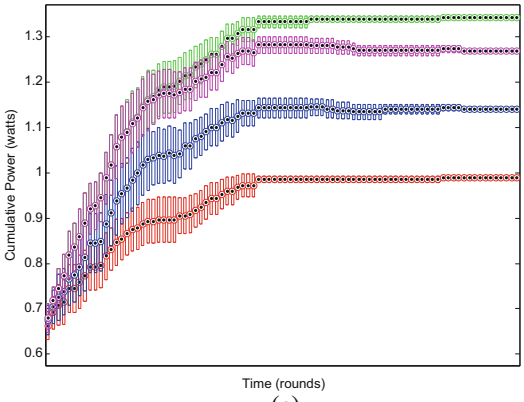

(c)

Fig. 10.4 Deployment and cumulative power for `IterativeMaxPower`. (**a**) Chargers' and nodes' deployment. (**b**) Cumulative power over time for different knowledge levels. (**c**) Confidence intervals for Fig. 10.4b. open 1 0.6, 0.4

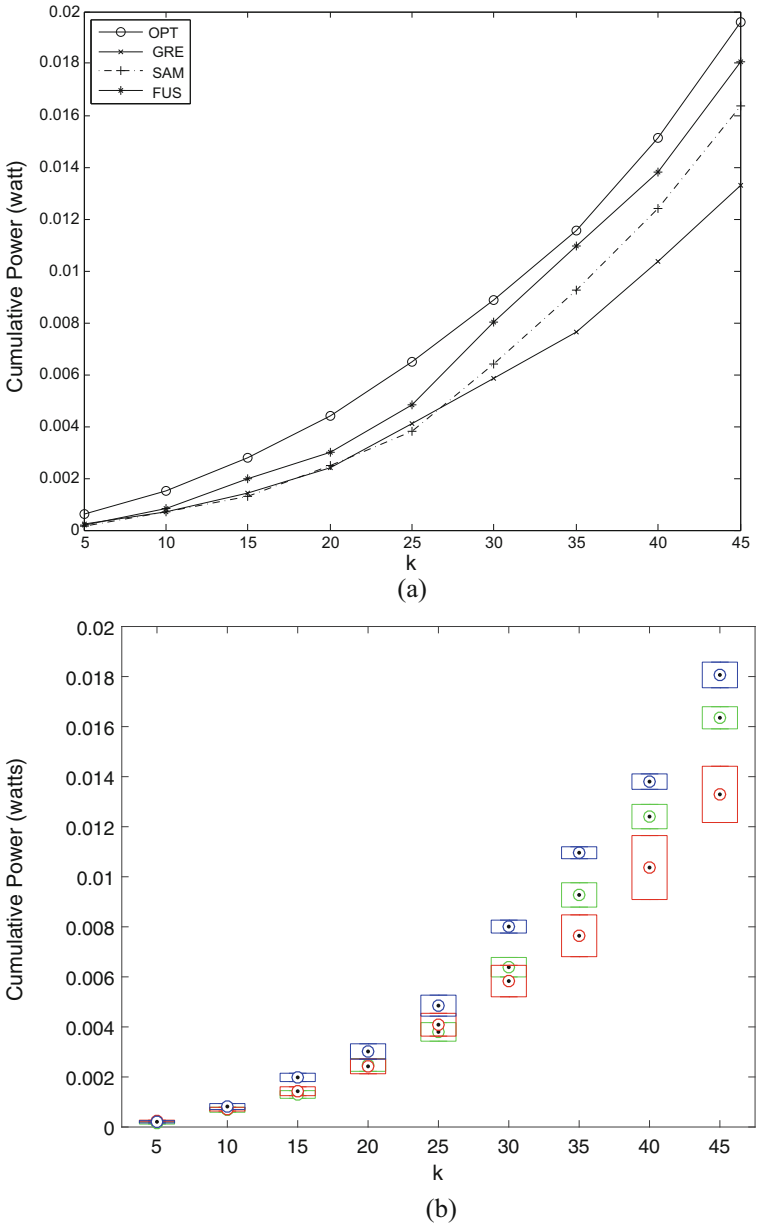

Fig. 10.5 Performance of different algorithms. (**a**) Cumulative power (of k-set with minimum power) for different values of k. (**b**) Confidence intervals for Fig. 10.5a. GRE SAM FUS

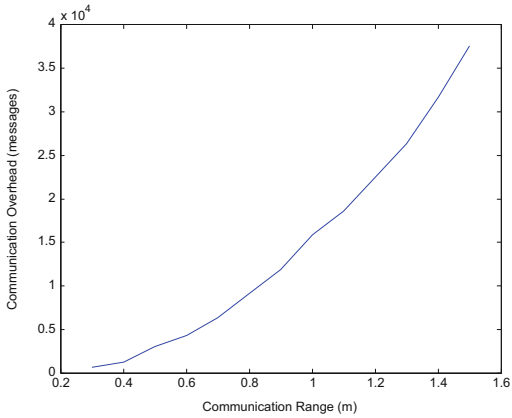

(a)

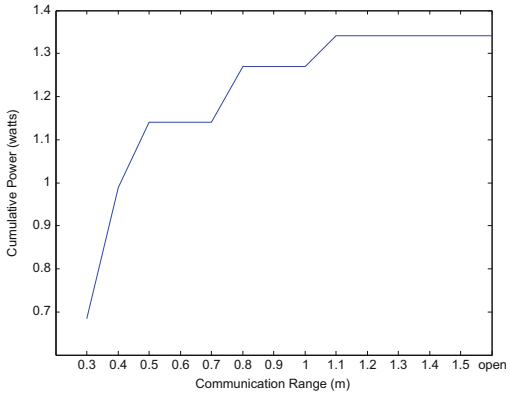

(b)

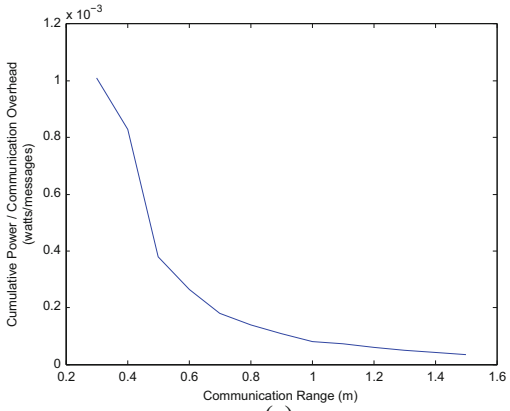

(c)

Fig. 10.6 Impact of communication range on different metrics. (**a**) Communication overhead over different communication ranges. (**b**) Cumulative power over different communication ranges at the 90th round of Algorithm 1. (**c**) Ratio of cumulative power to communication overhead over different communication ranges

other hand, for $k > 27$ we have a considerable improvement. The reason behind this is the sampling that SAM does. On the contrary, the rest of the algorithms compare the k least power values of all the system without any restriction. So for small k SAM by default has a disadvantage. For example, it is hard to sample in the same k-set for $k = 10$ even the two of the nodes with the least received power among 200 nodes. Thus, as k increases, the performance of SAM improves. At the experiments $\sigma = 30$ (the size of the sample for SAM). Different values of σ did not provide any significant improvement, but if it is too small the sample is not representative and poor. As expected, FUS outperforms the other two algorithms and it is the one that approximates OPT better. This is because FUS checks the power received for all the nodes and has more than one initial chargers' configuration unlike GRE. The confidence intervals are also presented in the Fig. 10.5b. As we claimed, the algorithms present high concentration around the mean and there are no overlaps as the value of k grows.

Communication Overhead Figure 10.6a meters the number of messages for ranges from 0.3 to 1.5 that have been exchanged in the system during the running time of the distributed algorithm. When the communication range of the chargers increases, the communication overhead goes up. Moreover, the effect of different communication ranges (from 0.3 to 1.5 and *open*) on the cumulative received power of the system is depicted in Fig. 10.6b. As we mentioned above, a limited communication range (1.1–1.5 m) can achieve the performance of *open*. We observe that there is a trade-off between the communication overhead and the cumulative power that the nodes receive (Fig. 10.6c). As the communication range grows, the ratio of cumulative received power to communication overhead decreases. It is evident that the contribution of the messages drops for communication range bigger than 1–1.2 m. After that point, the contribution of the extra messages, which are many, is very low. Note that the communication overhead depends on the relative position of the chargers and the nodes. As the number of nodes in the communication range of a charger increases, then the number of messages increases as well. The chargers' placement for communication optimization is not considered in this study.

Power Balance We finally study the impact of our methods on the system in relation to power balance (the variation of power among the various nodes). The simulation results are shown in Fig. 10.7 where we examine the performance of the algorithms in the general case. Obviously, there is room for improvement in this area, as our methods do not take power balance into consideration and we leave this as an open problem for future work.

10.8 Conclusion and Future Work

In this chapter, we studied the problem of finding the best configuration setup of the wireless power transmitters in a wireless system with respect to the maximization of the cumulative received power and we proposed heuristic algorithms to succeed

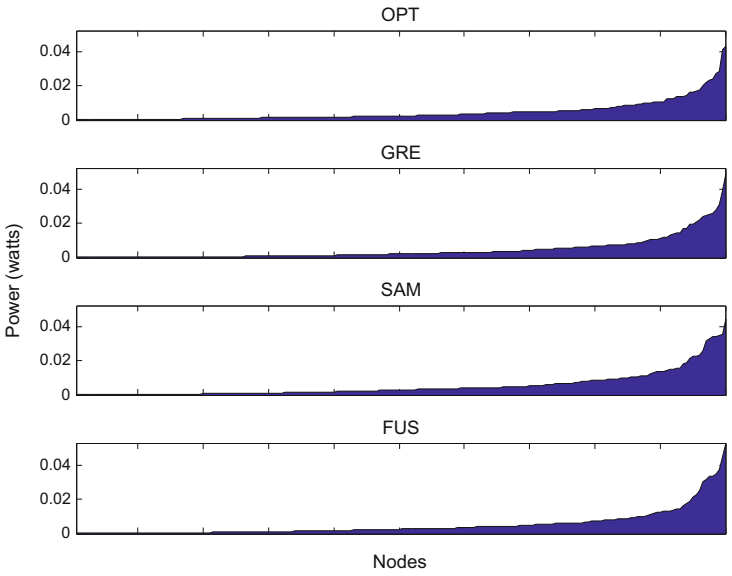

Fig. 10.7 Power balance achieved by different algorithms

in this goal. Finally, we evaluated the performance of the proposed algorithms through experimental simulation and provided numerical results to validate their efficiency. A main contribution of our work lies on the fact that, for the first time power maximization algorithms are given under the vector model which realistically addresses the superposition of energy fields.

In future work, we opt to improve the power balance of the algorithms in exchange of a small amount of the cumulative received power. We will also explore solutions with good approximation ratios to maximize the cumulative received power from the point of view of nodes or chargers deployment.

References

1. C.M. Angelopoulos, S. Nikoletseas, T.P. Raptis, Wireless energy transfer in sensor networks with adaptive, limited knowledge protocols. Comput. Netw. **70**, 113–141 (2014)
2. S. Boyd, L. Vandenberghe, *Convex Optimization* (Cambridge University Press, New York, 2004)
3. H. Dai, Y. Liu, G. Chen, X. Wu, T. He, Scape: safe charging with adjustable power, in *2014 IEEE 34th International Conference on Distributed Computing Systems (ICDCS)*, June (2014), pp. 439–448
4. D. Gao, G. Wu, Y. Liu, F. Zhang, Bounded end-to-end delay with transmission power control techniques for rechargeable wireless sensor networks. AEU Int. J. Electron. Commun. **68**(5), 395–405 (2014)

5. B. Griffin, C. Detweiler, Resonant wireless power transfer to ground sensors from a UAV, in *2012 IEEE International Conference on Robotics and Automation (ICRA)*, May (2012), pp. 2660–2665
6. S. Guo, C. Wang, Y. Yang, Mobile data gathering with wireless energy replenishment in rechargeable sensor networks, in *2013 Proceedings IEEE INFOCOM*, April (2013), pp. 1932–1940
7. S. He, J. Chen, F. Jiang, D.K.Y. Yau, G. Xing, Y. Sun, Energy provisioning in wireless rechargeable sensor networks. IEEE Trans. Mob. Comput. **12**(10), 1931–1942 (2013)
8. I. Katsidimas, S. Nikoletseas, T.P. Raptis, C. Raptopoulos, Efficient algorithms for power maximization in the vector model for wireless energy transfer, in *Proceedings of the 18th International Conference on Distributed Computing and Networking* (ACM, New York, 2017), pp. 30:1–30:10
9. Y. Li, L. Fu, M. Chen, K. Chi, Y.H. Zhu, RF-based charger placement for duty cycle guarantee in battery-free sensor networks. IEEE Commun. Lett. **19**(10), 1802–1805 (2015)
10. X. Lu, D. Niyato, P. Wang, D.I. Kim, Wireless charger networking for mobile devices: fundamentals, standards, and applications. IEEE Wirel. Commun. **22**(2), 126–135 (2015)
11. X. Lu, P. Wang, D. Niyato, D.I. Kim, Z. Han, Wireless networks with RF energy harvesting: a contemporary survey. IEEE Commun. Surv. Tutorials **17**(2), 757–789 (2015, Secondquarter)
12. X. Lu, P. Wang, D. Niyato, D.I. Kim, Z. Han, Wireless charging technologies: fundamentals, standards, and network applications. IEEE Commun. Surv. Tutorials **18**(2), 1413–1452 (2016, Second quarter)
13. A. Madhja, S. Nikoletseas, T.P. Raptis, Distributed wireless power transfer in sensor networks with multiple mobile chargers. Comput. Netw. **80**, 89–108 (2015)
14. A. Mittleider, B. Griffin, C. Detweiler, *Experimental Analysis of a UAV-Based Wireless Power Transfer Localization System* (Springer International Publishing, Cham, 2016), pp. 357–371
15. M.Y. Naderi, K.R. Chowdhury, S. Basagni, W. Heinzelman, S. De, S. Jana, Experimental study of concurrent data and wireless energy transfer for sensor networks, in *2014 IEEE Global Communications Conference*, Dec (2014), pp. 2543–2549
16. M.Y. Naderi, P. Nintanavongsa, K.R. Chowdhury, RF-MAC: a medium access control protocol for re-chargeable sensor networks powered by wireless energy harvesting. IEEE Trans. Wirel. Commun. **13**(7), 3926–3937 (2014)
17. M.Y. Naderi, K.R. Chowdhury, S. Basagni, Wireless sensor networks with RF energy harvesting: energy models and analysis, in *2015 IEEE Wireless Communications and Networking Conference (WCNC)*, March (2015), pp. 1494–1499
18. S. Nikoletseas, T.P. Raptis, C. Raptopoulos, Low radiation efficient wireless energy transfer in wireless distributed systems, in *2015 IEEE 35th International Conference on Distributed Computing Systems (ICDCS)*, June (2015), pp. 196–204
19. S. Nikoletseas, T.P. Raptis, C. Raptopoulos, Interactive wireless charging for energy balance, in *2016 IEEE 36th International Conference on Distributed Computing Systems (ICDCS)*, June 2016
20. S. Nikoletseas, Y. Yang, A. Georgiadis (eds.), *Wireless Power Transfer Algorithms, Technologies and Applications in Ad Hoc Communication Networks* (Springer International Publishing, Cham, 2016)
21. P. Nintanavongsa, M.Y. Naderi, K.R. Chowdhury, Medium access control protocol design for sensors powered by wireless energy transfer, in *2013 Proceedings IEEE INFOCOM*, April (2013), pp. 150–154
22. Powercast TX91501 Transmitter, http://www.powercastco.com/products/powercaster-transmitters/
23. TI BQ501210 Wireless Power Transmitter Manager, http://www.ti.com/product/BQ501210
24. B. Tong, Z. Li, G. Wang, W. Zhang, How wireless power charging technology affects sensor network deployment and routing, in *2010 IEEE 30th International Conference on Distributed Computing Systems (ICDCS)*, June (2010), pp. 438–447

25. L. Xie, Y. Shi, Y.T. Hou, H.D. Sherali, Making sensor networks immortal: an energy-renewal approach with wireless power transfer. IEEE/ACM Trans. Netw. **20**(6), 1748–1761 (2012)
26. L. Xie, Y. Shi, Y. T. Hou, A. Lou, Wireless power transfer and applications to sensor networks. IEEE Wirel. Commun. **20**(4), 140–145 (2013)
27. S. Zhang, Z. Qian, F. Kong, J. Wu, S. Lu, P3: joint optimization of charger placement and power allocation for wireless power transfer, in *2015 IEEE Conference on Computer Communications (INFOCOM)*, April (2015), pp. 2344–2352

Chapter 11
Enabling Green Heterogeneous Cellular Networks via Balanced Dynamic Planning

Muhammad Ismail, Mohamed Kashef, Erchin Serpedin, and Khalid A. Qaraqe

11.1 Introduction

The past decade has witnessed a wide deployment of wireless access networks, which is motivated by the increasing demand of wireless communication services. Moreover, mobile terminals (MTs) have evolved into more sophisticated devices with advanced processing and displaying capabilities that can support video streaming and data applications besides voice calls. Unfortunately, such a great advancement in wireless communication services has resulted in high energy consumption for both network operators and mobile users. Specifically, there exist 3 million base stations (BSs) and around 3 billion MTs worldwide that annually consume 4.5 GW and 0.2–0.4 GW of power, respectively [1]. The high energy consumption of network operators and mobile users has result in environmental, financial, and quality-of-experience (QoE) concerns. From an environmental point of view, the telecommunications industry is responsible for about 2% of the total CO_2 emissions worldwide, and the percentage is expected to double by 2020 [2]. Furthermore, the rechargeable batteries of MTs have an expected lifetime of 2–3 years, leading to 25,000 tons of annual disposed batteries, which has significant environmental (and financial) impacts [3]. From a financial standpoint, it has been estimated that the energy bills of service providers cost about 18–32% of their

M. Ismail (✉) • M. Kashef • K.A. Qaraqe
Electrical and Computer Engineering Department, Texas A&M University at Qatar, Education City, P.O. Box No. 23874, Doha, Qatar
e-mail: m.ismail@qatar.tamu.edu; mohamed.hany@qatar.tamu.edu; khalid.qaraqe@qatar.tamu.edu

E. Serpedin
Electrical and Computer Engineering Department, Texas A&M University, College Station, TX, USA
e-mail: serpedin@ece.tamu.edu

D.N.K. Jayakody et al. (eds.), *Wireless Information and Power Transfer: A New Paradigm for Green Communications*, DOI 10.1007/978-3-319-56669-6_11

operational expenditure [4]. From a QoE consideration, it has been estimated that almost 60% of mobile users suffer from a limited battery capacity, a problem that is further complicated by the slow advance in the battery technology. The aforementioned concerns have motivated the research in *green communications* for energy efficient wireless network operation.

In general, the green solutions that are deployed by network operators can be classified based on the call traffic load condition. At a high call traffic load, radio resource scheduling techniques are adopted to satisfy the MTs' required quality-of-service (QoS) at a reduced BS transmission power [5, 6]. At a low call traffic load, network operators switch-off some of their BSs to save energy and MTs are served by the remaining active BSs, which is referred to as *dynamic planning* [2, 7–9]. Such an approach is very useful in today's heterogeneous wireless medium where lightly loaded small cells (e.g., pico and femto cells) can be switched off and the call traffic load is mainly served by the remaining active macro/micro BSs, leading to a green heterogeneous cellular network. The main objective of the dynamic planning research is to switch off as many lightly loaded BSs as possible provided that the remaining active BSs satisfy the mobile users QoS in the downlink (e.g., the users minimum required downlink throughput). However, the existing research does not provide any QoS guarantee for the uplink mobile users and the relationship between the QoS of uplink mobile users and their incurred energy consumption is not well investigated. From a network operator's perspective, energy saving can be achieved by switching off dense small cells and radio coverage is provided by large cells. However, this could result in associating the uplink mobile users to a faraway BS which leads to higher energy consumption for MTs in the uplink due to larger transmission distances. Given the MT available energy, it might not be able under such circumstances to satisfy its minimum required throughput in the uplink. Even worse, high energy consumption in the uplink might lead the MT to drain its battery at a faster rate which might eventually result in call dropping due to battery depletion. However, the existing research does not quantify such a relationship between dynamic planning and the incurred uplink energy consumption and its impact on QoS degradation for uplink mobile users.

In this chapter, we aim to capture the trade-off between the mobile users' uplink energy consumption and their perceived QoS and employ such a relationship to design a balanced dynamic planning framework that can save energy for network operators while providing service quality guarantee for mobile users with data calls in the uplink and downlink. We first review the fundamentals of the traditional dynamic planning approaches along with the motivation for a dynamic planning framework with balanced energy efficiency [8]. Subsequently, we present a dynamic planning approach with balanced energy efficiency based on a multi-timescale decision process whose objective is to save energy for the service provider in a heterogeneous cellular network while ensuring the QoS of mobile users in the uplink and downlink [7]. The two-timescale problem decouples the BS operation (on–off switching) and MT association into two separate timescales, namely slow and fast timescales. The slow timescale captures the long-term temporal fluctuations in the call traffic load density while the fast timescale captures the short-term

temporal fluctuations in terms of mobile users arrivals and departures. Such a balanced dynamic planning formulation offers a novel BS switching criterion as BS switching-off might be infeasible due to service quality degradation in the uplink [9]. Due to the associated computational complexity of the decision problem, we present a sub-optimal dynamic planning framework following a feasibility analysis. We prove that the feasibility-based framework leads to an optimal BS switching decision from the downlink QoS perspective and a sub-optimal BS switching decision from the uplink QoS perspective. To further reduce the computational complexity, we present a tunable heuristic algorithm that iteratively activates the small cells until uplink and downlink QoS parameters are satisfied in an average sense. Simulation results indicate that the balanced dynamic planning framework can save energy for network operators (compared with an all active state that keeps all BSs active) while ensuring a target QoS for mobile users both in the uplink and downlink, unlike the unbalanced dynamic planning approach.

11.2 Dynamic Planning in Green Networks

This section discusses the motivation for adopting a dynamic planning approach to enable an energy efficient network operation. Furthermore, we discuss some design fundamentals and the motivation for a balanced dynamic planning approach [8].

11.2.1 Motivations and Design Principles of Dynamic Planning

In cellular network planning, the cell size and capacity are traditionally designed to satisfy the peak call traffic load. However, it has been shown that the call traffic load exhibits temporal and spatial fluctuations [4]. Specifically, real traffic traces have demonstrated a sinusoidal traffic profile in every cell. The call traffic load during day time (i.e., 11 am–9 pm) is much higher than that during the night (i.e., 10 pm–9 am) [10]. Furthermore, the peak call traffic load during weekends and holidays is much lower than that of a normal weekday. In addition, the real traffic traces have demonstrated a diverse behavior among closely located BSs [10]. Consequently, networks are over-provisioned at a low call traffic load, which lead to energy wastage. Thus, BS on–off switching is proposed to adapt the network energy consumption according to the call traffic load condition, an approach that is referred to as dynamic planning. Hence, at a low call traffic load, lightly loaded BSs are switched off and MTs are served by the remaining active BSs.

Two fundamental issues must be tackled while designing a dynamic planning mechanism, namely MT association and BS operation, as discussed in the following.

11.2.1.1 MT Association

This issue deals with associating each MT to a given BS for service. In the following, we discuss the design objectives of the MT association mechanism in the context of dynamic planning. Then, we review decision criteria of some existing MT association mechanisms.

11.2.1.2 Design Objectives

In literature, the MT association serves two objectives for dynamic planning deployment. The first objective is related to concentrating the MTs' traffic in a few BSs to switch off the remaining BSs. Hence, newly incoming MTs are associated with a subset of BSs. In addition, handover is triggered for MTs already in service to allow for traffic load concentration. The second objective aims to balance the trade-off between network energy efficiency and flow-level performance of the MTs (e.g., data rate, time delay, etc.) [11]. The rationale behind such an objective is to ensure that the target QoS of MTs is not jeopardized while reducing the network energy consumption. Hence, in [11], a weighted multi-objective function is introduced to control the MT association. Based on the weighting factor value, the MT association favors whether the network energy consumption or the users' received QoS. Furthermore, it has been shown that more energy is saved when mobile users can tolerate some service delay [12, 13].

11.2.1.3 Decision Criteria

Several decision criteria are defined in literature for the MT association problem to enable an efficient dynamic planning. The simplest decision criterion for the MT association problem is an MT-BS distance based, where MTs with downlink traffic are associated with the nearest BSs [14]. As a result, low transmission power is consumed due to the short transmission distances. The network impact is another decision criterion introduced in [15] where MTs' traffic is concentrated in the BSs that lead to lower intercell interference. Furthermore, coverage hole avoidance is a decision criterion that aims to concentrate the call traffic load in a subset of BSs that can provide an acceptable network coverage [16, 17].

11.2.1.4 BS Operation

The BS operation specifies which BSs are switched off, when to wake-up a given BS, and how to implement the switching decisions. The associated design issues are discussed in the following.

11.2.1.5 Prediction of Future Traffic Demands

The BS mode (on or off) lasts for a long duration (i.e., in hours) to avoid frequent BS on–off switching. This is mainly because frequent on–off switching of BSs is not favored as it leads to increased energy consumption during the BS start-up [2] and service unavailability for the inactive cells during the decision computation phase [18]. Hence, the BS on–off switching decision should consider not only the current traffic load (through MT association) but also the future demands to guarantee an acceptable QoS [2]. As a result, extra radio resources should be reserved at the active BSs to satisfy the future traffic demands [18]. Several studies in literature have demonstrated a repetitive call traffic load patterns for weekdays and weekends [19], a fact which can be used to predict the future call traffic demands. In addition, neighbor BSs can cooperate with each other to predict their future traffic profile via an online stochastic game as in [20].

11.2.1.6 BS Wake-Up Design

As a subset of BSs is switched off, the remaining active BSs should provide service coverage for the inactive cells. When the call traffic load served by the active BSs increases beyond their capacity limitation, some of the switched-off BSs have to be turned on. Hence, in dynamic planning, it is necessary to specify the wake-up instants for the inactive BSs. Different BS wake-up schemes are proposed in literature. For instance, in [21], an M-based and V-based wake-up schemes are proposed. Specifically, in the M-based scheme, an inactive BS wakes up only when M MTs request service, which is also investigated in [22] via queuing analysis techniques and in [23] based on game theory tools. On the other hand, in the V-based scheme, an inactive BS wakes up after a vacation time V. Moreover, the work in [24] presents a Markov decision problem (MDP) that employs optimal switching schemes to activate femto BSs in overlapping coverage with a macro BS by exploiting information about the call traffic load and user localization. In this context, the switching decision can be BS controlled, MT controlled, or network controlled [25]. A sleep femto BS monitors the user activity to wake up in the BS controlled mode, while the MT sends an activation message to the sleep femto BS in the MT controlled mode, and the core network sends activation messages to the sleep femto BS over the backhaul link in the network controlled mode.

11.2.1.7 Switching Off Mode Entrance and Exit

An MT may not be able to complete its handoff procedure to an active BS and suffers from call dropping if its associated BS is switched off too fast. This is due to the low received signal from the neighboring BSs and the limited signaling channel capacity. The switch-off mode entrance specifies how a BS transits from the on to the off state. In [26], BS wilting is proposed for a smooth switch-off mode entrance,

where the BS transmit power is progressively halved until the BS is turned off. Hence, the MTs initiate a handover process to the nearby BSs during the wilting process. Similarly, MTs in service can suffer from a strong interference if a BS is switched on too fast. The switch-off mode exit specifies how a BS transits from the off to the on state. A BS blossoming process is proposed in [26] for smooth switch-off mode exit, where the BS transmit power is progressively doubled until the BS is turned on.

11.2.2 Dynamic Planning with Balanced Energy Efficiency

A major limitation with the existing contributions on dynamic planning is that they focus only on enhancing energy efficiency of network operators regardless of the energy consumption performance of the mobile users. Specifically, the related research considers only MTs with downlink traffic. In this context, the main goal is to balance the BS energy consumption performance with the MTs' flow-level performance [11]. However, in reality, there exists a mixture of mobile users with uplink traffic and mobile users with downlink traffic. Unfortunately, the existing research does not pay attention to the relation between the mobile users' perceived service quality and their incurred uplink energy consumption. For instance, an MT might not be able to satisfy a target minimum uplink throughput due to the required high transmission power. Furthermore, if the MT is consuming high energy in the uplink, it is expected to drain its battery at a fast rate, eventually leading to call dropping. Consequently, dynamic planning approaches with balanced energy efficiency among network operators and mobile users should be investigated.

As discussed above, dynamic planning deals with two fundamental issues, namely user association and BS operation. When the main scope of dynamic planning is to enhance energy efficiency of network operators, which is the case for the existing research, the BSs' switch-off decisions can result in energy inefficient user association from the mobile users' standpoint. As shown in Fig. 11.1, accounting only for the downlink performance, MTs with uplink traffic can be associated with a faraway macro BS, due to a switched-off nearby femto/pico BS. Because of the long transmission distance, high energy consumption of MTs in the uplink is expected, which leads to energy depletion for MTs at a faster rate. Although energy consumption for MTs is not that much compared with the BS energy consumption, yet a fast rate battery depletion for MTs results in high rate of dropped services in the uplink, which jeopardizes the mobile users' perceived service quality. In addition, MTs might be incapable of supporting a minimum required throughput due to the associated high transmission power. Hence, the dynamic planning approach should be designed to capture and balance the trade-off in the resulting energy efficiency for network operators and mobile users. Towards this objective, in the following, we first quantify the impact of dynamic planning on the service quality of mobile users in the uplink and downlink. The uplink mobile users' QoS is measured in terms of supporting a minimum required throughput

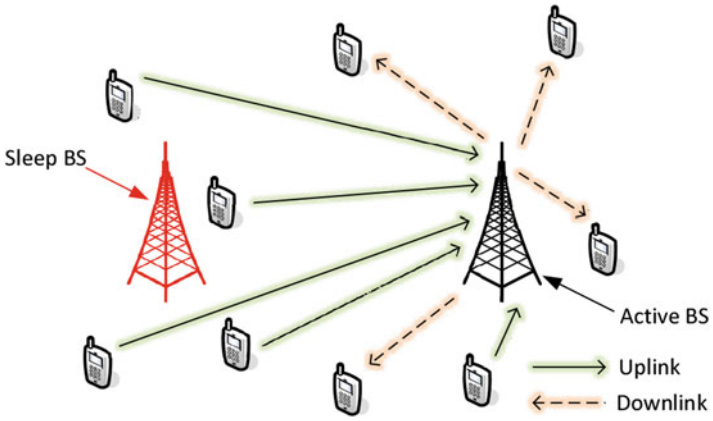

Fig. 11.1 Dynamic planning with unbalanced energy saving. MTs with uplink traffic are associated with faraway BSs [8]

(which is related to the MT transmission power, the available energy at the battery of the MT, and the number of uplink users) and satisfying a maximum threshold on call dropping probability due to the MT battery depletion (which is related to the available energy at the battery of the MT, the minimum required throughput, and the number of uplink users). On the other hand, the downlink mobile users' QoS is measured in terms of satisfying a minimum required throughput (which is related to the BS transmission power and the number of downlink users).

11.3 Impact of Dynamic Planning on Mobile Users' Service Quality

In this section, we aim to quantify the dynamic planning impact on mobile users' service quality [7, 9]. Such an investigation is very useful in designing dynamic planning approaches that can balance energy saving for network operators with uplink and downlink service quality. In the following, we first present the system model, then, we investigate the impact of dynamic planning on the mobile users' service quality.

11.3.1 System Model

This subsection presents the system model in terms of the employed heterogeneous cellular network, call traffic load fluctuations, power consum models, and QoS metrics. Mathematical symbols used in this chapter are summarized in Table 11.1.

Table 11.1 Summary of important symbols

Symbol	Definition
$B_s^{\mathrm{UL/DL}}$	Available bandwidths for uplink/downlink users at BS s
D_s	Separation distance between the macro BS and the pico/femto BS s
$E_{i,m}^{\mathrm{c}}$	MT m energy consumption till time slot $i+1$
$E_{\mathrm{trp},m}$	Trapping energy for MT m
$f_{\mathbf{P}_{its}}(\mathbf{p}_{its})$	PMF of vector of transmission power actions adopted by BS s over time slots
$f_{\mathbf{P}_{itm}}(\mathbf{p}_{itm})$	PMF of vector of transmission power actions adopted by MT m over time slots
$f_{E_m}(e_m)$	PDF of initial available energy e_m at MT m
$G_s^{\mathrm{UL/DL}}$	Average channel power gain for the uplink/downlink mobile users with BS s
H_s	Height of BS s
$\mathscr{I}$	Set of periods for the fast timescale
$\mathscr{K}$	Set of service areas
l_m	File size for MT m
$M_s^{\mathrm{UL/DL}}$	Maximum user capacity in the uplink/downlink at BS s
$\mathscr{M}_{1s}$	Set of MTs served by pico/femto BS s in the double coverage area
$\mathscr{M}_{2s}$	Set of MTs served by macro BS in the double coverage area
$\mathscr{M}_0$	Set of MTs served by macro BS in the single coverage area
$m_s^{\mathrm{UL/DL}}$	Number of MTs served by BS s in the uplink/downlink
$m_{\mathrm{UL/DL}}$	Number of MTs in the geographical region with uplink/downlink traffic
P_s	Average power consumption of BS s
$q(m_{\mathrm{UL/DL}})$	Steady state probabilities of having $m_{\mathrm{UL/DL}}$ mobile users in the uplink/downlink
$Q(m'_{\mathrm{UL/DL}}\|m_{\mathrm{UL/DL}})$	Transition probabilities of uplink/downlink queues
$R_{\min,m}^{\mathrm{UL/DL}}$	Minimum required data rate by MT m in the uplink/downlink
$R_{m,i,t}^{\mathrm{UL/DL}}$	Number of bits transmitted till time slot $i+1$ for MT m in the uplink/downlink
$\mathscr{S}$	Set of BSs covering the geographical region
$\mathscr{T}$	Set of periods for the slow timescale
X	Vector of the operation mode of all pico/femto BSs in the geographical region
ϵ_m	Upper bound on the call dropping probability
$\lambda_{\mathrm{UL/DL}}$	Call arrival rates (per unit τ) for uplink/downlink mobile users
ω	Duration of fast timescale period
$\rho_{k_s}^{\mathrm{UL/DL}}$	Spatial distributions of the MTs within service area covered by BS s
Δ_s	Slope of the load dependent power consumption for BS s

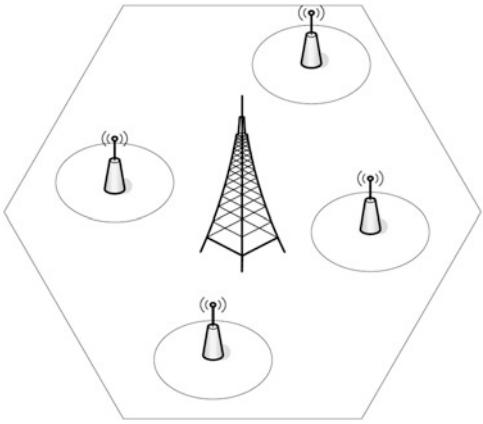

Fig. 11.2 Illustration of the heterogeneous wireless medium [9]

11.3.1.1 Heterogeneous Cellular Network

Consider a geographical region that is covered by a set $\mathscr{S} = \{0, 1, 2, \ldots, S\}$ of BSs where $s = 0$ denotes a macro BS and $s \in \mathscr{S} \setminus \{0\}$ represents small cells (i.e., pico and femto BSs), as shown in Fig. 11.2. A green hybrid solution is considered to power the BSs similar to the model described in [6] where a controller (switch) is utilized to power the BS either via energy harvesting or the grid energy. As a first step of research, in this work, it is assumed that the BS is connected to the grid. Using the insights obtained from this analysis, our future extension will investigate the case when the BS is powered via energy harvesting. The small cells follow a cell-on-edge deployment strategy, which is shown to be more energy efficient than a uniform distribution deployment strategy [27]. Interference mitigation techniques (e.g., enhanced intercell interference coordination (eICIC), adaptive frequency reuse [28] in the downlink, and successive group decoding [29] in the uplink) are adopted for interference avoidance among the macro and pico/femto BSs.

The BSs operate in the frequency division duplex (FDD) mode and the available bandwidths for uplink and downlink users are denoted by B_s^{UL} and B_s^{DL}, respectively, for $s \in \mathscr{S}$. Mobile users can be covered only by the macro BS or both macro and pico/femto BSs. Given the mobile users minimum required data rates and the BS maximum available bandwidth, each BS $s \in \mathscr{S}$ has a maximum user capacity M_s^{UL} and M_s^{DL} for uplink and downlink mobile users, respectively, which can be determined according to the call admission control policies [30]. The mobile user-BS association rules are as follows:

- In the single coverage area (i.e., the area covered solely by the macro BS), MTs are served by the macro BS. The set of MTs that fall under this category are denoted as $\mathscr{M}_0$.
- In double coverage areas (i.e., areas covered by both macro and pico/femto BSs), an MT is served by the active pico/femto BS if the BS has not reached its capacity limitation. The rationale behind this is the short transmission range between the

MT and the pico/femto BS compared with the distance to a macro BS, which leads to a lower transmission power consumption. The set of MTs that fall under this category are denoted as $\mathscr{M}_{1s}$.

- In double coverage areas where active pico/femto BSs have exceeded their capacity limitations, MTs are associated with the macro BS. The set of MTs which are in the coverage area of BS s that fall under this category are denoted as $\mathscr{M}_{2s}$.

Denote m_s^{UL} and m_s^{DL} as the number of MTs served by BS $s \in \mathscr{S}$ in the uplink and downlink, respectively, and $m_s^{\mathrm{UL}} \leq M_s^{\mathrm{UL}}$ and $m_s^{\mathrm{DL}} \leq M_s^{\mathrm{DL}}$. All mobile users are legitimate subscribers of the network (i.e., malicious users are not assumed). Each BS $s \in \mathscr{S}$ equally distributes its available bandwidth among its associated MTs. Let $m_{\mathrm{UL}} = \sum_s m_s^{\mathrm{UL}}$ and $m_{\mathrm{DL}} = \sum_s m_s^{\mathrm{DL}}$ denote the number of MTs in the geographical region with uplink and downlink traffic, respectively.

Let D_s represent the separation distance between the macro BS and the pico/femto BS $s \in \mathscr{S} \setminus \{0\}$. Denote H_s as the height of BS $s \in \mathscr{S}$. Let G_s^{UL} and G_s^{DL} denote the average channel power gain for the uplink and downlink mobile users served by BS $s \in \mathscr{S}$. The average channel power gains are characterized by the path loss ($G_s^{\mathrm{UL/DL}} = 10^{-\mathrm{PL[dB]}/10}$), and PL[dB] is given by

$$\mathrm{PL[dB]} = C_1 \log_{10}\left(d[\mathrm{m}]\right) + C_2 + C_3 \log_{10}\left(\frac{f_c[\mathrm{GHz}]}{5}\right), \tag{11.1}$$

where d denotes the average distance between the transmitter and receiver, f_c represents the carrier frequency, and C_1, C_2, and C_3 are model dependent constants. The average path loss is determined based on the MT location within the geographical region. Specifically, we use the results in [31] to estimate the average distance between a BS and an MT located in a specific coverage region, as follows:

- For MTs in the single coverage area that are served by the macro BS (i.e., $m \in \mathscr{M}_0$), the average distance d in (11.1) is calculated as the diagonal distance between the BS antenna (with height H_0) and an MT located at the coverage region. The average ground distance of an MT in a coverage region is calculated using the probability density function (PDF) derived in [31].
- For MTs in the double coverage area that are served by the pico/femto BS (i.e., $m \in \mathscr{M}_{1s}$), the distance d in (11.1) is calculated similarly to the above framework but using the pico/femto BS height and the average ground distance between pico/femto BS and the MT.
- For MTs in the double coverage area that are served by the macro BS (i.e., $m \in \mathscr{M}_{2s}$), the distance d in (11.1) is calculated as the diagonal distance using the height of the macro BS, while the average ground distance is dominated by the ground distance between the macro BS and the pico/femto BS.

Define x_s as a binary decision variable that represents the operation mode of the pico/femto BS $s \in \mathscr{S}$ where $x_s = 1$ indicates an active BS while $x_s = 0$ denotes a sleep BS. Let $\mathbf{X} = [x_1 x_2 \ldots x_S]$ be the operation mode vector of all pico/femto BSs in the geographical region. The macro BS is always active to provide radio coverage within the geographical region.

11.3.1.2 Call Traffic Load Fluctuations

The call traffic load in the geographical region exhibits temporal and spatial fluctuations as follows.

11.3.1.3 Temporal Traffic Fluctuations

Time is divided into slow and fast timescales to capture the long and short term temporal traffic fluctuations at both BS operation and MT association level, respectively.

11.3.1.4 Long-Term Temporal Traffic Fluctuations

At the slow timescale (in scale of hours), time is partitioned into a set of periods $\mathscr{T} = \{1, 2, \ldots, T\}$ with equal duration τ. The set $\mathscr{T}$ covers the 24 h of a day and captures the temporal variations in the call arrival rates (per unit τ). Let $\lambda_{\mathrm{UL}}(t)$ and $\lambda_{\mathrm{DL}}(t)$ represent the call arrival rates (per unit τ) for uplink and downlink mobile users, which are fixed during each period $t \in \mathscr{T}$ and vary from one period to another. The user arrival rates exhibit peak values by mid-day and low values at early morning and late night [2]. The values of $\lambda_{\mathrm{UL}}(t)$ and $\lambda_{\mathrm{DL}}(t)$ can be inferred from the historical traffic load patterns of the geographical region [2].

11.3.1.5 Short-Term Temporal Traffic Fluctuations

In order to determine the average MT dropping probability and uplink and downlink throughput within a specific long-term period, short-term traffic fluctuations are introduced. Each period $t \in \mathscr{T}$ is further partitioned into the set of periods $\mathscr{I} = \{1, 2, \ldots, I\}$ with equal duration $\omega = \lceil \tau / I \rceil$ and it represents the fast timescale (in scale of minutes) and captures the variations in the number of mobile users that are being served in the geographical region in the uplink and downlink. Specifically, let $m_{\mathrm{UL}}(i, t)$ and $m_{\mathrm{DL}}(i, t)$ represent the number of mobile users being served in the geographical region in the uplink and downlink during period $i \in \mathscr{I}$ of period $t \in \mathscr{T}$, respectively. Both $m_{\mathrm{UL}}(i, t)$ and $m_{\mathrm{DL}}(i, t)$ are fixed during the same $i \in \mathscr{I}$ and vary from one period i to another according to the users arrival and service rates. During period $i \in \mathscr{I}$, the mobile user arrivals in the uplink and downlink follow Bernoulli processes with probabilities $\eta_{\mathrm{UL}}(t) = \lambda_{\mathrm{UL}}(t)\omega/\tau$ and $\eta_{\mathrm{DL}}(t) = \lambda_{\mathrm{DL}}(t)\omega/\tau$, respectively [32]. Hence, the overall arrival process is memoryless and has a geometric distribution. The departure process depends on the taken actions, and hence, it does not follow a known distribution. Hence, we approximate the service process by a geometric distribution for mathematical tractability with service rates $\nu_{\mathrm{UL}}(i, t)$ and $\nu_{\mathrm{DL}}(i, t)$ (to be calculated in Sect. 11.3.2 as a function of the number of MTs served in the uplink/downlink, the MT/BS transmission

power, and the file size) [32]. The maximum number of MTs that can be served in the geographical region in the uplink and downlink (M_{UL} and M_{DL}, respectively) depends on the BS operation mode, i.e., $M_{\mathrm{UL}} = \sum_{s\in\mathscr{S}} x_s M_s^{\mathrm{UL}}$ and $M_{\mathrm{DL}} = \sum_{s\in\mathscr{S}} x_s M_s^{\mathrm{DL}}$. Consequently, the short-term temporal fluctuations in the uplink and downlink can be described by $Geo/Geo/M_{\mathrm{UL}}/M_{\mathrm{UL}}$ and $Geo/Geo/M_{\mathrm{DL}}/M_{\mathrm{DL}}$ queues, respectively. The conditional probability that a certain number of users $\tilde{m}_{\mathrm{UL}}$ has completed their uplink service given the number of users in the queue $\breve{m}_{\mathrm{UL}}$ is denoted by $c(\tilde{m}_{\mathrm{UL}}|\breve{m}_{\mathrm{UL}})$ and takes the expression [33]

$$c(\tilde{m}_{\mathrm{UL}}|\breve{m}_{\mathrm{UL}}) = \frac{\breve{m}_{\mathrm{UL}}!}{\tilde{m}_{\mathrm{UL}}!\,(\breve{m}_{\mathrm{UL}}-l)!}\nu_{\mathrm{UL}}^{\tilde{m}_{\mathrm{UL}}}(1-\nu_{\mathrm{UL}})^{\breve{m}_{\mathrm{UL}}-\tilde{m}_{\mathrm{UL}}}. \tag{11.2}$$

Define $q(m_{\mathrm{UL}}(i,t))$ and $q(m_{\mathrm{DL}}(i,t))$ as the steady state probabilities of having $m_{\mathrm{UL}}(i,t)$ and $m_{\mathrm{DL}}(i,t)$ mobile users in the uplink and downlink, respectively, during period $i \in \mathscr{I}$ in $t \in \mathscr{T}$. In (11.3) and for brevity, we refer to $m_{\mathrm{UL}}(i,t)$ and $m_{\mathrm{DL}}(i,t)$ by m_{UL} and m_{DL}, respectively. The balance equations for the uplink queue, for a given i and t, are

$$\begin{aligned}
\eta_{\mathrm{UL}} q(0) &= \sum_{l=1}^{M_{\mathrm{UL}}} q(l)(1-\eta_{\mathrm{UL}})c_{\mathrm{UL}}(l|l) \\
q(m_{\mathrm{UL}}) &= \sum_{l=m_{\mathrm{UL}}}^{M_{\mathrm{UL}}} q(l)[(1-\eta_{\mathrm{UL}})c_{\mathrm{UL}}(l-m_{\mathrm{UL}}|l) + \eta_{\mathrm{UL}}c_{\mathrm{UL}}(l+1-m_{\mathrm{UL}}|l)] \\
&\quad + q(m_{\mathrm{UL}}-1)\eta_{\mathrm{UL}}c_{\mathrm{UL}}(0|m_{\mathrm{UL}}-1), 1 \le m_{\mathrm{UL}} \le M_{\mathrm{UL}}-1 \\
q(M_{\mathrm{UL}}) &= q(M_{\mathrm{UL}}-1)\eta_{\mathrm{UL}}c_{\mathrm{UL}}(0|M_{\mathrm{UL}}-1) + q(M_{\mathrm{UL}})[\eta_{\mathrm{UL}}c_{\mathrm{UL}}(1|M_{\mathrm{UL}}) \\
&\quad + c_{\mathrm{UL}}(0|M_{\mathrm{UL}})].
\end{aligned} \tag{11.3}$$

Similar equations can be written for the downlink queue. Given the balance equations, the steady state probabilities $q(m_{\mathrm{UL}}(i,t))$ and $q(m_{\mathrm{DL}}(i,t))$ can be derived and the transition probabilities $Q(m_{\mathrm{UL}}(i+1,t)|m_{\mathrm{UL}}(i,t))$ and $Q(m_{\mathrm{DL}}(i+1,t)|m_{\mathrm{DL}}(i,t))$ can be found by solving a set of linear equations.

11.3.1.6 Spatial Traffic Fluctuations

Due to the overlapping coverage from macro and pico/femto BSs, the geographical region is partitioned into a set of service areas $\mathscr{K} = \{k_0, k_1, \ldots, k_S\}$, where k_0 represents the single coverage area (i.e., region covered only by macro BS) and k_s represents the double coverage area (i.e., region covered by both pico/femto BS s and the macro BS). The spatial distributions of the MTs within different service areas are captured using the probability mass functions (PMFs) $\rho_{k_0}^{\mathrm{UL}}$ and $\rho_{k_0}^{\mathrm{DL}}$ for the single coverage area and $\rho_{k_s}^{\mathrm{UL}}$ and $\rho_{k_s}^{\mathrm{DL}}$ for the double coverage areas, for uplink and downlink mobile users, respectively. Specifically, $\rho_{k_s}^{\mathrm{UL}}$ and $\rho_{k_s}^{\mathrm{DL}}$ yield the fraction

of uplink and downlink mobile users in the proximity of pico/femto BS s (i.e., in the double coverage area of pico/femto BS s and the macro BS) and $\rho_{k_0}^{\mathrm{UL}} = 1 - \sum_{s\in\mathscr{S}} \rho_{k_s}^{\mathrm{UL}}$ and $\rho_{k_0}^{\mathrm{DL}} = 1 - \sum_{s\in\mathscr{S}} \rho_{k_s}^{\mathrm{DL}}$ represent the fraction of users in the single coverage area.

11.3.1.7 Power Consumption Models

This subsection describes the power consumption models for the BSs (to serve the downlink traffic) and the MTs (to support the uplink traffic).

11.3.1.8 BS Power Consumption

The average power consumption of BS $s \in \mathscr{S}$ in the downlink depends on its mode of operation, and is given by Auer et al. [34]

$$P_s = \begin{cases} P_{\mathrm{F},s} + \Delta_s P_{\mathrm{tx},s}, & x_s = 1 \\ P_{\mathrm{L},s}, & x_s = 0, \end{cases} \tag{11.4}$$

where $P_{\mathrm{F},s}$ is the BS fixed power consumption that accounts for the power supply, cooling, backhaul, and other circuits, Δ_s represents the slope of the load dependent power consumption, $P_{\mathrm{tx},s}$ denotes the BS average transmission power, and $P_{\mathrm{L},s}$ stands for the BS sleep power. The BS transmission power is chosen from a discrete set of actions $\mathscr{P}_{\mathrm{tx},s} = \{P_{\min,s}, P_{1,s}, \ldots, P_{\max,s}\}$, which represent V_s power levels uniformly distributed in the range $[P_{\min,s}, P_{\max,s}]$. For a given period $t \in \mathscr{T}$, the selected BS transmission power action at time slot $i \in \mathscr{I}$ within period $t \in \mathscr{T}$ is denoted as $P_{\mathrm{tx},s}(i,t)$.

Let $\mathbf{P}_{its}$ represent a vector of transmission power actions adopted by BS s over time slots $1, 2, \ldots, i \in \mathscr{I}$ within period $t \in \mathscr{T}$, and which is assumed to have a PMF $f_{\mathbf{P}_{its}}(\mathbf{p}_{its})$. The PMF $f_{\mathbf{P}_{its}}(\mathbf{p}_{its})$ can be inferred from system dynamics as in [35].

11.3.1.9 MT Power Consumption

Each MT $m \in \mathscr{M}_0, \mathscr{M}_{1s}$, or $\mathscr{M}_{2s}$ with uplink traffic communicates with a macro or pico/femto BS using transmission power $P_{\mathrm{tx},m}$. Denote ζ as the transmission power amplifier efficiency. The MT circuit power consumption scales with the uplink achieved throughput $R_m(i,t)$ [36]. Hence, the overall power consumption of MT m is given by

$$P_m(i,t) = \frac{P_{\mathrm{tx},m}(i,t)}{\zeta} + \mu_m + \beta_m R_m(i,t), \tag{11.5}$$

where μ_m and β_m are two constants, measured in Watts and Watts per bit per second.

The MT transmission power is chosen from a discrete set of actions $\mathscr{P}_{\text{tx},m} = \{P_{\min,m}, P_{1,m}, \ldots, P_{\max,m}\}$, which represent V_m power levels uniformly distributed in the range $[P_{\min,m}, P_{\max,m}]$. For a given period $t \in \mathscr{T}$, the selected MT transmission power action at time slot $i \in \mathscr{I}$ within period $t \in \mathscr{T}$ is denoted as $P_{\text{tx},m}(i,t)$.

Let $\mathbf{P}_{itm}$ represent the vector of transmission power actions adopted by MT m over time slots $1, 2, \ldots, i \in \mathscr{I}$ within period $t \in \mathscr{T}$, which is also assumed to follow a PMF $f_{\mathbf{P}_{itm}}(\mathbf{p}_{itm})$. The PMF $f_{\mathbf{P}_{itm}}(\mathbf{p}_{itm})$ can be inferred from the system dynamics as in [35].

The initial available energy e_m at MT m is a random variable that follows a PDF $f_{E_m}(e_m)$, which can be inferred from behavioral studies as in [37]. The initial energy random variable takes a value within the range $[E_{\min}, E_{\max}]$. For a given MT $m \in \mathscr{M}_0, \mathscr{M}_{1s}$ or $\mathscr{M}_{2s}$ at a given period $t \in \mathscr{T}$, the energy consumed at time slot $i \in \mathscr{I}$ is given by $E^{\text{c}}_m(i,t) = P_m(i,t)\omega$. The MT energy consumption till time slot $i+1$ is given by $E^{\text{c}}_{i,m}(t) = \sum_{j=1}^{i} E^{\text{c}}_m(j,t)$.

11.3.1.10 QoS Guarantee

Mobile users request service for data calls, either in the uplink or the downlink (i.e., file uploading or file downloading). For MT $m \in \mathscr{M}_0, \mathscr{M}_{1s}$, or $\mathscr{M}_{2s}$, the file size l_m (in bits) is a random variable that follows a hyper-exponential distribution given by [30]

$$f_{L_m}(l_m) = \frac{a_m}{a_m+1}\frac{a_m}{\bar{L}_m}\exp\left(-\frac{a_m l_m}{\bar{L}_m}\right) + \frac{1}{a_m+1}\frac{1}{a_m\bar{L}_m}\exp\left(-\frac{l_m}{a_m\bar{L}_m}\right), \quad (11.6)$$

where $a_m \geq 1$ is a constant, $l_m \geq 0$, and $\bar{L}_m$ denotes the average file size.

11.3.1.11 Uplink Target QoS

Two QoS metrics are defined for the uplink users:

- Minimum required throughput: Each mobile user requires a minimum uplink throughput $R^{\text{UL}}_{\min,m}$. For an MT associated with BS s with m^{UL}_s uplink mobile users, the achieved uplink throughput at each time slot $i \in \mathscr{I}$ within period $t \in \mathscr{T}$ until file transmission completion given the MT uplink transmission power should satisfy

$$R^{\text{UL}}_m(i,t) = \frac{B^{\text{UL}}_s}{m^{\text{UL}}_s(i,t)}\log_2\left(1 + \frac{P_{\text{tx},m}(i,t)G^{\text{UL}}_s}{N_0\frac{B^{\text{UL}}_s}{m^{\text{UL}}_s(i,t)}}\right) \geq R^{\text{UL}}_{\min,m}, \quad (11.7)$$

where N_0 denotes the one-sided noise power spectral density and (11.7) follows Shannon's formula. The number of bits transmitted at time slot i is given by $R_m^{\mathrm{UL}}(i,t)\omega$ and the number of bits transmitted till time slot $i+1$ is represented by $R_{m,i,t}^{\mathrm{UL}} = \sum_{j=1}^{i} R_m^{\mathrm{UL}}(j,t)\omega$.

- Maximum dropping probability: It is required not to violate an upper bound on the call dropping probability ϵ_m due to depletion of MT batteries before transmission completion of their files. Such an upper bound is specified by the network operator in the network design stage. The trapping energy $E_{\mathrm{trp},m}(i,t)$ is defined as the minimum required energy available at the MT in order to satisfy the minimum required uplink throughput $R_{\mathrm{min},m}^{\mathrm{UL}}$. Using Shannon's formula, $E_{\mathrm{trp},m}(i,t)$ is given by

$$E_{\mathrm{trp},m}(i,t) = \frac{N_0 B_s^{\mathrm{UL}}}{m_s^{\mathrm{UL}}(i,t)} \frac{1}{G_s^{\mathrm{UL}}} \left(2^{\frac{m_s^{\mathrm{UL}}(i,t) R_{\mathrm{min},m}^{\mathrm{UL}}}{B_s^{\mathrm{UL}}}} - 1 \right) \omega. \tag{11.8}$$

Before file transmission completion, if the available energy at the battery of MT m is below $E_{\mathrm{trp},m}(i,t)$, the call is dropped.

11.3.1.12 Downlink Target QoS

Each mobile user requires a minimum downlink throughput $R_{\mathrm{min},m}^{\mathrm{DL}}$. For an MT associated with BS s with $m_s^{\mathrm{DL}}(i,t)$ downlink mobile users, the achieved downlink throughput at each time slot $i \in \mathscr{I}$ until file transmission completion given the BS downlink transmission power should satisfy the condition

$$R_m^{\mathrm{DL}}(i,t) = \frac{B_s^{\mathrm{UL}}}{m_s^{\mathrm{DL}}(i,t)} \log_2 \left(1 + \frac{P_{\mathrm{tx},s}(i,t) G_s^{\mathrm{DL}}}{N_0 \frac{B_s^{\mathrm{DL}}}{m_s^{\mathrm{DL}}(i,t)}} \right) \geq R_{\mathrm{min},m}^{\mathrm{DL}}. \tag{11.9}$$

In the downlink, it is assumed that the MT consumed power for file download is negligible since data transmission is performed by the BS, and hence, the call will not be dropped and the MT continues the file download as long as there is some energy E_{min} available at the MT battery. Such an assumption is reasonable when compared with the uplink energy consumption where the MT consumes high transmission power for file uploading. The number of bits transmitted at time slot i is given by $R_m^{\mathrm{DL}}(i,t)\omega$ and the number of bits transmitted till time slot $i+1$ is represented by $R_{m,i,t}^{\mathrm{DL}} = \sum_{j=1}^{i} R_m^{\mathrm{DL}}(j,t)\omega$.

11.3.2 Derivation of Service Process Parameters

The system short-term temporal fluctuations have been modeled in Sect. 11.3.1 as $Geo/Geo/M_{\mathrm{DL}}/M_{\mathrm{DL}}$ and $Geo/Geo/M_{\mathrm{UL}}/M_{\mathrm{UL}}$ queues for the downlink and uplink systems, respectively. The user arrivals follow a discrete geometric distribution and are assumed to depart following a similar model. In this subsection, we first derive the service rate to calculate the transition probability of the queue states using the solution of (11.3). The service process parameters are determined while taking into account the BS behavior (in terms of its mode of operation and available radio resources) and the mobile user behavior (in terms of file length, required throughput, and the MT available energy). The main aspect of data calls is the impact of allocated resources on the call presence in the system [38]. The allocated resources (e.g., transmission power) to a data call affect the call throughput, and hence, its duration, which also impacts energy consumption. Hence, the derived service rate is a function of the current number of users and the selected transmission power such that the transition probability is a function of the current queue state and the taken action.

11.3.2.1 Downlink Service Process Parameters

In the downlink, the mobile user leaves the system only when file download is complete. Hence, a mobile user remains in service at BS s during time slot $i+1$ with probability $\Pr(l_m > R^{\mathrm{DL}}_{m,i,t}|\mathbf{p}_{its})$ using BS s transmission power vector $\mathbf{p}_{its}$. Denote $f_{I,\mathbf{P}_{its}}(i|\mathbf{p}_{its})$ as the conditional PMF that MT m remains in service at BS s during time slot $i+1$ when the BS transmission power vector is $\mathbf{p}_{its}$ over time slots $1,2,\ldots,i$ during period $t \in \mathscr{T}$. Consequently, we have

$$f_{I,\mathbf{P}_{its}}(i|\mathbf{p}_{its}) = \Pr(l_m > R^{\mathrm{DL}}_{m,i,t}|\mathbf{p}_{its}) = 1 - \int_0^{R^{\mathrm{DL}}_{m,i,t}} f_{L_m}(l_m)dl_m. \tag{11.10}$$

Using the hyper-exponential distribution of the file size l_m and the distribution of $\mathbf{p}_{its}$, we have

$$f_{I,\mathbf{P}_{its}}(i,\mathbf{p}_{its}) = f_{\mathbf{P}_{its}}(\mathbf{p}_{its}) \left\{ \frac{a_m}{a_m+1} \exp\left(-\frac{a_m R^{\mathrm{DL}}_{m,i,t}}{\bar{L}_m}\right) + \frac{1}{a_m+1} \exp\left(-\frac{R^{\mathrm{DL}}_{m,i,t}}{a_m \bar{L}_m}\right) \right\}, \tag{11.11}$$

Let $\nu_{s,\mathrm{DL}}(m^{\mathrm{DL}}_s(i,t), P_{\mathrm{tx},s}(i+1,t))$ represent the exit probability (service rate), which denotes the probability that a mobile user exits the system at time slot $i+1$ if $m^{\mathrm{DL}}_s(i,t)$ users are being served by BS s in the downlink and the BS transmission power is $P_{\mathrm{tx},s}(i+1,t)$. The probability of a complete file download is given by

$$\Pr(R^{\mathrm{DL}}_{m,i,t} < l_m \le R^{\mathrm{DL}}_{m,i,t} + R^{\mathrm{DL}}_m(i+1,t) | R^{\mathrm{DL}}_{m,i,t} < l_m, P_{\mathrm{tx},s}(i+1,t))$$

$$= \sum_{i} \sum_{\mathbf{p}_{its}} \left\{ \frac{\int_{R^{\mathrm{DL}}_{m,i,t}}^{R^{\mathrm{DL}}_{m,i,t}+R^{\mathrm{DL}}_{m}(i+1,t)} f_{L_m}(l_m) dl_m}{\int_{R^{\mathrm{DL}}_{m,i,t}}^{\infty} f_{L_m}(l_m) dl_m} . f_{I,\mathbf{P}_{its}}(i, \mathbf{p}_{its}) \right\}. \tag{11.12}$$

In the downlink, the mobile user exits the system when the file download is complete. Following (11.11) and (11.12), the exit probability (service rate) $\nu_{s,\mathrm{DL}}(m^{\mathrm{DL}}_{s}(i,t), P_{\mathrm{tx},s}(i+1,t))$ can be expressed as

$$\nu_{s,\mathrm{DL}}(m^{\mathrm{DL}}_{s}, P_{\mathrm{tx},s}(i+1,t)) = \sum_{i} \sum_{\mathbf{p}_{its}} \left\{ f_{I,\mathbf{P}_{its}}(i, \mathbf{p}_{its}) \cdot \frac{N}{\frac{a_m}{a_m+1} \exp\left(-\frac{a_m R^{\mathrm{DL}}_{m,i,t}}{\bar{L}_m}\right) + \frac{1}{a_m+1} \exp\left(-\frac{R^{\mathrm{DL}}_{m,i,t}}{a_m \bar{L}_m}\right)} \right\}, \tag{11.13}$$

where

$$N = \left(\frac{a_m}{a_m+1} \left(\exp\left(-\frac{a_m R^{\mathrm{DL}}_{m,i,t}}{\bar{L}_m}\right) - \exp\left(-\frac{a_m (R^{\mathrm{DL}}_{m,i,t} + R^{\mathrm{DL}}_{m}(i+1,t))}{\bar{L}_m}\right) \right) + \frac{1}{a_m+1} \cdot \left(\exp\left(-\frac{R^{\mathrm{DL}}_{m,i,t}}{a_m \bar{L}_m}\right) - \exp\left(-\frac{\left(R^{\mathrm{DL}}_{m,i,t} + R^{\mathrm{DL}}_{m}(i+1,t)\right)}{a_m \bar{L}_m}\right) \right) \right). \tag{11.14}$$

For a given action vector $\mathbf{p}_{i+1,t} = P_{\mathrm{tx},0}(i+1,t), \ldots, P_{\mathrm{tx},s}(i+1,t), \ldots P_{\mathrm{tx},S}(i+1,t)$, the average downlink service rate in the geographical region is given by

$$\nu_{\mathrm{DL}}(m_{\mathrm{DL}}, \mathbf{p}_{i+1,t}) = \sum_{s} \rho^{\mathrm{DL}}_{k_s} \nu_{s,\mathrm{DL}}(m^{\mathrm{DL}}_{s}(i,t), P_{\mathrm{tx},s}(i+1,t)). \tag{11.15}$$

11.3.2.2 Uplink Service Process Parameters

In the uplink, the mobile user leaves the system based on which event occurs first: file upload is complete or due to MT battery depletion which leads to call dropping. Following (11.6), the conditional probability that file upload is not complete can be expressed as

$$\Pr(R^{\mathrm{UL}}_{m,i,t} < l_m | \mathbf{p}_{itm}) = \frac{a_m}{a_m+1} \exp\left(-\frac{a_m R^{\mathrm{UL}}_{m,i,t}}{\bar{L}_m}\right) + \frac{1}{a_m+1} \exp\left(-\frac{R^{\mathrm{UL}}_{m,i,t}}{a_m \bar{L}_m}\right). \tag{11.16}$$

On the other hand, the conditional probability that the MT battery is not depleted and can support the required QoS for $i+1$ can be expressed as

$$\Pr(\text{MT battery can hold for } i+1|\mathbf{p}_{itm}) = \begin{cases} 1, & E^{\mathrm{c}}_{i,m}(t) + E_{\mathrm{trp},m}(i,t) \le E_{\min} \\ 1 - F_{E_m}(E^{\mathrm{c}}_{i,m}(t) + E_{\mathrm{trp},m}(i,t))), & \\ & E_{\min} < E^{\mathrm{c}}_{i,m}(t) + E_{\mathrm{trp},m}(i,t) < E_{\max}, \\ 0, & E^{\mathrm{c}}_{i,m}(t) + E_{\mathrm{trp},m}(i,t) \ge E_{\max}, \end{cases} \tag{11.17}$$

where $F_{E_m}(e_m)$ is the cumulative density function of the initial available energy at MT m. Using (11.16) and (11.17), we have

$$f_{I,\mathbf{p}_{itm}}(i,\mathbf{p}_{itm}) = f_{\mathbf{p}_{itm}}(\mathbf{p}_{itm}) \cdot \Pr(R^{\mathrm{UL}}_{m,i,t} < l_m|\mathbf{p}_{itm}) \cdot \Pr(\text{MT battery can hold for } i+1|\mathbf{p}_{itm}). \tag{11.18}$$

The probability of call dropping in time slot $i+1$ if m^{UL}_s users are being served by BS s in the uplink and the MT transmission power is $P_{\mathrm{tx},m}(i+1,t)$ (and hence, the consumed energy is $E^{\mathrm{c}}_m(i+1,t)$) is expressed as

$$P_D(m^{\mathrm{UL}}_s, P_{\mathrm{tx},m}(i+1,t)) = \begin{cases} \sum_i \sum_{\mathbf{p}_{itm}} f_{I,\mathbf{p}_{itm}}(i,\mathbf{p}_{itm}) \cdot A(i,\mathbf{p}_{itm}), & \\ \quad E^{\mathrm{c}}_{i,m}(t) + E^{\mathrm{c}}_m(i+1,t) \ge E_{\min} + E_{\mathrm{trp},m}(i,t), & \\ 0, \quad E^{\mathrm{c}}_{i,m}(t) + E^{\mathrm{c}}_m(i+1,t) < E_{\min} + E_{\mathrm{trp},m}(i,t), & \end{cases} \tag{11.19}$$

where

$$A(i,\mathbf{p}_{itm}) = \frac{F_{E_m}(E^{\mathrm{c}}_{i,m}(t) + E^{\mathrm{c}}_m(i+1,t) + E_{\mathrm{trp},m}(i,t))}{1 - F_{E_m}(E^{\mathrm{c}}_{i,m}(t) + E_{\mathrm{trp},m}(i,t))} - \frac{F_{E_m}(E^{\mathrm{c}}_{i,m}(t) + E_{\mathrm{trp},m}(i,t))}{1 - F_{E_m}(E^{\mathrm{c}}_{i,m}(t) + E_{\mathrm{trp},m}(i,t))}. \tag{11.20}$$

For a given action vector $\mathbf{p}_{i+1} = P_{\mathrm{tx},0}(i+1,t), \ldots, P_{\mathrm{tx},m_{\mathrm{UL}}}(i+1,t)$, the average call dropping probability in the geographical region is given by

$$P_D(m_{\mathrm{UL}}, \mathbf{p}_{i+1}) = \sum_s \rho^{\mathrm{UL}}_{k_s} P_D(m^{\mathrm{UL}}_s, p(i+1,m)). \tag{11.21}$$

The uplink service rate $\nu_{s,\mathrm{UL}}(m^{\mathrm{UL}}_s, P_{\mathrm{tx},m}(i+1,t))$ represents the probability that a mobile user exits the system if m^{UL}_s user exists in the uplink and the MT transmits

with power $P_{\text{tx},m}(i+1,t)$ during time slot $i+1$, and it is expressed as follows:

$$\nu_{s,\text{UL}}(m_s^{\text{UL}}, P_{\text{tx},m}(i+1,t)) = \Pr\big(\text{File upload completion or MT battery depletion} | P_{\text{tx},m}(i+1,t)\big), \quad (11.22)$$

where the file upload completion event can be calculated similar to the downlink case in (11.12). Consequently, the uplink service rate is given by

$$\nu_{s,\text{UL}}(m_s^{\text{UL}}, P_{\text{tx},m}(i+1,t)) = \begin{cases} \sum_i \sum_{\mathbf{p}_{itm}} f_{I,\mathbf{P}_{itm}}(i,\mathbf{p}_{itm}) \cdot \{B + A - B \cdot A\}, \\ \quad E_{i,m}^{\text{c}}(t) + E_m^{\text{c}}(i+1,t) \geq E_{\min} + E_{\text{trp},m}(i,t), \\ \sum_i \sum_{\mathbf{p}_{itm}} f_{I,\mathbf{P}_{itm}}(i,\mathbf{p}_{itm}) \cdot \{B\}, \\ \quad E_{i,m}^{\text{c}}(t) + E_m^{\text{c}}(i+1,t) < E_{\min} + E_{\text{trp},m}(i,t), \end{cases} \quad (11.23)$$

where

$$B(i,\mathbf{p}_{itm}) = \frac{a_m}{a_m+1}\left(\exp\left(-\frac{a_m R_{m,i,t}^{\text{UL}}}{\bar{L}_m}\right) - \exp\left(-\frac{a_m(R_{m,i,t}^{\text{UL}} + R_m^{\text{UL}}(i+1,t))}{\bar{L}_m}\right)\right.$$
$$\left. + \frac{1}{a_m+1} \cdot \left(\exp\left(-\frac{R_{m,i,t}^{\text{UL}}}{a_m \bar{L}_m}\right) - \exp\left(-\frac{(R_{m,i,t}^{\text{UL}} + R_m^{\text{UL}}(i+1,t))}{a_m \bar{L}_m}\right)\right)\right), \quad (11.24)$$

and $A(i,\mathbf{p}_{itm})$ is given in (11.20).

The average service rate in the geographical region is given by

$$\nu_{\text{UL}}(m_{\text{UL}}, \mathbf{p}_{i+1}) = \sum_s \rho_{k_s}^{\text{UL}} \nu_{s,\text{UL}}(m_s^{\text{UL}}, p(i+1,m)). \quad (11.25)$$

11.3.3 Performance Evaluation

This subsection presents numerical results for the uplink QoS performance under dynamic planning. Two simulation set-ups are implemented. The first is used in Fig. 11.3 and it assumes an overlapping coverage between a macro BS and a pico BS with $\eta_{\text{UL}} = 0.3$ and $\rho_{k_1}^{\text{UL}} = 0.6$. Here, it is assumed that the pico BS is switched off. The second set-up is used in Fig. 11.4 and it considers an overlapping coverage between a macro BS and two pico BSs with $\eta_{\text{UL}} = 0.3$, and $\rho_{k_0}^{\text{UL}} = 0.4$. Simulation parameters are in Table 11.2. In the following, the low energy level available at MTs resembles a night time scenario where BS switching-off is practical.

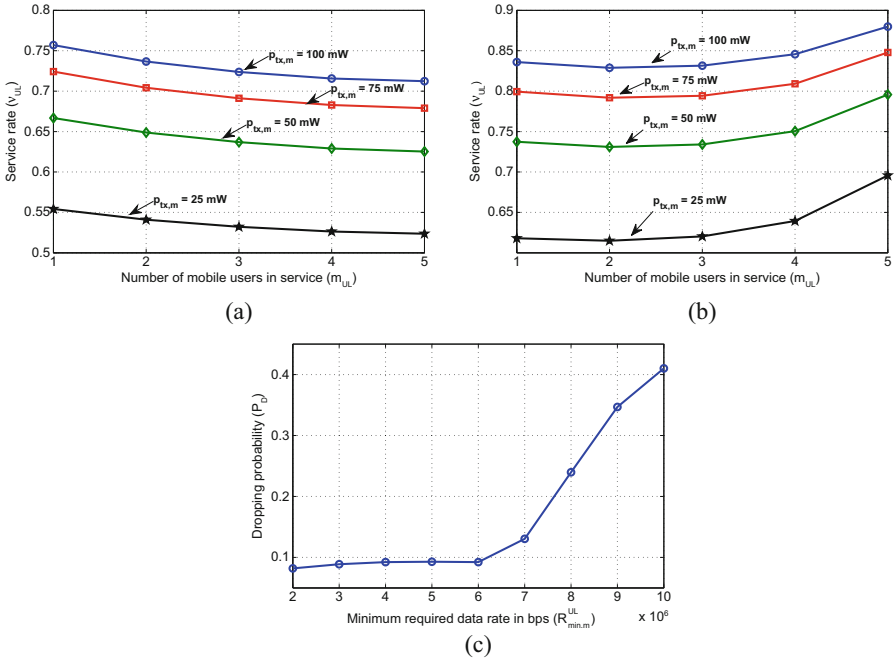

Fig. 11.3 Performance evaluation for the first simulation scenario [9]. (**a**) Service rate ν_{UL} for $E_{\max} = 500\,\mathrm{J}$. (**b**) Service rate ν_{UL} for $E_{\max} = 250\,\mathrm{J}$. (**c**) Call dropping probability for $E_{\max} = 250\,\mathrm{J}$

Table 11.2 Simulation parameters

Parameter	Value	Parameter	Value	Parameter	Value	Parameter	Value
B_0^{UL}	10 MHz	$B_{1,2}^{\mathrm{UL}}$	5 MHz	M_0^{UL}	10	$M_{1,2}^{\mathrm{UL}}$	5
D_1	110 m	D_2	130 m	H_0	100 m	$H_{1,2}$	50 m
C_1	18.7	C_2	46.8	C_3	20	N_0	−174 dBm/Hz
ω	5 min	μ_m	0.05 W	β_m	10^{-10} W/bps	$P_{\max,m}$	0.1 W
$\bar{L}_m$	2 Gbits	a_m	6	ϵ	0.1	$E_{\min}$	10 J

Figure 11.3a shows the service rate ν_{UL} at different transmission power levels for variable number of users being served in the uplink m_{UL} with $E_{\max} = 500\,\mathrm{J}$. Overall, the service rate increases with transmission power level due to faster file upload complete. On the other hand, the service rate decreases with m_{UL} because as the number of mobile users in service increases, the allocated bandwidth per user is decreased, which results in slower file upload complete. Figure 11.3b shows the service rate ν_{UL} at different transmission power levels for variable number of users being served in the uplink m_{UL} with $E_{\max} = 250\,\mathrm{J}$. In this figure, the performance is dominated by call dropping due to the low available energy level at the MT. As the transmission power level increases, the service rate increases either due to

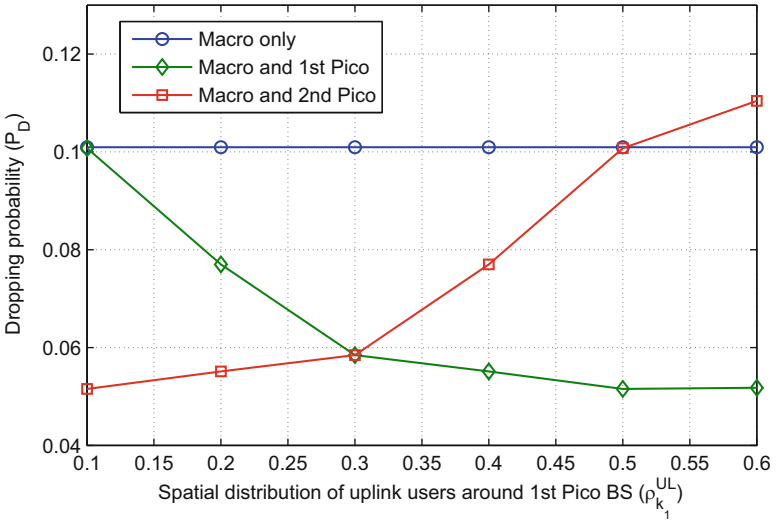

Fig. 11.4 Call dropping probability in the second simulation scenario [9]

file upload complete or faster battery depletion. Also, as the number of mobile users in service increases, the allocated bandwidth per user is decreased, which means slower file upload complete. Due to the low available energy at the MT, call dropping occurs before file upload complete, which results in higher service rate (due to MT battery depletion before file upload complete unlike Fig. 11.3a). Figure 11.3c shows the call dropping probability for variable target throughput with $E_{\max} = 250\,\text{J}$ and $P_{\text{tx},m} = 100\,\text{mW}$. As the required throughput increases, the trapping energy level is increased. Since mobile users are mainly concentrated around the pico BS (which is switched off), they suffer from long transmission distance with the macro BS. Due to the high transmission power, low available energy in MTs, and larger trapping energy level, high call dropping probability (exceeding ϵ) occurs with increased throughput.

Figure 11.4 shows the call dropping probability for variable user spatial distribution $\rho_{k_1}^{\text{UL}}$ with $E_{\max} = 250\,\text{J}$ and $P_{\text{tx},m} = 100\,\text{mW}$. Overall, activating only the macro BS leads to a high call dropping probability, since more users are concentrated around the pico BSs than around the macro BS, and hence, mobile users suffer from long transmission distance that depletes their MT batteries at faster rate. As $\rho_{k_1}^{\text{UL}}$ increases, more users are concentrated around the first pico BS leading to an improved call dropping probability when the macro and first pico BS are activated (unlike the case when the macro and second pico BS are activated).

11.4 Design of a Balanced Dynamic Planning Approach

Simulation results in Sect. 11.3.3 demonstrate that BS switching-off decisions that do not account for the uplink QoS requirements can result in severe service quality degradation. In this section, the derived QoS measures in Sect. 11.3.2 are used to develop dynamic planning approaches that can ensure QoS guarantee for mobile users both in the downlink and uplink.

11.4.1 Two-Timescale Optimal Switching Decision Problem

In this section, the optimal switching decision problem is formulated [7]. We start by formulating the minimization problem of the total average energy consumed by the BSs. The problem is constrained by the various QoS measures as follows:

$$\begin{aligned}
\min_{P_{\text{tx},s}(i,t),P_{\text{tx},m}(i,t),X(t)} \ & \frac{1}{IT}\sum_{i\in\mathscr{I}}\sum_{t\in\mathscr{T}}\sum_{s\in\mathscr{S}} P_s(i,t)\omega \\
\text{s.t.} \quad & R_m^{\text{DL}}(i,t) \geq R_{\text{min},m}^{\text{DL}}, \qquad \forall m,i,t, \\
& R_m^{\text{UL}}(i,t) \geq R_{\text{min},m}^{\text{UL}}, \qquad \forall m,i,t, \\
& P_D(t) \leq \epsilon, \qquad \forall t, \\
& X(t) = [x_1,\ldots x_S], x_s \in \{0,1\}, \qquad \forall t, \\
& P_{\text{tx},s}(i,t) \in \mathscr{P}_{\text{tx},s}, P_{\text{tx},m}(i,t) \in \mathscr{P}_{\text{tx},m}, \qquad \forall s,m,i,t. \qquad (11.26)
\end{aligned}$$

where $X(t)$ is the BS activation vector at the time slot t and $P_D(t)$ represents the value of the expected dropping probability calculated in (11.21) at the time slot t for the optimal transmission powers.

The objective function in (11.26) represents the expected energy consumed by all the BSs. The minimization problem in (11.26) is subject to uplink and downlink QoS in terms of achieved throughput and call dropping probability which reflects the mobile device lifetime in terms of battery energy depletion. The decisions are to select the downlink and uplink transmission powers at each time slot for the fast timescale. Moreover, the vector $X(t)$ is selected at every time slot at the slow timescale for switching the BSs. These decision variables are correlated on time as the evolution of the available number of users follows a geometric distribution. As a result, the problem can be considered as an average reward MDP with finite horizon. The value iteration technique can be optimally used to solve the formulated problem, which is computationally intensive due to employing the back-trace dynamic programming approach as shown in [39].

11.4.2 Feasibility Test-Based Balanced Dynamic Planning Approach

Due to the associated complexity, we split (11.26) into two sub-problems. The first sub-problem specifies the operation mode of the BSs and the second sub-problem determines the uplink and downlink transmission powers. Since the second sub-problem (i.e., determination of optimal transmission powers for an active BS in the downlink and MT in the uplink) has been extensively studied in literature, for example, in [40–43], we focus our attention on this work to specify the BS operation mode while accounting for uplink and downlink QoS requirements. In this section, a sub-optimal framework is proposed based on a feasibility test inspired by the optimal problem formulation for the downlink and uplink [7]. The rationale behind the feasibility test is as follows: activate the minimum number of BSs that can satisfy the target QoS for downlink and uplink mobile users. We will show that such a framework results in an optimal switching decision from the downlink perspective and a sub-optimal switching decision from the uplink perspective. We start with a simple case that investigates if only the macro BS is sufficient to satisfy the required QoS for uplink and downlink mobile users, and hence, all remaining pico/femto BSs can be switched off.

11.4.2.1 Downlink

In the downlink, the user minimum required data rate should be satisfied. To determine a performance upper bound at the beginning of some period $t \in \mathscr{T}$, we let $P_{\mathrm{tx},0}(i,t) = P_{\max,0}$ and $R_m^{\mathrm{DL}}(i,t) = R_{\min,m}^{\mathrm{DL}}\ \forall i \in \mathscr{I}$ and find the corresponding maximum number $\hat{m}_0^{\mathrm{DL}}$ of users that can be supported by the macro BS under these conditions. Two cases can be distinguished:

1. $\hat{m}_0^{\mathrm{DL}} < M_0^{\mathrm{DL}}$: In this case, the minimum required data rate cannot be supported for $\hat{m}_0^{\mathrm{DL}} < m_0^{\mathrm{DL}} \leq M_0^{\mathrm{DL}}$. Hence, we check if there is some probability that $\hat{m}_0^{\mathrm{DL}} < m_0^{\mathrm{DL}} \leq M_0^{\mathrm{DL}}$. Specifically, we determine $\nu_{0,\mathrm{DL}}(m_0^{\mathrm{DL}}, P_{\max,0})$ and use it in the balance equations of the downlink queue to determine the steady state probabilities $q(m_{\mathrm{DL}})$. If $\sum_{m_{\mathrm{DL}}=\hat{m}_0^{\mathrm{DL}}+1}^{M_0^{\mathrm{DL}}} q(m_{\mathrm{DL}}) \leq \varepsilon_{\mathrm{DL}}$ (for a small tolerance $\varepsilon_{\mathrm{DL}}$), then the minimum required data rate is satisfied in the downlink and it is sufficient to activate only the macro BS and switch off all other femto/pico BSs, from the downlink perspective. Otherwise, it is infeasible to activate only the macro BS, from the downlink perspective, since this will violate the minimum required data rate, and consequently, other femto/pico BSs should be activated.
2. $\hat{m}_0^{\mathrm{DL}} \geq M_0^{\mathrm{DL}}$: In this case, the minimum data rate requirement can be satisfied using only the macro BS for any $m_0^{\mathrm{DL}} \leq M_0^{\mathrm{DL}}$.

11.4.2.2 Uplink

In the uplink, two QoS measures should be satisfied which are the user minimum required data rate and the call dropping probability. To determine performance bounds at the beginning of some period $t \in \mathscr{T}$, we let $P_{\text{tx},m}(i,t) = P_{\max,m}$ and $R_m^{\text{UL}}(i,t) = R_{\min,m}^{\text{UL}}$ $\forall i \in \mathscr{I}$ and find the corresponding maximum number $\hat{m}_0^{\text{UL}}$ of users that can be supported by the macro BS under these conditions. Two cases can be distinguished:

1. $\hat{m}_0^{\text{UL}} < M_0^{\text{UL}}$: In this case, the minimum required data rate cannot be supported for $\hat{m}_0^{\text{UL}} < m_0^{\text{UL}} \leq M_0^{\text{UL}}$. Hence, we check if there is some probability that $\hat{m}_0^{\text{UL}} < m_0^{\text{UL}} \leq M_0^{\text{UL}}$. Specifically, we determine $\nu_{0,\text{UL}}(m_0^{\text{UL}}, P_{\max,m})$ and use it in the balance equations of the downlink queue to determine the steady state probabilities $q(m_{\text{UL}})$. If $\sum_{m_{\text{UL}}=\lfloor \hat{m}_0^{\text{UL}} \rfloor+1}^{M_0^{\text{UL}}} q(m_{\text{UL}}) > \varepsilon_{\text{UL}}$ (for a small tolerance ε_{UL}), then it is infeasible to activate only the macro BS, from the uplink perspective, since this will violate the minimum required data rate, and consequently, other femto/pico BSs should be activated. If $\sum_{m_{\text{UL}}=\lfloor \hat{m}_0^{\text{UL}} \rfloor+1}^{M_0^{\text{UL}}} q(m_{\text{UL}}) \leq \varepsilon_{\text{UL}}$, then the minimum required data rate is satisfied, and only the call dropping probability should be checked. Hence, we use (11.19) and (11.21) to find the call dropping probability for $P_{\text{tx},m}(i,t) = P_{\max,m}$ and $\hat{m}_0^{\text{UL}}$. If the call dropping probability is also satisfied, then it is sufficient to activate only the macro BS and switch off all other femto/pico BSs, from the uplink perspective since all constraints are satisfied. On the other hand, if the call dropping probability is not satisfied, it is not clear that it is infeasible to activate only the macro BS. The reason is that maybe there exists another transmission power level than the upper bound $P_{\max,m}$ that does not lead to a high rate of MT battery depletion, and hence, satisfies the call dropping probability along with the other constraints. In this case, we check a lower bound power level $P_{\text{tx},m}(i,t) = \hat{P}_m$ that satisfies $R_m^{\text{UL}}(i,t) = R_{\min,m}^{\text{UL}}$ for $m_0^{\text{UL}} = \lfloor \hat{m}_0^{\text{UL}} \rfloor$. This power level already satisfies the minimum data rate constraint. Hence, we only check the call dropping probability by substituting in (11.19) and (11.21) using $P_{\text{tx},m}(i,t) = \hat{P}_m$ and $\lfloor \hat{m}_0^{\text{UL}} \rfloor$. If the call dropping probability is also satisfied, then it is sufficient to activate only the macro BS and switch off all other femto/pico BSs, from the uplink perspective since all constraints are satisfied. Otherwise, it is not definite if it is insufficient to activate only the macro BS since there might exist another power level inside the range $\hat{P}_m$ and $P_{\max,m}$ that can satisfy all the constraints. In this condition, a conservative decision is to activate other femto/pico BSs besides the macro BS, which represents a sub-optimal decision.
2. $\hat{m}_0^{\text{UL}} \geq M_0^{\text{UL}}$: In this case, the minimum data rate requirement can be satisfied using only the macro BS for any $m_0^{\text{UL}} \leq M_0^{\text{UL}}$. The dropping probability needs to be checked to decide if it is sufficient to activate only the macro BS. Specifically, we determine $\nu_{0,\text{UL}}(m_0^{\text{UL}}, P_{\max,m})$ and use it in the balance equations of the uplink queue to determine the steady state probabilities $q(m_{\text{UL}})$. We substitute in (11.19) and (11.21) to find the call dropping probability for $P_{\text{tx},m}(i,t) = P_{\max,m}$ and

M_0^{UL}. If the call dropping probability is satisfied, then it is sufficient to activate only the macro BS and switch off all other femto/pico BSs, from the uplink perspective, since all constraints are satisfied. On the other hand, if the call dropping probability is not satisfied, it is not definite that it is infeasible to activate only the macro BS. In this condition, we check a lower bound power level $P_{\mathrm{tx},m}(i,t) = \hat{P}_m$ that satisfies $R_m^{\mathrm{UL}}(i,t) = R_{\mathrm{min},m}^{\mathrm{UL}}$ for $m_0^{\mathrm{UL}} = M_0^{\mathrm{UL}}$. If the call dropping probability is satisfied, then it is sufficient to activate only the macro BS and switch off all other femto/pico BSs, from the uplink perspective, since all constraints are satisfied. Otherwise, it is not definite if it is insufficient to activate only the macro BS since there might exist another power level inside the range $\hat{P}_m$ and $P_{\mathrm{max},m}$ that can satisfy all the constraints. In this condition, a conservative decision is to activate other femto/pico BSs besides the macro BS, which is a sub-optimal decision.

Theorem 1. *The feasibility tests result in optimal switching decisions from the downlink perspective and optimal or sub-optimal switching decisions from the uplink perspective.*

Proof. From the downlink perspective, the only QoS requirement is the minimum required data rate of each user. As a result, we let the macro BS operate at its maximum power $P_{\mathrm{max},0}$. From the monotonicity of Shannon's rate equation and for a fixed required rate, maximizing the power maximizes the number of supported users by the macro BS. Hence, the macro BS can optimally support the maximum number of users, which is denoted by $\hat{m}_0^{\mathrm{DL}}$ and it is obtained by solving Shannon's rate equation. Further, two cases need to be studied: (1) If the macro-cell user capacity, M_0^{DL}, is less than or equal to the obtained value $\hat{m}_0^{\mathrm{DL}}$, all the associated users can be supported by data rates larger than or equal to the minimum required data rate. Hence, it is optimal from the downlink perspective to switch on only the macro BS. (2) The second case occurs when M_0^{DL} is greater than $\hat{m}_0^{\mathrm{DL}}$. In this case, we employ queuing analysis to calculate the steady state probabilities of having m user in the system for all m between $\hat{m}_0^{\mathrm{DL}}$ and M_0^{DL}. If the sum of these probabilities is less than a very small threshold $\varepsilon_{\mathrm{DL}}$, then the minimum required rate is achieved as having a larger number of users presents a negligible probability tends to zero. Hence, the optimal decision is activating the macro BS only. Finally, if the sum of the steady state probabilities is greater than the threshold, the system will exhibit a situation where there exists a number of users greater than $\hat{m}_0^{\mathrm{DL}}$, and hence, they will not achieve the minimum required data rate. Then, it is optimal to switch on other small cells.

From the uplink perspective, two performance bounds are investigated, namely an upper bound with $P_{\mathrm{tx},m}(i,t) = P_{\mathrm{max},m}$ and $R_m^{\mathrm{UL}}(i,t) = R_{\mathrm{min},m}^{\mathrm{UL}}$ and a lower bound with $P_{\mathrm{tx},m}(i,t) = \hat{P}_m$ that satisfies $R_m^{\mathrm{UL}}(i,t) = R_{\mathrm{min},m}^{\mathrm{UL}}$ at the nearest lower feasible number of mobile users. The upper bound represents the case where the users operate at the maximum power while achieving the minimum data rate, and hence, the obtained number of users is the maximum number that satisfies these constraints. The lower bound represents the case in which we obtain the transmission power,

$\hat{P}_m$, corresponding to the number of users m such that the minimum data rate constraint is satisfied and the number of users in the system can be greater than m with probability $\varepsilon_{\mathrm{UL}}$ that tends to zero. If either bound satisfies the target QoS, then there exists a power level in the interval $[\hat{P}_m, P_{\max,m}]$ that can satisfy the target QoS and it is feasible to activate only the macro BS, which represents an optimal switching decision. If neither bound satisfies the target QoS, then there could exist a transmission power level inside the range $\hat{P}_m$ and $P_{\max,m}$ that can satisfy the target call dropping probability while supporting the minimum required data rate. Hence, the conservative solution of activating other femto/pico BSs represents a sub-optimal switching decision that preserves the uplink users QoS. The main difference between the downlink and uplink scenarios is the MT battery depletion effect in the uplink and its impact on the target call dropping probability. Hence, while $P_{\mathrm{tx},0}(i,t) = P_{\max,0}$ is a sufficient bound in the downlink case, no bound is sufficient in the uplink scenario to prove the infeasibility of activating only the macro BS (except for the case when $\hat{m}_0^{\mathrm{UL}} < M_0^{\mathrm{UL}}$ and $\sum_{m_{\mathrm{UL}}=\lfloor \hat{m}_0^{\mathrm{UL}} \rfloor+1}^{M_0^{\mathrm{UL}}} q(m_{\mathrm{UL}}) > \varepsilon_{\mathrm{UL}}$ which is infeasible due to the inability to support the target data rate, and represents an optimal switching decision).

If both downlink and uplink feasibility tests are passed, then it is sufficient to activate only the macro BS and switch off all other femto/pico BSs. Otherwise, more femto/pico BSs should be activated. In this case, all possible combinations of $\mathbf{X} = [x_1 x_2 \ldots x_S]$ will be checked where $x_s \in \{0,1\}$ and the set of possible combinations is denoted by $\mathscr{X}$. For each value of the vector $\mathbf{X}$, the association rules mentioned in Sect. 11.3.1 are applied and the downlink and uplink feasibility tests are checked for the active BSs. The value of $\mathbf{X}$ that passes the feasibility tests and incurs the minimum BS energy consumption represents the sub-optimal feasibility test-based switching decision. The proposed sub-optimal framework is described in Algorithm 1. While the feasibility-test-based algorithm has a reduced computational complexity compared with the optimal algorithm, the feasibility test-based algorithm is based on exhaustive search, and hence, presents an exponential time complexity $O(2^S)$, where S is the number of BSs. Consequently, the feasibility test-based algorithm requires intensive computation in a dense small cell deployment scenario.

11.4.3 Heuristic Balanced Dynamic Planning Approach

To further reduce the associated complexity, we propose a heuristic algorithm that iteratively activates the small cells until uplink and downlink QoS parameters are satisfied in an average sense [7]. For the uplink and downlink queues, the average service rate is given as the ratio of the minimum required throughput to the average file length (i.e., $\bar{\nu}_{\mathrm{UL}} = R^{\mathrm{UL}}_{\min,m}/\bar{L}$ and $\bar{\nu}_{\mathrm{DL}} = R^{\mathrm{DL}}_{\min,m}/\bar{L}$). Consequently, the uplink and downlink queues can be approximated by $M/D/\infty$ queues. The stationary distribution of such queues are given by

Algorithm 1: Sub-optimal balanced dynamic planning

for $\mathbf{X} \in \mathscr{X}$ **do**
  Downlink Feasibility Test
  Calculate $\hat{m}_s^{\mathrm{DL}}$ using $P_{\mathrm{tx},s} = P_{\max,s}$ and $R_m^{\mathrm{DL}} = R_{\min,m}^{\mathrm{DL}}$
  if $\hat{m}_s^{\mathrm{DL}} < M_s^{\mathrm{DL}}$ **then**
    Calculate $\nu_{s,\mathrm{DL}}(m_s^{\mathrm{DL}}, P_{\max,s})$
    if $\sum_{m_{\mathrm{DL}}=\hat{m}_s^{\mathrm{DL}}+1}^{M_s^{\mathrm{DL}}} q(m_{\mathrm{DL}}) \leq \varepsilon_{\mathrm{DL}}$ **then**
      $T_{\mathrm{DL}} = 1$
    else
      $T_{\mathrm{DL}} = 0$
    end if
  else
    $T_{\mathrm{DL}} = 1$
  end if
  Uplink Feasibility Test
  Calculate $\hat{m}_s^{\mathrm{UL}}$ using $P_{\mathrm{tx},m} = P_{\max,m}$ and $R_m^{\mathrm{UL}} = R_{\min,m}^{\mathrm{UL}}$
  if $\hat{m}_s^{\mathrm{UL}} < M_s^{\mathrm{UL}}$ **then**
    Calculate $\nu_{s,\mathrm{UL}}(m_s^{\mathrm{UL}}, P_{\max,m})$
    if $\sum_{m_{\mathrm{UL}}=\hat{m}_s^{\mathrm{UL}}+1}^{M_s^{\mathrm{UL}}} q(m_{\mathrm{UL}}) > \varepsilon_{\mathrm{UL}}$ **then**
      $T_{\mathrm{UL}} = 0$
    else
      Use (11.19) and (11.21) to calculate the call dropping probability for $P_{\mathrm{tx},m} = P_{\max,m}$ and $\hat{m}_s^{\mathrm{UL}}$
      if $P_D \leq \epsilon$ **then**
        $T_{\mathrm{UL}} = 1$
      else
        Calculate $\hat{P}_m$ that satisfies $R_m^{\mathrm{UL}} = R_{\min,m}^{\mathrm{UL}}$ for $m_s^{\mathrm{UL}} = \lfloor \hat{m}_s^{\mathrm{UL}} \rfloor$
        Use (11.19) and (11.21) to calculate the call dropping probability for $\hat{P}_m$ and $\hat{m}_s^{\mathrm{UL}}$
        if $P_D \leq \epsilon$ **then**
          $T_{\mathrm{UL}} = 1$
        else
          $T_{\mathrm{UL}} = 0$
        end if
      end if
    end if
  end if
  Calculate $\nu_{s,\mathrm{UL}}(m_s^{\mathrm{UL}}, P_{\max,m})$
  if $P_D \leq \epsilon$ **then**
    $T_{\mathrm{UL}} = 1$
  else
    Calculate $\hat{P}_m$ that satisfies $R_m^{\mathrm{UL}} = R_{\min,m}^{\mathrm{UL}}$ for $m_s^{\mathrm{UL}} = M_s^{\mathrm{UL}}$
    Calculate $\nu_{s,\mathrm{UL}}(M_s^{\mathrm{UL}}, \hat{P}_m)$
    if $P_D \leq \epsilon$ **then**
      $T_{\mathrm{UL}} = 1$
    else
      $T_{\mathrm{UL}} = 0$
    end if
  end if
  if $T_{\mathrm{DL}} = 1$ AND $T_{\mathrm{UL}} = 1$ **then**
    Calculate the total energy consumption of active BSs
    Save $\mathbf{X}$ in $\tilde{\mathscr{X}}$
  end if
end for
$\mathbf{X}^* = \arg \min_{X \in \tilde{\mathscr{X}}}$ Total energy consumption of active BSs

$$q(m) = \frac{(\eta\bar{\nu})^m \exp(-\eta\bar{\nu})}{m!}, \quad m \geq 0. \tag{11.27}$$

Define M_κ to be an upper bound on the number of mobile users in service (in the uplink or the downlink) such that

$$\sum_{m=0}^{M_\kappa} q(m) \geq \kappa. \tag{11.28}$$

The heuristic algorithm starts with only the macro BS active and all the small cells are assumed deactivated. The algorithm iteratively activates the small cells until uplink and downlink QoS are satisfied in an average sense.

In the uplink, when only the macro BS is activated, we first determine $\bar{p}$ using the Shannon's data rate formula for M_κ^{UL} and $R_{\min,m}^{\mathrm{UL}}$. If $\bar{p} \in [P_{\min}, P_{\max}]$, we check the condition on call dropping probability. The average energy required to complete the file upload is approximated as $\bar{p}/\bar{\nu}_{\mathrm{UL}}$. Then, the average call dropping probability in the uplink is approximated as

$$\bar{P}_D = 1 - \int_{\bar{p}/\bar{\nu}_{\mathrm{UL}}}^{E_{\max}} f_{E_m}(e_m) dE. \tag{11.29}$$

If either the minimum required throughput or the uplink call dropping probability threshold is not satisfied, the heuristic algorithm iteratively activates the small cells starting from the small cell with the largest $\rho_{k_s}^{\mathrm{UL}}$. We calculate for each BS, $\bar{p}_s$ using the Shannon's data rate formula for $\rho_{k_s}^{\mathrm{UL}} M_\kappa^{\mathrm{UL}}$ and $R_{\min,m}^{\mathrm{UL}}$. If $\bar{p}_s \in [P_{\min}, P_{\max}]$, the average uplink call dropping probability is calculated for each cell ($\bar{P}_{Ds}$) using (11.29) and the average uplink call dropping probability for the geographical region is determined as $\sum_s \rho_{k_s}^{\mathrm{UL}} \bar{P}_{Ds}$. At each iteration, one small cell is activated until all QoS conditions are satisfied.

In the downlink, we first use the combination of small cells activated according to the uplink test. We ensure that $\rho_{k_s}^{\mathrm{DL}} M_\kappa^{\mathrm{DL}}$ mobile users can satisfy their minimum required throughput $R_{\min,m}^{\mathrm{DL}}$ when the BS transmits with its maximum transmission power. If this condition is not satisfied, we iteratively activate additional small cells starting from the small cell with maximum $\rho_{k_s}^{\mathrm{DL}}$ until all conditions are satisfied. The proposed heuristic algorithm is summarized in Algorithm 2, which decides at the beginning of each slow timescale slot if a given BS should be activated or switched off. The algorithm presents a worst case computational complexity of $O(S)$, which represents a polynomial time complexity.

Algorithm 2: Heuristic balanced dynamic planning

Determine M_{κ}^{UL} and M_{κ}^{DL} for a specific tolerance κ using (11.27) and (11.28)
Set $T_{\mathrm{UL}} = 0$ and $T_{\mathrm{DL}} = 0$
Activate only the macro-cell and deactivate all small cells
Determine $\bar{p}$ and $\bar{P}_D$
if $\bar{p} \in [P_{\min}, P_{\max}]$ AND $\bar{P}_D \leq \epsilon$ **then**
  $T_{\mathrm{UL}} = 1$
end if
Define ρ_{UL} as a descending order of $\rho_{k_s}^{\mathrm{UL}}$, $\forall s \in \mathscr{S}$
while $T_{\mathrm{UL}} = 0$ **do**
  Set $x_s = 1$ for $s = \arg\max \rho_{\mathrm{UL}}$ and update $\mathbf{X}$
  Update ρ_{UL} to exclude the activated small cell
  Determine $\bar{p}_s$ and $\bar{P}_D$
  if $\bar{p} \in [P_{\min}, P_{\max}]$ AND $\bar{P}_D \leq \epsilon$ **then**
    $T_{\mathrm{UL}} = 1$
  end if
end while
Define ρ_{Dl} as a descending order of $\rho_{k_s}^{\mathrm{DL}}$, $\forall s \in \mathscr{S}$
while $T_{\mathrm{DL}} = 0$ **do**
  Calculate R_m^{DL} given $\rho_{k_s}^{\mathrm{DL}} M_{\kappa}^{\mathrm{DL}}$ mobile users and BS maximum transmission power
  if $R_m^{\mathrm{DL}} \geq R_{\min,m}^{\mathrm{DL}}$ **then**
    $T_{\mathrm{DL}} = 1$
  else
    Set $x_s = 1$ for $s = \arg\max \rho_{\mathrm{DL}}$ and update $\mathbf{X}$
    Update ρ_{DL} to exclude the activated small cell
  end if
end while

11.4.4 Performance Evaluation

In this section, we present simulation results for the optimal balanced dynamic planning framework (using (11.26)), feasibility test-based framework (using Algorithm 1), heuristic framework (using Algorithm 2), and the traditional unbalanced approach (which accounts only for the downlink QoS in determining the BS switching decision) that resembles the state-of-the-art research efforts. Three simulation scenarios are investigated. The first scenario considers a macro BS that presents overlapping coverage with one pico BS. In this scenario, we compare the performance of the optimal framework, the feasibility test-based framework, and the heuristic approach with the traditional dynamic planning approach. The second scenario considers a macro BS that presents overlapping coverage with two pico BSs. Due to the high computational complexity, only the performances of the feasibility test-based framework and the heuristic approach are compared with the traditional dynamic planning approach. In the last simulation scenario, we consider an overlapping coverage between one macro BS and 50 pico-cells that represent a dense small cell-on-edge deployment. Due to the extensive computation complexity, only the proposed heuristic approach is compared with the traditional

Table 11.3 Simulation parameters

Parameter	Value	Parameter	Value	Parameter	Value	Parameter	Value
$B_0^{\mathrm{UL/DL}}$	10 MHz	$B_{1,2}^{\mathrm{UL/DL}}$	5 MHz	$M_0^{\mathrm{UL/DL}}$	10	$M_{1,2}^{\mathrm{UL/DL}}$	5
D_1	110 m	D_2	130 m	H_0	100 m	$H_{1,2}$	50 m
C_1	18.7	C_2	46.8	C_3	20	N_0	−174 dBm/Hz
ω	5 min	Δ_0	4.7	$\Delta_{1,2}$	2.6	$P_{\mathrm{F},0}$	390 W
$P_{\mathrm{F},1,2}$	120 W	$P_{\mathrm{L},0}$	75 W	$P_{\mathrm{L},1,2}$	39 W	$P_{\max,0}$	23.4 W
$P_{\max,1,2}$	3.1 W	$P_{\min,0,1,2}$	0	$V_{0,1,2}$	5	μ_m	0.05 W
β_m	10^{-10} W/bps	$P_{\min,m}$	0	$P_{\max,m}$	0.1 W	V_m	5
$\bar{L}_m$	2 Gbits	a_m	6	ϵ	0.1	$E_{\min}$	10 J
$E_{\max}$	250 J	$R_{\min,m}^{\mathrm{DL}}$	15 Mbps	$R_{\min,m}^{\mathrm{UL}}$	6 Mbps	τ	1 h

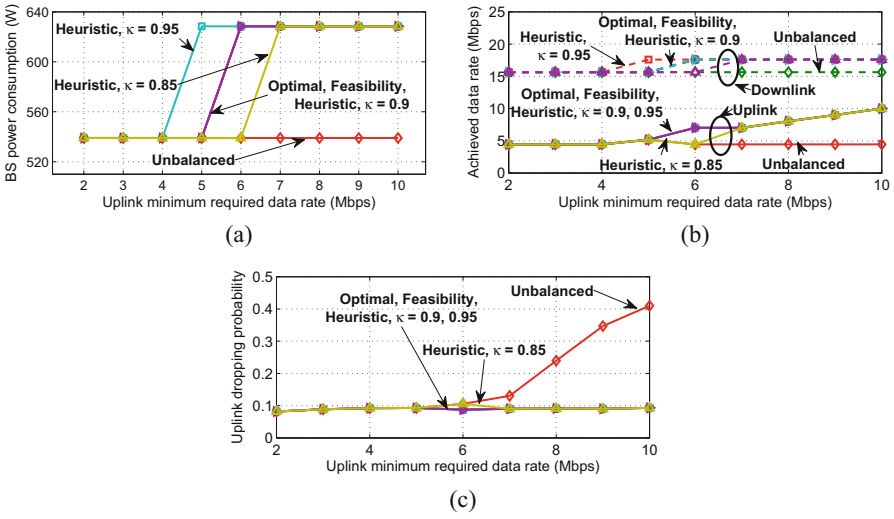

Fig. 11.5 Performance of dynamic planning for the first simulation scenario [7]. (**a**) BS power consumption vs. $R_{\min,m}^{\mathrm{UL}}$. (**b**) Achieved data rate vs. $R_{\min,m}^{\mathrm{UL}}$. (**c**) Uplink call dropping vs. $R_{\min,m}^{\mathrm{UL}}$

dynamic planning approach. Simulation parameters are adopted from [30, 34] and summarized in Table 11.3 unless otherwise stated. The low energy level at the MTs represents a night time scenario which is practical for BS switching-off.

In Fig. 11.5, the following parameters are assumed: $\eta_{\mathrm{UL}} = 0.6$, $\eta_{\mathrm{DL}} = 0.6$, $\rho_{k_1}^{\mathrm{UL}} = 0.6$, and $\rho_{k_1}^{\mathrm{DL}} = 0.3$. In Fig. 11.5a, the unbalanced approach activates only the macro BS, and hence, leads to the minimum BS energy consumption as compared with the balanced approach that activates both the macro and pico BSs whenever the uplink QoS is violated. As shown in figure, the resulting switching decision for the feasibility test-based framework matches the decision for the optimal framework. In addition, by varying κ, the heuristic approach can either be less conservative or more conservative depending on the choice of κ. As the value of κ increases, the heuristic algorithm accounts for the presence of more number of mobile users in the

uplink and downlink, and hence, it is more inclined towards the activation of the pico BS. While Fig. 11.5a suggests that the unbalanced dynamic planning approach is more energy efficient than the balanced dynamic planning framework, this is not true when the uplink QoS is considered. Figure 11.5b plots the achieved data rate for the different dynamic planning approaches. As shown in figure, the unbalanced dynamic planning approach fails to satisfy the target uplink throughput for high values of $R^{\mathrm{UL}}_{\mathrm{min},m}$. This is mainly because it activates only the macro BS which faces high uplink traffic demand that cannot be satisfied for all the mobile users as $R^{\mathrm{UL}}_{\mathrm{min},m}$ increases. On the other hand, the balanced dynamic planning approaches satisfy the target $R^{\mathrm{UL}}_{\mathrm{min},m}$ by activating the pico-cell and associating some mobile users to it. For the heuristic dynamic planning approach with smaller values of κ, the minimum required uplink throughput can be violated for some values of $R^{\mathrm{UL}}_{\mathrm{min},m}$, as the heuristic planning algorithm accounts for the presence of less number of users. However, for larger values of κ, the uplink minimum required throughput will always be satisfied. All the dynamic planning algorithms can satisfy the minimum required throughput in the downlink, as shown in figure. In addition, the unbalanced dynamic planning approach cannot satisfy the target threshold on uplink call dropping probability for large values of $R^{\mathrm{UL}}_{\mathrm{min},m}$ due to the associated high target trapping energy and the limited available transmission power, as shown in Fig. 11.5c. On the other hand, the balanced dynamic planning approaches activate the pico BS, and hence, mobile users in proximity of the small cell can enjoy a minimum transmission distance, and hence, can satisfy the target trapping energy with low transmission power. This signifies the trade-off between energy saving for network operator and uplink service quality guarantee.

In Fig. 11.6, the following simulation set-up is adopted. The minimum required data rate in the uplink is 5 Mbps, $\eta_{\mathrm{UL}} = \eta_{\mathrm{DL}} = 0.6$, $\rho^{\mathrm{DL}}_{k_0} = 0.7$, $\rho^{\mathrm{DL}}_{k_1} = 0.2$, $\rho^{\mathrm{UL}}_{k_0} = 0.4$, and $\epsilon = 0.07$. As shown in Fig. 11.6a, the balanced dynamic planning approach always activates the macro and one pico BS, which presents a total power consumption of 630 W. When uplink mobile users are concentrated more around the second pico BS $\rho^{\mathrm{UL}}_{k_1} \leq 0.3$, the balanced planning approach chooses to activate the second pico BS and switch off the first pico BS (switching decision 3). As more users are concentrated around the first pico BS, the balanced dynamic planning approach chooses to activate the first pico BS and switch off the second pico BS (switching decision 2). The unbalanced dynamic planning approach activates only the macro BS and deactivates both pico BSs resulting in a minimum power consumption of 540 W, however, it fails to satisfy the uplink QoS. As shown in Fig. 11.6b, both uplink and downlink required throughput are satisfied for all planning algorithms. For the feasibility test-based algorithm uplink throughput, as more users are concentrated around the first pico BS, activating the second pico BS presents a longer transmission distance which reduces the achieved throughput in the range $\rho^{\mathrm{UL}}_{k_1} \in [0.1, 0.3]$. Switching off the second pico BS and activating the first one presents a lower transmission distance which leads to an improved throughput in the range $\rho^{\mathrm{UL}}_{k_1} \in [0.3, 0.5]$. For $\rho^{\mathrm{UL}}_{k_1} \geq 0.5$, more users are concentrated around the pico BS and compete over the limited available bandwidth which results in the

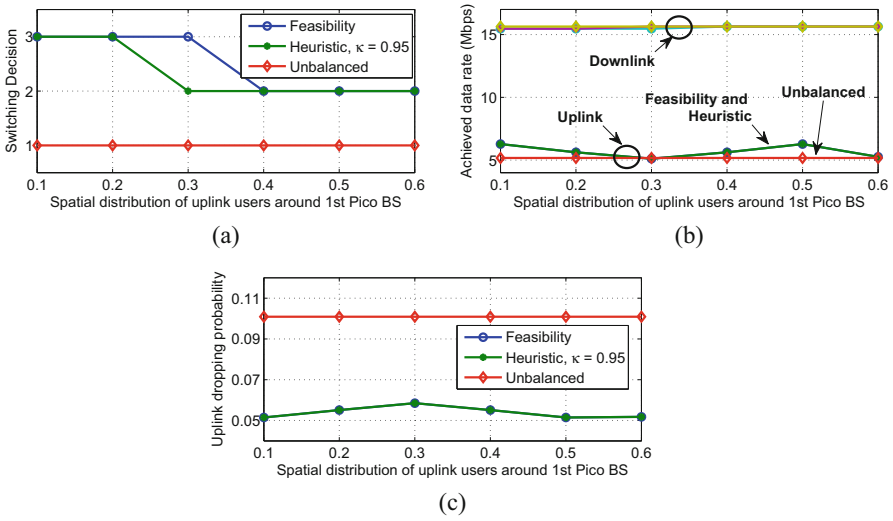

Fig. 11.6 Performance of dynamic planning for the second simulation scenario [7]. (**a**) Switching decision vs. $\rho_{k_1}^{\mathrm{UL}}$. (**b**) Achieved data rate vs. $\rho_{k_1}^{\mathrm{UL}}$. (**c**) Uplink call dropping vs. $\rho_{k_1}^{\mathrm{UL}}$

reduced throughput. While the unbalanced dynamic planning approach can satisfy the target uplink and downlink throughput, it cannot satisfy the target call dropping probability, as shown in Fig. 11.6c, unlike the balanced dynamic planning approach. The behavior of the uplink call dropping probability for the sub-optimal algorithms follows the same argument made for the uplink throughput.

In Fig. 11.7a, the minimum required data rate in the uplink is 10 Mbps, $\eta_{\mathrm{DL}} = 0.6$, $\rho_{k_0}^{\mathrm{DL}} = 0.7$, $\rho_{k_0}^{\mathrm{UL}} = 0.4$, $\rho_{k_s}^{\mathrm{UL}}$ and $\rho_{k_s}^{\mathrm{DL}}$ are uniformly distributed among the pico-cells. In Fig. 11.7a, the switching decisions are shown for the heuristic planning approach, where the red cross indicates an inactive pico-cell, while the green circle denotes an active pico-cell, while the unbalanced approach activates only the macro BS. As η_{UL} increases, the geographical region experiences an increasing number of mobile users, which are more concentrated around the cell edge since $\rho_{k_0}^{\mathrm{UL}} = 0.4$. As a result, the heuristic algorithm activates more pico-cells to serve the increasing number of uplink mobile users who compete over the available radio resources to satisfy their minimum required QoS. This in turn results in increased BS power consumption as shown in Fig. 11.7b, unlike the unbalanced approach which presents the minimum power consumption of 540 W. Both balanced and unbalanced approaches satisfy the target call dropping threshold. However, only the heuristic algorithm can support the increasing uplink traffic demand and satisfies the minimum required throughput, unlike the unbalanced approach which suffers from a decreasing achieved uplink throughput with the increasing number of uplink mobile users (see Fig. 11.7c).

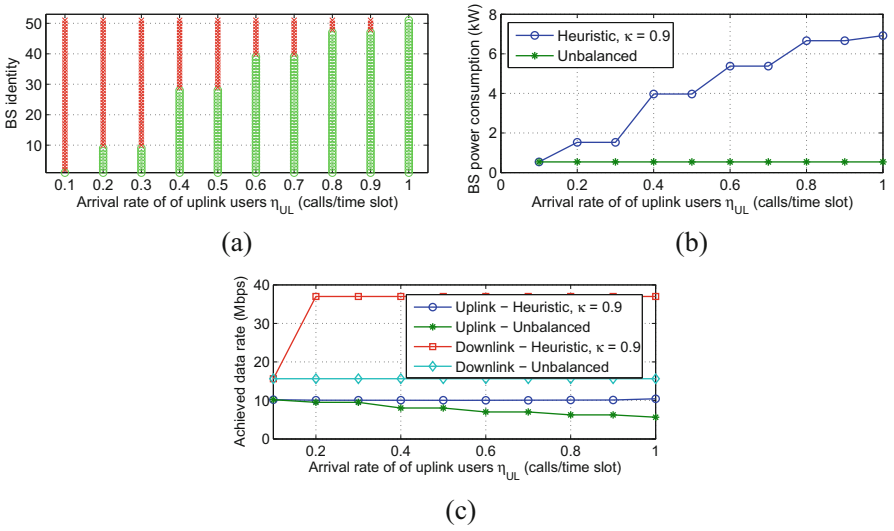

Fig. 11.7 Performance of dynamic planning for the third simulation scenario [7]. (**a**) Switching decision vs. η_{UL}. (**b**) BS power consumption vs. η_{UL}. (**c**) Achieved data rate vs. η_{UL}

Discussion *Gains:* In Fig. 11.7a, b, based on the uplink call arrival rate, only 1 BS can be switched off when $\eta_{\mathrm{UL}} = 0.1$ and 49 pico BSs can be switched off, which presents an energy saving of 92.8% compared with an all active state (which keeps all BSs active). When the call arrival rate increases to 0.3, an energy saving of 75.7% can be achieved. At a half load state (i.e., call arrival rate of 0.5), the balanced approach still can achieve an energy saving of 42.8%. *Trade-offs:* From Fig. 11.7b, while the unbalanced approach can save 92.8% of energy compared with the all active state for the entire range of η_{UL}, it violates the uplink required throughput as in Fig. 11.7c. Although the unbalanced approach achieves more energy saving compared with the balanced approach, the latter one always satisfies the uplink service quality, which demonstrates the trade-off between energy saving and uplink QoS guarantee. The same arguments hold for the gains and trade-offs for Figs. 11.5 and 11.6.

11.5 Conclusions

This chapter presents a balanced dynamic planning approach that can save energy for the network operators by switching off lightly loaded BSs while satisfying the user required QoS in the uplink and downlink. First, we have quantified the impact of dynamic planning on the service quality of mobile users in the uplink and downlink. For uplink mobile users, the QoS is measured in terms of the minimum required throughput and call dropping probability due to MT battery depletion. For

downlink mobile users, the QoS is measured in terms of the minimum required throughput. Then, the balanced dynamic planning problem is formulated as a two-timescale problem that decouples the BS operation (on–off switching) and MT association into two separate timescales. Due to computational complexity, we have presented a sub-optimal dynamic planning framework based on the analysis of the decision problem behavior. In addition, we have proposed a less complex tunable heuristic dynamic planning algorithm (with tuning parameter κ). The selection of κ can lead to a performance that ranges from the unbalanced approach performance which overlooks the uplink QoS requirement for small values of κ, and as κ increases the performance of the heuristic algorithm gets closer to the performance of the optimal and sub-optimal algorithms. Simulation results have indicated that the balanced dynamic planning framework can save energy for network operators while ensuring a target QoS for mobile users both in the uplink and downlink, unlike the unbalanced dynamic planning approach. Future extension of this work will investigate balanced dynamic planning when the BS is powered via energy harvesting.

Acknowledgements This publication was made possible by NPRP grant # NPRP 9-055-2-022 from the Qatar National Research Fund (a member of Qatar Foundation). The statements made herein are solely the responsibility of the authors.

References

1. S. Mclaughlin, P.M. Grant, J.S. Thompson, H. Haas, Techniques for improving cellular radio base station energy efficiency. IEEE Wirel. Commun. **18**(5), 10–17 (2011)
2. M. Ismail, W. Zhuang, Network cooperation for energy saving in green radio communications. IEEE Wirel. Commun. **18**(5), 76–81 (2011)
3. K. Pentikousis, In search of energy-efficient mobile networking. IEEE Commun. Mag. **48**(1), 95–103 (2010)
4. L. Budzisz et al., Dynamic resource provisioning for energy efficiency in wireless access networks: a survey and an outlook. IEEE Commun. Surv. Tutorials **16**(4) 2259–2285 (2014)
5. M. Ismail, W. Zhuang, Green radio communications in a heterogeneous wireless medium. IEEE Wirel. Commun. **21**(3), 128–135 (2014)
6. M. Ismail, M. Shakir, K. Qaraqe, E. Serpedin, *Green Heterogeneous Wireless Networks* (Wiley-IEEE Press, Hoboken, 2016)
7. M. Kashef, M. Ismail, E. Serpedin, K. Qaraqe, Balanced dynamic planning in green heterogeneous cellular networks. IEEE J. Sel. Areas Commun. **34**(12), 3299–3312 (2016)
8. M. Kashef, M. Ismail, E. Serpedin, K. Qaraqe, On balancing energy efficiency for network operators and mobile users in dynamic planning. IEEE Commun. Mag. **53**(11), 158–165 (2015)
9. M. Kashef, M. Ismail, E. Serpedin, K. Qaraqe, Impact of dynamic planning on uplink service quality in heterogeneous cellular networks, in *IEEE Vehicular Technology Conference (VTC)-Fall, 1–5, September* (2016)
10. E. Oh, B. Krishnamachari, X. Liu, Z. Niu, Toward dynamic energy-efficient operation of cellular network infrastructure. IEEE Commun. Mag. **49**(6), 56–61 (2011)
11. K. Son, H. Kim, Y. Yi, B. Krishnamachari, Base station operation and user association mechanisms for energy-delay tradeoffs in green cellular networks. IEEE J. Sel. Areas Commun. **29**(8), 1525–1536 (2011)

12. S. Gamboa, A. Pelov, P. Maille, X. Lagrange, N. Montavont, Reducing the energy footprint of cellular networks with delay-tolerant users. IEEE Syst. J. (2015, to appear)
13. J. Wu, Y. Bao, G. Miao, S. Zhou, Z. Niu, Base station sleeping control and power matching for energy-delay tradeoffs with bursty traffic. IEEE Trans. Veh. Technol. **65**(5), 3657–3675 (2016)
14. T. Han, N. Ansari, On greening cellular networks via multicell cooperation. IEEE Wirel. Commun. **20**(1), 82–89 (2013)
15. E. Oh, K. Son, B. Krishnamachari, Dynamic base station switching-on/off strategies for green cellular networks. IEEE Trans. Wirel. Commun. **12**(5), 2126–2136 (2013)
16. C.Y. Chang, W. Liao, H.Y. Hsieh, D.S. Shiu, On optimal cell activation for coverage preservation in green cellular networks. IEEE Trans. Mob. Comput. **13**(11), 2580–2591 (2014)
17. C. Liu, B. Natarajan, H. Xia, Small cell base station sleep strategies for energy efficiency. IEEE Trans. Veh. Technol. **65**(3), 1652–1661 (2016)
18. Z. Niu, Y. Wu, J. Gong, Z. Yang, Cell zooming for cost-efficient green cellular networks. IEEE Commun. Mag. **48**(11), 74–79 (2010)
19. T. Han, N. Ansari, On optimizing green energy utilization for cellular networks with hybrid energy supplies. IEEE Trans. Wirel. Commun. **12**(8), 3872–3882 (2013)
20. N. Saxena, B.J.R. Sahu, Y.S. Han, Traffic-aware energy optimization in green LTE cellular systems. IEEE Commun. Lett. **18**(1), 38–41 (2014)
21. J. Wu, S. Zhou, Z. Niu, Traffic-aware base station sleeping control and power matching for energy-delay tradeoffs in green cellular networks. IEEE Trans. Wirel. Commun. **12**(8), 4196–4209 (2013)
22. Z. Niu, X. Guo, S. Zhou, P.R. Kumar, Characterizing energy-delay tradeoff in hyper-cellular networks with base station sleeping control. IEEE J. Sel. Areas Commun. **33**(4), 641–650 (2015)
23. J.B. Seo, Rewarded access to a sleeping base station. IEEE Commun. Lett. **19**(9), 1612–1615 (2015)
24. L. Saker, S.E. Alayoubi, R. Combes, T. Chahed, Optimal control of wake up mechanisms of femtocells in heterogeneous networks. IEEE J. Sel. Areas Commun. **30**(3), 664–672 (2012)
25. S. Navaratnarajah, A. Saeed, M. Dianati, M.A. Imran, Energy efficiency in heterogeneous wireless access networks. IEEE Wirel. Commun. **20**(5), 37–43 (2013)
26. A. Conte et al., Cell wilting and blossoming for energy efficiency. IEEE Wirel. Commun. **18**(5), 50–57 (2011)
27. M.Z. Shaker, K.A. Qaraqe, M.S. Alouini, E. Serpedin, M.A. Imran, Green heterogeneous small-cell networks: toward reducing the CO2 emissions of mobile communications industry using uplink power adaptation. IEEE Wirel. Commun. **51**(6), 52–61 (2013)
28. G. Huang, J. Li, Interference mitigation for femtocell networks via adaptive frequency reuse. IEEE Trans. Veh. Technol. **65**(4), 2413–2423 (2016)
29. P. Liu, X. Wang, J. Li, Uplink co-tier interference management in femtocell networks with successive group decoding. IEEE Trans. Commun. **14**(9), 4797–4809 (2015)
30. W. Song, Y. Cheng, W. Zhuang, Improving voice and data services in cellular/WLAN integrated network by admission control. IEEE Trans. Wirel. Commun. **6**(11), 4025–4037 (2007)
31. Y. Zhuang, Y. Luo, L. Cai, J. Pan, A geometric probability model for capacity analysis and interference estimation in wireless mobile cellular systems, in *IEEE Global Telecommunications Conference (GLOBECOM)* (2011), pp. 1–6
32. B. Chandrasekaran, Survey of network traffic models (2006). http://www.cs.wustl.edu/~jain/cse56706/ftp/traffic_models3/index.html
33. V. Goswami, U.C. Gupta, Analyzing the discrete-time multiserver queue Geom/Geom/m queue with late and early arrivals. Inf. Manag. Sci. **9**(2), 55–66 (1998)
34. G. Auer, V. Giannini, C. Desset, I. Godor, How much energy is needed to run a wireless network? IEEE Wirel. Commun. **18**(5), 40–49 (2011)
35. W. Wiesemann, D. Kuhn, B. Rustem, Robust Markov decision processes. Math. Oper. Res. **38**(1), 153–183 (2013)

36. C. Isheden, G.P. Fettweis, Energy-efficient multi-carrier link adaptation with sum rate-dependent circuit power, in *IEEE Global Telecommunications Conference (GLOBECOM)* (2010), pp. 1–6
37. D. Ferreira, A.K. Dey, V. Kostakos, Understanding human-smartphone concerns: a study of battery life. Pervasive Comput. **6696**, 19–33 (2011)
38. R. Litjens, H. van den Berg, R.J. Boucherie, Throughputs in processor sharing models for integrated stream and elastic traffic, in *MobiHeld*, vol. 65, no. 2 (ACM, New York, 2008), pp. 152–180
39. E. Altman, *Constrained Markov Decision Processes* (Chapman & Hall/CRC, Boca Raton, 1999)
40. C.W. Tan, Optimal power control in Rayleigh fading heterogeneous wireless networks. IEEE/ACM Trans. Networking **24**(2), 940–953 (2016)
41. M. Monemi, M. Rasti, E. Hossain, Low-complexity SINR feasibility checking and joint power and admission control in prioritized multi-tier cellular networks. IEEE Trans. Wirel. Commun. **15**(3), 2421–2434 (2016)
42. A. Zappone et al., Energy-efficient power control: a look at 5G wireless technologies. IEEE Trans. Signal Process. **64**(7), 1668–1683 (2016)
43. C. Yang, J. Li, A. Anpalagan, M. Guizani, Joint power coordination for spectral-and-energy efficiency in heterogeneous small cell networks: a bargaining game-theoretic perspective. IEEE Trans. Wirel. Commun. **15**(2), 1364–1376 (2016)

Index

A
AF. *See* Amplify-and-forward (AF)
Age of information, xxviii, 254–255
Amplify-and-forward (AF), 13, 123–125, 132–139, 147, 152, 270

B
Beamforming, xxvii, xxviii, 12, 18–20, 31, 33, 34, 41, 44–48, 52, 66, 67, 69, 70, 75, 78, 82, 84, 85, 93, 97, 102–109, 111, 112, 114–118, 169, 193, 210, 216, 219–220, 226, 253
Beamforming optimization, 38–43, 45
BS on-off switching, 322, 323, 325, 354

C
Cognitive network, 5, 21, 195, 226, 271, 281
Cognitive radios (CRs), 5, 30, 95, 195, 199, 225–226, 271, 281
Constructive interference, xxvii, 12, 68, 87–119
Cooperative communications, 10, 11
Cooperative relay communications, 11
Cooperative relaying, 270, 271
Cooperative spectrum sharing (CSS), xxix, 270–272, 281, 282, 293
CRs. *See* Cognitive radios (CRs)
CSS. *See* Cooperative spectrum sharing (CSS)

D
Decode and forward (DF), 20, 21, 43, 123–132, 272
Delay analysis, 255–265
DF. *See* Decode and forward (DF)
Dynamic planning, xxix, 321–354

E
EH. *See* Energy harvesting (EH)
Energy costs of sensing and transmission., 254–265
Energy efficiency, xxvi, xxviii, xxix, 3, 8, 18, 19, 32, 88, 153, 158, 172–173, 177, 183, 272, 322, 324, 326–327
Energy harvesting (EH), xxv, xxvi, xxvii, xxviii, xxix, 5–13, 15–22, 30–33, 44, 45, 47, 51, 55, 57–60, 65–68, 70, 78, 85, 114–116, 123–153, 157–183, 189–227, 240–249, 251, 253–257, 260, 269–293, 297, 329, 354
Error rate, 125

F
5G and beyond, xxv, xxvii, xxix, 4, 14, 19–22, 24, 30, 32, 43, 113, 269
5G communications, 4, 14, 20, 22

G
Green networking, 321–354

H
Heterogeneous networks, xxix, 321–354

D.N.K. Jayakody et al. (eds.), *Wireless Information and Power Transfer: A New Paradigm for Green Communications*, DOI 10.1007/978-3-319-56669-6

I
Interference, xxvi, xxvii, 11, 12, 18, 20, 51, 53, 58, 67, 68, 70, 71, 73, 76, 80, 84, 87–119, 125–133, 135, 153, 174, 212, 223, 225, 271, 272, 275, 281, 297, 324, 326, 329
Interference exploitation, xxvii, 16, 58, 88, 95, 96, 100, 103–114, 117, 118
Internet of Things (IoT), 3, 5, 14, 15, 17, 21, 33, 65, 157, 160, 223, 227, 240, 242, 248, 254, 269

M
Massive MIMO, 6, 19, 20, 85
Millimeter wave (mm wave) communications, 14–15
Molecular communication, 172–174, 178–181, 183
Multi-objective optimization (MOO), xxvii, 5, 65–85
Multi-scale, xxviii, 157–183

O
Outage probability, 49–52, 125, 134, 256, 275–281, 289–293, 297

P
Performance analysis, xxvii, 13, 47–53, 133, 162, 195, 247–248, 253–254, 272–278, 282–288, 390–391
Precoding, 12, 13, 55–58, 95–103, 107, 109, 111–114

R
Radiofrequency identification (RFID), 11, 159, 192, 199, 210–216, 225
Relay and multiple-input-multiple-output (MIMO), 5, 6, 8–11, 13, 17, 19–21, 33–35, 41, 43–46, 49, 52, 53, 59, 67, 85, 110, 123, 125, 126, 129, 132, 133, 138–141, 146–151, 153, 159, 169, 180, 183, 251, 270–272, 283, 289
Relaying, xxvii, 8–11, 17, 20, 33, 47, 123–153, 169, 182, 251, 270, 271
Resource allocation, xxvii, 10, 18, 19, 31, 34, 65–85, 109–114, 219, 250, 252, 336
RFEH. *See* RF energy harvesting (RFEH)
RF energy harvesting, xxv, xxvi, xxviii, 5, 10, 17, 158, 160, 161, 169, 181, 189–227, 252, 253, 270, 271
RF energy harvesting (RFEH), 4, 6–8, 11, 12, 16–19, 24, 158, 160, 161, 169, 189–227, 253, 270, 271
RFID. *See* Radiofrequency identification (RFID)
RF wireless power transfer, 214

S
Satellite communications, 22–23, 193
Simultaneous wireless information and power transfer (SWIPT), xxv, xxvi, xxvii, xxviii, 4–16, 18–24, 31–35, 59, 65–85, 115–119, 158, 169, 173, 217, 219, 220, 226, 251–253
Small-cell network, xxvii, 30, 65–85, 162
Stochastic geometry, 125, 161, 170, 181, 195
Supercapacitors, 203, 204, 206–209, 214, 222
SWIPT. *See* Simultaneous wireless information and power transfer (SWIPT)
Symbol-level precoding, 12–13

T
Throughput, xxvi, 10, 21, 22, 30, 33, 35, 43, 47–50, 52, 53, 59, 60, 67, 68, 124, 125, 127–131, 133, 135–138, 141–143, 153, 247, 251, 253, 254, 272, 322, 326, 327, 331, 333–336, 341, 342, 346, 348, 351–354
Time switching (TS), 8, 15, 20, 32, 66–75, 84, 115, 124, 203, 218, 219, 251, 271, 272, 282, 283

U
Update age, xxviii, 254, 255, 258–263, 265
Update cycle, xxviii, 254, 255, 258–265

W
Wireless energy harvesting (WEH), xxvi, 6–7, 12, 15, 31
Wireless information and power transfer, xxv, xxvi, 3–24, 219
Wirelessly powered communications, 29–60
Wireless power, 5, 22, 31, 33, 59, 114, 115, 153, 189, 199, 214, 216, 217, 248
Wireless power transfer (WPT)
  charger configuration, 301–303, 305–307, 309–312, 317
  distributed algorithm, 296, 305, 306, 313, 317

power management, 296, 303–307, 313–317
power transfer models, 251–252, 295–318
wireless power networks, 7–8, 297, 301
Wireless sensor networks (WSN), xxvi, xxviii, 5–7, 15, 16, 65, 195, 206, 209, 210, 213, 214, 220, 223, 239–265, 269, 270, 282, 290–292, 295, 297, 298
Wireless sensor nodes, xxviii, 4, 15, 16, 226, 241, 242, 269–293
WSN. *See* Wireless sensor networks (WSN)